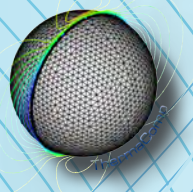

ThermaComp2014

Third International Conference on

COMPUTATIONAL METHODS FOR THERMAL PROBLEMS

JUNE
2-4, 2014
LAKE BLED,
SLOVENIA

Edited by
Božidar Šarler
Nicola Massarotti
Perumal Nithiarasu

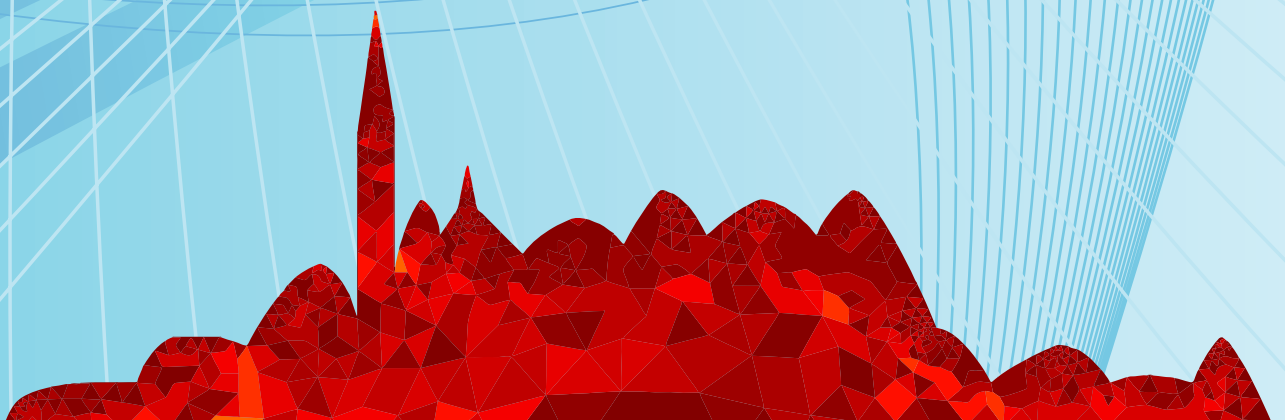

THERMACOMP2014

THIRD INTERNATIONAL CONFERENCE ON COMPUTATIONAL METHODS FOR THERMAL PROBLEMS

JUNE 2-4, 2014, LAKE BLED, SLOVENIA

EDITED BY:

BOŽIDAR ŠARLER
LABORATORY FOR MULTIPHASE PROCESSES
UNIVERSITY OF NOVA GORICA
NOVA GORICA, SLOVENIA
LABORATORY FOR SIMULATION OF MATERIALS AND PROCESSES
INSTITUTE OF METALS AND TECHNOLOGY
LJUBLJANA, SLOVENIA

NICOLA MASSAROTTI
DIPARTIMENTO DI INGEGNERIA
UNIVERSITÀ DEGLI STUDI DI NAPOLI "PARTHENOPE"
NAPOLI, ITALY

PERUMAL NITHIARASU
CIVIL AND COMPUTATIONAL ENGINEERING CENTRE
SCHOOL OF ENGINEERING, SWANSEA UNIVERSITY
SWANSEA, UNITED KINGDOM

WITH THE SUPPORT OF:
ALESSANDRO MAURO AND SIMONA DI FRAIA
UNIVERSITÀ DEGLI STUDI DI NAPOLI "PARTHENOPE"

3rd International Conference on Computational Methods for Thermal Problems, 2014, Lake Bled, Slovenia

Third Edition, June 2014

ISBN 978-88-7431-727-1

Publisher: Giannini Editore
Via Cisterna dell'Olio 6/b, 80134 Napoli
www.gianninispa.it

Finito di stampare nel mese maggio 2014
nelle Officine Grafiche Francesco Giannini & Figli SpA
di Napoli

PREFACE

It is our pleasure to welcome all participants of the *Third International Conference on Computational Methods for Thermal Problems* (THERMACOMP2014) to Lake Bled. Computational and mathematical methods have a profound impact on the understanding and advancement of engineering science and technology. When this series of Conferences was started in 2009, we thought that even though there were many conferences in the area of computational methods serving the community, a focused conference in the area of computational methods for thermal problems had been long overdue. This Conference aims to convene a diverse scientific audience of mathematicians, physicists and computational scientists that have a communal interest in modelling thermal problems. It is encouraging to learn that this conference represents an interdisciplinary forum of scientists with expertise ranging from heat conduction, convection and radiation to CFD and micro and nano heat transfer. We hope that the interaction between scientists during the conference leads to new topics of research, new collaborations, and possibly new friends.

THERMACOMP2014 consists of three plenary lectures, six keynote lectures, seven organized mini-symposia and seven parallel sessions. We are grateful to all invited speakers for accepting our invitation.

We would also like to take this opportunity to thank THERMACOMP2014 sponsors, mini-symposium organizers, executive and advisory committee members, as well as everyone who has been involved in the organization for their support.

Božidar Šarler
University of Nova Gorica
Institute of Metals and Technology
Slovenia

Nicola Massarotti
Università di Napoli Parthenope
Italy

Perumal Nithiarasu
Swansea University
United Kingdom

SPONSORS

UNIVERSITY OF NOVA GORICA

INSTITUTE OF METALS AND TECHNOLOGY

UNIVERSITÀ DEGLI STUDI DI NAPOLI "PARTHENOPE"

SWANSEA UNIVERSITY

SUPPORTING ORGANIZATIONS

DIPARTIMENTO DI INGEGNERIA

CONSORZIO DI RICERCA PER L'AMBIENTE, L'ENERGIA I VEICOLI E I BIOCOMBUSTIBILI

UNIVERSITÁ DEGLI STUDI DI CASSINO E DEL LAZIO MERIDIONALE

ZIENKIEWICZ FOUNDATION

COMMITTEES

HONORARY CHAIR
R.W. Lewis, Swansea University, UK

CO-CHAIRS
N. Massarotti, University of Naples "Parthenope", Italy
P. Nithiarasu, Swansea University, UK
B. Šarler, University of Nova Gorica & Institute of Metals and Technology, Slovenia

INTERNATIONAL EXECUTIVE COMMITTEE
P. Cheng, Shanghai Jiao Tong University, China
G. Comini, CISM, Italy
Y. Jaluria, Rutgers, The State University of New Jersey, USA
X. K. Li, Dalian University of Technology, China
V. Naso, Università di Napoli Federico II, Italy
K.N. Seetharamu,PES Institute of Technology, India
B. Sunden, Lund University, Sweden
K. Vafai, University of California, Riverside, USA

INTERNATIONAL ADVISORY COMMITTEE
F. Arpino, Università di Cassino, Italy
B.R. Baliga, McGill University, Canada
S.W. Baek, Korea Advanced Institute of Science & Technology, South Korea
G. Biswas, Indian Institute of Technology Kanpur, India
A. Carotenuto, Università di Napoli "Parthenope", Italy
A.J. Chamkha, Public Authority for Applied Education and Training, Kuwait
S. Chang, National University of Singapore, Singapore
F. Chinesta, Ecole Centrale de Nantes, France
R. Codina, Universitat Politècnica de Catalunya, Spain
H. Combeau, Ecole des Mines de Nancy, France
R.M. Cotta, Universidade Federal do Rio de Janeiro, Brazil
D. Drikakis, Cranfield University, UK
D. Givoli, Technion - Israel Institute of Technology, Israel
D. Gobin, CNRS, France
S. Idelsohn, International Center for Numerical Methods in Engineering, Spain
Y. Joshi, Georgia Institute of Technology, USA
A. Kassab, University of Central Florida, USA
M. Li, Taiyuan University of Technology, China
R. Lohner, George Mason University, USA
A.G. Malan, Council for Scientific and Industrial Research, South Africa
O. Manca, Seconda Università di Napoli, Italy
J.C. Mandal, Indian Institute of Technology Bombay, India
C. Meola, Università di Napoli Federico II, Italy
C. Nonino, Università di Udine, Italy
A.J. Nowak, Silesian Polytechnic University, Poland
J. Patterson, University of Sydney, Australia
I. Pop, University of Cluj, Romania
J. Reese, University of Strathclyde Glasgow, UK
W. Shyy, Hong Kong University of Science and Technology, Hong Kong
Siraj-ul-Islam, University of Engineering and Technology Peshawar, Pakistan
B. A. Schrefler, Università di Padova, Italy
V.R. Voller, University of Minnesota, USA
I. Vušanović, University of Montenegro, Montenegro
W. Wall, Technische Universität München, Germany

ORGANISING COMMITTEE
A.Z. Gustin, Institute of Metals and Technology, Slovenia
A. Mauro, University of Napoli "Parthenope", Italy
E. Sincich, University of Nova Gorica, Slovenia

CONTENTS

PLENARY LECTURES

KEYNOTE LECTURES

MINI-SYMPOSIA

HEAT TRANSFER IN FOAMS AND NANOFLUIDS

MINI-SYMPOSIUM ORGANISED BY N. BIANCO AND S. NARDINI

MODELLING & APPLICATIONS OF BIOHEAT & MASS TRANSFER

MINI-SYMPOSIUM ORGANISED BY P. NITHIARASU AND E. BOILEAU

MULTI-STREAM HEAT EXCHANGERS

MINI-SYMPOSIUM ORGANISED BY K.N. SEETHARAMU, V. KRISHNA, K.H. JYOTHIPRAKASH AND C. RANGANAYAKULU

PARALLEL SESSIONS

CONDUCTION, CONVECTION AND RADIATION

REACTIVE HEAT AND MASS TRANSPORT

HEAT AND MASS TRANSFER IN POROUS MEDIA

NUMERICAL METHODS

MICRO- AND NANO- HEAT TRANSPORT

PLENARY LECTURES

Third International Conference on Computational Methods for Thermal Problems
THERMACOMP2014, June2-4, 2014, Lake Bled, Slovenia
N. Massarotti, P.Nithiarasuand B. Sarler(Eds.)

UNIFIED INTEGRAL TRANSFORMS IN CONJUGATED HEAT AND FLUID FLOW

***Renato M. Cotta, [+]Diego C. Knupp, and Carolina P. Naveira-Cotta**
Federal University of Rio de Janeiro, UFRJ
Laboratory of Transmission and Technology of Heat - LTTC
Department of Mechanical Engineering, POLI/COPPE, Rio de Janeiro, Caixa Postal 68503,
Cidade Universitária, 21941-972, Brazil
[+]Dept. of Mechanical Eng. and Energy, Instituto Politécnico, IPRJ/UERJ, Nova Friburgo, RJ, Brazil

([*]Corresponding author: cotta@mecanica.coppe.ufrj.br)

ABSTRACT

The present lecture reviews recent developments on the Generalized Integral Transform Technique (GITT) in the analysis of internal and external conjugated heat transfer problems, by combining this hybrid numerical-analytical approach with a reformulation strategy into a single domain that envelopes all of the physical and geometric sub-regions in the original problem. Space variable coefficients and source terms with abrupt transitions between the various sub-regions interfaces are then defined and incorporated into this single domain representation for the governing convection-diffusion equations of the conjugated heat and fluid flow problem. Eigenfunction expansions are then proposed based on eigenvalue problems that carry along the information on the space variable coefficients of the reformulated spatial operators. Such differential eigenvalue problems are then integral transformed to yield algebraic eigensystems that are computationally solved through reliable and readily available solvers. The same idea is employed in solving both the fluid flow and the conjugated heat transfer problems, including the direct integral transformation of irregular regions. An application is considered more closely to illustrate this straightforward and robust hybrid solution path, for a multi-stream micro-heat exchanger.

Key Words: *Conjugated Heat Transfer, Single Domain Formulation, Forced Convection, Hybrid Methods, Integral Transforms, Micro-heat exchangers.*

1. INTRODUCTION

The method of integral transforms for solving partial differential equations dates back to Fourier´s classical treatise on heat conduction first published in 1822 [1], and has been widely used and developed since then in the analytical solution of linear heat and mass diffusion problems [2-7]. It is essentially based on the proposition of eigenfunction expansions, associated with the eigenvalue problems that naturally appear after application of the method of separation of variables to the homogeneous versions of the originally posed problems. The integral transformation process is in general applied to all but one independent variable, then in such transformable cases, yields a decoupled linear system of ordinary differential equations for the transformed potentials, for which analytical solutions can be readily obtained. Only in the 80´sand 90´sthis classical approach gained a hybrid numerical-analytical structure, known as the Generalized Integral Transform Technique (GITT) [8-21], for overcoming the barrier of handling a priori non-transformable problems, including some wide classes of problems of interest in heat and fluid flow, such as nonlinear diffusion problems, irregular geometries, moving boundaries, boundary layer equations, Navier-Stokes equations, etc, as later on consolidated in [22]. In the hybrid approach, the concept is to alleviate the need for obtaining the exact integral transformation, and thus accepting the derivation of a coupled system of transformed ordinary differential equations from a chosen auxiliary eigenvalue problem, which is then either analytically or numerically handled to provide error

controlled robust solutions to the original potentials, after the inverse formulae from the eigenfunction expansions are recalled to reconstruct the solution. The integral transforms method provides an alternative for benchmarking purposes in such cases when exact solutions are not obtainable by the classical analytical methods. It may also be an alternative to purely numerical solutions, not only for analytically oriented users, when combined with symbolic computation platforms for reducing the derivation effort. In this context, an open source unified integral transforms code named **UNIT** (**UN**ified **I**ntegral **T**ransforms) [23-25], was recently constructed in the *Mathematica* system (v.7 and above), which provides a development platform for applying the GITT in multidimensional nonlinear convection-diffusion problems.

Among other challenging extensions, the analysis of complex physical and geometrical configurations such as in conjugated heat transfer problems with irregular domains, have been also recently dealt with, by combining the ideas in the Unified Integral Transforms algorithm with a problem reformulation strategy based on a single domain representation, as here demonstrated. The so called conjugated heat transfer problems were first identified as such by Perelman (1961) [26] and Luikov et al. (1971) [27], and extensively studied along more than fifty years, including previous developments with the GITT itself [28-32]. Conjugation effects are in fact avoided in many practical situations due to their inherent mathematical complexity, by adopting sometimes over-simplified boundary conditions that decouple the heat transfer processes in the fluid and solid regions. Otherwise, it should be handled by solving the energy balance differential equations in all the problem sub-regions (solids and fluids), coupling them using continuity conditions at the interfaces, eventually leading to time consuming iterations.

This lecture provides an overview of this unified integral transforms algorithm combined with the single domain formulation, and illustrates this computational tool in the solution of conjugated problems with complex configurations, first introduced in the context of internal flows [33] and progressively extended in recent contributions dealing with internal [34-36] and external flows [37].The approach is illustrated in the analysis of multi-channel micro-heat exchangers, including the model validation through infrared thermography.

2. ANALYSIS

We consider transient diffusion or convection-diffusion in a complex multidimensional configuration that is represented by n_V different sub-regions with volumes V_l, l=1,2,…n_V, with potential and flux continuity at the interfaces among themselves, as illustrated in Figure 1(a). We consider that a number of potentials are to be calculated in each sub-region, $T_{k,l}(\mathbf{x},t)$, k=1,2,…n_T, for instance temperature, velocity components, and pressure, governed in its corresponding sub-region through a fairly general formulation including non-linear coefficients and convective terms, incorporated into the source terms, $P_{k,l}(\mathbf{x},t,\mathbf{T})$, given by:

$$w_{k,l}(\mathbf{x})\frac{\partial T_{k,l}(\mathbf{x},t)}{\partial t}=\nabla\cdot\left(K_{k,l}(\mathbf{x})\nabla T_{k,l}(\mathbf{x},t)\right)-d_{k,l}(\mathbf{x})T_{k,l}(\mathbf{x},t)+P_{k,l}(\mathbf{x},t,\mathbf{T}),$$
$$\mathbf{x}\in V_l,\ \ t>0,\ \ k=1,2,...,n_T,\ \ l=1,2,...,n_V \tag{1a}$$

with initial, interface and boundary conditions given, respectively, by

$$T_{k,l}(\mathbf{x},0)=f_{k,l}(\mathbf{x}),\qquad \mathbf{x}\in V_l \tag{1b}$$

$$T_{k,l}(\mathbf{x},t)=T_{k,m}(\mathbf{x},t),\ \mathbf{x}\in S_{l,m},\ t>0 \tag{1c}$$

$$K_{k,l}(\mathbf{x})\frac{\partial T_{k,l}(\mathbf{x},t)}{\partial \mathbf{n}} = K_{k,m}(\mathbf{x})\frac{\partial T_{k,m}(\mathbf{x},t)}{\partial \mathbf{n}},\ \mathbf{x}\in S_{l,m},\ t>0 \tag{1d}$$

$$\left[\alpha_{k,l}(\mathbf{x})+\beta_{k,l}(\mathbf{x})K_{k,l}(\mathbf{x})\frac{\partial}{\partial \mathbf{n}}\right]T_{k,l}(\mathbf{x},t)=\phi_{k,l}(\mathbf{x},t,\mathbf{T}),\ \mathbf{x}\in S_l,\ t>0 \tag{1e}$$

where**n** denotes the outward-drawn normal to the interfaces, $S_{l,m}$, and external surfaces, S_l.

The Generalized Integral Transform Technique (GITT) can be directly applied to solve system (1) above, either by constructing an individual eigenfunction expansion basis for each potential, and then coupling all the transformed systems and potentials for each sub-region, or by constructing a multiregion eigenvalue problem that couples all of the sub-regions into a single set of eigenvalues, which in general involves cumbersome computations in multidimensional applications. However, in this case, one single transformed system and one single set of transformed potentials is obtained by employing the appropriate orthogonality property.

Figure 1 provides two possibilities for representation of the single domain, either by keeping the original overall domain after definition of the space variable coefficients, Fig. 1(b), or, if desired, by considering a regular overall domain that envelopes the original one, Fig. 1(c). Irregular domains can be directly integral transformed, as demonstrated in several previous works [9, 16, 22], and in principle there is no need to consider this second representation possibility. However, computational advantages may be achieved by enveloping the original irregular domain by a simple regular region in a number of situations.

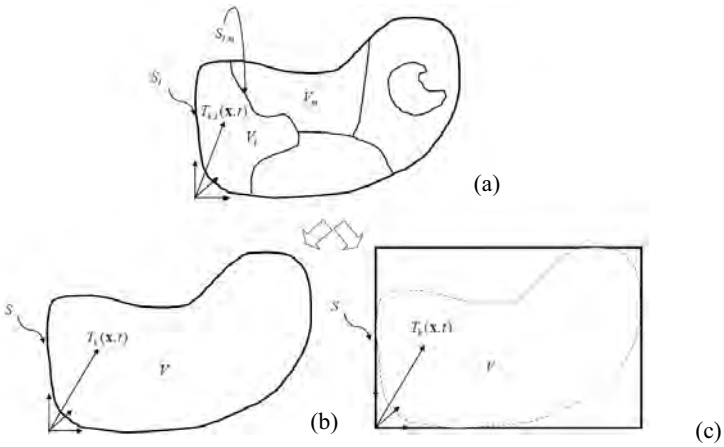

FIGURE 1. (a) Diffusion or convection-diffusion in a complex multidimensional configuration with n_V sub-regions; (b) Single domain representation keeping the original overall domain; (c) Single domain representation considering a regular overall domain that envelopes the original one

Therefore, as already demonstrated in the analysis of specific conjugated problems [33-37], it is possible to rewrite problem (1) as a single domain formulation with space variable coefficients and source terms, given by:

$$w_k(\mathbf{x})\frac{\partial T_k(\mathbf{x},t)}{\partial t}=\nabla\cdot\left(K_k(\mathbf{x})\nabla T_k(\mathbf{x},t)\right)-d_k(\mathbf{x})T_k(\mathbf{x},t)+P_k(\mathbf{x},t,\mathbf{T}),\quad \mathbf{x}\in V,\ \ t>0 \tag{2a}$$

with initial and boundary conditions given, respectively, by

$$T_k(\mathbf{x},0)=f_k(\mathbf{x}),\quad \mathbf{x}\in V \tag{2b}$$

$$\left[\alpha_k(\mathbf{x})+\beta_k(\mathbf{x})K_k(\mathbf{x})\frac{\partial}{\partial\mathbf{n}}\right]T_k(\mathbf{x},t)=\phi_k(\mathbf{x},t,\mathbf{T}),\ \mathbf{x}\in S,\ t>0 \tag{2c}$$

where

$$V=\sum_{l=1}^{n_V}V_l,\quad S=\sum_{l=1}^{n_V}S_l \tag{2d}$$

and where the potentials vector is given by

$$\mathbf{T}=\left\{T_1,T_2,...,T_k,...,T_{n_T}\right\} \tag{2e}$$

The space variable coefficients in eqs.(2), besides the new equation and boundary source terms and initial conditions, now without the subscript *l* for the sub-regions V_l, incorporate the abrupt transitions among the different sub-regions and permit the representation of system (1) as a single domain formulation to be directly handled by integral transforms.

The formal integral transform solution of problem (2) requires the proposition of eigenfunction expansions for the associated potentials. The linear situation, when the equation and boundary source terms in eqs. (2) do not depend on **T**, i.e. with $P_k(\mathbf{x},t,\mathbf{T})\equiv P_k(\mathbf{x},t)$ and $\phi_k(\mathbf{x},t,\mathbf{T})\equiv\phi_k(\mathbf{x},t)$, allows for an exact solution via the classical integral transform approach [7], and naturally leads to the eigenvalue problems to be preferred in the analysis of the nonlinear situation. They appear in the direct application of the separation of variables methodology to the linear homogeneous purely diffusive version of the proposed problem. Thus, the recommended set of uncoupled auxiliary problems is given by:

$$\nabla\cdot\left(K_k(\mathbf{x})\nabla\psi_{ki}(\mathbf{x})\right)+[\mu_{ki}^2w_k(\mathbf{x})-d_k(\mathbf{x})]\psi_{ki}(\mathbf{x})=0,\quad \mathbf{x}\in V \tag{3a}$$

$$\left[\alpha_k(\mathbf{x})+\beta_k(\mathbf{x})K_k(\mathbf{x})\frac{\partial}{\partial\mathbf{n}}\right]\psi_{ki}(\mathbf{x})=0,\quad \mathbf{x}\in S \tag{3b}$$

where the eigenvalues, μ_{ki}, and related eigenfunctions, $\psi_{ki}(\mathbf{x})$, are assumed to be known from application of the GITT itself in the solution of Sturm-Liouville type problems [16, 38], as briefly described in the Appendix. In fact, the written form of eqs. (2) already reflects this choice of eigenvalue problems, eqs.(3), via prescription of the linear coefficients in both the equations and boundary conditions, since any remaining term is directly incorporated into the general nonlinear equation and boundary condition source terms, without loss of generality. Problem (3) allows, through the associated orthogonality property of the eigenfunctions, the definition of the following integral transform pairs:

$$\overline{T}_{ki}(t)=\int_V w_k(\mathbf{x})\tilde{\psi}_{ki}(\mathbf{x})T_k(\mathbf{x},t)\mathrm{d}V\ ,\qquad \text{transforms} \tag{4a}$$

$$T_k(\mathbf{x},t)=\sum_{i=1}^{\infty}\tilde{\psi}_{ki}(\mathbf{x})\bar{T}_{k,i}(t),\qquad \text{inverses} \tag{4b}$$

where the symmetric kernels $\tilde{\psi}_{ki}(\mathbf{x})$ are given by

$$\tilde{\psi}_{ki}(\mathbf{x})=\frac{\psi_{ki}(\mathbf{x})}{\sqrt{N_{ki}}};\quad N_{ki}=\int_{\mathrm{v}} w_k(\mathbf{x})\psi_{ki}^2(\mathbf{x})\mathrm{d}V \tag{4c,d}$$

with N_{ki} being the normalization integral.

The integral transformation of eq. (2a) is accomplished by applying the operator $\int_V \tilde{\psi}_{ki}(\mathbf{x})(\cdot)\mathrm{d}V$ and making use of the boundary conditions given by eqs. (2c) and (3b), yielding:

$$\frac{d\bar{T}_{ki}(t)}{dt}+\mu_{ki}^2\bar{T}_{ki}(t)=\bar{g}_{ki}(t,\mathbf{T})+\bar{b}_{ki}(t,\mathbf{T}),\ i=1,2,\ldots,\quad t>0,\quad k=1,2,\ldots,n_T \tag{5a}$$

where the transformed source term $\bar{g}_{ki}(t,\mathbf{T})$ is due to the integral transformation of the equation source term, and the other, $\bar{b}_{ki}(t,\mathbf{T})$, is due to the contribution of the boundary source term:

$$\bar{g}_{ki}(t,\mathbf{T})=\int_V \tilde{\psi}_{ki}(\mathbf{x})P_k(\mathbf{x},t,\mathbf{T})dV \tag{5b}$$

$$\bar{b}_{ki}(t,\mathbf{T})=\int_S K_k(\mathbf{x})\left[\tilde{\psi}_{ki}(\mathbf{x})\frac{\partial T_k(\mathbf{x},t)}{\partial \mathbf{n}}-T_k(\mathbf{x},t)\frac{\partial \tilde{\psi}_{ki}(\mathbf{x})}{\partial \mathbf{n}}\right]ds \tag{5c}$$

The boundary conditions contribution may also be expressed in terms of the boundary source terms, after manipulating eqs. (2c) and (3b), to yield:

$$\bar{b}_{ki}(t,\mathbf{T})=\int_S \phi_k(\mathbf{x},t,\mathbf{T})\left[\frac{\tilde{\psi}_{ki}(\mathbf{x})-K_k(\mathbf{x})\dfrac{\partial \tilde{\psi}_{ki}(\mathbf{x})}{\partial \mathbf{n}}}{\alpha_k(\mathbf{x})+\beta_k(\mathbf{x})}\right]ds \tag{5d}$$

The initial conditions given by eq. (2b) are transformed through the operator $\int_V w_k(\mathbf{x})\tilde{\psi}_{ki}(\mathbf{x})(\cdot)dV$, to provide:

$$\bar{T}_{ki}(0)=\bar{f}_{ki}\equiv\int_V w_k(\mathbf{x})\tilde{\psi}_{ki}(\mathbf{x})f_k(\mathbf{x})dV \tag{5e}$$

Equations (5) form an infinite coupled system of nonlinear ordinary differential equations for the transformed potentials, $\bar{T}_{ki}(t)$, which is unlikely to be analytically solvable. Nevertheless, reliable algorithms are readily available to numerically handle this ODE system, after truncation to a sufficiently large finite order. The *Mathematica* system [39] provides the routine NDSolve for solving stiff ODE systems such as the one here obtained, under automatic absolute and relative error control. Once the transformed potentials have been numerically computed, the *Mathematica* routine automatically provides an interpolating function object that approximates the t variable behavior of the

solution in a continuous form. Then, the inversion formula, eq. (4b), can be recalled to yield the potential field representation at any desired position $\mathbf{x}$ and time t.

The formal solution above derived provides the basic working expressions for the integral transform method. However, for an improved computational performance, it is always recommended to reduce the importance of the equation and boundary source terms, for instance through analytical filtering, so as to enhance the eigenfunction expansions convergence behavior [20]. The constructed multidimensional UNIT code in the *Mathematica* platform [23-25] encompasses all of the symbolic derivations that are required in the above GITT formal solution, besides the numerical computations that are required in the solutions of the chosen eigenvalue problem and the transformed differential system.

3. APPLICATION

The conjugated heat transfer analysis here considered comes from an application related to waste heat recovery formicro-reactors in biodiesel synthesis, employing multi-stream micro-heat exchangers. A model for flow visualization made on PMMA through laser ablation is shown in Figure 2a, while the employed experimental apparatus for the infrared thermography analysis is presented in Figure 2b.The heat exchanger is graphically represented in Figures3a,b for the whole set of channels and for a single microchannel.

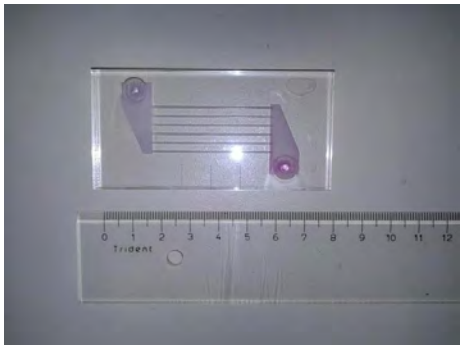

FIGURE 2a. PMMA model of the micro-heat exchanger made by laser ablation.

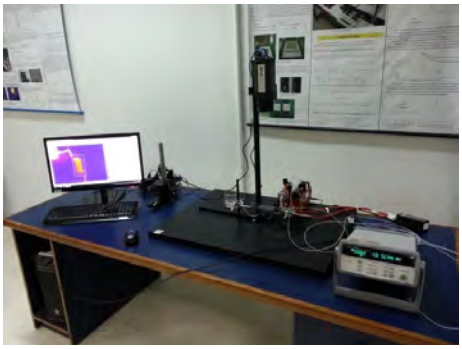

FIGURE 2b. Experimental apparatus for infrared thermography analysis of micro-heat exchanger.

The conjugated heat transfer problem involving conduction in the acrylic substrate and laminar forced convection in the water flow within the six triangular shaped microchannels, is thus combined into a single domain formulation. Then, the steady-state temperature fields at the substrate surface obtained from the GITT solution and from infrared thermography are critically compared. Numerical results from the finite elements commercial code COMSOL Multiphysics are also obtained and presented.

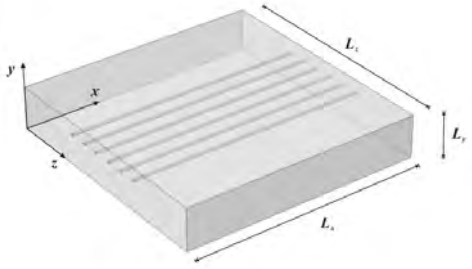

FIGURE 3a. Representation of the micro-heat exchanger for the single domain formulation.

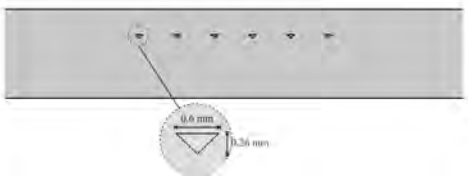

FIGURE 3b. Details of the micro-channel geometry.

Motivated by the fairly high values of the Péclet number and the relatively low thermal conductivity of the substrate, the longitudinal conduction terms both in the fluid and along the plate are neglected for the sake of simplicity. Therefore, the formulation of the steady state conjugated problem as a single region model is achieved by making use of space variable coefficients represented as functions with abrupt transitions at the fluid-wall interfaces, as follows:

$$w(y,z)\frac{\partial T(x,y,z)}{\partial x}=\frac{\partial}{\partial y}\left(k(y,z)\frac{\partial T}{\partial y}\right)+\frac{\partial}{\partial z}\left(k(y,z)\frac{\partial T}{\partial z}\right), \qquad 0<y<L_y,\quad 0<z<L_z,\quad 0<x<L_x \tag{6a}$$

$$T(0,y,z)=T_{in}(y,z) \tag{6b}$$

$$-k_s\left.\frac{\partial T}{\partial y}\right|_{y=0}+h_{eff}T(x,0,z)=h_{eff}T_\infty, \qquad k_s\left.\frac{\partial T}{\partial y}\right|_{y=L_y}+h_{eff}T(x,L_y,z)=h_{eff}T_\infty \tag{6c,d}$$

$$-k_s\left.\frac{\partial T}{\partial z}\right|_{z=0}+h_{eff}T(x,y,0)=h_{eff}T_\infty, \qquad k_s\left.\frac{\partial T}{\partial z}\right|_{z=L_z}+h_{eff}T\left(x,y,L_z\right)=h_{eff}T_\infty \tag{6e,f}$$

with

$$w(y,z)=\begin{cases}w_f\overline{u}_f, & \text{fluid}\\ 0, & \text{solid}\end{cases} \quad \text{and} \quad k(y,z)=\begin{cases}k_f, & \text{fluid}\\ k_s, & \text{solid}\end{cases} \tag{6g,h}$$

where $\overline{u}_f$ is the average flow velocity in the micro-channel, w_f is the fluid thermal capacitance, k_f and k_s are the thermal conductivities of the fluid (water) and the solid (PMMA), respectively. The inlet condition $T(0,y,z)=T_{in}(y,z)$ given by eq. (6b), refers to the temperatures at the channel inlets.

To improve the computational performance of the formal solution to be derived below using the integral transforms method, the boundary conditions are filtered to become homogeneous, and in this work if suffices to propose as filter just the room temperature, T_∞ :

$$T(x,y,z) = T_\infty + T^*(x,y,z) \tag{7}$$

resulting in the following homogenous problem:

$$w(y,z)\frac{\partial T^*(x,y,z)}{\partial x} = \frac{\partial}{\partial y}\left(k(y,z)\frac{\partial T^*}{\partial y}\right) + \frac{\partial}{\partial z}\left(k(y,z)\frac{\partial T^*}{\partial z}\right), \quad 0 < y < L_y, \quad 0 < z < L_z, \quad 0 < x < L_x \tag{8a}$$

$$T^*(0,y,z) = T^*_{in}(y,z) = T_{in}(y,z) - T_\infty \tag{8b}$$

$$-k_s\left.\frac{\partial T^*}{\partial y}\right|_{y=0} + h_{eff}T^*(x,0,z) = 0, \qquad k_s\left.\frac{\partial T^*}{\partial y}\right|_{y=L_y} + h_{eff}T^*(x,L_y,z) = 0 \tag{8c,d}$$

$$-k_s\left.\frac{\partial T^*}{\partial z}\right|_{z=0} + h_{eff}T^*(x,y,0) = 0, \qquad k_s\left.\frac{\partial T^*}{\partial z}\right|_{z=L_z} + h_{eff}T^*\left(x,y,L_z\right) = 0 \tag{8e,f}$$

Following the Generalized Integral Transform Technique formalism, it is desirable that the eigenvalue problem be chosen in order to contain as much information as possible about the original problem. The eigenvalue problem is formulated by directly applying separation of variables to problem (8) so that all the information concerning the transitions of the original domains are represented within the eigenvalue problem, by means of the space variable coefficients $k(y,z)$ and $w(y,z)$:

$$\nabla\cdot\left[k(y,z)\nabla\psi(y,z)\right] = \mu^2 w(y,z)\psi(y,z), \quad 0 < y < L_y, \quad 0 < z < L_z \tag{9a}$$

$$-k_s\left.\frac{\partial\psi}{\partial y}\right|_{y=0} + h_{eff}\psi\left(0,z\right) = 0, \qquad \left.\frac{\partial\psi}{\partial y}\right|_{y=L_y} + h_{eff}\psi\left(L_y,z\right) = 0 \tag{9b,c}$$

$$-k_s\left.\frac{\partial\psi}{\partial z}\right|_{z=0} + h_{eff}\psi\left(y,0\right) = 0, \qquad k_s\left.\frac{\partial\psi}{\partial z}\right|_{z=L_z} + h_{eff}\psi\left(y,L_z\right) = 0 \tag{9d,e}$$

and then problem (9) is solved, yielding the eigenvalues μ_i and corresponding normalized eigenfunctions, $\tilde{\psi}_i(y,z)$, with:

$$\tilde{\psi}_i(y,z) = \frac{\psi_i(y,z)}{\sqrt{N_i}}, \quad N_i = \int_0^{L_z}\int_0^{L_y} w(y,z)\psi_i^2(y,z)dydz \tag{10a,b}$$

Problem (8) can be exactly transformed by operating eq. (8a) with $\int_0^{L_z}\int_0^{L_y}\tilde{\psi}_i(y,z)(\cdot)dydz$ and making use of the boundary conditions, eqs. (8e-f) and (9b-e), yielding:

$$\frac{d\overline{T}_i^*(x)}{dx} + \mu_i^2\overline{T}_i^*(x) = 0, \quad i = 1,2,... \tag{10a}$$

The initial condition given by eq. (8b) is transformed through the operator $\int_0^{L_z}\int_0^{L_y} w(y,z)\tilde{\psi}_i(y,z)(\cdot)dydz$:

$$\overline{T}^*(0) = \overline{T}^*_{in,i} \equiv \int_0^{L_z}\int_0^{L_y} w(y,z)\tilde{\psi}_i(y,z)T^*_{in}dydz \tag{10b}$$

Problem (10) can be analytically solved to provide:

$$\overline{T}^*_i(x) = \overline{T}^*_{in,i}\exp\left(-\mu_i^2 x\right) \tag{11}$$

and the solution of Problem (6) can be analytically expressed by making use of the inversion formula:

$$T(x,y,z) = T_\infty + T^*(x,y,z) = T_\infty + \sum_{i=1}^{\infty}\tilde{\psi}_i(y,z)\overline{T}^*_i(x) \tag{12}$$

Therefore, the main task in this solution path is associated with the solution of the two-dimensional eigenvalue problem with space variable coefficients, eqs. (9a-e), which can also be achieved by means of integral transforms. This solution procedure is described with further details in the Appendix.

4. RESULTS AND DISCUSSIONS

Results are now reported for the considered micro-heat exchanger conjugated problem, in terms of the external surface temperatures in steady-state as obtained from the infrared thermography images, such as those shown in Figures 5a,b below, for the front and back faces of the acrylic substrate, respectively. For more accurate temperature evaluations, the surfaces are uniformly covered with a graphite ink of known emissivity of 0.97.

(a) (b)

FIGURE 5. Infrared thermographic images of micro-heat exchanger external surfaces: (a) front face; (b) back face with coolant inlet-outlet

The experiment is conducted with a prescribed total volumetric flow rate of 2mL/min, yielding $\bar{u}_f = 0.0712$ m/s in each channel. Using empirical correlations for natural convection [40], the value $h_{eff} = 15\text{W/m}^3\text{K}$ was used for the heat transfer coefficient in problem (6). Additionally, the following thermophysical properties were employed [40]: $k_f = 0.64\text{W/mK}$ and $w_f = 4.186\times10^6$ J/m^{3}K (water), and $k_s = 0.17\text{W/mK}$ (PMMA).

Figure 6 depicts the theorectical predictions obtained with both the single domain model solved throughGITT, and the COMSOLMultiphysics commercial code, together with the infrared experimental measurements obtained at the transversal centerline of the substrate external surfaces. In figure 6aare provided the results corresponding to the micro-heat exchanger front face, whereas in figure 6b the back face is considered. Similar comparative results are presented in figures 7a,b, which depict the surface temperature profiles in the longitudinal direction at the centerline along the length of the micro-heat exchanger, corresponding to the front face (fig. 7a) and the back face (fig. 7b).

From this results sample, it is clear that a good adherence between the hybrid theoretical prediction via GITT and the experimental measurements, could be achieved, indicating the adequacy of the proposed model and solution methodology. It should also be observed the good agreement between the solution provided by GITT employing the single domain model and the numerical finite element solution (COMSOL) of the conjugated problem, with the difference between these predictions remaining within the experimental error.

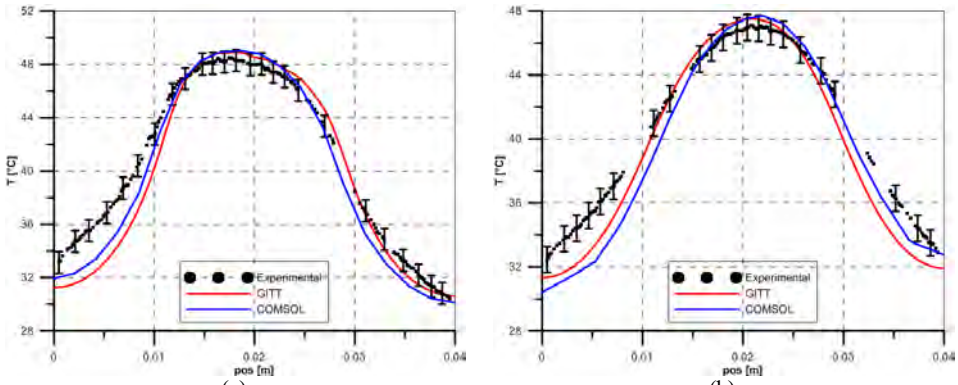

FIGURE 6. Comparison of infrared thermography temperature measurements at the external surfaces (transversal centerline) against the GITT (red) and COMSOL (blue) solutions: (a) front face; (b) back face with coolant inlet-outlet

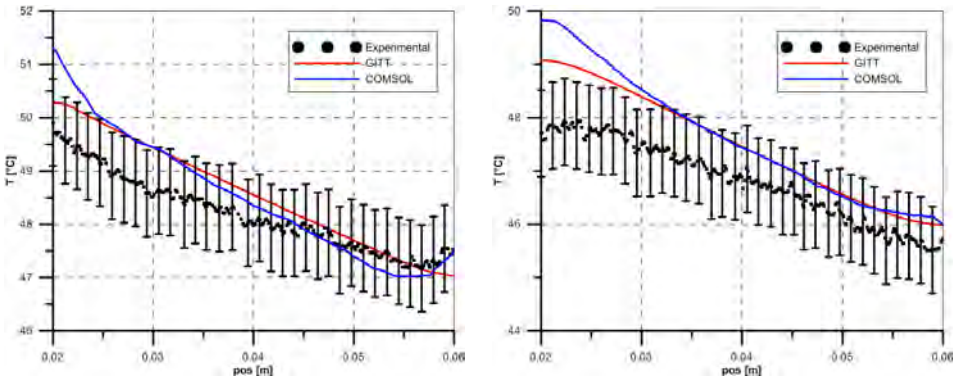

FIGURE 7. Comparison of infrared thermography temperature measurements at the external surfaces (longitudinal centerline) against the GITT (red) and COMSOL (blue) solutions: (a) front face; (b) back face with coolant inlet-outlet

5. CONCLUSIONS

The combination of the Generalized Integral Transform Technique (GITT) with a single domain reformulation strategy is reviewed, as applied in the hybrid numerical-analytical treatment of multi-region convection-diffusion problems, here illustrated for conjugated conduction-convection problems. A multi-stream micro-heat exchanger application is more closely considered, involving a three-dimensional configuration with irregular channels, and the methodology here advanced is carefully validated against experimental results from non-intrusive infrared thermography measurements of the substrate external surface temperatures. Critical comparisons with a commercial CFD code (COMSOL Multiphysics) are also provided. Excellent agreement among the theoretical predictions and the experimental findings has been achieved. The proposed methodology has been demonstrated to be quite flexible, robust, and accurate. Most important, the hybrid nature of the approach, providing analytical expressions in all but one independent variable, and requiring numerical treatment at most in one single independent variable, makes it particularly well suited for computationally intensive tasks such as in optimization, inverse problem analysis and simulation under uncertainty.

REFERENCES

[1] Fourier, Joseph, 1822, Théorie analytique de la chaleur. Paris: Firmin Didot Père et Fils., 1822, http://books.google.com/books?id=TDQJAAAAIAAJ.

[2] Koshlyakov, N.S., Fundamental Differential Equations of Mathematical Physics, Moscow, 1936.

[3] Luikov, A.V.,Analytical Heat Diffusion Theory, Academic Press, New York, 1968.

[4] Ozisik, M.N., Boundary Value Problems of Heat Conduction, Int. Textbooks Co., 1968.

[5] Luikov, A.V., Heat and Mass Transfer, Mir Publishers, Moscow, 1980.

[6] Ozisik, M.N., Heat Conduction, John Wiley, New York, 1980.

[7] Mikhailov, M.D., and Özisik, M.N., Unified Analysis and Solutions of Heat and Mass Diffusion, John Wiley, New York, 1984; also, Dover Publications, 1994.

[8] Cotta, R.M. and Ozisik, M.N., Laminar Forced Convection in Ducts with Periodic Variation of Inlet Temperature, Int. J. Heat Mass & Transfer, vol. 29, no. 10, pp. 1495-1501, 1986.

[9] Aparecido, J.B., Cotta, R.M. and Ozisik, M.N., Analytical Solutions to Two-Dimensional Diffusion Type Problems in Irregular Geometries, J. of the Franklin Institute, V. 326, pp. 421-434, 1989.

[10] Cotta, R.M., Hybrid Numerical-Analytical Approach to Nonlinear Diffusion Problems, Num. Heat Transfer, Part B, V. 127, pp. 217-226, 1990.

[11] Serfaty, R. and Cotta, R.M., Integral Transform Solutions of Diffusion Problems With Nonlinear Equation Coefficients, Int. Comm. Heat & Mass Transfer, vol. 17, no. 6, pp. 851-864, 1990.

[12] Diniz, A.J., Aparecido, J.B., and Cotta, R.M., Heat Conduction with Ablation in a Finite Slab, Int. J. Heat & Technology, vol. 8, pp. 30-43, 1990.

[13] Cotta, R.M. and Carvalho, T.M.B., Hybrid Analysis of Boundary Layer Equations for Internal Flow Problems, 7th Int. Conf. on Num. Meth. in Laminar & Turbulent Flow, Part 1, pp. 106-115, Stanford CA, July, 1991.

[14] Serfaty, R. and Cotta, R.M., Hybrid Analysis of Transient Nonlinear Convection-Diffusion Problems, Int. J. Num. Meth. Heat & Fluid Flow, vol. 2, pp. 55-62, 1992.

[15] Perez Guerrero, J.S. and Cotta, R.M., Integral Transform Method for Navier-Stokes Equations in Stream Function-Only Formulation, Int. J. Num. Meth. in Fluids, vol. 15, pp. 399 – 409, 1992.

[16] Cotta, R.M., Integral Transforms in Computational Heat and Fluid Flow, CRC Press, Boca Raton, FL, 1993.

[17] Cotta, R.M., The Integral Transform Method in Computational Heat and Fluid Flow, Special Keynote Lecture, Proc. of the 10th Int. Heat Transfer Conf., Brighton, UK, SK-3, vol. 1, pp. 43-60, August, 1994a.

[18] Cotta, R.M., Benchmark Results in Computational Heat and Fluid Flow: - The Integral Transform Method. Int. J. Heat Mass Transfer (Invited Paper), vol. 37, pp. 381-394, 1994b.

[19] Quaresma, J.N.N. and Cotta, R.M., Integral Transform Method for the Navier-Stokes Equations in Steady Three-Dimensional Flow, Proc. of the 10th ISTP - Int. Symp. on Transport Phenomena, pp.281-287, Kyoto, Japan, November, 1997.

[20] Cotta,R.M. and Mikhailov, M.D., Heat Conduction: Lumped Analysis, Integral Transforms, Symbolic Computation, Wiley-Interscience, Chichester, UK, 1997.

[21] Cotta, R.M. (Ed.), The Integral Transform Method in Thermal and Fluids Sciences and Engineering. Begell House, New York, 1998.

[22] Cotta, R.M. and Mikhailov, M.D., Hybrid Methods and Symbolic Computations, in: Handbook of Numerical Heat Transfer, 2nd edition, Chapter 16, Eds. W.J. Minkowycz, E.M. Sparrow, J.Y. Murthy, John Wiley, New York, 2006.

[23] Cotta, R.M., Quaresma, J.N.N., Sphaier, L.A. , and Naveira-Cotta, C.P., Unified Integral Transform Approach in the Hybrid Solution of Multidimensional Nonlinear Convection-Diffusion Problems, 14th Int. Heat Transfer Conf., Washington, DC, USA, August, 2010.

[24] Sphaier, L.A., Cotta, R.M., Naveira-Cotta, C.P., and Quaresma, J.N.N., The UNIT Algorithm for Solving One-Dimensional Convection-Diffusion Problems via Integral Transforms, Int. Comm. in Heat and Mass Transfer, Vol. 38, pp. 565-571, 2011.

[25] Cotta, R.M., Knupp, D.C., Naveira-Cotta, C.P., Sphaier, L.A., and Quaresma, J.N.N., Unified Integral Transform Algorithm for Solving Multidimensional Nonlinear Convection-Diffusion Problems, Num. Heat Transfer, Part A, Vol. 63, No. 11, pp. 840-866, 2013.

[26] Perelman, Y.L., On Conjugate Problems of Heat Transfer, Int. J. Heat and Mass Transfer, Vol. 3, pp.293-303, 1961.

[27] Luikov, A.V., Aleksashenko, V.A., and Aleksashenko, A.A., Analytical Methods of Solution of Conjugated Problems in Convective Heat Transfer, Int. J. Heat and Mass Transfer, Vol. 14, pp. 1047-1056, 1971.

[28] Guedes, R.O.C., Cotta, R.M., and Brum, N.C.L., Heat Transfer in Laminar Tube Flow with Wall Axial Conduction Effects, J. Thermophysics and Heat Transfer, Vol. 5, No 4, pp. 508-513, 1991.

[29] Guedes, R.O.C., and Cotta, R.M., Periodic Laminar Forced Convection Within Ducts Including Wall Heat Conduction Effects, Int. J. Eng. Science, Vol. 29, No. 5, pp. 535-547, 1991.

[30] Naveira, C.P., Lachi, M., Cotta, R.M., and Padet, J., Hybrid Formulation and Solution for Transient Conjugated Conduction-External Convection, Int. J. Heat and Mass Transfer, Vol. 52, Issues 1-2, pp. 112-123, 2009.

[31] Naveira-Cotta, C.P., Lachi, M., Rebay, M., and Cotta, R.M., Experiments and Simulations in Transient Conjugated Conduction-Convection-Radiation, Heat Transfer Research, Vol.43, No.3, pp. 209-231, 2010.

[32] Souza, J.R.B., Lisboa,K.M., Cerqueira, I.G., Naveira-Cotta,C.P.,Cotta, R.M.,and Zotin,J.L.Z.,Conjugated Heat Transfer Analysis of Heated Aeronautical Pitot Probes with Flight Tests Experimental Validation, Heat Transfer Eng, 2014 (in press).

[33] Knupp, D. C., Naveira-Cotta, C.P.,and Cotta, R.M.,Theoretical Analysis of Conjugated Heat Transfer with a Single Domain Formulation and Integral Transforms, Int. Comm. Heat & Mass Transfer, V.39, no.3, pp.355-362, 2012.

[34] Knupp, D.C., Naveira-Cotta, C.P.,and Cotta, R.M.,Conjugated Convection-Conduction Analysis in Micro-Channels with Axial Diffusion Effects and a Single Domain Formulation, ASME J. Heat Transfer, Special Issue on Micro/Nanoscale Heat and Mass Transfer, V.135, no.9, pp. 091401- 091411, 2013.

[35] Knupp, D.C., Cotta, R.M.,and Naveira-Cotta, C.P., Conjugated Heat Transfer in Micro Channels with Upstream-Downstream Regions Coupling, Num. Heat Transfer, Part B - Fundamentals, Vol.64, pp.365-387, 2013.

[36] Knupp, D.C., Cotta, R.M., and Naveira-Cotta, C.P.,Conjugated Heat Transfer in Heat Spreaders with Micro-Channels, Proc. of the ASME 2013 Summer Heat Transfer Conference, HT2013, Minneapolis, MN, USA, July 14-19, 2013.

[37] Lisboa, K.M. and Cotta, R.M., External Flow Conjugated Problem Analysis via Integral Transforms and Single Domain Formulation, 3rd International Conference on Computational Methods for Thermal Problems - ThermaComp2014, pp.1-4, Lake Bled, Slovenia,June, 2014.

[38] Sphaier, L.A., and Cotta, R.M., Integral Transform Analysis of Multidimensional Eigenvalue Problems Within Irregular Domains, Numerical Heat Transfer, Part B-Fundamentals, Vol.38, pp.157-175, 2000.

[39] Wolfram, S., *The Mathematica Book*, Wolfram Media, Cambridge, UK, 2005.

[40] Lienhard IV, J. H., and Lienhard V, J. H., *A Heat Transfer Textbook*, Phlogiston Press, Cambridge, MA, US, 2008.

APPENDIX

Solution of Eigenvalue Problems with the Generalized Integral Transform Technique

The auxiliary eigenvalue problems that provide the basis for the eigenfunction expansions can be efficiently solved through the generalized integral transform technique itself, as introduced in [16] and successfully employed in several works, such as [34,35], just to cite a few recent contributions. The procedure constitutes a very straightforward approach to handle more general eigenvalue problems, such as multidimensional problems, complex domain, and non-classical systems, and, therefore, is essential for the solution through integral transforms of the problem proposed in this work.

The basic idea is to employ the GITT formalism to reduce the eigenvalue problem described by partial differential equations into standard algebraic eigenvalue problems, which can be solved by existing codes for matrix eigensystem analysis. Therefore, the eigenfuctions of the original auxiliary problem can be expressed by eigenfunction expansions based on a simpler auxiliary eigenvalue problem, for which exact analytic solutions are known.

Consider the following eigenvalue problem defined in region V and boundary surface S:

$$L\psi(\mathbf{x}) = \mu^2 w(\mathbf{x})\psi(\mathbf{x}), \quad \mathbf{x} \in V \tag{A1a}$$

$$B\psi(\mathbf{x}) = 0, \quad \mathbf{x} \in S \tag{A1b}$$

where the operators L and B are given by:

$$L = -\nabla \cdot \left(k(\mathbf{x})\nabla\right) + d(\mathbf{x}) \tag{A1c}$$

$$B = \alpha(\mathbf{x}) + \beta(\mathbf{x})k(\mathbf{x})\frac{\partial}{\partial \mathbf{n}} \tag{A1d}$$

where $w(\mathbf{x})$, $k(\mathbf{x})$, and $d(\mathbf{x})$ are known functions in region V, and $\alpha(\mathbf{x})$, $\beta(\mathbf{x})$ are known functions on the boundary surface S.

The problem given by eqs. (A1a-d) can be rewritten as:

$$\hat{L}\psi(\mathbf{x}) = \left(\hat{L} - L\right)\psi(\mathbf{x}) + \mu^2 w(\mathbf{x})\psi(\mathbf{x}), \quad \mathbf{x} \in V \tag{A2a}$$

$$\hat{B}\psi(\mathbf{x}) = (\hat{B} - B)\psi(\mathbf{x}), \quad \mathbf{x} \in S \tag{A2b}$$

where $\hat{L}$ and $\hat{B}$ are the operators given by:

$$\hat{L} = -\nabla \cdot \left(\hat{k}(\mathbf{x})\nabla\right) + \hat{d}(\mathbf{x}) \tag{A2c}$$

$$\hat{B} = \hat{\alpha}(\mathbf{x}) + \hat{\beta}(\mathbf{x})\hat{k}(\mathbf{x})\frac{\partial}{\partial \mathbf{n}} \tag{A2d}$$

which are employed in the selection of an appropriate auxiliary problem:

$$\hat{L}\Omega(\mathbf{x}) = \lambda^2 \hat{w}(\mathbf{x})\Omega(\mathbf{x}), \quad \mathbf{x} \in V \tag{A3a}$$

$$\hat{B}\Omega(\mathbf{x}) = 0, \quad \mathbf{x} \in S \tag{A3b}$$

where $\hat{w}(\mathbf{x})$, $\hat{k}(\mathbf{x})$, $\hat{d}(\mathbf{x})$, $\hat{\alpha}(\mathbf{x})$, and $\hat{\beta}(\mathbf{x})$ are user selected coefficients in V and S, properly chosen so that the eigenvalue problem given by eqs. (A3a,b) has known analytic solution for the corresponding eigenfunctions $\Omega(\mathbf{x})$.

Therefore, making use of these eigenfunctions orthogonality property, problem (A3) allows the definition of the following integral transform pair:

$$\text{transform: } \bar{\psi}_i = \int_V \hat{w}(\mathbf{x})\tilde{\Omega}_i(\mathbf{x})\psi(\mathbf{x})dV \tag{A4a}$$

$$\text{inverse: } \psi(\mathbf{x}) = \sum_{i=1}^{\infty} \tilde{\Omega}_i(\mathbf{x})\bar{\psi}_i \tag{A4b}$$

where

$$\tilde{\Omega}_i(\mathbf{x}) = \frac{\Omega_i(\mathbf{x})}{\sqrt{N_{\Omega_i}}} \text{ , with } N_{\Omega_i} = \int_V \hat{w}(\mathbf{x})\Omega_i^2(\mathbf{x})dV \tag{A4c,d}$$

Eq. (A1a) is now operated on with $\int_V \tilde{\Omega}_i(\mathbf{x})(\cdot)dV$, to yield the transformed algebraic system:

$$\lambda_i^2\bar{\psi}_i = \int_S \gamma_i(\hat{B}-B)\psi(\mathbf{x})dS + \int_V \tilde{\Omega}_i(\mathbf{x})(\hat{L}-L)\psi(\mathbf{x})dV + \\ + \mu^2 \int_V \tilde{\Omega}_i(\mathbf{x})w(\mathbf{x})\psi(\mathbf{x})dV, \quad i = 1,2,... \tag{A5a}$$

$$\gamma_i = \frac{\tilde{\Omega}_i(\mathbf{x}) - \hat{K}(\mathbf{x})\dfrac{\partial\tilde{\Omega}_i(\mathbf{x})}{\partial\mathbf{n}}}{\hat{\alpha}(\mathbf{x}) + \hat{\beta}(\mathbf{x})} \tag{A5b}$$

After introducing the truncated to the Mth term inversion formula, eq. (A4b), into eq. (A5a), the resulting system is written in matrix form as:

$$(\mathbf{A}+\mathbf{C})\{\bar{\boldsymbol{\psi}}\} = \boldsymbol{\mu}^2\mathbf{B}\{\bar{\boldsymbol{\psi}}\} \tag{A6a}$$

with the elements of the M x M matrices, and vector $\boldsymbol{\mu}^2$ given by:

$$A_{ij} = -\int_S \gamma_i(\hat{B}-B)\tilde{\Omega}_j(\mathbf{x})dS - \int_V \tilde{\Omega}_i(\mathbf{x})(\hat{L}-L)\tilde{\Omega}_j(\mathbf{x})dV \tag{A6b}$$

$$C_{ij} = \lambda_i^2 \delta_{ij} \tag{A6c}$$

$$B_{ij} = \int_V w(\mathbf{x}) \tilde{\Omega}_i(\mathbf{x}) \tilde{\Omega}_j(\mathbf{x}) dV \tag{A6d}$$

$$\boldsymbol{\mu}^2 = \left\{ \mu_1^2, \mu_2^2, ..., \mu_M^2 \right\} \tag{A6e}$$

where δ_{ij} is the Kronecker delta.

By choosing to use the relation

$$\begin{aligned} \int_V \tilde{\Omega}_i(\mathbf{x}) \nabla \cdot \left(\hat{k}(\mathbf{x}) \nabla \tilde{\Omega}_j(\mathbf{x}) \right) dV = \int_S \hat{k}(\mathbf{x}) \tilde{\Omega}_i(\mathbf{x}) \frac{\partial \tilde{\Omega}_j(\mathbf{x})}{\partial \mathbf{n}} dS - \\ - \int_V \hat{k}(\mathbf{x}) \nabla \tilde{\Omega}_i(\mathbf{x}) \cdot \nabla \tilde{\Omega}_j(\mathbf{x}) dV \end{aligned} \tag{A7}$$

the elements of $\mathbf{A}$ can be calculated through the following working formula:

$$\begin{aligned} &\int_S \frac{\tilde{\Omega}_i(\mathbf{x}) - \hat{k}(\mathbf{x}) \dfrac{\partial \tilde{\Omega}_i(\mathbf{x})}{\partial \mathbf{n}}}{\hat{\alpha}(\mathbf{x}) + \hat{\beta}(\mathbf{x})} \left[\left(\alpha(\mathbf{x}) - \hat{\alpha}(\mathbf{x}) \right) \tilde{\Omega}_j(\mathbf{x}) + \left(\beta(\mathbf{x}) k(\mathbf{x}) - \hat{\beta}(\mathbf{x}) k(\mathbf{x}) \right) \frac{\partial \tilde{\Omega}_j(\mathbf{x})}{\partial \mathbf{n}} \right] dS - \\ &- \int_S \left(k(\mathbf{x}) - \hat{k}(\mathbf{x}) \right) \tilde{\Omega}_i(\mathbf{x}) \frac{\partial \tilde{\Omega}_j(\mathbf{x})}{\partial \mathbf{n}} dS + \int_V \left(k(\mathbf{x}) - \hat{k}(\mathbf{x}) \right) \nabla \tilde{\Omega}_i(\mathbf{x}) \cdot \nabla \tilde{\Omega}_j(\mathbf{x}) dV + \\ &+ \int_V \left(d(\mathbf{x}) - \hat{d}(\mathbf{x}) \right) \tilde{\Omega}_i(\mathbf{x}) \tilde{\Omega}_j(\mathbf{x}) dV \end{aligned} \tag{A8}$$

Therefore, the eigenvalue problem given by eqs. (A1a,b) is reduced to the standard algebraic eigenvalue problem given by eq. (A6a), which can be solved with existing software for matrix eigensystem analysis, directly yielding the eigenvalues μ, whereas the corresponding calculated eigenvectors from this numerical solution, $\bar{\psi}_i$, are to be used in the inversion formula, given by eq. (A4b), to find the desired originally proposed eigenfunction. By increasing the number of terms in the truncated expansion, one can obtain the results to within user prescribed accuracy.

Third International Conference on Computational Methods for Thermal Problems
THERMACOMP2014, June 2-4, 2014, Lake Bled, Slovenia
N. Massarotti, P. Nithiarasu and B. Sarler (Eds.)

COMPUTATIONAL MODELLING OF COUPLED PROCESSES IN GROUND ENERGY PROBLEMS

Hywel R. Thomas and Majid Sedighi

Geoenvironmental Research Centre, Cardiff School of Engineering, Cardiff University, The Queen's Buildings, Newport Road, Cardiff, CF24 3AA, UK.

ThomasHR@cf.ac.uk, SedighiM@cf.ac.uk

ABSTRACT

This paper presents some aspects of the computational modelling of coupled processes related to geoenergy problems. Experiences gained from model development, validation and application in the areas of i) ground source heat and ii) carbon dioxide sequestration in coal are presented. A field scale validation exercise of ground source heat application is presented. Aspects related to the coupled physical, chemical and mechanical modelling of carbon sequestration in coal are presented.

Key Words: *Geoenergy, computational modelling, ground source heat, carbon dioxide sequestration, coalbed methane, coupled processes.*

1. INTRODUCTION.

Ground energy sources such as ground source heat, geothermal energy and the exploitation of unconventional gas from coal and shale are generally thought to be important areas to be considered as part of a spectrum of energy sources to ensure energy security needs. Understanding the processes involved in geoenergy exploitation requires the consideration of highly coupled phenomena in extreme or unconventional environments. The development of an improved understanding of the behaviour of the ground under such circumstances remains an interesting challenge.

Computational modelling of the ground energy aspects may involve various complexities due to i) the coupled nature of the processes involved, ii) heterogeneity of the ground system, iii) multi-scale interactions and dynamics of the system and components, iv) the extreme environmental conditions which exist in technology applications, e.g. elevated temperature effects in underground coal gasification, iv) computational efforts required for an efficient numerical solution for large scale simulations and v) limited applications or scarcity of trial tests with high resolution results which can be used for validation of the models. To address such complexities, further investigation and development areas ranging from theoretical formulations and advanced numerical/computational algorithms to validation tests are of importance.

This paper presents experiences gained from a programme of computational modelling in that area. Various aspects related to sustainable energy extraction from the ground have been studied; including field scale studies, laboratory experiments, advanced computational modelling and geoinformatic applications. Areas of geoenergy applications including ground source heat, carbon sequestration in coal/enhanced coalbed methane recovery and underground coal gasification have been studied as part of this programme.

The work performed includes: i) the development of a theoretical formulation of coupled physical, chemical and mechanical behaviour, ii) the inclusion of advanced computational techniques and iii) the development of validation exercises along with field and laboratory research. In this paper, a

review of the model developed to study the coupled thermal, hydraulic, chemical and mechanical (THCM) behaviour are provided. Two example developments in the areas of ground source heat and coalbed methane gas are described and the results achieved are presented.

2. A COUPLED THCM MODEL – DEVELOPMENT AND APPLICATION IN GEOENERGY PROBLEMS.

The computational modelling work described in this paper is based on a numerical model of coupled thermal, hydraulic, chemical and mechanical behaviour of geomaterials developed by Thomas and co-workers at the Geoenvironmental Research Centre, i.e. COMPASS [e.g. 1, 2, 3] The model is based on a mechanistic approach in which physical, chemical and mechanical processes are included in an additive manner with inter-related couplings being accommodated in the governing equations of the model (Figure 1).

The main features of ground behaviour included in model are: i) the heat transfer via the mechanisms of conduction, convection and latent heat of vaporisation, ii) moisture transfer which includes water and vapour flow due to various driving potentials, iii) transfer of gas phase or air, iv) transport of multicomponent chemicals present in the liquid and gas phases, v) geochemical reactions including heterogeneous and homogenous reactions between/in solid, liquid and gas phases and vi) deformation behaviour which is based on stress-strain equilibrium, considering appropriate constitutive relationships describing the behaviour of soil or rock.

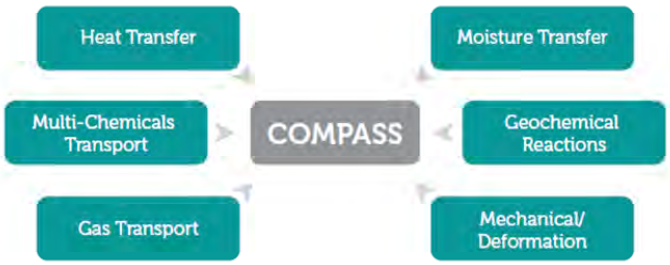

FIGURE 1. Schematic of coupled physical, chemical and mechanical modelling features included in COMPASS model.

The governing equation of heat transfer has been developed based on the energy conservation law in unsaturated porous media [1], given as:

$$\frac{\partial\left[H_c\left(T-T_r\right)\delta V+L\theta_a\rho_v\delta V\right]}{\partial t}=-\delta V\nabla\cdot\left[-\lambda_T\nabla T+L\left(\rho_l\mathbf{v}_\mathbf{v}+\rho_v\mathbf{v}_\mathbf{g}\right)+A\left(T-T_r\right)\right] \quad (1)$$

where, H_c is the heat storage capacity. T and T_r represents temperature and the reference temperature, respectively. δV is the incremental volume, L represents the latent heat of vaporisation. θ_a is the volumetric air (gas) content. ρ_l and ρ_v is the water and vapour density, respectively. $\mathbf{v}_\mathbf{v}$ and $\mathbf{v}_\mathbf{g}$ represents the vapour velocity and gas (air) velocity, respectively. λ_T represents the thermal conductivity and A stands for the sum of the heat conduction components [2]. t is time.

The governing equation for moisture flow is based on a mass conservation law. The flow of water (liquid) in unsaturated porous medium is explained using Darcy's law and the vapour flow is considered to be driven by diffusion and advection processes [2]:

$$\frac{\partial(\rho_l \theta_l \delta V)}{\partial t} + \frac{\partial(\rho_v \theta_a \delta V)}{\partial t} = -\delta V \nabla \cdot \left(\rho_l \mathbf{v_l} - \rho_l \mathbf{v_v} - \rho_v \mathbf{v_g}\right) \tag{2}$$

where, θ_l is the volumetric liquid content. $\mathbf{v_l}$ represents the water velocity.

The formulations of the reactive transport of chemicals in liquid are also expressed based on a mass conservation law. Multiple chemical/geochemical reactions that may occur in the systems causing loss or gain of each component are considered via a sink/source term in the formulation [2, 3,4]:

$$\frac{\partial\left(\theta_l c_d^i \delta V\right)}{\partial t} + \frac{\partial\left(\theta_l s_i \delta V\right)}{\partial t} = -\delta V \nabla \cdot \left(c_d^i \mathbf{v_l} - \sum_{j=1}^{nc} D_{ij} \nabla c_d^j - \mathbf{D}_m \nabla c_d^i \right) \tag{3}$$

where, c_d^i denotes the concentration of the i^{th} chemical component, dissolved in liquid phase. s_i is a geochemical sink/source term which stands for the amount of the i^{th} chemical component which is produced or depleted due to geochemical reactions. D_{ij} is the effective diffusion coefficient of the i^{th} chemical due to the chemical gradient of the j^{th} component and $\mathbf{D}_m$ is the matrix of the effective dispersion coefficients.

Similarly, the formulation for the reactive transport of chemicals in gas phase is expressed as [5, 6]:

$$\frac{\partial\left(\theta_g c_g^i \delta V\right)}{\partial t} + \frac{\partial\left(\theta_g s_i \delta V\right)}{\partial t} = -\delta V \nabla \cdot \left(c_g^i \mathbf{v_g} - \sum_{j=1}^{nc} D_{ij} \nabla c_g^i \right) \tag{4}$$

where, c_g^i denotes the concentration of the i^{th} chemical component which exist in the gas phase.

The expanded form of the governing equation of each flow process, i.e. thermal, hydraulic and chemical is expressed in a general and coupled form as:

$$\begin{aligned} &C_{\alpha l} \frac{\partial u_l}{\partial t} + C_{\alpha T} \frac{\partial T}{\partial t} + C_{\alpha a} \frac{\partial u_a}{\partial t} + \sum_{j=1}^{nc_d} C_{\alpha c_d^j} \frac{\partial c_d^j}{\partial t} + \sum_{k=1}^{nc_g} C_{\alpha c_g^j} \frac{\partial c_g^k}{\partial t} + C_{\alpha \mathbf{u}} \frac{\partial \mathbf{u}}{\partial t} = \\ &\nabla \cdot \left[K_{\alpha l} \nabla u_l\right] + \nabla \cdot \left[K_{\alpha T} \nabla T\right] + \nabla \cdot \left[K_{\alpha a} \nabla u_a\right] + \nabla \cdot \left[\sum_{j=1}^{nc_d} K_{\alpha c_d^j} \nabla c_d^j\right] + \nabla \cdot \left[\sum_{k=1}^{nc_g} K_{\alpha c_g^j} \nabla c_g^k\right] + J_\alpha \end{aligned} \tag{6}$$

where, C and K terms are the coefficients of each process, i.e. α, due to the coupled potentials. u_l is the pore water pressure and $\mathbf{u}$ represents the displacement matrix. nc_d and nc_g are the number of chemical components in the liquid and gas phases, respectively.

The numerical solution of the highly coupled and non-linear transient formulations presented has been achieved through the application of the finite element and the finite difference methods [1,7]. The Galerkin weighted residual method has been adopted by which the special discretisation is developed. Temporal discretisation is achieved by applying an implicit finite difference algorithm [1,7]. A sequential (time-splitting) approach is employed to solve the chemical transport and reaction equations [2,3]. The geochemical modelling was achieved by coupling an advanced geochemical model into the model [3,4]. High Performance Computation (HPC) version using parallel computing architecture has also been developed for coupled THM behaviour [8]. The

model has been extensively applied to study the coupled behaviour of unsaturated soils, in particular, the behaviour of highly compacted swelling clays in relation to geological disposal of high level radioactive waste [e.g. 9, 10].

In the context of geoenergy applications, theoretical aspects of the model have been further developed. Validation and applications are being pursued to study the coupled phenomena related to ground energy themes described in section 1. Ground behaviour in response to heat extraction is studied via a programme of field scale investigation and numerical modelling [11,12]. In addition, coal behaviour under gas injection and potential of methane extraction has also been studied through experimental and numerical investigations [13,14,15]. Recent modelling and computational developments from the above mentioned programmes are described in the following sections.

3. GROUND SOURCE HEAT – A FIELD SCALE VALIDATION EXERCISE.

The performance and sustainability of ground source heat systems dependents on the ground's thermal behaviour and its response to energy extraction. The behaviour of a horizontal ground source heat system which provides space heating to a domestic property, located in Mid-Wales, UK has been studied [11,12]. The experimental study comprised of a field scale monitoring scheme which has produced a high resolution ground temperature data-set since May 2012 via 112 temperature sensors, i.e. thermistors, buried at various depths and locations at the site. Furthermore datasets representing the soil properties, climatic variables and heat pump behaviour have also been compiled. Figure 2 shows the general layout of the horizontal ground source heat system monitored and the arrangement of the thermistors.

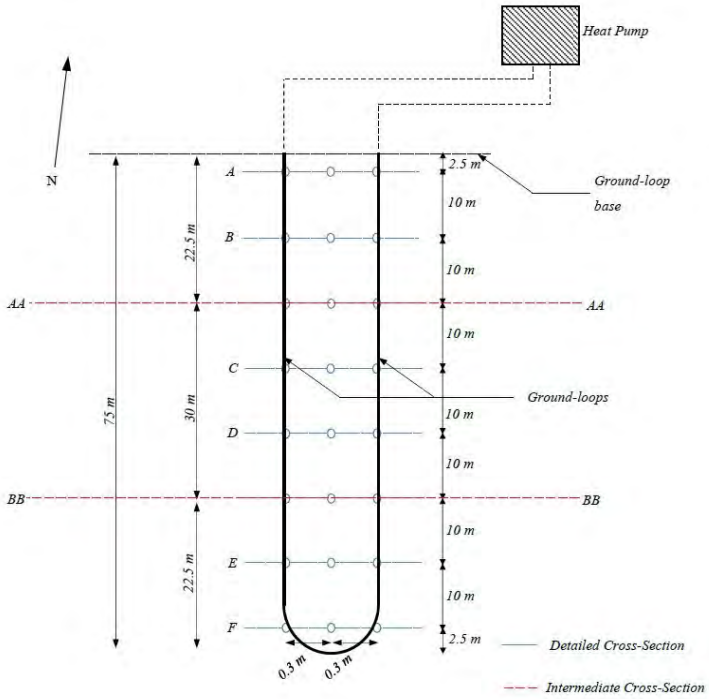

FIGURE 2. Plan schematic of the horizontal ground source heat system monitored and the position of the thermistor installed at the site [12].

The numerical model described above was extended to include the appropriate boundary conditions for the coupled thermo-hydraulic simulation of ground's response to heat extraction. The interactions of the soil with atmosphere, i.e. surface boundary, were included, considering a range of climatic variables and mechanisms. The surface boundary condition developed allows the overall radiant energy being exchanged between an upper layer of the ground surface and atmosphere to be simulated.

The resolution and duration of the collected data-set facilitated extensive analysis and validation, including a thorough investigation of the ground thermal distributions resulting from heat extraction and recharge. The validation exercise was carried out in two stages which included: i) modelling the ground thermal behaviour during the initial period of the instalment when the system was not in use and ii) modelling the ground during the period of heat extraction. The theoretical description of the surface boundary conditions implemented in the model was tested during the first stage of the exercise.

Figures 3 presents two examples of the results obtained from the ground temperature evolution with time, as monitored at the site together with those obtained from the numerical simulation of the period of heat extraction. In general, a good correlation between the modelling results and field data can be observed.

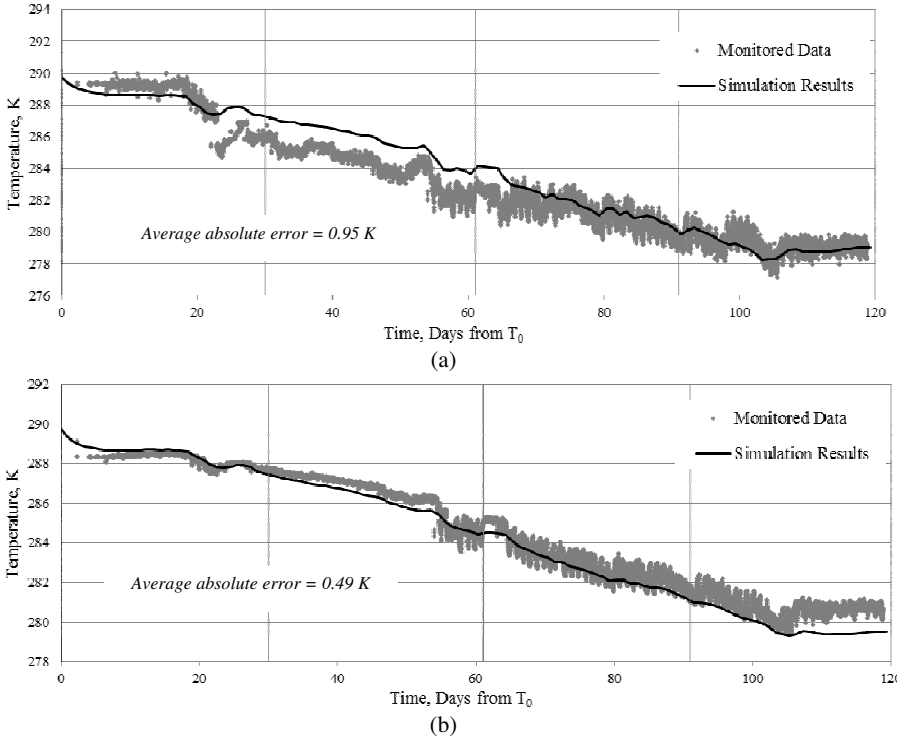

FIGURE 3. Evolution of the ground temperature with time at the depth of 1.9m and distance from the trench centre of approximately 0.37m (a) and 0.55m (b) [11].

4. CARBON SEQUESTATION IN COAL.

A programme of research has been pursued on aspects related to carbon dioxide sequestration in coal. The model described in section 2, has been extended to study the processes involved in high pressure gas injection with coal. In the new model, the coal is described via a dual continuum system, i.e. a dual porosity, dual permeability approach [14]. This approach has been selected as the structure of coal exhibits a non-uniform porosity system which contains a dispersed fracture network and blocks of rock matrix. Figure 4a presents a cross-section of a coal sample showing fractures and a matrix. The idealised system of a dual continuum system considered in the modelling is shown in Figure 4b.

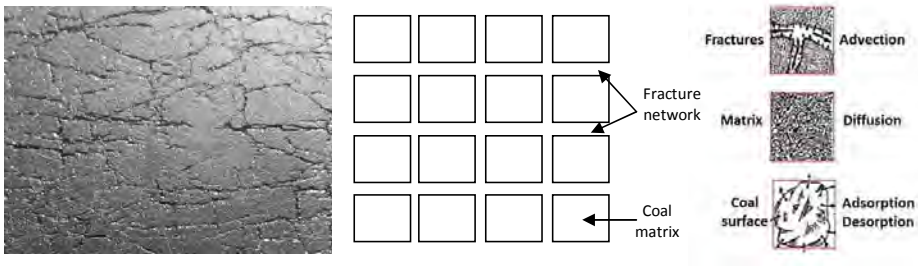

FIGURE 4. (a) A cross section of a coal sample, (b) Schematic of a double porosity system considered for the model development and (c) Major transport mechanisms and reactions in coal.

The dominant transport mechanisms of gas in coal can be described as advection in the fracture domain and reactive diffusion in the matrix (Figure 4c). The properties of gas at high pressure can have a significant impact on the transport/interaction behaviour, e.g. the effects of the phase change of carbon dioxide to supercritical state at high pressure. The major properties of a gas species and gas mixtures are highly dependent on pressure, temperature and composition. These have been incorporated in the constitutive relationships of the transport model [14, 15]. The key gas properties included in the formulation are i) non-ideal bulk gas compressibility, ii) bulk gas viscosity and iii) diffusivity of gas species. The non-ideal behaviour of the gas phase was included using an appropriate equation of state (EoS) which provides a relationship between pressure, volume and temperature.

Experimental results indicate that coal exhibits a higher affinity to carbon dioxide than to methane and nitrogen [14]. In addition, adsorption of carbon dioxide has been found to induce considerable matrix swelling. This in fact affects the flow regime for the gas. This effect can be observed from the permeability evolutions of coal samples, from experimental research, as shown in Figure 5 [13]. The permeability of coal to N_2 increases as the increase as the gas pressure increases which can be related to changes in the effective stress and cleat porosity. However, the permeability of coal to carbon dioxide shows a gradual decrease with injection pressure which is due to the adsorption of carbon dioxide into the coal matrix and consequent swelling.

A schematic of the matrix porosity evolution when nitrogen and carbon dioxide is injected into coal is presented in Figure 6a and 6b, respectively. The interaction of the gas with the coal matrix and the effects of porosity/permeability changes impose additional complexity therefore to the modelling of processes. Such deformation which is caused by chemical interactions and its effect on flow behaviour in the model have been included in the model via a porosity/permeability feedback from physical and chemical interactions between gases and coal.

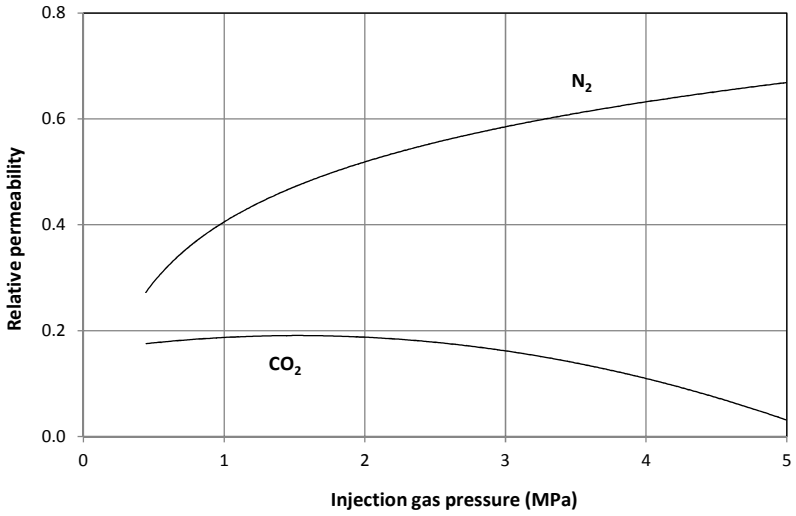

FIGURE 5. Relative permeability of coal to N_2 and CO_2 at different gas injection pressures [14].

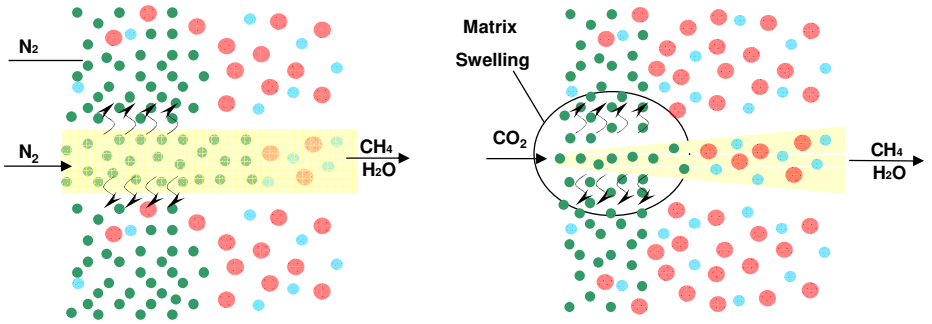

(a) CH_4 recovery with N_2 injection (b) CH_4 recovery with CO_2 injection

FIGURE 6. Schematics of injecting N_2 (a) and CO_2 (b) into the coal in which the matrix swelling due to the adsorption of carbon dioxide is also shown.

The model developed has been used to study the injection of a mixture of 80% CO_2 and 20% N_2 into coal. The mixed gas was injected at 8 MPa into a 100m coal domain with unit surface area. The coal is initially saturated with CH_4 with an initial pressure of 3MPa. Matrix deformation due to sorption of gas was included via a Langmuir type strain curve. Using this approach an implicit geomechanical model was applied that describes the evolution of porosity and permeability during coal-matrix deformation. Figure 7 shows the gas composition profiles at the end of the simulation period for the injection of the binary CO_2:N_2 mixture.

The nature of in situ gas replacement by gas injected at high pressure is strongly affected by the adsorption/desorption characteristics of the components involved. More strongly adsorbing components fully displace in situ gas with a sharp injection front and little mixing. Less strongly adsorbing components produce a smoother injection front with significant mixing [15].

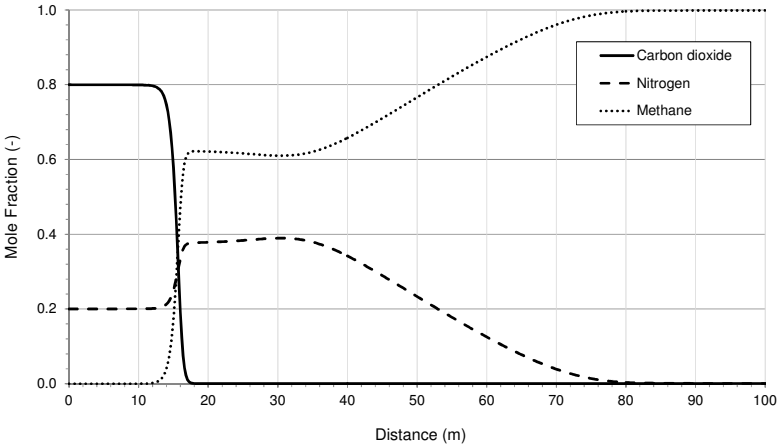

FIGURE 7. Gas profiles after 16 days of simulation for the replacement of CH_4 with a gas mixture consisting of 80% CO_2 and 20% N_2 [15].

5. CONCLUSIONS

A model developed using a coupled thermal, hydraulic, chemical and mechanical formulation has been used to study some aspects of energy extraction from the ground. An example of model validation is provided for ground source heat technology. The work presented is one of only a few tests at this scale and duration. The results provided an improved insight into the performance of the system and the sustainably of heat extraction.

Experience in modelling the coupled processes involved in carbon sequestration in coal has been presented. Chemical aspects of gas interactions with coal and the effects on the flow regime of the gas are important components when modelling carbon sequestration in coal. The developments presented here provide advanced capabilities to simulate processes related to some emerging deep geoenergy applications.

AKNOWLEDGMENT

Mr Benjamin D. Hepburn, Mr Lee J. Hosking and Mrs Mojgan Hadi Mosleh are currently pursuing PhD programmes in this area. Financial support received by the Welsh European Funding Office (WEFO) for this purpose is gratefully acknowledged.

REFERENCES

[1] H.R. Thomas and Y. He, Analysis of coupled heat, moisture and air transfer in a deformable unsaturated soil. *Géotechnique*, 45(4), 677-689, 1995.

[2] S.C. Seetharam, H.R. Thomas and P.J. Cleall, Coupled thermo/hydro/chemical/mechanical model for unsaturated soils-numerical algorithm, *International Journal of Numerical Methods in Engineering*, 70 (12), 1480-1511, 2007.

[3] H.R. Thomas, M. Sedighi, and P.J. Vardon, Diffusive reactive transport of multicomponent chemicals under coupled thermal, hydraulic, chemical and mechanical conditions, *Geotechnical and Geological Engineering*, 30(4), 841-857, 2012.

[4] M. Sedighi, H.R. Thomas, P.J. Vardon and S.C. Seetharam, *Advances in modelling the non-isothermal behaviour of multicomponent chemicals in unsaturated soils*, Proceedings of the 6th International Congress Environmental Geotechnics (6ICEG), 1619-1622, 2010.

[5] S.A. Masum, P.J. Vardon, H.R. Thomas, Q. Chen, and D. Nicholso, Multicomponent gas flow through compacted clay buffer in a higher activity radioactive waste disposal facility, *Mineralogical Magazine*, 75 (8), 3337-3344, 2012.

[6] H.R. Thomas, M. Sedighi, S.A. Masum, P.J. Vardon, D. Nicolson, A. Chen, *Gas-flow/geochemistry interactions in unsaturated bentonite buffer*, Gas Generation and Migration, FORGE Symposium, 109-112, 2013.

[7] H.R. Thomas, Y. He and C. Onofrei, An examination of the validation of a model of the hydro/thermo/mechanical behaviour of engineered clay barriers, *International Journal of Numerical and Analytical Methods in Geomechanics*, 22(1), 49-71, 1998.

[8] P.J. Vardon, P.J. Cleall, H.R. Thomas, R.N. Philp and I. Banicescu, Three-dimensional field-scale coupled thermo-hydro-mechanical modeling: Parallel computing implementation, *International Journal of Geomechanics*, 11(2), 90-98, 2010.

[9] H.R. Thomas, P.J. Cleall, N. Chandler, D. Dixon and H.P. Mitchell, Water infiltration into a large-scale in-situ experiment in an underground research laboratory. *Géotechnique*, 53(2), 207-224, 2003.

[10] H.R. Thomas and M. Sedighi, *Modelling the engineering behaviour of highly swelling clays*, Keynote Paper, Proceeding of the 4th International Conference on Problematic Soils, 21-33, 2012.

[11] B.D.P. Hepburn, *An investigation of the behaviour of the ground in response to energy extraction*. PhD Thesis, Cardiff University, 2014 (Submitted).

[12] H.R. Thomas, B.D.P. Hepburn and M. Sedighi, Soil thermal behaviour of a horizontal ground source heat system, *Coupled Phenomena in Environmental Geotechnics (Manassero et al. Eds)*, 525-530, 2013.

[13] M. Hadi Mosleh, *An investigation of gas transport and reactions in coal*, PhD Thesis, Cardiff University, Cardiff, 2014 (In preparation).

[14] L.J. Hosking, *On the reactive transport of gases in fractured rock under coupled physical and chemicals effects*, PhD Thesis, Cardiff University, Cardiff, 2014 (In preparation).

[15] L.J. Hosking, M. Sedighi, H.R. Thomas, *High pressure gas transport under coupled thermal, hydraulic, chemical and mechanical behaviour*, Proceeding of the 3rd International Symposium in Computational Geomechanics (COMGEOIII), 381-388, 2013.

Third International Conference on Computational Methods for Thermal Problems
THERMACOMP2014, June 2-4, 2014, Lake Bled, Slovenia
N. Massarotti, P. Nithiarasu, B. Sarler (Eds.)

Fast local transient thermal analysis of Fourier and non-Fourier heat conduction using AWE

K N Seetharamu

Department of Mechanical Engineering, PES University, Bangalore 560085. INDIA
(Formerly Professor of Mechanical Engineering, IIT, Madras)

Key Words: *Asymptotic waveform evaluation (AWE); Fourier; Non-Fourier; Transient; Conduction; Local.*

ABSTRACT

Implementation of Finite Element Method (FEM) in transient thermal analysis usually will produce a formulation in space/time domain. This kind of space/time domain formulation leads to a set of ordinary differential equation and have to be solved in the time domain. But, the size of the equations or matrices in FEM usually are large, thus the conventional algorithms involve considerable computational time. The conventional methods have to take a very small time step size to avoid undesirable numerically induced oscillations or numerical instabilities.

In this lecture, asymptotic waveform evaluation (AWE) has been successfully used for fast transient solution of Fourier and non-Fourier heat conduction. The Fourier and non-Fourier equations are reduced to a system of linear differential equations ,using finite element method and then solved with AWE. Besides providing equivalent accuracy in its solution, it is also shown that AWE is at least three orders faster in term of computational time as compared to conventional solvers. Its accuracy is also independent of the time step used and it has the capability of providing local transient solution. However, the moment matching processin AWE is inherently ill-conditioned and thus may yield unstable response even for stable system. This numerical instability is addressedand two stability schemes are also successfully implemented to yield stable and accurate solutions from AWE. The limitation of AWE is also discussed. Some of the applications of this method are illustrated in Microchannels, Heat Exchangers etc.

1. INTRODUCTION

Asymptotic waveform evaluation (AWE), which has been used for fast transient circuit simulation, is based on the concept of approximating the original system with a reduced order system. The inspiration of AWE came from Rubinstein et al. [1], where RC-tree networks were estimated using efficient Elmore delay approach. However, these estimates were not always accurate. A second break- through came from the work of McCormick [2], in which he has used the interconnect circuit moments to form a lower order circuit models to predict transient responses accurately. The efforts of these authors lead to the formalization and generalization of AWE algorithms [3, 4].

For more than a decade, extensive works on AWE has been carried out. AWE has been successfully applied or fast transient circuit simulation [5–7]. AWE also has a lot of successes in electromagnetic simulations. However, there are only two papers available on the application of AWE in transient thermal simulation. Da et al. [8] have published the first paper on thermal analysis of PCB using AWE scheme, but the details of incorporating the initial conditions were not addressed. Then, Ooi et al. [9] has success- fully extended the AWE algorithm to incorporate the initial conditions. They created a generalized formulation using the concept of zero state response and zero input response,

which is used in control system. However, Ooi et al. [9] did not address the inherent numerical instability of AWE, which may yield incorrect solutions. Both papers also only focused on solving Fourier heat conduction equation with AWE. On the other hand, finite element method (FEM) has been extensively used to solve hermal problems because it is capable to account for complicated three-dimensional geometry. Besides that, the governing equations for Fourier and non-Fourier heat conduction are also parabolic and hyperbolic in nature, respectively, and they are difficult to be solved analytically. Using FEM, the transient heat conduction equation (partial differential equation) is reduced to a set of linear differential equations through the process of discretization. This set of differential equations can then be solved in time domain to obtain its transient solution.

Usually, this set of equations is solved using conventional iterative solvers such as Crank–Nicolson, Runge–Kutta and the famous Newmark algorithm. These conventional numerical solvers require the whole set of equations to be solved at each increment of time step, even though only the solution at a particular node is of interest. Solving this large set of equations is very time consuming, especially when the time step required is also very small in order to yield accurate solutions. In contrast, AWE is actually approximating the original system with reduced order system and thus, it is a few orders faster than conventional iterative solvers in term of computational time. It is also independent of time step because it produces the transient solutions in a form of equation, rather than numerical solutions at every increment of time step. AWE is also capable of producing local solution because it can obtain the solution for each node independently and thus further reducing the amount of computational time. However, the drawback of AWE is that the moment matching process in AWE is inherently ill-conditioned and thus may produce unstable response even for stable system [10]. Higher order approximation will lead to a more accurate solution but not always guarantee a stable solution.

In this work, FEM is coupled with AWE to efficiently solve the transient Fourier and non-Fourier heat conduction equations. FEM is used to reduce the Fourier (parabolic) and non-Fourier (hyperbolic) equations to a set of first and second order linear differential equations, respectively. AWE is then used to obtain the transient solutions instead of using conventional iterative solvers. The inherent instability of AWE is also addressed and two stability schemes are also introduced to yield accurate and yet stable solution even using higher order approximation. In recent times, surgeons would like to have the effect of some parameters during the operation processes like the prostate cancer and modify the parameters to avoid damage to healthy tissues. This needs fast transient solutions.

2. MATHEMATICAL MODEL FOR FOURIER AND NON-FOURIER HEAT CONDUCTION

Classical Fourier's law is based on diffusion model with assumption of infinite thermal wave propagation speed, which leads to simultaneous development of heat flux and temperature gradient. Classical Fourier's law also assumes that instantaneous local thermal equilibrium occurs between electrons and phonons. In other words, classical Fourier's law dictates that the thermal effect is felt instantaneously throughout the system if the surface of a material is heated. The governing equation for non-dimensionlized two-dimensional Fourier heat conduction is a parabolic equation as shown by Eq. (1).

$$\frac{\partial^2\theta}{\partial\delta^2}+\frac{\partial^2\theta}{\partial\varepsilon^2}=\frac{\partial\theta}{\partial\beta} \tag{1}$$

where h is the dimensionless temperature and b is the dimensionless time. The dimensionless distance x and y are represented by d and e, respectively. After discretization Eq. (1) with

Galerkin's weighted residual method, a set of first order linear differential equations is obtained as given by Eq. (2). The detailed formulations of Eq. (2) can be obtained from Logan [11].

$$C\dot{\theta} + K\theta = f \tag{2}$$

where C is known as the capacitive matrix, while K is the conductivity matrix. f represents the load vector, which can be time-dependent or time-independent.

Classical Fourier law is sufficient for most heat conduction phenomena, but it is inadequate to describe rapid heating response, such as VLSI interconnection heating. Thus, many non-Fourier heat conduction equations are proposed by many researchers to account for the finite thermal wave propagation speed and/or finite relaxation time to establish local thermal equilibrium between electrons and phonons. The non-Fourier model discussed in this paper is a two-phase lag model proposed by Tzou [12]. Cheah et al. [13] has generalized it into a non-dimensionlized two-dimensional hyperbolic equation given by sT is the phase lag of spatial temperature gradient with respect to the local temperature (to account for finite relaxation time for electron–phonon equilibrium), while sq is the phase lag of heat flux with respect to the local temperature (to account for finite thermal wave speed). The dimensionless variables for these phase lags are represented by ZT and Zq, respectively. The length and width are given by l and h, respectively, whereas a is the thermal diffusivity. Cheah et al. [13] has also discretized Eq. (3)

$$\frac{\partial^2\theta}{\partial\delta^2} + \frac{\partial^2\theta}{\partial\varepsilon^2} + Z_T\frac{\partial^3\theta}{\partial\beta\partial\delta^2} + Z_T\frac{\partial^3\theta}{\partial\beta\partial\varepsilon^2} = \frac{\partial\theta}{\partial\beta} + Z_q\frac{\partial^2\theta}{\partial\beta^2} \tag{3}$$

where

$$\theta = \frac{T - T_o}{T_w - T_o}, \quad \beta = \frac{t}{l^2/\alpha}, \quad \delta = \frac{x}{l}, \quad \varepsilon = \frac{y}{h},$$

$$Z_T = \frac{\tau_T}{l^2/\alpha} \quad \text{and} \quad Z_q = \frac{\tau_q}{l^2/\alpha}$$

using Galerkin's weighted residual method to form a set of second order linear differential equations, as shown by Eq. (4).

τ_T is the phase lag of spatial temperature gradient with respect to the local temperature (to account for finite relaxation time for electron–phonon equilibrium), while sq is the phase lag of heat flux with respect to the local temperature (to account for finite thermal wave speed). The dimensionless variables for these phase lags are represented by ZT and Zq, respectively. The length and width are given by l and h, respectively, whereas a is the thermal diffusivity.

Cheah et al. [13] has also discretized Eq. (3) using Galerkin's weighted residual method to form a set of second order linear differential equations, as shown by Eq. (4).

Where,

$$A_{\text{element}} = \frac{Z_q\bar{A}}{12}\begin{bmatrix} 2 & 1 & 1 \\ 1 & 2 & 1 \\ 1 & 1 & 2 \end{bmatrix}$$

$$C_{\text{element}} = \frac{\bar{A}}{12}\begin{bmatrix} 2 & 1 & 1 \\ 1 & 2 & 1 \\ 1 & 1 & 2 \end{bmatrix} + \frac{Z_T}{4\bar{A}}\left\{\begin{bmatrix} b_i^2 & b_ib_j & b_ib_k \\ b_jb_i & b_j^2 & b_jb_k \\ b_kb_i & b_kb_j & b_k^2 \end{bmatrix} + \begin{bmatrix} c_i^2 & c_ic_j & c_ic_k \\ c_jc_i & c_j^2 & c_jc_k \\ c_kc_i & c_kc_j & c_k^2 \end{bmatrix}\right\} \tag{4}$$

$$K_{\text{element}} = \frac{1}{4\bar{A}}\left\{\begin{bmatrix} b_i^2 & b_ib_j & b_ib_k \\ b_jb_i & b_j^2 & b_jb_k \\ b_kb_i & b_kb_j & b_k^2 \end{bmatrix} + \begin{bmatrix} c_i^2 & c_ic_j & c_ic_k \\ c_jc_i & c_j^2 & c_jc_k \\ c_kc_i & c_kc_j & c_k^2 \end{bmatrix}\right\}$$

3. THE AWE ALGORITHM

The concept of AWE is to approximate the original response of a system with a reduced order system. Fig. 1 shows the flow of AWE algorithm, which can be categorized into three major steps. The response of a system can be represented by a polynomial equation in s-domain, where the coefficients of this polynomial are known as the moments [2, 3]. In moment generation, the moments are determined for zero state response (ZSR) and zero input response (ZSR). The concept of ZSR and ZIR is used by Ooi et al. [9] to account for the boundary and initial conditions, respectively. In ZSR, the initial conditions of the system are assumed to be zero, while the forcing functions are assumed to be zero in ZIR. In moment matching, the order

of the system response is reduced using Pade approximation, and then further simplified to a set of partial fractions, where each partial fraction contains a pole and also a zero. Finally, each partial fraction is inversed Laplace back to time domain and summed up to provide the transient solution.

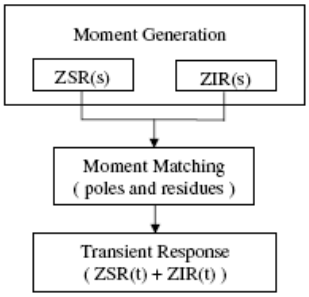

Fig. 1 Flow of AWE algorithm.

3.1. First order differential equation

As discussed in Section 2, parabolic heat conduction equation can be discretized into a set of first order linear differential equations using Galerkin's weighted residual method.

Where,
$$C\dot{T} + KT = F(t) \tag{5}$$

$$C \in R^{N\times N},\ K \in R^{N\times N} \text{ and } F(t) \in R^{N}$$

Taking Laplace transform of Eq. (5),

$$C(sT(s) - T(0)) + KT(s) = f \tag{6}$$

The system solution, T(s) can be approximated by using polynomial equation in s-domain, as given by Eq. (7)

$$T(s) = \sum_{n=0}^{\infty} M_n s^n \tag{7}$$

The moments, Mn, are the coefficients of Taylor series expansion about s = 0 (Maclaurin series) [2–4]. Moments are generated, respectively, for ZSR and ZIR by substituting Eq. (7) into Eq. (6) as following.

3.1.1. Zero state response (ZSR)

In ZSR, the initial condition is assumed to be zero, T (0) = 0.

$$(Cs+K)(M_0+M_1s+M_2s^2+\cdots+M_ns^n)=f \tag{8}$$

By equating the same powers of s, the moments are generated from Eq. (9).

$$\begin{aligned} KM_0 &= f \\ KM_n &= -CM_{n-1} \quad \text{for } n=1,2,3,\ldots,(2q-1) \end{aligned} \tag{9}$$

where q = order of Pade´ approximation

3.1.2. Zero input response (ZIR)

In ZIR, the forcing function is assumed to be zero, f = 0.

$$(Cs+K)(M_0+M_1s+M_2s^2+\cdots\cdots+M_ns^n)=CT(0) \tag{10}$$

Again by equating the same powers of s, the moments are generated from Eq. (11).

$$\begin{aligned} KM_0 &= CT(0) \\ KM_n &= -CM_{n-1} \quad \text{for } n=1,2,3,\ldots,(2q-1) \end{aligned} \tag{11}$$

3.2. Second order differential equation

For hyperbolic heat conduction equation as shown by Eq. (3), it can be reduced to a set of second order differential equations using Galerkin's weighted residual method [13, 14].

$$A\ddot{T}+C\dot{T}+KT=F(t)$$

Where, $A\in R^{N\times N}$, $C\in R^{N\times N}$, $K\in R^{N\times N}$ and $F(t)\in R^N$.

Following the formulation above, the moments for ZSR and ZIR can be obtained from Eqs. (12) and (13), respectively.

3.2.1. Zero state response (ZSR)

$$\begin{aligned} KM_0 &= f \\ KM_1 &= -CM_0 \\ KM_n &= -(AM_{n-2}+CM_{n-1}) \quad \text{for } n=2,3,4,\ldots\ldots,(2q-1) \end{aligned} \tag{12}$$

3.2.2. Zero input response (ZIR)

$$\begin{aligned} KM_0 &= CT(0)+A\dot{T}(0) \\ KM_1 &= AT(0)-CM_0 \\ KM_n &= -(AM_{n-2}+CM_{n-1}) \quad \text{for } n=2,3,4,\ldots\ldots,(2q-1) \end{aligned} \tag{13}$$

3.3. Moment matching

In moment matching, only the moments for an arbitrary node of interest, i are used for computing its local transient response. This further reduces the computational time, in contrast to conventional iterative solver which requires computing the solutions of all the nodes at all time. The nodal moments of interest, [m], are extracted from global moment matrix, [M] as shown by Eq. (14).

$$[m_n]_i = [M_n]_i \quad \text{for } n = 0, 1, 2, \ldots, (2q-1) \tag{14}$$

$$\begin{aligned} T_i(s) &= m_0 + m_1 s + m_2 s^2 + \cdots + m_n s^n \\ &= \frac{b_0 + b_1 s + \cdots + b_{q-1} s^{q-1}}{1 + a_1 s + \cdots + a_q s^q} \end{aligned} \tag{15}$$

$$\frac{b_0 + b_1 s + \cdots + b_{q-1} s^{q-1}}{1 + a_1 s + \cdots + a_q s^q} = \frac{k_1}{s - p_1} + \frac{k_2}{s - p_2} + \cdots + \frac{k_q}{s - p_q} \tag{16}$$

The transient response at an arbitrary node of interest, I can be approximated by a lower order polynomial fraction using Pade´ approximation as shown in Eq. (15) and can be further simplified to partial fractions as given by Eq. (16).

The poles and residues of the respective partial fractions can be obtained by solving Eqs. (17)-(19) [3, 9].

$$\begin{bmatrix} m_0 & m_1 & m_2 & \cdot & m_{q-1} \\ m_1 & m_2 & m_3 & \cdot & m_q \\ m_2 & m_3 & m_4 & \cdot & m_{q+1} \\ \cdot & \cdot & \cdot & \cdot & \cdot \\ m_{q-1} & \cdot & \cdot & \cdot & m_{2q-2} \end{bmatrix} \begin{Bmatrix} a_q \\ a_{q-1} \\ a_{q-2} \\ \cdot \\ a_1 \end{Bmatrix} = \begin{Bmatrix} -m_q \\ -m_{q+1} \\ -m_{q+2} \\ \cdot \\ -m_{2q-1} \end{Bmatrix} \tag{17}$$

$$\sum_{j=1}^{q} (a_j p^j) + 1 = 0 \tag{18}$$

$$\begin{bmatrix} p_1^{-1} & p_2^{-1} & p_3^{-1} & \cdot & p_q^{-1} \\ p_1^{-2} & p_2^{-2} & p_3^{-2} & \cdot & p_q^{-2} \\ p_1^{-3} & p_2^{-3} & p_3^{-3} & \cdot & p_q^{-3} \\ \cdot & \cdot & \cdot & \cdot & \cdot \\ p_1^{-q} & p_2^{-q} & p_3^{-q} & \cdot & p_q^{-q} \end{bmatrix} \begin{Bmatrix} k_1 \\ k_2 \\ k_3 \\ \cdot \\ k_q \end{Bmatrix} = \begin{Bmatrix} -m_0 \\ -m_1 \\ -m_2 \\ \cdot \\ -m_{q-1} \end{Bmatrix} \tag{19}$$

3.4. Transient response

The transient response at an arbitrary node, i is given by the sum of ZSR and ZIR in time domain

$$T_i(t) = \mathrm{ZSR}(t) + \mathrm{ZIR}(t) \tag{20}$$

Where,

$$\mathrm{ZSR}(t) = \sum_{r=1}^{q} \frac{k_r}{p_r} (e^{p_r t} - 1) \tag{21}$$

$$\mathrm{ZIR}(t) = \sum_{r=1}^{q} k_r (e^{p_r t} - 1) \tag{22}$$

4. UNSTABLE SOLUTIONS AND STABILITY SCHEMES

4.1. Inherent instability of AWE in Fourier heat conduction

The moment matching process in AWE is inherently ill conditioned because Pade´ approximation is well-known for yielding unstable poles [10]. In the scope of finite element analysis, AWE can produce correct solutions for most of the nodes, but may yield incorrect solutions for some arbitrary nodes. A one-dimensional transient Fourier heat conduction example

from Logan [11] is taken as case study. Using finite element method (FEM), it is discretized into 19 line elements (20 nodes) as shown in Fig. 2 and subjected to higher step temperature at the base as boundary condition. Solutions from AWE and also Crank–Nicolson (conventional iterative solver) agree well for all the nodes, except for nodes 6, 7, 14 and 15. This is because Pade´ approximation is known for producing unstable response even for stable system [15, 16].

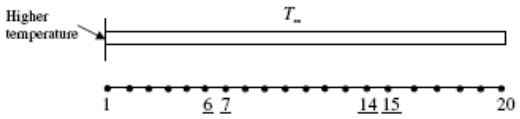

Fig. 2 Example from Logan [11] and its finite element representation.

To further elaborate the weakness of Pade´ approximation, consider a stable system, H(s), with two negative value poles and it is to be approximated by a one pole system, G(s) using Pade´ approximation, as follows:

$$H(s) = \frac{k_1}{s - p_1} + \frac{k_2}{s - p_2} \quad \text{and} \quad G(s) = \frac{\bar{k}}{s - \bar{p}} \tag{23}$$

With some mathematical manipulation, it can be shown that are related to the original poles and residues by Eq. (24) [17]. has to be a negative value left-half plane pole in order to have a stable reduced order system, G(s). However, as per Eq. (24), can still be rendered to become a positive value right-half plane pole depending on the values of the residues (k1 and k2), even though both p1 and p2 are negative value left-half plane poles. The process of yielding undesirable positive poles is random, but it can be overcome by using the stability schemes as will be discussed in Sections 4.2 and 4.4 below.

$$\bar{p} = \frac{\frac{k_1}{p_1} + \frac{k_2}{p_2}}{\frac{k_1}{p_1^2} + \frac{k_2}{p_2^2}} \tag{24}$$

4.2. Stability schemes for Fourier heat conduction

AWE is based on approximating an original system with a reduced order system. So, higher order approximation is vital in ensuring that the exact response is successfully captured by the reduced order system. Besides yielding higher accuracy at the cost of slightly more computational time, higher order approximation is also prone to numerical instability. In most cases, stable and accurate solutions can be obtained by using lower order approximation. It was found that using 4th order Pade´ approximation is sufficient to provide accurate solutions for most Fourier heat conduction problems, and yet minimizing the number of unstable nodal solutions. However, this scheme may not always guarantee that the solutions are both stable and accurate for all the nodes, as in this case.

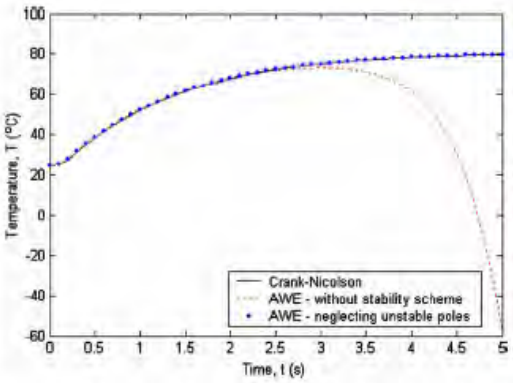

Fig. 3. Comparison between Crank–Nicolson and AWE (before and after applying stability scheme) solutions at node 14.

Fig. 3 shows that the AWE solution at node 14 starts to diverge from the Crank–Nicolson solution after 2.5 s. The divergence is due to unstable positive real poles. It is well known in linear feedback control system that a system becomes unstable if any of the poles fall on the right-hand side of s-plane. Mathematically, poles with real positive value will cause magnitude of ZSR or ZIR to become very large over time, and thus causing the solution to differ greatly from the correct response.

As given by Eqs. (21) and (22), ZSR and ZIR consist of the e^{pt} term. If any of the pole, p, has only real positive value, then the system response will be unable to converge to a steady-state solution. Instead, it will keep on increasing with time and consequently deviates from the correct transient response. Thus, it is reasonable to just simply neglect these unstable real positive poles [18]. This stability scheme proves to be valid as shown in Fig. 3, where the AWE solution agrees well with Crank–Nicolson solution even after 2.5 s.

4.3. Inherent instability of AWE in non-Fourier heat conduction

AWE is extended to model the transient non-Fourier heat conduction of two-dimensional slab subjected to instantaneous temperature rise on one edge [13], as shown in Fig. 4. The dimensionless parameters used are d = e = 1(size) and Zq = 0.05. ZT is taken at three different values, which are 0.5 (over-diffusion), 0.05 (diffusion) and 0.0001(wave-like). Without implementing any stability scheme, some arbitrary nodes are expected to have positive real poles and the solutions at these nodes are going to be unstable and incorrect. As explained above, the generation of unstable positive real poles is due to the inherently ill conditioned moment matching process in AWE.

In this case, higher order approximation is also more prone to yielding unstable response, whereas lower order approximation will reduce the number of nodes with unstable response. Similar to Fourier heat conduction problems, it was found that 4th order Pade´ approximation is best at yielding sufficiently accurate solutions with minimum number of nodes with unstable response for most non-Fourier heat conduction problems.

However, AWE does not produce reasonable solutions for the case with ZT = 0.0001 using this stability scheme.

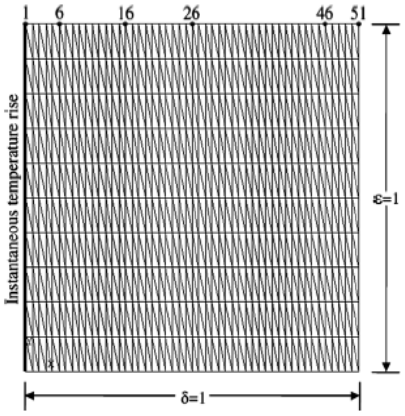

Fig. 4 2-D slab subjected to instantaneous temperature rise on left edge.

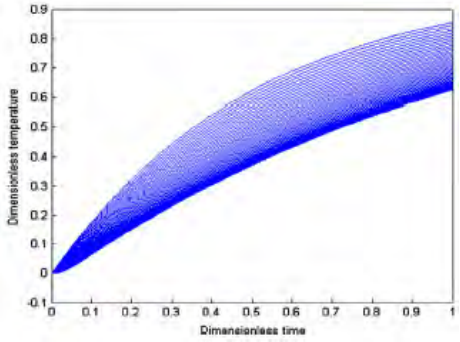

Fig. 5 Dimensionless temperature distribution along the top edge of slab at ZT = 0.0001 after applying partial Pade´ approximation.

4.4. Stability schemes for non-Fourier heat conduction

The response of Fourier heat conduction has been successfully stabilized by neglecting the unstable real positive poles, as discussed in Section 4.2. Thus, this stability scheme is also implemented for two-dimensional non-Fourier heat conduction, in an attempt to stabilize all the temperature responses. The stabilized temperature responses for nodes along the top edge of the slab (from node 2 to node 51 as shown by Fig. 4) are plotted on Figs. 5–7 for three different values of ZT, respectively. Figs. 5 and 6 do not show any unstable response along the slab, which indicates that this stability scheme has worked well for cases with ZT = 0.5 and ZT = 0.05.

However, AWE does not produce reasonable solutions for the case with ZT = 0.0001 using this stability scheme.

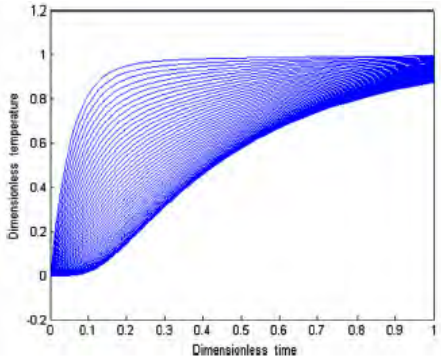

Fig. 6 Dimensionless temperature distribution along the top edge of slab at ZT = 0.05.

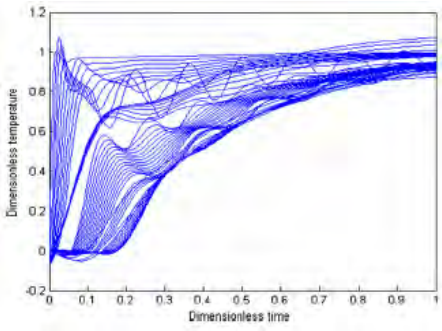

Fig. 7 Dimensionless temperature distribution along the top edge of slab at ZT = 0.0001.

There is no smooth and continuous trend for the nodal responses along the top edge of slab, and the solutions at some nodes are also fluctuating incorrectly as shown in Fig. 7. The applied stability scheme does manage to suppress all unstable poles because there will be responses with very large magnitude if unstable poles exist. Yet, AWE solutions are still incorrect at some nodes because AWE fails to actually approximate the high frequency responses for nodes adjacent to the instantaneous temperature rise boundary condition, and thus causing the approximations for other nodes to deviate from the actual responses as well. In other words, AWE is incapable to fully represent the steep responses at some nodes since it is making use of only exponential terms (as shown by Eqs. (21) and (22)) to make approximation of the original response. Thus, this failure also renders the solutions at other nodes to be incorrect as well.

In addition, partial Pade´ approximation [15, 16] is also introduced to stabilize the AWE solutions for the case ZT = 0.0001. In this stability scheme, the set of poles at an arbitrarily chosen node is used to approximate the responses of other nodes. In other words, this means that only the set of poles at an arbitrarily chosen node is calculated and it is used throughout the calculations of ZSR and ZIR for all other nodes. Usually, the node selected to approximate other nodes has high frequency response, and definitely it has to be stable. Therefore, it will eliminate the need to monitor the stability at every node.

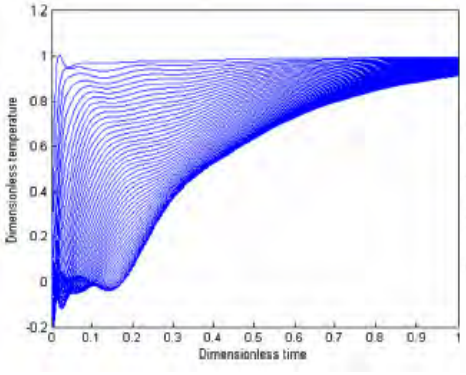

Fig.8 Dimensionless temperature distribution along the top edge of slab at Z_T = 0.0001 after applying partial Pade´ approximation.

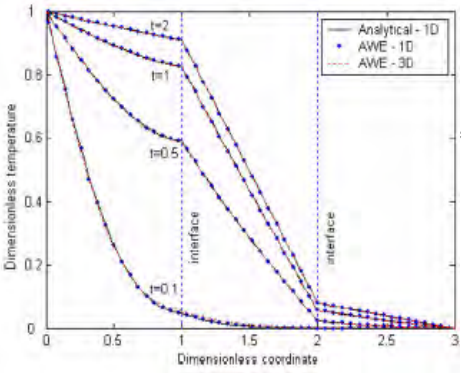

Fig. 9 Comparison between AWE and Eigen-function expansion method for dimensionless temperature across the layers at different dimensionless time.

In this case, the node closest to the temperature load is chosen to approximate the temperature rise for other nodes along the top edge of slab, and only the poles at this chosen node are calculated. This node is chosen because it has the fastest temperature rise, or in other words, the response at this node is of high frequency. The temperature responses for nodes along the top edge of the slab are plotted on Fig. 8. There is no unreasonable solution as compared to the former stability scheme because the poles used are selected from a chosen node, which is stable and also representing the correct response. This eliminates the generation of incorrect poles at some nodes (when using former stability scheme), which may renders the solutions to be incorrect. One way to determine a suitable node is to check the responses by using former stability scheme before applying partial Pade´ approximation. The accuracy of this scheme will be discussed in Section 5.2.

5. PERFORMANCE OF AWE WITH STABILITY SCHEMES

5.1. Fourier heat conduction

Analytical solution is always more preferred because it provides an algebraic relationship equation that will generate solutions instantaneously, just by inputting the related parameter values. However, analytical method may not be viable for problems involving complex geometry and in most cases; it will also involve complicated mathematical derivations to arrive at the solution. One example is the eigenfunction expansion method, which has been used to solve the transient heat conduction for a one-dimensional three layers composite slab [19]. This method involves complicated mathematical derivations and also requires Newton iterative procedure to solve a non-linear equation for obtaining the eigenvalues. When more parameters (more layers) are involved, the eigenvalues become more difficult to obtain as the nonlinear equation becomes more complicated to be solved.

In comparison, finite element method (FEM) coupled with AWE as solver can provide accurate solution in a more efficient manner. FEM can be easily implemented to solve one-dimensional thermal problem, and also can be extended to solve two-dimensional or three-dimensional

problems. AWE is also capable of providing the solution in equation form for each node. Besides that, moments in AWE are generated through direct solving of a system of linear equations. This will not be an issue even if the number of equations involved is large [20].

Fig. 9 compares the eigenfunction expansion solution with AWE solution for the one-dimensional three layers composite slab. It shows that AWE solutions are identical to the analytical solutions. In addition, this one-dimensional three layers composite slab is also extended into a three-dimensional problem with cross-sectional area of one and solved using AWE. Fig. 9 shows that there is slight difference between one-dimensional solution and three dimensional solution (nodal temperatures taken across the centers of layers) because in-plane heat conduction effect is not considered in formulation for one-dimensional heat conduction.

5.2. Non-Fourier heat conduction

In Section 4.3, it is shown that both stability schemes are capable to suppress the generation of unstable poles for case ZT = 0.0001. However, only partial Pade´ approximation can yield reasonable responses for all the nodes by using only one set of poles from a stable and reasonable chosen node. In order to check the accuracy, it is compared with Runge-Kutta solutions at node 6, 16, 26 and 46 along the slab. Positions of these nodes on the slab are shown in Fig. 4.

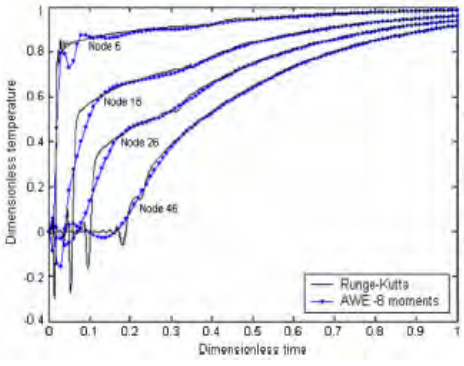

Fig. 10 Comparison between AWE (after applying partial Pade´ approximation) and Runge-Kutta for case ZT = 0.0001.

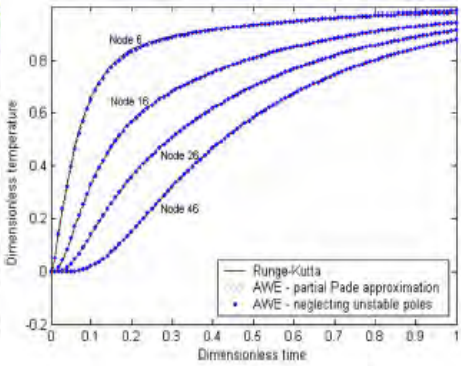

Fig. 11 Comparison between AWE (after applying stability schemes) and Runge-Kutta for case Z_T = 0.05.

Runge-Kutta fourth order method has been used by Cheah et al. [13] to obtain his results. Fig. 10 shows that AWE solutions differ from the Runge–Kutta solutions at the initial time and only agree well approximately after 0.2 dimensionless time. This is expected because the concept of AWE is to extract the dominant poles from the full system [18] and these dominant poles are usually of low frequency. Thus, AWE responses are not able to match the high frequency temperature responses at the initial time for case ZT = 0.0001. In other words, initial steep response cannot be approximated by AWE using exponential terms, as shown in Eq. (21).

In addition, Fig. 10 also shows that AWE is not able to approximate the delay accurately since the response only consists of real and complex conjugate exponentials. This is because, to represent a pure delay, AWE is employing decaying sinusoids to artificially force the response close to zero

for some initial period. This will lead to spurious ringing effects in the AWE waveforms [18] as shown in Fig. 10.

For case ZT = 0.05 and ZT = 0.5, the AWE solutions can be successfully stabilized with both stability schemes, which are neglecting unstable real positive poles and partial Pade´ approximation. For accuracy check, AWE solutions after applying these stability schemes are compared with Runge–Kutta solutions. For case ZT = 0.05, the comparison is shown on Fig. 11, where the results from using both stability schemes agree well with Runge–Kutta solutions, respectively. AWE shows similar accuracy for case ZT = 0.5 as well, but the results are not depicted in this paper.

In term of computational time, AWE only needs 1.2 s for case ZT = 0.0001 while Runge–Kutta requires 31 min even though the same total number of nodes is used. For case ZT = 0.05, AWE can produce the result in less than 1.5 s using both stability schemes while Runge–Kutta requires 1.8 hours. In this case, Runge–Kutta requires approximately 3.5 times more than for case ZT = 0.0001because smaller time step is required to attain convergence. However, AWE can still produce the solutions at approximately the same amount of computational time for both cases. This is because AWE is independent of time step size used. Thus, AWE is much more efficient than Runge-Kutta in terms of speed but still it can produce accurate results equivalent to Runge–Kutta.

6. CONCLUSION

AWE has proven itself to be a powerful solver for fast transient thermal characterization of Fourier and non-Fourier heat conduction. When AWE is coupled with FEM, it is capable of solving one-dimensional, two-dimensional and even three-dimensional heat conduction problems. AWE is also at least three orders faster in terms of computational time as compared to conventional iterative solvers, but still providing equivalent accuracy. The drawback of AWE is its inherent instability of Pade´ approximation, which may yield unstable solutions even for stable system. However, this instability can be overcome by applying any of the two stability schemes that has been introduced in this paper. Besides that, AWE does have the limitation of approximating very high frequency response for non-Fourier heat conduction case with ZT = 0.0001. This limitation is indicated by incorrect responses even after neglecting the unstable positive poles, and thus AWE is not recommended for use. Even though applying partial Pade´ approximation may help to yield reasonable responses, but the initial high frequency response still cannot be approximated accurately.

REFERENCES

[1] J. Rubinstein, P. Penfield Jr., M. Horowitz, Signal delay in RC tree networks, IEEE Trans. Comput. Aided Design (1983) 202–211.

[2] S.P. McCormick, Modeling and simulation of VLSI interconnections with moments, Ph.D. thesis, Massachusetts Institute of Technology, June, 1989.

[3] L.T. Pillage, R.A. Rohrer, Asymptotic waveform evaluation for timing analysis, IEEE Trans. Comput. Aided Design 9 (4) (1990) 352 - 366.

[4] L.T. Pillage, X.L. Huang, R.A. Rohrer, AWEsim: Asymptotic waveform evaluation for timing analysis, in: Proceedings of the 26th ACM/IEEE Design Automation Conference, 1989, pp. 634 - 637.

[5] S.Y. Kim, N. Gopal, L.T. Pillage, AWE macromodels in circuit simulation, in: Technical Digest of IEEE International Conference on Computer-Aided Design, 1992.

KEYNOTE LECTURES

Third International Conference on Computational Methods for Thermal Problems
THERMACOMP2014, June 2-4, 2014, Lake Bled, Slovenia
N. Massarotti, P. Nithiarasu and B. Sarler (Eds.)

HYBRID NUMERICAL METHODS COMBINING SEGMENTED NETWORK AND MULTIDIMENSIONAL MODELS FOR SIMULATING THERMOFLUID SYSTEMS

Alexandre Lamoureux[†] and Bantwal R. (Rabi) Baliga
Heat Transfer Laboratory, Department of Mechanical Engineering, McGill University
817 Sherbrooke St. W., Montreal, Quebec H3A 0C3, Canada
alexander.lamoureux@mail.mcgill.ca; bantwal.baliga@mcgill.ca
[†]Currently at: Hatch, 5 Place Ville Marie, Montreal, Quebec H3B 2G2, Canada

ABSTRACT

Hybrid numerical methods based on a combination of segmented quasi-one-dimensional and multidimensional mathematical models of complex thermofluid systems allow cost-effective computer simulations. An overview of such a method for simulations of a closed-loop thermosyphon, operating with slurries of a micro-encapsulated phase-change material, is presented along with some results.

Key Words: *Hybrid Numerical Methods, Coupled Segmented Network-Multidimensional Models, Thermosyphon, Microencapsulated Phase-Change Materials, Slurries.*

1. INTRODUCTION

Hybrid numerical methods based on a combination of quasi-one-dimensional and multidimensional mathematical models of complex thermofluid systems enable computer simulations of acceptable accuracy at affordable costs. Such methods have been used for cost-effective computer simulations, parametric studies, and optimizations of the following systems, for example: closed-loop thermosyphons operating with liquids and slurries of microencapsulated solid-liquid phase-change materials suspended in liquids [1-3]; loop heat pipes [4-6]; nuclear reactors and power-generation systems [7-9]; and cooling systems of power and distribution transformers [10-12].

The key features of the above-mentioned hybrid numerical methods are the following: relatively simple elements, such as ducts for transporting fluids, for example, are segmented into cells (control volumes that span their cross-sectional extent) over which quasi-one-dimensional models are used to impose conservation principles (typically, mass, momentum, and energy), with semi-empirical correlations as inputs, and finite volume methods are used to discretize the governing equations; multidimensional mathematical models are used for thermofluid phenomena in more complex and/or critically important elements, such as active heating and cooling sections, and discretized using finite volume, finite element, and/or control-volume finite element methods; and the resulting sets of coupled discretized equations are solved iteratively.

2. HYBRID METHOD FOR SIMULATIONS OF A CLOSED-LOOP THERMOSYPHON

An overview of a hybrid numerical method for simulations of a closed-loop thermosyphon, operating with slurries of a micro-encapsulated phase-change material suspended in distilled water, some results, and related discussions are presented in this section. This material is based mainly on the research works and contributions reported in Bernier and Baliga [1], Lamoureux [2], Lamoureux and Baliga [3], Scott [13], and Scott et al. [14].

Enhancement of convective heat transfer using slurries of solid-liquid phase-change materials (PCMs) suspended in a carrier liquid has received considerable attention over the last 48 years [2,3,13-20]. When the PCM undergoes melting or freezing, its latent heat of fusion increases the effective specific heat of the slurry, which, in turn, could increase the rate of convective heat

transfer relative to that obtained with just the conveying liquid. In practice, it is advantageous to use slurries of microencapsulated phase-change materials (MCPCMs) suspended in the conveying liquid because of their following desirable characteristics: no drastic changes in the effective viscosity and no clumping (or agglomeration) of the PCM during the phase-change (melting and freezing) processes; and with the proper choice of the encapsulation material and size of the particles, no agglomeration and no significant separation of the MCPCM from the conveying liquid.

Most of the published investigations of convective heat transfer with MCPCM slurries pertain to forced convection in tubes of circular cross-section [20], but there a few related to mixed convection in such tubes [13, 14]. Reviews of works related to the preparation, characterization, and applications of MCPCMs and slurries made by suspending them in liquids are available, for example, in the Refs. [2,3,13-20].

Examples of engineering heat transfer systems that employ closed-loop thermosyphons include the following [1,2,19,21-23]: cooling systems for large electrical transformers and electronics; systems for emergency cooling of nuclear reactor cores; chillers used in HVAC (heating, ventilating, and air-conditioning); and solar water heaters, geothermal heat pumps, and natural circulation loops for heating buildings. Reviews and examples of investigations of closed-loop thermosyphons operating with single-phase working fluids are available in the works of Grief [22] and Bernier and Baliga [1], for example. Haider and Nakayama [23] present an investigation of closed-loop thermosyphons operating with liquid-vapor phase-change, along with a review of pervious works on this topic. The works of Ho et al. [19], Lamoureux [2], and Lamoureux and Baliga [3] appear to be the only published investigations of closed-loop thermosyphons operating with MCPCM slurries. Details of a closed-loop thermosyphon operating under steady-state laminar-flow conditions with slurries of a MCPCM suspended in distilled water, properties of these MCPCM particles and slurries, and a hybrid numerical method for computer simulations of this thermosyphon are presented briefly in the remainder of this section.

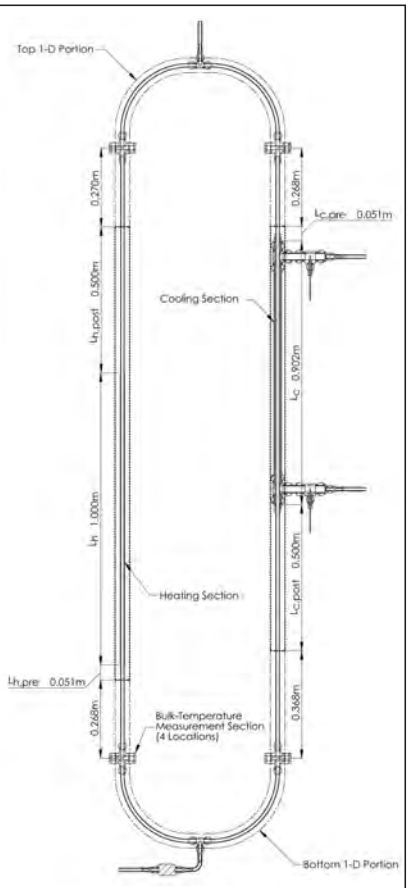

FIGURE 1. Schematic of the closed-loop thermosyphon, some of its dimensions, and associated notation [2].

2.1 Details of the closed-loop thermosyphon: The thermosyphon considered in this work is illustrated in Figure 1, along with some of its dimensions and the associated notation [2]. It consists of two vertical straight pipes connected together by two vertical 180-degree bends (made of the same pipe) of radius, R_{bend} = 0.229 m All these pipes are of circular cross-section, made of stainless steel 316 (smooth), with inside and outside diameters of 0.01021 m and 0.01270 m, respectively. The left vertical pipe includes the heating section, which has an active length of L_h (electrically heated to provide an essentially uniform wall-heat-flux condition) and pre- and post-heating sections of lengths $L_{h,pre}$ and $L_{h,post}$, respectively. The right vertical pipe includes the cooling section, which has an active cooling length of L_c (maintained at an essentially constant temperature, T_{cool}, using a

concentric annular heat exchanger and distilled water supplied from a constant-temperature bath) and pre- and post-cooling sections of lengths $L_{c,pre}$ and $L_{c,post}$, respectively. The center of the active cooling section is a vertical distance $\Delta z = 0.5$ m above the center of the active heating section [2]. The pre- and post-heating and pre- and post-cooling lengths ($L_{h,pre}$, $L_{h,post}$, $L_{c,pre}$ and $L_{c,post}$) are not actively heated or cooled, and they are included for the following reasons: 1) the local buoyancy effects in the active sections could also influence the flow to some extent upstream of the entrance to these sections, but they do not extend over the full length of the pre-sections (as they are made sufficiently long), so fully-developed flow conditions (without local buoyancy effects) prevail at the entrance to these section; and 2) the extent of the post-sections is sufficiently long to allow the velocity and temperature profiles leaving them to achieve essentially fully-developed conditions (without local buoyancy effects). These features of the heating and cooling sections allowed convenient formulation of the proposed hybrid model of the closed-loop thermosyphon. The whole closed-loop thermosyphon is very well insulted on its outer surfaces, to minimize rates of heat loss (or gain) from the ambient environment.

2.2 Properties of the MCPCM particles and slurries: The MCPCM particles have a core of solid-liquid PCM enclosed in a thin polymer resin shell, as shown in Figure 2(a). The slurries consist of suspensions of these MCPCM particles in distilled water. Experimental investigations were undertaken to determine the effective properties of the MCPCM particles [2,3,13, 14]. Their size distribution was determined using photomicrographs, similar to that shown in Figure 2(b). The variations with temperature of the effective density of the MCPCM particles, ρ_{MCPCM}, are illustrated in Figure 2(c). Variations of the effective specific heat at constant pressure of the MCPCM particles, $c_{p,MCPCM}$, during heating (from the fully-solid to the fully-melted state of the PCM core) followed by cooling (from the fully-melted to the fully-frozen state of the PCM core) are shown in Figure 2(d).

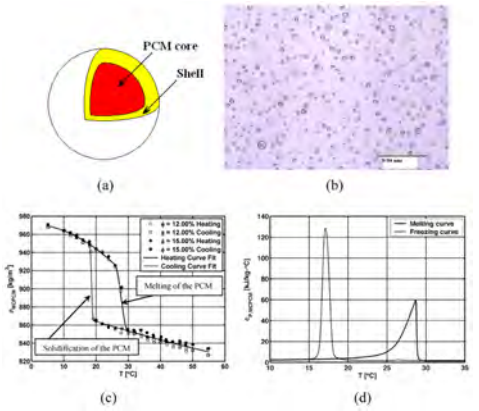

FIGURE 2. Properties of the MCPCM particles: (a) schematic of a particle; (b) photomicrograph [21]; (c) variation of effective density with temperature during heating and cooling [2,3]; (d) variation with temperature of the effective specific heat at constant pressure during heating (melting curve) followed by cooling (freezing curve) [2,3].

The mean effective diameter of the MCPCM particles, was determined to be 2.5 μm, with a standard deviation of 1.0 μm [13]. Quantitative data obtained using a differential scanning calorimeter (DSC) [2,3] showed that starting with the PCM in its solid state, during monotonic heating, melting is initiated gradually at 20 ^{o}C, occurs mainly in a the range 25.8 ^{o}C $\leq T \leq$ 28.6 ^{o}C, and is completed by 32.5 ^{o}C. During cooling after complete melting ($T \geq$ 32.5 °C), supercooling of the liquid PCM to 18.06 ^{o}C is needed for the onset or initiation of freezing, which is then completed by 15.0 ^{o}C. The acronym FMSCWFH is used to denote this full-melting-supercooling-with-freezing-and-hysteresis process. The DSC tests also showed that no supercooling is required to initiate the freezing process if cooling is started after only partial melting, with all temperatures less than 28.0 ^{o}C, and the freezing curve is then essentially the same as the melting curve in reverse: this partial-melting-no-supercooling-no-hysteresis process is denoted by the acronym PMNSCNH. In addition, the DSC tests showed that if the melting process of a slurry is halted at temperatures between 28.0 ^{o}C and 32.5 ^{o}C, and it is then cooled, part of the PCM freezes in the range 25.8 ^{o}C $\leq T \leq$ 28.6 ^{o}C, but cooling to below 15.0 ^{o}C is required for full freezing: this two-stage freezing process was not investigated in this work. Techniques to mitigate the aforementioned subcooling are

available [20], but they were not considered in this work. Using the DSC data, the effective latent heats of melting and freezing of the MCPCM particles (when supercooling is required) were determined to be $\lambda_{melting,MCPCM}$ = 129.5 kJ/kg and $\lambda_{freezing,MCPCM}$ = 134.0 kJ/kg, respectively [2,3]. Least-squares polynomial fits to the experimental data pertaining to the variations of ρ_{MCPCM} and $c_{p,MCPCM}$ with temperature during the FMSCWFH process (Figures 2(c) and 2(d)) were used in the numerical simulations; details of these curve-fits are available in Refs. [2,3].

Experiments undertaken by Scott [13] for determining the effective thermal conductivity of the MCPCM particles (polymer resin shell, PCM core, and residual impurities), k_{MCPCM}, yielded the following results (which were used in the numerical simulations): during monotonic heating, k_{MCPCM} = 0.171 W/m.^{o}C and 0.097 W/m.^{o}C for 5 ^{o}C $\leq T \leq$ 28.64 ^{o}C and 28.64 ^{o}C $\leq T \leq$ 55 ^{o}C, respectively; and during monotonic cooling in the FMSCWFH process, k_{MCPCM} = 0.171 W/m.^{o}C and 0.097 W/m.^{o}C for 5 ^{o}C $\leq T \leq$ 18.06 ^{o}C and 18.06 ^{o}C $\leq T \leq$ 55 ^{o}C, respectively.

For the density, specific heat at constant pressure, thermal conductivity, and dynamic viscosity of water, least-squares curve-fits to well-established data [24] in the range 5 ^{o}C $\leq T \leq$ 55 ^{o}C were used.

The effective density, ρ_s, and effective specific heat at constant pressure, $c_{p,s}$, of the slurries were calculated using the corresponding properties of the MCPCM particles and distilled water, and the mass concentration of the MCPCM [2,3]. The values of the effective thermal conductivity of the slurries, k_s, were calculated from the corresponding values of the MCPCM particles and distilled water, and the volume concentration of MCPCM in the slurry [2,3,13,14]. The MCPCM slurries considered in this work show a shear-thinning power-law rheological behavior [2,3], that conforms to the Ostwald and de Waele model [25,26]: details of the corresponding expression for the apparent or effective dynamic viscosity of the slurries are available in Refs. [2,3].

2.3 Synopsis of mathematical models: The proposed hybrid method is based on an amalgamation of a steady-state two-dimensional axisymmetric model and a quasi-one-dimensional model of laminar fluid flow and heat transfer phenomena in the vertical (heating and cooling) sections and the remaining portions, respectively, of the closed-loop thermosyphon shown in Figure 1. The slurry flows of interest belong to the class of disperse two-phase (liquid-solid-particle) flows [2,27]. In addition, for these flows, the velocity and temperature differences between the dispersed and conveying phases are negligibly small, so a homogeneous model is applicable [2,14,27]. In such a model, the governing equations are reduced to forms similar to those of the equations that govern single-phase flow and heat transfer, but effective thermophysical properties pertaining to the homogeneous mixture of the phases are used (see discussions in the previous subsection). It should also be noted that latent heat of fusion (or solidification) of the MCPCM particles when they undergo solid-liquid or liquid-solid phase-change processes in the heating and cooling sections of the closed-loop thermosyphon, respectively, is taken into account using an effective specific heat function [2,3,13,14] (again, see discussions in the previous subsection).

The following assumptions (in addition to those stated above) were invoked in this work [2]: viscous dissipation and the pressure-work terms in the energy equation are negligibly small (Eckert number << 1); the effective thermophysical properties of the MCPCM slurries are functions of the local temperature, the MCPCM mass concentration, and the local rate of strain (for the dynamic viscosity only), and they are essentially independent of pressure; the effective density of the slurries can be considered constant (at a suitably-averaged value, $\rho_{s,ref}$) in all terms of the governing equations, except in the buoyancy terms; the effects of an MCPCM-free layer along the inner surface of the pipe wall are negligible; the effective properties of the MCPCM slurries do not drift over time, nor are they altered by successive thermal cycling while flowing in the closed-loop thermosyphon (confirmed by experiments [2]); and the rates of axial heat conduction in the pipe wall and in the surrounding insulation layer are negligible compared to the rate of radial heat conduction through them.

The curvature effects and related additional head losses that occur in the semicircular (180-degree) pipe bends that join the vertical heating and cooling sections of the closed-loop thermosyphon (see Figure 1) were taken into account using empirical correlations applicable to Newtonian fluids and also non-Newtonian fluids [2,28,29]. Heat losses from the various sections of the thermosyphon to the environment were assessed in the proposed models using overall heat loss coefficients, the values of which were determined via complementary experiments [2].

The equations of the homogeneous mathematical model that governs steady, two-dimensional axisymmetric, laminar fluid flow and heat transfer in the vertical heating and cooling sections are cast in generalized forms, so that they are applicable to both distilled water (a Newtonian fluid) and the MCPCM slurries (which behave as non-Newtonian fluids with shear-thinning behavior). Thus, with respect to a cylindrical (*r*-*z*) coordinate system, the governing equations (steady, two-dimensional axisymmetric) are the continuity equation, *r*- and *z*-momentum equations (which have the same form as the Navier-Stokes equations, accounting for a variable effective dynamic viscosity prescribed using the Ostwald and de Waele model [25,26]); and the energy equation in which the latent-heat effects during melting and freezing (including possible super cooling) are taken into account by using an effective specific heat [2,3,13,14,30]. Boundary conditions are prescribed, along with inlet and outlet conditions that allow matching up with the quasi-one-dimensional model of the fluid flow and heat transfer in the other portions of the closed-loop thermosyphon [1-3].

In the portions of the closed-loop thermosyphon that join the vertical heating and cooling sections, quasi-one-dimensional (1-D) models of the fluid flow and heat transfer phenomena were used [1,2], as the local buoyancy effects are essentially negligible. The upper 1-D portion starts at the exit plane of the post-heating length, includes the top 180º bend, and ends at the entry plane of the pre-cooling length (see Figure 1). The lower 1-D portion starts at the exit plane of the post-cooling length, includes the bottom 180º bend, and ends at the entry plane of the pre-heating length (see Figure 1). Even though the outer surfaces of these 1-D portions are well insulated, they experience some heat exchange with the ambient environment. So the temperature of the working fluid in these 1-D portions changes (albeit slightly). Thus, to enhance the accuracy of the numerical simulations, a segmented approach was adopted in the proposed 1-D models of the fluid flow and heat transfer in these portions. Examples of segments of the upper 180º bend are schematically illustrated in Figure 3, along with the related notation used in the formulation of the 1-D models [2]. The non-Newtonian behavior of the slurries was handled using the Ostwald and de Waele model, and procedures described in Refs. [2,25,26,28,29]. In the pipe bends, an empirical correlation proposed by Gupta and Mishra [28] to take into account the additional head losses.

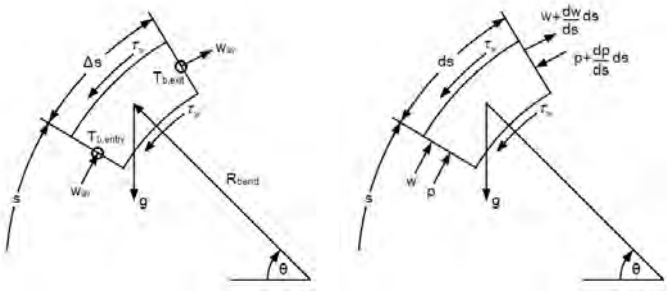

(a) (b)

FIGURE 3. Segments of the upper 180º bend of the closed-loop thermosyphon and related notation used in the proposed hybrid model [2].

The well-established definition of the bulk temperature for single-phase fluid flows [24] is not adequate as the specific heat of the slurries change significantly with temperature when the

encapsulated PCM undergoes phase change [14]. Thus, a modified bulk temperature proposed by Scott et al. [14] (which for convenience is referred to as the bulk temperature in this paper) is used in the proposed hybrid model. Finally, it should be noted that an overall momentum balance, applied over the entire closed-loop thermosyphon, was used to determine an average velocity of the working fluid [1,2].

2.4 Notes on the numerical methods used for solving the proposed mathematical models: A co-located equal-order control-volume finite element method (CVFEM) was specially formulated, implemented, tested, and then used to solve the two-dimensional axisymmetric (2-D) models of the steady fluid flow and heat transfer phenomena in the vertical heating and cooling sections of the closed-loop thermosyphon. This CVFEM is an axisymmetric version of a CVFEM proposed by Lamoureux and Baliga [31] for the solution of two-dimensional planar fluid flow and heat transfer problem. The conservation equations of the segmented quasi-one-dimensional model were discretized using well-established finite volume methods [32,33], when required. An iterative procedure was used to solve the coupled, nonlinear, sets of discretized equations [1,2,31,33].

3. RESULTS

3.1 Preamble: The proposed hybrid model was formulated, implemented, and tested (benchmarked) using simulations of the closed-loop thermosyphon (see Figure 1) operating with distilled water and checking the results against those of complementary experiments [2]. Following that, the hybrid method was used for simulations of the thermosyphon operating with the above-mentioned MCPCM slurries, and the results were again checked against those of a complementary experimental investigation [2]. In all, six runs with distilled water and 17 runs with slurries (of different mass concentrations of MCPCM) were investigated experimentally and numerically [2]. The results obtained in the experimental investigation are available in Lamoureux and Baliga [3]. The grids for the final simulations were chosen on the basis of numerous preliminary computations and grid-independence studies [2].

3.2 Sample results: To demonstrate the capabilities of the proposed hybrid method, results for four different runs (denoted as Runs 9-S, 10-S, 11-S, and 12-S), each with the thermosyphon operating with a slurry of MCPCM mass concentration 12.49%, are presented here. Runs 9-S and 10-S correspond to the FMSCWFH process; and Runs 11-S and 12-S correspond to the PMNSCNH process. The input parameters and some experimental and numerical results (bulk temperatures at the inlet and outlet planes of the heating and cooling sections of the thermosyphon; and w_{av}) for these four runs are presented below in Table 1; and graphical presentations of some results pertaining to the vertical heating section are presented in Figures 4 and 5.

The results in Figure 4(a) for the dimensionless velocity distribution in the vertical heating section show the following features: 1) at the inlet to the heating section ($z = 0$) it corresponds to the fully-developed velocity profile (without local buoyancy effects) for non-Newtonian flows; 2) it gets increasingly influenced by local buoyancy and latent-heat heat effects as the fluid travels through the active heating section; 3) for $z \geq L_{h,pre} + 0.8L_h$, it attains shapes that are not influenced by latent-heat effects (as the PCM has fully melted before this location is reached); and 4) at the outlet of the heating section ($z = L_{h,pre} + L_h + L_{h,post}$), it reverts back to a shape essentially akin to the fully-developed velocity profile (without local buoyancy effects) for non-Newtonian flows. The results in Figure 4(b) for the dimensionless temperature distribution in the heating section show the following features: 1) at the inlet to the heating section, it is uniform and essentially zero, as the inlet temperature was set equal to $T_{b,in}$; 2) it gets increasingly influenced by local buoyancy and latent-heat effects as the fluid travels through the active heating section; 3) in the active heating section, for $z \geq L_{h,pre} + 0.8L_h$, it attains an essentially fully-developed shape for the thermal boundary condition imposed in this section (same shape, but temperature at all r locations increases

essentially linearly with *z*); and 4) at the outlet of the heating section ($z = L_{h,pre} + L_h + L_{h,post}$), it is essentially uniform again, but at a value of one (unity), indicating that $T = T_{b,out}$ for $0 \le r \le r_i$.

Run	Input Parameters		Results	$T_{b,in,heating}$ [°C]	$T_{b,out,heating}$ [°C]	$T_{b,in,cooling}$ [°C]	$T_{b,out,cooling}$ [°C]	w_{av} [m/s]
9-S	$q_{heating,total}$ [W]	42.33	Expt.	15.06	37.39	36.12	14.56	4.67×10^{-3}
	T_{cool} [°C]	13.08	Num.	15.42	37.85	36.22	14.66	4.66×10^{-3}
	T_{∞} [°C]	22.18	% Diff.	2.39	1.23	0.28	0.69	0.21
10-S	$q_{heating,total}$ [W]	31.95	Expt.	14.82	33.42	32.34	14.27	4.12×10^{-3}
	T_{cool} [°C]	13.09	Num.	15.26	33.96	32.56	14.39	4.09×10^{-3}
	T_{∞} [°C]	22.02	% Diff.	2.88	1.59	0.68	0.83	0.73
11-S	$q_{heating,total}$ [W]	8.315	Expt.	15.75	26.72	26.35	14.67	2.04×10^{-3}
	T_{cool} [°C]	13.05	Num.	16.46	26.68	26.12	14.86	2.14×10^{-3}
	T_{∞} [°C]	22.67	% Diff	4.51	0.15	0.87	1.30	4.90
12-S	$q_{heating,total}$ [W]	5.066	Expt.	20.04	26.83	26.34	20.11	1.61×10^{-3}
	T_{cool} [°C]	19.62	Num.	20.68	26.76	25.98	20.20	1.72×10^{-3}
	T_{∞} [°C]	22.22	% Diff	3.19	0.26	1.37	0.45	6.83

TABLE 1. Input parameters, experimental results, and numerical results for runs with an MCPCM slurry of mass concentration 12.49%: Runs 9-S and 10-S correspond to the FMSCWFH process; and Runs 11-S and 12-S correspond to the PMNSCNH process.

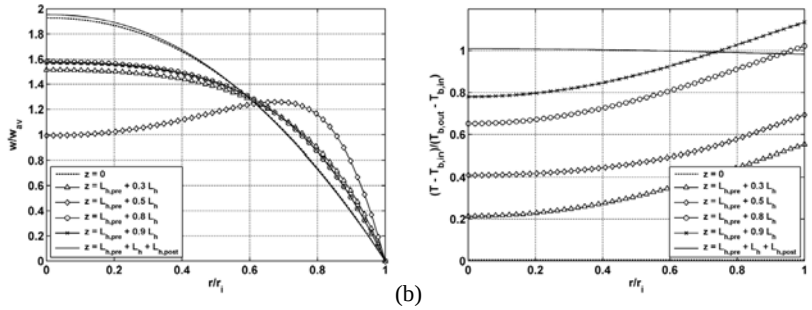

(a) (b)

FIGURE 4. Results for the closed-loop thermosyphon operating with a slurry of ϕ = 12.49%: (a) numerical predictions of the distributions of dimensionless axial velocity in the vertical heating section; and (b) numerical predictions of dimensionless temperature in the vertical heating section.

The $T_{r=r_o}$ *vs.* z plots in Figure 5 for Runs 9-S and 10-S, which correspond to the FMSCWFH process, have the following features: in the region $0 \le z \le 0.6\,\text{m}$ (roughly), the joint (and coupled) effects of the developing flow, buoyancy, and latent heat of the PCM during the solid-liquid phase-

change phenomenon cause these plots to be nonlinear; the region $0.6\,\mathrm{m} \le z \le 0.8\,\mathrm{m}$ (roughly) corresponds to sensible heating of the slurry (as the melting of the PCM is fully completed before the start of this region), and the plots indicate a second region of development for this condition; and for $z > 0.8\,\mathrm{m}$ (roughly), these plots are almost linear, indicating an essentially fully-developed regime (with local buoyancy effects). The $T_{r=r_o}$ *vs.* z plots in Figure 5 for Runs 11-S and 12-S, which correspond to the PMNSCNH process, exhibit the joint (and coupled) effects of the developing flow, buoyancy, and latent heat of the PCM during the solid-liquid phase-change phenomenon throughout the active heating section, $0 \le z \le 1.0\,\mathrm{m}$.

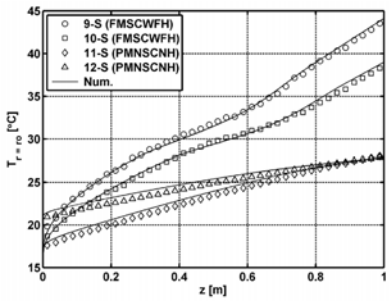

FIGURE 5. Results for the closed-loop thermosyphon operating with a slurry of ϕ = 12.49%: experimental and numerical result for the axial distributions of the temperature of the outer surface of the tube wall in the active heating section.

4. CONCLUSIONS

In the previous sections of this paper, to demonstrate the key features of hybrid numerical methods for simulations of complex thermofluid systems, the formulation of such a method was presented in the context of a closed-loop thermosyphon, operating under steady-state conditions with slurries consisting of a micro-encapsulated phase-change material (MCPCM) suspended in distilled water. This hybrid numerical method is based mainly on the research works and contributions reported in Refs. [1-3,13,14,30,31,33]. The details of the closed-loop thermosyphon and the effective properties of the aforementioned MCPCM slurries (and the experiments that were undertaken to determine them [2]) were also discussed. In particular, these slurries can be considered as homogeneous non-Newtonian fluids that display a shear-thinning power-law rheological behavior [2,3,25], analogous to that of fluids that conform to the Ostwald and de Waele model [25,26]. The sample results presented in the previous section show that the proposed hybrid numerical method produces predictions that are in very good agreement with results obtained in a complementary experimental investigation [2]. In this work, the two-dimensional axisymmetric models of the fluid flow and heat transfer in the vertical heating and cooling sections of closed-loop thermosyphon (see Figure 1) were solved using a control-volume finite element method [2,31,33]. However, other suitable numerical methods [32,34] could be used for this purpose.

5. ACKNOWLEDGEMENTS

The authors are grateful to the Natural Sciences and Engineering Research Council (NSERC) of Canada and the Fonds québécois de la recherche sur la nature et les technologies (FQRNT) for financial support of this work. The second author would like to thank Professors N. Massarotti, P. Nithiarasu, and B. Sarler for inviting him to present this keynote lecture at ThermaComp2014. The second author and his students would also like to express their gratitude to the Honorary Chair of ThermaComp2014, Professor R.W. Lewis, for being a big source of inspiration to them.

REFERENCES

[1] M.A. Bernier, and B.R. Baliga, A 1-D/2-D model and experimental results for a closed-loop thermosyphon with vertical heat transfer sections, *Int. J. Heat Mass Tran.*, 35, 2969-2982, 1992.

[2] A. Lamoureux, A., Investigations of a closed-loop thermosyphon operating with slurries of a microencapsulated phase-change material, *Ph.D. Thesis*, McGill University, Montreal, Quebec, Canada, 2012.

[3] A. Lamoureux and B.R. Baliga, Experimental study of a closed-loop thermosyphon operating with slurries of a microencapsulated phase-change material, *Proc. ASME Summer Heat Transfer Conference*, Paper # HT2013-17547, pp. 1-13, Minneapolis, MN, July 14-19, 2013.

[4] Y.F. Maydanik, Loop heat pipes, *Appl. Therm. Eng.*, 25, 635-657, 2005.

[5] A. Faghri, Review and advances in heat pipe science and technology, *ASME J. Heat Transfer*, 134, 123001-1-18, 2012.

[6] M.A. Chernysheva and Y.F. Maydanik, 3D-model for heat and mass transfer simulation in flat evaporator of copper-water loop heat pipe, *Appl. Therm. Eng.*, 33-34, 124-134, 2012.

[7] K. Ivanov and M. Avramova, Challenges in coupled thermal-hydraulics and neutronics simulations for LWR safety analysis, *Annals Nuclear Energy*, 34, 501-513, 2007.

[8] J.J. Jeong, S.W. Lee, J.Y. Cho, B.D. Chung, and G.C. Lee, A coupled analysis of system thermal-hydraulics and three-dimensional reactor kinetics for a 12-finger control element assembly drop event in a PWR plant, *Annals Nuclear Energy*, 37, 1580-1587, 2010.

[9] R. Bonifetto, S. Dulla, P. Ravetto, L.S. Richard, and R. Zanino, A full-core coupled neutronic/thermal-hydraulic code for the modeling of lead-cooled nuclear fast reactors, *Nuclear Eng. and Design*, 261, 85-94, 2013.

[10] F. Torriano, M. Chaaban, and P. Picher, Numerical study of parameters affecting the temperature distribution in a disc-type transformer winding, *Appl. Therm. Eng.*, 30, 2034-2044, 2010.

[11] J. Gastelurrutia, J.C. Ramos, A. Rivas, G.S. Larraona, J. Izagirre, and L. del Rio, Zonal thermal model of distribution transformer cooling, Applied Thermal Engineering, 31, 4024-4035, 2011.

[12] M.A. Tsili, E.I. Amoiralis, A.G. Kladas, and A.T. Souflaris, A. T., Power transformer thermal analysis by using an advanced coupled 3D heat transfer and fluid flow FEM model, *Int. J. Therm. Sci.*, 53, 188-201, 2012.

[13] Scott, D.A., Heat transfer in pipes conveying slurries of microencapsulated phase-change materials in water, *Ph.D. Thesis*, McGill University, Montreal, Canada, 2006.

[14] D.A. Scott, A. Lamoureux, and B.R. Baliga, Modeling and simulations of laminar mixed convection in a vertical pipe conveying slurries of a microencapsulated phase-change material in distilled water, *ASME J. Heat Transfer*, 135, 011013-1-13, 2013.

[15] L. Katz, Natural convection heat transfer with fluids using suspended particles which undergo phase change, *Ph.D. Thesis*, Massachusetts Institute of Technology, Cambridge, MA, 1967.

[16] P. Charunyakorn, S. Sengupta, and S.K. Roy, Forced convection heat transfer in microencapsulated phase change material slurries: flow in circular ducts, *Int. J. Heat and Mass Transfer*, 34, 819-833, 1991.

[17] J.C. Mulligan, D.P. Colvin, and Y.G. Bryant, Microencapsulated phase-change material suspensions for heat transfer in spacecraft thermal systems, *J. Spacecraft and Rockets*, 33, 278-284, 1996.

[18] H. Inaba, M.J. Kim, and A. Horibe, Melting heat transfer characteristics of microencapsulated phase change material slurries with plural microcapsules having different diameters, *ASME J. Heat Transfer*, 126, 558-565, 2004.

[19] C.J. Ho, S.Y. Chiu, and J.F. Lin, Heat transfer characteristics of a rectangular natural circulation loop containing solid-liquid phase-change material suspensions, *Int. J. Num. Meth. Heat & Fluid Flow*, 15, 441-461, 2005.

[20] J.L. Alvarado, C. Marsh, C. Sohn, G. Phetteplace, and T. Newell, Thermal performance of microencapsulated phase change material slurry in turbulent flow under constant heat flux, *Int. J. Heat and Mass Transfer*, 50, pp. 1938-1952, 2007.

[21] D. Japikse, Advances in thermosyphon technology, *Advances in Heat Transfer*, 9, 1-111, 1973.

[22] R. Greif, Natural circulation loops, *ASME J. Heat Transfer*, 110, pp. 1243-1258, 1988.

[23] S.I. Haider and W. Nakayama, A natural circulation model of the closed loop, two-phase thermosyphon for electronics cooling, *ASME J. Heat Transfer*, 124, 881-890, 2002.

[24] F.P. Incropera and D.P. DeWitt, *Fundamentals of Heat and Mass Transfer*, 5th Ed., John Wiley, New York, 2002.

[25] R.B. Bird, R.C. Armstrong, and O. Hassager, *Dynamics of Polymeric Liquids, Vol. 1*, 2nd Ed., Wiley, New York, 1987.

[26] J. Ferguson, J. and Z. Kembłowski, *Applied Fluid Rheology*, Elsevier, New York, 1991.

[27] C.E. Brennen, *Fundamentals of Multiphase Flow*, Cambridge Univ. Press, U.K., 2005.

[28] S.N. Gupta and P. Mishra, Isothermal laminar flow of non-Newtonian fluids through helical coils, *Indian J. Technology*, 13, 245-250, 1975.

[29] R.P. Chhabra and J.F. Richardson, *Non-Newtonian Flow in the Process Industries: Fundamentals and Engineering Applications*, Butterworth-Heinemann, Boston, USA, 1999.

[30] N. Elkouh and B.R. Baliga, Effect of variable properties on natural convection in water near its density inversion temperature, *Proc. 30th ASME National Heat Transfer Conference*, Portland, Oregon, August 6-8, HTD 33**,** 53-63, 1995.

[31] A. Lamoureux and B.R. Baliga, Improved formulations of the discretized pressure equation and boundary treatments in co-located equal-order control-volume finite-element methods for incompressible fluid flow", *Num. Heat Transfer Part B: Fundamentals*, 59, 442-472, 2011.

[32] S.V. Patankar, *Numerical Heat Transfer and Fluid Flow*, Hemisphere, Washington, U.S.A., 1980.

[33] B.R. Baliga and N. Atabaki, Control-volume-based finite difference and finite element methods, in *Handbook of Numerical Heat Transfer*, 2nd Edition, W.J. Minkowycz, E.M. Sparrow, and J.Y. Murthy (Eds.), John Wiley, New York, U.S.A. Chapter 6, 191-224, 2006.

[34] N. Massarotti, F. Arpino, R.W. Lewis, and P. Nithiarasu, Fully explicit and semi-implicit CBS procedures for incompressible flows, *Int. J. Num. Methods in Eng.*, 66, 1618-40, 2006.

Third International Conference on Computational Methods for Thermal Problems
THERMACOMP2014, June 2-4, 2014, Lake Bled, Slovenia
N. Massarotti, P. Nithiarasu and B. Sarler (Eds.)

MULTIPHYSICS AND MULTISCALE MODELS IN MODELING AND SIMULATION OF SOLIDIFICATION PROCESSES

H. Combeau and M. Založnikž

Institut Jean Lamour, CNRS – Université de Lorraine, Dep. SI2M, F-54011 Nancy cedex, France
herve.combeau@univ-lorraine.fr

ABSTRACT

Prediction of solidification defects like macro and mesosegregations and of microstructures constitutes a key issue for the industry. The development of models needs to account for several imbricated length scales and different physical phenomena. The goal of this presentation is to introduce the existing models and their principles. The most recent applications of these models to solidification processes will be presented (steel ingot, aluminum direct-chill casting). Their ability to help in the understanding of complex phenomena, such as the competition between nucleation and growth of grains in the presence of convection of the liquid and of grain motion, will be demonstrated, and their predictive capabilities will be discussed. Finally, the main remaining key issues will be addressed.

Key Words: *Multiscale modeling, Solidification processes, Macrosegregation, Grain structure.*

1. INTRODUCTION

In the metallurgical production chain, the solidification step sets the basic microstructure of the material. The modification of this structure during subsequent processing steps is limited. During solidification several types of defects form, such as heterogeneities of composition: microsegregation at the microstructure scale, macrosegregation at the scale of the product; heterogeneities of structures in terms of grain orientation, size and morphology [1]. The reduction of these defects is an important issue for the industry because they impair the final properties of products. Numerical simulation is a valuable tool for progress in this direction. The prediction of macrosegregation and microstructure in solidification processes, such as: casting of steel ingots, continuous casting of steel and direct-chill (DC) casting of aluminum alloys, needs in a first step the derivation of a model accounting for nucleation, growth and motion of grains, thermal and solutal natural convection. The volume averaging technique is often used to incorporate microscopic phenomena into macroscale models. The difficulty of this technique lies in the closure relations. The second step consists of defining an efficient and robust algorithm that can solve a large number of strongly coupled partial differential equations. A model and its solution procedure are presented in the next section. Then we show the applications of this model to two industrial processes: casting of steel ingots and DC casting of aluminum alloys. We finish by discussing possible issues for the future.

2. PHYSICAL MODEL AND SOLUTION PROCEDURE

The multiscale two-phase model SOLID, which we have developed, is presented in entirety in [2]. The model is based on a volume-averaged Euler-Euler two-phase model that consists of two parts: of a macroscopic part with momentum, mass, heat, solute mass, and grain-population conservation equations, and of a microscopic part that describes the nucleation and growth of grains. At the macroscopic level, the model accounts for heat and solute transport coupled with two-phase flow driven by thermal and solutal buoyancy. Flow induced by shrinkage i.e. difference of densities between the solid and the liquid phases is also accounted for. Depending on the behaviour of the

solid phase, we consider two flow regimes in the mushy zone. Where the solid volume fraction g_s is larger than the packing limit ($g_s > g_{s,pack}$) the solid grains are considered to be blocked and the velocity of the solid phase is set to the product velocity (i.e. zero in case of static castings, the casting velocity in case of continuous casting). The flow of intergranular liquid through the porous solid matrix is described by a momentum equation including a Darcy term for the drag interactions, with the permeability modeled by the Kozeny-Carman law. The density of the solid phase is assumed to be constant and for the liquid density the Boussinesq assumption is employed. At solid fractions smaller than the packing limit ($g_s < g_{s,pack}$) the solid phase is considered to be in the form of free floating grains. Their motion is described by a balance of buoyancy, drag and pressure forces acting on the grains. In this way, the solid and liquid have locally different velocities. The interfacial particle drag is considered dependent on the grain size, which produces the tendency that the larger the grains are, the stronger their tendency to settle; contrarily, smaller grains are more easily entrained by the liquid motion. In order to simulate the columnar zone, the grains in a predefined region close to the mould are imposed to be fixed. The microscopic level is treated locally; within SOLID, this means within each discrete volume element. The apparition of new grains is modeled by a distribution of nuclei per unit volume. In case of steel ingots, nuclei are assumed to be constituted of dendrite fragments that are activated at the liquidus temperature. In aluminium DC casting, nucleation on TiB_2 or TiC inoculant particles is considered. An inoculant particle triggers nucleation at a critical undercooling that is inversely proportional to its size. The size distribution of these particles must therefore be considered. Additionally, the transport of inoculant particles with the flow is described. The phase change (solidification and melting) is controlled by solute diffusion in both phases at the grain scale, assuming local thermal equilibrium and thermodynamic equilibrium at the solid-liquid interface. We solve the macroscopic equations with a finite volume method. The local microscopic growth model is integrated implicitly and is coupled with the macroscopic model via an operator-splitting integration method [2] that separates the integration of the macroscopic terms, and the growth and nucleation terms.

3. APPLICATION TO A 65-TON STEEL INGOT

The simulation results obtained with SOLID in the case of the solidification of a 65 t ingot are presented in this section as an illustration of its prediction capabilities. More details concerning this case can be found in [3]. This 65 t ingot was cast by ArcelorMittal Industeel. Metal samples were taken during solidification, the temperature were measured in the mould and in the ingot core and a sulphur injection was performed to mark the position of the mushy zone.

C	S	P	Si	Mn	Ni	Cr	Mo
0.22	0.007	0.008	0.18	0.25	1.14	1.6	0.19

Table 1: Steel grade of the 65 ton ingot cast for this study (solute content in mass %)

A liquidus temperature of 1507°C corresponds to this steel grade. The steel was bottom poured in a cast iron mould. The ingot dimensions were: 3.5 m height and 1.8 m diameter (in average). The mould was hot topped with refractory materials along a height of 0.6 m. Steel was poured with 48°C of superheat, the solidification time was of the order of 20 hours. Two simulation results are presented below in Figure 1. In the first simulation the solid phase was assumed to be fixed. In the second simulation, the motion of equiaxed grains was accouted for and the solid was fixed only in a zone of several cm from the outer surface in order to describe the columnar zone. The grain morphology was approximated as globular in both simulations. The ingot geometry was modeled as axisymmetric. The comparison between the two simulations shows that the settling of globular equiaxed grains is the predominant cause for the formation of the macrosegregations in this ingot.

These results are encouraging and show that the model is on a good way to being fully predictive. In the next step, a model that includes the description of the globular-dendritic transitions of the grain morphology should be applied to this ingot. This will test the ability of the model to predict the grain-morphology transitions at the process scale. Some remaining points have also to be addressed, such as the number of nuclei, which needs to be related to the fragmentation of the dendritic structures, and the possibility for the growth of a columnar zone from the packed equiaxed zone (equiaxed-to-columnar transition) when equiaxed nucleation is exhausted.

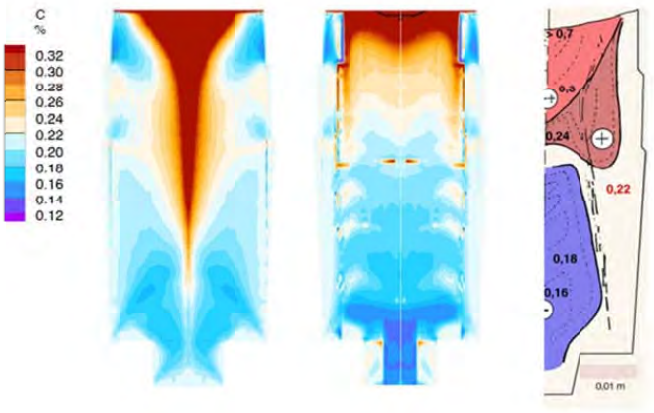

Figure 1: Macrosegregation in the 65-ton steel ingot: model prediction with fixed solid (left), with moving grains (center) and experimental determination (right).

4. APPLICATION TO ALUMINIUM DC CASTING

The most recent development of SOLID is its application to the direct-chill casting of aluminum alloys. The structure and macrosegregation formation in this process is characterized by a very intricate interplay of the melt flow, the grain settling and the flow of intergranular liquid in the packed-grain layer. Furthermore, as the nucleation of the grains is controlled by the addition of Al-Ti-B or Al-Ti-C inoculant particles to the molten metal, the modeling of the grain formation requires a detailed description of inoculant particle motion and activation. With the strongly coupled modeling of all these phenomena we have succeeded for the first time to predict the structure and macrosegregation in direct-chill castings [4]. In the following examples, DC casting of a 7449 aluminium alloy extrusion ingot of 350 mm thickness is studied. A simplified 2D geometry with symmetry, i.e. a domain of 175x800 mm was considered. In Figure 2a, we illustrate the role of grain motion in the formation of macrosegregation. When a part of the grains growing in the mushy zone of a DC cast ingot are free to move, these grains, as they are usually heavier than the surrounding liquid, have a tendency to settle. They settle along the inclined mushy zone towards the center, where they accumulate at the bottom of the sump. In this way they create a negative macrosegregation in the center. It can be seen in Figure 2a, that the fluid flow and the negative macrosegregation are strongly dependent of the packing fraction. In Figure 2b, we illustrate the capability of the model to identify the characteristic zones for nucleation and growth of the grains in the non-packed (slurry zone). Notably, we can see that the nucleation zone is restricted to a region located in the top part of the slurry zone and close to the packing front. Along the packing front, the growth of the grains is the fastest, whereas the central region of the solidification zone corresponds to slow growth or remelting of the grains.

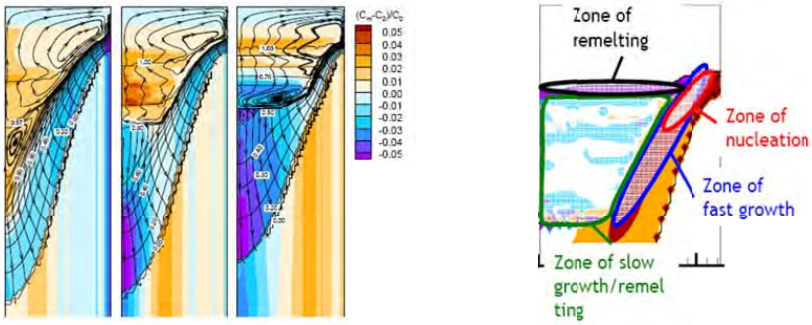

(a) (b)

Figure 2: Illustration of the capabilities of the model.

a) Sensitivity to grain motion: segregation and streamlines of the relative liquid velocity for different packing fractions. Left: $g_{s,pack}$=0.03. Middle: $g_{s,pack}$=0.2. Right: $g_{s,pack}$=0.5.
b) Description of the origin of the equiaxed grains: identification of the different zones for nucleation and growth of the grains ($g_{s,pack}$=0.3).

5. CONCLUSIONS

We have briefly described the principles of a solidification model predicting the macrosegregation and the microstructure in metal castings and have shown its capabilities through two industrial applications. Although these results are promising, some further efforts in different directions are needed. A first axis concerns the improvement of the understanding of phenomena such as dendrite fragmentation, grain packing, nucleation and growth of grains in presence of convection. This will require dedicated experiments and models at a scale smaller than that of the product. A second axis concerns the accuracy of the numerical solutions. This was tackled by a numerical benchmark exercise [5], which showed that more work needs to be done in order to determine the limitations of this type of model from a numerical point of view.

REFERENCES

[1] Dantzig J.A., Rappaz M., Solidification, EPFL Press, ISBN: 9780849382383, 2009.
[2] Založnik, M.; Combeau, H.: An operator splitting scheme for coupling macroscopic transport and grain growth in a two-phase multiscale solidification model: Part I – model and solution scheme; *Comp. Mater. Sci.*, 48, 1–10, 2010.
[3] Combeau H., Kumar A., Založnik M., Poitrault I., Lacagne G., Gingell A., Mazet T., Lesoult G., Macrosegregation prediction in a 65 ton steel ingot, *International Conference on Ingot Casting, Rolling and Forging*, 2012, 27.
[4] Založnik M., Kumar A., Combeau H., M. Bedel, Jarry P., Waz E., The Coupling of Macrosegregation With Grain Nucleation, Growth and Motion in DC Cast Aluminum Alloy Ingots, In J. F. Grandfield & D. G. Eskin (Eds.), *Essential Readings in Light Metals*, Volume 3, *Cast Shop for Aluminum Production, Hoboken (NJ), USA : John Wiley& Sons*, ISBN: 978−1−118−63571−1, 848–853, 2013.
[5] Combeau H. and col., Analysis of a Numerical Benchmark for Columnar Solidification of Binary Alloys, *IOP Conference Series: Materials Science and Engineering*, 33 (2012), 012086.

Third International Conference on Computational Methods for Thermal Problems
THERMACOMP2014, June 2-4, 2014, Lake Bled, Slovenia
N. Massarotti, P. Nithiarasu and B. Sarler (Eds.)

THERMAL SIMULATIONS IN SUPPORT OF MULTI-SCALE CO-DESIGN OF ENERGY EFFICIENT INFORMATION TECHNOLOGY SYSTEMS

Y. Joshi, B. Barabadi, R. Ghosh, Z. Wan, H. Xiao, S. Yalamanchili, and S. Kumar
G.W. Woodruff School of Mechanical Engineering
Georgia Institute of Technology, Atlanta, Georgia 30332, U.S.A
yogendra.joshi@me.gatech.edu

ABSTRACT

Information technology (IT) systems are already ubiquitous, and their future growth is expected to drive the global economy for the next several decades. Energy consumption by these systems is growing rapidly, and their sustained growth requires curbing the energy consumption, and the associated heat removal requirements. Currently, 20%-50% of the incoming electrical power is used to meet the cooling demands of IT facilities. Careful co-optimization of electrical power and thermal management is essential for reducing this requirement. Such modelling based co-optimization is further complicated by the presence of several decades of spatial and temporal scales. In this paper, we illustrate the challenges and possible modelling approaches by considering three examples. The multi-scale modelling of chip level transient heating using a combination of progressive-zoom in, and proper orthogonal decomposition (POD) is an effective approach for chip level electrical/thermal co-design for mitigation of reliability concerns, such as Joule heating driven electromigration. In the second example, we will illustrate the optimal microfluidic thermal management of hot spots, and large background heat fluxes associated with future high performance microprocessors. Through modelling based electrical/thermal co-design, dramatic savings in energy usage for cooling are possible. In the third example, data centre facility level energy usage reduction through a transient measurements based POD modelling framework will be illustrated.

Key Words: *Multi-Scale, Thermal Modelling, Co-Design, POD, Microfluidic Cooling.*

1. INTRODUCTION

Thermal management of information technology (IT) systems involves over ten decades of length scales, from on chip interconnects (currently ~22 nm) to large data centre facilities (~50-100 m in length), and a multitude of time scales. Thermal modelling at various scales is essential during design phase to insure performance and reliability. An emerging focus area is co-design, involving the consideration of two or more aspects of the overall design, with the objective of reducing overall energy consumption. Energy consumption in IT facilities and equipment is a growing concern, which is driving this interest. Figure 1 shows two dissimilar length scales, where the thermal analysis for co-design is illustrated in this paper. On the left is a chip package. The current baseline is a single tier package with air cooling. Temperature computations within such packages with multi-scale resolution are needed under both steady state and transient operation, for assessing reliability. These are explored in Sections 2-4. The packaged two-tier chip stack incorporating microfluidic cooling, shown in Figure 1 illustrates future packaging direction, to achieve the continuing goals of faster and more functional systems. In Section 5, this configuration is analysed in an electrical/thermal co-design framework to optimize cooling. The image on the right in Figure 1 illustrates a data centre aisle, with perforated tiles for cooling air delivery. Efficient computations of inlet air temperatures at servers allow for controlling cooling hardware to optimize energy consumption. A data driven modelling framework for achieving this is presented in Sections 6-8.

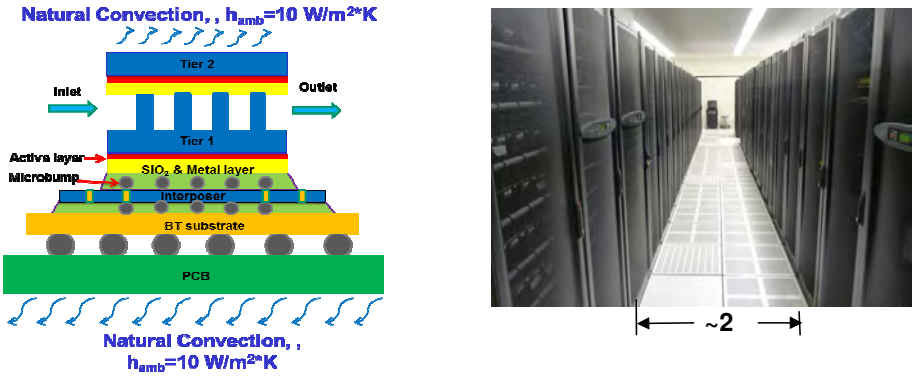

FIGURE 1. A cm scale chip/package (left), and data centre (right) illustrate the multi-scale spatial nature of thermal modelling needs in information technology systems. Both are considered in this paper to illustrate co-design approaches.

2. CHIP/PACKAGE LEVEL THERMAL MODELLING FOR IC DESIGN AND RELIABILITY ANALYSIS

Key factors impacting integrated circuit (IC) chip performance and reliability are the knowledge of thermal and electrical performance. As the size of on-chip interconnects reduces below the electron mean free path (~40 nm in Cu at room temperature), electron transport becomes dominated by scattering at the metal-dielectric interface, and at grain boundaries. This scattering can decrease the electrical and thermal conductivity to less than half that of the bulk value [1-6], making Joule heating a major concern in IC industry, requiring a comprehensive predictive framework.

It is important to note that on-chip interconnects are not isolated entities. They are arranged as a stack of metal lines, vias, and dielectric layers, as a part of a chip that is ultimately enclosed in a package. The majority of heat is generated in the transistors and metallic interconnects, with characteristic length scale of tens of nm (~10^{-8} m). This heat is then conducted through the passive/active components, substrate, and heat sink, prior to being convectively removed by the ambient environment. At this level, the characteristic length scale is on the order of tens of cm (10^{-1} m). Therefore, the effect of the entire structure should be accounted for, to acquire an accurate and realistic thermal simulation of interconnects. In addition, transient thermal events in the interconnect structure can vary from tens of s (10^{2} s) at the package level to □s (10^{-6} s) at the interconnect level. Thus, the heat diffusion problem in interconnects is a multi-scale problem, both in length and time scales.

The traditional finite difference (FD) and finite element (FE) methods require a large number of computational nodes for such problems. As a result, computational times are long, even for a unit cell (micro-model), and hence unfeasible for parametric studies. Analytical methods, less complex in geometry, are not able to capture the important features of the thermal problem. Additionally, previous models have been primarily concerned with the steady-state Joule heating in interconnects, while the pulsed nature of the electric currents necessitates studying the effects of transient heat conduction in the interconnects as well. This confirms the need for the development of high fidelity transient multi-scale thermal models that can address the aforementioned issues.

Barabadi et al. [7] developed a computationally efficient hybrid multi-scale transient thermal modelling methodology. It incorporates two different multi-scale modeling approaches: "Progressive Zoom-in" (e.g. [8]), and "Proper Orthogonal Decomposition (POD)"([9]). This integration resulted in a model that has the capability of handling several decades of length scales, from tens of mm at "package" level to several nm at "interconnects", corresponding to various thermal events. This ability also applies for time scales from s to □s, at significantly lower computational cost, without compromising the desired accuracy. Hybrid scheme also provides the ability to rapidly predict thermal responses under different power input patterns, based on only a few representative detailed simulations [10]. It is demonstrated that utilizing the proposed model, the computational time is reduced by at least two orders of magnitude at every step of modeling.

To further describe the hybrid scheme, a chip and its function blocks, in a Flip Chip Ball Grid Array (FCBGA) package are considered. The hybrid scheme utilizes a combination of progressive-zoom in, and proper orthogonal decomposition (POD) as an effective approach for chip level electrical/thermal co-design for mitigation of reliability concerns, such as Joule heating driven electromigration. Random transient power distributions were assumed for the chip and its individual function blocks to demonstrate the capability of POD method in predicting different thermal scenarios. To validate this methodology, the results were compared with a finite element (FE) model developed in COMSOL®. The results of the model developed through hybrid scheme were in good agreement with the corresponding FE models.

3. HYBRID SCHEME FOR MULTI-SCALE THERMAL MODELING

As mentioned earlier, hybrid scheme combines the implementation of POD technique and progressive zoom-in approach:

3.1. POD Method: POD is a powerful method of data analysis that offers low-dimensional but accurate descriptions of a high-dimensional system. A comprehensive summary for applications of POD is given by Holmes et al. [11]. A detailed procedure to generate a 2-D POD based reduced order model is provided in [12]. The primary steps to generate a POD based reduced order model are: 1. Generating the observation matrix; 2. Calculating basis functions (POD modes); 3. Calculating POD coefficients, b_i; and 4. Generating the POD temperature field [10]. Combining POD with the Progressive Zoom-in approach greatly improves the computational efficiency.

3.2. Progressive Zoom-in Approach: Progressive zoom-in method is a top-down approach to model transient thermal problems. It integrates package, chip, sub-chip level analyses, acquiring the advantages of each (e.g. [8]). It has the capability of covering several orders of magnitude in length and time scale [12].

The overall hybrid approach is demonstrated in the flowchart provided in Fig. 2. The section marked via dashed lines represents the area used in this paper to illustrate the proposed multi-scale transient thermal modelling approach. The scheme is further explained through a case study.

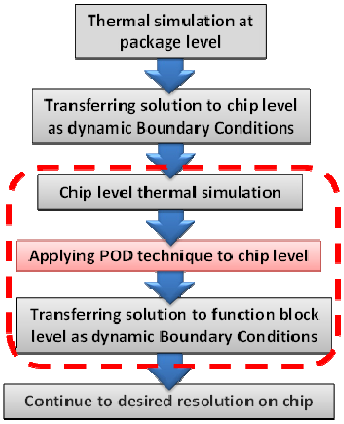

FIGURE 2. Flowchart of the hybrid scheme for multi-scale thermal modelling

4. CASE STUDY AND RESULTS

The focus of this study is to develop a transient thermal model at the chip and its function block level, with a spatial resolution of 1 □m. The modeling steps are described below:

4.1. Thermal Simulation at the Package Level: In order to have a realistic thermal solution at the chip level, we start from modelling the entire FCBGA package (shown in Fig. 3 (a)), including the surrounding mold, underfill, solder bumps, substrate, etc., using COMSOL software. At this level, the chip is treated as a solid block with effective material and thermal properties, without considering internal details. The details of the package level modelling including the thermal and material property calculations are provided in [10]. This package is used for low power portable systems where compact form factor prohibits the use of heat sinks and forced cooling. Natural convection boundary condition with a heat transfer coefficient of h=15 W/m^{2}K (typical range for air [8]) was applied to the top surface and a constant temperature boundary condition is assigned to the bottom surface.

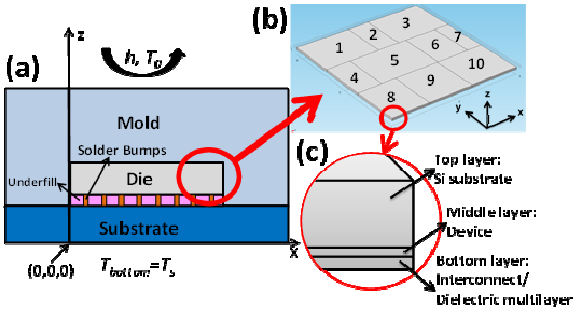

FIGURE 3.(a) Schematic of a simplified FCBGA for package level modeling, (b) zoomed-in outline of the chip with artificial block, and (c) zoomed-in schematic of the layers of the die used in chip level modeling ((a) and (c) are adapted from [10])

A full finite element (FE) model is developed for the entire package consisting of 75,919 elements, of which 343 are for the chip. The grid size is chosen after performing mesh independence analysis. Total power to the chip is Q=3 sin $2\pi t+3$ (W), which is applied for 1 s. The FE results for the spatial distribution of temperature in the package and chip after 1 s is displayed in Fig. 4 (a) and (b) respectively.

4.2. Transferring the Solution from Package Level to the Chip Level: Once the transient thermal solution is obtained at the package level for 1 s, the solution is then dynamically transferred in to the chip every 0.1 s as boundary conditions. On the top surface temperature, and on the bottom surface heat flux are applied to the chip. Due to the high aspect ratio of the chip, the side walls are considered adiabatic. Afterwards, the thermal solution is then linearly interpolated on each surface with much higher spatial resolution (268,033 elements to model the chip at this level vs. 343 elements to model the chip at the package level).

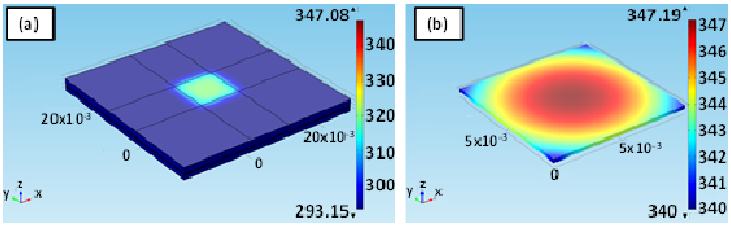

FIGURE 4. Spatial distribution of temperature rise extracted from FE method after 1 μs for (a) FCBGA package and (b) chip (adapted from [10])

4.3. Chip Level Thermal Simulation: At this level, chip is no longer assumed to be a solid block. It is now divided into 10 subdomains called function blocks which symbolize various components on the chip (shown in Fig. 3 (b)). Each block has three layers, displayed in Fig. 3 (c). These layers are: 1. Top Si layer with the thickness of 0.249 mm, 2. Middle layer which is a 5 μm-thick device layer, and 3. Interconnect/Dielectric multilayer at the bottom with the thickness of 16.72 μm. The third layer consists of 21 sub-layers including 10 metal layers. Details on the calculation of thermal and material properties of the function blocks can be found in [10]. In order to have a realistic and accurate thermal simulation, a detailed dynamic power map of the function blocks are required which is discussed in the following section.

4.4. Applying POD Technique to Chip Level: After determining the temperature distribution at package level and transferring it to the chip level as boundary conditions, a POD model is developed for chip level analysis using the procedure discussed in section 3.1. Total of 6 observations based on the transient temperature solution were taken in the first 0.5 s using the package level FE thermal solution that is transferred on to the chip level model setup. These observations correspond to the temperature solutions obtained at different time instants. As previously demonstrated by Barabadi et al. [12], for any linear system, POD method has the ability to predict transient thermal solution regardless of the temporal or spatial dependence of the applied heat source. In other words, the POD solutions of these transient thermal scenarios are independent of the initial observations. Essentially, for any linear system, once the solution to a sample case of chip total power is obtained, there is no need to generate new observations, or full field FE simulations. This feature provides the ability to predict temperature distributions for arbitrary heat

inputs, by using a smaller sample set of applied heat sources and power maps, which results in considerably decreased simulation time.

To further verify this feature of POD, a randomly generated transient power distribution, shown in Fig. 5 (d), is used in the POD thermal model development. As can be implied from Fig. 5 (d) the new power profile differs from the chip power in duration, magnitude, and temporal dependency. Furthermore, since at this level of simulation the chip is no longer treated as a solid block and is divided into subdomains, the dynamic power grid also needs to be assigned to individual function blocks. Therefore, 10 random power profiles with minimum and maximum values of 0 and 3 W were generated between 0 and 1s and assigned to each block in such a way that their sum will equal the total chip power as shown in Fig. 5 (d). The power sources for blocks 1, 2, and 10 are presented in Fig. 5 (a-c) as representatives.

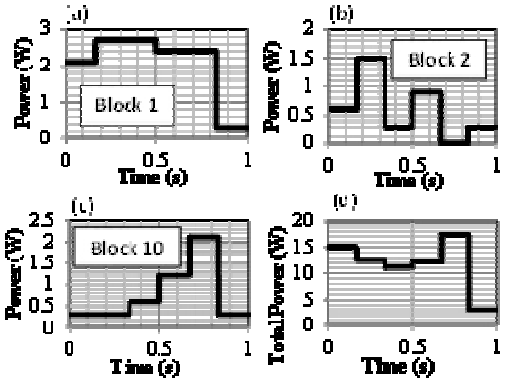

FIGURE 5. Dynamic randomly generated power profile for function blocks 1, 2, 3 (a-c) and randomly generated total chip power (d) (adapted from [10])

After assigning the function blocks power profiles, the POD modes are calculated. In order to have a reliable but fast model, only five POD modes are utilized. This is selected such that the cumulative correlation energy, E_m, [13], is larger than 99.0%. Because the POD modes are three-dimensional, for better visualization, 2D contour plots of the first 6 POD modes at the interface of device and interconnect/dielectric layers are depicted in Fig. 6. In this figure, POD modes are normalized with respect to the total sum of the generated modes. The POD coefficients, b_i, were then calculated as functions of time using the method of Galerkin Projection [10].

After calculating the POD modes and coefficients, the transient thermal solution can be obtained. Fig. 7 shows the spatial distribution of temperature after 0.95 s based on POD method (Fig. 7 (a)) and full field FE model (Fig. 7 (c)) inside the chip and its function blocks (Fig. 7 (b)). The temporal distribution of temperature based on POD model and FE analysis at four different points inside the function blocks are also provided in Fig. 8. The mean absolute error between the POD and FE model is 8 % over the entire space and time domain. It must be noted that the computational time required for POD model is approximately 20 s, which is 2 orders of magnitude less than that of FE results (~ 27 min).

4.5. Transferring the Solution from Chip level to the Function Block Level: If higher spatial resolution on the function blocks are required, the procedure in section 3.2 can be repeated and transient thermal solution can be transferred to any of the function blocks in terms of boundary conditions. In general, procedures 3.1- 3.4 can be repeatedly applied, until the desired resolution on the chip is achieved.

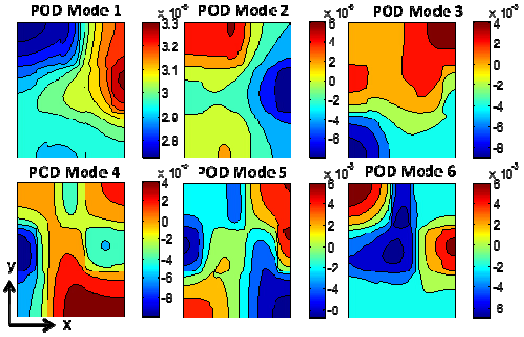

FIGURE 6. 2D contour plots of the first 6 POD Modes at the interface of device and interconnect/dielectric layers.

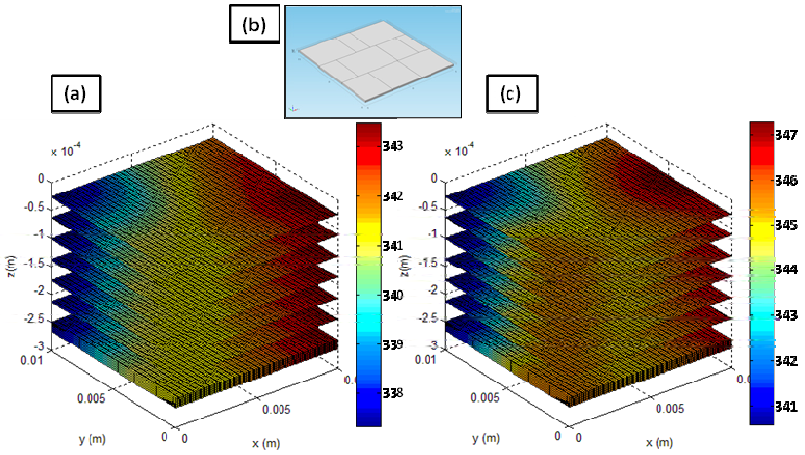

FIGURE 7. Spatial distribution of temperature rise at 0.95 s extracted from the POD model (a) and FE simulation (c). The domain is sliced horizontally along the XY plane. The outline of chip with the function blocks are shown in (b).

5. THERMAL MODELING FOR CO-DESIGN OF MICROFLUIDICALLY COOLED 3D ICs

Wire interconnections become longer in 2D topology, with increasing number of transistors, which can increase the latency in the wire and reduce the expected benefit from integration [14]. 3D ICs as the next generation IC technology achieve higher integration with the technology of through-silicon vias (TSVs). The vertical integration

can reduce the global wire length by as much as 50% [15]. The wire limited clock frequency could be increased nearly four-fold [16]. However, the increased power density due to the stack results in great thermal challenges. If the heat cannot be removed effectively, the temperature rise will degrade the electrical performance, and adversely impact reliability. One important drawback of high temperature in ICs is the non-linear increase in leakage power [17]. The leakage power cannot be used by the transistors and will further exacerbate the thermal stress. Inter-tier microfluidic cooling has been proposed as a possible solution to the thermal problem of 3D ICs due to its high performance and scalability [18].

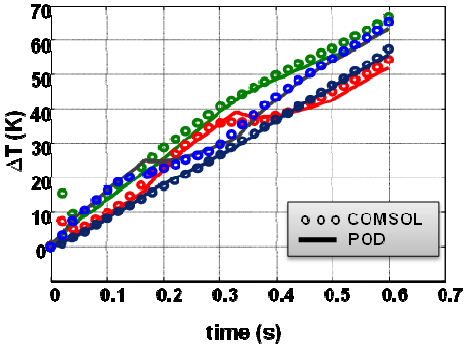

FIGURE 8. Comparison of Temporal dependence of temperature rise between FE (markers) and POD (solid lines) models at 4 different points inside the die.

Figure 9 shows the schematic of physical model of 3D ICs with inter-tier microfluidic cooling [19]. The 2-tiers stack with processor and L2 cache memory is placed on the substrate through interposer. Each tier consists of a SiO_2 & Metal layer, an active layer, and a silicon base layer. SiO_2 is used for insulation and bonding. Active layer is a thin layer in which most of the heat is generated. Staggered micro pin fin array used for cooling is fabricated between the two tiers by Deep Reactive Ion Etching (DRIE). Signal vias are embedded in the pin fins to provide communication between the two tiers. The stack is electrically connected to the outside through the Si interposer. The chip size is 8.4 mm X 8.4 mm. Thickness of the silicon base and is 100 μm. Thickness of SiO_2 & Metal is 10 μm. The active layer is assumed zero thickness for simplicity.

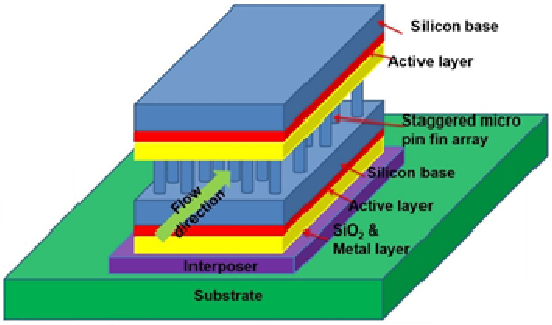

FIGURE 9. Schematic of physical model of 3D ICs with inter-tier microfluidic cooling.

The pin fin diameter is 100 μm, heigh 300 μm, and pitches in both direction are 200 μm. DI-water with inlet temperature 20 $^{\circ}C$ is used for cooling.

A coupled power-thermal mode is used to model the 3D ICs in Figure 9. Figure 10 shows the floorplans for processor and L2 cache. The processor is a x86 16-cores processor resemble the Intel Nehalem structure, a typical Out-of-Order microarchitecture including: FE (pipeline frontend and L1 instruction cache), SC (Out-of-Order scheduler), INT (integer unit), FPU (float-point unit) and DL1 (L1 data cache). Each core has a private L1 data cache of 128KB and a shared L2 cache. The L2 cache layer consists of 16 SRAM banks each with size of 2MB.

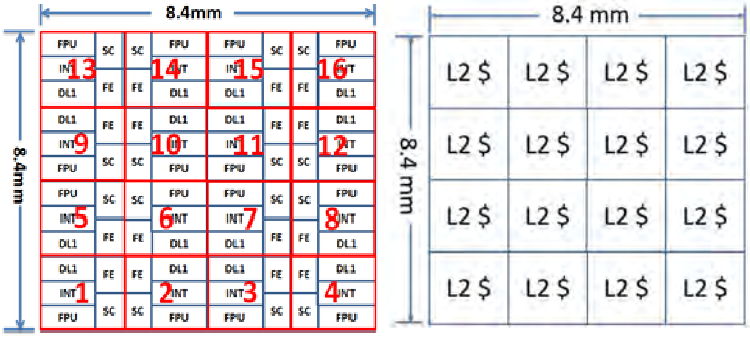

FIGURE 10: Floor plans (a) processor, and (b) L2 cache [19].

A cycle-level timing model is used to execute compiled 32-bit x 86 binaries. Simulations are run for 500M clock cycles to warm up the processor state and reach a "region of interest" where the computational characteristics are representative in the benchmark program. The power at each block in the processor floor plan is sampled every 10 microseconds to produce a power trace. Table 1 shows the power distribution for each module. The total power of processor is 165.5 W with maximum heat flux 301.3 W/cm^2. The total power of L2 cache is 49.6 W. The power distribution will in input to the thermal model.

	FPU (W)	INT (W)	DL1 (W)	SC (W)	FE (W)	L2 (W)
Core 9	1.16	1.52	2.68	1.73	0.96	3.1
Other cores	1.69	2.06	2.81	2.31	1.63	3.1

TABLE 1. Power distribution for each module.

First, the 3D stack is discretized into multiple control volumes. Each of the control volumes is around one pin and consists of the fluid and solid domain. The temperatures of the two active layers and the fluid within each control volume are assumed uniform and stored in 3 2D matrix. Figure 11 shows the energy flow within each control volume. Each tier has in-plane conduction from four directions. Also there are conduction between the two tiers, conduction between the stack and PCB, convection between the stack and coolant.

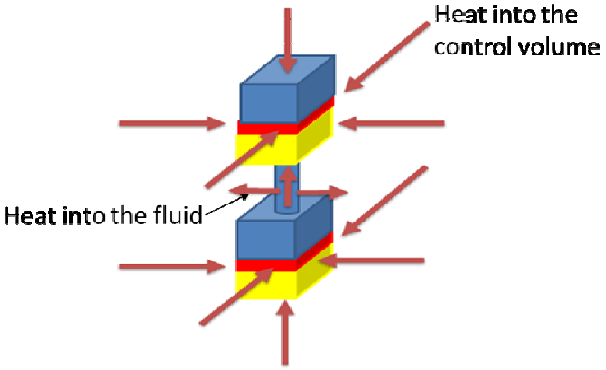

FIGURE 11. Energy flow within one control volume.

The thermal model is based finite volume approximation of the energy equations for both the solid and fluid within the control volumes:

$$Solid: \dot{q_{gen}} + \dot{q_{cond}} + \dot{q_{conv}} = 0 \quad (1)$$

$$Fluid: \dot{m}C_p(T_{f,in} - T_{f,out}) + \dot{q_{conv}} = 0 \quad (2)$$

where $\dot{q}_{gen}$ is power dissipation. It consists of two part: dynamic power from the power simulation, and static power which depends on temperature. $\dot{q}_{cond}$, $\dot{q}_{conv}$ are the heat conduction and heat convection rate terms. $\dot{m}$ is the mass flow rate into the control volume. C_p is the heat capacity of the fluid. A system of energy equations could be built for the 3D ICs. The conduction and convection heat rate can be determined by the temperatures of two tiers and fluid. So the system of energy equations could be transferred to a system of equations with only temperatures as variables. After iterative calculations, the temperature within each control volume can be obtained.

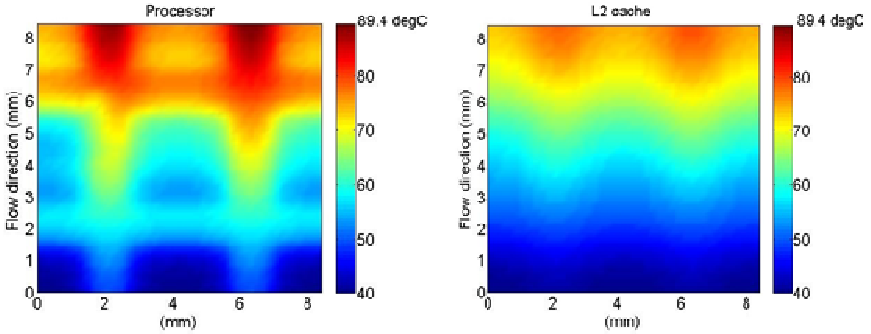

FIGURE 12: Temperature distribution of processor and L2 cache, pumping power 0.02 W.

Figure 12 shows the temperature distribution of processor and L2 cache when the pumping power is 0.02 W and processor is located at the bottom of the stack. The temperature of processor is non-uniform due to the non-uniform power distribution. The maximum temperature is near the exit of the fluid due to the bulk fluid temperature. Although the power distribution of L2 cache is uniform, its temperature distribution is non-uniform due to the cross-tier heat conduction. Table 2 shows the

maximum temperature and leakage power under various pumping power. When the pumping power is 0.005 W, the maximum temperature is 123.1 °C and the leakage power is 26.7 W. If the air cooled heat sink instead of inter-tier microfluidic cooling is used for cooling, the temperature and leakage power would be much higher. When the pumping power is increased to 0.12 W, the maximum temperature is reduced to 65.7 °C and leakage power is reduced to 7.3 W. This proves the inter-tier microfluidic cooling could achieve significant performance enhancement.

Pumping power (W)	Tmax(°C)	Leakage power (W)
0.005	123.1	26.7
0.01	110.5	17.2
0.015	101.6	12.1
0.02	89.4	8.9
0.04	80.1	7.6
0.08	70.9	7.4
0.12	65.7	7.3

TABLE 2. Maximum temperature and leakage power under various pumping power.

6. DATA DRIVEN MODELING OF AIR TEMPERATURES NEAR DATA CENTER RACKS

Proper orthogonal decomposition (POD), introduced in Section 3.1, can pave the way for an efficient decision support system to optimize the energy consumption of a data center. The most attractive feature of POD is its computational efficiency and flexibility. Currently, data center cooloing hardware is controlled based on air temperature measurements. Sampling rate is a critical cost item for such transient temperature data acquisition. High sampling rate means larger sampling cost and vice versa. To solve this problem, we conducted a case-study with the hypothesis that a POD-based data-driven algorithm can improve the temporal granularity of the temperature data, acquired using selected sensors. Data center air temperatures are a function of time and rack heat load. Depending upon the sampling intervals of time and rack heat load, air temperature interrogation point can lie on one of the nine possible interrogation spaces, as shown in Figure 13. Four of these nine zones, namely Zones A, B, C, and D convey most physical significance. Zone A represents normal mode of operation, Zone B represents failure mode, Zone C represents critical mode, and Zone D represents retrofit mode. The modeling fidelity is documented in Figure 14. It shows the maximum errors for Zones A, B, C, and D are equal to 5%, 9%, 12.5%, and 12.5%, respectively, similar to [20] for slightly different conditions.

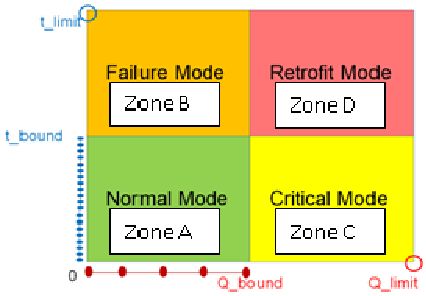

FIGURE 13: Two dimensional parametric space, comprising heat load and time, for data center air temperature predictor space.

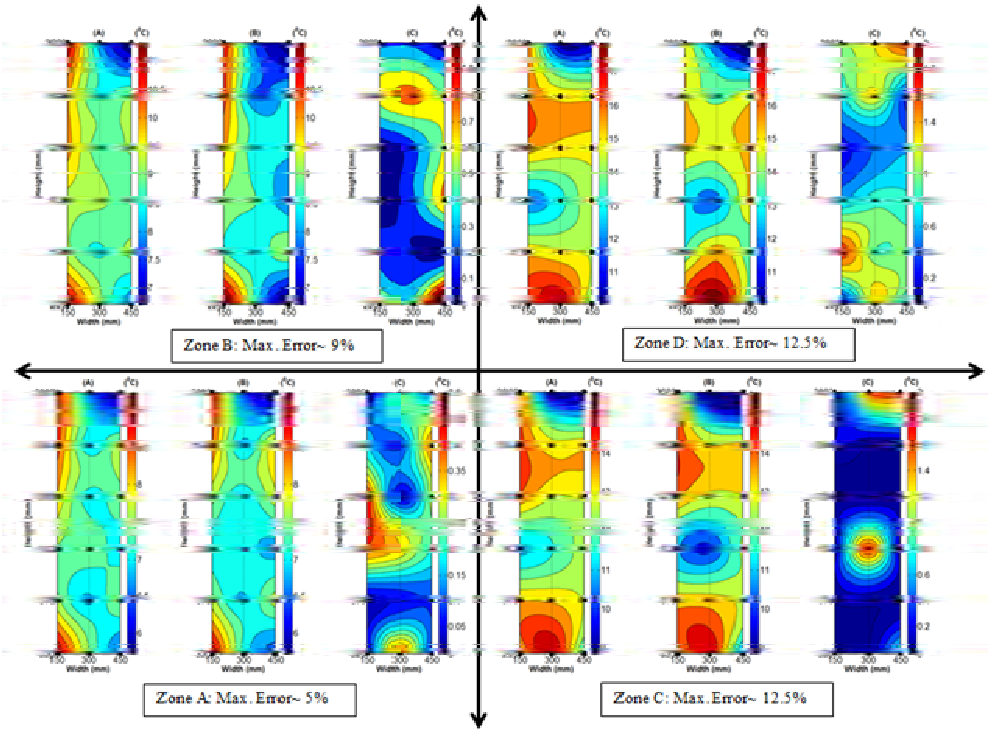

FIGURE 14. Fidelity of POD-based prediction framework

7. PROGNOSIS-BASED RELIABILITY MODELLING OF DATA CENTER AIR TEMPERATURES

Temperature prognosis, or future prediction, at critical locations, especially at sever inlets, is potentially befeficial for the reliability monitoring of data centers. POD facilitates an efficient temperature prediction tool; however, the modeling accuracy is a critical concern for the prognosis.

Therefore, error conditioning is an important requirement. The error--defined as the differences between data and corresponding predictions--can be computed using a data-driven approach or by a semi-analytical formulation. The semi-analytical formulation is more cost-effective because it requires minimal hardware deployment. The analytical error is given by:

$$E = c_1(g+h) + \left[\frac{l\exp(\theta)}{1-\theta}(c_2 + c_3 g)\sum_{i=k+1}^{n}\lambda_i\right]^{\frac{1}{2}} \tag{3}$$

Where, g is the normalized temporal resolution, h is the normalized spatial resolution, l is the size of input space, θ is the normalized time, λ_i is the eigenvalue corresponding to POD modes, k is the number of retained POD modes, c_1, c_2, c_3 are arbitrary constants.

Figure 15 shows the numerical matching procedure to determine the empirical constants (c_1, c_2, c_3). The redline with open triangular markers shows how the data-driven prediction errors—deviations between data and predictions—vary with time. The predictions are computed using input data generated by measuring transient response of air temperature ensuring sudden switch-on of the test computer room air conditioning (CRAC) unit. The temperature data are collected in [10-200] s interval at 10 s sampling period. Figure 15 shows the extrapolation horizon staring from 201 s. The extrapolation window lasts till 224 s, because the error becomes higher than an arbitrarily-specified absolute error bound of 2 ℃. The empirical constants (c_1, c_2, c_3) are determined by the conjugate gradient method. This matching shown in Figure 15 is conducted for the average air temperature. Similar procedure can be performed for all sensor points. Unless the data center condition is drastically changed, the calibration constants once determined can be used repeatedly over time.

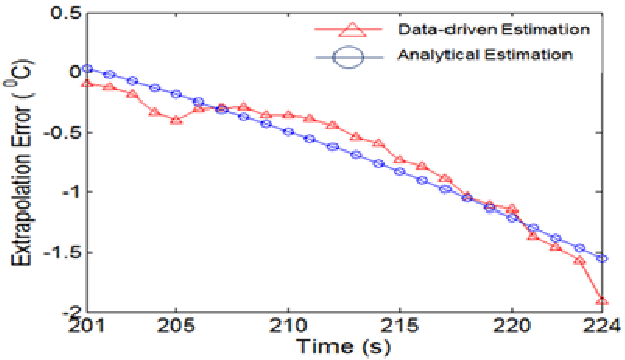

FIGURE 15. Specification of a priori error by the conjugate gradient method. For this particular dataset, c_1=3.1, c_2=-0.02, c_3=-0.02

The importance of the error conditioning is evident from Figure 16, comprising the contour plots generated from the air temperature data, predictions, and deviations at the test server inlet at 206 s. Figure 16(c) shows the deviations are considerably large ranging from -2.0 ℃ to 0 .5 ℃, i.e., more than 10% of the maximum inlet air temperature. These are consistent with [21].

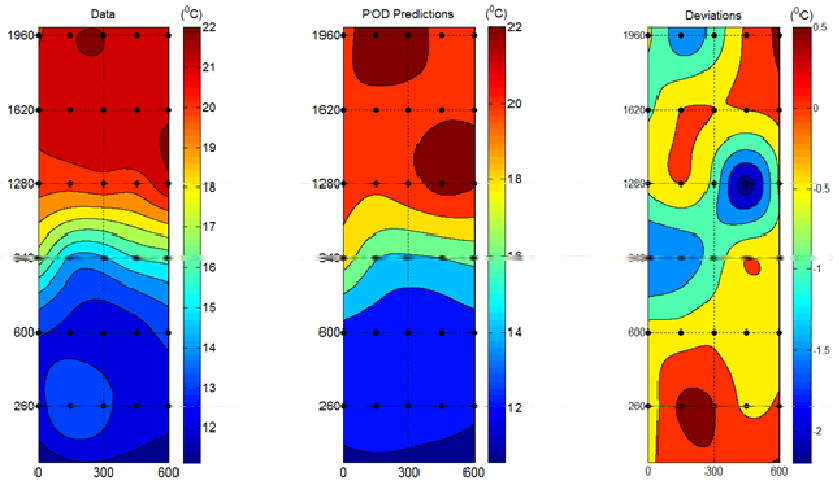

(a) (b) (c)

FIGURE 16. Fidelity of POD-based temperature prognosis at 206 s at the test rack inlet.

8. SENSOR FUSION FOR REDUCING TEMPERATURE MONITORING COST

Measurement-based thermal control is of paramount importance to optimize energy consumption in data centers. Therefore, cost-effective data center management demands optimizing sensor number for monitoring air temperatures at critical locations. The optimization problem pertains to minimizing sensor numbers, while the error remains below a certain pre-assigned limit.

$$\min \text{ (sensor number)}$$
$$\text{such that, deviation} < \text{error limit.}$$

The effectiveness of POD for reducing the number of sensors is assessed using the temperature data collected at the test rack exhaust located near the top of the test rack as shown in Figure 17. The input air temperature data are collected by 13 sensors at the locations marked by black filled circles. These are used to predict air temperatures at the locations indicated by open circles. The prediction accuracy of the POD-based framework shows a maximum relative deviation of 2.2%. The high predictive accuracy at new locations indicates the usefulness of POD in reducing the number of monitoring sensors. In this particular case, the required sensor number has been reduced to 13 from 21, a 38% savings in number of sensors.

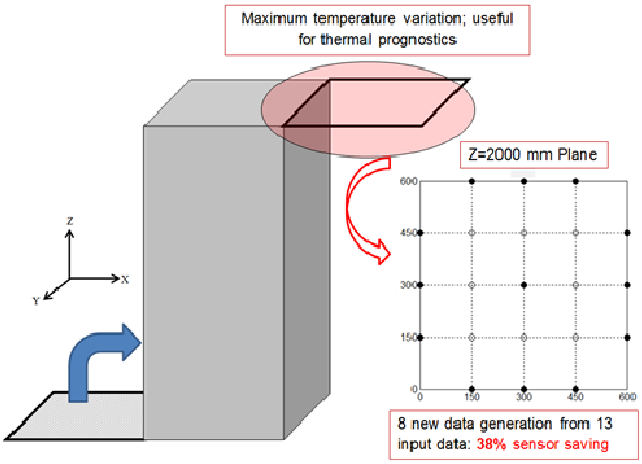

FIGURE 17. Test plane for the sensor reduction

9. CONCLUSION

Three examples are presented to illustrate the emerging thermal modelling needs to enable co-design of multi-scale IT systems, with the objective of energy efficient operation, while meeting the performance and reliability targets. Reduced order thermal modelling techniques are employed, in order to couple the thermal analyses with the overall co-design framework. Two such techniques illustrated are based on control volume energy balances, and POD. For the POD technique, both computational observations as well as a data driven framework are presented.

REFERENCES

[1] K. Fuchs, The conductivity of thin metallic films according to the electron theory of metals, eds., 34, 100-108, 1938.

[2] E. Sondheimer, The mean free path of electrons in metals, *Advances in Physics*, 1, 1-42. 1952.

[3] J. M., Ziman, and P. W. Levy, Electrons and phonons, *Physics Today*, 14, 64, 1961.

[4] Y. Namba, Resistivity and temperature coefficient of thin metal films with rough surface, *Japanese Journal of Applied Physics*, 9(11), pp. 1970.

[5] S. B. Soffer, Statistical model for the size effect in electrical conduction, Journal of Applied Physics, 38, 1710-1715, 1967.

[6] S. P. Gurrum, Y. Joshi, W. P. King, and K. Ramakrishna, Numerical simulation of electron Transport through Constriction in a Metallic Thin Film," *Electron Device Letters, IEEE*, 25(10), pp. 696-698, 2004.

[7] B. Barabadi, S. Kumar, V. Sukharev, and Y. Joshi, Multi-scale transient thermal analysis of microelectronics, eds., Houston, TX, pp. 2012

[8] L. Tang, and Y. Joshi, A multi-grid based multi-scale thermal analysis approach for combined mixed convection, conduction, and radiation due to discrete heating, *Journal of Heat Transfer*, 127(1), 18-26, 2005.

[9] J. L. Lumley, The structure of inhomogeneous turbulent flows, Atmospheric turbulence and radio wave propagation, 166-178, 1967.

[10] B. Barabadi, Y. Joshi, and S. Kumar, Multi-scale transient thermal analysis of microelectronics, *Electronic Packaging,* pp. 2014.

[11] P. Holmes, J. L. Lumley, and G. Berkooz, Turbulence, coherent structures, dynamical systems and symmetry, *Cambridge University Press*, 1998

[12] B. Barabadi, Y. Joshi, and S. Kumar, Prediction of transient thermal behavior of planar interconnect architecture using proper orthogonal decomposition method, *ASME InterPACK*, 213-224, 2011.

[13] K. Bizon, G. Continillo, L. Russo, and J. Smula, On POD reduced models of tubular reactor with periodic regimes, *Computers & Chemical Engineering*, 32(6), 1305-1315, 2008.

[14] J. D. Meindl, Beyond Moore's law: the interconnect era, *Computing in Science & Engineering*, 5(1), 20-24, 2003.

[15] N. H. Khan, S. M. Alam, and S. Hassoun, System-level comparison of power delivery design for 2D and 3D ICs, *Proc. 3DIC 2009*, San Francisco, CA, USA, 1-7, 2009.

[16] M. Bamal et al., Performance comparison of interconnect technology and architecture options for deep submicron technology nodes, *2006 International Interconnect Technology Conference*, San Francisco, CA, USA, 202-204, 2006.

[17] K. Roy, S. Mukhopadhyay, H. Mahmoodi-Meimand, Leakage current mechanisms and leakage reduction techniques in deep-submicrometer CMOS circuits, *Proc. of IEEE*, 91, 305-327, 2003.

[18] M. S. Bakir, J. D. Meindl Eds, *Integrated interconnect technologies for 3D nanoelectronic systems*, Artech House, 2008.

[19] Z. Wan., H. Xiao, Y. Joshi, S. Yalamanchili, Electrical/thermal co-design of multi-core architectures and microfluidic cooling for 3D stacked ICs, *Proc. of 2013 19th Int. Workshop on Thermal Investigations of ICs and Systems*, 237-242, 2013.

[20] R. Ghosh and Y. Joshi, Rapid temperature predictions in data centers using multi-parameter proper orthogonal decomposition, *Numerical Heat Transfer*, Part A: Applications, 66, 41-63, 2014.

[21] R. Ghosh and Y. Joshi, Error estimation in POD-based dynamic reduced-order thermal modeling of data centers, *International Journal of Heat and Mass Transfer*, 57, 698-707, 2013.

Third International Conference on Computational Methods for Thermal Problems
THERMACOMP2014, June 2-4, 2014, Lake Bled, Slovenia
N. Massarotti, P. Nithiarasu and B. Sarler (Eds.)

Shock boundary layer interactions: a gradient smoothed method

G. R. Liu[1,2] and Jianyao Yao[1]
[1]Department of Aerospace Engineering and Engineering Mechanics, University of Cincinnati
Cincinnati, Ohio 45221-0070, United States
[2]Summer Consultant, Taiyuan University of Technology, Taiyuan, Shanxi, 030024, China
liugr@uc.edu, yaojy@uc.edu

ABSTRACT

A GSM-CFD solver is newly developed based on the gradient smoothing theory for both compressible and incompressible flows. In the GSM-CFD solver, all the first and second order spatial gradient are calculated using the gradient smoothing operation to improve the accuracy and robustness since all the gradient approximations are carried out on the locally and globally conservative gradient smoothing domains (GSD). An efficient matrix-based algorithm and the corresponding edge-based data structure are devised for the spatial gradient approximation using GSM. With the GSM for gradient calculation, the flow governing equations can be discretized and solved in a strong form, and higher accuracy can be achieved. To get better resolution near the shock region, a solution-based adaptive mesher is integrated with the solver to form an adaptive GSM-CFD solver. In the adaptive solver, the solution domain is divided into two parts, the shock-wave-driven and the boundary-layer-driven zone, and proper meshes are generated separately in these two regions. Numerical examples are given to show the effectiveness of the proposed adaptive GSM-CFD solver.

Key Words: *Gradient Smoothing Method, CFD, Solution-Based Adaptation, Shock-Boundary Layer Interaction.*

1. INTRODUCTION

After decades of development, CFD has become a standard tool which is widely used for both engineering and scientific purpose. There are three kinds of numerical methods for the fluid governing equations, namely the finite difference method (FDM), the finite element method (FVM) and the finite volume method (FVM) [1]. There are also some other approaches like smoothed-particle hydrodynamics (SPH) [2][3] and lattice Boltzmann method that are developed for complex flows [4][5]. Recently, gradient smoothing methods has been developed as a strong-form method for solving the general partial differential equations, named as smoothed finite element method [6][7] for solid and GSM-CFD for fluid [1][8][9][10], respectively.

Although the GSM-CFD solver is like a combination of strong-form (equation discretization) and the weak-form (gradient approximation), there still are some obvious features distinguish it from conventional FDM or FVM. First, different kinds of smoothing functions can be chosen for the gradient approximation to provide results with desired accuracy. That means the GSM is a more versatile, flexible and designable method. Second, both first- and second-order gradients are always approximated on compact and conservative gradient smoothing domains. Therefore, the GSM for gradient calculation is stable, accurate, robustness and insensitive to mesh distortions.

A matrix-based algorithm and corresponding edge-based data structure for GSM are devised to improve the computational efficiency. The edge-based data structure stores the geometrical information of the smoothing domains, and is used to form the element (local) and the global B-matrix, which relates the field variables at nodes and the gradients at nodes. In the matrix-based method, the spatial gradient can be simply calculated as the multiplication of a sparse matrix and a vector.

The solution based adaptive GSM-CFD solver for turbulent flow is developed based on the inviscid adaptive GSM-CFD solver [8] to obtain better resolution at the shock and shock-boundary layer interaction regions. In this adaptive solver, the solution domain is divided into two parts, the shock-wave-driven and the boundary-layer-driven zone. In the shock-wave-driven zone, the adaptive unstructured mesh is generated using the advancing front method to handle the complex geometry, while in the boundary-layer-driven zone, the structured layered mesh is adopted to generate meshes with very large aspect ratio to resolve the boundary-layer flows with less number of cells and nodes. Several numerical examples are presented to show the effectiveness of the proposed GSM-CFD solver.

2. METHOD

2.1 Gradient smoothing method and gradient smoothing domains

The gradients of a field variable U at point x_i in domain Ω_i can be approximated using a weak-form of

$$\nabla U_i \equiv \nabla U_i(x_i) \approx \int_{\Omega_i} \nabla U(x)\hat{w}(x-x_i)\mathrm{d}\Omega \tag{1}$$

where ∇ is the gradient operator, and $\hat{w}$ is a smoothing function which can be chosen properly based on the requirement of gradient accuracy. The integration in Eq. (1) can be written as the sum of two parts, the integration on the domain and on the domain boundary:

$$\nabla U_i \approx \int_{\partial\Omega_i} U(x)\hat{w}(x-x_i)\mathbf{n}\mathrm{d}s - \int_{\Omega_i} U(x)\nabla\hat{w}(x-x_i)\mathrm{d}\Omega \tag{2}$$

where $\partial\Omega$ represents the boundary of the domain and $\mathbf{n}$ denotes the outward unit normal vector on boundary. The most efficient smoothing function is the piecewise constant function defined as

$$\hat{w}(x-x_i) = \begin{cases} 1/V_i, & x \in \Omega_i \\ 0, & x \notin \Omega_i \end{cases} \tag{3}$$

where V_i is the volume of the smoothing domain. By using this kind of smoothing function, the first- and second-order gradients at x_i can be written as

$$\nabla U_i \approx \frac{1}{V_i}\int_{\partial\Omega_i} U(x)\mathbf{n}\mathrm{d}s, \quad \text{and} \quad \nabla(\nabla U_i) \approx \frac{1}{V_i}\int_{\partial\Omega_i} \nabla U(x)\mathbf{n}\mathrm{d}s \tag{4}$$

The gradient smoothing domains (GSDs) can be constructed from the primitive meshes. There are two kinds of GSDs, one is node-associated GSD (denoted as nGSD) for gradient approximation at nodes, and the other one is midpoint-associated GSD (denoted as mGSD) for gradient approximation at edge midpoint. The illustrations of 3D GSDs are shown in Figure 1.

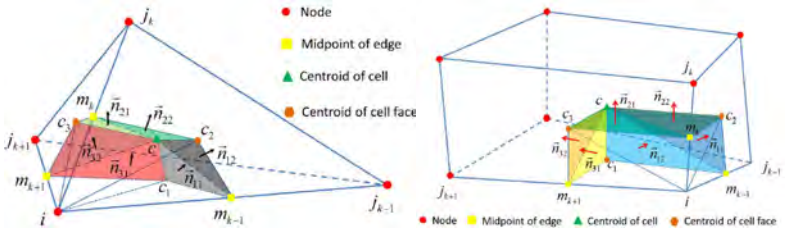

(a) nGSD of tetrahedron (b) nGSD of hexahedron

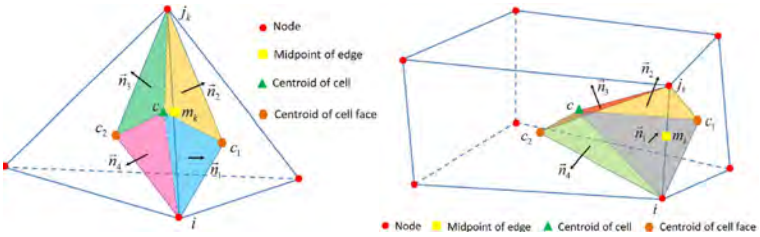

(c) nGSD of tetrahedron (d) nGSD of hexahedron

Figure 1. Illustration of 3D gradient smoothing domains

2.2 Matrix-based GSM for gradient approximation

After the GSDs are constructed, the gradients at nodes or edge midpoints can be calculated as boundary integration shown in Eq. (4). The Gauss integration scheme is used for boundary integration, and we can choose the number of integration points according to the accuracy requirement. Usually, the one-point quadrature is adopted for GSM, which means one integration point on each cell edge. The matrix form for gradient calculation using GSM can be expressed as:

$$\frac{\partial \mathbf{U}}{\partial s} = \mathbf{B}\square\mathbf{U} \tag{5}$$

where **B** is the geometrically dependent block-wise sparse matrix, and **U** is the vector of field variables. The matrix **B** can be assembled from the each cell of the primitive mesh, and corresponding new types of edge-based data structures can be constructed as in Figure 2.

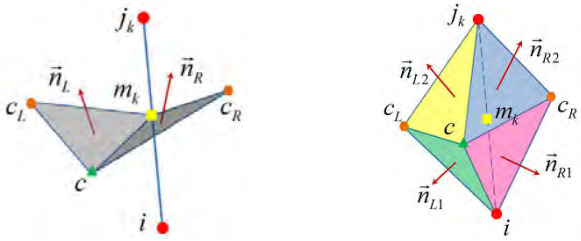

(c) nGSD (d) mGSD

Figure 2. Illustration of 3D edge-based data structure

2.3 Solution-based adaptive GSM-CFD solver for turbulent flows

There are two main parts in the adaptive GSM-CFD solver, the adaptive mesher and the GSM-CFD solver. The flow chart is shown in Figure 3.

3. RESULTS

3.1 Results of gradient approximation

Here we present the results for gradients approximation on linear, polynomial, harmonic and exponential variable fields. The error norms of the gradient approximation calculated using conventional finite volume method (here the open source SU2 package is used for comparison [11]) and the proposed GSM on hexahedral and prismatic meshes. We can see the proposed GSM preforms consistently better than FVM for gradient approximation.

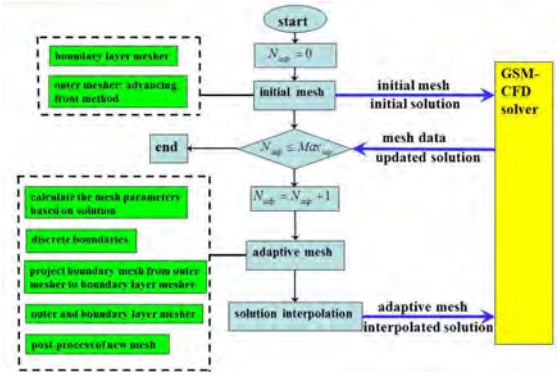

Figure 3. Flowchart of the adaptive GSM-CFD solver

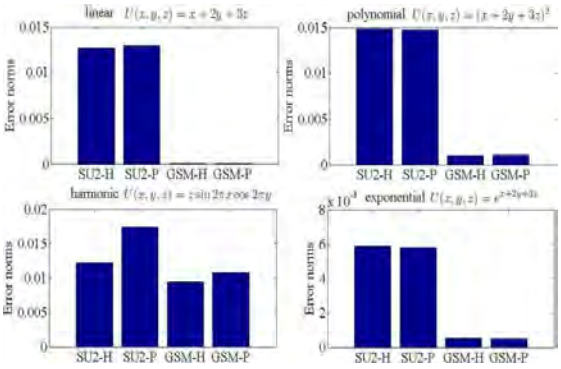

Figure 4. Results of error norms for gradient approximation on various variable fields. In the figure, SU2 denotes the conventional FVM, -H denotes the hexahedral mesh, and -P denotes the prismatic mesh.

3.2 Example of adaptive GSM-CFD solver

Here, the transonic flow over RAE 2822 airfoil is used as the example for adaptive GSM-CFD solver. The density results and adaptive mixed meshes are shown in Figure 5. We can see that the mesh is automatically refined around the shock region.

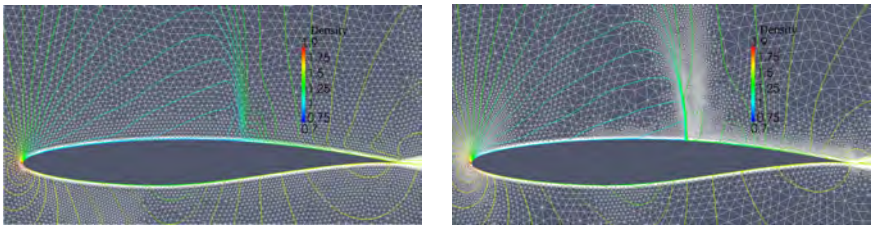

(a) initial mesh (b) 1st adaptive mesh

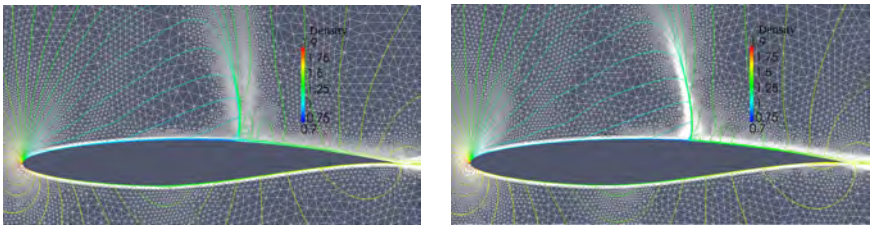

(c) 2nd adaptive mesh (d) final adaptive mesh

Figure 5. Adaptive mesh for RAE 2822 transonic airfiol. Flow conditions: $T_\infty = 255\text{K}$, $p_\infty = 1.07\times10^5\,\text{Pa}$, $Re = 6.5\times10^6$, $Ma = 0.729$ and $\alpha = 2.31^o$.

4. CONCLUSIONS

The matrix-based GSM and corresponding edge-based data structures are described and the solution-based adaptive solver for compressible transonic turbulent flows is also introduced in this paper. The numerical examples for both gradients approximation and the transonic turbulent flow show the effectiveness of the proposed GSM-CFD solver.

ACKNOWLEDGMENTS

This work is partially supported by the United States NSF Grant under the award No. 1214188, and partially supported by the United States ARO contract: No.W911NF-12-1-0147.

REFERENCES

[1] Liu G. R., Xu G. X. A gradient smoothing method (GSM) for fluid dynamics problems. International Journal for Numerical Methods in Fluids, 58(10):1101-1133, 2008.
[2] Liu G. R., Liu M. B. Smoothed particle hydrodynamic: a meshfree particle method. World Scientific, Singapore, 2003.
[3] Liu M. B., Liu G. R. Smoothed particle hydrodynamics (SPH): an overview and recent developments. Arch Comput Methods Eng, 17:25–76, 2010.
[4] Chen S., Doolen G. D. Lattice Boltzmann method for fluid flows. Annu Rev Fluid Mech 30:329–364, 1998.
[5] Aidun C. K., Clausen J. R. Lattice–Boltzmann method for complex flows. Annu Rev Fluid Mech 42:439–472, 2010.
[6] Liu G. R. Smoothed finite element methods. CRC Press, Boca Raton, 2010.
[7] Liu G. R., Dai K. Y., Nguyen T. T. A smoothed finite element method for mechanics problems. Computational Mechanics, 39(6):859-877, 2007.
[8] Xu G. X., Liu G. R., Tani A. An adaptive gradient smoothing method (GSM) for fluid dynamics problems. Int J Numer Method Fluids 62:499–529, 2009.
[9] Yao J., Liu G. R., Chen C.-L. A moving-mesh gradient smoothing method for compressible cfd problems. Math Models Methods Appl Sci 23(2):273–305, 2013.
[10] Yao J., Liu G. R. A matrix-form GSM–CFD solver for incompressible fluids and its application to hemodynamics, Computational Mechanics, 2014.
[11] Palacios F., Colonno M. R., et al. Stanford University Unstructured (SU2): an open-source integrated computational environment for multi-physics simulation and design. AIAA 2013-0287.

Third International Conference on Computational Methods for Thermal Problems
THERMACOMP2014, June 2-4, 2014, Lake Bled, Slovenia
N. Massarotti, P. Nithiarasu and B. Sarler (Eds.)

FEM ANALYSIS OF CONJUGATE CONDUCTION-CONVECTION HEAT TRANSFER IN MICRODEVICES

Nonino Carlo, Savino Stefano, Del Giudice Stefano
Università degli Studi di Udine, Dipartimento di Energetica e Macchine,
Via delle Scienze 206, 33100 Udine, Italy
carlo.nonino@uniud.it, stefano.savino@uniud.it, stefano.delgiudice@uniud.it

ABSTRACT

A summary is given of the results obtained by the authors' research group using, as an alternative to massive CFD, an efficient finite element procedure to solve even geometrically complex conjugate heat conduction-forced convection problems with limited computational resources. Parametric studies have been carried out on the thermal behaviour of thick-walled microchannels and on the performances of cross-flow micro heat exchangers.

Key Words: *Micro Heat Transfer, Finite Elements, Conjugate Conduction-Convection.*

1. INTRODUCTION

The coupling between the heat conduction in the solid walls and the forced convection inside the flow passages must be taken into account in the numerical analysis of thermal performances of most micro thermal devices because the thickness of the solid walls is usually comparable with the transverse size of the flow passages.

In this work, an efficient finite element procedure is used to solve conjugate heat conduction-forced convection problems with limited computational resources, but good accuracy, even in complex geometries such as those occurring in cross-flow micro heat exchangers. The adopted technique implies the step-by-step solution of the parabolised momentum equations in the fluid domain, followed by the solution of the energy equation in the entire domain, corresponding to both its solid and the fluid parts [1].

First, parametric studies were carried out on the thermal behaviour of thick-walled microchannels [1]. Then, the performances of cross-flow micro heat exchangers are analysed. With reference to this class of problems, to reduce CPU time and computer memory requirements, different parts of the computational domain are meshed separately with optimal structured grids that, however, do not match at the common interface. An original method is used to preserve the compatibility of temperature and heat flux across the artificial internal boundaries.

2. MATHEMATICAL AND NUMERICAL MODELS

Many flows in microscale thermal devices develop in straight microchannels with a characteristic transverse dimension of the cross-section that is much smaller that the duct length. Moreover, due to the small hydraulic diameter, the flow is laminar. If, in the steady state thermal analysis of this kind of devices, the fluid properties can be considered temperature independent, it is often very convenient to first calculate the velocity field by solving the momentum equations in their parabolised form and then compute the temperature distribution by solving the energy equation in its elliptic form in a domain that includes both fluid and solid parts [1]. This approach, which can be considered adequate, except for the immediate neighbourhood of the duct inlet, for values of the Reynolds number larger than about 50, allows significant savings in computer time while preserving a good accuracy of the solution. Therefore, it was adopted in this research to carry out

the analysis of the conjugate conduction-convection heat transfer in the hydrodynamically and thermally developing flow in microchannels when the effects of the axial conduction in the solid walls cannot be neglected, and in cross-flow micro heat exchangers, which consist of many layers of parallel microchannels with the microchannels of each layer perpendicular to those of the two adjacent layers.

The procedure consists of few steps. First, a finite element code is employed to repeatedly solve, while marching in the axial direction, the parabolised Navier-Stokes equations in a domain corresponding to the cross-section of a single microchannel. Then, the three-dimensional hydrodynamically developing laminar velocity field thus determined is used in the finite element solution of the steady-state energy equation in the domain corresponding to both solid and fluid parts. This requires that the velocity field calculated for one microchannel be mapped onto the portions of the grid corresponding to all the microchannels of the same size and with the same mass flow rate. Since the grids involved in this mapping may have different nodal densities, local and total mass conservation might be affected. Therefore, the fulfilment of the discrete mass conservation constraint for the velocity field mapped onto the new grid must be enforced before solving the energy equation. This is achieved by resorting to a technique which is standard in the context of fractional step methods for the solution of the continuity and the Navier-Stokes equation: a Poisson equation for a velocity correction potential is solved to compute appropriate velocity corrections.

The computer time required to compute and map the velocity field is negligible if compared to that required by the solution of the energy equation, which, in turn, is only a small fraction of that necessary if also the Navier-Stokes equations have to be solved in their elliptic form. However, even if the above procedure allows substantial savings in terms of computational resources, this is not sufficient if one wants to tackle practical problems concerning cross-flow micro heat exchangers using structured grids and have a sufficiently high nodal density in the regions of the domain close to the fluid-solid interfaces. Using unstructured meshes of tetrahedral elements would not make things better since, in both cases, it would not be possible to employ elongated elements in the flow direction, and, thus, the grids would be unnecessarily fine in the axial direction. Therefore, the possibility was implemented of independently meshing the layers of perpendicular microchannels with structured grids that do not match at the common interface. A detail of one of such grids is shown in Figure 1, where the regions corresponding to perpendicular microchannels carrying the hot and cold fluids are shown in red and blue, respectively.

Several methods are described in the literature to deal with non-matching grids, but they are either iterative (e.g. Schwartz and Dirichlet-Neumann methods), which is an undesired feature considering that the problem is linear, or they require the evaluation of integrals of the jump of one or more functions across the common interface between two different subdomains (e.g. mortar element and Nitsche methods), which is complicated to implement. Therefore, an original, non-iterative and easy-to-implement method was developed. It is based on the idea of pointwise imposing the transmission conditions of equal temperature and normal heat flux at the common interface of two

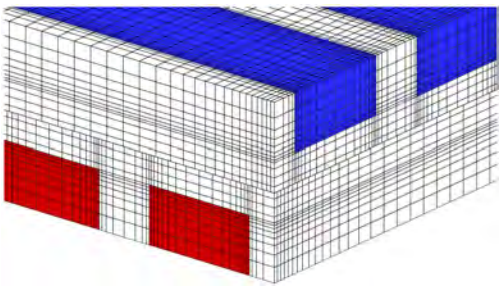

FIGURE 1. Detail of a non-matching grid used in analysis of cross-flow micro heat exchangers.

subdomains, which are discretised using non-matching structured grids. To this purpose, both temperature and nodal heat flow rates on the common interface are interpolated using the shape functions to allow the calculation of their values in element face positions of one subdomain that correspond to nodal positions of the other subdomain. The method has proven to be second order accurate both in the Euclidean and in the energy norms when the subdomains are discretised with uniform structured grids of linear elements. Second order accuracy in the Euclidean norm (but not in the energy norm) is preserved even if non-uniform grids are used.

3. RESULTS AND DISCUSSION

The procedure described in the previous section was first used to systematically study the effects of axial conduction in thick-walled circular microchannels with a constant wall heat flux imposed on the outer surface [1]. A sketch of the axisymmetric computational domain with the imposed thermal boundary conditions is shown in Figure 2(a). The effects of wall thickness, solid to fluid thermal conductivity ratio, channel length to inner diameter ratio and Reynolds number were investigated. The corresponding ranges of dimensionless parameters were D_o/D_i =1÷5, k_s/k_f =1÷5, L/D_i=25÷100, Re=50÷200, with the obvious meaning of symbols. The effects of possible heat losses at both end sections of the microchannel towards environments at temperatures equal to those of the fluid at inlet and outlet were also considered by assuming the following values of the end section Nusselt number $\mathrm{Nu}_e=h_a D_i/k_f$: 0 (adiabatic wall), 1 and 10.

It was found that the effects of axial conduction are similar when either the wall thickness or the thermal conductivity of the solid are increased. In fact, in both cases there is a reduction of the local Nusselt number at the inner wall, which is more pronounced towards the microchannel ends and for lower values of the Reynolds number. Two examples of the local Nusselt number axial distributions for the considered values of D_o/D_i are reported in Figures 2(b) and 2(c), where $X^* = x/(D_i \mathrm{Pe})$. It was also found that heat losses at microchannel ends produce an increase of the local Nusselt number with respect to the case with adiabatic ends in the first part of the microchannel and a reduction near the microchannel exit. Finally, in Figure 2(d), a plot is shown of the values of the ratio of the length averaged Nusselt numbers Nu, pertaining to all the test cases considered, and Nu_0, pertaining to the corresponding microchannels with wall thickness equal to zero (D_o/D_i =1), as a function of the so-called axial conduction parameter M, defined as the ratio of the nominal axial heat transfer rate by conduction in the wall to the heat transfer rate by convection in the fluid.

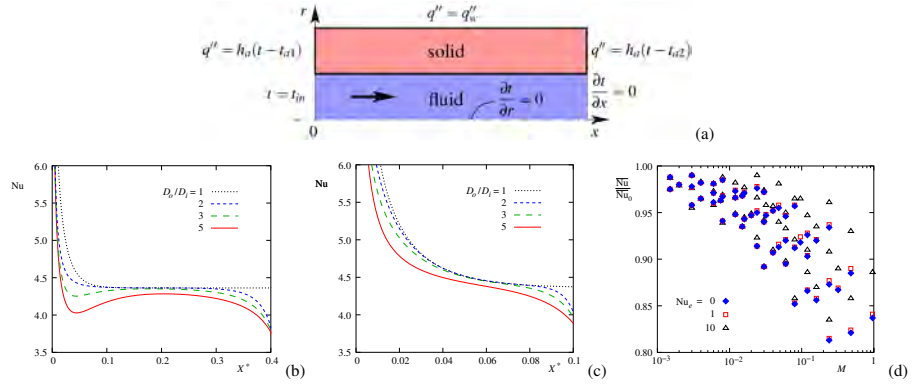

FIGURE 2. Thick-walled circular microchannels: (a) sketch of the computational domain; axial distributions of the local Nusselt number for L/D_i=100, k_s/k_f =250, Nu_e=0: (b) Re=50 and (c) Re=200; (d) Nusselt number ratio as a function of the axial conduction parameter M for all the cases considered.

The same finite element procedure was then used to study thermal behaviour of cross-flow micro heat exchangers for different thermal conductivities of the solid material and different numbers of microchannels per layer. By taking advantage of the possibility of separately meshing the subdomains corresponding to each layer and of reducing the computational domain by taking into account the existing symmetries, it was possible to carry out numerical simulations concerning micro heat exchangers with up to 50 microchannels per layer using single core CPU workstations and grids with up to 15 million nodes. An example of a temperature colour map on the outer surface of the computational domain corresponding to such a micro heat exchanger is shown in Figure 3(a). As an additional example, in Figures 3(b) and (c) the axial profiles of the bulk temperature, calculated for each microchannel of the hot and cold layers, and the temperature colour maps on the top, mid and bottom planes of the computational domain are shown with reference to a cross-flow micro heat exchanger with 32 rectangular (100μm×200μm) microchannels per layer and 25 layers per passage, for a mass flow rate of 150 kg/h of water (Re = 326). With inlet temperatures of 10°C and 95°C, the total heat flow rate is about 3.7 kW.

4. CONCLUSIONS

In this work the results of a parametric study on the thermal behaviour of thick-walled microchannels are summarised. It was shown that the main effect of axial heat conduction in thick-walled microchannels is a reduction of the Nusselt number. The performances of cross-flow micro heat exchangers were also analysed. To reduce CPU time and computer memory requirements, an original method was developed to make it possible to separately mesh different parts of the computational domain with optimal structured grids that do not match at the common interface.

REFERENCES

[1] C. Nonino, S. Savino, S. Del Giudice, L. Mansutti, Conjugate forced convection and heat conduction in circular microchannels, *Int. J. Heat Fluid Flow*, 30, 823–830, 2009.

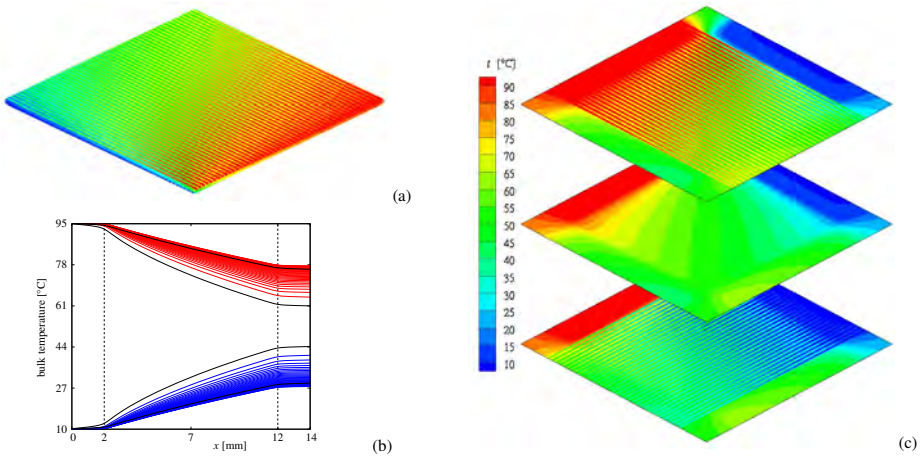

FIGURE 3. Cross-flow micro heat exchangers: (a) example of temperature colour map (50 microchannels per layer); examples of (b) axial profiles of the bulk temperature along the microchannels of hot and cold layers, and (c) temperature colour maps maps on the top, mid and bottom planes of the computational domain (32 microchannels per layer).

Third International Conference on Computational Methods for Thermal Problems
THERMACOMP2014, June 2-4, 2014, Lake Bled, Slovenia
N. Massarotti, P. Nithiarasu and B. Sarler (Eds.)

COMPUTATIONAL MODELLING OF SELECTED THERMAL PROBLEMS OCCURRING IN NEONATOLOGY

Andrzej J. Nowak, Joanna Laszczyk
Institute of Thermal Technology, Silesian University of Technology,
Konarskiego 22, 44-100 Gliwice, Poland,
E-mail addresses: andrzej.j.nowak@polsl.pl, joanna.laszczyk@polsl.pl

ABSTRACT

This work discusses a computational modelling of thermal problems occurring in neonatology in two following situations: i.e. newborn is placed inside an infant incubator of different type to be treated or newborn is suffering from a hypoxia which eventually leads to increase of his brain temperature. To solve this kind of problems the advanced thermoregulation model for neonates coupled with a model of heat transfer and fluid flow processes inside the incubator have been developed. CFD techniques are applied in those models to study interactions of newborn with the closed incubators, radiant warmers, heating mattresses and oxygen hoods. Models incorporate also the effect of cerebral blood flow on the metabolic heat rate via the Pennes bioheat equation. Some results obtained through numerical simulations are compared to results of medical trials published in the medical literature and also carried out in the hospital.

Key Words: *Bioheat Transfer, Infant Incubator, Brain Cooling..*

1. INTRODUCTION

The maintenance of an optimal thermal environment, particularly in the case of very low birth weight infants, is regarded as a priority in neonatology. On the other hand, maintaining a thermal neutral environment became nowadays a routine practice because the number of very specialised medical devices. This includes infant incubators, radiant warmers, heated mattresses, oxygen hoods etc. While closed incubators are design to provide a warm air circulating inside this device and compensate heat losses from the newborn, the radiant warmers are open devices, consisting of a radiant heater placed above a neonate lying on a crib. The main advantage of these devices over closed incubators is the ease of access to the neonate during various medical interventions. The main drawback is that they increase evaporative heat losses, which may result in dehydration in the case of very premature babies.

Oxygen hoods are commonly used devices to deliver supplemental oxygen to neonates. An air-oxygen blender is often used with oxygen hoods to administer gas when a precise dose of oxygen is required. Hoods are a versatile method of oxygen delivery that can be used on neonates in an incubator or under a radiant warmer. However, great care and constant monitoring must be in place as delivering a cold, wet mist to the infant's face will chill the infant, causing cold stress. Conversely, delivery of an overheated gas has the potential to induce hyperthermia, dehydration or pulmonary burns.

The perinatal hypoxic-ischemic encephalopathy is nowadays a relatively frequent problem which the neonatologists have to cope with. In order to perform the treatment in a proper way a distribution of the temperature inside the neonatal body (especially inside the brain) during the whole therapy should be known. It has been already proved that temperature level of 34-34.5^{o}C is secure during brain cooling, and at the beginning of the therapy the deep body temperature is decreased to that level. In the case of neonate suffering from the hypoxia his temperature is usually decreasing spontaneously and at certain moment neonatologists can start therapy. If not, his

temperature has to be reduced utilising cooling helmet or other device. Next, during the therapy [7], the deep body temperature is maintained at the constant level. Since the most vulnerable organ is the brain, the temperature of the scalp is kept by cooling helmet at the lowered level equal to about 24^{o}C. Simultaneously, in order to maintain the deep body temperature at the secure level, the skin of the rest of the neonatal body has to be heated by the radiant warmer. The therapy is carried out for 72 hours [7] and then the deep body temperature is gradually increased to the normal level (about 37^{o}C). It is very important to guarantee that temperature augments not faster than 0.5 K per hour, what entails many enormous difficulties.

This work discusses selected coupled thermal problems occurring in above mentioned neonatal situations. To solve those problems the advanced thermoregulation model for neonates has been developed. CFD techniques are applied in those models to study the fluid flows as well as heat and mass transfer in closed incubators, radiant warmers, heating mattresses and oxygen hoods. Model incorporates also the effect of cerebral blood flow on the metabolic heat rate via the Pennes bioheat equation. Some results obtained through numerical simulations are compared to results of medical trials published in the medical literature but also carried out in the hospital.

2. GOVERNING EQUATIONS AND MODELLING

The present paper is analysing the heat and fluid flow processes resulting from the metabolic heat generation, sensible and latent heat losses, including heat conduction, convection, radiation and evaporation. The paper follows previous studies by Ginalski, Fic, Wrobel et al. [1 - 3, 9], who presented a model for analysing the total heat balance of the neonate using CFD techniques. Moreover, significant improvements have been made to the geometric representation of the infants and the process of data generation. These developments gave rise to a supplementary model, entitled Infant Heat Balance Module (IHBM), which has been fully integrated with the CFD solver and graphical interface. The module is capable of calculating all the heat balance components that are present during the intensive care of neonates under different treatment scenarios. Details can be found in [1, 9].

In the case of brain cooling treatment the model of transient heat transfer in human tissues is needed and in this work Pennes bioheat equation [8] is applied. This governing equation is coupled with a passive and active thermoregulation [4] as well as with blood flow model based on the concept of blood pool. Finally it allowed us to build up the computational model of newborn consisted of few segments (head, shoulders, legs etc.) inside of which some tissues are distinguished and 3D heat transfer is taken into account. Parameter in this model are determined as result of inverse analysis utilising skin temperature measurements and details can be found in [5, 6].

3. SELECTED RESULTS

Developed models of closed incubator with double walls and radiant warmer have already been extensively tested. Results of carried out simulations have been compared with results of experimental studies published in medical literature. Unfortunately, those articles did not include all the data required to reconstruct accurate representations of the infants analysed, and the properties of the incubator and the environment in which they were nursed. In this sense, the comparison of the CFD results with data published in these articles can only provide limited validation of the CFD models. Anyway obtained CFD results agree well with experimental data and details can be found [1 – 3,.9]. Example of the geometrical model of the newborn inside a closed incubator with double walls and exemplary resulting temperature field is shown in Figure 1.

In should also be mentioned that the mean skin temperature for the infant was calculated in the CFD simulations as a weighted average of each computational face representing the infant's skin. Only in those cases when infrared camera was used to measure skin temperature, detailed comparison of

very local temperatures was possible. Temperature measurements using IR camera were first of all needed to determine parameters of the computational model of newborn. The model consists of few segments (head, shoulders, legs etc.) inside of which some tissues are distinguished and 3D heat transfer is taken into account. Then this model is further tuned by collecting temperatures during brain cooling therapy and carrying out inverse thermal analysis. based on above mentioned temperature measurements. Exemplary IR measurements of skin temperatures obtained from neonatologists and exemplary simulated temperature fields are demonstrated in Figure 2. Due to symmetry only half of the infant is presented.

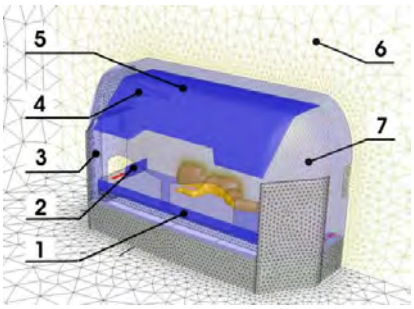

1 Internal front screen, 2 Internal top screen, 3 Top corner, 4 Internal thermometer, 5 Internal screen, 6 Exterior domain, 7 Interior domain.

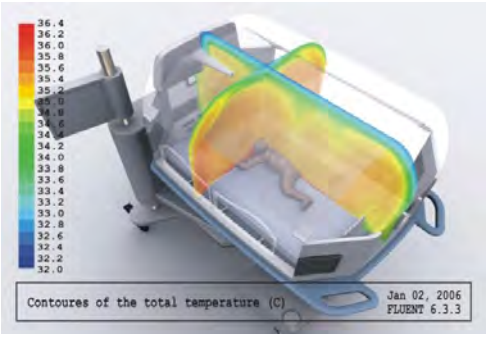

FIGURE 1. Geometrical model of the newborn inside closed incubator with double walls and exemplary resulting temperature field

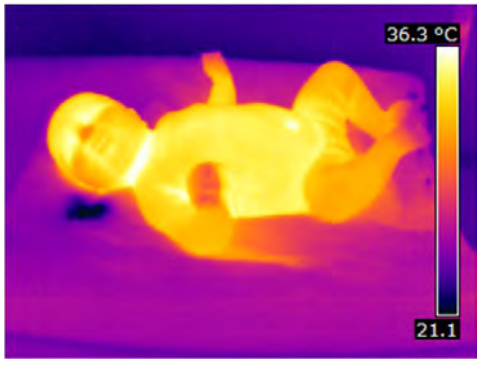

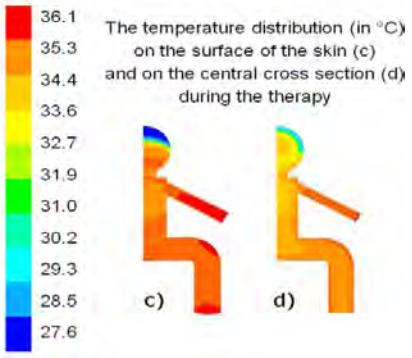

FIGURE 2. Exemplary IR measurements of skin temperatures obtained from neonatologists and exemplary resulting temperature field

4. CONCLUSIONS

The obtained results of extensive numerical studies confirm capabilities and usefulness of developed computational models of thermal problems occurring in modern neonatology. Those models are still being extended to tune them and to base them on as realistic geometrical models of the newborns as possible. Developed models can also be used as educational software for medical staff.

ACKNOWLEDGMENT

This paper was partially elaborated within the frame of the grant No N519 657840 entitled *The analysis of the brain cooling process supported by the National Centre for Research*. This financial support is gratefully acknowledged hereby.

REFERENCES

[1] Ginalski M.K., Nowak A.J., Wrobel L.C., Modelling of Heat and Mass Transfer Processes in Neonatology, *Biomedical Materials*, **3** (2008) 034113 (11pp),

[2] Fic A.M, Ingham D.B., Ginalski M.K., Nowak A.J., Wrobel L.C., Heat and mass transfer under an infant radiant warmer — development of a numerical model, *Journal of Medical Engineering and Physics* , Volume 32, Issue 5, Pages 497-504 (June 2010),

[3] Fic A.M, Ingham D.B., Ginalski M.K., Nowak A.J., Wrobel L.C., Modelling and optimisation of the operation of a radiant warmer, *Journal of Medical Engineering and Physics*. Vol. **36**, Issue 1, pp 81–87, January 2014.

[4] Janssen, F., Van Leeuwen, G., Van Steenhoven, A. (2005), Modelling of temperature and perfusion during scalp cooling, *Physics in Medicine and Biology*, Institute of Physics Publishing, Vol. 50, pp. 4065-4073.

[5] Laszczyk J., Maczko A., Walas W., Nowak A.J. (2012), The numerical modelling of the heat transfer processes within neonate's body based on the simplified geometric model, *Information Technologies in Biomedicine*, Lecture Notes in Computer Science, Vol. 7339, Springer Verlag, pp. 310-318.

[6] Laszczyk J., Maczko A., Walas W., Nowak A.J., Inverse thermal analysis of the neonatal brain cooling process, *International Journal of Numerical Methods for Heat and Fluid Flow*, Vol. 24, in press.

[7] Olympic Cool-Cap System Trainer (2007), The operating instruction Olympic Medical, a division of Natus, USA.

[8] Pennes, H.H. (1948), Analysis of Tissue and Arterial Blood Temperatures in the Resting Human Forearm, *J. Appl. Physiology*, Vol. 1 No. 2 pp. 93-122.

[9] Wrobel, L. C., Ginalski, M. K., Nowak, A. J., Ingham, D. B., Fic, A. M. (2010), "An overview of recent applications of computational modelling in neonatology", Phil. Trans. The Royal Society A 368, pp. 2817-2834.

MINI-SYMPOSIA

MINI-SYMPOSIUM

HEAT TRANSFER IN FOAMS AND NANOFLUIDS

MINI-SYMPOSIUM ORGANISED BY N. BIANCO AND S. NARDINI

Third International Conference on Computational Methods for Thermal Problems
ThermaComp2014, June 2-4, 2014, Lake Bled, Slovenia
N. Massarotti, P. Nithiarasu and B. Sarler (Eds.)

STABILITY ANALYSIS OF MIXED CONVECTION IN A VERTICAL POROUS CHANNEL WITH ASYMMETRIC HEATING

Antonio Barletta, Eugenia Rossi di Schio
Department of Industrial Engineering, Alma Mater Studiorum Università di Bologna,
Viale Risorgimento 2, 40136 Bologna
antonio.barletta@unibo.it eugenia.rossidischio@unibo.it

ABSTRACT

Parallel mixed convection in a vertical porous channel filled with a saturated porous medium is analysed. The case where one boundary wall is subject to a uniform heat flux and the other wall is thermally insulated is considered. The stability analysis versus small-amplitude disturbances is carried out.

Key Words: *Porous Medium; Darcy's Law; Convective Instability; Vertical Channel; Mixed Convection; Normal Modes.*

1. INTRODUCTION

The analysis of mixed convection in a vertical channel filled with a porous medium saturated by a fluid is an important task to evaluate the performances of several heat transfer systems. Among them, a special interest emerges relative to all those applications based on metal foams. Metal foams are in fact special porous media endowed with a high thermal conductivity. The employment of metal foams in devices for the heat transfer enhancement is based on the foam internal ligaments acting as fins.

A previous analysis of the stable/unstable nature of fully-developed mixed convection in a vertical porous channel with plane parallel walls subject to uniform and symmetric heating was carried out recently by Barletta [1].

The purpose of this contribution is to investigate the effect of an asymmetric basic flow state, induced by an asymmetry in the thermal boundary conditions. One vertical wall is modelled as isoflux while the facing wall is considered as thermally insulated. A linear stability analysis of the fully-developed mixed convection is carried out relative to the buoyancy-assisted and buoyancy-opposed regimes. The solution of the eigenvalue problem for the perturbations is found analytically for the longitudinal modes, while it has to be obtained numerically for general normal modes.

2. MATHEMATICAL MODEL

We consider a vertical porous channel saturated by a fluid. Here, the $y^\star-$axis is vertical, while the $x^\star-$axis and the $z^\star-$axis are horizontal. The boundary walls, at $x^\star = 0, L$, are impermeable. The boundary $x^\star = 0$ is considered as thermally insulated, while a uniform flux $q_{\rm w} > 0$ expresses the heating at $x^\star = L$.

The saturated porous medium is considered isotropic and homogeneous. Local thermal equilibrium between the solid and the fluid is assumed. Thus, according to Darcy's law and to the Oberbeck-Boussinesq approximation, the local mass, momentum and energy balance equations can be written in a dimensionless form as [2]

(1a) $$\boldsymbol{\nabla}\cdot\boldsymbol{u} = 0,$$

(1b) $$\boldsymbol{\nabla} \times \boldsymbol{u} = R\, \boldsymbol{\nabla} \times (T\, \hat{\boldsymbol{e}}_y)\,,$$

(1c) $$\frac{\partial T}{\partial t} + \boldsymbol{u} \cdot \boldsymbol{\nabla} T = \nabla^2 T.$$

The dimensionless quantities employed in Eqs. (1) are defined as

(2) $$(x, y, z) = (x^\star, y^\star, z^\star)\, \frac{1}{L}, \quad t = t^\star\, \frac{\varkappa}{\sigma L^2}, \quad \boldsymbol{u} = \boldsymbol{u}^\star\, \frac{L}{\varkappa}, \quad T = \frac{T - T_0}{\Delta T}, \quad R = \frac{g\beta \Delta T K L}{\varkappa \nu},$$

where

(3) $$\Delta T = \frac{q_\mathrm{w}\, L}{\lambda}.$$

The stars denote the dimensional time t, coordinates (x, y, z), velocity field $\boldsymbol{u} = (u, v, w)$ and temperature field T. Here, g is the modulus of the gravitational acceleration $\boldsymbol{g} = -\, g\, \hat{\boldsymbol{e}}_y$ with $\hat{\boldsymbol{e}}_y$ the unit vector along the $y-$axis, K is the permeability, λ is the average thermal conductivity, $\varkappa$ is the average thermal diffusivity, σ is the ratio between the average heat capacity of the porous medium and that of the fluid, while β is the thermal expansion coefficient and ν the kinematic viscosity of the fluid. The dimensionless parameter R is the Darcy-Rayleigh number.

The dimensionless boundary conditions are expressed as

(4a) $$x = 0: \qquad u = 0, \qquad \frac{\partial T}{\partial x} = 0,$$

(4b) $$x = 1: \qquad u = 0, \qquad \frac{\partial T}{\partial x} = 1.$$

A steady basic solution of Eqs. (1) and (3) exists given by

(5) $$u_\mathrm{b} = 0, \quad v_\mathrm{b} = R\, F(x), \quad w_\mathrm{b} = 0, \quad T_\mathrm{b} = F(x) + \frac{y}{P},$$

where "b" stands for basic solution and

(6) $$F(x) = -\, \frac{\cos(\alpha x)}{\alpha \sin \alpha}, \qquad \alpha^2 = -\, \frac{R}{P}.$$

Here, P is the Péclet number associated with the average channel velocity in the basic flow state. The solution exists as far as we have a nonzero flow rate, $P \neq 0$.

On account of Eqs. (5) and (6), there are different features of the basic solution depending on the sign of R/P. When α^2 is negative and hence α is imaginary, trigonometric functions are transformed into hyperbolic functions. Thus, we define

(7) $$\begin{aligned} &R/P > 0 \quad (\alpha^2 < 0), \qquad \text{buoyancy-assisted flow,} \\ &R/P < 0 \quad (\alpha^2 > 0), \qquad \text{buoyancy-opposed flow.} \end{aligned}$$

For a buoyancy-opposed regime, the basic solution Eqs. (5) and (6) may display singularities when the denominator in the expression of $F(x)$ vanishes, and this happens when $\alpha^2 = n^2\pi^2$, where $n = 1,\ 2,\ 3\ \ldots$. This odd mathematical behaviour is likely to be unobservable due to a possible instability of buoyancy-opposed flows where α^2 is as large as π^2.

3. LINEAR STABILITY ANALYSIS

The basic velocity and temperature fields, Eqs. (5) and (6), are perturbed with small-amplitude disturbances,

(8) $$\boldsymbol{u} = \boldsymbol{u}_\mathrm{b} + \varepsilon \hat{\boldsymbol{u}}, \qquad T = T + \varepsilon \hat{T},$$

where $\varepsilon \ll 1$ is a perturbation parameter. By employing Eq. (8), Eqs. (1) yield

(9a) $$\boldsymbol{\nabla} \cdot \hat{\boldsymbol{u}} = 0,$$

(9b) $$\boldsymbol{\nabla} \times \hat{\boldsymbol{u}} = R\, \boldsymbol{\nabla} \times \left(\hat{T}\, \hat{\boldsymbol{e}}_y \right),$$

(9c) $$\frac{\partial \hat{T}}{\partial t} + F'(x)\, \hat{u} + \frac{1}{P}\, \hat{v} + R\, F(x)\, \frac{\partial \hat{T}}{\partial y} = \nabla^2 \hat{T},$$

where the terms $\mathrm{O}(\varepsilon^2)$ have been neglected, and primes denote ordinary derivatives with respect to x. The boundary conditions (4) return

(10) $$x = 0, 1: \qquad \hat{u} = 0, \qquad \frac{\partial \hat{T}}{\partial x} = 0.$$

Eq. (9b) can be satisfied identically by adopting a pressure formulation,

(11) $$\hat{\boldsymbol{u}} = R\, \hat{T}\, \hat{\boldsymbol{e}}_y - \boldsymbol{\nabla} \hat{\Phi},$$

where $\hat{\Phi}$ is an auxiliary scalar field. Eqs. (9) and (10) can be reformulated as

(12a) $$\nabla^2 \hat{\Phi} = R\, \frac{\partial \hat{T}}{\partial y},$$

(12b) $$\nabla^2 \hat{T} = \frac{\partial \hat{T}}{\partial t} - F'(x)\, \frac{\partial \hat{\Phi}}{\partial x} + \frac{1}{P} \left(R\, \hat{T} - \frac{\partial \hat{\Phi}}{\partial y} \right) + R\, F(x)\, \frac{\partial \hat{T}}{\partial y},$$

(12c) $$x = 0, 1: \qquad \frac{\partial \hat{\Phi}}{\partial x} = 0, \qquad \frac{\partial \hat{T}}{\partial x} = 0,$$

We now test the stability to normal modes, such that

(13) $$\hat{\Phi} = \varphi(x)\, e^{\eta t}\, e^{i(k_y y + k_z z)}, \qquad \hat{T} = \theta(x)\, e^{\eta t}\, e^{i(k_y y + k_z z)},$$

where $k = (k_y^2 + k_z^2)^{1/2}$ is the wave number, and (k_y, k_z) is the wave vector which defines the wave direction in the $(y, z)-$plane. Here, k_y and k_z are real numbers. The parameter η is complex such that $\omega = -\,\mathrm{Im}(\eta)$ is the angular frequency, and $\mathrm{Re}(\eta)$ is positive for unstable modes, negative for stable modes and zero for neutral stability. Substitution of Eq. (13) into Eqs. (12) yields

(14a) $$\varphi'' - k^2\, \varphi + i\, k_y\, P\, \alpha^2\, \theta = 0,$$

(14b) $$\theta'' - \left[k^2 + \eta - \alpha^2 - i\, k_y\, P\, \alpha^2\, F(x) \right] \theta + F'(x) \varphi' + \frac{i\, k_y}{P}\, \varphi = 0,$$

(14c) $$x = 0, 1: \qquad \varphi' = 0, \qquad \theta' = 0.$$

Longitudinal modes are such that $k_y = 0$. In this case we have a drastic simplification of Eqs. (14), namely

(15a) $$\varphi'' - k^2\, \varphi = 0,$$

(15b) $$\theta'' - \left(k^2 + \eta - \alpha^2 \right) \theta + F'(x) \varphi' = 0,$$

(15c) $$x = 0, 1: \qquad \varphi' = 0, \qquad \theta' = 0.$$

4. DISCUSSION OF THE RESULTS

4.1. **Longitudinal modes.** For the longitudinal modes, Eq. (15a) with $\varphi'(0) = \varphi'(1) = 0$ can be satisfied for a generic $k \geqslant 0$ only if φ is identically zero or an arbitrary constant, in the special case $k = 0$. Thus, the solution of Eq. (15b) with $\varphi(x) = constant$ and $\theta'(0) = \theta'(1) = 0$ is given by

(16) $$\theta(x) = \cos(n \pi x), \quad \text{with} \quad n = 0,\ 1,\ 2,\ \ldots\ ,$$

provided that the dispersion relation,

(17) $$\eta = -\,k^2 + \alpha^2 - n^2 \pi^2 \quad n = 0,\ 1,\ 2,\ \ldots\ ,$$

is satisfied. On account of Eq. (17), we immediately see that $\mathrm{Im}(\eta) = 0$ and, as a consequence, we may conclude that longitudinal modes have a vanishing angular frequency, ω. The main information gathered from Eq. (17) is that instability, *viz.* the condition $\mathrm{Re}(\eta) = \eta > 0$, is ensured whenever,

$$\alpha^2 > k^2 + n^2\pi^2 \quad \text{with} \quad k \geqslant 0, \quad n = 0,\ 1,\ 2,\ \ldots\ . \tag{18}$$

Thus, the critical condition for the onset of instability arises when the right hand side of the inequality (18) is at its minimum, namely for $k = 0$ and $n = 0$. The conclusion is that all buoyancy-opposed flows, $\alpha^2 > 0$, are unstable. On the other hand, all buoyancy-assisted flows turn out to be stable versus longitudinal mode perturbations, as Eq. (18) cannot be satisfied whenever $\alpha^2 < 0$.

4.2. **General normal modes.** When $k_y \neq 0$, there is a convenient rescaling of the eigenfunction φ, namely by defining

$$\phi = \frac{\varphi}{k_y\, P}. \tag{19}$$

Then, Eqs. (14) are rewritten as

$$\phi'' - k^2\,\phi + i\,\alpha^2\,\theta = 0, \tag{20a}$$

$$\theta'' - \left[k^2 + \eta - \alpha^2 - i\,k_y\,P\,\alpha^2\,F(x)\right]\theta + k_y\,P\,F'(x)\phi' + i\,k_y^2\,\phi = 0, \tag{20b}$$

$$x = 0, 1: \qquad \phi' = 0, \qquad \theta' = 0. \tag{20c}$$

For general normal modes, the eigenvalue problem (20) can be solved only numerically. There exist many numerical methods developed for this kind of differential eigenvalue problems. A descriptive and thorough analysis of such methods is given, for instance, in Chapter 9 of Straughan [3].

In the present contribution, the numerical solution of Eqs. (20) will be achieved by adopting the shooting method. The basic idea is to complete artificially the conditions on ϕ and θ at $x = 0$, so that Eqs. (20a) and (20b) can be solved as an initial value problem starting at $x = 0$. Numerical solvers for initial value problems are manifold. Our computation will be based on the Runge-Kutta method, implemented within the environment *Mathematica 9* (© Wolfram Research). Completion of the set of boundary conditions at $z = 0$, Eq. (20c), is achieved by writing

$$\phi(0) = 1, \quad \phi'(0) = 0, \quad \theta(0) = \xi_1 + i\,\xi_2, \quad \theta'(0) = 0. \tag{21}$$

Here, $\phi(0) = 1$ is a scale-fixing condition needed to gauge the otherwise indeterminate scale of the eigenfunctions. Real parameters ξ_1 and ξ_2 are unknown. They are to be evaluated, together with the eigenvalue pair (ω, α^2), for assigned input data $(\mathrm{Re}(\eta), k_y, k, P)$, by imposing the target conditions at $x = 1$ defined by Eq. (20c),

$$\phi'(1) = 0, \quad \theta'(1) = 0. \tag{22}$$

Since the eigenfunctions are complex-valued in general, Eq. (22) actually provides four real constraints, sufficient to compute the four unknown parameters $(\xi_1, \xi_2, \omega, \alpha^2)$. Setting $\mathrm{Re}(\eta) = 0$ allows one to draw the neutral stability curves $\alpha^2(k)$ for every assignment of the input data $(k_y/k, P)$.

REFERENCES

[1] A. Barletta, *Instability of mixed convection in a vertical porous channel with uniform wall heat flux*, Physics of Fluids **25** (2013), 084108.

[2] D. A. Nield and A. Bejan, *Convection in Porous Media*, 4th ed., Springer, New York, 2013.

[3] B. Straughan, *Stability and Wave Motion in Porous Media*, Springer, New York, 2008.

Third International Conference on Computational Methods for Thermal Problems
THERMACOMP2014, June 2-4, 2014, Lake Bled, Slovenia
N. Massarotti, P. Nithiarasu and B. Sarler (Eds.)

EFFECTS OF LIGAMENTS SHAPE ON RADIATIVE HEAT TRANSFER IN METAL FOAMS

Dominique Baillis
Laboratorie de Mecanique des Contacts et des Structures - INSA de Lyon
20, Avenue Albert Einstein – 69 621 - Villeurbane Cedex (Lyon) - France
dominique.baillis@insa-lyon.fr

Nicola Bianco, Salvatore Cunsolo, Vincenzo Naso
Dipartimento di Ingegneria Industriale - Università degli studi di Napoli Federico II
P.le Tecchio, 80 – 80125 - Napoli - Italy
nicola.bianco@unina.it; sal.cuns@gmail.com, vincenzo.naso@unina.it

Maria Oliviero
Istituto per i materiali compositi e biomedici - Consiglio Nazionale delle Ricerche
P.le Fermi, 1 - 80055 - Portici (Napoli) – Italy - maria.oliviero@unina.it

ABSTRACT

The radiative behavior of metal foams has been studied using analytical, numerical and experimental approaches. However, only few researches focused their attention on the assessment of the relevance of specific micro-structural (i.e. sub-cell size) characteristics.

In this study, using internally developed MATLAB and C++ codes and the free-to-use software Surface Evolver, the impact of ligaments shape on radiative behavior is investigated, with a specific focus on the interdependence among porosity, ligaments shape and radiative characteristics.

Key Words: *Metallic foams, Radiative characteristics, Monte Carlo Ray Tracing, Ligaments shape*.

1. INTRODUCTION

The radiative heat transfer in porous media has inspired many analytical and numerical studies. Combining geometric optics, diffraction theory, and Mie scattering theory and assuming an independent scattering, various authors have evaluated analytically the radiative characteristics of foams, modelled as sets of cubic [1], dodecahedral [2] or tetradecahedrical [3] cells.

A weak point of the above mentioned studies is the difficulty of accounting for the role played by the geometrical structure of the foam and the near field effects. Though it is known that the geometrical characteristics of the foam, such as the ligaments shape, have a complex relation with parameters, such as porosity and PPI [4], few of the existing models take them into account [3].

Studies based on numerical methods can account for the foam structure and the near-field effects, and thus allow an improvement of the models for metal and ceramic foams. Numerical methods can be employed on computer generated models. A common method to obtain these models is to make reference to idealized structures, such as the Kelvin [5] one. Pusterla et al. [6] used such a structure to assess the effect of the foam microstructure on convective heat transfer.

Recently Andreozzi et al. [7], applying Monte Carlo Ray Tracing methods described in Tancrez and Taine [8] and Coquard et al. [9], used Kelvin and Weaire Phelan structures to model radiation at the pore level. The comparison of their results with those obtained by using tomographic data showed that the ligaments shape strongly affects the radiative behavior of the foam.

The objective of this study is to systematically assess the influence of the ligaments shape on radiation heat transfer in foams, focusing on the porosity dependence of ligaments shape.

2. METHODOLOGY

A number of idealized structures, based on the Kelvin structure, were generated, in order to evaluate the effects of the ligaments shape. A method to create them using the free software Surface Evolver [10] for use in Monte Carlo codes was described in [7]. However this method works only for the generation of structures with concave-shaped ligaments. For this reason, another procedure has been devised, that allows to obtain structures whose ligaments shape varies with porosities, as reported in the literature [4]. A base structure with 99% porosity was initially obtained using Surface Evolver, and then it was manipulated using a MATLAB code. The MATLAB code first transforms the triangular mesh into a volumetric representation with binary (filled/void) voxels, and then applies a number of simulated growth steps to the structure. Each growth step can be decomposed in three sub steps:

- the binary voxels are converted into real-valued (grey-scale) voxels;
- a "diffusion" step: by applying a spherical box filter to the 3D image, the filled part of the structure "diffuses" towards the void part;
- a “threshold” step: by choosing a threshold level such that the desired decrease in porosity is obtained, the real-valued voxels are converted back again into binary voxels.

A 2D example of this process is shown in Fig.1. The step-size of the growth process is chosen by calibrating it in such a way that the resulting structures match the representation typically given by manufacturers and by the literature (see Fig.2). For each route, four different structures have been generated, with porosities, ε, equal to 0.86, 0.90, 0.94 and 0.98, for a total of 8 structures. A 1 mm cell diameter (defined as in [7]) has been chosen for each structure.

3. RESULTS

The free path distribution functions and the consequent values of the extinction coefficient have been estimated for the generated structures. An example of the full free path distribution is given in Fig.3. The free path distribution obtained from a tomographically acquired structure [7]. is also reported in the figure, that points out a free path distribution function of the structure with variable ligaments shape closer to that of the real one.

The extinction coefficient as a function of the porosity, for the structures with both concave and variable ligaments shape is reported in Fig.4. One can notice that the structure with concave ligament shape always exhibits a substantially larger (up to about 50%) extinction coefficient than the variable ligaments shape structures. It is also interesting to point out that the percent difference is a function of the porosity, i.e. the higher the porosity the smaller the difference.

Furthermore, expressing the extinction coefficient as a function of porosity in a power law form:

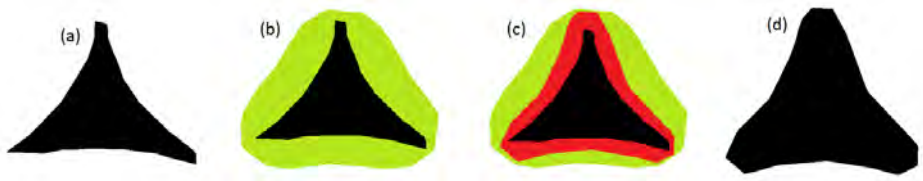

FIGURE 1. 2D example of the growth process (single growth step):
(a) Initial structure (b) “Diffusion” step (c) “Threshold” step (d) Final structure.

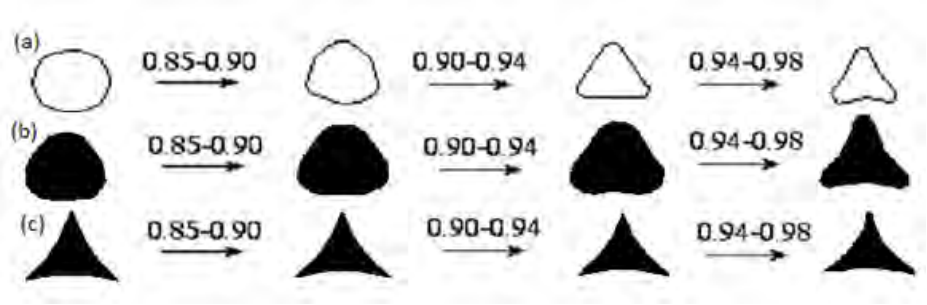

FIGURE 2. Examples of ligaments cross section:
(a) Bhattacharya et al. [4] (b) Variable ligament shape (c) Concave ligament shape.

$$\beta = A(1-\varepsilon)^B$$

we found that for constant concave ligaments shape structures B is nearly equal to 0.53, close to the 0.5 value used in expressions such as those given in [2] and larger than the 0.44 value we found for variable ligaments shape structures. This implies that accounting for variable ligaments shape makes the dependence of extinction coefficient on the porosity weaker than that found in the literature. The above mentioned weaker dependence was also observed experimentally [11].

One can also remark that a variation in the ligaments shape affects the specific surface area, which in turn influences the extinction coefficient. The specific surface area as a function of the porosity, for the structures with concave ligaments and the structures with variable ligaments shape is presented in Fig.5.

In order to separate the effects of the specific surface area from the pure shape effects, the dimensionless parameter β^+, defined as in [8], has been calculated for all the structures, and results, as a function of the porosity, are reported in Fig.6. The figure shows that, even after accounting for the effects of the specific surface area, the same qualitative considerations can be made as those made observing Fig.4. About 1⁄3 of the previously discussed effects depends on pure shape, while the remaining 2⁄3 is given by variations in the specific surface area.

4. CONCLUSIONS

The effect of the ligaments shape on radiative heat transfer in metal foams was evaluated. Concave

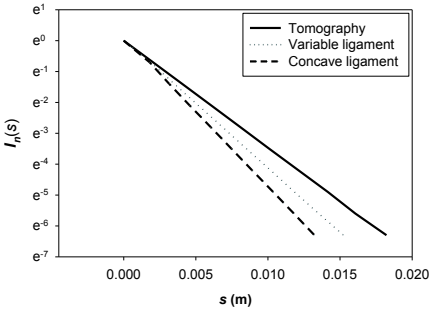

FIGURE 3. Free path distribution for three different structures: tomography [7], variable ligaments, concave ligaments.

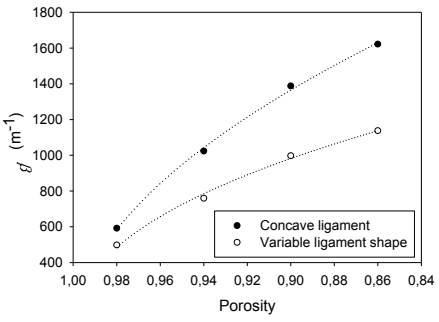

FIGURE 4. Extinction coefficient *vs* porosity, for all investigated structures.

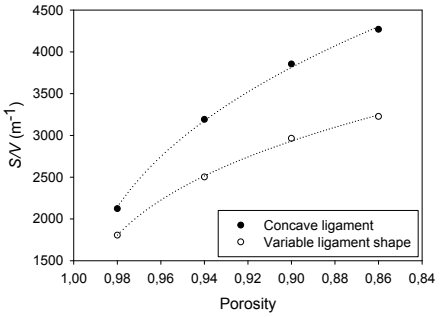

FIGURE 5. Specific surface area *vs* porosity, for all investigated structures.

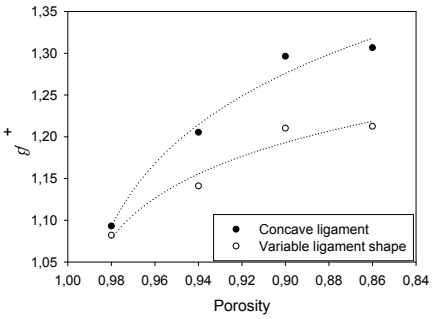

FIGURE 6. Dimensionless extinction coefficient *vs* porosity, for all investigated structures.

triangular ligaments shaped structures and structures with the ligaments shape depending on the porosity were considered. The ligaments shape strongly affects the predictions of numerical models; differences up to 50% in the extinction coefficient were found. The effects of the shape variations have been separated by those of the specific surface area, and have been found to be significant.

REFERENCES

[1] C.Y. Zhao, S.A. Tassou, and T.J. Lu, Analytical considerations of thermal radiation in cellular metal foams with open cells, *IJHMT*, 51, 929-940, 2008.

[2] L.R. Glicksmann, M.A. Schuetz, and M. Sinofsky, Radiation heat transfer in foam insulation, *J. Heat Transfer,* 109, 809-812, 1987.

[3] M. Loretz, R. Coquard, D. Baillis, E. Maire, Metallic foams: radiative properties/comparison between different models, *J. Quant. Spectrosc. Radiat. Transfer,* 109, 16-27, 2008.

[4] A. Bhattacharya, V.V. Calmidi, and R.L. Mahajan, Thermophysical properties of high porosity metal foams, *IJHMT*, 45, 1017–1031, 2002.

[5] Lord Kelvin (Sir W. Thomson), On the Division of Space with Minimum Partitional Area, *Acta Mathematica*, 11, 121-134, 1887.

[6] S. Pusterla, M. Barbato, A. Ortona, and C. D'Angelo, Numerical study of cell morphology effects on convective heat transfer in reticulated ceramics, *IJHMT*, 55, 7902-7910, 2012.

[7] A. Andreozzi, N. Bianco, W.K.S. Chiu, S. Cunsolo, W.M. Harris, V. Naso, and M. Oliviero, Monte Carlo determination of radiative properties of metal foams: comparison between idealized and real cell structures, *Proceedings of 31st UIT Heat Transfer Conference*, Como, Italy, June 25-27, 127-139, 2013.

[8] M. Tancrez, and J. Taine, Direct identification of absorption and scattering coefficients and phase function of a porous medium by a Monte Carlo technique, *IJHMT*, 47, 373-383, 2004.

[9] R. Coquard, D. Baillis, J. Randrianalisoa, Homogeneous phase and multi-phase approaches for modeling radiative transfer in foams, Int. J. Thermal Sciences 50 (2011) 1648-1663.

[10] K. A. Brakke, The surface evolver, *Experimental Mathematics,* 1, 141-165, 1992.

[11] R. Coquard, D. Rochais, and D. Baillis, Experimental investigations of the coupled conductive and radiative heat transfer in metallic/ceramic foams, *IJHMT*, 52, 4907-4918, 2009.

Third International Conference on Computational Methods for Thermal Problems
THERMACOMP2014, June 2-4, 2014, Lake Bled, Slovenia
N. Massarotti, P. Nithiarasu and B. Sarler (Eds.)

FORCED CONVECTIVE HEAT TRANSFER IN METAL FOAMS: THE CHARACTERISTIC LENGTH ISSUE

Marcello Iasiello, Salvatore Cunsolo, Nicola Bianco, Vincenzo Naso
Dipartimento di Ingegneria Industriale – Università degli Studi di Napoli Federico II
P.le Tecchio, 80 – 80125 – Napoli – Italy – marcello.iasiello@unina.it, sal.cuns@gmail.com, nicola.bianco@unina.it, vincenzo.naso@unina.it

Maria Oliviero
Istituto per i materiali compositi e biomedici - Consiglio Nazionale delle Ricerche
P.le Fermi, 1 - 80055 - Portici (Napoli) – Italy - maria.oliviero@unina.it

William M. Harris, Wilson K. S. Chiu
Department of Mechanical Engineering - University of Connecticut, 191 Auditorium Road, Unit 3139, 06269-3139 – Storrs (CT) – USA – wmh07001@engr.uconn.edu， wchiu@engr.uconn.edu

ABSTRACT

The choice of the characteristic length in dimensionless parameters is an important issue in the determination of correlations among dimensionless parameters in the convective heat transfer in open cell metal foams. Various characteristic lengths have been proposed in the literature but the effect of different choices has not been investigated thoroughly. In this paper the current state-of-art of the characteristic length issue is first presented. Then, with reference to a structure reconstructed with tomographic scans of a real foam sample, heat transfer coefficients obtained numerically for air forced convection are presented in a dimensionless form, for different characteristic lengths. Two characteristic lengths are chosen as the most suitable to describe the physical problem.

Key Words: *Forced convection, Metal foams, Finite element method, Characteristic length.*

1. INTRODUCTION

The heat transfer rate in heat exchangers, volumetric solar air receivers, burners and fire barriers can be suitably enhanced by employing porous materials, like open cell metal foams, because of their extended specific surface area and tortuosity.

The choice of the characteristic length in the dimensionless parameters is an important issue in convective heat transfer. Various characteristics lengths for open cell foams have been proposed in the literature [1, 2], but the effect of different choices is limited, and the choice for real foam structures is unclear.

Because of the difficult evaluation of the pore structure of a porous medium [3], the square root of the permeability, $K^{1/2}$, or sometimes $K^{1/2}/\varepsilon$, with ε the porosity, is often assumed as the characteristic length. This is a reliable choice when the velocity of the fluid is rather low [2], whereas it isn't for non-Darcian flows.

The characteristic length $\beta \times K$, where β is the form coefficient in the Forchheimer's equation, was proposed for non-Darcian flows, but this characteristic length may be incorrect, since experimental results [3] showed that the larger K, the smaller βK.

Nowadays the evaluation of morphological characteristics of a foam, such as the cell size, d_c, the pore size, d_p, and also the ratio of the surface area to volume, S/V, has become easier. This allows one to select d_c [4], d_p [2] or S/V [5] as the characteristic length. Manufacturers generally provide the number of pores per inch (*PPI*) of a foam, that in theory is the reciprocal of d_p. However the

comparison of the value given by the manufacturer with the measured value shows its inaccuracy [6].

Dietrich et al. [7] assumed the hydraulic diameter, d_h, as the characteristic length.

The effect of the choice of the characteristic length for the convective heat transfer problem in open cell foams is analyzed in this paper, with reference to a structure reconstructed with tomographic scans of a real foam sample. Heat transfer coefficients for air forced convection obtained numerically in [4] are presented in a dimensionless form, for different characteristic lengths.

NUMERICAL DATA AND ANALYSIS

A cylindrical foam sample (Duocel Al6101-T6, 90% porosity, 40 pores per inch (PPI)), 10.1 mm in diameter and 10.3 mm in height (Fig. 1a), was provided by the manufacturer (Erg Aerospace Corporation, USA). A tomographic scan of the foam 3-D structure was performed with an Xradia MicroXCT 400 scanner. Some key parameters, such as the porosity, ε, the surface area to the total volume ratio, S/V, the tortuosity, τ, the cell size, d_c, and the pore size, d_p, were obtained and listed in Tab.1. A Representative Volume Element (RVE), shown in Fig. 1b, that represents the entire foam sample, was extracted from the tomography data. A tetrahedral mesh was built on the RVE for the numerical analysis of the air domain in the porous medium using a Finite Element (FE) commercial code (COMSOL). The equations governing the problem, the boundary conditions and the details of their numerical solution are reported in [4].

The knowledge of velocity, pressure and temperatre fields for the air domain, allows the calculation of the average heat transfer coefficient as

$$\overline{h_c} = q/\Delta T \tag{1}$$

where q is the 5,000 W/m^2 imposed heat flux, and $\Delta T = \overline{T_s} - \overline{T_f}$ with $\overline{T_s}$ the average solid-fluid boundary surface temperature and $\overline{T_f}$ the volume average of local adiabatic mixing temperatures.

The average Nusselt number and the Reynolds number are defined in the following way

$$\overline{\mathrm{Nu}} = h_c L/k_f \tag{2}$$

$$\mathrm{Re} = uL/\nu \tag{3}$$

where L is a characteristic length, k_f is the thermal conductivity of the air, u is the inlet velocity of the air (frequently referred as the superficial or Darcian velocity), equal to the ratio of the volumetric flow rate to the inlet cross-section, and ν is the kinematic viscosity of the air. Because of the complexity of the geometry of a porous medium, the volume averaging technique is frequently used in the study of thermo-fluid-dynamic phenomena, that allows to define an average volumetric Nusselt number

$$\overline{\mathrm{Nu_v}} = \mathrm{Nu} \cdot L \cdot S/V = \overline{h_v}\ L^2/k_f \tag{4}$$

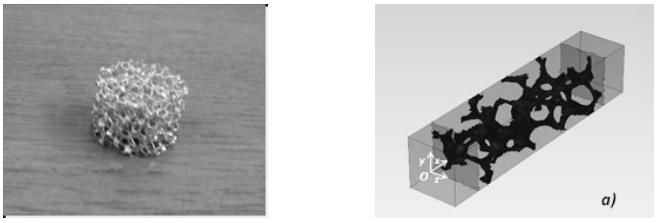

FIGURE 1. Aluminum foam: a) sample; b) RVE extracted from the CT data.

TABLE 1. Morphological parameters of the foam [4]

S/V (m^{-1})	ε	d_c (mm)	d_p(mm)	τ
1,116	0.894	2.64	0.91	1.04

where $\overline{h_v}$ is the average volumetric heat transfer coefficient.

With reference to the foam analyzed in [4], numerical values of the characteristic lengths reported in the introduction, with d_h defined in the following way

$$d_h = 4 \cdot \frac{\text{cross section available for flow}}{\text{wetted perimeter}} = 4 \cdot \varepsilon \, (S/V)^{-1} \tag{5}$$

together with the characteristic length proposed in this paper, d_c/ε, are reported in Tab.2. All the analysed characteristic lengths have the same pore level order of magnitudes.

The average Nusselt and volumetric Nusselt numbers as a function of the Reynolds number, for each characteristic length, are presented in Fig. 2.

The morphology of a foam can be univocally determined by knowing a couple of parameters selected from two different sets among the following:

a) S/V; b) d_c, d_p, PPI; c) ε; d) d_f, where d_f is the fiber diameter.

Whenever it is possible, the assumption of a parameter as the characteristic length, that univocally defines the morphology of the foam, is to be preferred. This can be accomplished only by choosing either d_h or d_c/ε among the parameters presented in Tab.2.

While the hydraulic diameter is a common concept in convective problems and it can be very useful in the comparison among geometries, a sufficiently accurate evaluation of S/V is still a challenging task.

As far as d_c/ε is concerned, the characteristic length could make reference both to d_c and d_p, that play an important physical role in heat transfer in foams. However, since the pore size distribution is more dispersed than the cell size distribution [4], the cell size has been preferred to the average pore size.

The porosity at the denominator of the characteristic length allows to account for the pore velocity, u_p, in the Reynolds number, according to the Dupuit-Forcheimer relation $u_p = u/\varepsilon$. It also permits to take into account the effective fluid conductivity for a porous medium, $k_{f,eff} = k_f \, \varepsilon$, in the Nusselt numbers.

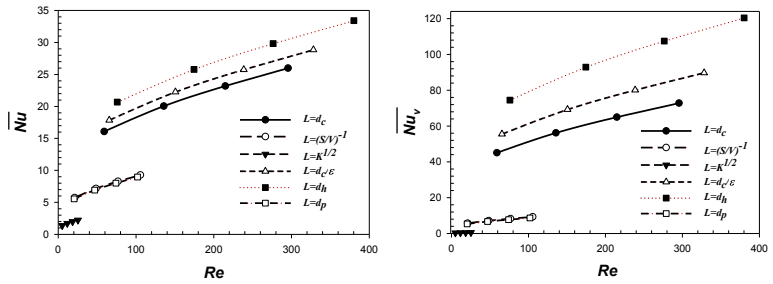

FIGURE 2. Average Nusselt and volumetric Nusselt number *vs*. Reynolds number.

TABLE 2. Characteristic lengths (mm)

d_c	$(S/V)^{-1}$	$K^{1/2}$	d_h	d_p	d_c/ε
2.64	0.94	0.23	3.40	0.91	2.93

4. CONCLUSIONS

The choice of a characteristic length for forced convection heat transfer in open cell metal foams has been investigated. A selection of characteristic lengths taken from the literature and a new one proposed in the present paper have been presented.

The importance of choosing a characteristic length univocally defining the foam morphology has been pointed out. The ratio of the cell size to the porosity seems to be a good choice in terms of measurements easiness and physical significance of dimensionless parameters.

REFERENCES

[1] F. Xu, R. Viskanta and J.P. Gore, Measurement and correlation of volumetric heat transfer coefficient of cellular ceramics, *Exp. Thermal Fluid Science*, 17, 285-93, 1998.

[2] J.P. Bonnet, F. Topin and L. Tadrist, Flow laws in metal foams: compressibility and pore size effects, *Transport in Porous Media*, 73, 233-54, 2008.

[3] R. Noman and M.Z. Kalam, Transition from laminar to non-darcy flow of gases in porous media, *in Advances in core evaluation – Accuracy and precision in reserves estimation*, P. F. Worthington ed., Gordon and Breach Science Publishers, Amsterdam, The Netherlands, 447-62, 1990.

[4] M. Oliviero, S. Cunsolo, W.M. Harris, M. Iasiello, W.K.S. Chiu V. Naso and N. Bianco, Microtomography-based analysis of pressure drop and heat transfer through open cell metal foams, in *Proc. ASME Summer Heat Transfer Conference 2013 (HT 2013),* Minneapolis (Minnesota, USA), 14-19 July 2013, paper HT2013-17237, 2013.

[5] Dukhan and P. Patel, Equivalent particle diameter and length scale for pressure drop in porous metals, *Exp. Thermal and Fluid Science*, 32, 10567, 2008.

[6] J. Petrasch, F. Meier, H. Friess and A. Steinfeld, Tomography based determination of permeability, Dupuit-Forchheimer coefficient, and interfacial heat transfer coefficient in reticulate porous ceramics, *Int. J. Heat and Fluid Flow*, 29, 315-26, 2008.

[7] B. Dietrich, W. Schabel, M. Kind and M. Holger, Pressure drop measurements for ceramic sponges – Determining the hydraulic diameter, *Chem. Eng. Science*, 64, 3633-40, 2009.

Third International Conference on Computational Methods for Thermal Problems
ThermaComp2014, June 2-4, 2014, Lake Bled, Slovenia
N. Massarotti, P. Nithiarasu and B. Sarler (Eds.)

NONLINEAR STABILITY ANALYSIS OF FLUID FLOW WITH VISCOUS DISSIPATION IN A POROUS CHANNEL

Michele Celli
Department of Industrial Engineering - Alma Mater Studiorum - Università di Bologna
Viale Risorgimento 2 - 40136 - Bologna - Italy
michele.celli3@unibo.it

Leonardo Santos de Brito Alves
Departamento de Engenharia Mecânica - Universidade Federal Fluminense
Rua Passo da Pátria 156 - 24210 240 - Niteroi, RJ - Brasil
leonardo.alves@mec.uff.br

Antonio Barletta
Department of Industrial Engineering - Alma Mater Studiorum - Università di Bologna
Viale Risorgimento 2 - 40136 - Bologna - Italy
antonio.barletta@unibo.it

ABSTRACT

The nonlinear convective instability of flow in a fluid saturated rectangular porous channel of arbitrary aspect ratio is here investigated by taking into account the effect of viscous dissipation. A laminar throughflow of constant velocity is assumed. The system is characterized by a unique source of thermal instability identified in the internal heat generation due to the viscous dissipation. The nonlinear analysis is performed by means of the generalized integral transform technique (GITT). The results obtained are compared with those coming from the linear analysis carried out numerically by means of the normal modes method.

Key words: *Nonlinear Stability, GITT, Porous Media, Viscous Dissipation, Thermal Convection*

1. INTRODUCTION

The study of the onset of the thermal instabilities is an important topic with a deep engineering impact. The stability analyses of fluid saturated porous media have indeed several applications for the oil extraction engineering and is strongly relevant in geological and geophysical studies. The thermal convection in porous media may be generated by heating from below or internal heat generation [1]. In this paper, the role of the viscous dissipation for the onset of convective instability in fluid saturated porous media is investigated. The analysis of this topic is relatively recent [2, 3, 4]. The novel feature introduced in the present paper is the fully nonlinear approach to the stability analysis. The results obtained by the linear stability analysis are here used as a benchmark [5]. The technique employed in order to investigate the nonlinear problem is the generalized integral transform technique [6, 7]. The GITT is a technique characterised by an alternative hybrid numerical analytical approach, based on the formal analytical principles in the classical integral transform method, for the solution of a priori non transformable diffusion and convection-diffusion problems. The computational task relative to the integral transformation procedure and the solution of the differential equations obtained are heavily based on a software that allow for mixed symbolic and numerical computations such as *Mathematica*.

2. MATHEMATICAL MODEL

A rectangular porous channel saturated by fluid with longitudinal throughflow is here studied. The geometry of the system is characterized by an arbitrary aspect ratio. The vertical boundaries as well as the lower horizontal boundary of the channel are considered adiabatic whereas the horizontal top boundary is kept at uniform temperature. A sketch of the system

is drawn in Fig. 1. The problem is modelled by assuming the Oberbeck-Boussinesq approx-

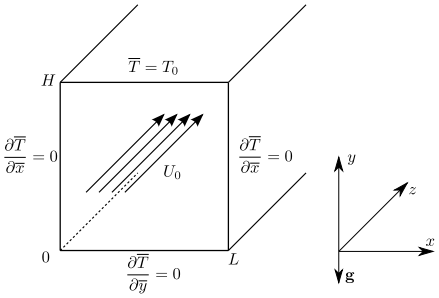

FIGURE 1. Sketch of the system

imation, by employing Darcy's law in order to define the momentum balance equation and by taking into account the viscous dissipation contribution inside the energy balance equation as internal heat source. The set up of the problem defines the viscous dissipation phenomenon as the only possible source of thermal instability. On applying the curl operator to the momentum balance equation, governing equations lose the pressure gradient contribution. In order to perform a stability analysis of the system just described, a nondimensional approach to the problem is needed. The governing equations together with the boundary conditions in their nondimensional form are given by

$$
\begin{aligned}
&\boldsymbol{\nabla} \cdot \boldsymbol{u} = 0, \\
&\boldsymbol{\nabla} \times \boldsymbol{u} = \boldsymbol{\nabla} \times T \boldsymbol{e}_y, \\
&\frac{\partial T}{\partial t} + \boldsymbol{u} \cdot \boldsymbol{\nabla} T = \nabla^2 T + Ge\, \boldsymbol{u} \cdot \boldsymbol{u}, \\
&y = 0: \quad v = 0, \quad \frac{\partial T}{\partial y} = 0, \qquad y = 1: \quad v = 0, \quad T = 0, \\
&x = 0: \quad u = 0, \quad \frac{\partial T}{\partial x} = 0, \qquad x = s: \quad u = 0, \quad \frac{\partial T}{\partial x} = 0,
\end{aligned}
\tag{1}
$$

where Ge the Gebhart number and s is the aspect ratio. The following scaling has been employed in order to obtain Eqs. (1)

$$
\overline{t} = \frac{\sigma H^2}{\alpha} t, \quad \overline{\boldsymbol{x}} = H \boldsymbol{x}, \quad \overline{\boldsymbol{u}} = \frac{\alpha}{H} \boldsymbol{u}, \quad \overline{T} = T_0 + \frac{T \nu \alpha}{g \beta K H}, \quad Ge = \frac{g \beta H}{c}, \quad s = \frac{L}{H},
\tag{2}
$$

where the overlined symbols refer to dimensional quantities, σ is the ratio between the heat capacity of the saturated medium and that of the fluid, α is the average thermal diffusivity, ν is the kinematic viscosity, g is the modulus of gravitational acceleration, β is the fluid thermal expansion coefficient, K is the permeability of the porous medium and c is the fluid specific heat.

3. BASIC SOLUTION AND DISTURBANCES

The stability analysis starts with perturbing the stationary solution of the problem. This solution is named basic state, the velocity field is assumed as constant in the x-direction and the temperature field is taken to be dependent only on the vertical y-coordinate. This stationary basic state can be obtained by solving Eqs. (1), namely

$$
\boldsymbol{u}_b = (0, 0, Pe), \qquad T_b = \frac{GePe^2}{2}(1 - y^2),
\tag{3}
$$

where, Pe is the Péclet number $Pe = U_0\, L/\alpha$ and U_0 the prescribed basic velocity. The velocity and temperature fields may be now rewritten as composed by a basic state and perturbed fields

$$\boldsymbol{u} = \boldsymbol{u}_b + \boldsymbol{U}, \quad T = T_b + \Theta, \tag{4}$$

where the subscript b refers to the basic state and the capital letters refer to the disturbances. The initial condition for the temperature field is defined as

$$T(x, y, z, 0) = T_b(y) + \Theta(x, y, z, 0). \tag{5}$$

In order to investigate the nonlinear stability of system (1), the analysis is focused only on the perturbed fields and their interaction with the basic state. The investigation may be reduced in complexity by focusing the attention only on the longitudinal rolls and avoiding the other possible inclinations of the disturbances. Since the longitudinal rolls lie on the (x, y)-plane, the contributions coming from the z-axis are neglected. On introducing the streamfunction $U = \partial\Psi/\partial y$ and $V = -\partial\Psi/\partial x$, Eqs. (1) reduce to

$$\begin{aligned}
&\nabla^2\Psi = -\frac{\partial\Theta}{\partial x},\\
&\frac{\partial\Theta}{\partial t} - \frac{\mathrm{d}T_b}{\mathrm{d}y}\frac{\partial\Psi}{\partial x} + \frac{\partial\Psi}{\partial y}\frac{\partial\Theta}{\partial x} - \frac{\partial\Psi}{\partial x}\frac{\partial\Theta}{\partial y} = \frac{\partial^2\Theta}{\partial x^2} + \frac{\partial^2\Theta}{\partial y^2} + Ge\left[\left(\frac{\partial\Psi}{\partial y}\right)^2 + \left(\frac{\partial\Psi}{\partial x}\right)^2\right],\\
&y = 0: \qquad \Psi = 0, \quad \frac{\partial\Theta}{\partial y} = 0, \qquad y = 1: \qquad \Psi = 0, \quad \Theta = 0,\\
&x = 0: \qquad \Psi = 0, \quad \frac{\partial\Theta}{\partial x} = 0, \qquad x = s: \qquad \Psi = 0, \quad \frac{\partial\Theta}{\partial x} = 0.
\end{aligned} \tag{6}$$

4. GENERALIZED INTEGRAL TRANSFORM TECHNIQUE

The generalized integral transform technique (GITT) is here employed in order to perform the fully nonlinear analysis of the problem described by Eqs. (6). The GITT method is based first on eigenfunction expansions for the problem potentials in the spatial variables and on the integral transformation of the expanded governing equations. A system of ordinary differential equations in time is thus obtained. The auxiliary eigenvalue problems in x and y directions for both the streamfunction and the temperature fields are defined as

$$\begin{aligned}
&\bar{\psi}_i''(x) + \lambda_i^2\bar{\psi}_i(x) = \bar{\psi}_i(0) = \bar{\psi}_i(s) = 0, \quad \tilde{\psi}_j''(y) + \omega_j^2\tilde{\psi}_j(y) = \tilde{\psi}_j(0) = \tilde{\psi}_j(1) = 0,\\
&\bar{\theta}_m''(x) + \gamma_m^2\bar{\theta}_m(x) = \bar{\theta}_m'(0) = \bar{\theta}_m'(s) = 0, \quad \tilde{\theta}_n''(y) + \sigma_n^2\tilde{\theta}_n(y) = \tilde{\theta}_n'(0) = \tilde{\theta}_n(1) = 0.
\end{aligned} \tag{7}$$

We need now to define the relations that allow us to transform, by means of an integration procedure, the governing equations. Once the problem is solved we also need the the inverse-transform relations. These relations are needed both for the streamfunction and for the temperature field but, for the sake of brevity, they will not be reported here. The governing equations (6) are thus modified to obtain

$$\begin{aligned}
&(\lambda_i^2 + \omega_j^2)\tilde{\bar{\Psi}}_{i,j}(t) = \sum_{n=1}^{\infty}\sum_{m=0}^{\infty}\tilde{A}_{j,n}\bar{A}_{i,m}\tilde{\bar{\Theta}}_{m,n}(t),\\
&\tilde{\bar{\Theta}}_{m,n}'(t) - \sum_{i=1}^{\infty}\sum_{j=1}^{\infty}\left[B_{m,n,i,j}\tilde{\bar{\Psi}}_{i,j}(t) + \sum_{o=0}^{\infty}\sum_{p=1}^{\infty}\left(C_{m,n,i,j,o,p} - D_{m,n,i,j,o,p}\right)\tilde{\bar{\Psi}}_{i,j}(t)\tilde{\bar{\Theta}}_{o,p}(t)\right]\\
&= -(\gamma_m^2 + \sigma_n^2)\tilde{\bar{\Theta}}_{m,n}(t) + Ge\left[\sum_{i=1}^{\infty}\sum_{j=1}^{\infty}\sum_{o=1}^{\infty}\sum_{p=1}^{\infty}\left(E_{m,n,i,j,o,p} + F_{m,n,i,j,o,p}\right)\tilde{\bar{\Psi}}_{i,j}(t)\tilde{\bar{\Psi}}_{o,p}(t)\right].
\end{aligned} \tag{8}$$

Where the tensors $\tilde{A}, \bar{A}, B, C, D, E, F$ arising from of the integration. The set of ordinary differential equations (8) are now solved numerically by means of software *Mathematica 9* (© Wolfram Research). The indexes present in Eq. (8) are reordered in order to minimize the number of equations needed to obtain an accurate solution. The system solved in the following is truncated to a total number of 100 equations in order to have a four digits accuracy in the results.

5. RESULTS

Figure (2) is composed by two frames where different neutral stability curves are drawn: the threshold values of the governing parameter $Ge\,Pe^2$ for the onset of the instability are shown as functions of the aspect ratio. The left frame of Fig. 2 shows a comparison between the benchmark solution coming from the linear stability analysis [5] and the solutions obtained by GITT. In order to compare the results of linear stability analysis with the nonlinear ones, Fig. 2 refers to the case $Ge \to 0$: in this limit the nonlinear contribution of the viscous dissipation terms is, in fact, neglected. This frame shows a good agreement between the benchmark solution and the results obtained in this paper. The right frame of Fig. 2 refers to results relative to two different values of the Gebhart number. Different values of Ge refer to different values of the heat generated by viscous dissipation effect: $Ge \to 0$ refers to negligible viscous dissipation and $Ge = 1$ refers to an extremely high viscous heating. The right frame highlights the almost vanishing sensitivity of the critical values of $Ge\,Pe^2$ with respect to the value of Ge. The limit $Ge \to 0$ together with the limit $Pe \gg 1$ can be taken in order to have $Ge\,Pe^2 \approx O(1)$. This is a physically sensible case to have a important effect of viscous dissipation even with small values of the Gebhart number. From the physical viewpoint the high velocity of the basic flow balances the weakness of buoyancy force with the strength of viscous heating.

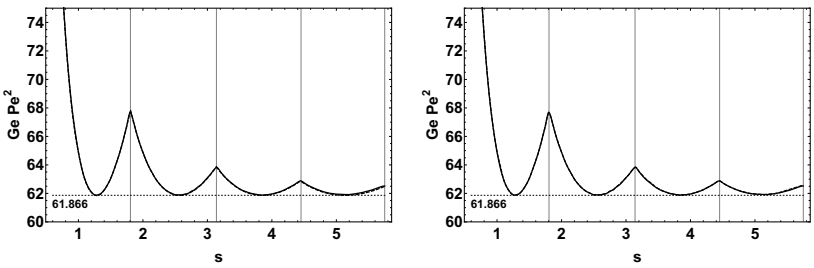

Figure 2. Left frame: neutral stability curves comparison between the benchmark case (linear analysis, dashed line) and the nonlinear analysis (continuous line). Right frame: neutral stability curves for $Ge \to 0$ (continuous line) and for $Ge = 1$ (dashed line).

6. CONCLUSIONS

The paper deals with the thermoconvective stability analysis of a fluid saturated rectangular porous channel. The stability analysis performed is fully nonlinear and has been carried out by means of the generalized integral transform technique. The results coming from the fully nonlinear analysis show a good agreement with the results found in the literature for the linear stability analysis of the same setup. The nonlinear terms in the disturbances produce no appreciable differences with respect to the linear analysis for what concerns the threshold for the onset of the thermoconvective instability.

REFERENCES

[1] A.D. Nield and A. Bejan. *Convection in Porous Media (3rd edition)*. Springer, New York, 2006.
[2] L. Storesletten and A. Barletta. Linear instability of mixed convection of cold water in a porous layer induced by viscous dissipation. *International Journal of Thermal Sciences*, 48:655–664, 2009.
[3] D.A. Nield. The modeling of viscous dissipation in a saturated porous medium. *ASME Journal of Heat Transfer*, 129:1459–1463, 2007.
[4] A. Barletta, M. Celli, and D.A.S. Rees. Darcy-forchheimer flow with viscous dissipation in a horizontal porous layer: onset of convective instabilities. *Journal of Heat Transfer*, 131:072602, 2009.
[5] A. Barletta and L. Storesletten. Viscous dissipation and thermoconvective instabilities in a horizontal porous channel heated from below. *International Journal of Thermal Sciences*, 49:621–630, 2010.
[6] R.M. Cotta. *The integral transform method in thermal & fluids sciences & engineering*. Begell House, 1998.
[7] J. Pontes L.S. de B. Alves, R.M. Cotta. Stability analysis of natural convection in porous cavities through integral transforms. *International Journal of Heat and Mass Transfer*, 45:1185–1195, 2002.

Third International Conference on Computational Methods for Thermal Problems
THERMACOMP2014, June 2-4, 2014, Lake Bled, Slovenia
N. Massarotti, P. Nithiarasu and B. Sarler (Eds.)

LAMINAR FORCED CONVECTION IN FLAT TUBES WITH NANOFLUIDS FOR AUTOMOTIVE APPLICATIONS

Bernardo Buonomo, Oronzio Manca, Lorenzo Marinelli, Sergio Nardini
Dipartimento di Ingegneria Industriale e dell'Informazione, Seconda Università degli Studi di Napoli, Via Roma 29, 81031 - Aversa, Italy, bernardo.buonomo@unina2.it, oronzio.manca@unina2.it, lorenzo.marinelli@unina2.it, sergio.nardini@unina2.it

ABSTRACT

A numerical investigation on laminar forced convection with nanofluid in a flat tube is accomplished. A constant and uniform heat flux on the surfaces is applied and single-phase model approach is employed. The analysis is performed in steady state regime for nanofluids with water (W) or water-ethylene glycol (EG) as base fluid and spherical nanoparticles with a diameter equal to 38 nm. The governing equations are solved by a finite volume method employed in a CFD code. Results are presented in terms of heat transfer convective coefficient and pressure drops for different values of Reynolds number and volumetric concentration.

Key Words: *Laminar Flow, Nanofluids, Convective Heat Transfer, Forced Convection, Automotive.*

1. INTRODUCTION

Convective heat transfer can be enhanced passively by changing flow geometry, boundary conditions or by enhancing the thermal conductivity of the working fluid [1]. A technique which is employed for heat transfer augmentation is the use of flattened tubes. There are only a few articles which have reported the advantages of these kinds of tubes in the favour of heat transfer augmentation which are focused mainly on the two phase flow regimes [2].

The use of nanofluids instead of the conventional fluids in car radiators is recently studied for the first time in [3]. In this study was reported a project to target fuel savings for the automotive industries through the development of energy efficient nanofluids and smaller and lighter radiators.

Some numerical and experimental investigations have been accomplished on the use of nanofluids in automotive car radiators. One of the first study was presented in [4] where was studied the specific heat of Al_2O_3/ethylene glycol and water (EG/W) nanofluid to influence the cogeneration efficiency of a 45 kW diesel electric generator (DEG) in 2008. A numerical study of fluid dynamic and heat transfer performance of Al2O3 and CuO nanoparticles in an ethylene glycol and water mixture under laminar flow in the flat tubes of an automobile radiator was presented in [5]. Performances of an automotive car radiator operated with ethylene glycol and Cu nanoparticles were investigated in [6]. In another study, Peyghambarzadeh et al. [7] have used different base fluids including pure water, pure ethylene glycol, and their binary mixtures with Al2O3 nanoparticles. It was proved that nanofluids improves the cooling performance of the car radiator extensively. The heat transfer and pressure drop characteristics of CuO/oil nanofluid flow inside horizontal flattened tubes under constant heat flux were studied in [8]. Application of CuO-water nanofluid with size of the nanoparticles of 20 nm and volume concentrations up 2% was numerically investigated in [9] for a radiator of Chevrolet Suburban diesel engine A numerical investigation on the cooling performances of an automotive radiator using ethylene glycol based CuO nanofluids as coolants was presented in [10]. A three-dimensional analysis was used to study the heat transfer performance of nanofluid flows through a flattened tube in a laminar flow regime and constant heat flux boundary condition. More recent experimental study are reported in [11,12].

In this paper a numerical investigation on laminar forced convection flow of Al_2O_3 nanosize particles, dispersed in base fluids, made up by water or water and glycol, in a flat tube, with opposite flat sides and two lateral circular sides, is accomplished. A constant and uniform heat flux on the surfaces is applied and single-phase model approach is employed.

2. PHYSICAL PROBLEM AND GOVERNING EQUATIONS

The geometrical configuration under consideration consists in a with two parallel flat plates and the lateral sides with a circular shape as shown in Fig. 1. The length of the duct, the edge one and the channel height is 0.5 m, 0.0081 m and 0.00254 m, respectively. In this way, the hydraulic diameter is set equal to 4.58×10^{-3} m. A steady laminar flow and different nanoparticle volume fractions have been considered. The analysis has been performed for nanofluids with water or water/glycol, at different concentrations, as base fluid and spherical nanoparticles of alumina (Al_2O_3) with a diameter equal to 38 nm. Thermophysical properties are considered constant with temperature [13]. The CFD commercial code Ansys-Fluent has been employed in order to solve the 3-D numerical model. A grid independence analysis has been accomplished to evaluate the optimal node number in terms of computational time and accuracy. Moreover, the validation procedure have been performed in the case of pure water and fully developed laminar flow, with data reported by [14].

3. RESULTS

Results are presented in terms of average convective heat transfer coefficient, pressure drops and required pumping power profiles, as a function of Re, ranging from 100 to 1000, and particle concentrations, in the range 0%-5% in pure water and water/ ethylene glycol (W/EG) mixture. A constant and uniform heat flux of 2 kW/m^2 is applied on all the channel walls. In Figs. 2and 3 are given some results.

In Fig. 2a, it is interesting to observe the significant increase of average convective heat transfer due to the presence of nanoparticles. As expected the enhancement increases with the increase of the volumetric concentration. However, the pressure drop, in Fig. 2b, presents an increase due to the increase of viscosity at increase of the nanoparticles volumetric concentration.

The ratio between the average convective heat transfer coefficient for nanofluids with base fluid the W/EG mixture and the one for nanofluids with water, as base fluid, reported in Fig. 3a, indicates that W/EG mixtures present improved heat transfer behaviour. The improvement decreases as the Re value increases. In any cases the higher the EG concentration is the higher the convective heat transfer. The convective heat transfer coefficient increases with respect to the simple water is presented in Fig. 3b. In the diagrams the ratio significantly decreases as Re increases, but for Re>500 the values present a slight increase and a minimum value is reached at about Re=600.

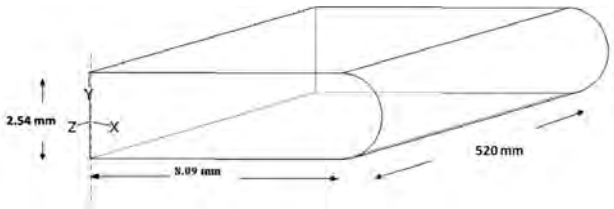

Figure 1 - Sketch of the geometrical model.

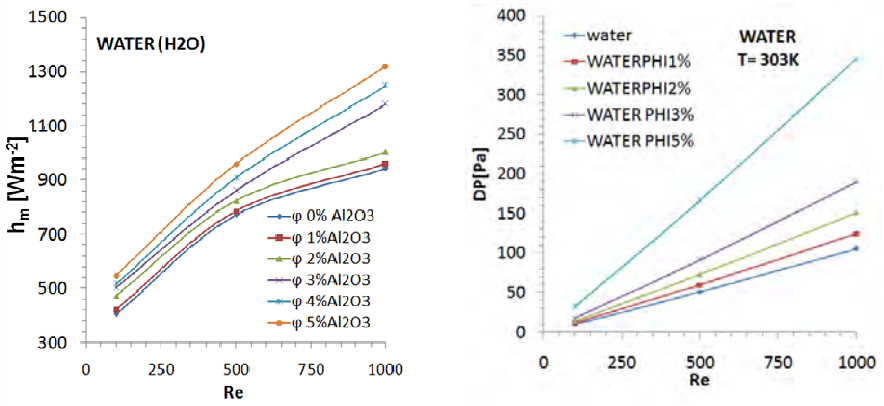

(a) (b)

Figure 2. Profile as a function of Reynolds number for different volumetric concentrations: (a) average convective heat transfer coefficient and (b) pressure drop.

4. CONCLUSIONS

Steady state laminar convection in a flat tube with nanofluids was numerically investigated. The nanofluids were Al_2O_3 in water or in water-ethylene glycol mixture. Results in terms of average convective heat transfer and pressure drop are presented together with the ratio between average convective heat transfer for nanofluids and pure water. The increases in convective heat transfer and in pressure drop are detected for all mixture. The improvement of W/EG nanofluid mixture average convective heat transfer increased with the volumetric concentration of EG in water but decreased with the Reynolds number increase. The ratio between average convective heat transfer for W/EG nanofluids and the pure water presented minimum values at Re=600 for all considered W/EG mixture.

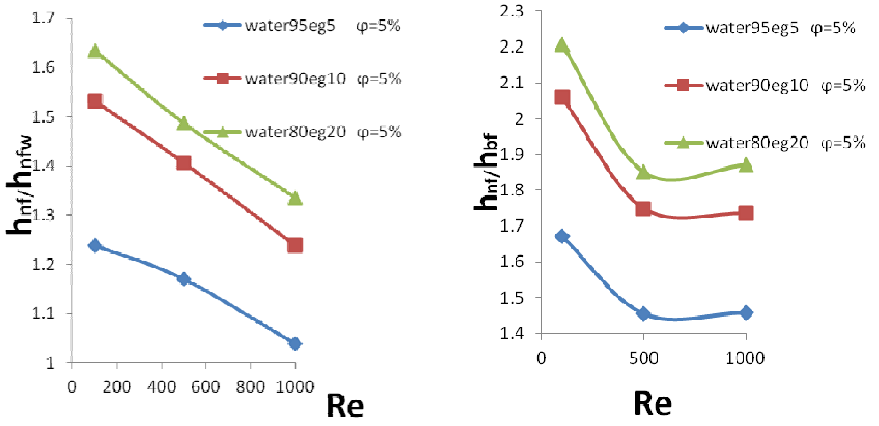

(a) (b)

Figure 3. Average convective heat transfer coefficient ratios as a function of Reynolds number and different W/EG mixtures with respect to: a) water based nanofluid and b) pure water.

REFERENCES

[1] R.L. Webb, and N.H. Kim, *Principles of Enhanced Heat Transfer*, 2nd ed., Taylor&Francis Group, New York.

[2] M. Nasr, M.A. Akhavan Behabadi, and S.E. Marashi, Performance evaluation of flattened tube in boiling heat transfer enhancement and its effect on pressure drop, *International Communication in Heat and Mass Transfer*, 37, 430–36, 2010.

[3] S. Choi, Nanofluids for improved efficiency in cooling systems, *Heavy Vehicle Systems Review,* Argonne National Laboratory, April 18-20, 2006.

[4] D.P. Kulkarni, R.S. Vajjha, D.K. Das, and D. Oliva, Application of aluminum oxide nanofluids in diesel electric generator as jacket water coolant, *Applied Thermal Engineering*, 28, 1774-81, 2008.

[5] R.S. Vajjha, D.K. Das, and P.K. Namburu, Numerical study of fluid dynamic and heat transfer performance of Al2O3 and CuO nanofluids in the flat tubes of a radiator, *International Journal of Heat and Fluid Flow*, 31, pp. 613–621, 2010.

[6] K.Y. Leong, R. Saidur, S.N. Kazi, and A.H. Mamun, Performance investigation of an automotive car radiator operated with nanofluid-based coolants (nanofluid as a coolant in a radiator), *Applied Thermal Engineering*, 30, 2685-92, 2010.

[7] S.M. Peyghambarzadeh, S.H. Hashemabadi, S.H. Hoseini, and M.S. Jamnani, Experimental study of heat transfer enhancement using water/ethylene glycol based nanofluids as a new coolant for car radiators, *International Communication in Heat and Mass Transfer*, 38, 1283-90, 2011.

[8] P. Razi, M.A. Akhavan-Behabadi, and M. Saeedinia, Pressure drop and thermal characteristics of CuO–base oil nanofluid laminar flow in flattened tubes under constant heat flux, *International Communication in Heat and Mass Transfer*, 38, 964–71, 2011.

[9] N. Bozorgan, K. Krishnakumar, and N. Bozorgan, Numerical study on application of CuO-water nanofluid in automotive diesel engine radiator, *Modern Mechanical Engineering*, 2, 130-36, 2012.

[10] G. Huminic, and A. Huminic, Numerical analysis of laminar flow heat transfer of nanofluids in a flattened tube, *International Communication in Heat and Mass Transfer*, 44, 52–57, 2013.

[11] S.M. Peyghambarzadeh, S.H. Hashemabadi, M. Naraki, and Y. Vermahmoudi, Experimental study of overall heat transfer coefficient in the application of dilute nanofluids in the car radiator, *Applied Thermal Engineering*, 52, 8–16, 2013.

[12] H.M. Nieh, T.P. Teng, and C.C. Yu, Enhanced heat dissipation of a radiator using oxide nano-coolant, *International Journal of Thermal Sciences*, 77, 252–261, 2014.

[13] O. Manca, P. Mesolella, S. Nardini, and D. Ricci, Numerical study of a confined slot impinging jet with nanofluids, *Nanoscale Research Letters*, 6, art. no. 188, 2011.

[14] Fluent v.6.3 user guide, Fluent corporation, Lebanon, 2006.

Third International Conference on Computational Methods for Thermal Problems
THERMACOMP2014, June 2-4, 2014, Lake Bled, Slovenia
N. Massarotti, P. Nithiarasu and B. Sarler (Eds.)

TANSIENT ANALYSIS OF LAMINAR SLOT-JET IMPINGING ON CONFINED POROUS MEDIUM WITH BOTTOM SURFACE AT UNIFORM HEAT FLUX

B. Buonomo[1], G. Lauriat[2], O. Manca[1] and S. Nardini[1]

[1]Dipartimento di Ingegneria Industriale e dell'Informazione, Seconda Università degli Studi di Napoli, Via Roma 29, Aversa (CE) 81031, Italy,

[2]Laboratoire MSME, UMR CNRS 8208, Université Paris-Est, 77454 Marne-la-Vallée Cedex 2, France

bernardo.buonomo@unina2.it, lauriat@univ-mlv.fr, oronzio.manca@unina2.it, sergio.nardini@unina2.it

ABSTRACT

This paper presents the results of a numerical investigation in transient regime on a single slot jet impinging in a porous parallel-plate channel containing an air-saturated high permeability porous medium. The bottom wall is partially heated, the effect of buoyancy is also taken into account. The fluid flow is assumed two dimensional, laminar and the porous medium is modelled using the Brinkman–Forchheimer-extended Darcy model in local thermal non-equilibrium hypothesis. Results in terms of non-dimensional average wall temperature profiles and average Nusselt numbers are given.

Key Words: *Heat Transfer, Finite Volumes, Impinging Jet, Porous Medium, Local Thermal Non-Equilibrium, Mixed Convection.*

1. INTRODUCTION

A very efficient method for cooling heated surfaces is the jet impingement of a cold fluid. This is employed in several engineering applications such as in refrigeration, automotive, aerospace, process industry and solar energy heaters. An intensive research activity has been developed on impinging jets as reported in the review [1]. As indicated in literature, jets employed together with porous media with high porosity and thermal conductibility, such as aluminum foams, allows to improve the heat removal from a heated surface. Moreover, it has been observed that several parameters have effects on the fluid and thermal behaviors and they should be investigated to evaluate optimal configurations in order to enhance the heat transfer. But also some fundamental studies need to understand and characterize the thermal and fluid dynamic behaviors of this system. In fact, except the study given in [2], there is a lack of knowledge on impinging jet on a heated surface at assigned wall heat flux in porous media with assumption of local thermal non-equilibrium condition. This assumption should take into account for highly conducting and highly porous material attached to the hot wall, as indicated in [3].

The present study presents the results of an numerical investigation in transient regime on a porous parallel-plate channel containing a fluid-saturated high permeability porous medium and a single

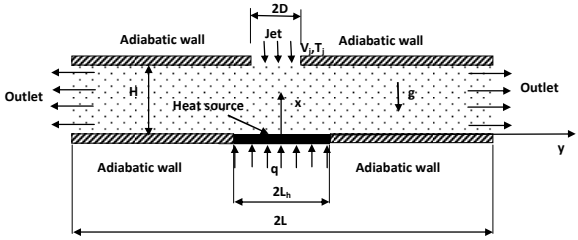

FIGURE 1. Sketch of geometrical and physical model with coordinate system

slot jet impinging on the porous medium. The opposite wall to the slot jet is heated at uniform heat flux and the buoyancy effect are taken into account. The fluid flow in the porous medium is modeled using the Brinkman–Forchheimer extended Darcy model. The fluid flow is laminar and unsteady. The analysis is accomplished under local thermal non-equilibrium conditions. Results in terms non-dimensional average wall temperature and average Nusselt numbers profiles are given.

2. GEOMETRY AND NUMERICAL MODEL

The investigated configuration is a confined impinging slot jet on a heated surface in a porous foam with the lower impinging surface partially heated at uniform heat flux, q, and the upper surface adiabatic. Figure 1 shows the physical problem and geometry under investigation. The flow is assumed two-dimensional, unsteady, laminar and incompressible and the inlet section of the slot jet wide D. The jet impinges through a saturated porous medium on a horizontal surface with a heat source, wide $2L_h$. The inlet slot jet velocity and temperature are V_j and T_j, respectively. The distance between the upper confining surface and the lower partially heated surface is H. The length of the lower plate is 2L and the unheated symmetrical zone of the lower surface is assumed adiabatic. Fully developed fluid dynamic and thermal flow is assumed at the outlet sections and the fluid is air, Pr=0.71. The effect buoyancy is taken into account. The porous material is considered as homogeneous and isotropic. All the thermophysical properties of the fluid and the solid matrix of the porous medium are assumed constant except for the variation in density with temperature (Boussinesq approximation) giving rise to the buoyancy forces. In the porous medium, the Brinkman-Forchheimer-extended Darcy model is used in the momentum equations to enable the study of Darcian and non-Darcian effects. The local thermal non-equilibrium (LTNE) is used in the energy equations the solid and the fluid phase whereas the dissipation effect is assumed negligible. The numerical computation was carried out by means of the finite volume method, using rectangular cells with constant mesh spacing along the coordinate directions, X and Y. More details on the used numerical method are reported in [4].

3. RESULTS

In Fig.2 non-dimensional average temperature profiles are reported as a function of non-dimensional time for Ra=100, Da=10^{-6}, Bi=10, ε=0.80, α_f/α_s=1.0 and for different non dimensional jet radius d_j=D/H. For Pe=1 and $k_{f,eff}/k_{s,eff}$=0.001, Fig.2a, non-dimensional average temperature is slightly independent on jet diameter because the solid phase is much more conductive than the

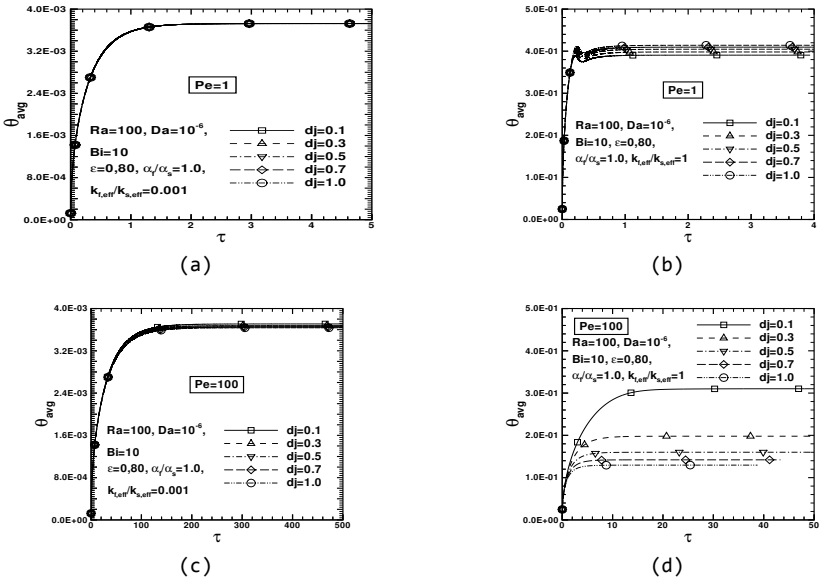

FIGURE 2. Non-dimensional avarage wall temprature vs non-dimensional time for Ra=100, $Da=10^{-6}$, Bi=10, ε=0.80, α_f/α_s=1.0 and for different jet diameter: (a) Pe=1 and $k_{f,eff}/k_{s,eff}$=0.001; (b) Pe=1 and $k_{f,eff}/k_{s,eff}$=1; (c) Pe=100 and $k_{f,eff}/k_{s,eff}$=0.001; (d) Pe=100 and $k_{f,eff}/k_{s,eff}$=1

fluid one and due to the low value of the Peclet number. For $k_{f,eff}/k_{s,eff}$=1, Fig.2b, temperature profiles depend on jet diameter after a maximum value is reached. In particular as jet diameter increases non-dimensional temperature is higher. For each jet diameter temperature profile presents a relative maximum and a minimum. In the first instants buoyancy effect is negligible and, therefore, the regime is only conductive. When temperature riches a value so to activate natural convection temperature profile has a maximum (overshoot) and then temperature decreases till a minimum. For Pe=100 and $k_{f,eff}/k_{s,eff}$=0.001, Fig.2c, the effect of jet diameter is higher and heat removal increases as diameter is higher. Non-dimensional average temperature profiles for Pe=100 and $k_{f,eff}/k_{s,eff}$=1, Fig.2d, do not show the presence of the overshoot for each jet diameter.

Nusselt numbers at the steady state as a function of Peclet number is presented in Fig.3 for $k_{f,eff}/k_{s,eff}$=0.001 and 1 and for different non dimensional jet radius d_j=D/H. For $k_{f,eff}/k_{s,eff}$=0.001, Fig.3a, the dominant effect is associated with the conduction in the solid phase. For low values of the Peclet number the effect of natural convection is negligible compared to that associated to the heat transfer in the conductive porous medium. As the Peclet number increases the differences between the Nusselt number values for the various diameters of the jet increase because the forced convection in the medium due to the jet is more significant. This effect is more marked as jet diameter increases. For the same conductivity value of the two phases, $k_{f,eff}/k_{s,eff}$=1, Fig.3b, it is worth noticing that Nusselt number decreases in the range $1 \leq Pe \leq 10$ and this effect is more marked for high jet diameter. This is due to the fact that in this range the effect of buoyancy is not negligible respect to the one of the opposing forced convention therefore as Peclet number increases

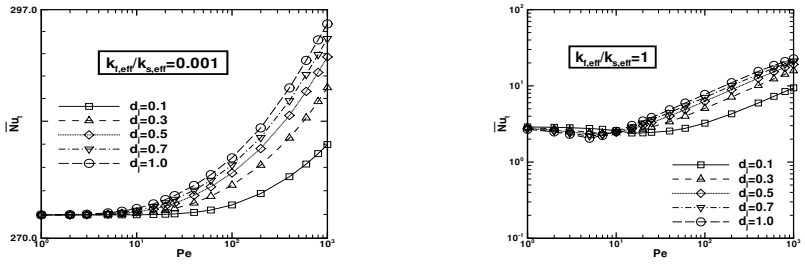

(a) (b)

FIGURE 3 Nusselt number vs Peclet number for different jet diameter values: (a) for $k_{f,eff}/k_{s,eff}$=0.001; (b) for $k_{f,eff}/k_{s,eff}$=1

heat removal worsen. For Pe>10 forced convection prevails on buoyancy effect.

4. CONCLUSIONS

Two dimensional impinging slot jet in laminar unsteady state flow in a saturated porous medium was numerically investigated. The fluid phase was air with constant temperature properties. The slot jet impinged on a partially heated plate at uniform heat flux. Governing equations given in terms of stream function and vorticity and in local thermal non-equilibrium hypothesis and Brinkman-Forchheimer-extended Darcy model. They were solved by a finite volume method. For $k_{f,eff}/k_{s,eff}$=1 and Peclet number lower than 10 the effect of buoyancy is not negligible respect to the one of opposing forced convention and Nusselt number decreases. This effect is more marked for high jet diameters. Non-dimensional wall average temperature profiles were not dependent on jet diameters in the first instants till a maximum was reached (overshoot). For $k_{f,eff}/k_{s,eff}$=0.001 the dominant effect is that associated with the conduction in the solid phase. Non-dimensional average temperature profiles are slightly dependent on jet diameters in particular for low Peclet numbers. The overshoot in not present even for Pe=1.

REFERENCES

[1] A. Dewan, R. Dutta, and B. Srinivasan, Recent trends in computation of turbulent jet impingement heat transfer, *Heat Transfer Engineering*, 33, 447-460, 2012.

[2] T.M. Jeng, and S.C. Tzeng, Height effect on heat transfer characteristics of sintered porous blocks with a confined slot jet, *Int. Communications in Heat and Mass Transfer*, 35, 30-38, 2008.

[3] F.T.,Dórea and M.J.S. de Lemos, Simulation of laminar impinging jet on a porous medium with a thermal non-equilibrium model, *Int. Journal of Heat and Mass Transfer*, 53, 5089-5101, 2010.

[4] B. Buonomo, O. Manca, S. Nardini, Laminar Slot-Jet Impinging on Confined Porous Medium in Local Thermal non-Equilibrium Conditions with Bottom Surface at Uniform Heat Flux, Proc. Of 4th International Conference on Porous Media and its Applications in Science and Engineering ICPM4, June 17-22, 2012, Potsdam, Germany.

Third International Conference on Computational Methods for Thermal Problems
THERMACOMP2014, June 2-4, 2014, Lake Bled, Slovenia
N. Massarotti, P. Nithiarasu and B. Sarler (Eds.)

Adjoint-based cooling efficiency optimization of turbulent ducted flows

Hauke Narten, Claudenê Correia, Carsten Othmer
Volkswagen AG, PO 011/1750 38440 Wolfsburg, Germany, Hauke.Narten@volkswagen.de

Rolf Radespiel
Institute of Fluid Mechanics, Technical University Braunschweig, Hermann-Blenk-Str 37, 38108 Braunschweig, Germany

ABSTRACT

We present a new method to optimize the cooling efficiency of ducted flows by using surface sensitivities obtained from multi-objective continuous adjoint fluid simulations. A surrogate cost function that approximates the heat transfer coefficient is proposed and the corresponding adjoint boundary conditions are derived. The method is applied to a turbulent pipe flow, which is iteratively morphed into a more beneficial shape. The improvements in its cooling efficiency at the cost of total pressure loss are validated with a conjugate heat transfer simulation for each morphing step.

Key Words: *Heat Transfer, Continuous Adjoint Optimization, OpenFoam®, Forced Convection, Internal Flow, Ducted Flow, One-Shot*

1. INTRODUCTION

Due to downsizing in automotive internal combustion engines the thermal power densities are rising and sufficient cooling of the solid regions becomes increasingly difficult. In order to optimize the flow of liquid coolant inside the engine block a stable optimization method is needed that handles complex geometries at a reasonable calculation cost. Adequate parameterization of those geometries is nigh on impossible and computation of sensitivities for a large number of parameters is very costly [1]. Therefore, the presented optimization method is based on the calculation of surface sensitivities by means of the adjoint method.

Ideally the cost function for cooling optimization involves the temperature distribution in a selected region of the solid domain. But for complex geometries, already primal conjugate heat transfer (CHT) calculations are quite inaccurate because of the delicacy of reliable heat transfer coefficient computation. Therefore, adjoint CHT is not our first choice. This study rather aims at approximating the heat transfer via the Reynolds analogy [2] as follows:

$$\dot{q}_W \approx \frac{\tau_W c_p (T_W - T_\infty)}{c_\infty}. \tag{1}$$

Here $\dot{q}_W$ is the heat flux per unit wall area and τ_W is the wall shear stress. $(T_W - T_\infty)$ represents the fluid temperature difference between wall and free stream, with c_∞ being the free stream velocity. c_p is the thermal capacity at constant pressure. This equation states an approximate correlation between heat transfer and wall shear stress, that allows to compute sensitivities w.r.t. cooling efficiency by isothermal primal and adjoint simulations. As a surrogate cost function J for optimizing cooling efficiency of ducted flows we therefore propose the integral of the wall shear stress τ_W over the heated surface Γ_0:

$$\mathrm{J} = \int_{\Gamma_0} \mathrm{d}\Gamma_0 \sqrt{\tau^2} \ . \tag{2}$$

An adjoint topology optimization method including heat transfer was recently presented by Kontoleontos et al. [3]. Their approach proved successful for laminar and turbulent flow conditions in two- and three-dimensional geometries. However, we decided for shape morphing as opposed to porosity-based topology optimization in order to avoid the inherent inaccuracies of the velocity profile along the porous/non-porous interface.

2. ADJOINT-BASED SHEAR STRESS OPTIMIZATION METHOD

The optimization method presented here is based on the implementation outlined in [4], where a continuous adjoint formulation with the frozen turbulence assumption was derived for various ducted flow cost functions. We extended this formulation to allow the computation of sensitivities w.r.t. our wall shear stress cost function J (Equation 2).

Optimizing the cooling efficiency means in general to find a suitable trade-off between pressure drop and heat transfer. For this reason, this optimization method uses a multi-objective approach, which in addition to maximizing the wall shear stress on the objective surface according to Equation 2, aims at minimizing the total pressure loss between inlet and outlet. This is accomplished by introducing a combined cost function with suitably weighted contributions from pressure drop and shear stress, respectively.

Altering the mesh according to the surface sensitivities G_J is done with the OpenFoam® mesh motion utility using a standard Laplacian solver and quadratic inverse distance diffusivity. The face centres of the surface mesh are displaced by $\overrightarrow{y_d}$ as follows:

$$\overrightarrow{y_d} = \vec{n} \cdot c \cdot \tan^{-1}\left(b \cdot G_J\right), \tag{3}$$

where $\vec{n}$ is the surface normal. This trigonometric conversion serves as a scalable limiter. For very high magnitudes of sensitivities the displacement y_d approaches its maximum value while values close to zero still result in significant enough mesh deformation. Parameter b is used to scale the sensitivities into a usable range and c defines the maximum mesh deformation per Iteration. The displacement is interpolated onto the vertices which are finally moved, dragging along the internal mesh.

3. APPLICATION TO PIPE BEND FLOW

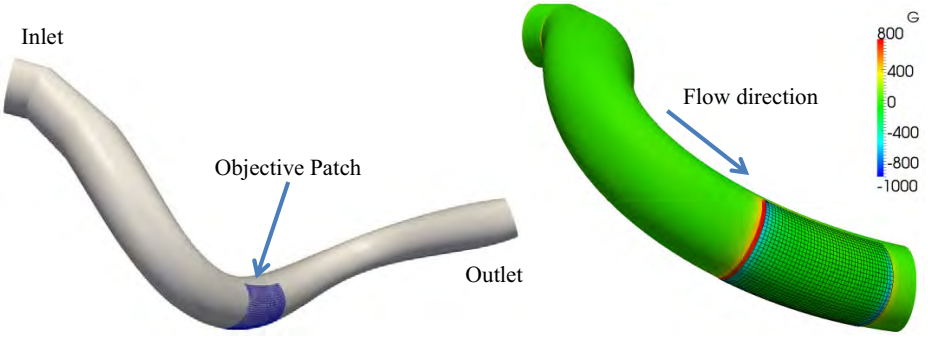

FIGURE 1. Pipe bend test case with highlighted objective patch (left) and combined surface sensitivities (right)

The surface sensitivities are fed into the above mentioned morphing algorithm in order to perform geometrical updates in a one-shot fashion. Once the mesh deformation reaches a level where certain mesh quality criteria are violated, the optimization process is terminated. Figure 2 (left) depicts the evolution of the cost functions pressure drop and wall shear stress (Equation 2), and the final shape of the geometry upstream of the objective patch (which itself is kept frozen) after 39 geometry updates is shown in Figure 2 (right).

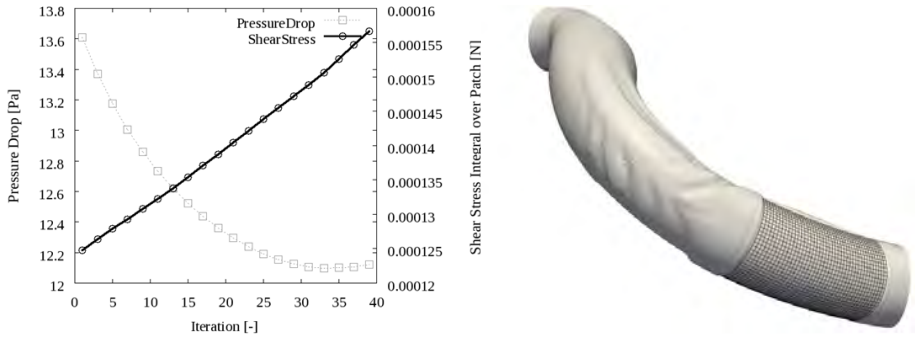

FIGURE 2. Optimization history of pressure drop and wall shear stress cost function (left) and the final shape of the pipe bend (right)

The optimization method succeeded in increasing the shear stress magnitude on the objective patch by approximately 26 % while lowering the total pressure loss by 10 %. The improvement in the pressure drop is mainly due to rounding sharp edges present in the original duct, while the increase in wall shear stress is invoked by the appearance of steps and fins upstream, which disturb the thermal boundary layer and expose the objective patch to higher shear stress. How these geometric modifications increase the shear stress on the objective patch is detailed in Figure 3.

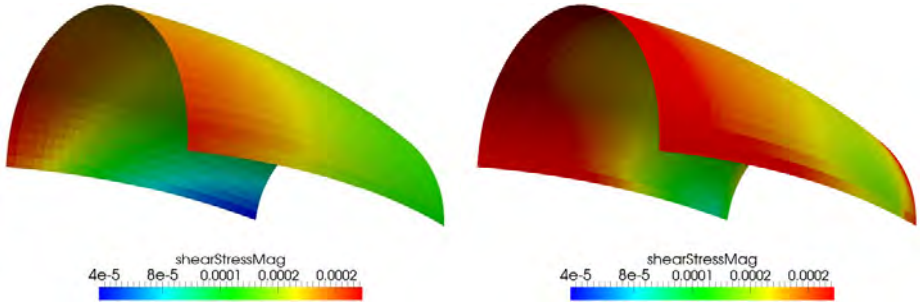

FIGURE 3. Shear stress distribution on the objective patch before (left) and after the optimization (right).

For validation purposes the pipe bend was fitted with a heat conducting solid domain of fixed temperature on the outer diameter interfacing at the objective patch (Figure 4, left). For every updated geometry a separate conjugate heat transfer computation was set up and the heat flux across the fluid/solid interface was computed. As can be seen from Figure 4 (right), the heat flux across the interface increased by approximately 5 % in the course of the optimization, thus demonstrating the

improved heat transfer capabilities of the new geometry and the applicability of the proposed surrogate cost function (Equation 2) for cooling efficiency optimization.

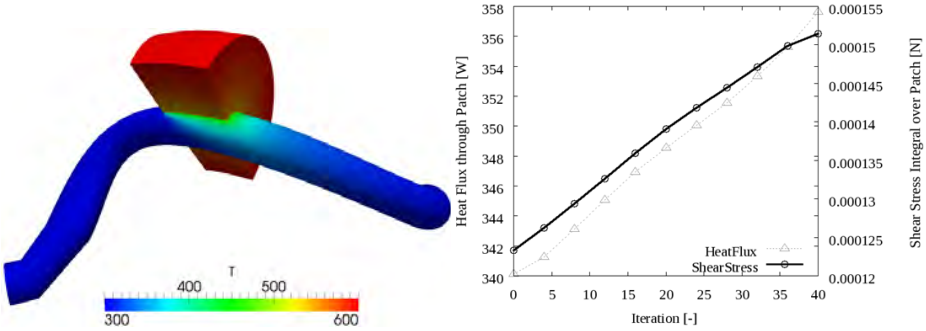

FIGURE 4. Pipe bend with attached solid (left) and the evolution of heat flux and shear stress as obtained from the CHT validation simulations (right)

4. CONCLUSIONS

A new method for optimizing the cooling capabilities of internal flows has been introduced. The outlined workflow has been successfully demonstrated on a small yet industrial relevant 3D case. Heat flux across the objective patch has been increased by 5 % while pressure drop has been reduced by 10 %. This result was confirmed by independent conjugate heat transfer computations simultaneously justifying the application of the Reynolds analogy in the derivation of the presented cost function. The overall computational effort of the optimization is comparable to three times of the cost of a single primal solution. Considering the multi-objective approach, this is a very promising outlook for the intended industrial applications on complex geometries with large meshes.

REFERENCES

[1] G. Janiga and D. Thevenin. *Optimization and Computational Fluid Dynamics*. Optimization and Computational Fluid Dynamics. Springer, 2008.

[2] D. Shang. *Theory of Heat Transfer with Forced Convection Film Flows*. Heat and mass transfer. Springer, 2010.

[3] E. A. Kontoleontos, E. M. Papoutsis-Kiachagias, A. S. Zymaris, D. I. Papadimitriou, and K. C. Giannakoglou. Adjoint-based constrained topology optimization for viscous flows, including heat transfer. *Engineering Optimization*, 45(8):941–961, 2013.

[4] C. Othmer. A continuous adjoint formulation for the computation of topological and surface sensitivities of ducted flows. *Int J. Num. Meth. Fluids*, 58(1770):861 – 877, 2008.

Third International Conference on Computational Methods for Thermal Problems
THERMACOMP2014, June 2-4, 2014, Lake Bled, Slovenia
N. Massarotti, P. Nithiarasu and B. Sarler (Eds.)

DESIGN OF A PCM LATENT HEAT ENERGY STORAGE SYSTEM THROUGH ENTROPY GENERATION ANALYSIS

Adriano Sciacovelli
Politecnico di Torino, Dipartimento Energia, c.so Duca degli Abruzzi 24, Torino, Italy,
adriano.sciacovelli@polito.it

Vittorio Verda
Politecnico di Torino, Dipartimento Energia, c.so Duca degli Abruzzi 24, Torino, Italy,
vittorio.verda@polito.it

ABSTRACT

In this paper entropy generation analysis is used as a design tool to perform a pseudo-optimization of a shell-and-tube latent heat thermal energy storage (LHTES) system. An initial configuration is gradually varied by introducing design modifications with the aim of improving the performance of the system. The different configurations are investigated by means of a CFD code that adopts the enthalpy method to take in account of the phase change phenomenon in the system. Unsteady-state numerical simulations are performed to characterize the thermal behaviour of the system and to evaluate the various contributions of the entropy generation rate. The design improvements are introduced on the basis of a careful examination of the local entropy generation rate distribution. Results show that an unconventional fins arrangement allows to reduce the solidification time and increase system efficiency.

Key Words: *Second Law, Thermal Storage, Phase Change, Performance Enhancement.*

1. INTRODUCTION

Thermal energy storage is of great importance to various engineering fields and renewable energy systems. It limits the mismatch between energy demand the energy supply that affects various kinds of energy systems. Latent heat thermal energy storage (LHTES) is one of the most effective ways to store thermal energy. It involves heating or cooling a phase change material (PCM) across its melting temperature. In such a way PCM absorbs (or release when cooled) its latent heat of fusion, thus storing energy. LHTES systems allow one to achieve large energy storage density and are able to store heat at nearly constant temperature. On the other hand, low thermal conductivity of PCMs should be overcame to achieve good performance. The goal of this paper is to improve a shell-and-tube LHTES system through the entropy generation analysis. The investigation is carried out by means of a CFD model. Fin arrangement is arrangement is modified according to results of the entropy generation analysis. The results indicate that the improved system brings a reduction of PCM solidification and an increase of Second-law efficiency.

2. SYSTEM DESCRIPTION AND MODEL

Figure 1.left illustrates the shell-and-tube LHTES system considered in this paper. Water flows through the inner pipe and acts as heat transfer fluid (HTF). The PCM is placed in the gap between the outer shell and the HTF pipe. The HTF pipe has a diameter of 16 mm while diameter of the shell is 100 mm. The discharge process, i.e. PCM solidification is here considered. Initially, the PCM is liquid while water inlet temperature (20°C) is below PCM melting temperature. Thus, heat transfer is established between the HTF and the phase change material. The heat transfer process persists until PCM is completely solid and the energy stored in the unit is retrieved. In this work

various fin designs are considered to enhance the heat transfer between the PCM and the HTF. The governing equations adopted here for the PCM are [1]:

Continuity:

$$\frac{\partial \rho}{\partial t} + \nabla \cdot \mathbf{v} = 0 \tag{1}$$

Momentum:

$$\rho \frac{\partial \mathbf{v}}{\partial t} + \rho(\mathbf{v} \cdot \nabla)\mathbf{v} = -\nabla p + \mu \nabla^2 \mathbf{v} + \rho \mathbf{g} \beta (T - T_0) + \frac{(1+\gamma)^2}{\gamma^3 + \varepsilon} A_{\text{mushy}} \mathbf{v} \tag{2}$$

Energy:

$$\frac{\partial}{\partial t}(\rho h) + \nabla \cdot (\rho \mathbf{v} h) = \nabla \cdot (k \nabla T) \tag{3}$$

where **v** is the velocity vector of the liquid PCM, p is the pressure and μ is the viscosity. Boussinesq approximation is used to model natural convection in the liquid PCM. A paraffin wax produced by SER S.p.A. was considered as PCM. The enthalpy method [1] is used to deal with the phase change problem and solid-liquid presence is tracked through liquid fraction γ. The modelling was conducted using the finite-volume code Fluent.

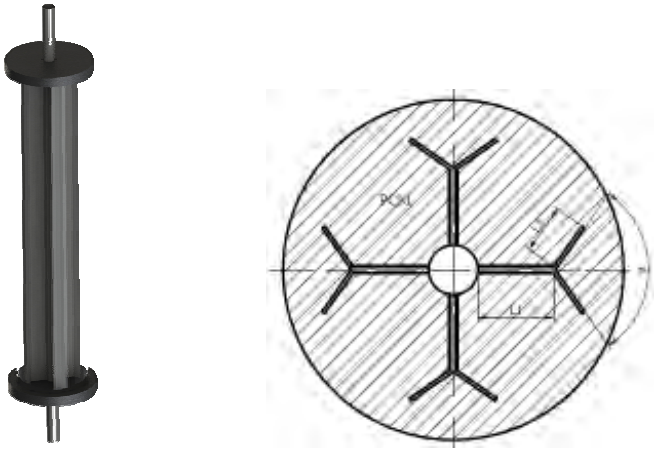

FIGURE 1. Left) LHTES unit. Right) A possible fin design.

Entropy generation analysis is here adopted to point out possible design improvements of the LHTES unit. The local entropy generation *rate* is evaluated as follows [2]:

$$\dot{s}_{gen} = -\frac{\Delta : \boldsymbol{\tau}}{T} + \frac{k(\nabla T)^2}{T^2} \tag{4}$$

Based on Eq. (4) a novel approach to entropy generation analysis is proposed in this work. The *local entropy generation over time span* [0 t_1]

$$s_{gen} = \int_0^{t_1} \dot{s}_{gen} dt \tag{5}$$

is investigated to introduce design changes. This approach is more suitable for systems that operates under transient conditions, such as the LHTES unit here analysed. Figure 1.right illustrates a possible fin design and the design parameters allowed to vary. That is, the length of main and secondary branch and the angle θ. In order to consider comparable cases the total volume occupied by the fins was considered constant for all the designs.

3. RESULTS

The first design consists in a LHTES unit with radial fins. Figure 2.left depicts the liquid fraction contour along two orthogonal planes for t = 1500 s. It can be noted that solidification begins along the solid walls, i.e. HTF pipe and the fins. A larger amount of solid PCM is found in the bottom part of the system. This is due to the natural convection that occurs in the liquid PCM. Heat transfer is enhanced by the radial fins. In fact most of the solidification front is aligned with the solid surfaces. However, most of the PCM is liquid in the zone between fins. Figure2.right shows the local entropy generation over the time interval [0 1500s]. It can be noticed that thermodynamic irreversibilites are predominant in the proximity of the fins and HTF pipe. In such location of the system temperature gradient is particularly pronounced. Consequently, the second contribution of Eq. (4) is also significant through the entire solidification process. The opposite condition occurs in the zone between the two fins where thermodynamic irreversibilities are not significant. According to the results reported in Figure 2.right, geometry changes are more appropriate where s_{gen} is larger and in the region between two fins. The design should tend to make s_{gen} more homogeneous as possible, without necessarily minimize it [2].

In Figure 3 a possible design improvement is shown: Y-shaped fins are adopted to achieve a more uniform distribution of s_{gen} in the region between two fins. The design parameters that specify the Y-shaped fin are L_1 = 11 mm, L_2 = 22 mm and θ = 30°. Figure 3.right indicates that s_{gen} is more evenly distributed in the system. This leads to a significant enhancement of the heat transfer process. In fact Figure 3.left shows that a significant higher amount PCM is solid compared to the radial fins case. Figure 4 compares the global performance of Y-shaped fins and radial fins designs. Figure 4.left plots the liquid fraction time evolution. It can be observed that Y-shaped fins brings a reduction of solidification decreases of about 50% compared to radial fins. Furthermore, averaged time second law efficiency is higher of about 10% in the case of Y-shaped fins, despite the enhanced heat transfer process.

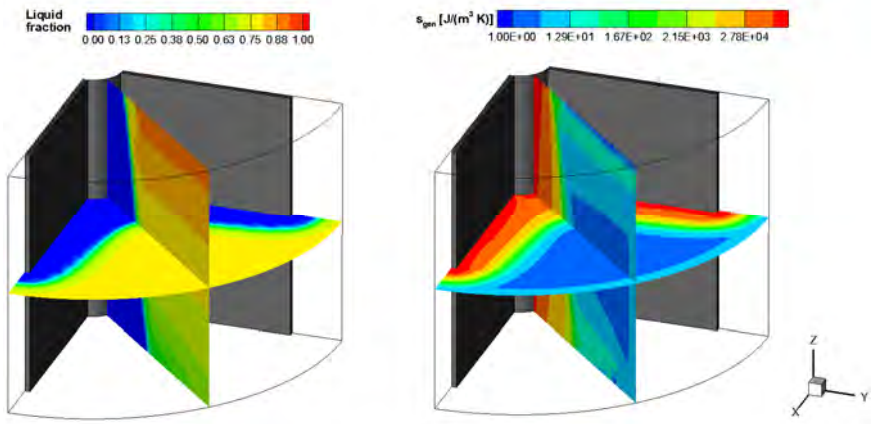

FIGURE 2. Radial fins. Left) Liquid fraction. Right) s_{gen}. t = 1500s.

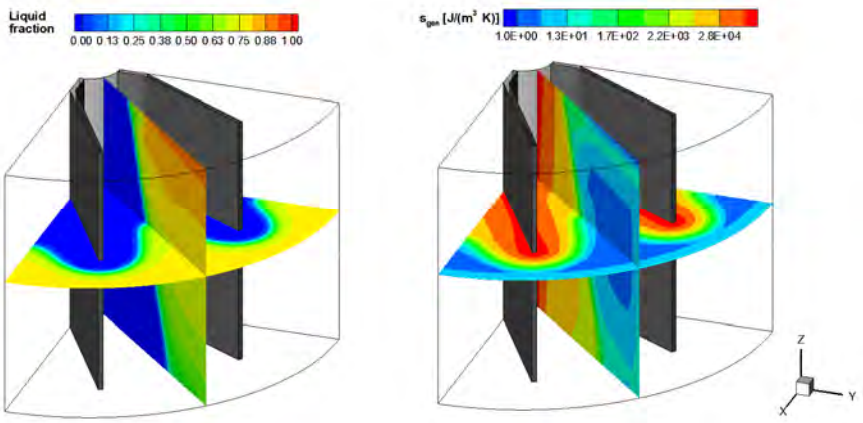

FIGURE 3. Y-shaped fins. Left) Liquid fraction. Right) s_{gen}. t = 1500s.

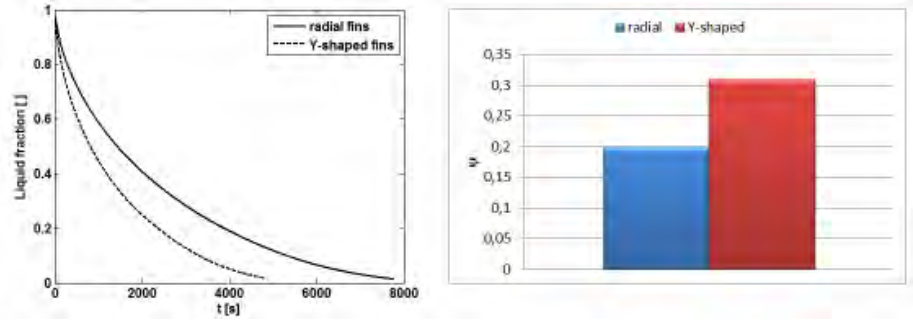

FIGURE 4. Left) Liquid fraction time evolution. Right) time-averaged second law efficiency.

4. CONCLUSIONS

In this paper entropy generation analysis used to perform a design improvement of a latent heat thermal energy storage unit with longitudinal fins. The analysis is carried out by means of a CFD models that implements the enthalpy method to deal with the phase change problem. The distribution of cumulative entropy generation pointed out that geometry changes are appropriate in the PCM region between two fins. As a result, Y-shaped fins are proposed to improve the performance of the system. The results indicate that solidification time is reduced of 50%. Furthermore, second-law efficiency shows an increase of 10% compared to the radial fins configuration.

REFERENCES

[1] A.A. Al-abidi , S.B. Mat, K. Sopian, M.Y. Sulaiman, A.Th. Mohammed. CFD applications for latent heat thermal energy storage: a review, *Renewable and Sustainable Energy Reviews*, 20, 353–363, 2013.

[2] E. Guelpa, A. Sciacovelli, V. Verda. Entropy generation analysis for the design improvement of a latent heat storage system, *Energy*, 53, 128-138, 2013.

MINI-SYMPOSIUM

MODELLING & APPLICATIONS OF BIOHEAT & MASS TRANSFER

MINI-SYMPOSIUM ORGANISED BY P. NITHIARASU AND E. BOILEAU

Third International Conference on Computational Methods for Thermal Problems
THERMACOMP2014, June 2-4, 2014, Lake Bled, Slovenia
N. Massarotti, P. Nithiarasu and B. Sarler (Eds.)

Computational modeling of skin electroporation: reconciliation between experimental observations and anticipated physics

Sid Becker
University of Canterbury, Christchurch New Zealand sid.beckercanterbury.ac.nz
Barbara Zorec, Nataša Pavšelj, Damijan Miklavčič
University of Ljubljana, Ljubljana, Slovenia Natasa.Pavselj@fe.uni-lj.si

ABSTRACT

The subject of this study concerns modeling and treatment of mass transport associated with electroporation of the skin. When the skin is exposed to sufficient intense electric pulses, its outer barrier membrane may experience a breakdown in its barrier properties as evidenced in the local alteration of the microstructure of the *Stratum Corneum* lipds. Our experimental findings that indicate that when long moderate voltage pulses are preceded by short intense pulses, the total transport is less compared to the case when long moderate pulses are administered alone. This is in conflict with the general view held by the field: that more pulses result in more transport. We conduct a theoretical study to reconcile this apparent disagreement. We show that the type of pulse must be considered as well as the number of pulses. The computational study indicated that the conditions of the skin that are associated with high pulses prohibit the development of large regions of increased permeability if they are followed by long duration electric pulses.

Key Words: *Electroporation, Transdermal Transport, Thermodynamic, Electrophoresis, Diffusion*.

1. INTRODUCTION

The skin's outer barrier, the *Stratum Corneum* (SC), offers the greatest resistance to transport. Transdermal drug delivery methods focus on methods of overcoming this barrier function of the SC. By exposing the skin to electroporation pulses, the SC experiences a structural alteration that results in order of magnitude increases in molecular diffusivity, electrophoretic mobility, and electrical conductivity. It has been shown that these structural alterations are highly localized in sites termed "local transport regions" (LTRs) [1]. The expert opinions in the field are in general agreement that there are to two primary pulsing regimes: (1) that short duration-high intensity pulses (HV) result in a non thermal alteration of the SC that is characterized by nm sized aqueous "pores", and (2) that long duration medium intensity pulses (LV) result thermally initiated regions of increased permeability within the SC that are relatively large (up to hundreds of μm) but that occur at a much lower density (number of pores per lateral SC surface area) than the HV electropores [1, 2]. A generally held view in the field of skin electroporation is that the skin's drop in resistance (to transport) is proportional to the number of pulses administered. However recently the authors have conducted experimental electroporation tests whose results are not in agreement with the general belief held by the field [3].

2. Unanticipated Experimental Observation

The experimental component of this paper follows an identical methodology to that reported by this group in [3]. The resulting experimental data depicted in Fig. 1 shows the total concentration of calcein in the receiver solution for 5 hours of passive diffusion after pulse delivery. We found that

HV pulses have a negative effect on transport compared to LV pulses alone (see Figure 1). Thhis result disagrees to the anticipated physics which would result in a two step process: 1) the short, HV pulses result in the creation of small cell-level permeation pathways through the SC and then 2) that by following the HV pulses with the LV pulses, these pathways would evolve into the much larger LTRs. The transport data indicate that the anticipated physics are not correct. Its is the motivation of the computational component of this study: to try to reconcile the experimental results with the generally accepted belief that more pulses equal greater drops in the resistance to transport.

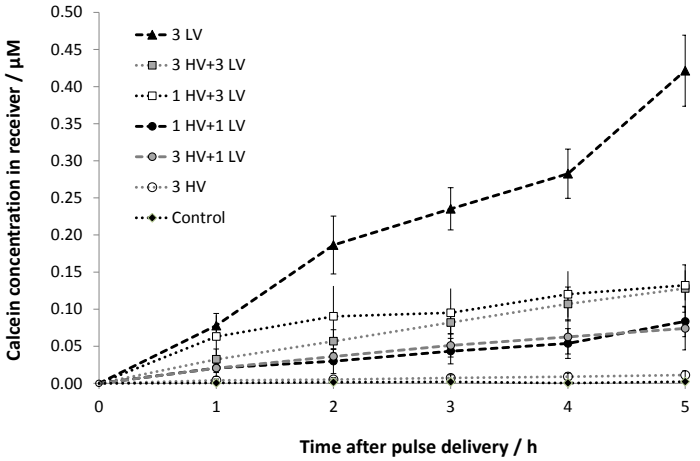

Figure 1: Comparison of different combinations of HV and LV pulses and their effect on calcein concentration in the receiver solution for 5 hours of passive diffusion after pulse delivery.

3. Theoretical Model

A computational finite volume model previously developed and detailed in reference [4] was implemented to predict the thermo-electrical behavior in a small region of radius R_o that centered directly about an evolving LTR that is expanding about a small SC defect of size R_P. The domain is modeled as a composite system with layers: donor solution, electrode, SC, epidermis or dermis, and receiver solution.

Briefly the physics of the model (the details of which are explained at length in Reference [4]) couple the equations governing the heat transfer, the electric field, and the conservation of specied in the mass transport. The LTR is a consequence of the SC lipids thermal reorganization in response to the temperature rise associated with resistive Joule heating during the applied pulse. To capture the sudden temperature rise, the transient heat equation is used to describe the transient distribution of thermal energy within each layer of the skin. The localized resistive heating that occurs during the applied electric pulse and contributes to the thermal alterations of the SC microstructure is included in the heat equation as a source term and is most prominent in the strong variation in electrical conductivity within the SC just about the evolving LTR. Transport is derived from the modified transient Nernst-Planck equation which describes the transport of a charged solute in the presence of an electric field.

The evolving LTR, from a mass transport perspective, represents a region within the SC where the electrical conductivity, electrophoretic mobility, and diffusion coefficient are orders of magnitude

higher than in the surrounding SC. To link the thermal model to the alteration of the SC lipids that exist within the SC's LTR, a parameter called the lipid melt fraction is introduced. It represents the ratio of heat added to the SC lipids (above phase transition temperatures) to the total heat required to complete a full transition of the SC lipd structure:

$$\varphi = \left(H(T) - c_{SC}T\right)/\Delta H \tag{1}$$

where ΔH is the latent heat associated with the phase transition, and $H(T)$ is total enthalpy. The melt fraction is description of the state of the lipids within the developing LTR. Using a linear dependence on melt fraction, the increase in SC the transport coefficients and electrical conductivity may be represented:

$$\begin{aligned} m_{SC} &= m_{SC-U} + \varphi\left(m_{SC-M} - m_{SC-U}\right) \\ D_{SC} &= D_{SC-U} + \varphi\left(D_{SC-M} - D_{SC-U}\right) \\ \sigma_{SC} &= \sigma_{SC,U} + \varphi\left(\sigma_{SC,M} - \sigma_{SC,U}\right) \end{aligned} \tag{2}$$

where the subscripts $SC-U$ are the property values associated with the unaltered lipid structure and those with $SC-M$ are associated with the SC after full lipid melting . The conductivity values and transport coefficients have been chosen as suggested by reference [3].

3. RESULTS

In this section, we use the results of the computational model to answer the question:

"Why does preceding a long duration, low voltage electroporation pulse with a short duration high intensity pulse result in much less transport than when the skin is exposed to a low intensity pulse by itself?"

The answer is that HV pulses result in an SC with a very high density of very small regions of high electrical conductivity. These influence the thermo-electrical behavior of the skin during an LV pulse. We first consider that the pore formations created by the HV pulse result in a small region of higher electrical conductivity. These may be represented by a pre-existing pore of radius R_p. The pre-existing pore size strongly influences the electrical distribution that is evaluated from the Laplace equation near the LTR centre which in turn is reflected in the Joule heat that is seen in the heat equation. Figure 2 shows a prediction in much smaller LTR's (represented by R^+) when the pre-existing defect region is small.

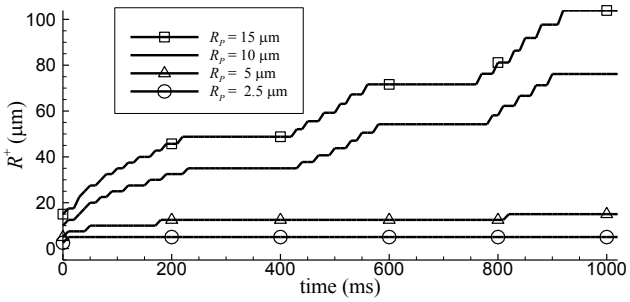

Figure 2: Influence of pre-existing pore size on the LTR evolution.

Next we consider that HV electroporation pulses result in more pores per cm^2 occurring across the lateral surface of the SC. To investigate the effect of pore density, we consider varying the radial size of the computational domain, R_O. Figure 3 shows that the LTR evolution during the LV pulse is strongly affected by the outer computational domain radius (which is related to the inverse of the density distribution. The physical explanation of this phenomenon lies in the consideration of the electric field. When the pore density is increased, for a given global domain, the global distribution of electric current is distributed among more pre-existing pores. This is likely to result in a lower electric current within each pore (and thus less heating).

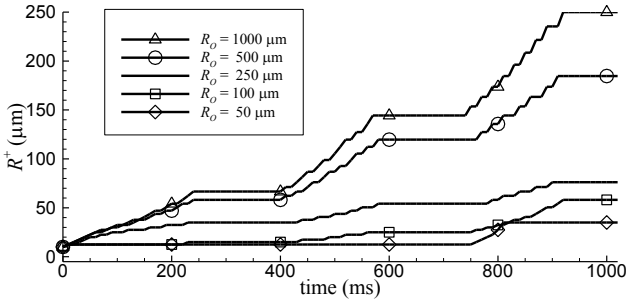

Figure 3: Influence of pore density on the LTR evolution.

4. CONCLUSIONS

Experimental measurements of calcein delivery through dermatomed skin have shown that the total transport is not simply directly related to the total number of applied pulses. A computational study using a thermodynamically based theoretical description of the skin's response to an electric field concludes that *any* influence that acts to increase the density distribution of SC regions of higher electrical conductivity or that acts to decrease the continuous local area of higher electrical conductivity will result in the evolution of smaller LTR's and greatly reduced transdermal drug delivery. Because the application of the high voltage pulses has been shown to encourage both of these and because the LTR is associated with a higher permeability to mass transport, transport is inhibited when LV pulses are preceded by HV pulses. This discounts the unsubstantiated generalizations that blindly relate total pulse energy to total solute transport.

ACKNOWLEDGEMENT

Research was supported by the Marsden Fund Council from Government funding administered by the Royal Society of New Zealand.

REFERENCES

[1] Pliquett U, Gusbeth C. Surface area involved in transdermal transport of charged species due to skin electroporation. Bioelectrochemistry. 2004 Dec;65(1):27–32.

[2] A.R Denet., R Vanbever., V Preat., Skin electroporation for transdermal and topical delivery, *Advanced Drug Delivery Reviews*, 56 659-674, 2004.

[3] B. Zorec, S. Becker, M.Reberšek, D.Miklavčič, N.Pavšelj Skin electroporation for transdermal drug delivery: the influence of the order of different square wave electric pulses, *International Journal of Pharmaceutics*, 457(1), 214-23, 2013

[4] S. Becker, Transport modeling of skin electroporation and the thermal behavior of the stratum corneum, *International Journal of Thermal Sciences*. 54 48–61, 2012.

Third International Conference on Computational Methods for Thermal Problems
THERMACOMP2014, June 2-4, 2014, Lake Bled, Slovenia
N. Massarotti, P. Nithiarasu and B. Sarler (Eds.)

ARTERIAL TRANSPORT AND WALL DYNAMICS

Etienne Boileau, Perumal Nithiarasu
Civil and Computational Engineering Centre, College of Engineering
Swansea University, Swansea, SA2 8PP, UK

ABSTRACT

Transport of chemical species is modelled in anatomical geometries, with the aim of integrating large and small scale phenomena within an image-based computational domain. To provide a better understanding of the mechanisms that underlie blood flow regulation, we consider the effects of direct, wall shear stress (WSS)-mediated, and indirect receptor-ligand interactions in a generic transport model, and the coupling with models for arterial wall dynamics.

Key Words: Mass transfer, wall-shear stress, endothelium, arterial disease.

1. INTRODUCTION

In recent years, an increasing number of computational studies have dealt with mass transfer in anatomical geometries, with the aim of correlating disturbed flow patterns and the onset of arterial disease. Our understanding of the impact of transport on flow control mechanisms rely on realistic hæmodynamics of blood flow and chemical species, but also on an accurate characterisation of the biomechanical and biochemical processes involved. We present herein a first attempt to integrate large and small scale phenomena within an image-based computational domain, to provide a better understanding of the processes involved in the pathways to endothelial dysfunction.

Healthy vessels are characterised by an ability to adapt to the conditions imposed by the local environment, and respond to changes in blood flow by dilating or contracting. The progressive impairment of this dilator function is known as endothelial dysfunction, and it has been shown to predict long-term development of arterial disease. Although smooth muscles are responsible for vascular tone and contractile phenomena, the endothelium act as an active interface between the lumen and the inner layers of the blood vessel wall.

The endothelium consists of a single layer of cells that cover the inner surface of blood vessels. In addition to providing a non-thrombogenic surface and a semi-selective barrier between the lumen and the surrounding tissue, it plays a critical role in the local regulation of blood flow. In the surface boundary layer, blood flow affects cellular responses by modifying the interactions between blood-borne agonists and endothelial receptors, and these signal transduction pathways can be altered by mass transport phenomena and reaction kinetics.

At a smaller scale, arterial contractions are dependent on cellular ionic transport mechanisms. A number of mathematical models have been proposed to described smooth muscle dynamics, inter-cellular communication and ion wave propagation. We propose to use some of these models, in combination with our previously developed models, as a first attempt in describing the interactions between the blood flow, the endothelium and the arterial wall.

2. METHODS

The release of the nucleotide adenosine-5' triphosphate (ATP) by endothelial cells, via WSS-dependent mechanisms, is thought to play an important role in endothelium-mediated vasodilation. Its influence on regional blood flow is also seen through the effects of its end-products, such as adenosine diphosphate (ADP). Plasma concentrations of ATP and ADP are obtained by successively solving the conservation of species equation:

$$\frac{\partial[n]}{\partial t} + (\mathbf{u} \cdot \nabla)[n] = D_n \nabla^2 [n]$$

where D_n is the corresponding diffusion coefficient for n = ATP, ADP. The Reynolds number is relatively small, in comparison with a very large Peclet number, of the order of 10^6, based on D_{ATP}. Mass transport is highly convection dominated, and variations of the concentration field near the boundary impose severe restrictions either on the spatial discretisation or on the accuracy of the computational method.

Rates of heterogeneous biochemical reactions such as receptor desensitisation during cellular transduction or enzyme catalysed reactions are often almost linear for relatively small concentration of substrate, but levels out as the concentration increases. This phenomenon is usually represented by a Hill-type equation, following Michaelis-Menten kinetics. The reaction rate is approximately 1st order, and the reactive surface boundary condition, representing the hydrolysis of ATP/ADP and ATP-derived ADP at the endothelium, is expressed as:

$$D_n \frac{\partial[n]}{\partial \mathbf{n}} = \frac{V_{max,n}[n]}{K_n} - S_n \qquad S_{ADP} = \frac{V_{max,ATP}[ATP]}{K_{ATP}}$$

where n is the vector normal to the arterial wall, $V_{max,n}$ is the maximum enzyme reaction velocity and K_n is the Michaelis-Menten constant for species n. Flow-mediated ATP release is included as a separate source term S_{ATP} , which depends on WSS and/or time. The boundary condition for ADP is determined by substituting the term corresponding to S_{ADP}.

3. RESULTS

We investigate the dependence of the surface concentration of nucleotides (especially ATP) on the instantaneous WSS, the rate of mass transfer, both spatially and temporally, as represented by the Sherwood number, and the influence of geometry. Lumenal and surface concentration of species are obtained for different patient-specific geometries (see Figure 1). Production and degradation at the endothelium is affected by numerous flow features.

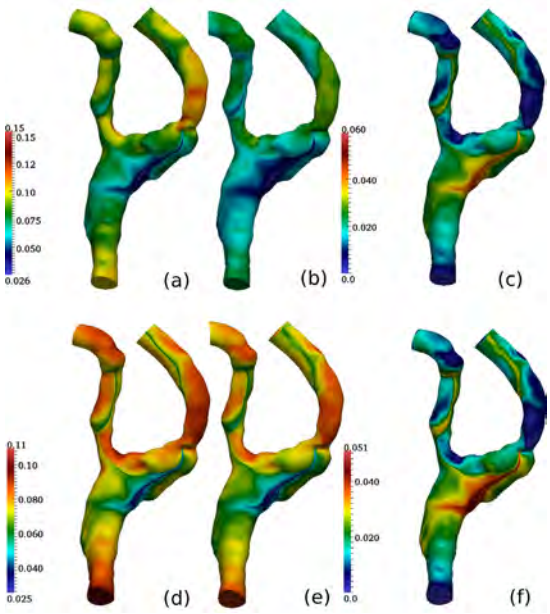

Figure 1. Upper row: distribution on one arterial surface of [ATP] (μM) during (a) systole and (b) diastole and [ADP] (μM) during (c) diastole. Lower row: distribution on the arterial surface of [ATP] (μM) using a different source term, during (d) systole and (e) diastole and [ADP] (μM) during (f) diastole. For each time instant, the scale covers the maximum concentration range obtained with the model.

Preliminary results of an integrated strategy, and further manifestations of blood-wall and arterial dynamics coupling will be investigated, through computational manipulation of a number of potential mechanisms underlying flow-endothelium interactions. Such mechanisms potentially include WSS, which can modulate responses in smooth muscles cells indirectly, via mass transfer of agonist and receptor-ligand interactions, and directly through WSS operated channels. In this context, ATP and its products derived from hydrolysis will be considered. Concentration of ATP (and its derived products) will be related to arterial wall dynamics via a catalytic term, through one or more of the mechanisms known to influence wall dynamics.

REFERENCES

[1] J.P.J. Halcox, A.E. Donald, E. Ellins, D.R. Witte, M.J. Shipley, E.J. Brunner, M.G. Marmot, J.E. Deanfield, Endothelial function predicts progression of carotid intima-media thickness,Circ., 119, 1005-12, 2009.

[2] C.R. Ethier, Computational modeling of mass transfer and links to atherosclerosis, AnnalsBiomed. Eng., 30, 461-471, 2002.

[3] K. Perktold, M. Prosi, P. Zunino, Mathematical models of mass transfer in the vascular walls, in L. Formaggia, A. Quarteroni, A. Veneziani (Eds.) Cardiovascular Mathematics. Modeling and simulation of the circulatory system., Vol. 1, Springer-Verlag, 2009.

[4] A.W. Lohman, M. Billaud, B.E. Isakson, Mechanisms of ATP release and signalling in the blood vessel wall, Cardiovasc. Res., 95, 269-80, 2012.

[5] E. Boileau, R.L.T. Bevan, I. Sazonov, M.I. Rees, P. Nithiarasu, Flow-induced ATP release in a patient-specific arterial geometries – a comparative study of computational models, Int. J. Numer. Meth. Biomed. Engng., 2013.

[6] Parthimos D, Haddock RE, Hill CE and Griffith TM. Dynamics of a three-variable nonlinear model of vasomotion: comparison of theory and experiments. Biophys. J. 2007; 93:1534-1556.

.

Third International Conference on Computational Methods for Thermal Problems
THERMACOMP2014, June 2-4, 2014, Lake Bled, Slovenia
N. Massarotti, P. Nithiarasu and B. Sarler (Eds.)

A THREE-DIMENSIONAL GEOMETRIC MONTE-CARLO METHOD FOR THE SIMULATION OF LIGHT PROPAGATION IN BIO-TISSUE

Yong Zhang, Bin Chen*, Dong Li
State Key Laboratory of Multiphase Flow in Power Engineering, Xi'an Jiaotong University, Xi'an, Shaanxi, 710049, China, Email: chenbin@mail.xjtu.edu.cn

Guo-Xiang Wang
Department of Mechanical Engineering, The University of Akron, Akron, Ohio, 44325-3903, USA

E-mail: gwang@uakron.edu

ABSTRACT

A geometric Monte-Carlo (GMC) algorithm is proposed based on accurate calculation of optical transmission on the material interface for the simulation of light propagation in turbid media (e.g. bio-tissue). Grid is not necessary for the computation of photons' motion and the memory of optical parameters can be saved. Optical transmission is exactly simulated at material interfaces with curved boundary according to the principles of geometric optics, while energy deposition in different structures can be precisely counted. The validity of GMC method is confirmed by the comparison with voxels based Monte-Carlo method. Time consumed by GMC method is dramatically shortened compared with the hexahedral voxels based Monte-Carlo (VMC) method: about 25 times faster than VMC with a grid of 140×140×100 cells. In addition, the present GMC method shows better portability when raising the geometric complexity.

Key Words: *geometric Monte-Carlo* algorithm*, light propagation, bio-tissue, geometric optics*

1. INTRODUCTION

In order to improve the efficiency of laser treatment, it's important to reveal the mechanism of laser-tissue interaction. Numerical simualtion is a powerful tool, among which Monte Carlo method has been widely adopted for the light (laser) propagation in bio-tissue. Wang et al [1] introduced a Multi-Layered Monte Carlo (MCML) algorithm for the tissue slab with homogeneous layers parallel to each other. Pfefer et al [2] developed a voxels based Monte-Carlo (VMC) method and demonstrated its ability in the simulation for light propagation in multi-layered tissue slab with embedded blood vessels. However, one of the major problems of the VMC is that it is difficult to incorporate precise boundary information, which will introduce significant errors. Moreover, VMC method is extremely time consuming because the photon motion need to be calculated in each voxel, which becomes another apparent bottleneck for the application of VMC method.

In this paper, we propose a geometric MC (GMC) method to overcome the drawbacks of VMC mentioned above. We not only testify the validity and accuracy of GMC method but also extend its application to some more complicated skin geometric structures, such as vascular cluster of multi-homoaxial vessels, single vessel with an optional trend and two bridge intersection vessels.

2. MODEL OF LIGHT PROPAGATION BY GMC METHOD

The general Monte Carlo procedure[1, 2] includes launching, hopping, interface calculation, dropping and spining, which is designed for a tissue model illustrated in Figure 1. A normal incidence photon will randomly shift before being reflected or refracted by interfaces, or scattered, as shown in Figure 2. The major difference of GMC lies in the process of interface calculation, which will be shown below.

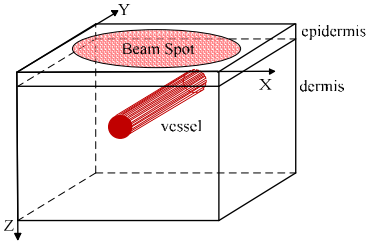

FIGURE 1. Simplified skin model

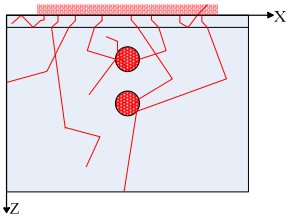

FIGURE 2. Schematic of photon's random motion

Let $\mathbf{r}=(x,y,z)$, $\boldsymbol{\mu}=(\mu_x,\mu_y,\mu_z)$, which represent the photon's current location and the directional cosines, respectively. Then its new location after a pretend step s is:

$$\mathbf{r}_1=\mathbf{r}+\boldsymbol{\mu}\cdot s \tag{1}$$

In the GMC method, we should firstly check whether the photon's location before and after a pretend step is in different tissue structures or not, which will not be difficult because all the boundaries have been mathematically depicted. With this check, it will be determined that whether a photon will cross the material boundaries and then move along the path from the current location to the intersection on the interface, where reflection or refraction will happen, or the end of the pretend step. So interface calculations include: 1) path length (d); 2) propagation behaviors of reflection and refraction on the interfaces.

1) There are two situations for the calculation of path length (d): plane boundaries and curved boundaries. For the former, $d=\min(D_1/|\mu_z|, D_2/|\mu_y|, D_3/|\mu_x|)$, where D_1, D_2, D_3 are the distances from photon's current location to the three potential faces that the photon might cross respectively. For the latter, it is convenient to conduct a projection on xoz plane for calculation. Assuming that points A and B are the projections of the photon's current location and the impact point if the photon cross the boundary from the outside to inside (oi), A_1 and B_1, on the contrary (io), as shown in Figure 3(a), then

$$\begin{cases} d_{oi}=\left(\sqrt{\mathrm{OA}^2-\mathrm{OC}^2}-\sqrt{r^2-\mathrm{OC}^2}\right)\Big/\sqrt{1-\mu_y^{\,2}} \\ d_{io}=\min(d_c, D/|\mu_y|), d_c=\left(\sqrt{r^2-\mathrm{OC}_1^{\,2}}-\mathrm{sign}(\mathbf{OA_1}\cdot\mathbf{A_1B_1})\sqrt{\mathrm{OA}_1^{\,2}-\mathrm{OC}_1^{\,2}}\right)\Big/\sqrt{1-\mu_y^{\,2}} \end{cases} \tag{2}$$

where D is the distance from photon's current location to the undersurface of the cylindrical vessel, OC and OC_1 are the distances from point O to lines ABC and $A_1C_1B_1$ respectively.

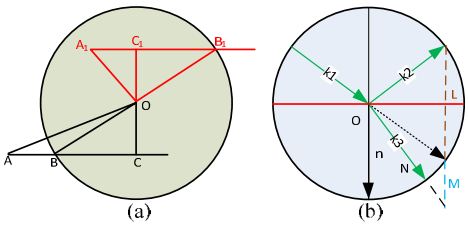

FIGURE 3. Diagrams for interface alculation

2) A common approach for describing the propagation behaviors on the interfaces is introduced below. As shown in Figure 3(b), **k1**, **k2**, **k3** and **n** are normalized vectors of incidence, reflection, refraction and normal, respectively. L, M, N separately denotes the length of the segments they mark. Then we can decuce that

$$\mathbf{k2} = \mathbf{k1} - \mathrm{L} \cdot \mathbf{n},\ \mathrm{N} \cdot \mathbf{k3} = \mathbf{k1} + \mathrm{M} \cdot \mathbf{n} \tag{3}$$

where $\mathbf{k1} = \boldsymbol{\mu}$, and $\mathbf{n}$ is normal to the local interface. $\mathrm{L} = 2\cos\theta_i$, $\mathrm{N} = \sin\theta_i / \sin\theta_t$, $\mathrm{M} = \sin\theta_i / \tan\theta_t - \sin\theta_i / \tan\theta_i$ where θ_i, θ_t denote the angles that $\mathbf{k1}, \mathbf{k3}$ make to $\mathbf{n}$ respectively.

3. RESULTS

Skin model in Figure 2 is used to validate the GMC algorithm. As shown in Figure 4, our result agrees very well with that of the Pfefer et al [2]. We also compare the efficiency of GMC and VMC methods for the identical problems with different vessels number. As shown in Fig. 5, time consumed by GMC method is dramatically shortened: about 25 times faster than VMC for the single vessel case. When increasing the number of blood vessels, there is a slightly and restrictively rise of computing time by GMC method. But apparently, it's still much lower than that of VMC.

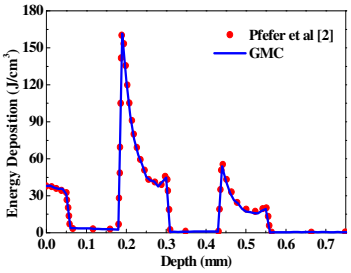

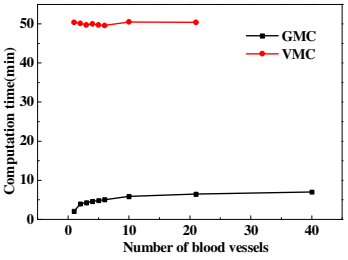

FIGURE 4. Comparision between GMC and VMC FIGURE 5. Computation time vs number of blood vessels

Afterwards, the present GMC method was adopted to simulate light propagation in some more complicated skin geometric structures. Assuming that the volume fraction of blood vessels is 5%, we calculate the energy deposition under different vessels number. It can be found that the largest amplitude of energy deposition in vessels is 9% (with 3 vessels) and it will decrease (to 4% with 20 vessels) with the increase of vessels number.

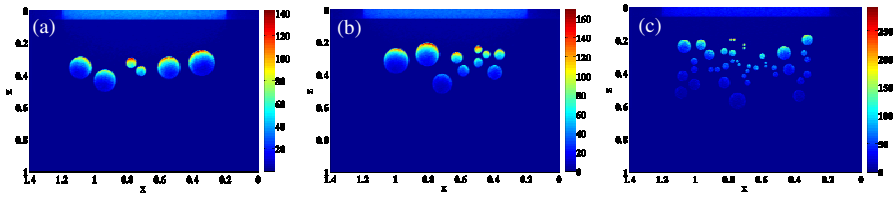

FIGURE 6. Energy depositon on center plane with (a) 6, (b)10 and (c) 40 random vessels

Furthermore, we develop a GMC method based on coordinate rotation (CR-GMC) for cases in which a vessel is positioned with arbitrary angle rather than parallel to skin surface in all the cases above. By rotating the coordinates, a mapping relationship between the arbitraily placed vessel and the one parallel to skin surface in Figure 1 can be set up through

$$\mathbf{r}_2 = \mathbf{rotate} \cdot \mathbf{r}_1 \tag{4}$$

where **rotate** is the rotation matrix, $\mathbf{r}_1$ and $\mathbf{r}_2$ are the photon's position vectors before and after ratation. To illustrate the convenience of CR-GMC, we demonstrate another two cases: 1) a 0.8 mm long cylindrical vessel rotates on a plane parallel to *xoz*; 2) a superficial vessel (1.4 mm long) is parallel to *y* axis and a deep one (1.4 mm long) rotates on a plane parallel to *xoy*. As can be seen

from Figure 7, the position of the vessel in a turbid medium with a high scattering coefficient mainly affects the energy distribution instead of energy deposition. In addition, for the two bridge intersection vessels in case 2, no matter the superficial vessel is a totally geometric shelter or not, the shading effect on the deep vessel will definitely occur, as shown in Figure 7 (b).

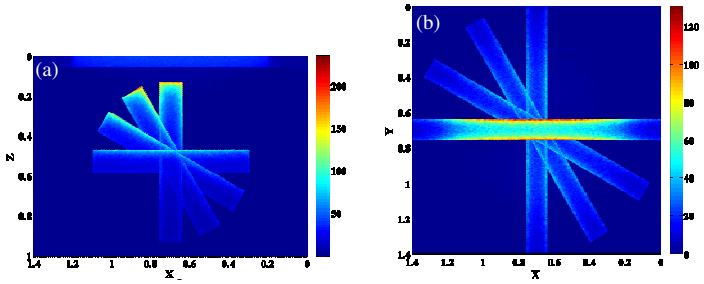

FIGURE 7. Energy depositon on the vessels' centeral planes: (a) parallel to *xoz*, (b) parallel to *xoy*

4. CONCLUSIONS

Geometric Monte-Carlo (GMC) method has been proved to be an effective approach for the general simulation of light propagation in bio-tissue. Compared with the traditional voxels based Monte-Carlo (VMC) method, GMC is not only physically credible in the calculation of energy deposition and photon transport on the interfaces, but also efficient for computing photon's motion process. Each coin has two sides, so does the GMC method. GMC is accurate and high-efficiency for the common problems, while its flexibility for a realistic situation is still far from satisfaction. But we have already extended the application of GMC method to situations of vascular cluster of multi-homoaxial vessels, single vessel with an optional trend and two bridge intersection vessels, and have gained a few useful conclusions. In general, for the simulation of light propagation in tissue models that can be simplified as the ones GMC can handle, GMC should be the first choice.

In the future, the GMC method would be implemented in the simulation of the energy deposition during laser treatment of cutaneous vascular lesions such as port wine stains. Based on the simulation result, the optimal treatment parameters would be examined. The new treatment wavelength and clinic protocol would be explored for the better clinic clearance of the vascular lesions as well.

ACKNOWLEDGMENTS

The work is supported by Joint Research Fund for National Natural Science Foundation of China (51336006, 51228602), the International Science & Technology Cooperation Plan of Shanxi Province (No. 2013KW30-05) and the Fundamental Research Funds for the Central University.

REFERENCES

[1] Wang L H, Jacques S L, and Zheng L Q. MCML – Monte Carlo modeling of photon transport in multi-layered tissues.*Computer Methods Programs Biomed*, 47:131–146, 1995.

[2] Pfefer T J, Kehlet Barton J, Chan E K, et al. A three-dimensional modular adaptable grid numerical model for light propagation during laser irradiation of skin tissue[J]. *Selected Topics in Quantum Electronics*, 2(4): 934-942, 1996.

Third International Conference on Computational Methods for Thermal Problems
THERMACOMP2014, June 2-4, 2014, Lake Bled, Slovenia
N. Massarotti, P. Nithiarasu and B. Sarler (Eds.)

THEORETICAL INVESTIGATION ON THERMAL RESPONSES OF BLOOD VESSELS TO 595NM AND 1064NM LASER

Dong Li, Bin Chen*, WenJuan Wu, YaLing He
State Key Laboratory of Multiphase Flow in Power Engineering, Xi'an Jiaotong University, Xi'an, Shaanxi, 710049, China, E-mail: chenbin@mail.xjtu.edu.cn

Guo-Xiang Wang
Department of Mechanical Engineering, University of Akron, Akron, Ohio 44325-3903, USA,

E-mail: gwang@uakron.edu

ABSTRACT

As a kind of congenital vascular malformations, port wine stain is composed of ectatic venular capillary blood vessels buried within healthy dermis. In clinic, pulsed dye laser in visible band (e.g. 595nm) together with cryogen spray cooling have become the golden standard for treatment of PWS. However, due to the limited energy deposition of the PDL in blood, large blood vessels are likely to survive from the laser irradiation and complete clearance of the lesions is rarely achieved. Nd:YAG laser in near infrared 1064nm has deeper penetration depth in tissue, which has great potential in laser treatment of PWS. In this study, a multi-component bio-heat transfer model is developed to demonstrate the blood vessel thermal responses to two lasers. The results show that large and deeply buried blood vessels, which are likely to survive from 595nm laser irradiation, can be coagulated by 1064 nm laser. Meanwhile, the heating patterns within the vessel lumen for two lasers are also different. The 595 nm laser heated the superior portions of large blood vessels more than the inferior portions, while the 1064 nm laser produced uniform heating.

Key Words: *Port wine stain; Pulsed dye laser; Nd:YAG laser; Multi-component bio-heat transfer model*

1. INTRODUCTION

Port wine stains (PWS) are congenital vascular birthmarks that occur in approximately 0.3% of children. The selective photothermolysis theory of Anderson and Parrish [1] provides a basic principle for selection of the wavelength in laser treatment of PWS. Pulsed dye lasers (PDL) of 595 nm together with cryogen spray cooling (CSC) are now served as golden standard for treatment of PWS. CSC can protect the epidermis from unwanted thermal injury by energy absorption of melanin with cold cryogen spray prior to laser irradiation. However, clinical studies have shown that completely clearing of the vascular lesions is less than 20% [2]. The possible reasons for the limited therapeutic outcomes are the limited light penetration depth in large-sized or deeply extended blood vessels [3]. Near-infrared wavelengths penetrate deeper into skin tissue than visible wavelengths. Therefore, laser irradiation using near-infrared wavelengths may be promising to treat resistant blood vessels. In this paper, discrete blood vessels with various diameters are embedded into a two-layer skin model (epidermis and dermis) to simulate the thermal response of PWS during laser treatment by a multi-component bio-heat transfer model. Typical PDL with 595 nm and near-infrared Nd:YAG laser with 1064 nm are used to compare the coagulation depth in tissue and the large blood vessels lumen. Some suggestions will be given for the treatment of PWS containing large or deeply-buried blood vessels and the selection of treatment end-point for two lasers.

2. PHYSICAL MODEL AND MATHEMATICAL DESCRIPTION

The skin tissue containing PWS is assumed to be a two-layered geometry, consisting of the epidermal layer and the dermal layer of 60 and 940μm thickness, respectively. The irregular distributed PWS blood vessels are simplified as parallel distributed cylindrical tubes in dermis.

There are total 9 discrete blood vessels used in the skin model. Small blood vessels buried at tissue depth of 250μm with the diameter of 10, 30 and 50μm to represent the normal capillary, smallest PWS blood vessels and normal PWS blood vessels, respectively. Six larger target blood vessels with 120μm diameter buried in the skin tissue with the depth of 450 and 650 μm to represent large blood vessels which is typical resistant to PDL irradiation.

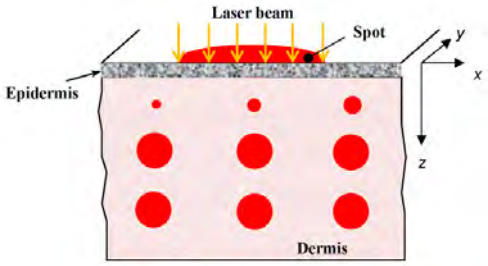

FIGURE 1. Two-layer skin model with 9 blood vessels

The heat transfer during pulsed laser heating and CSC within the skin model can be described by a multi-component bio-heat transfer model as below:

$$\rho_i c_i \frac{\partial T(x,z,t)}{\partial t} = k_i \nabla^2 T(x,z,t) + Q_i(x,z) \qquad \text{i = e, d, b} \tag{1}$$

where the subscript i (= e, d, or b) represents, the epidermis, the dermis or the blood vessels; ρ is the density, c_p is the specific heat, k is the thermal conductivity, T is the temperature, and t is the time. $Q_i(x,z)$ is the heat generation due to laser energy absorption and can be determined from the multi-layer Monte Carlo simulation [3]. Blood perfusion and metabolic heat generations are not included in above equations because of the short pulse (typically < 40 ms). Early works demonstrated that these effects were small, compared to laser energy absorption [4]. The cooling effect of CSC is quantified by a convective heat transfer coefficient which can be determined from an experimental correlation [5], while the thermal damages in the skin tissue are obtained by the Arrhenius rate process integral. All thermal and optical properties of the tissues can be found in reference [3].

3. RESULTS

The theoretical model is solved to compare the effect of typical PDL (595 nm) with near infrared laser (1064 nm). Prior to the laser irradiation, cryogen was sprayed to the skin surface to prevent the epidermal overheating with spurt duration of 100ms. Acoording to the clinical experience, a flat hat-beam with diameter of 6 mm is chosen. The laser incident energy used are 12 J/cm^2 for 595nm laser and 80 J/cm^2 for 1064nm laser, which are just below the minimum radiant exposure that causes irreversible thermal injury to the epidermis for two lasers.

3.1 Treatment of large and deeply-buried blood vessels with 595nm and 1064 nm laser irradiation

The temperature distribution and corresponding thermal damage after 6ms 595nm pulsed dye laser irradiation were shown in Figure 2. As shown in the Figure 2a, the temperature of the blood vessels is much higher than that of dermis because of the selective erngy aborption by blood compare to the water in dermis to 595nm laser. Meanwhile, the temperature within larger blood vessels (120μm diameter) is evidently decayed. As shown in the Figure 2b, the thermal damage area (red area) was almost cover the entire vessel lumen in small blood vessels with diameter of 30 and 50μm. However, only a small part of the top area within center large blood vessel in the sencond row was damaged. The large blood vessels in the thrid row are all intact. In comparison, the temperature distribution and corresponding thermal damage after 6ms 1064nm Nd:YAG laser irradiation was

shown in Figure 3. As the light absorption in blood is much lower in 1064nm than that in 595nm, the temperature distributions in all 9 blood vessels are uniform even in six large blood vessels (Figure 3a). Completely coagulations were observed within eight vessel lumens, except for the 10μm normal capillary (Figure 3b), which is a result of heat dispersion to the surrounding tissue when the pulse duraiotn (6ms) is much longer than thermal relaxation time of 10μm blood vessel (≈0.1ms).

The above results imply an insufficient coagulation for large diameter and deeply buried PWS blood vessels at traditional PDL with 595nm laser irradiation, while a much better coagulation can be achieved with 1064nm laser.

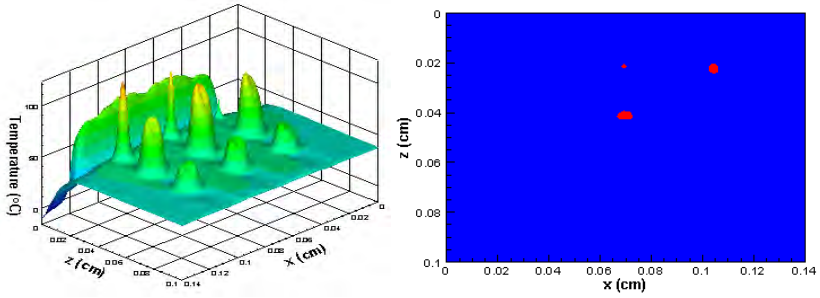

a) b)

FIGURE 2. Predicted temperature (a) and thermal damage (b) after 6 ms 595nm laser irradiation

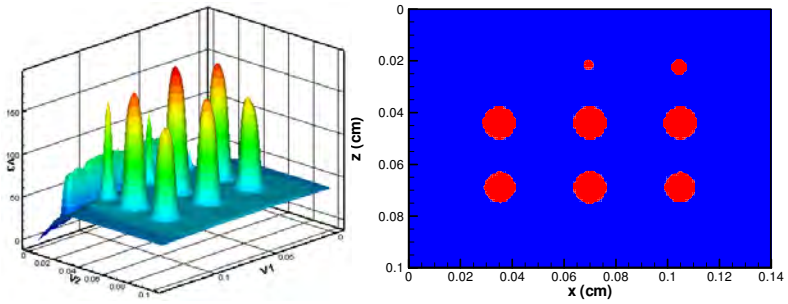

a) b)

FIGURE 3. Predicted temperature (a) and thermal damage (b) after 6 ms 1064nm laser irradiation

3.2 Distinct heating pattern of blood within vessel lumen to 595nm and 1064nm laser

Figure 4 shows the calculated temperature at top and bottom vessels at end of 6ms 595 and 1064nm lasers. 50μm and 120μm diameter blood vessels are selected at the center of laser spot. As displayed in Figure 4a, the temperature at top blood vessel is always higher than the bottom since the attenuation of 595nm laser light within vessels is large. As the diameter increased from 50 to 120μm, the light attenuation got even larger. As displayed in Figure 4b, the temperature at top and bottom of the vessel is almost uniform even within the large vessels with diameter of 120μm during Nd:YAG laser irradiation since 1064nm laser light penetration is much deeper than 595nm laser.

The above results imply that heatng pattern within vessels lumen is greatly different between 595nm and 1064nm lasers, leading to distinct damage pattern. This explains the different observable clinical treatment end points when using two lasers, e.g. instant purpura for PDL and

immediate blood vessel clearing for Nd:YAG laser [2] and is also consistent with the animal experiment observation in our previous study [6].

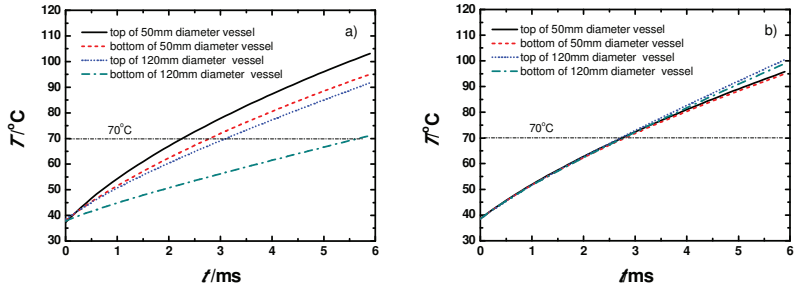

FIGURE 4. Temperature variation at top and bottom of blood vessel with diameter of 50 and 120μm after irradiation with 595nm (a) and 1064nm (b) lasers

4. CONCLUSIONS

This study demonstrates the different blood vessel thermal responses to visible and near infrared laser irradiation by theoretical investigation. The simulated results show that: 1) Large-sized and deep-extending blood vessels, which are likely to survive from the 595nm laser irradiation, can be completely coagulated by 1064 nm laser. 2) Heating patterns within the blood vessel lumen for two lasers are different. The 595 nm laser heated the superior portions of large blood vessels more than the inferior portions. Conversely, the 1064 nm laser produced uniform heating. The distinct heating patterns can explain the different observable clinical treatment end points for two lasers.

ACKNOWLEDGMENTS

The work is supported by Joint Research Fund for National Natural Science Foundation of China (51336006, 51228602), the International Science & Technology Cooperation Plan of Shaanxi Province (No. 2013KW30-05) and the Fundamental Research Funds for the Central University.

REFERENCES

[1] R.R. Anderson, J.A. Parrish, Microvasculature can be selectively damaged using dye laser: a basic theory and experimental evidence in human skin, *Lasers Surg. Med.*, 1, 263-276, 1981.

[2] M.U. Yang, A.N. Yaroslavsky, W.A. Farinelli, T.J. Flotte, F. Rius-Diaz, S.S. Tsao and R.R. Anderson, Long-pulsed neodymium: yttrium-aluminum-garnet laser treatment for port-wine stains, *J Am Acad Dermatol*, 52, 480-490, 2005.

[3] T. Dai, B.M. Pikkula, L.H. Wang, B. Anvari, Comparison of human skin opto-thermal response to near-infrared and visible laser irradiations: a theoretical investigation, *Phys. Med. Biol.*, 49, 4861-4877, 2004.

[4] A.J. Welch, E.H. Wissler, L.A. Priebe, Significance of blood flow in calculation of temperature in laser irradiated tissue, *IEEE Trans. Biomed. Eng.*, BME-27, 164-166, 1980.

[5] D. Li, G.X. Wang, Y.L. He, K.M. Kelly, W.J. Wu, Y.X. Wang and Z.X. Ying, A two temperature model for selective photothermolysis laser treatment of port wine stains, *Applied Thermal Engineering*, 59, 41-51, 2013.

[6] W.J. Wu, D. Li, L.Z Xing, B. Chen, G.X. Wang, Dynamic characteristics of vascular morphology after 1064nm laser exposure, Chin J Lasers, 41, 0304001-0304006, 2013.

Third International Conference on Computational Methods for Thermal Problems
THERMACOMP2014, June 2-4, 2014, Lake Bled, Slovenia
N. Massarotti, P. Nithiarasu and B. Sarler (Eds.)

MULTI-DISCIPLINARY ANALYSIS OF COOLING PROTOCOLS FOR HUMAN HEART DESTINED FOR TRANSPLANTATION

Abas Abdoli[1], George S. Dulikravich[1]
[1]Department of Mechanical and Materials Engineering, MAIDROC Laboratory, Florida International University, Miami, FL 33174, aabdo004@fiu.edu, dulikrav@fiu.edu.

Chandrajit Bajaj[2], David F. Stowe[3], M. Salik Jahania[4]
[2]Department of Computer Sciences, Computational Visualization Center, Institute of Computational Engineering and Sciences, University of Texas at Austin, Austin, TX 78712, bajaj@cs.utexas.edu.
[3]Department of Anesthesiology, Physiology, Cardiovascular Research Center, Anesthesiology Research Laboratory, Medical College of Wisconsin, Milwaukee, WI 53226, dfstowe@mcw.edu.
[4]Department of Surgery, Division of Cardiothoracic Surgery, School of Medicine, Wayne State University, Detroit, MI 48202, jahaniam@med.wayne.edu.

ABSTRACT

A new cooling protocol for realistic human heart preservation was designed and investigated numerically with an objective to extend the usable life of an organ between its harvesting and implantation. A high resolution MRI imaging of actual human heart was used to create a 3D geometric model used for simulations based on OpenFOAM software platform. The conjugate cooling protocol uses internal cooling by perfusing a liquid inside the heart and external cooling by submersing the heart inside cooling gelatine. Multi-domains, multi-physics, three-dimensional simulation was performed to obtain unsteady temperature and stress fields inside the heart during the shortest cooling process.

Key Words: *heart simulation, organ preservation, transplantation, heart cooling, stress analysis, blood flow, conjugate heat transfer.*

1. INTRODUCTION

The main current problem of organ transplantation is the relatively short time that organs can survive from the moment of their harvesting to the moment of their surgical transplantation into the recipient's body. Currently, human hearts can be used for transplantation only during 4 hours between harvesting to its implantation when kept submerged in a saline solution at temperature close to freezing of water [1]. Cold preservation is using the advantages of decreasing cell temperature, thus causing the cell metabolism to be decreased. As a result, oxygen and glucose consumption and carbon dioxide production will be decreased as well [2]. Thus the cell damage due to lack of oxygen will be decreased [3]. Numerical studies in this field are very challenging due to geometric complexity and lack of certain experimental data. Dulikravich [4] demonstrated, in the case of two dimensions, that it is possible to maintain specified cooling rates at any point of the cooled object by varying container wall temperature distribution. Dennis and Dulikravich [5] used 3-D spectral finite elements to simulate unsteady temperature field and thermal stress field during freezing of an idealized canine kidney submerged in gelatine without perfusion. They also for the

first time demonstrated the optimized time-varying thermal boundary conditions use on the surface of a spherical freezing container and suggested use of optimized internal perfusion of the organ during the cooling process.

2. SIMULATIONS AND RESULTS

Complex geometry of human heart is one of the challenges of this work. Zhang and Bajaj [6] applied finite element method for meshing the 3-D human heart from MRI scan data. In this research, human heart geometry presented by Bajaj has been used for simulations. Multi-physics nature of this research requires having three separate domains; inside the heart, heart, and outside the heart. The first step in creating the required domains is to separate innermost (blood contact) surfaces from outermost surfaces which are shown in figure 1.

a) b)

Figure 1. Heart model: a) whole heart, and b) blood contact and outermost surfaces.

For each of the two heart circulation systems, two inlets and two outlets were designed to circulate the perfusate inside the heart. Heart was treated as submersed in a cooling gelatin in order to have pure conduction cooling from outside. Heat conduction will give an ability to apply different cooling rates on heart by using different temperatures on the walls of the cooling container.

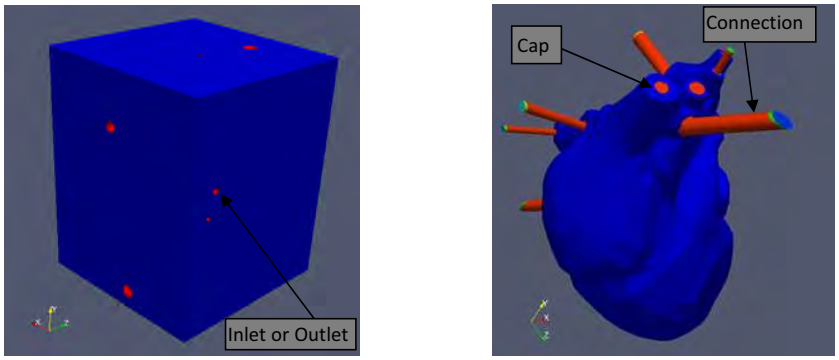

a) b)

Figure 2. Cooling system: a) cooling container, and b) connections and caps.

Figure 2a shows a designed cooling container of 214 mm in length, 212 mm in width and 282 mm in height, with 4 inlets and 4 outlets for cooling the heart. Figure 2b shows the all connections and caps for pumping coolant through the heart right and left circulation systems.

Conjugate heat transfer simulation was performed in OpenFOAM environment [7]. Perfusate flow was considered a laminar flow due to low Reynolds number, and was modeled by using Navier–Stokes equations. In this research, very low inlet and wall temperature were applied in order to better demonstrate variations of the temperature field during cooling process and the capacity of cooling system in removing heat from the heart. The inlet temperature of the perfusate was set to -10°C. Cooling container wall temperature was also set to -10°C. Figures 3a and 3b show that the average heart temperature was reduced 22°C in 300 s. Figure 3c and 3d demonstrate the temperature distributions of perfusate during cooling process.

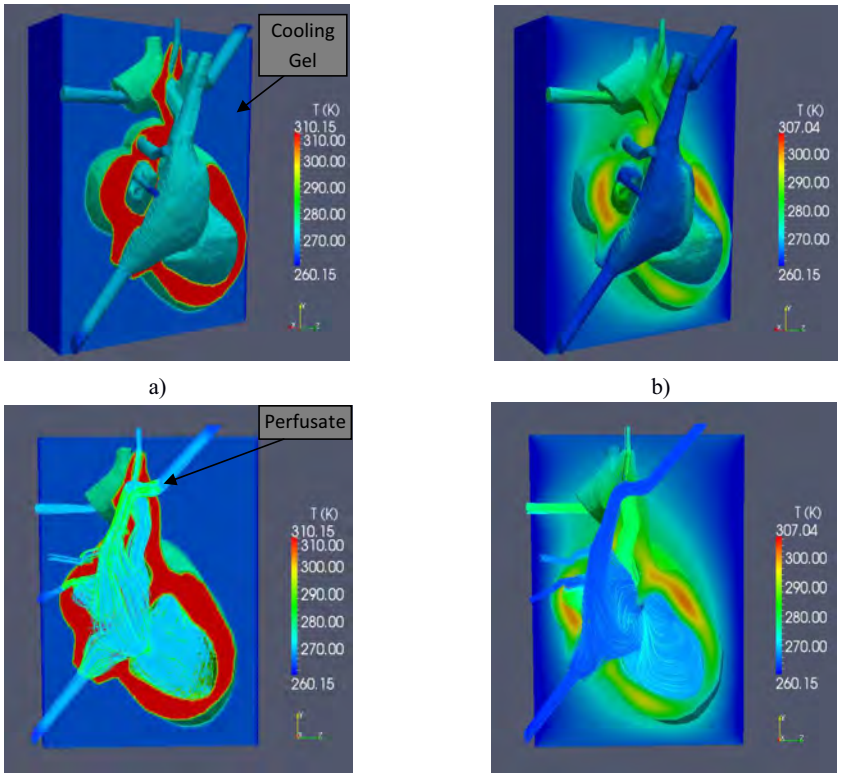

Figure 3. Temperature distribution (sagittal view) after: a) 0.5 s, b) 300 s, c) 0.5 s with perfusate view, and d) 300 s with perfusate.

Stress analysis with small deformations was also performed using OpenFOAM to calculate normal and shear stresses applied to the heart tissue during the cooling process. The ultimate allowable stress of the heart tissue is 110 kPa [8]. Magnitude of stress inside the entire heart at 5 s was higher

than at 300 s. This was due to larger variation of temperature at the 0.5 s compared to 300 s. The calculated stress was lower than the ultimate allowable stress during the entire cooling process.

3. CONCLUSIONS

A cooling protocol simulation for human heart preservation was designed. In this protocol, external cooling takes place via conduction by using a cooling gelatin between the heart and the walls of the cooling container. Heart internal cooling is by perfusate convection. Different temperature was applied on the cooling container walls in order to have different cooling rates. Gelatin was chosen as the cooling conduction medium and water as perfusate. Three-dimensional, conjugate thermo-fluid-stress analysis was performed using high resolution realistic human heart geometry during 25 minutes of the cooling process. OpenFOAM software was used to perform all numerical time-dependent simulations. The combined conduction/convection cooling is capable of lowering the heart temperature much faster than typically used conduction alone.

ACKNOWLEDGEMENTS

Authors are grateful for partial financial support of this research provided by DARPA via GaTech in the framework of ICECool project under supervision of Dr. Avram Bar-Cohen. The lead author would like to acknowledge the financial support of a Florida International University Dissertation Year Fellowship. The research of Chandrajit Bajaj was supported in part by NIH grant R01-EB004873. The authors also gratefully acknowledge the FIU Instructional and Research Computing Center for providing HPC resources to perform calculations for this project.

REFERENCES

[1] E.M. Moore, A.D. Nichol, S.A. Bernard and R. Bellomo. Therapeutic hypothermia: Benefits, mechanisms and potential clinical applications in neurological, cardiac and kidney injury. *Injury, Int. J. Care Injured*, 42 (9), 843-54, 2011.

[2] K.H. Polderman and I. Herold. Mechanisms of action, physiological effects, and complications of hypothermia. *Critical Care Med.,* 37, S186–202, 2009.

[3] F.M. Wagner. Donor heart preservation and perfusion. *Applied Cardiopulmonary Pathophysiology,* 15, 198-206, 2011.

[4] G.S. Dulikravich. Inverse design and active control concepts in strong unsteady heat conduction. *Applied Mechanics Reviews*, 41 (6) 270-277, June 1988.

[5] B.H. Dennis and G.S. Dulikravich. Determination of unsteady container temperatures during freezing of three-dimensional organs with constrained thermal stresses. *International Symposium on Inverse Problems in Engineering Mechanics – ISIP' 2k*, (eds: M. Tanaka and G. S. Dulikravich), Nagano, Japan, Elsevier Science Ltd, Amsterdam, 139-148, 2000.

[6] Y. Zhang and C. Bajaj. Finite element meshing for cardiac analysis. *ICES Technical Report 04-26*, University of Texas at Austin, 2004.

[7] J. Peltola, T. Pättikangas, T. Brockmann, T. Siikonen, T. Toppila and T. Brandt, Adaptation and validation of OpenFOAM®CFD-solvers for nuclear safety related flow simulations, *SAFIR2010*, CSC, Espoo, Finland, May 17, 2011.

[8] H. Yamada, Strength of biological materials. *Williams & Wilkins*, ISBN-13: 978-0683093230, 1970.

Third International Conference on Computational Methods for Thermal Problems
THERMACOMP2014, June 2-4, 2014, Lake Bled, Slovenia
N. Massarotti, P. Nithiarasu and B. Sarler (Eds.)

POROUS MEDIUM BIO-HEAT TRANSFER MODELING OF HYPOTHERMIA TREATMENT IN HUMAN BRAIN

Arunn Narasimhan

Heat Transfer and Thermal Power Laboratory, Dept Mechanical Engg, IIT Madras, Chennai-600036, India
arunn@iitm.ac.in

ABSTRACT

In this study we present a transient porous medium bio-heat transfer model of human brain and head region to simulate ischemic stroke and subsequent focused therapeutic hypothermia of the head. Partial geometry of the Circle of Willis (COW) and major veins in brain were constructed in a 3D model of head region. Scalp cooling with a cooling helmet termed as selective brain cooling (SBC) is employed as a cooling protocol. Results of finite volume method calculation on the domain suggested that SBC alone is ineffective to induce even mild hypothermia (35°C) but under extreme cooling conditions (< -20°C) of the coolant it would achieve target temp at superficial regions but not of deep brain. Intracarotid cold saline infusion (ICSI) is another cooling protocol simulated to attain the target temperature of the whole brain with 30 ml/min and 20 ml/min saline infusion rates respectively.

Key Words: *Transient, Porous medium, Bio-heat transfer, Brain Stroke, Hypothermia.*

1. INTRODUCTION

Ischemic stroke is followed by a series of biochemical reactions initiated in the brain called the "ischemic cascade" [1]. During and after ischemic stroke, even any small changes in tissue temperature has been shown to cause highly variable rate of brain injury [2] as progressively more number of cells proceed to the apoptotic cell death pathway with continued absence of local blood flow. Most clinical trials focus on inducing hypothermia by way of systemic cooling which can take more than three hours to reach target temperatures [3] which falls outside the window for the effectiveness of hypothermia [4].

Among several methods for selective induction of hypothermia in the brain are cooling helmets which utilizes either frozen material like ice or circulating cold fluid or forced cold air circulation [25]. We simulate two of these basic methods, viz. the scalp cooling via cooling helmet which we term as selective brain cooling (SBC) and intracarotid cold saline infusion (ICSI).

2. MATHEMATICAL MODELING AND NUMERICAL PROCEDURE

A 3D model was developed to analyze the coupled fluid flow and heat transfer processes in a semi-realistic geometry of the human head. The model enabled realistic simulation of pathological conditions such as stroke as well as induced effects such as introduction of cold saline in one of the arteries nourishing the brain. The model also captured the non-homogeneity of the brain region and set different thermal and perfusion properties for different regions of the brain.

The model contains layers of concentric solid shells consisting of scalp, skull, cerebrospinal fluid (CSF). The brain was an ellipsoidal domain at the middle. Even though CSF is not a solid region, it is a very thin layer and we model it as a solid and ignore any convection inside the layer. The brain tissue region is constructed as a porous domain while the large blood vessels modeled inside the

tissue are fluid regions. The porous bio-heat transport equations [5], along with the standard Navier-Stokes solved in the computational domain of the brain region are given below.

$$\rho_f \left[\frac{1}{\phi}\frac{\partial \vec{u}}{\partial t} + \frac{1}{\phi}\vec{u}\cdot\frac{1}{\phi}\nabla\vec{u}\right] = -\nabla P + \mu_{eff}\nabla^2\vec{u} - \frac{\mu}{K}\vec{u} - \rho C\left|\vec{u}\right|\vec{u} \quad (1)$$

$$\left(\rho c_p\right)_e \frac{\partial T_f}{\partial t} + \left(\rho c_p\right)_f \vec{u}\cdot\nabla T = \nabla\cdot\left(k_e\nabla T\right) + Q'''_{met} \quad (2)$$

$$\rho\left(\frac{\partial \vec{u}}{\partial t} + \vec{u}\cdot\nabla\vec{u}\right) = -\nabla p + \mu\nabla^2\vec{u} + \vec{F} \quad (3)$$

$$\rho c_p\left(\frac{\partial T}{\partial t} + \vec{u}\cdot\nabla T\right) = k_f\nabla^2 T \quad (4)$$

$$\rho c_p\frac{\partial T}{\partial t} = k_s\nabla^2 T + Q'''_{met} \quad (5)$$

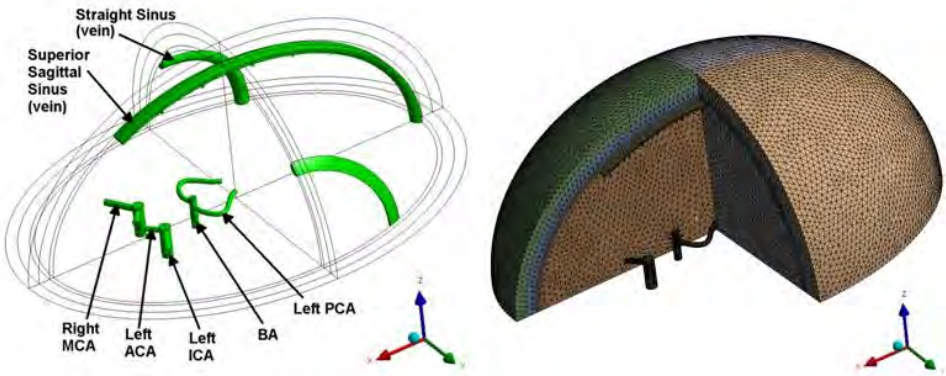

FIGURE 1. (left) 3D model skeletal view of human brain showing the COW vessels and major veins and (right) representative computational domain.

The computational model was solved for the boundary conditions listed in Table 1. The cerebrospinal fluid (CSF), skull and scalp regions were created as concentric elliptic shells of $2 mm$, $5 mm$ and $5 mm$ respectively. The major arteries of the brain constituting the Circle of Willis (COW) are included in the model as shown in Figs. 1 and 2. The diameters of the capillaries in the brain region are between 5 and 10 μm. The permeability (K, m^2) of the porous medium model of the brain is estimated in some regions from the MR image as shown in Fig. 2B. It is determined [5] to be in the range of 10^{-9} m^2 and 10^{-14} m^2 in other regions. In our model, we use a uniform homogeneous value of permeability 10^{-10} m^2. The thermo-physical properties of the biomaterials used in the model are given in Table 2. Further details of the computational domain construction, grid independence and model validation studies are available in Reference [6].

Boundary Condition	Condition	Type	Value
Top External Walls	Normal	Convective	$h = 8\frac{W}{m^2K}, T_{\infty} = 300K$
Internal Walls	Flow	Wall	$v = 0\, m/s$
	Energy	Coupled	$T_1 = T_2$ $k_1\frac{\partial T_1}{\partial n} = k_2\frac{\partial T_2}{\partial n}$
Left, Right ICA	Normal	Velocity Inlet	$v = 0.125\, m/s, T = 310K$
BA	Normal	Velocity Inlet	$v = 0.25\frac{m}{s}, \quad T = 310K$
Head Bottom Wall	Flow	Wall	$v = 0\, m/s$
	Energy	Adiabatic	$\frac{\partial T_1}{\partial n} = 0$
Vein Outlets	Flow	Pressure Outlet	Gauge Pressure P = 0 Pa

TABLE 1. Boundary conditions for solving transport equations in the computational domain.

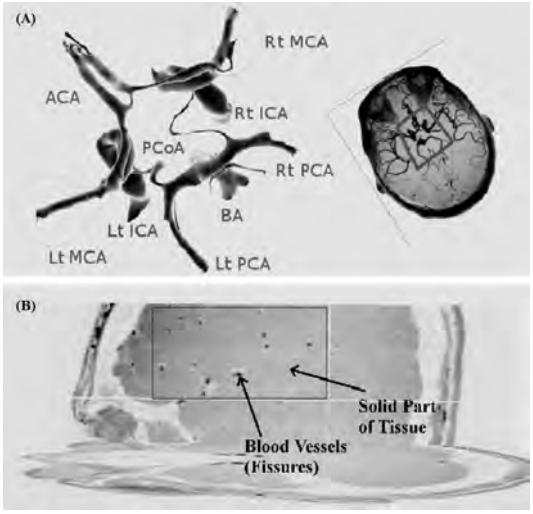

FIGURE 2. (A) Volume rendering of Circle of Willis geometry used in the 3D model taken from Magnetic Resonance image using 3D Slicer software http://www.slicer.org (B) MRI scan of volunteer to determine the permeability of the brain tissue.

3. RESULTS AND DISCUSSION

Initially a healthy brain at steady state was simulated giving an average temperature \$0.12 K\$ higher than body core temperature. Hypothermia application was done by two methods primarily. 1) Selective Brain Cooling (SBC) which was attempted via scalp cooling simulating application of cooling helmets or direct application of ice on the scalp and 2) Intracarotid Cold Saline Infusion (ICSI) which simulated infusion of saline at very low temperatures into the carotid artery and a mixture of artery blood and saline reaching the brain at a temperature between body core temperature and the cold saline temperature.

In both cooling mechanisms, treatment was started 30 minutes after the onset of the ischemic event to simulate a more realistic time window of therapeutic procedures. For simulation of SBC, a convective boundary condition was implemented on the top surface of the scalp with different heat transfer coefficients and different temperatures of the coolant fluid. A situation where ice was put on the scalp directly was also simulated by setting the scalp surface temperature to $273 K$. In case of ICSI, the cold saline was input at a certain rate and a corresponding temperature which resulted in certain mixture temperatures after mixing with arterial blood.

Material	Specific Heat W/kgK	Thermal Conductivity W/mK	Density kg/m^3	Viscosity $kg/m \cdot s$	Metabolism W/m^3
Blood	3800	0.505	1050	0.0035	N/A
Brain	3700	0.528	1030	N/A	10437
CSF	3800	0.500	1000	N/A	0
Skull	2300	1.160	1500	N/A	363
Scalp	4000	0.342	1000	N/A	365
Saline	4213	0.500	1006	0.0035	N/A

TABLE 2. Thermophysical properties of the bio-materials in the brain.

Figure 3 shows the transient temperature history for left MCA occlusion under different cooling conditions with SBC. The effect of high rate of warm blood perfusion in the brain is the main reason for the failure of the scalp cooling. The temperature history in different hemispheres reveals the thermal effects of blood perfusing the brain. The maximum temperature reached in brain is 310.25 K. In the affected left hemisphere the temperature is low (307.5 K) while the temperature in the normal right hemisphere is high (309.5 K) and is much closer to the artery inlet temperature due to higher rate of perfusion. The perfusion is lowest (307 K) in particular inside the left front quadrant and as such scalp cooling is most effective there. At the ischemic zone the target temperature may be reached even with h=50W/m^{2}K. In combination ICSI and SBC cooling, a shown in Fig. 4, the final temperatures reached are lower than with any single cooling method.

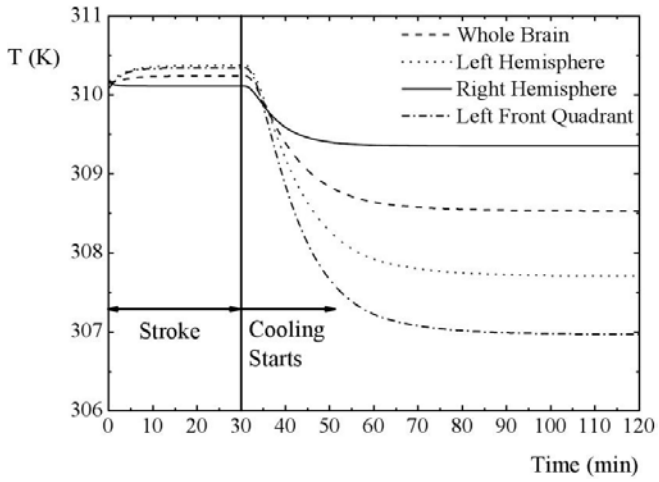

FIGURE 3. Temperature history for selective brain cooling with cooling cap and ice packing as average of whole brain for different methods of cooling and (b) different segments of brain under selective brain cooling with h = 50W=m^{2}K and T_{amb} = 253K after left MCA occlusion.

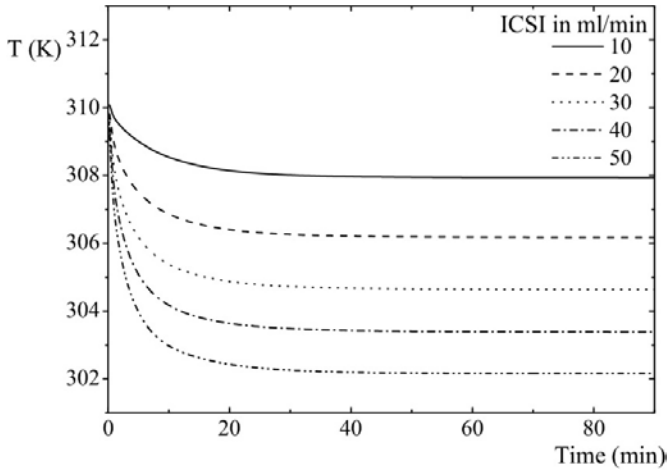

FIGURE 4. Whole brain average temperature history during combination cooling using ICSI and SBC methods with h = 50W=m^{2}K and T_{amb} = 253K.

4. CONCLUSION

The novel 3D porous medium model of human brain allowed for conveniently simulating several brain stroke conditions and two different types of treatment methods -- selective brain cooling (SBC) and intracarotid cold saline infusion (ICSI) -- and a third which consisted of a combination of the first two methods. The scalp cooling method alone proved to be insufficient to achieve hypothermia of the total brain under moderate cooling conditions (T = 273 K) but it did achieve hypothermia (307 K) in the affected quadrant of the brain for left MCA occlusion. This aspect of the study has not been considered in previous studies which discarded scalp cooling as an effective protocol to achieve rapid hypothermia in affected regions of the brain. The combination cooling strategy of using both scalp cooling and ICSI proved to be the most efficient method of reaching and maintaining hypothermia in the brain.

REFERENCES

[1] Deb, P., Sharma, S., Hassan, K.M.. Pathophysiologic mechanisms of acute ischemic stroke: An overview with emphasis on therapeutic significance beyond thrombolysis. Pathophysiology 2010;17(3):197{218.

[2] Busto, R., Dietrich, W.D., Globus, M.Y., Ginsberg, M.D.. The importance of brain temperature in cerebral ischemic injury. Stroke 1989;20(8):1113-1114.

[3] Krieger, D.W., De Georgia, M.a., Abou-Chebl, a., Andrefsky, J.C., Sila, C.a., Katzan, I.L., et al. Cooling for Acute Ischemic Brain Damage (COOL AID): An Open Pilot Study of Induced Hypothermia in Acute Ischemic Stroke. Stroke 2001;32(8):1847-1854.

[4] Hemmen, T.M., Lyden, P.D.. Hypothermia after acute ischemic stroke. Journal of Neurotrauma 2009;26(3):387-91.

[5] Narasimhan, A., 2012. Essentials of Heat and Fluid Flow in Porous Media. CRC Press, NY.

[6] Jaichandar, S., 2012. Porous Medium Bio-heat Transfer Modelling in the Human Head. BTech. Thesis, ME Dept., IIT Madras.

Third International Conference on Computational Methods for Thermal Problems
THERMACOMP2014, June 2-4, 2014, Lake Bled, Slovenia
N. Massarotti, P. Nithiarasu and B. Sarler (Eds.)

STUDY OF THERMAL DAMAGE OF TISSUE EMBEDDED WITH BLOOD VESSELS DURING PHOTO-THERMAL HEATING

Anup Paul, Arunn Narasimhan*, Sarit K. Das
Heat Transfer and Thermal Power Laboratory, Department of Mechanical Engineering, IIT Madras, Chennai, Tamilnadu 600036, India
*Corresponding author: Tel.: +91-44-22574696, E-mail: arunn@iitm.ac.in

ABSTRACT

The cooling effect of large blood vessels on tissue temperature distribution during photo-thermal heating is predicted using finite element based simulation. A modified Beer-Lambert law is used to model the laser heating. Experiments have been performed on equivalent tissue mimic embedded with simulated blood vessel to validate the simulated results. The result shown that the large blood vessel can take away a significant amount of heat during photo-thermal heating and the corresponding value of damage parameter obtained is insufficient for tissue irreversible damage.

Key Words: *Conjugate Heat Transfer, Photo-thermal Heating, Large Blood Vessels, Damage Integral, Finite Elements simulation.*

1. INTRODUCTION

The blood flow through large blood vessels (LBV) can take away a significant amount of heat during thermal therapy, which results in incomplete tissue necrosis. Until now, there have been a lot of studies to investigate the effect of LBV on tissue temperature distribution during thermal therapy. Chato [1] studied theoretically, the heat transfer in three different configurations of blood vessels near the skin surface. A steady temperature distribution has been obtained for several tissue-vascular network model [2] during simulated hyperthermia treatment. Different power deposition pattern in the tumor region has been discussed and finally determined an optimal power deposition pattern to reduce the cold spot from tumor. Horng et al. [3] studied the effect of pulsatile blood flow on thermal lesion distribution on tumor tissue embedded with LBV. This paper demonstrates the effect of LBV on tissue damage during Near infra-red (NIR) radiation. A modified Beer-Lambert law has been used to simulate the laser light propagation in bio-tissues with or without introducing LBVs and the rate process Arrhenius equation to investigate the irreversible thermal damage to the bio-tissues.

2. MATERIALS AND METHODS

2.1. Experimental set-up

Briefly, the set-up consists of a test section made of acrylic which contains equivalent tissue phantom, a continuous wave diode-pumped solid state laser source system of 1064 nm wavelength with TEC driver, a dual syringe pump to regulate the flow and an Infra-red (IR) thermal camera. A teflon tube of 2.2 mm OD/1.6 mm ID was used to simulate the LBV. The surface temperature distribution were captured at different time intervals using a stop watch. The laser intensity at the tissue surface was kept constant at 2.8 W/cm^2 (an average laser power of 0.558 W and a spot size of 5 mm).

2.2. Mathematical model and Numerical scheme

In this study, two tissue vascular models viz tissue in absence of LBV and Single vessel transiting tissue (SVTT) were discussed as shown in Figure 1. The energy transport in tissue and blood vessel were modelled by heat diffusion equations and a convective diffusion equation were used to take care of blood flow. The top surface of the tissue was under natural convection with convective heat

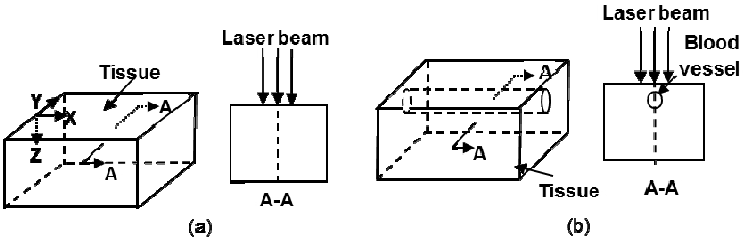

FIGURE 1. Illustration of physical model. (a) tissue in absence of LBV and (b) Single vessel transiting tissue (SVTT)

transfer coefficient to ambient was taken as 10 W/m^{2}K [4] and with different ambient temperatures of 28.8 ºC in case of tissue in absence of LBV and 29.7 ºC in case of SVTT respectively since the experiments were conducted in two different days. The radiation effect at the surface was neglected due to the small temperature difference. An adiabatic boundary condition was imposed on all other tissue boundaries. The temperature of the blood at the inlet of the blood vessel was considered as 29.48 ºC based on the experimental conditions and outflow condition was applied at the exit. The inlet of blood vessel was considered as a parabolic velocity profile and no slip boundary condition was imposed on vessel wall. Welch [5] has derived a model for penetration of laser light in bio-tissue assuming Gaussian distribution of the laser beam, which comprises of tunable optical properties in the form of absorption (α) and scattering coefficients (β). Once the temperature distribution has been obtained the tissue damage were predicted. Based on the assumption that, the protein denaturation occurs due to the burning of tissue, [6] hypothesized the Arrhenius damage integral equation to compute the tissue damage distribution.

A numerical software COMSOL multiphysics (COMSOL Multiphysics 4.3, Burlington, MA) was used to solve the conjugate heat transfer with a relative tolerance limit of 0.001 and absolute tolerance of 0.0001 in both velocity and temperature. The meshed model was solved transiently by GMRES (Generalized Minimum Residual) iterative method with geometric multigrid pre conditioner and Forward Difference Formula for time stepping method were used with time step of 0.1 second.

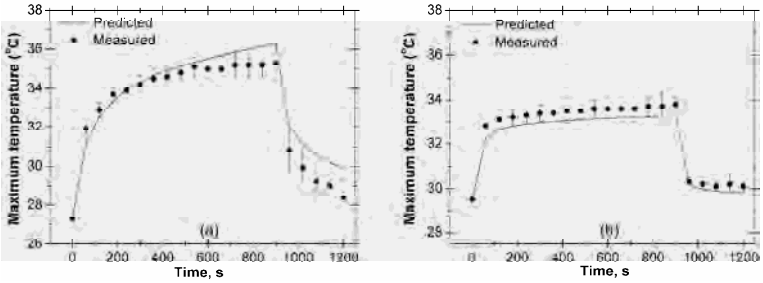

FIGURE 2. Unsteady temperature distribution at the center of the heated area of tissue surface. (a) tissue in absence of LBV and (b) Single vessel transiting tissue (SVTT) (laser power=558 mW, spot size=5 mm, flow rate=10 ml/min)

3. RESULTS AND DISCUSSIONS

The thermal properties of equivalent tissue phantom were measured and thermal as well as optical properties of blood vessel, blood presented in Table 1. The model presented in this paper is validated with the experiment of laser irradiation on equivalent tissue phantom. A comparison of temperature distribution at the top tissue surface (below laser spot) is shown in Figure 2 and a good agreement with numerical has been obtained. During the experiment the laser was continuously irradiated for 15 minutes and then it was allowed to cool for 5 minutes. Figure 2(a) depicts the temperature distribution for the case of bare tissue and the maximum rise in temperature obtained in this case was approximately 9 ºC whereas it was approximately 5 ºC in case of SVTT for same heating period as shown in Figure 2(b). Hence, due to the cooling effect of LBV, the maximum rise in surface temperature was drops down to 4 ºC (however, there was a difference in tissue initial temperature of 1 °C between the two cases). Moreover, due to the heat sink effect of LBV the system is approaching steady state much quicker than the case with bare tissue. In both the two cases, identical laser power and spot size of 558 mW and 5 mm respectively were maintained.

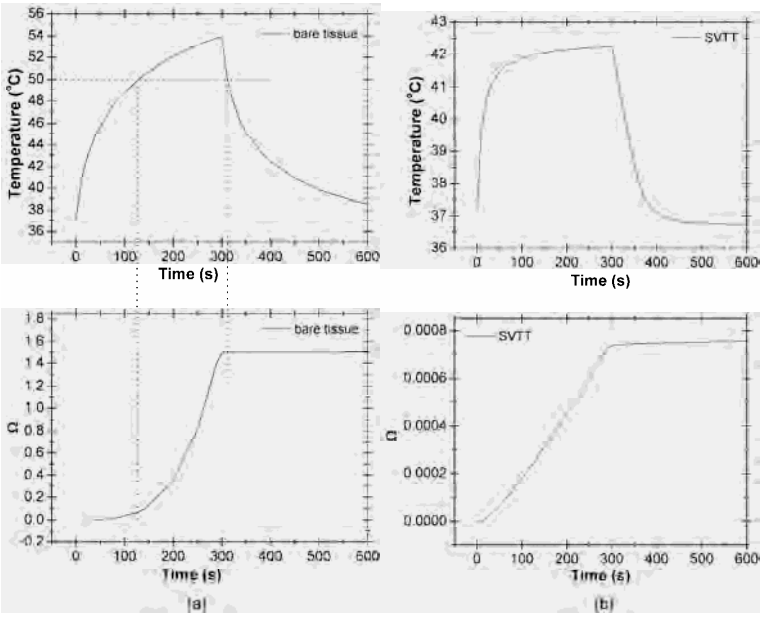

FIGURE 3. Prediction of temperature and damage integral at the center of top tissue surface (below laser spot) as a function of time (laser power=1.5 W, spot size=5 mm, flow rate=10 ml/min) (a) bare tissue, (b) SVTT.

The thermal damage was calculated using Arrhenius equation, temperature was evaluated as a function of time based on the transient temperature data available for different times of heating and cooling of bio tissue. Figure 3 depicts the temperature and damage parameter (Ω) at the center of top tissue surface (below laser spot) as a function of time. In this case, initial tissue temperature and blood inlet temperature were taken as 37 °C, the laser intensity of 7.6 W/cm^2, beam radius of 0.0025 m, exposure time of 300 s and then allowed to cool up to another 300 s. The temperature rises with increase in time till the laser is switched off and then drops down due to the diffusion of heat to the neighbouring tissues and due to maintaining convective cooling boundary condition at the top surface. The damage parameter is very low until the temperature rises to about 50 ºC and then a steep rise is observed till the laser is turned off. There is a continuous increase in damage

parameter even after the laser is turned off till the temperature cools down to 50 ºC and afterwards it becomes constant. The predicted damage parameter beyond 50 ºC is >1 [5] and hence sufficient for the irreversible damage. The maximum thermal damage parameter obtained in case of bare tissue at the centre of the top tissue surface was evaluated to be 1.5. For the SVTT case (Figure 3(b)), the damage value was 0.00075 which is insufficient for irreversible tissue damage.

	Density (ρ) (kg/m^3)	Specific heat (C) (J/kg.K)	Thermal conductivity (k) (W/m.K)	Absorption coefficient (α) (m^{-1})	Scattering coefficient (β) (m^{-1})
Phantom	1050	4219	0.66	40	530
Blood	1000	4200	0.6	200	150
Blood vessel	2200	1200	0.25	45	140

TABLE 1. Physical and optical properties [4,5]

4. CONCLUSIONS

A three dimensional computational model for conjugate heat transfer has been developed during photo-thermal heating to predict the temperature distribution at the tissue surface with or without introducing LBV. Experiments have been performed on equivalent tissue mimic embedded with simulated blood vessel to validate the simulated results. The maximum rise in temperature at the surface of tissue drops down significantly due to the heat sink effect of LBV and it has been also observed that the maximum thermal damage parameter drops down to 0.00075 from 1.5 which is insufficient for irreversible tissue damage. Hence, it is very much essential to ascertain the position of LBV and fixing the laser spot position during photo-thermal heating.

REFERENCES

[1] J. C. Chato, Heat transfer to blood vessels, *Journal of Biomechanical Engineering,* 102, 110-118, 1980.

[2] Z. P. Chen, R. B. Roemer, The effects of large blood vessels on temperature distributions during simulated hyperthermia, *Journal of Biomechanical Engineering*, 114, 473-481, 1992.

[3] T. L. Horng, W. L. Lin, C. T. Liauh, T. C. Shih, Effects of pulsatile blood flow in large vessels on thermal dose distribution during thermal therapy, *Medical Physics*, 37(4), 1312-1320, 2007.

[4] G. V. Maltzahn, J. H. Park, A. Agrawal, N. K. Bandaru, S. K. Das, M. J. Sailor, S. N. Bhatia, Computationally guided photothermal tumor therapy using long-circulating gold nanorod antennas, *Cancer Research*, 69(9), 3892–3900, 2009.

[5] A. Welch, The thermal response of laser irradiated tissue, *Quantum Electronics, IEEE Journal of Quantum Electronics,* 20, 1471–1481, 1984.

[6] F. C. Henriques, Studies of thermal injury, *Archives of pathology,* 43, 489–502, 1947.

Third International Conference on Computational Methods for Thermal Problems
THERMACOMP2014, June 2-4, 2014, Lake Bled, Slovenia
N. Massarotti, P. Nithiarasu and B. Sarler (Eds.)

Numerical modeling of drug delivery to posterior segment of eye

Sundarraj C, Arunn Narasimhan
Heat Transfer and Thermal Power lab, Dept Mechanical Engg, IIT Madras, Chennai. India-600036
sundarrajchandran@gmail.com, arunn@iitm.ac.in

ABSTRACT

Intravitreous injection and transscleral drug delivery are numerically modeled in the present study. Two dimensional computational domain, generated with the actual eye geometry, is used for simulation. Laser heated vitrectomized eye showed better drug transport to the retinal region. For a centrally injected drug, the convection assisted diffusion transported drug in 30 minutes to the retinal region as compared to the 2.7 hours for the pure diffusion case. Also transscleral drug transport of direct injection route and from implant, has been simulated and preliminary results are presented.

Key Words: *Intravitreous drug delivery, Transscleral drug delivery, vitrectomized eye*

1. INTRODUCTION

Drug delivery to posterior segment of eye is done through various methods. Topical administration, systemic administration, intravitreal injection, transscleral drug delivery are some of the existing techniques [1-4]. Polymer based drug delivery, photodynamic therapy, nanoparticulate drug delivery are also gaining momentum in this field recently. The highly protective structure of human eye, makes it difficult for the drug to reach the posterior segment. Drug delivery methods that overcome or circumvents all the barrier are expected to deliver the adequate therapeutic level of drug to the eye tissue.

Intravitreous drug delivery, places the drug directly in the vitreous by which it bypasses all the barrier in the anterior segment of the eye. Upon placed in the vitreous, the drug reaches the retinal region where the therapeutic effect is required. In vitrectomized human eye, the vitreous substitute, upon heating, exhibits convection flow [5]. The drug transport can very well be augmented by this convection.

Transscleral delivery is a minimally invasive method which achieves targeted delivery of high molecular weight compounds to the posterior segment of eye. It can be used to deliver different kinds of drugs- anti-angiogenic drugs, neuroprotective agents or vectors for gene transfer. With these drugs, glaucoma and other chorioretinal degenerations can be treated [6]. Potential barrier for the periocular injection is the diffusion away from the scleral surface and adsorption into the systemic circulation. By placing the drug in an impermeable reservoir, this loss could be limited [7].

The present work numerically models the intravitreal injection and the laser assisted intravitreal injection. Also transscleral drug delivery in two forms- injection and implant is being numerically modeled.

2. DRUG DELIVERY

For the intravitreous method, direct injection of the drug is modeled and also the drug transport influenced by the laser heating is simulated. In the transscleral delivery, both the direct injection and implant transport are modeled. Direct injection technique releases the drug instantaneously from a specified volume. Controlled release systems places the drug in a polymeric system or an implant in which the drug release rate is limited. It is designed for long-term administration of drug to maintain required levels of drug in the target region [8].

3.NUMERICAL METHODOLOGY

For intravitreous injection, geometrical model of the eye has been developed based on the human eye data as available in the literature. The meshing is refined near the retina. Inside the eye domain, the energy equation and momentum equations are solved to obtain the velocity and temperature profile. Blood perfusion effect in the choroid is accounted by solving Pennes bio heat equation in it. The natural convection in the vitreous due to laser heating is studied by solving appropriate form of Navier-Stokes equation containing buoyancy term. Boussinesq approximation is invoked while solving the momentum equations. Once the drug (fluorescein) is placed in the vitreous humour, the diffusion equations are also solved to obtain the concentration distributions of the drug inside the eye. The drug is initially assumed to be in a circle of radius 1.3 mm. Finite volume based solver is used for solving the governing equations. Separate sub-routines (programs) are used for specifying volumetric heat generation and laser path through the eye domain.

In case of transscleral delivery, only the posterior segment containing sclera and choroid, is modeled in the present study. The drug (anecortave acetate) is placed in the posterior justascleral location. The sclera and the choroid are considered as porous medium with porosity of 0.39. The porous medium mass transport equation is solved in the computational domain. ANSYS FLUENT has been used for solving the equations.

4.RESULTS AND DISCUSSION

4.1 Intravitreous injection:

The natural convection in the vitreous humour, induced by laser heating (with laser power 300mW and spot diameter of 4 mm) is solved initially to give the velocity field inside the vitreous. Details of convection induced by laser heating and the assumptions used may be found elsewhere [5]. The drug transport for a drug placed in a stagnant vitreous humour and convection induced vitreous are studied.

The drug is placed in different initial locations- central, bottom, near lens, near retina. The drug transport for the pure diffusion case and the convection enhanced diffusion case are studied. Figure 1 compares the two cases for centrally injected drug. As observed, the drug reaches the retinal region after time of 2.7 hours in pure diffusion case whereas for the convection case, it reaches by 30 minutes. Further results, including comparative study for various initial drug depot may be seen in related works [9,10].

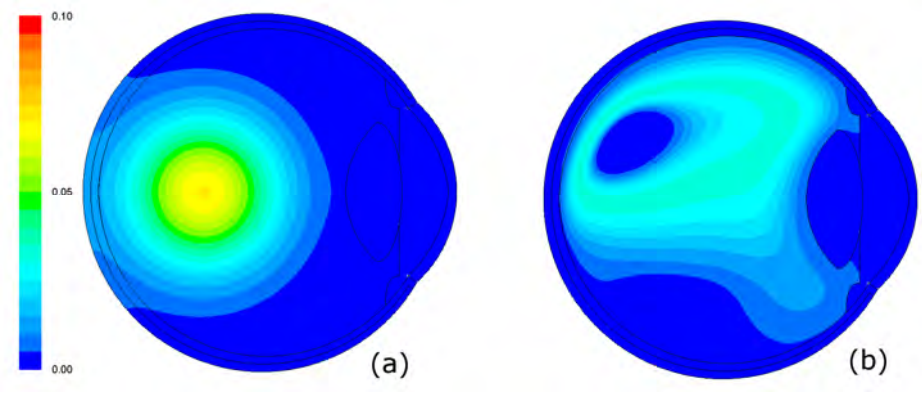

FIGURE 1. Concentration profile showing drug reaching the posterior segment for a Central deposit (a)Diffusion case at t=2.7 h (b) Convection enhanced diffusion at t=0.5h.

4.2 Transscleral delivery:

The model drug anecortave acetate is placed in the scleral surface. The drug tansport for a time period of 30 minutes is simulated. Figure 2 shows the concentration profiles of transscleral drug depot for a period of 30 minutes. The difference between the two modes will be evident for long durations of drug deposit.

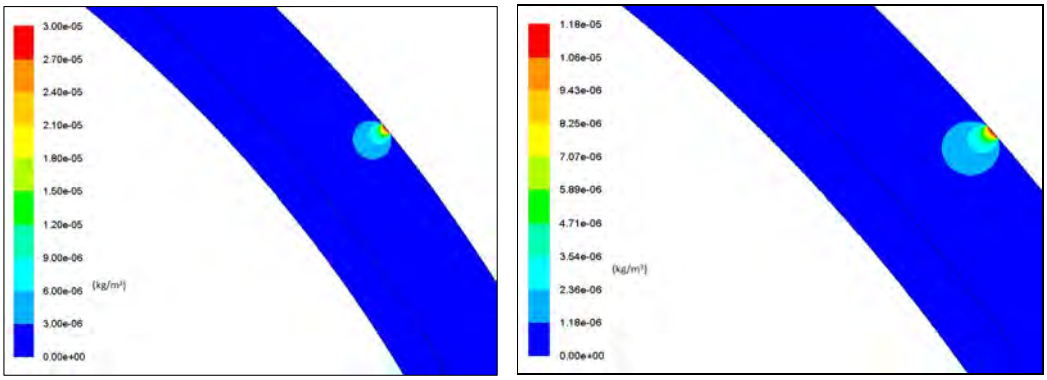

Figure 2. Concentration profile of drug during transscleral drug delivery (a) Injection (b) Implant for a period of 30 minutes after placement.

5.CONCLUSIONS

Numerical modeling of intravitreous and transscleral drug delivery were done in a two dimensional computational domain. Convection assisted intravitreous drug delivery showed enhanced drug transport compared to pure diffusion of drug in the vitreous. Transscleral delivery of direct drug injection and delivery from implant were simulated.

Comparison of all the methods of drug delivery will be made and experiments to simulate possible drug delivery methods will be attempted.

REFERENCES

[1] Gaudana, R. et al., Ocular drug delivery. The AAPS journal, 2010, 12, 348-60
[2] Thrimawithana, T. R. et al, Drug delivery to the posterior segment of the eye. Drug discovery today, Elsevier Ltd, 2011, 16, 270-7
[3] Edelhauser, H. F. et al., Ophthalmic drug delivery systems for the treatment of retinal diseases: basic research to clinical applications. Investigative ophthalmology & visual science, 2010, 51, 5403-20
[4] Ambati, J. and Adamis, A. P. Transscleral drug delivery to the retina and choroid Progress in Retinal and Eye Research, 2002, 21, 145-151
[5] Narasimhan, A. and Sundarraj, C, Effect of choroidal blood perfusion and natural convection in vitreous humor during transpupillary thermotherapy (TTT), International Journal for Numerical Methods in Biomedical Engineering, 29(4),530–541, 2013
[6] Jayakrishna Ambati, Transscleral Drug Delivery to the Retina and Choroid, Intraocular Drug Delivery, Taylor and Francis, Ch.13, 193-202, 2006
[7] Ricardo A. Pontes de Carvalho et al., Delivery from Episcleral Exoplants, Investigative Ophthalmology & Visual Science, Vol. 47, No. 10, 2006
[8] Jyoti Kathawate and Sumanta Acharya, Computational modeling of intravitreal drug delivery in the vitreous chamber with different vitreous substitutes, *International Journal of Heat and Mass Transfer*, 51, 5598–5609, 2008
[9] Sundarraj,C and Narasimhan,A, Convection enhanced intravitreous drug delivery, Proceedings of the 22nd National and 11th International ISHMT-ASME Heat and Mass Transfer Conference December 28-31, 2013, IIT Kharagpur, India, HMTC1300187
[10] Narasimhan, A and Sundarraj,C, Convection enhanced intravitreous drug delivery, Biomech and jour. mechan. biology,2014, under review

Third International Conference on Computational Methods for Thermal Problems
THERMACOMP2014, June 2-4, 2014, Lake Bled, Slovenia
N. Massarotti, P. Nithiarasu and B. Sarler (Eds.)

Simulation of HIFU Heating in Solid Tumour: Comparison of Different Temperature Control Modes

Wenbo Zhan, Xiao Yun Xu*
Department of Chemical Engineering, South Kensington Campus
Imperial College London, UK
yun.xu@imperial.ac.uk

ABSTRACT

Three different temperature control modes used in high intensity focused ultrasound (HIFU) heating of solid tumour are compared in this study. Results show that the control mode with an independent temperature monitor for each focused region is effective in achieving a rapid temperature rise and maintaining a stable temperature level in tumour.

Key Words: *Bio-heat Transfer, HIFU Heating, Cancer Therapy.*

1. INTRODUCTION

Delivery of anticancer drugs via specially designed nanoparticle drug carriers (e.g. thermo-sensitive liposomes) is an important attempt to overcome some of the drawbacks associated with standard chemotherapies, such as side effects caused by high drug concentration in normal tissue and insufficient drug delivery to tumour interior. In thermo-sensitive liposome-mediated delivery, drug cannot be released until tissue temperature is raised above the phase transition temperature of the liposome. High intensity focused ultrasound (HIFU) is a non-invasive, highly effective and reliable method of heating which can be applied locally to trigger the release of encapsulated drug.

For thermo-sensitive liposome-mediated drug delivery to be used in cancer treatment, it is necessary to keep the tumour temperature within a narrow mild hyperthermia range which should not exceed 45 ^{o}C [1]. Experimental work shows that the most effective drug release takes place at around 42 ^{o}C [2]. In order to achieve a target temperature range, a feedback system with an appropriate temperature control mechanism must be incorporated into the heating device. In the present study, a mathematical bio-heat transfer model is developed and applied to an idealized tumour model. The aim is to quantify the effect of temperature control mode on the spatial and temporal distributions of tissue temperature by HIFU heating.

2. Methods

A computational model is developed which incorporates the key physical and biological processes involved in the transport and release of thermo-sensitive liposomal drugs. These include the propagation of acoustic energy generated by a single element ultrasound transducer, heat absorption by blood, tumour and normal tissues, as well as heat transfer between these compartments.

Tissue and blood temperatures (T) can be calculated by solving the following energy balance equations

$$\rho_t c_t \frac{\partial T_t}{\partial t} = k_t \nabla^2 T_t - \rho_b c_b w_b (T_t - T_b) + q_t \tag{1}$$

$$\rho_b c_b \frac{\partial T_b}{\partial t} = k_b \nabla^2 T_b + \rho_b c_b w_b (T_t - T_b) - \rho_b c_b w_b (T_b - T_n) + q_b \tag{2}$$

where ρ is density, c is specific heat and w is the perfusion rate of blood flow. Ultrasound power deposition is denoted by q, and subscripts b and t represent blood and tissue, respectively. T_n is the normal body temperature, which is assumed to be 37 ˚C in this study.

Assuming negligible non-linear propagation, the ultrasound power deposition per unit volume can be considered to be proportional to the local acoustic intensity I_a as follows

$$q = 2\alpha I_a = \alpha p^2 / \rho v \tag{3}$$

where α is the absorption coefficient, v is the speed of ultrasound waves, and p is the acoustic pressure which is represented by the real part of the following equation, where k refers to the acoustic velocity potential.

$$p = ik\rho v\psi \tag{4}$$

The acoustic velocity potential, Ψ, can be evaluated based on the geometry of the ultrasound radiator using the method described in [4].

The model is applied to an idealised tumour geometry with six focused regions. The duration of sonication is 1.0 second for each of the focused region, and the six regions are heated sequentially. To maintain a desired temperature range over the treatment period, a temperature controller needs to be implemented which is capable of adjusting power input based on the maximum temperature in the heated region (T_{max}).

Three temperature control modes are simulated and compared; details of these are given below.

Range Control (RC)

To ensure T_{max} in the range 42±0.5 ^{o}C, the ultrasound transducer is controlled as follows:

$$\begin{aligned} T_{max}(t) &< 41.5\ ^{o}\text{C, the transducer is switched on} \\ T_{max}(t) &> 42.5\ ^{o}\text{C, the transducer is switched off} \end{aligned} \tag{6}$$

Proportional-Integral (PI) Control

The transducer power is timed by the PI controller output (P) temporally according to the following equation

$$P(t) = k_p\left[T_{target} - T_{max}(t)\right] + k_i \sum \left[T_{target} - T_{max}(t)\right] \tag{7}$$

here k_p and k_i are PI control parameters, which are set as 5.0 and 0.006 respectively [3].

In Mode 2, the maximum temperature in each of the focused region is monitored by an independent controller during the entire heating period, whereas there is only one PI controller in Mode 3. The output is cleared when the transducer moves to the next focused region.

3. RESULTS

Equations governing the acoustic pressure propagation and heat transfer, together with the controllers described above are solved numerically. The maximum and spatial mean temperature profiles in the tumour are compared for different temperature control modes.

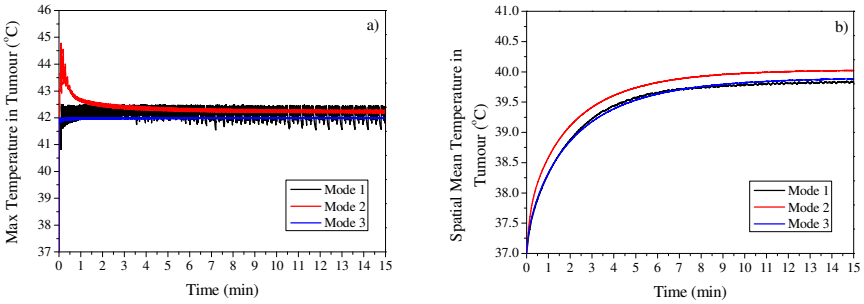

Figure 1. Variations of tumour temperature with time for different temperature control modes. a) max temperature, and b) spatial-mean temperature

The maximum temperature in tumour presented in Figure 1a shows that all the simulated temperature control modes can effectively raise the maximum temperature to the target level within a short time. As expected, T_{max} oscillates in the specified range (41.5~42.5°C) with Mode 1. Since the PI control output will continue to rise while other regions are being heated in Mode 2, T_{max} may jump to a high level in the first few seconds which will then fall to and sustain at a low level after self-adjustment. Comparison of spatial-mean temperature in tumour is presented in Figure 1b. Results show that the spatial-mean temperature reaches a steady level after approximately 7 to 8 minutes. This is because 1) the maximum temperature is maintained within a narrow range by temperature control, and 2) a steady state is established for heat transfer between blood and tissue. Results also show that Mode 2 leads to higher average temperature in tumour.

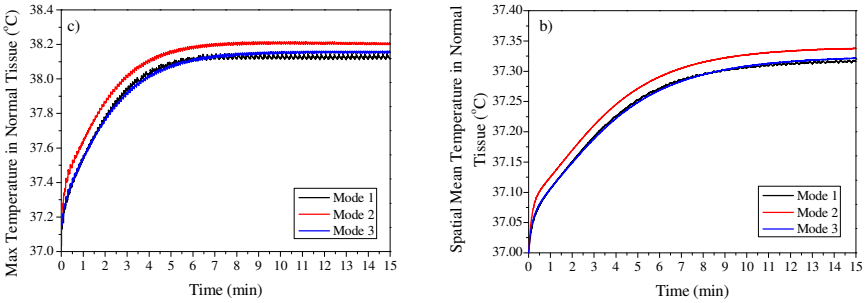

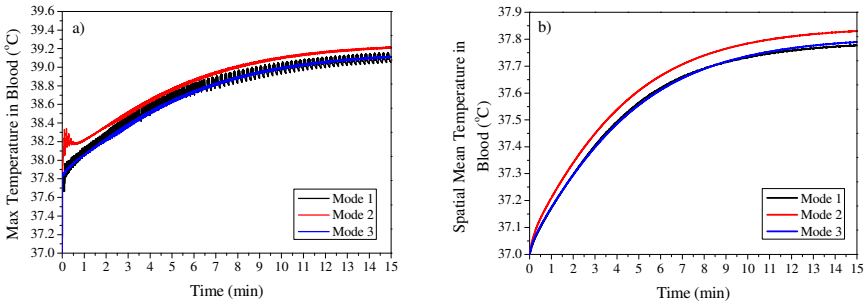

Figure 2. Variations of temperature in blood and normal tissue with time for different temperature control modes. a) max and b) spatial-mean temperature in normal tissue, and c) max and d) spatial-mean temperature in blood

The maximum and spatial-mean temperatures in normal tissue and blood are shown in Figure 2. Results show that all the temperature profiles reach a constant level after a certain period of time, and Mode 2 leads to higher temperature in both blood and normal tissue than the other temperature control modes.

4. CONCLUSIONS

This numerical study is concerned with the comparison of temperature profiles obtained with different temperature control modes in HIFU heating of solid tumour. Results show that the region-dependent proportional-integral control is more effective than the other modes at achieving faster temperature elevation and maintaining a higher stable temperature level in tumour.

REFERENCES

[1] S. Krishnan, D. Parmeswaran, and H.C. Sang, Nanoparticle-mediated thermal therapy: evolving strategies for prostate cancer therapy, *International journal of Hyperthermia* 26, 775-789, 2010.

[2] T. Tagami, J.P. May, M.J. Ernsting, and S.D. Li, A thermosensitive liposome prepared with a Cu^{2+} gradient demonstrates improved pharmacokinetics, drug delivery and antitumor efficacy. *Journal of Controlled Release*, 161, 142-149, 2012.

[3] R. Staruch, R. Chopra, and K. Hynynen, Localised drug release using MRI-controlled focused ultrasound hyperthermia, *International Journal of Hyperthermia*, 27, 156-171, 2010.

[4] H.T. O'Neil, Theory of focusing radiators, *The Journal of the Acoustical Society of America*, 21 516~526, 1949.

MINI-SYMPOSIUM

NUMERICAL MODELING OF SYSTEMS FOR THE EXPLOITATION OF LOW ENTHALPY GEOTHERMAL ENERGY SOURCES

MINI-SYMPOSIUM ORGANISED BY A. CAROTENUTO AND A. MAURO

Third International Conference on Computational Methods for Thermal Problems
THERMACOMP2014, June 2-4, 2014, Lake Bled, Slovenia
N. Massarotti, P. Nithiarasu and B. Sarler (Eds.)

THE IMPROVED MODEL CaRM FOR THE SIMULATION OF VERTICAL GROUND-COUPLED HEAT EXCHANGERS

Antonio Capozza
RSE SpA, Via Rubattino 54, 20134 Milano, Italy, antonio.capozza@rse-web.it
Angelo Zarrella, Michele De Carli
University of Padova, DII, Via Venezia 1, 35131 Padova, Italy, angelo.zarrella@unipd.it, michele.decarli@unipd.it

ABSTRACT

A model is presented to simulate the thermal processes in ground heat exchangers connected to ground-source heat pumps. The considered approach is based on the electrical analogy, for this reason named CaRM (CApacity Resistance Model). The model here presented allows to consider the fluid flow pattern along the classical vertical ground heat exchangers shaped as a single U-tube, a double U-tube, helix or coaxial pipes. Besides, ground temperature at different distances from borehole are calculated, taking into account also the thermal interference between more boreholes. Starting from the supply temperature to the heat exchanger, the outlet fluid temperature and the ground temperature are calculated in each node, step by step. The model has been validated and its exemplary use has been shown extensively with reference to a real plant.

Key Words: *Heat Transfer, heat pumps, geothermal systems, HVAC.*

1. INTRODUCTION

Ground-Source Heat Pump (*GSHP*) systems are a particular *HVAC* solution which relies on the ground as a low enthalpy heat source or sink.

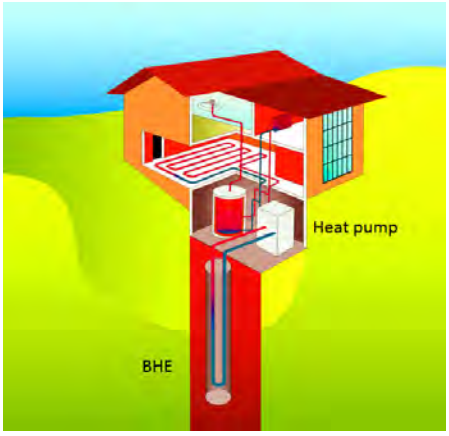

FIGURE 1. Scheme of a GSHP with vertical BHE

The most common solution is the *closed loop* system with vertically oriented borehole heat exchangers (*BHE* – see FIGURE 1), since they allow small land area requirements. The design of *BHE* is a crucial item, since an incorrect evaluation of its length strongly affects the energy efficiency and/or the investment costs of the whole plant system. This aspect was deemed crucial in

the perspective of a long-lived and efficient operation of the designed plants; the thermal behaviour of these systems has then to be designed thoroughly.
An analytical simulation tool is presented in this paper, aimed at assessing and optimising *GSHP* systems when alternative typologies and layouts are available for BHEs, with aims of evaluation and comparison.
The developed tool was validated in the past and it is now used to analyse the thermal behaviour of a real case study. In these particular conditions, the present paper quantifies the different expected plant performances versus three selected BHE geometries and two different horizontal layouts.

2. THE MODEL

Model CaRM, presented in Ref. [1], is based on the electrical analogy to solve the heat conduction equation under unsteady state conditions. For a homogeneous isotropic solid material whose thermal conductivity is independent of temperature T and within which no heat is generated, the heat conduction equation is:

$$\frac{\partial T}{\partial \tau} = \alpha \cdot \nabla^2 T \qquad (1)$$

where τ is the time and α is the thermal diffusivity of the material.
The thermal influence of the external air temperature, the incident solar radiation and the radiant heat exchange with the sky are considered. FIGURE 2 identifies three characteristic zones of the

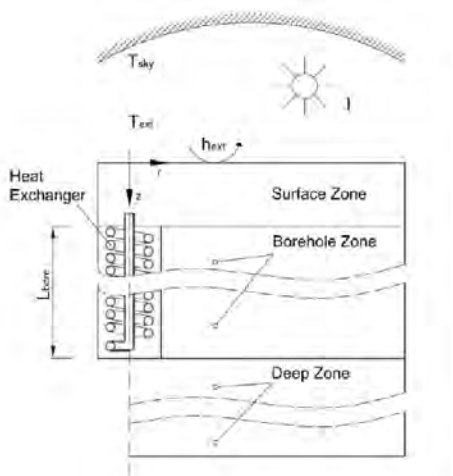

FIGURE 2. Modelling approach.

ground: the borehole zone, surrounding the heat exchanger; the surface zone, between the top of the heat exchanger and the ground surface where the boundary conditions are applied; the deep zone, beyond the end of the heat exchanger. The ground of the borehole zone is divided into m slices and each slice is consequently divided into n annular regions. Four possible geometries of GHE pipes are taken into account: single U-tube, double U-tube, coaxial pipe and helix pipe.
Further details on the adopted models and discretization criteria can be extensively found in Reff. from [1] to [4]. The developed CaRM software was widely validated against experimental data and results of acknowledged software (HEAT2, COMSOL), see [1][2].

3. ANALYSIS OF A REAL CASE

A real ground-source heat pump plant was then considered, devoted to heating and sanitary hot water supply to a residential building in North Italy. It entails from two to three floors, beside a ground floor hosting garages and cellars. The building dwells twelve middle-size lodges (about 80 m^2 each), which are supplied with central heating. The geothermal field is made up of 15 vertical single U-tube BHEs, whose depth is 100 m; the heat that the BHEs subtract yearly from the ground is about 118,000 kWh. Calibration was preliminarily performed on the thermal-physic ground and grouting parameters against the experimental results collected by RSE during the 2009-2010 operation [5]. The assumed ground thermal conductivity was 1.5 W/m K. Once this procedure was accomplished, a parametric analysis was carried out in order to exemplify the elective use of CaRM in refining an already designed plant, while comparing the performance of different geometries of the BHEs and different layouts of the BHE cluster.
The behaviour of the existing plant was considered over a period of two years, starting from undisturbed ground conditions of 15°C and assuming as forcing condition the measured time-history of the thermal power extracted from the ground. A careful tuning of the ground thermal-physical parameters was obtained in the first simulation, aimed at the best possible agreement with the experimental results. The time-history of the output temperature of the heat carrier fluid leaving the BHE is shown for this simulation in FIGURE 3. The values of the temperature Tg_m of the ground at 1.3 m from the BHE axis, averaged over the BHE depth, are shown in the same figure as well.

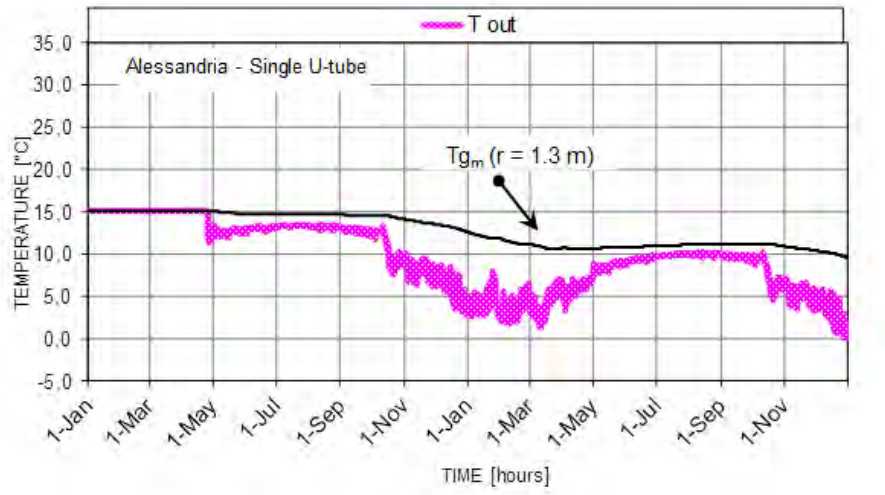

FIGURE 3**.** CaRM tuning simulation of Alessandria geothermal field

The parametric analysis was then performed assuming a double U-pipe or a helix geometry for the BHEs (in the latter case, a depth H of 50 m and a helix pitch of 0.1 m were assumed). For each of the three above geometries, a pipe-to pipe distance $d_{p\text{-}p}$ of 4.5 m and 9 m and a thermal conductivity λ_{grout} of 1.8 and 2.5 W/(m K) for the grouting were assumed. We remind that all the examined cases involve same behaviour of the forcing quantity, the thermal power delivered from the ground to the BHEs. The results are graphically summarized in FIGURE 4 in terms of maximum and minimum values of the temperature of the fluid entering the BHEs during the examined two transient years. It can be remarked that all the adopted BHE geometries show comparable quantitative behaviour as for maximum values, whereas the helix geometry leads to lower minimum values (then to actual

efficiency decrease of the related heat pump). Conversely, a substantial upgrading of the performance is originated by the increase of the pipe-to-pipe distance from 4.5 m to 9 m, as well as some improvement can be expected adopting a better conductive grouting.

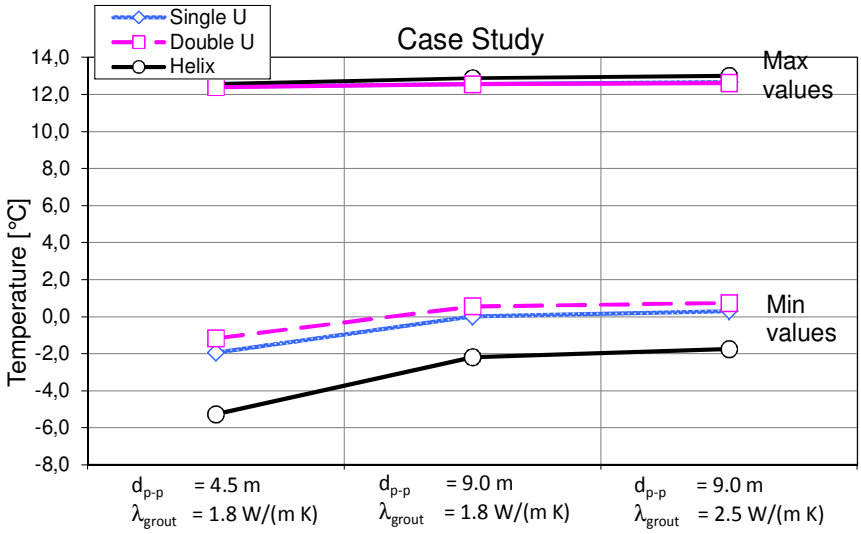

FIGURE 4**.** Results of parametric analysis

4. CONCLUSIONS

A simulation software of ground heat exchangers connected to ground-source heat pumps was set up and validated. The optimal use of a best-estimate software such as CaRM was outlined, consisting of a preliminary step of tuning operation and of proper detailed analyses of the influence of thermal physical and geometrical parameters, in view of expected improvements to a possible already existing rough draft design of the examined plant.

REFERENCES

[1] M. De Carli, M. Tonon, A.Zarrella, R. Zecchin, *A computational capacity resistance model (CaRM) for vertical ground-coupled heat exchangers*, Renewable Energy 35 (2010) 1537–1550.

[2] A. Zarrella A, Scarpa M, De Carli M. *Short time step analysis of vertical ground coupled heat exchangers: the approach of CaRM.* Renew Energy 2011;36(9):2357–67.

[3] A. Zarrella, A. Capozza, M. De Carli, *Analysis of short helical and double U-tube borehole heat exchangers: A simulation-based comparison*, Applied Energy 112 (2013) 358–370.

[4] A. Zarrella, A. Capozza, M. De Carli, *Performance analysis of short helical borehole heat exchangers via integrated modelling of a borefield and a heat pump: A case study*, Applied Thermal Engineering 61 (2013) 36-47

[5] F. Bazzocchi, L. Croci, *Monitoraggio delle prestazioni energetiche di impianti di climatizzazione*, RSE report, 1300058, 2013

Third International Conference on Computational Methods for Thermal Problems
THERMACOMP2014, June 2-4, 2014, Lake Bled, Slovenia
N. Massarotti, P. Nithiarasu and B. Sarler (Eds.)

MODELING GROUND-SOURCE HEAT EXCHANGERS: A REVIEW

Alberto Carotenuto, Michela Ciccolella, Nicola Massarotti, Alessandro Mauro
Dipartimento di Ingegneria, University of Naples "Parthenope", Centro Direzionale, Isola C4, 80143 Naples, Italy,
alberto.carotenuto@uniparthenope.it, michela.ciccolella@uniparthenope.it, massarotti@uniparthenope.it, alessandro.mauro@uniparthenope.it

ABSTRACT

The need to increase energy efficiency for heating and cooling has promoted the development of Ground-Source Heat Pumps; in particular a large number of vertical ground-coupled heat pumps have been installed thanks to their high energy efficiency and little land area requirement. This work, presents an overview of the numerical models available for the thermo-fluid dynamic phenomena which occur in the surroundings of Ground Heat Exchangers (GHEs). After a brief introduction on the subject, the available analytical and numerical models are summarized, underlining recent developments in modeling approach.

Key Words: *Ground-Source Heat Pump systems*, *numerical modeling*, *heat transfer*

1. INTRODUCTION

In this work models available for the simulation of heat transfer phenomena in surroundings of Ground-Source Heat Pumps (GSHP) systems are analyzed. GSHP systems use the ground as heat source/sink to provide space heating and cooling. These systems can be basically grouped into three categories according to ASHRAE [1]: (1) Surface Water Heat Pump (SWHP) systems, (2) Ground-Water Heat Pump (GWHP) systems and (3) Ground-Coupled Heat Pump (GCHP) systems. Among different GSHP systems, vertical GCHP have attracted the greatest interest in research and practical engineering, due to its advantages in terms of less land requirements and wide range of applicability. Several literature reviews on the GCHP technology have been produced; a recent overview on the subject is given by Yang's work [2].

2. ANALYTICAL MODELS

As a correct analysis of thermal response of ground surrounding GHE is crucial for the design of GCHP systems, several models of different complexity have been developed for the design and performance prediction of the GHEs. The earliest analytical approach is the Kelvin's line-source model (LSM), i.e. the infinite source line (ref. 2 of [2]). The ground is considered as an infinite medium with an initial uniform temperature and the borehole is treated as an infinite line source. This one-dimensional model, characterized by simplicity and low computing time, can only be applied to small pipes within a narrow time from few hours to months. Later, Ingersoll et al. (ref. 14 of [2]) developed the infinite cylindrical source model (CSM), applying the mathematical results of Carslaw and Jaeger (ref. 18 of [2]) to boreholes (BHE). Assuming an infinite length of the BHE, axial effects are neglected, with an effect on long term simulations. The need for a correct prediction of GCHP performance during all its technical life has promoted the development of new analytical models which take into account the finite length of boreholes. Claesson and Eskilson (ref. 40 of [2]), first, developed an analytical model in which the borehole is approximated as a linear heat source of finite length H, buried into a semi-infinite homogeneous and isotropic medium; a constant heat transfer per unit length rate is assumed. The solution is obtained starting from the solution for the point heat source developed by Carslaw and Jaeger (ref. 18 of [2]), by assuming that finite line source is composed of series of point sources; to take into account the ground surface boundary the method of images is applied, by considering a "virtual" line source of length H, located symmetrically above the line sink, with an opposite heat transfer rate per unit length. The same model is studied by Zeng et al. (ref. 24 of [2]) for long-term analysis of a GCHP and recently, Lamarche and Beauchamp [3] suggested improvements to the solution of Finite Line Source (FLS) models to decrease computational burden. Another improvement has been recently proposed by Bandos et al. [4]: in their model, these authors take into account also the geothermal gradient and seasonal variations of ground surface temperature. In order to analyze the thermal response of ground in presence of inclined boreholes, Cui et al. [5] developed a new tridimensional analytical solution by applying the same approach of Eskilson's work (ref. 40 of [2]) to an inclined line source. All analytical models previously considered, neglect the effect of groundwater flow. Sutton et al. [6], developed an analytical

model which considers groundwater advection, through the classical LSM assumptions with a constant fluid velocity; the solution is obtained observing that advection-conduction equation is the same in mathematical formulation as the conduction equation with a moving heat source when an equivalent velocity, veff , replaces the moving speed of the heat source. Solution in polar coordinate is given in Carslaw and Jaeger (ref 18 of [2]). A same model is used by Diao et al. [7]; an improvement was given by Molina-Giraldo et al. [8] by considering also the finite length of the BHE. Classical analytical solutions are applicable with a good approximation to boreholes, which are characterized by a small value of the ratio radius/length, but fail in modeling geothermal piles which are much thicker in diameter but shorter in depth as pile thermo-physical properties become significant in the global heat transfer process. Man et al. [9] developed a new analytical cylindrical solution for modeling geothermal piles with spiral coils, which are usually disposed in the proximity of the pile circumference. The new "solid" cylindrical heat source model, considers the cylinder no longer as an empty cavity, but filled with a medium equal to that out of the cylinder, so that the whole infinite domain is composed of a homogeneous medium. A one-dimensional solution is obtained considering an infinite medium; in order to take into account axial effects, a two-dimensional solution is obtained by considering the finite length of the cylindrical source and the ground surface boundary, by using the method of images. An improvement of this model was been later proposed by Cui et al. [10] and Man et al. [11] , in order to take into account the geometrical characteristics of the spiral coils, which determines that the temperature distribution fluctuates significantly along the axial direction in the vicinity of the cylindrical surface due to the particular spatial distribution of the heat source. Both models consider the cylinder filled with a medium identical to that out of it; in reference [10], the spiral coils buried in the pile, are simplified as a number of separated rings on the cylindrical surface of radius rb, with the pitch b being coincident with z-axis. Two analytical models are developed, considering first an infinite ring-coils source buried into an infinite medium and then the finite length of the heat source. The model proposed by Man et al. [11] gives a better approximation of the real geometry of the spiral coil which is modeled as a spiral line heat source of infinite length, that emits heat at intensity $q_l b$ for each pitch section. The tridimensional analytical solution, written in a r-φ-z coordinate system is obtained by applying the Green's function theory; then, the finite length of the heat source is considered by using the method of images. Recently, Li and Lai [12] proposed a modification of the classical heat point source solution, in order to take into account the anisotropy of the medium; by applying the Green's function theory, analytical solutions for line, cylindrical and spiral-line heat sources of finite or infinite length are obtained for application to pile and borehole buried into an anisotropic medium. To take into account the heat capacity of borehole and pile heat exchanger, the authors developed a second model [13] in which each pipe of the U-tube is considered as a finite line source in a composed medium. Finally, Zhang et al. [14] considered the effects of groundwater advection on an energy pile foundation; the solution is obtained by combining the approaches used by Molina-Giraldo [8] et al. and by Man et al. [9].

3. NUMERICAL MODELS

Although analytical models allow to use minimal computational time, these cannot model the spatial complexity of a geothermal heat exchanger and they fail in predicting short-time response. For this reason, several numerical models of different complexity have been developed for the design and performance prediction of the GHEs. Most of the developed models analyze heat transfer mechanisms by considering two separated regions: one is the solid soil/rock outside the borehole, where the heat conduction and advection occur and the other one is the region inside the borehole, including grout, the U-tube pipes and the circulating fluid inside the pipes. This region is both analyzed under steady-state or quasi-steady-state conditions, and in transients. The analyzes on the two spatial regions are linked at the borehole wall, and the assumption of a steady-state heat transfer in the region inside the borehole has been proved appropriate and convenient for most engineering applications, except for dynamic responses within a few hours. The interconnection between the two sub-domains, soil and BHE is realized by imposing a Neumann condition on the borehole wall; this imposed heat flux is related to the thermo-physical properties of the BHE through a parameter, called borehole thermal resistance; an overview on the different methods of calculation for this coefficient is given by Lamarche et al. [15].

The first numerical models solve heat conduction equation in soil domain, for long-term performance analysis of the system; an example is given in [16]. In order to take into account the effects of groundwater advection, first, Chiasson et al. [17] studied diffusion-advection equation coupled to fluid mass conservation law, considering four-by-four configuration for the borehole field.

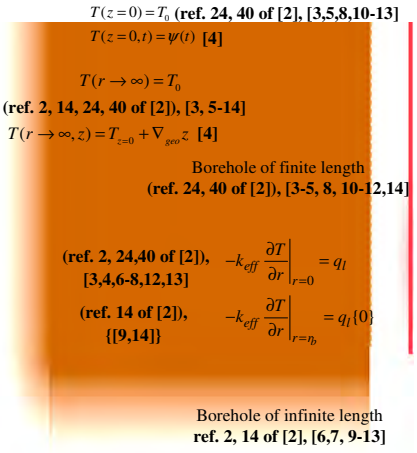

FIGURE 1. Reference geometry and boundary conditions for analytical models.

Model equation:	Heat conduction equation **(ref. 2, 14,24,40 of [2]), [3-5,9-12]** Heat advection-conduction equation **[6-8, 13]**
Solution Type:	1-D: T(r,t) **(ref. 2,14 of [2]), [9,12]** 2-D: T(r,z,t) **(ref. 24, 40 of [2]), [3,4,10]** 2-D: T(r,θ,t) **[6,7,13]** 3-D: T(x,y,z,t) **[5]** 3-D: T(r,θ,z,t) **[8,11,12,14]**
General characteristics	BHE or pile foundation is approximated by a straight **(ref. 2, 24, 40 of [2]),[3,4,6-8,12,13],** helical **[10,11]** or inclined **[5]** line heat source or by a hollow **(ref. 14 of [2])** or solid **[9,12,14]** cylindrical heat source. Source terms are introduced in **[4,8-10,12]**, using a Delta of Dirac function.
Domain properties:	The whole domain is treated as an homogeneous, isotropic medium in all analytical works; only Li et Lai consider and anisotropic medium in **[12]** and a composite medium in **[13].**
Verification and Validation:	All the models lack of an experimental validation; a numerical verification is conducted with a comparison with Eskilson's g-function **[3,4]** or with classical analytical models **[6,7,11,13].** A comparison with numerical model is conducted in **[8,9]**.

TABLE 1. Characteristics of analytical models.

Fan et al. [18] solved the advection-conduction equation for a borehole field in an integrated soil cold storage and ground-source heat pump, considering the latent heat due to phase changes, the transient heat transfer through the pipe wall and the convective transfer between the working fluid and the pipe wall; a constant groundwater velocity is assumed and an equivalent single straight pipe is assumed to represent the actual U-shape. The effects of both direction and rate of groundwater flow on the performance of various type of BHE arrays are taken into account in the model of Choi et al. [19]. This two-dimensional coupled heat conduction-advection model is written considering a numerical domain in which the BHE is not included; heat transfer inside the borehole is assumed to be steady. In recent years, there has been a great interest in the three-dimensional modeling of borehole and its surroundings, as it offers most generality and potentially most accurate representation of heat transfer. Lee developed two three-dimensional models for the analysis of heat conduction process [20] and groundwater heat advection [21] in presence of multiple ground layers. Li and Zheng [22] solved the heat conduction equation in the soil and the grout and energy balance equation for the working fluid referring to a three-dimensional polar system, assuming a vertical physical symmetry plane passing through the centers of the pipes so that only half of the bore-field is modeled; conductive heat transfer along the fluid channels is neglected. The inlet temperature of the U-tube is imposed as a boundary condition, so that conjugate heat transfer occurring between the fluid in the pipes and the soil around it and between the two pipes of the U-tube are considered all together. A fully three-dimensional model is proposed by Florides et al. [23] ; this model is solved with FlexPDE software package and takes into account also heat conduction through the pipe-wall and the presence of a multiple-layers substrate. Finally, three-dimensional models for the analysis of heat advection-conduction equations have been proposed by Nabi and Al-Khoury [24-25] and Rees and He [26]. As the numerical simulation requires long computational time and a large CPU memory, reduced models have been developed by Kim et al. [27] starting from a two-dimensional and a three-dimensional numerical models; only heat conduction is taken into account and the state model size reduction technique is applied, using the linear aggregation method.

4. CONCLUSIONS

During the past few decades, a large number of geothermal heat pumps have been largely applied thanks to their efficiency and low CO2 emissions. Beside, a large number of simulation tools and analytical and numerical models have been developed since the 1970's. In this paper, a review on the subject has been underlined that recent researches are focused on the development of analytical tools for coupled modeling of BHE and surrounding ground to overcome inaccuracies due to the common approximations of the initial

models. Existing numerical models are based on a two-region simulation approach that generally neglect the real geometry of the BHE, the presence of which is taken into account by an overall thermal resistance. In order to evaluate the errors introduced in two-dimensional numerical models, in the recent years a number of three-dimensional numerical models have been developed, which take into account not only heat conduction but also the heat transfer due to groundwater advection and the heat convection inside the pipes. Although the great development of the numerical modeling of GCHP systems, authors note a lack of interest in the numerical investigation of convective phenomena which involve groundwater-filled boreholes and, according to authors' opinion, a great interest should be given to the development of reduced models which are able to take into account not only the heat conduction but also groundwater advection.

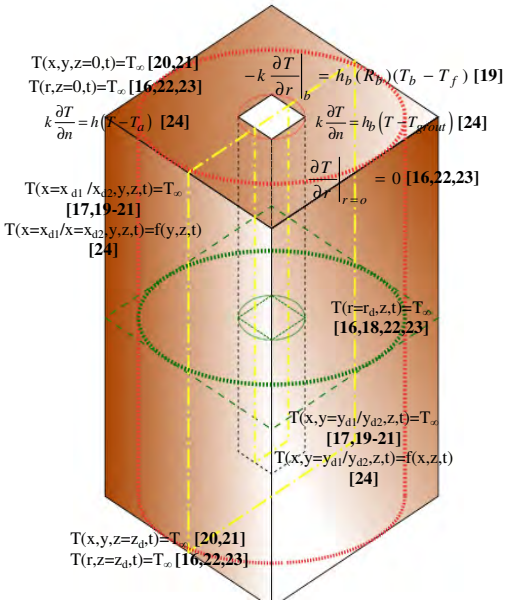

FIGURE 2. Reference geometry and boundary conditions for numerical models.

Analyzed equation:	Heat conduction equation **[16,20,22,23]** Heat advection-conduction equation **[18, 24-26]** coupled to fluid flow equation **[17,19,21]**
Solution Type:	2-D: T(r,z,t) **[16]** 2-D: T(r,θ,t) **[18]** 2-D: T(x,y,t) **[17,19]** 3-D: T(x,y,z,t) **[20,21,24-26]** 3-D: T(r,θ,z,t) **[22,23]**
Spatial discretization	The finite difference technique is applied in **[16,20,21]**; finite element discretization is applied in **[17,19,22,23]** while a finite volume discretization is applied in **[18,24,26]**.
Domain properties:	The whole domain is treated as an homogeneous, isotropic medium in all numerical models presented here; only Lee and Lam **[20,21]** and Florides et al. **[23]** consider an anisotropic medium
Borehole modeling	The presence of borehole is taken into account introducing a source term in **[16-18,20,21]**; a boundary condition of an imposed heat flux related to a borehole thermal resistance R_b is applied in **[19]**. Finally, the temperature field inside the borehole is an output of the model in **[22,26]**: in these models, thermo-physical properties of borehole are taken into account and the inlet temperature of work fluid is set as a boundary condition or setting a constant ΔT between inlet and output work fluid temperature **[23]**. A model for the borehole is developed by **[24]**.
Verification and Validation:	An experimental validation is conducted by **[16,22,23,25,26]**; a numerical verification is conducted with a comparison with TRNSYS' model, TRNVDSTP **[20]** or with other commercial software **[21]** or with classical analytical solutions **[19,25]**. Any validation or verification is conducted in **[17,18]**

TABLE 1. Characteristics of numerical models.

ACKNOWLEDGMENTS

The authors gratefully acknowledge the financial support of Poligrid "Smart Grid con Sistemi di Poligenerazione Distribuita" and FC Smartgen "Fuel Cell and Smart Hybrid Generation from fossil and renewable sources" projects.

REFERENCES

[1] ASHRAE, *ASHRAE handbook, HVAC applications*, Atlanta, ASHRAE Inc. (2011).

[2] H. Yang, P. Cui, Z. Fang, *Vertical borehole ground-coupled heat pumps: A review of models and systems*, Applied Energy 87 (2010), 16-27.

[3] L. Lamarche, B. Beauchamp, *A new contribution to the finite line-source model for geothermal boreholes*, Energy and Buildings 39 (2007) 188-198.

[4] T. V. Bandos, A. Montero, E. Fernandes, J. L. G. Santander, J. M. Isidro, J. Perez, P. J. Fernandez de Cordoba, J. F. Urchueguía, *Finite line-source model for borehole heat exchangers: effect of vertical temperature variations*, Geothermics 38 (2009) 263-270.

[5] P. Cui, H. Yang, Z. Fang, *Heat transfer analysis of ground heat exchangers with inclined boreholes*, Applied Thermal Engineering 26 (2006) 1169-1175.

[6] M. G. Sutton, D. W. Nutter, R. J. Couvillion, *A Ground Resistance for Vertical Bore Heat Exchangers With Groundwater Flow*, Journal of Energy Resources Technology – Transactions of ASME 125 (2003), 183-189.

[7] N. Diao, Q. Li, Z. Fang, *Heat transfer in ground heat exchangers with groundwater advection*, International Journal of Thermal Sciences 43 (2004) 1203–1211.

[8] N. Molina-Giraldo, P. Blum, K. Zhu, P. Bayer, Z. Fang, *A moving finite line source model to simulate borehole heat exchangers with groundwater advection*, International Journal of Thermal Sciences 50 (2011), 2506-2513.

[9] Y. Man, H. Yang, N. Diao, J. Liu, Z. Fang, *A new model and analytical solutions for borehole and pile ground heat exchangers*, International Journal of Heat and Mass Transfer 53 (2010) 2593-2601.

[10] P. Cui, X. Li, Y. Man, Z. Fang*, Heat transfer analysis of pile geothermal heat exchangers with spiral coils*, Applied Energy 88 (2011) 4113-4119.

[11] Y. Man, H. Yang, N. Diao, P. Cui, L. Lu, Z. Fang, *Development of spiral heat source model for novel pile ground heat exchangers*, HVAC&R Research 17 (2011), 1075-1088.

[12] M. Li, C. K. Lai, *Heat-source solutions to heat conduction in anisotropic media with application to pile and borehole ground heat exchangers*, Applied Energy 96 (2012), 451-458.

[13] M. Li, C. K. Lai, *New temperature response functions (G functions) for pile and borehole ground heat exchangers based on composite-medium line-source theory*, Energy 38 (2012) 255-263.

[14] W. Zhang, H. Yang, L. Lu, Z. Fang, *The analysis on solid cylindrical heat source model of foundation pile ground heat exchangers with groundwater flow*, Energy 55 (2013) 417-425.

[15] L. Lamarche, S. Kajl, B. Beauchamp, *A review of methods to evaluate borehole thermal resistances in geothermal heat-pump systems*, Geothermics 39 (2010) 187-200.

[16] Y. Bi, L. Chen, C. Wu, *Ground heat exchanger temperature distribution analysis and experimental verification*, Applied Thermal Engineering 22 (2002) 183-189.

[17] A. D. Chiasson, S. J. Rees, J.D. Spitler, *A preliminary assessment of the effects of groundwater flow on closed-loop ground-source heat pump systems*, ASHRAE Trans. 106 (2000) 380–393.

[18] R. Fan, Y. Jiang, Y. Yao, D. Shiming, Z. Ma, *A study on the performance of a geothermal heat exchanger under coupled heat conduction and groundwater advection*, Energy 32 (2007) 2199–2209.

[19] Jung Chan Choi, Joonsang Park, Seung Rae Lee, *Numerical evaluation of the effects of groundwater flow on borehole heat exchanger arrays*, Renewable Energy 52 (2013) 230-240.

[20] C. K. Lee, *Effects of multiple ground layers on thermal response test analysis and ground-source heat pump simulation*, Applied Energy 88 (2011) 4405-4410.

[21] C.K. Lee, H.N. Lam, *A modified multi-ground-layer model for borehole ground heat exchangers with an inhomogeneous groundwater flow*, Energy 47 (2012) 378-387.

[22] Z. Li, M. Zheng, *Development of a numerical model for the simulation of vertical U-tube ground heat exchangers*, Applied Thermal Engineering 29 (2009) 920–924.

[23] G. A. Florides, P. Christodoulides, Panayiotis Pouloupatis, *Single and double U-tube ground heat exchangers in multiple-layer substrates*, Applied Energy (2012).

[24] M. Nabi, R. Al-Khoury, *An efficient finite volume model for shallow geothermal systems. Part I: Model formulation*, Computers & Geosciences 49 (2012) 290–296.

[25] M. Nabi, R. Al-Khoury, *An efficient finite volume model for shallow geothermal systems. Part II: Verification,validation and grid convergence*, Computers & Geosciences 49 (2012) 297–307.

[26] S. J. Rees, M. He, *A three-dimensional numerical model of borehole heat exchanger heat transfer and fluid flow*, Geothermics 46 (2013) 1– 13.

[27] E. J. Kim, J. J. Roux, G. Rusaouen, F. Kuznik, *Numerical modelling of geothermal vertical heat exchangers for the short time analysis using the state model size reduction technique*, Applied Thermal Engineering 30 (2010) 706–714.

Third International Conference on Computational Methods for Thermal Problems
THERMACOMP2014, June 2-4, 2014, Lake Bled, Slovenia
N. Massarotti, P. Nithiarasu and B. Sarler (Eds.)

NUMERICAL SIMULATION OF A GROUND SOURCE HEAT PUMP COUPLED TO A DESICCANT WHEEL

Giovanni Angrisani, Giuseppe Diglio, Maurizio Sasso
DING, Department of Engineering, Università degli Studi del Sannio, Piazza Roma 21, 82100 Benevento, Italy, E-mail addresses: giovanni.angrisani@unisannio.it; diglio@cheapnet.it; sasso@unisannio.it

ABSTRACT

Ground Source Heat Pump (GSHP) coupled with a Micro Combined Cooling, Heating and Power (MCCHP) system, consisting of a hybrid desiccant-based Air Handling Unit (AHU) and a microcogenerator is investigated in this paper. Software TRNSYS is used to simulate heat and fluid flow in a heat exchange system interacting with low enthalpy geothermal reservoirs.

Key Words: *Ground Source Heat Pump, Desiccant Wheel, TRNSYS.*

1. INTRODUCTION

Desiccant cooling systems (DCS) are air conditioning devices that can be seen as an alternative or as a supplement to traditional cooling dehumidification systems. For example, DCS can help to solve problems of electrical over-consumption in traditional vapour compression units. These systems comprise three main components: the dehumidifier, the regeneration heat source and the cooling device [1].

The dehumidifying device is often a wheel made of inert material coated with an adsorbent (Desiccant Wheel – DW). In order to ensure continuous operation of the system, the DW has to be regenerated; as consequence, two section of the wheel can be identified: a process section, through which air to be dehumidified passes, and a regeneration section, where water vapour is removed from the adsorbent medium by means of a dry air flow, heated up to a suitable temperature (from 60 °C up to 140 °C, depending on the adsorbent material and the desired humidity ratio reduction). Thermal energy required to heat regeneration air can be supplied as waste heat from cogenerators, or as solar thermal energy, typically integrated with an auxiliary fossil-fuelled system.

The desiccant dehumidification process is exothermic and determines a sensible heating of the air flow being dehumidified; hence it has to be cooled down to the supply thermal-hygrometric conditions required to handle the thermal loads [2].

At “Università degli Studi del Sannio”, in Benevento (Southern Italy), a desiccant Air Handling Unit (AHU) coupled to a natural gas-fired reciprocating internal combustion engine cogenerator (Micro Combined Heat and Power – MCHP), an electric chiller and a natural gas-fired boiler has been installed. The system is based on the dehumidification of outdoor air by a desiccant wheel and its subsequent cooling by the electric chiller.

Since the energy and environmental savings are maximized when DCS interact with renewable energy resources, this paper aims to simulate operation of the described system by substituting the installed air-cooled electric chiller with a Ground Source Heat Pump (GSHP). This coupling is not widespread, although in recent years countless systems of heat exchange with the ground have been tested, mainly because of the diffusion of heat pumps which have made the use of subsoil as reservoir of thermal energy economically viable.

2. NUMERICAL SIMULATION

The coupling of the DCS and the GSHP is investigated by TRNSYS software, that enables the dynamic simulation and analysis of transient systems. The model consist of components that interact with each other. The subsystem components included in the standard library are programmed in Fortran language. Each component has a unique TYPE number that relates this component to the Fortran subroutine to model it. Moreover, each component is represented by a number of parameters and time-dependent inputs, and produces time dependent outputs. The output of a specific component can be used as input to other components. TRNSYS has the capability of interconnecting system components in any desired manner.

The simulation model developed (Fig. 1) uses TMY weather data for the city of Naples (Type 109), while standard control models (type 14h, type 41a and type 141), combined with several external equations are employed to mimic ON/OFF control scheme of the boiler (type 6), heat pump (type 668) and desiccant wheel (type 683). Type 33e provides thermo-hygrometric properties of humid air. Types 91, 508f, 670, 506c and 744-1 mimic the operation of cross-flow heat exchanger, cooling coil, heating coil, humidifier and variable speed fan. The experimental calibration and validation of the main components of the AHU can be found in [3].

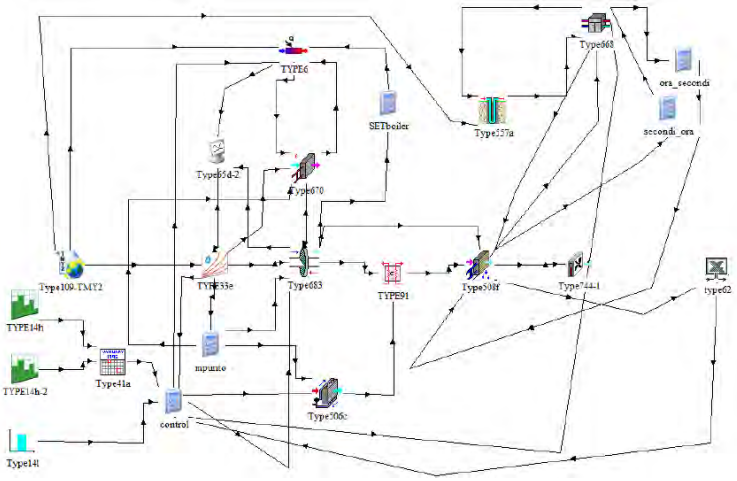

FIGURE 1. Simulation model of the system, in TRNSYS environment.

The vertical borehole heat exchangers is modelled using component type 557a of TRNSYS. This type uses the duct storage model (DST model) developed at Lund Institute of Technology in Sweden [4] which is incorporated in TRNSYS by Pahud and Hellström [5]. The storage volume has a cylindrical shape with rotational symmetry. There is convective heat transfer within the pipes and conductive heat transfer to the storage volume. The temperature of surrounding ground is calculated, using superposition methods, on three parts: a global temperature, a local solution and a steady-flux solution. The global and local problems are solved with the use of an explicit finite-difference method and the steady-flux solution is obtained analytically.

Considering average properties of the subsoil, relative to normal rocky subsoil, the method proposed by ASHRAE [6] to design vertical borehole heat exchangers was used. Thus, for type 557, considering double U-tube as heat exchangers type, the parameters reported in table 1 were used.

Distance between boreholes was set to 5 m and “reverse-return” was chosen as layout of boreholes. Pure water as heat carrier fluid inside the ground heat exchangers was used.

Parameters	Value	Unit
Storage volume	4976	m^3
Borehole depth	115	m
Number of boreholes	2	-
Borehole radius	0.132	m
Outer radius of U-tube	0.040	m
Inner radius of U-tube	0.037	m
Storage thermal conductivity	1.83	W/m·K
Storage heat capacity	$2.420 \cdot 10^6$	$J/m^3 \cdot K$

TABLE 1. Parameters used to simulate vertical borehole heat exchangers

The heat pump model is performance map-based. In particular, considering 8 kW as nominal cooling power of the water-to-water heat pump, data of cooling capacity and electric power drawn by the heat pump in cooling mode have been specified, considering various temperature of the fluids exiting the evaporator and the condenser.

Supply air conditions, after cooling coil, of 18 °C and 8 g/kg were set.

The simulation was carried out in the period 1st June – 15th September, assuming an activation schedule of the AHU from Monday to Friday, from 8:00 a.m. to 19:00 p.m.

3. RESULTS

In the initial period of June, free-cooling of process air exiting the DW allows to meet the cooling energy demand. The trend of the temperature of the geothermal source, that increase as thermal energy is transferred to the subsoil, and the external air, throughout the summer season, are shown in Fig. 2, while Coefficient Of Performance (COP) of GSHP, which reaches values up to about 6.0, are shown in Fig. 3. According to a typical thermo-economic analysis, the performances of a reference conventional system, constituted by the heat-led microcogenerator, that satisfies electric energy demand and provides thermal energy to regenerate the DW (with partial integration by the natural gas boiler), and by an air-cooled electric chiller for sensible cooling, [7], was compared to those of the alternative system (AS), whose only difference is that the air-cooled electric chiller is replaced with the GSHP. The average Italian power plant efficiency and equivalent CO_2 emission factor are 46.1% and 0.531 $kgCO_2/kWh_{el}$, respectively. Primary energy saving equal to 20.9% and reduction of equivalent CO_2 emission equal to 22.8% was obtained.

As regards the economic analysis, three scenarios were considered: incentives for MCHP system, (tax exemption on the purchase cost of natural gas), MCHP system without incentives, MCHP system with incentives and running at full electric power, with electric energy surplus exported to the electric grid. Results are shown in Fig. 4 in terms of yearly cash flow of the alternative system, with an extra installation cost of about 6'600 € for the AS. Economic feasibility can be achieved only in the case of the "full load with incentives" scenario, with a pay-back period of less than 12 years.

4. CONCLUSIONS

Ground Source Heat Pumps are very interesting, especially during the hot summer periods. The higher value of COP, greater than that of the conventional air-cooled electric chiller (about 2.5), is optimal for the interaction with air conditioning systems that integrate desiccant rotors. The system provides good performance in terms of primary energy savings and reduction of CO_2 emission, with respect to conventional systems. However, as in the investigated plant the GSHP is used only in summer, the economic feasibility is achieved only if economic incentives are considered and the MCHP runs at full electric power, with a quite long pay-back period is obtained (about 12 years).

The system must work also in winter, when the GSHP offers higher performance, to make the application more economically feasible.

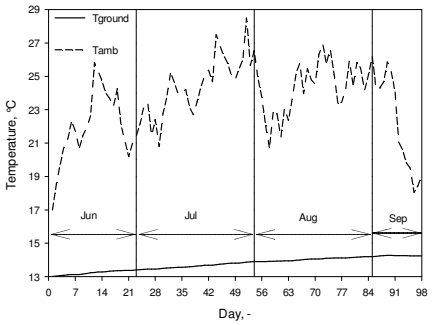

FIGURE 2. Geothermal source and air temperature

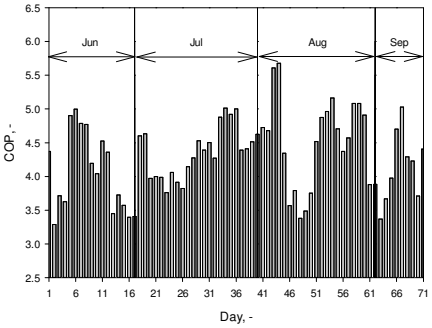

FIGURE 3. COP of GSHP

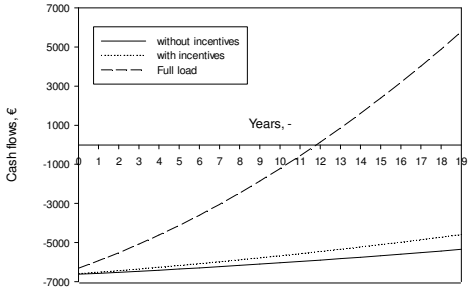

FIGURE 4. Economic analysis

REFERENCES

[1] G. Angrisani, Experimental and simulative analysis of a microtrigeneration system based on an air handling unit with desiccant wheel, *PhD Thesis*, 2011.

[2] M. Cargocaire, *The Dehumidification Handbook,* 2nd Edition, Amesbury, 1990.

[3] G. Angrisani, C. Roselli, M. Sasso, Experimental validation of constant efficiency models for the subsystems of an unconventional desiccant-based Air Handling Unit and investigation of its performance, Applied Thermal Engineering 33-34 (2012) 100-108.

[4] G. Hellström, Duct ground heat storage model, *Manual for Computer Code*, 44, 1989.

[5] D. Pahud, G. Hellström, L. Mazzarella, Duct ground heat storage model for TRNSYS (TRNVDST), *Laboratoire de systems énergétique,* 9, 1997.

[6] P. K. Kavanaugh, K. Rafferty, GROUND SOURCE HEAT PUMP – Design geothermal systems for commercial and institutional buildings, *ASHRAE*, 1997.

[7] G. Angrisani, C. Roselli, M. Sasso, F. Tariello, Dynamic performance assessment of a micro-trigeneration system with a desiccant-based air handling unit in Southern Italy climatic conditions, Energy Conversion and Management 80 (2014) 188–201.

Third International Conference on Computational Methods for Thermal Problems
THERMACOMP2014, June 2-4, 2014, Lake Bled, Slovenia
N. Massarotti, P. Nithiarasu and B. Sarler (Eds.)

ANALYSIS OF THE POSSIBLE THERMAL STORAGE WITH GROUND HEAT EXCHANGERS

M. De Carli, D. Favaretto, A. Galgaro, A. Zarrella
DFT, University of Padova, Via Venezia 1 – 35131, Italy
michele.decarli@unipd.it, diego.favaretto.1@studenti.unipd.it, antonio.galgaro@unipd.it, angelo.zarrella@unipd.it,

ABSTRACT

This work is the first stage of an analysis aiming to check the possible use of the ground as thermal storage. Two models (CaRM and COMSOL) have been used. Results have shown that, the thermal energy stored in the ground grows when the distance between the vertical ground heat exchangers increases. Once fixed the distance between the probes, the value of the thermal energy stored in the ground remains almost unchanged even if the number of probes changes, if the total length of the heat exchangers is constant.

Key Words: *Thermal storage in the ground, vertical ground heat exchangers*

1. INTRODUCTION

The possibility to meet the thermal energy availability and production with the user requests is a concrete and interesting solution voted to maximize the efficiency and to reduce the energy losses and greenhouse emissions. During the last decades, the increasing number of biomass co-generation power plants and solar thermal system developed worldwide and the growing needs for more efficient energy use in buildings due to heating and cooling made the employment of Underground Thermal Energy Storage (UTES) systems increasingly interesting. The possibility to store the waste heat and the excessive heat production in the underground in the warm season to recover it during cold periods enables energy cost saving and environmental protection.

This work is the first step of an analysis aiming to check the possible use of the ground as thermal storage both with solar systems and with biomass heat waste. For this reason simulations have been performed with two models CaRM and COMSOL. The first one has been mainly used to investigate the shape of the borehole field and the distance between boreholes. The second one has been used to check the results of CaRM.

2. MAIN BODY

For the purposes of this research, two different software (CaRM and COMSOL) have been used. CaRM is a model to simulate ground heat exchangers based on electrical analogy. The model allows to consider the fluid flow pattern along the double U-tube vertical ground heat exchangers. Besides, ground temperature at different distances from borehole are calculated, taking into account also the thermal interference between different boreholes. Starting from the supply temperature of the heat exchanger, CaRM calculates the outlet fluid temperature, the heat flow and the ground temperature in each node, step by step (usually one hour) [1].

For the simulations in CaRM as heat transfer fluid water was used ($\dot{m}_w$=0.25kg s^{-1}, $c_{p,w}$=4186 J $kg^{-1}\cdot K^{-1}$, λ_w=0.60 W $m^{-1}\cdot K^{-1}$, ν_w=0.014 m^2 s^{-1}, ρ_w=1001 kg m^{-3}); for thermo-physical properties of surrounding ground the following parameters have been adopted: $c_{p,g}$= 1460.1 J $kg^{-1}\cdot K^{-1}$, λ_g= 1.5 W $m^{-1}\cdot K^{-1}$, ρ_g= 1438.10 kg m^{-3}. As geometric characteristics of the vertical ground heat exchangers, an external diameter of borehole equal to 0.140 m has been used, with pipes of 0.026 m, and 0.032 m as internal and external diameter respectively, while the distance between pipes is 0.083m. The thermal conductivity of pipes λ_{pipe} has been set equal to 0.4 W $m^{-1}\cdot K^{-1}$, the thermal conductivity of

the filler material λ_f is 2.5 W $m^{-1} \cdot K^{-1}$ and the specific heat of the filler material $c_{p,f}$ is 2000 J $kg^{-1} \cdot K^{-1}$, density of the filler material ρ_f= 1850.10 kg m^{-3}. As average annual temperature it was used 13°C and it was considered an hourly time profile of temperature repeated for 5 years. For the supply temperature to the heat exchanger two temperature profiles were used: the first one with six months at 5°C (winter season) and six months at 25 °C (summer season), and the second one with six months at 5°C (winter season) and six months at 50 °C (summer season). The first one could be supposed to be representative of solar collectors recharging the ground, the second one could be representative of energy waste used for recharging the ground. The simulated fields of vertical ground heat exchangers are shown in Table 1. The parameter that has been kept constant in the various cases is the total length of the heat exchanger, which is equal to L= 1600 m.

Case	Number of probes	Depth of probes [m]	Distance between boreholes [m]
1	16	100	7
2	16	100	5.5
3	16	100	4
4	32	50	7
5	32	50	5.5
6	32	50	4
7	64	25	7
8	64	25	5.5
9	64	25	4

TABLE 1. The types of field of the vertical ground heat exchangers

COMSOL Multiphysics is a powerful interactive tool for modeling and solving many kinds of scientific and engineering problems based on partial differential equations (PDEs). When solving the models, COMSOL Multiphysics uses the Finite Element Method (FEM). The software runs the finite element analysis together with adaptive meshing and error control using a variety of numerical solvers. PDEs form the basis for the laws of science and provide the foundation for modeling a wide range of scientific and engineering phenomena, in particular for the heat transfer[2].

For the comparison, as reference a borehole field of 16 vertical ground heat exchangers has been considered; the distance between probes has been changed, simulating 7 m, 5.5 m and 4 m. Two types of two-dimensional geometry have been considered, as shown in Figures 1.a and 1.b.

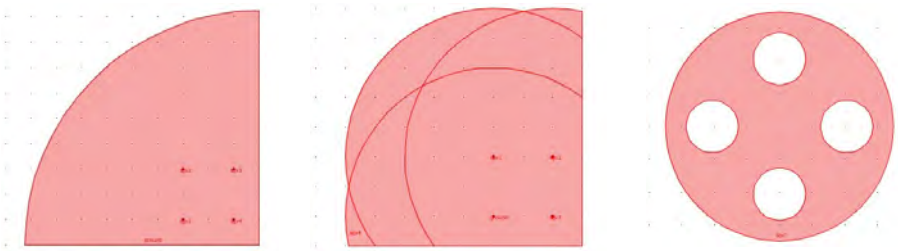

a **b** **c**

FIGURE 1. Geometries used in COMSOL: domains (a and b) and subdomain (c).

It was assumed the symmetry in the field of probes, thus reducing to a quarter the simulation domain. There are two types of sub-domains. The subdomains "sgv1", "sgv2", "sgv3", "sgv4" represent the vertical ground heat exchangers: they have the same geometry used in CaRM, they are characterized by the presence of the 4 pipes (the probes have double-U pipes i.e. two supply pipes and two return pipes) and they have the same thermal properties of the filling material of the probes used in CaRM. In Figure 1.c in detail the subdomain sgv1 is shown. The subdomain "ground" is, instead, characterized by the thermo-physical properties of the ground used in CaRM.

3. RESULTS

For each case of Table 1 the CaRM simulation has been run and the resulting heat flow has been calculated (Table 2). Values are positive if the heat flow is extracted (winter), while values are negative if the heat is rejected (summer). Adding together the values of the energy exchanged with the ground, the thermal energy extracted or released in the ground can be estimated.

Simulation	E_c [MWh]	E_h [MWh]	E_c+E_h [MWh]
1	25.395	-33.023	-7.628
2	25.956	-32.732	-6.776
3	26.537	-32.234	-5.697
4	24.750	-32.273	-7.523
5	25.337	-31.950	-6.613
6	25.995	-31.339	-5.344
7	24.199	-31.958	-7.759
8	24.788	-31.561	-6.774
9	25.513	-30.807	-5.294

TABLE 2. Values of the energy exchanged in the ground for the first profile of supply water temperature

For a better understanding of the results, a graphical representation of the values obtained in the different simulations is shown in Figure 2. As can be seen, assuming the same supply water temperature and the overall length of probes installed, the thermal energy stored in the ground grows when the distance between the vertical ground heat exchangers increases.

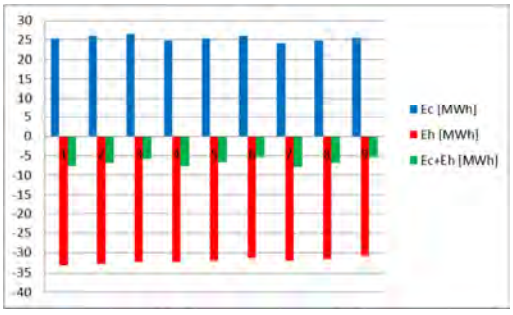

FIGURE 2. Values of heat flow for the first profile of supply temperature

By assuming constant the total length of the heat exchangers, once fixed constant the distance between the probes, set of three simulations 1-4-7, 2-5-8 and 3-6-9, the value of the thermal energy stored in the ground remains almost unchanged even if the number of probes changes.

As for the comparison against COMSOL simulations, the results have shown a very good accuracy. As an example in Figure 3 the temperatures on the edge of probe "sgv4" can be seen.

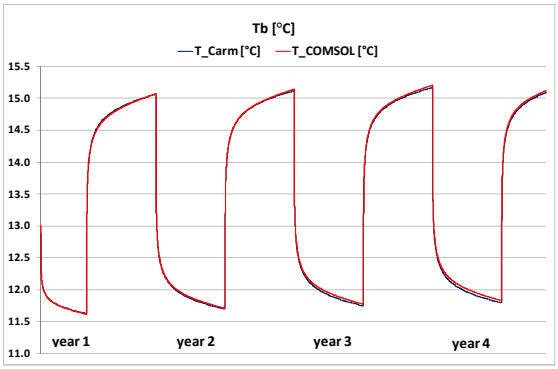

FIGURE 3. Example of CaRM and COMSOL temperatures on the edge of the probe "sgv4"

4. CONCLUSIONS

This work is the first stage of an analysis aiming to check the possible use of the ground as thermal storage both with solar systems and with biomass heat waste. Two models (CaRM and COMSOL) have been used. COMSOL has shown that the accuracy of CaRM is guaranteed for any shape of boreholes.

CaRM results have shown that, assuming the same supply water temperature and the overall length of probes installed, the thermal energy stored in the ground grows when the distance between the vertical ground heat exchangers increases.

On the other hand, by assuming constant the total length of the heat exchangers, once fixed the distance between the probes, the value of the thermal energy stored in the ground remains almost unchanged even if the number of probes changes.

REFERENCES

[1] M. De Carli, M. Tonon, A. Zarrella, R. Zecchin, *A computational capacity resistance model (CaRM) for vertical ground-coupled heat exchanger*, Department of Applied Physics – DFT, University of Padova, Via Venezia 1 – 35131, Italy, 2006.

[2] COMSOL Multiphysics User's guide.

Third International Conference on Computational Methods for Thermal Problems
THERMACOMP2014, June 2-4, 2014, Lake Bled, Slovenia
N. Massarotti, P. Nithiarasu and B. Sarler (Eds.)

LOSS OF PERFORMANCE OF DOUBLE U-TUBE BOREHOLE HEAT EXCHANGERS DUE TO THERMAL SHORT-CIRCUITING

Stefano Lazzari, Enzo Zanchini
Department of Industrial Engineering, University of Bologna, Viale Risorgimento 2, I-40136 Bologna, Italy, stefano.lazzari@unibo.it , enzo.zanchini@unibo.it

Antonella Priarone
DIME, University of Genova, Via all'Opera Pia 15/A, I-16145, Genova, Italy, a.priarone@unige.it

ABSTRACT

The loss of performance of double U-tube Borehole Heat Exchangers due to the thermal short-circuiting between the incoming and the outgoing fluid is studied by means of 3-D finite element simulations performed through COMSOL Multiphysics. Reference is made to a well-designed BHE with a length of 100 m, in winter working conditions, with two different values of the thermal conductivity of the grout and of the volume flow rate.

Key Words: *Borehole Heat Exchangers, Thermal Short-Circuiting, 3-D Finite Element Simulations*

1. INTRODUCTION

Ground-Coupled Heat Pumps normally employ vertical ground heat exchangers, called Borehole Heat Exchangers (BHEs). BHEs are usually composed of a single U-tube or a double U-tube, made of high density polyethylene, inserted in a drilled bore and sealed by a proper grout. Other BHEs, less widely employed, are composed of two coaxial circular tubes which form an inner circular tube and an outer annular duct, and are called coaxial BHEs. Since the temperature of the circulating fluid changes along the flow direction, an energy transfer occurs between the fluid which goes down and that which returns up: this phenomenon is called thermal short-circuiting and causes a loss of performance of the BHE.

Some research papers on the effects of the thermal short-circuiting are available in the literature. The decrease in performance of coaxial BHEs caused by the thermal short-circuiting was studied by Zanchini, Lazzari and Priarone [1, 2]. The authors recommended to replace the inner polyethylene tube by a polypropylene one, in order to reduce the internal heat transfer. Muraya, O'Neal and Heffington [3] analyzed, by a 2-D finite difference model, the effects of the thermal interference between the legs of a single U-tube BHE. Li et al [4] studied the effects of thermal short-circuiting for a single U-tube BHE by means of 3-D numerical simulations in steady-state conditions. Zeng, Diao and Fang [5] studied the heat transfer within the BHE, excluding the ground. They considered steady-state conditions and, through some simplifying assumptions, determined analytical expressions of the fluid bulk temperature along the channels, both for single U-tube and double U-tube BHEs. Through the temperature distributions, they evaluated the effective borehole thermal resistance per unit length R_b. They took into account, but did not single out, the effects of thermal short-circuiting.

A satisfactory analysis of the effects of thermal short-circuiting on the performance of double U-tube BHEs is not yet available in the literature. Some accurate results are provided in the present paper, by means of 3-D finite element simulations.

2. NUMERICAL MODEL

A 3-D finite element model for the simulation of a double U-tube BHE was implemented by means of COMSOL Multiphysics, with reference to a double U-tube BHE commonly employed in North Italy: length 100 m; diameter 152 mm; external diameter of each tube 32 mm and wall thickness 2.9 mm; distance between the axes of opposite tubes of 85 mm (see sketch in Figure 1). The flow of a water/ethylene glycol 20% solution inside the tubes was considered, with constant volume flow rate and inlet temperature. The adopted values for the physical properties of the high density polyethylene (PE100) tubes, of the water/glycol solution, of the sealing grout and of the ground are listed in Table 1. The ground around the BHE was modelled as a solid cylinder, coaxial with the BHE, having a radius of 10 m and a length of 104 m; the top surface was assumed isothermal at 4°C, while the lateral and bottom surfaces were modelled as thermally insulated. Winter working conditions were considered, with inlet temperature T_{in} = 4 °C. As initial condition, a temperature distribution varying with the depth z from the ground surface was assumed: parabolic for $0 \le z \le 10$ m, with values 4°C at $z = 0$ and 14 °C for $z = 10$ m; linear with a geothermal gradient equal to 0.03 °C/m for $z > 10$ m. Starting from the initial condition, a period of five days of operation at constant values of T_{in} and of $\dot{V}$ was considered, with time steps variable from 1 s to 3600 s.

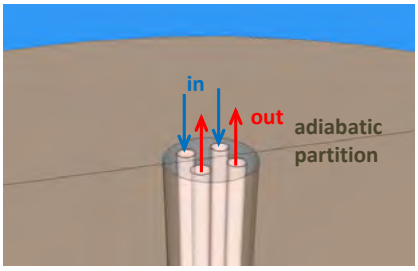

FIGURE 1. Sketch of the BHE

The unsteady conjugate convection-conduction heat transfer problem in the tubes was studied by means of the Pipe Flow Module of COMSOL Multiphysics, which models the tubes as 1-D domains where the governing equations are solved only for the average values of pressure, velocity and temperature of the fluid in each cross section.

Physical quantity	PE100 tubes	Water/Glycol 20% solution	Grout	Ground
Thermal conductivity [W/(m K)]	0.4	0.5036	1 ; 1.6	1.8
Heat capacity per unit volume [MJ/(m^3 K)]	1.824	4.012	1.600	2.500
Roughness [μm]	2			
Dynamic viscosity [mPa s]		2.672		
Volume flow rate [dm^3/min]		12 ; 18		

TABLE 1. Physical properties of the materials and volume flow rates

The mesh independence was checked by comparing the results obtained by two unstructured meshes, with 91291 elements and 248374 elements respectively. The relative mean square deviation between the results obtained by the first and by the second mesh was lower than 0.6%. The finer mesh was adopted for final computations.

3. RESULTS

Two values of the thermal conductivity of the grout, k_{gt} = 1 and 1.6 W/(m K), and two values of the volume flow rate, $\dot{V}$ = 12 and 18 dm^3/min, were considered. For each case, the effects of the thermal short-circuiting were singled out by comparing the results with those that would be obtained if the computational domain were divided in two parts by a central adiabatic vertical plane, as sketched in Figure 1.

Plots of the power exchanged between BHE and ground for k_{gt} = 1.6 W/(mK) and $\dot{V}$ = 18 dm^3/min, both in the real case and in the presence of the adiabatic partition, are illustrated in Figure 2. The figure shows that the thermal short-circuiting between tubes yields a decrease of the power extracted from the ground. The decrease in performance is not due to an increase of the thermal resistance between the fluid and the undisturbed ground, but to an increase of the mean temperature of the flowing fluid with respect of the arithmetic mean of inlet and outlet temperature.

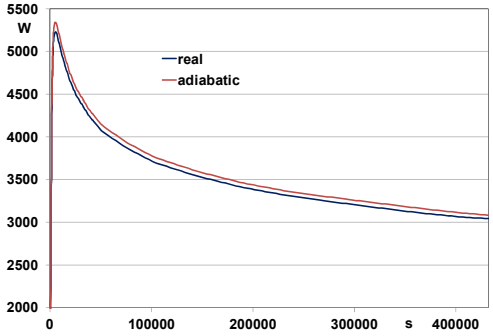

FIGURE 2. Power extracted from the ground, for k_{gt} = 1.6 W/(mK) and $\dot{V}$ = 18 dm^3/min

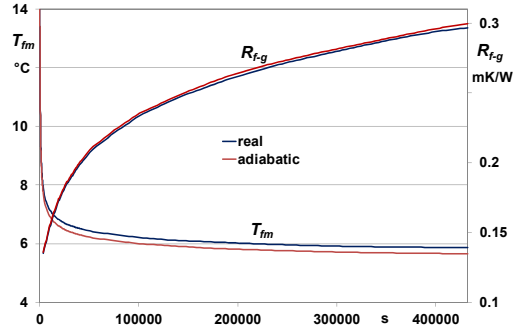

FIGURE 3. Mean fluid temperature and thermal resistance fluid-ground per unit length, for k_{gt} = 1.6 W/(mK) and $\dot{V}$ = 18 dm^3/min

Indeed, one can define a (generalized, unsteady) thermal resistance per unit length between the fluid in the tubes and the undisturbed ground as

$$R_{f-g} = \left(T_g - T_{fm}\right) \Big/ \dot{q}_l \quad , \tag{1}$$

where T_g is the undisturbed ground temperature, averaged along the BHE length and equal to 14.88 °C in the case considered, T_{fm} is the mean value of the fluid bulk temperature, and $\dot{q}_l$ is the power extracted from the ground per unit length of the BHE. Plots of T_{fm} and of $R_{f\text{-}g}$ versus time, for k_{gt} = 1.6 W/(mK) and $\dot{V}$ = 18 dm^3/min, are illustrated in Figure 3, both in the real case and in the presence of the adiabatic partition. The plots show that the thermal short-circuiting does not yield an increase of $R_{f\text{-}g}$, but rather a very slight decrease. On the other hand, it causes an increase in T_{fm}, with the same value of T_{in} (4 °C) and a slight decrease of T_{out}; the latter is not illustrated here for brevity, but is an obvious consequence of the lower value of the power extracted from the ground.

Values of the ratio between the energy E extracted from the ground and the energy E_{ad} which would be extracted in the presence of an adiabatic partition between the cooler and the warmer half-domain are reported in Table 2. The table shows that, for operating periods longer than 1 h, the per cent reduction in energy extracted from the ground does not depend on the operation time, and reaches 3% for $\dot{V} = 12$ dm^3/min and $k_{gt} = 1.6$ W/(m K) .

	$\dot{V} = 12$ dm^3/min		$\dot{V} = 18$ dm^3/min	
time [h]	$k_{gt} = 1$ W/(m K)	$k_{gt} = 1.6$ W/(m K)	$k_{gt} = 1$ W/(m K)	$k_{gt} = 1.6$ W/(m K)
1	0.988	0.979	0.992	0.984
12	0.980	0.968	0.989	0.982
24	0.981	0.969	0.990	0.982
48	0.981	0.969	0.990	0.983
120	0.982	0.970	0.990	0.984

TABLE 2. Values of the ratio E/E_{ad}

4. CONCLUSIONS

For double U-tube BHEs with a well designed cross section, the decrease in energy-exchange with the ground due to the thermal short-circuiting ranges between 1% and 3%, with the highest values for low flow rate and high conductivity of the grout. The decrease of performance is not due to an increase of the thermal resistance between fluid and ground, but to an increase of the difference between the mean temperature of the fluid and the arithmetic mean of inlet and outlet temperature.

REFERENCES

[1] E. Zanchini, S. Lazzari, and A. Priarone, Effects of flow direction and thermal short-circuiting on the performance of small coaxial ground heat exchangers, *Renewable Energy*, 35, 1255-56, 2010.

[2] E. Zanchini, S. Lazzari, and A. Priarone, Improving the thermal performance of coaxial borehole heat exchangers, *Energy*, 35, 657-66, 2010.

[3] N. K. Muraya, D.L. O'Neal, and W. M. Heffington, Thermal Interference of Adjacent Legs in a Vertical U-Tube Heat Exchanger for a Ground-Coupled Heat Pump, *ASHRAE Transactions*, 102 (2), 12-21, 1996.

[4] Y. Li, J. Mao, S. Geng, X. Han and H. Zang, Evaluation of thermal short-circuiting and influence on thermal response tests for borehole heat exchangers, *Geothermics*, 50, 136-47, 2014.

[5] H. Zeng, N. Diao, and Z. Fang, Heat transfer analysis of boreholes in vertical ground heat exchangers, *International Journal of Heat and Mass Transfer*, 46, 4467-81, 2003.

Third International Conference on Computational Methods for Thermal Problems
THERMACOMP2014, June 2-4, 2014, Lake Bled, Slovenia
N. Massarotti, P. Nithiarasu and B. Sarler (Eds.)

FINITE ELEMENT MODELING OF VERTICAL ENERGY PILES

A. Carotenuto, S. Di Fraia, N. Massarotti, A. Mauro, G. Paderni
Dipartimento di Ingegneria, Università degli Studi di Napoli "Parthenope", Centro Direzionale, Isola C4, Napoli, Italy, alberto.carotenuto@uniparthenope.it; massarotti@uniparthenope.it, alessandro.mauro@uniparthenope.it, gabriella.paderni@uniparthenope.it.

ABSTRACT

In this study, the authors have developed a model to study heat transfer in energy piles. The model has been validated against experimental data available from the literature, and the influence of different parameters has been analyzed. In particular, the authors have varied the volumetric flow rate of water entering the probe and the thermal conductivity of the concrete, showing that these parameters significantly influence the heat transfer mechanism.

Key Words: *Heat Transfer, Thermal conductivity, Flow rate, geothermal energy.*

1. INTRODUCTION

Foundation piles employed as ground coupled heat exchangers are currently under investigation, since can ensure significant reduction of installation costs [1]. The equipment used for air conditioning are essentially constituted by three main components: energy pile, heat pump and secondary system. These three components constitute the GCHPs, where the heat transfer fluid flows in a closed circuit in contact with the ground [2]. The authors have developed a reduced model, taking into account both three-dimensional heat transfer of a single energy pile with the surrounding ground and one-dimensional heat and fluid flow in the probe. In this way, it is possible to obtain accurate results and to save on computational costs at the same time. The pile is supposed to be not affected by the presence of the other elements of the piling. The time considered in the transient analysis is of three hours, on the basis of the data reported by Gao et al. [1]. The effects of the fluid flow rate injected into the probe and of the reinforced concrete thermal conductivity have been evaluated by the authors.

2. NUMERICAL MODEL

In this section, the methodology proposed for the numerical simulation of the geothermal system sketched in Figure 1 is presented, in terms of governing equations and boundary conditions employed. The pile-foundation heat exchanger has a length of 25 m and is vertically laid at a depth of 5 m. The outer diameter of the pile is 600mm. The fluid employed in the heat exchanger is water, and the material employed for the probe is high-density polyethylene (HDPE). The authors have considered one U-shaped probe. The case taken into account concerns the cooling mode operation of the system. The characteristics of the materials are reported in Table 1. The ground subdomain taken into account in the simulations has a volume of $5x5x35m^3$, while the foundation pile has a radius of 0.6 m and a length of 25 m. The authors have developed a reduced model taking into account three-dimensional heat transfer in the pile and surrounding ground, and one-dimensional heat and fluid flow in the probe.

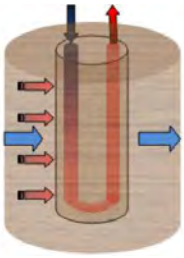

FIGURE 1. Heat exchange for an energy pile.

FIGURE 2. Adopted mesh

Materials	Thermal conductivity W/(m · K)	Density kg/m^3	Heat capacity J/(kg · K)
Soil (sandy silt)	1.3	1847	1200
Reinforced concrete	1.628	2500	837
HDPE (DN 20 mm)	0.42	1100	1465

TABLE 1. Physical property of materials [1].

This model allows to reproduce accurately the energy pile behavior and to save computational resources at the same time. The partial differential equations governing the physical phenomena are the following:

Continuity

$$\frac{\partial(A\rho)}{\partial t}+\frac{\partial(A\rho u)}{\partial z}=0$$

Momentum Conservation

$$\frac{\partial(\rho u)}{\partial t}=-\frac{\partial p}{\partial z}-f_d\frac{\rho}{2D_h}u|u|+F$$

Energy conservation in the fluid

$$\frac{\partial(\rho A c_f T)}{\partial t}+\frac{\partial(\rho A c_f u T)}{\partial z}=\frac{\partial}{\partial z}\left(Ak\frac{\partial T}{\partial z}\right)+f_d\frac{\rho}{2D_h}|u|^3+Q_{wall}$$

Energy conservation in the ground

$$\rho c_g\frac{\partial T}{\partial t}-\nabla(k\nabla T)=0$$

where: u is the average velocity of the fluid along the cross section of the probe; p is the fluid pressure; $f_D = f_D(Re, \varepsilon/d)$ is the friction coefficient; F is the volume force; ρ is the density of the fluid; c_f and c_g are the specific heat of fluid and ground, respectively; k is the thermal conductivity of the fluid; D_h is the hydraulic diameter of the probe; Q_{wall} is the thermal power per unit of length

exchanged between the ground and the fluid flowing into the probe, through the walls of the probe (W/m). The governing equations have been solved with the following boundary conditions:
inlet velocity and temperature of the fluid in the probe: u_{in}=0.3m/s and T_{in}=35.12°C, respectively. The vertical surfaces and top surface of the ground are assumed adiabatic, while bottom surface is maintained at a temperature of 18.2°C. The initial temperature of the computational domain is 18.2°C. The volumetric fluid flow rate at the entrance of the probe is 0.342 m^3/h.

3. RESULTS

A mesh sensitivity analysis has been carried out, in order to produce grid independent results, and the computational grid is shown in Figure 2. The obtained results have been compared with data available in the literature [4]. Table 2 shows that there is a good agreement between the present results and the in situ experimental data reported by Gao et al. [4]. In fact the difference in terms of fluid outlet temperature in the probe after 3 hours is of 0.38 °C (Case 1). After validation against experimental data, the model has been employed to evaluate the effects of variation of the fluid volumetric flow rate and thermal conductivity of the concrete. Firstly, the influence of the concrete thermal conductivity has been studied, increasing its value from 10% to 30% with respect to the value taken from the literature [4], as reported in Table 2 (Case 2). The results in terms of temperature profile of the fluid in the probe are shown in Figure 3. Secondly, the influence of the fluid volumetric flow rate has been studied, decreasing its value of 40% and increasing its value of 70%, with respect to the value taken from the literature, as reported in Table 2 (Case 3). From the analysis of these results, shown in Figure 3, it is clear that the outlet temperature of the fluid in the probe is significantly influenced both by the variation of the thermal conductivity of the concrete and the volumetric flow rate of the fluid. The thermal power obtained in Case 1 is 1.61 kW. Therefore, the performance of energy piles are comparable to those of vertical probes. Moreover, the use of concrete with thermal conductivity of 10% and 30% higher than the reference one [4], brings to an increase of thermal power of 6% and 15%, respectively. Therefore, it is useful to study concrete mixtures with better thermal properties, such as those obtained with recycled ferrous aggregates. The variation of the volumetric flow rate has a smaller influence on the thermal power. In fact, the performance in terms of thermal power decrease of 6% after decreasing the volumetric flow rate of 40%, while increase of 12% after increasing the volumetric flow rate of 70%.

Case	T_{out} (°C)	Flow rate (m^3/h)	Conductivity W/(m·K)
Gao et al. [4]	31.56	0.342	1.628
Present results - Case 1	31.18	0.342	1.628
Present results - Case 2	30.83 30.48	0.342 0.342	1.8 2.1
Present results - Case 3	28.65 32.53	0.2 0.6	1.628 1.628

TABLE 2. Obtained results and comparison with experimental data.

4. CONCLUSIONS

The authors present a numerical model, taking into account three-dimensional heat transfer in concrete and surrounding ground and one-dimensional heat and fluid flow in the probe, that represents a useful tool for the design of energy piles. The model has been validated against experimental data available from the literature, and the influence of different parameters has been analyzed. In particular, the authors have varied the volumetric flow rate of water entering the probe

and the thermal conductivity of the concrete, showing that these parameters significantly influence the heat transfer mechanism. Highly conductive concrete mixtures, such as the ones obtained from recycled ferrous aggregates, could be studied in order to increase heat transfer in energy piles, ensuring at the same time the required mechanical characteristics of the foundation. Instead, the increase of the fluid flow rate in the probe beyond a certain value could be not favorable from both thermal and economic point of views. This work is part of a broader research activity regarding the thermo-mechanical analysis of pilings, conducted in collaboration between the research groups of Thermal Sciences and Geotechnic at the University of Napoli "Parthenope".

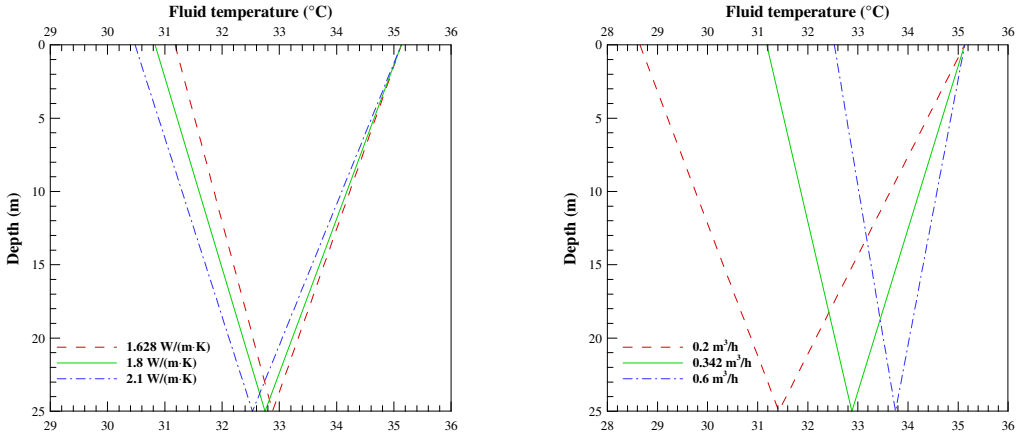

FIGURE 3. Comparison of the fluid temperature profiles.

ACKNOWLEDGEMENTS

The authors gratefully acknowledge the financial support of Poligrid "Smart Grid con Sistemi di Poligenerazione Distribuita" and GAIA "Geotermia Avanzata per Impianti Autonomi" projects.

REFERENCES

[1] J. Gao, X. Zhang, J. Liu, K. Li, J. Yang, Numerical and experimental assessment of thermal performance of vertical energy piles: An application, *Applied Energy*, 85(10), 901-910, 2008.

[2] A. Carotenuto, N. Massarotti, A. Mauro, A new methodology for numerical simulation of geothermal down-hole heat exchangers, *Applied Thermal Engineering*, 48, 225-236, 2012.

[3] L. Laloui, M. Nuth, L. Vulliet, Experimental and numerical investigations of the behavior of a heat exchanger pile, *International Journal for Numerical and Analytical Methods in Geomechanics*, 30, 763-781, 2006.

[4] J. Gao, X. Zhang, J. Liu, K.S. Li, J. Yang, Thermal performance and ground temperature of vertical pile-foundation heat exchangers: A case study, *Applied Thermal Engineering*, 28, 2295-2304, 2008.

Third International Conference on Computational Methods for Thermal Problems
THERMACOMP2014, June 2-4, 2014, Lake Bled, Slovenia
N. Massarotti, P. Nithiarasu and B. Sarler (Eds.)

NUMERICAL MODELING OF COUPLED GROUNWATER FLOW AND HEAT EXTRACTION FROM SUBSOIL

Ciccolella M.
Department of Technologies, University of Naples "Parthenope", Centro Direzionale Isola 4, 80143, Napoli, michela.ciccolella@uniparthenope.it

D'Acunto B.
Department of Mathematics and Applications "Renato Caccioppoli", University of Naples "Federico II", Via Claudio 21, 80125, Napoli, dacunto@unina.it;

Pirone M., Urciuoli G.
Department of Civil, Architectural and Environmental Engineering, University of Naples "Federico II", Via Claudio 21, 80125, Napoli, mariannapirone@unina.it; gianurci@unina.it

ABSTRACT

The subsoil can be used to store or extract heat for cooling or heating buildings, respectively, via a ground-coupled heat pump (GCHP) and the Ground heat exchanger (GHE) commonly used consist of HPDE pipes. The present contribution deals with the role of groundwater flow in the performance of GHEs installed in vertical boreholes. A mathematical model in 2D space is introduced, comprising a pair of partial differential equations of parabolic and elliptic type for soil temperature and ground water velocity field, respectively. The equations have been solved numerically by mean of Difference Finite method and Finite Element Method. The numerical model has been validated by comparing the results with the solutions of Moving infinite line source (MILS) model. The soil temperatures established in a sand around GHE operating in heat mode are calculated either assuming a uniform velocity field and by taking into account the correct seepage around the GHEs to investigate how much the proper modelling of groundwater flow around the borehole affects the results.

Key Words: *Heat Transfer, Gorundwater flow, Numerical modelling*

1. INTRODUCTION

The paper focuses on heat exchangers installed in vertical boreholes. About the estimation of the heat transfer in and around GHE boreholes, many methods are based on Fourier's law of heat conduction and do not take into account the effects of groundwater flow. First, Chiasson et al. [1] reported the effect of groundwater flow in various geological conditions using a 2-D finite element method. Indeed, various analytical models are available including the line source model with groundwater advection, i.e. [2]. All these models assume a horizontal and uniform seepage velocity and neglect the obstacles represented by GHEs that deflect the flow. The main goal of this work is to investigate how much the proper modelling of groundwater flow around the borehole affects the performance of GHEs; a mathematical model in which the heat advection–diffusion equation is considered coupled with the groundwater velocity equation is introduced. The soil temperatures established in a soil sand by the GCHP system operating in heating mode are calculated in 2D plan-view, solving the heat convection-diffusion equation via the Finite Difference Method. The equation for velocities is integrated by using the Finite Element Method on Matlab platform. First the model is validated by comparing the results with the solutions of Moving infinite line source (MILS) [2]. Then the soil temperatures established in soil sand, referring to a typical building located in Naples (Southern Italy) are computed; the solutions calculated by assuming uniform and unidirectional water velocity are compared to these obtained by coupled groundwater flow and heat extraction model taking in account the effect of GHE on the groundwater flow.

2. MODELLING OF COUPLED GROUNDWATER FLOW AND HEAT TRANSPORT

The equation governing heat transport in a saturated porous medium through which water flows is a partial differential equation of the convection-diffusion type. For 2-D problems, i.e. plan view, the heat equation can be rewritten as:

$$\rho_g c_g \frac{\partial T}{\partial t} + \rho_w c_w \left(v_x \frac{\partial T}{\partial x} + v_y \frac{\partial T}{\partial y} \right) - k_{eff} \left(\frac{\partial^2 T}{\partial x^2} + \frac{\partial^2 T}{\partial y^2} \right) = 0 \quad (1), \quad v_x = -K \frac{dh}{dx}; v_y = -K \frac{dh}{dx} \quad (2)$$

where T is the temperature of the rock matrix and water, v_x and v_y are the Darcy velocities on the x-and y-axes, K is the hydraulic conductivity of the medium and h is the hydraulic head. The effective thermal conductivity, k_{eff}, is a volume-weighted average thermal conductivity of the saturated soil medium and the volumetric heat capacity of the bulk porous medium, $\rho_g c_g$, can be computed as the weighted arithmetic mean of solid $\rho_s c_s$ and water $\rho_w c_w$ capacity. By applying the law of mass conservation to a control homogeneous soil volume, characterized by isotropic permeability, K, and making use of Darcy's law, the equation defining the hydraulic head distribution for 2D problem in steady conditions may expressed as:

$$K \left(\frac{\partial^2 h}{\partial x^2} + \frac{\partial^2 h}{\partial y^2} \right) = 0 \quad (3)$$

The soil temperature field established in a soil sand volume around a GHE operating in heating mode is calculated in 2D plan-view (considering an infinite GHE in the vertical direction), solving the heat convection-diffusion equation via a finite difference method. The following assumptions are made: *(i)* the soil is a homogeneous porous medium (a sand); *(ii)* a rectangular plan-view of the system at a depth greater than 2 m from the ground surface, where the temperature is not influenced by seasonal fluctuations, is analysed (fig.1a);*(iii)* the sizes of the rectangular domain investigated are respectively L_y= 576 m and L_y= 6 m; the borehole is placed at y_b=35.7 m away from one of the side of the rectangle; *(iv)* a square geometry is adopted to approximate the real shape of the borehole acting as a GHE; the borehole is modelled empty, directly at contact with the soil (fig.1a); only heat advection-conduction outside the borehole (in the ground) is modelled, having assumed the whole concrete section at the same temperature of the edge of the borehole. The sizes of the borehole are l_x= l_y =0.6 m; *(v)* a system of boreholes aligned normal to the direction of water flow are simulated, so the sides in direction y are impermeable to heat and water flow (axes of symmetry). The governing equation of heat transfer is solved numerically by using the Upwind Method, [3], with dt =15minutes and dx=dy=0.075 m. The far-field boundary conditions are imposed on the x sides of the analysed domain: the temperature is always equal to the initial one; Neumann's boundary conditions of zero heat flux are imposed on the y sides, that are considered axes of symmetry. At the interface between the soil and the borehole, heat exchange can be expressed by means of Neumann's boundary condition. The eq. (3) is solved by FEM on Matlab platform and the total head is set equal to pressure head, in fact the elevation doesn't contribute to the flow as the horizontal domain is analysed. Zero flux is applied on the y-edges that are axes of symmetry respect to velocity too. The values of pore pressure heads assumed on the horizontal-edges, h_{y1} (=h(0,x)) and h_{y2} (=h(256,x)), provide groundwater flow parallel to the slope and the mean unit gradient equal to 0.1 and 0.02, calculated as $(h_{y1}- h_{y2})/L_y$, these concurrently with the permeability, K (table 1) are able to reproduce the constant velocity of 10^{-5} and $2 \cdot 10^{-6}$ m/s respectively some distance from the GHE. Moreover, since the water flow cannot cross the borehole, flux null is applied around the borehole. The velocities calculated by the FEM are loaded in the solving code which integrates the heat-transfer equation.

Analysis	n	k_{eff} [W/(m °C)]	$\rho_g c_g$ [J/(m³°K)]	$\rho_w c_w$ [J/(m³°K)]	$\rho_s c_s$ [J/(m³°K)]	v_y [m/s]	K [m/s]	q [m/s]
Validation	0.39	2.4	$2.5 \cdot 10^6$	$4.19 \cdot 10^6$	$1.45 \cdot 10^6$	$1 \cdot 10^{-5}$	10^{-4}	10
GHPE working	0.39	2.4	$2.5 \cdot 10^6$	$4.19 \cdot 10^6$	$1.45 \cdot 10^6$	$1 \cdot 10^{-5}$, $2 \cdot 10^{-6}$	10^{-4}	21

TABLE 1. Parameters used in the analyses

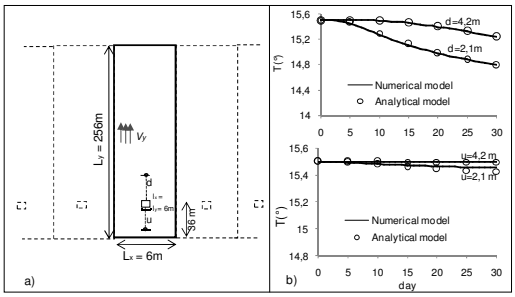

FIGURE 1. a) Plan-view of the domain analysed; b) validation of the numerical model

The numerical model is validated by comparing the results with the solutions of MILS[2]:

$$T = \frac{q}{4\pi k_{eff}} \exp\left[\frac{Pe}{2}\frac{r}{r_b}\cos(\vartheta)\right] \int_{\left(\frac{r}{r_b}\right)^2/4F_o}^{\infty} \frac{\exp\left(-\xi - \frac{Pe^2\left(\frac{r}{r_b}\right)^2}{16}\frac{1}{\xi}\right)}{\xi} d\xi \quad (4)$$

where $\xi = \frac{r^2}{4\alpha_{eff}(t-\tau)}; F_0 = \frac{\alpha_{eff} t}{r_b^2}; Pe = \frac{U_{eff} r_b}{\alpha_{eff}}$

For the meaning of parameters, the readers can refer to [2]. Here, the solution of 'generalized incomplete gamma function' of Chaudhry and Zubair [4] are used to solve the integral in eq. (4) and the spatial superimposition is considered due to the geometry of the model. The solution for an heat extraction of 10 W/m^2 for 30 days are compared to the numerical calculations; in particular the solution are estimated at a distance of 2.1 and 4.2 m along y-axis either downstream and upstream the borehole. The analytical and numerical solutions are reported in fig.1b and they are in good agreement.

3. RESULTS OF THE NUMERICAL MODEL

The analyses are carried out over one year, T_t=365 days, referring to a typical building located in Naples (Climatic Zone C, DPR 412/93), heated only during the winter and for part of the day; the system operating in heating mode is modelled by extracting a heat flow, q, equal to 50 W/m per unit length at the interface between the soil and the borehole over 137 days per year (that is the period over which the system works, T_w). Otherwise zero heat flux is assumed. However, the system works ten hours per day; during the other 14 hours of the day there is no flow extracted. The initial temperature is equal to 15.5°. In order to evaluate the effects of the GHE on water flow, the groundwater velocity field is calculated by two different approaches: (i) the water velocity is set as uniform and horizontal; (ii) the field velocity is calculated by using the Finite Element Method (FEM) implemented in Matlab platform and then loaded in the solving code of the heat-transport equation; in this way the effects of the borehole on the groundwater field, especially around the borehole, are correctly taken into account. In both the ways, two constant velocities establishing everywhere (approach i)) or at least far from the borehole (approach ii)) are considered: $10^{-5}$and $2\cdot10^{-6}$ m/s. In Figure 2a-d the soil mean daily temperatures at four different distances from the borehole (u=0 and 1.2 m upstream, d=0m and 1.2m downstream, see fig.1a), for two different values of velocity and the two different approaches are reported against time. The groundwater flow affects the soil temperature variation especially downstream, in fact the highest soil temperature reduction occurs downstream of the pile, where heat extraction and groundwater flow follow opposite directions. Thanks to groundwater flow, steady-state conditions both in operating times and in switching-off times are very quickly established and initial conditions are restored 140 days

after the beginning of operations. However, assumption of unidirectional uniform velocity overestimates and underestimates the reduction in the soil temperature respectively downstream and upstream the borehole. If the proper field velocity is taken in account, a better balance between the reductions in soil temperature upstream and downstream the borehole is carried out. Nevertheless the benefit to use a coupled model depends on the magnitude of velocity, in fact for $v=2\cdot10^{-6}$ m/s the uniform seepage field velocity may be already used without committing considerable errors in the temperature estimation. Therefore in order to perform a proper energy balance, a good estimation of groundwater flow is necessary when high velocity occurs into subsoil.

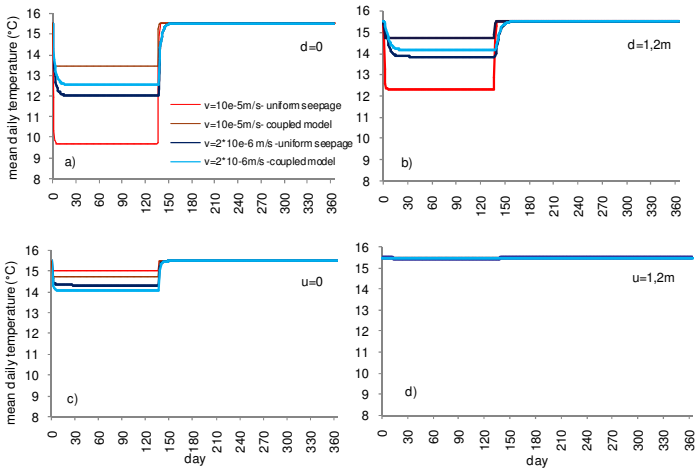

FIGURE 2. Mean soil temperature a) on the upper -y-edge of borehole; b) at 1.2 m downstream the borehole; c) on the lower –y- edge of borehole; d) at 1.2 m upstream the borehole

4. CONCLUSIONS

The groundwater flow greatly influences the temperature field in the subsoil as modified by heat extraction, improving the performance of the system. However, when the velocity is higher than10^{-5} m/s, sure the groundwater flow field has to be correctly evaluated, taking into account the influence of boreholes on the water velocity field to determine a good energy balance in the subsoil. Velocities included between the two values used here, should be investigated to catch the precise threshold beyond which it is necessary using a coupled model. Otherwise the decrease/increase in soil temperature is overestimated.

REFERENCES

[1] A.D. Chiasson, S.J. Rees, J.D. Spitler, A preliminary assessment of the effects of groundwater flow on closed-loop ground-source heat pump systems, *ASHRAE Trans.*, 106, 380-384,2000.

[2] M.G. Sutton, D.W. Nutter, R.J. Couvillon, A Ground Resistance for Vertical bore heat exchangers with groundwater flow, *J. of Energy Resour. Tech.*, , 125,183-189, 2003.

[3] B. D'Acunto, Computational Partial Differential Equations for Engineering Science, Nova Science Publishers, New York, 2012.

[4] M.A. Chaudhry, S.M. Zubair. Generalized incomplete gamma function with Application. *J.Comp.and Appl. Math.,* 55, 99-124, 1994

Third International Conference on Computational Methods for Thermal Problems
THERMACOMP2014, June 2-4, 2014, Lake Bled, Slovenia
N. Massarotti, P. Nithiarasu and B. Sarler (Eds.)

NUMERICAL MODEL OF HEAT FLOW IN A GEOTHERMAL BOREHOLE HEAT EXCHANGER

Esad Tombarević, Igor Vušanović
Faculty of Mechanical Engineering, University of Montenegro, Džordža Vašingtona bb, 81000 Podgorica, Montenegro. E-mail: esad.tombarevic@ac.me, igor.vusanovic@ac.me

ABSTRACT

This paper presents a three dimensional numerical model for the simulation of heat flow in a geothermal borehole heat exchanger. Two equations of the mathematical model are simultaneously solved to arrive at the solution: energy equation for the fluid flowing in the U-bended tube and energy equation for the heat flow in the pipe, grout and surrounding soil. The results obtained are validated against the available reference data sets from a large laboratory "sandbox" containing a borehole with a U-tube.

Key Words: *Borehole heat exchanger, CVFEM method.*

1. INTRODUCTION

Borehole heat exchangers are often used to couple the heat pump with the ground to use it as a heat source or sink. This technical solution provides more efficient operation of the heat pump since the ground usually has more favourable temperatures than air to be used as a heat source in winter, or as a heat sink in summer. An illustration of the typical borehole heat exchanger horizontal and vertical cross section is given in Figure 1. Heat extraction and rejection is performed by circulating of heat transfer fluid (usually water, brine or antifreeze solution) in a U-bended high density polyethylene pipe buried in a vertical borehole. Borehole is backfilled with appropriate grouting material which purpose is to improve heat transfer between the pipe legs and the surrounding soil.

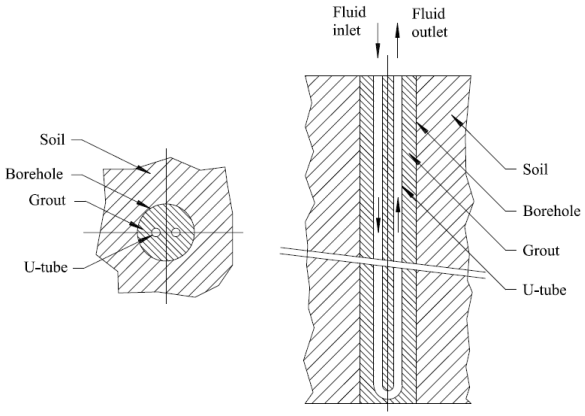

FIGURE 1. Sketch of the horizontal and vertical cross section of the borehole heat exchanger

Numerical models of heat flow taking place between the fluid circulating in the pipe and the surrounding soil are of crucial importance for the dimensioning and efficiency of long term operation of the system. Extensive review of systems and models is given in the paper by Yang [1]. Most of analytical models are based either on Kalvin's solution for the infinite line source [2] or Carslaw's and Jaeger's solution for the cylindrical source [3]. Analytical models are attractive because of computational efficiency and have been incorporated in several design methods but with

a number of simplifying assumptions. Rottmayer et al. [4] presented a finite deference model for U tube heat exchanger with geometric factor that takes into account the noncircular geometry used to represent the pipes in the borehole. Tago et al. [5] developed a three dimensional control volume based model with U-tube of square cross section. Many other numerical models also assumes a number of simplifying assumptions regarding the geometry. However, the geometry of the U-tube heat exchanger is more challenging. First, heat transfer within the borehole is not simple radial conduction. Then the temperatures of the circulating fluid in the two legs of the U-tube are different, and therefore the pipes do not exchange heat only with the soil, but also with each other. Therefore, it is evident that in general the borehole heat exchanger presents a transient three dimensional problem because the temperature of circulating fluid changes with depth. Li and Zheng [6] developed a three-dimensional unstructured finite volume model which uses Delaunay triangulation method to mesh the cross-section of the borehole. Three-dimensional models offer most generality and potentially most accurate representation of heat transfer, but at the cost of considerable computation time.

2. PHYSICAL AND MATHEMATICAL MODEL

Physical model is sketched in Figure 1. Mathematical model of the borehole heat exchanger consists of the two energy conservation equations, one for the fluid that circulate in the U pipe and another for the pipe, grout and soil. Neglecting the conductive heat transfer, energy equation for the fluid in the U-pipe is:

$$(\rho c_p)_{HTF}\frac{\partial T_{HTF}}{\partial t}+(\rho c_p)_{HTF}\frac{\partial}{\partial z}\left(\mathbf{v}_{HTF}T_{HTF}\right)=\frac{4h}{d_p}\left(T_w-T_{HTF}\right) \tag{1}$$

where d_p is the inner pipe diameter and $(\rho c_p)_{HTF}$, $\mathbf{v}_{HTF}$ and T_{HTF} are volumetric heat capacity, velocity and temperature of the heat transfer fluid (*HTF*) respectively. T_w is the temperature of the pipe wall and h is the heat transfer coefficient which is calculated using the correlation of Gnielinski for the turbulent flow in the circular pipes. This equation is dicretized using control volume method with implicit integration in time and with quadratic upwind interpolation for convective kinetics.

With the assumption that the heat transfer in the vertical direction is negligibly small compared to the radial, corresponding energy equation for the U-pipe, grout and soil is:

$$(\rho c_p)\frac{\partial T}{\partial t}=\frac{\partial}{\partial x}\left(\lambda\frac{\partial T}{\partial x}\right)+\frac{\partial}{\partial y}\left(\lambda\frac{\partial T}{\partial y}\right) \tag{2}$$

In the case of considerable groundwater flow, equation (2) could be expanded by advective term where the velocity components can be computed using expressions for potential flow. The whole domain is divided in layers in vertical z direction to take into account the change of heat transfer fluid with depth. Each horizontal layer is discretized by a mesh of triangular elements (Figure 2). Solutions of the two equations are coupled through the source term on the RHS of equation (1) and the boundary conditions on the pipe falls for equation (2) on the way that the continuity of heat flux on this mutual interface is preserved.

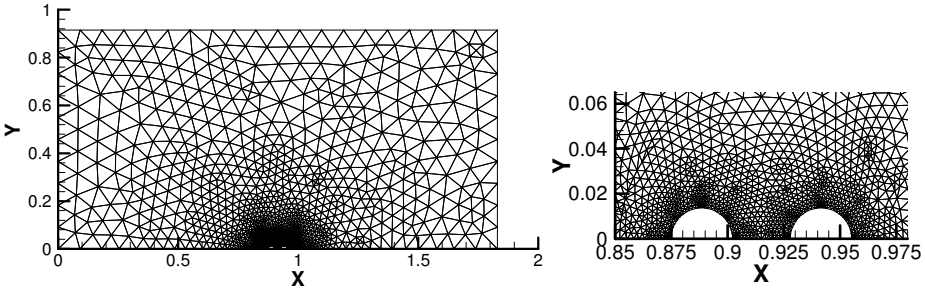

FIGURE 2. Triangular mesh of the domain cross section and zoom of the mesh near the borehole

3. RESULTS AND DISCUSSION

The developed model is validated through comparing its results with the available reference data sets from a large laboratory "sandbox" with a borehole and U-tube. This experimental installation is developed by Building and Environmental Thermal Systems Research Group at the Department of Mechanical Engineering Technology of Oklahoma State University [7]. Large wooden box has a horizontal layout, 18.3 m in length with square vertical cross section with side of 1.83 m. Borehole in the form of an aluminium pipe with an inner diameter 12.6 cm is cantered horizontally along the length of the box. U-tube made of HDPE (high density polyethylene) with the inner diameter of 27.33 mm and the outer diameter 33.40 mm is centred with spacers in the borehole which is then filled with a bentonite grout. The box is filled with sand which is saturated with water. Constant far field temperature (ground temperature away from the borehole) is simulated by circulating air of the constant temperature through the gap around sandbox and the outer surrounding box. The ends of the sand box are insulated. In the experiments, water is circulated through the U-tube and heated by means of an electric heater. Temperatures of water at the inlet and outlet of the U-tube, temperature of sand at various positions as well as the voltage and current at electric heater are recorded once every minute. Relevant parameters for the model validation are given in Table 1.

Parameter	Description	Value
L	Borehole length	18,30 m
d_b	Borehole diameter	0,126 m
d_i	U-tube inner diameter	0,02733 m
d_o	U-tube outer diameter	0,0334 m
s	Distance between centres of U-tube legs	0,053 m
k_p	Thermal conductivity of U-tube	0,39 W/mK
k_g	Thermal conductivity of grout	0,73 W/mK
k_s	Thermal conductivity of wet sand	2,82 W/mK
C_p	Estimated volumetric heat capacity of U-tube	2137500 J/m^{3}K
C_g	Estimated volumetric heat capacity of grout	3800000 J/m^{3}K
C_s	Estimated volumetric heat capacity of wet sand	2000000 J/m^{3}K

TABLE 1. Geometrical data and physical properties of the U-tube model verification

Two tests are performed. In the first, uninterrupted test, circulating pump and electric heater are operated constantly for the period of 52 hours, more or less without variations in the flow rate and electric power (average values 0.1968 l/s and 1051 W). Measured outlet water temperature as well as measured and calculated outlet water temperatures are shown on Figure 3. Calculated outlet water temperature shows good agreement with values measured in the experiment.

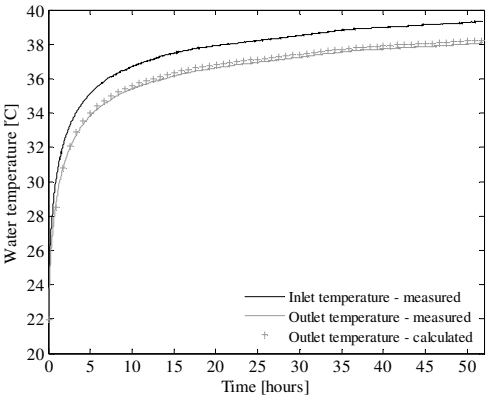

FIGURE 3. Uninterrupted test - numerical vs. experimental data

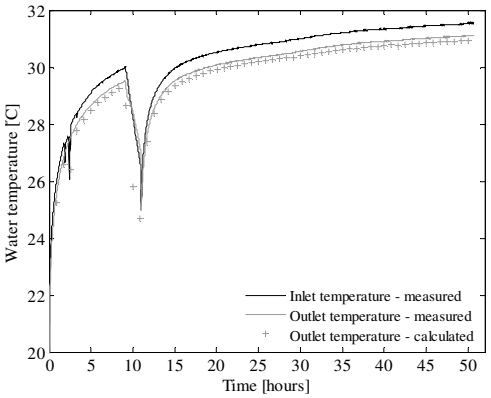

FIGURE 4. Interrupted test - numerical vs. experimental data

Another test performed by Beier et al. includes a two hour interruption of the electric power to the heater and circulating water pump, between 9 and 11 hours of operation. Figure 4 compares the measured water temperature at the outlet of the U-tube with model predictions. The proposed numerical model reproduces with acceptable accuracy the trend of the fluid temperatures over the entire period of interrupted test.

4. CONCLUSIONS

The paper presents a numerical model for the simulation of borehole U-tube heat exchanger. The proposed model allows the calculation of temperature of heat transfer fluid as well as temperature distribution in the surrounding grout and soil. The results are validated against experimental data. It is shown that the proposed model successfully reproduce the measured data. Small discrepancies between the model prediction and experimental data can be contributed to various factors like uncertainties in the measurements of thermal properties (conductivity and heat capacity) of pipe, grout and wet sand.

REFERENCES

[1] H. Yang, P. Cui, Y. Fang, Vertical-borehole ground-coupled heat pumps: A review of models and systems, *Applied Energy*, 87, 16-27, 2010.

[2] L.R. Ingersoll, H.J. Plass, Theory of the ground pipe source for the heat pump, *ASHVE Transactions*, 54, 339-48, 1948.

[3] H.S. Carslaw, J.C. Jaeger, *Conduction of Heat in Solids*, 2nd edition, Clarendon Press, Oxford, 1959.

[4] S.P. Rottmayer, W.A. Beckman, J.W. Mitchell, Simulation of a single vertical U tube ground heat exchanger in an infinite medium, *ASHRAE Transactions*, 103, 651-9, 1997.

[5] M. Tago, K. Morita, M. Sugawara, Heat extraction characteristics of a single U-tube downhole heat exchanger with square cross section, *Heat and Mass Transfer*, 42, 608-616, 2006.

[6] Z. Li, M. Zheng, Development of a umerical model for simulation of vertical U-tube ground heat exchangers, *Applied Thermal Engineering*, 29, 920-4, 2009.

[7] R.A. Beier, M.D. Smith, J.D. Spitler, Reference data sets for vertical borehole ground heat exchanger models and thermal response test analysis, *Geothermics*, 40, 79-85, 2011.

MINI-SYMPOSIUM

NUMERICAL MODELLING FOR VOLCANOES AND HIGH ENTHALPY GEOTHERMAL SYSTEMS

MINI-SYMPOSIUM ORGANISED BY G. DE NATALE AND C. TROISE

Third International Conference on Computational Methods for Thermal Problems
THERMACOMP2014, June 2-4, 2014, Lake Bled, Slovenia
N. Massarotti, P. Nithiarasu and B. Sarler (Eds.)

The role of stress-dependent permeability in enhanced geothermal systems modelling.

M. G. Di Giuseppe, A. Troiano, C. Troise, G. De Natale
INGV - Osservatorio Vesuviano, Via Diocleziano, 328, Naples (Italy),
mariagiulia.digiuseppe@ov.ingv.it

ABSTRACT

We present a procedure for testing the interpretation of the induced seismicity. The procedure is based on Coulomb stress changes induced by deep fluid injection during well stimulation, providing a way to estimate how the potential for seismic failure in different volumes of a geothermal reservoir might change due to the water injection. It was successfully applied to reproduce the observations collected during and after the complex stimulation cycle of the GPK2 and GPK3 wells at the Soultz sous Foret Enhanced Geothermal System EGS site (Alsace, France).

In this paper, a conceptual model that links the induced stress tensor and the permeability modifications is considered, with the aim to estimate the permeability change induced during the water injection. In this way, we can adapt the medium behaviour to mechanical changes, in order to better evaluate the effectiveness of the stimulation process for the enhancement of the reservoir permeability, while also refining the reconstruction of the Coulomb stress change patterns. Numerical tests have been developed that consider a physical medium comparable with the granitic basement of the Soultz EGS site, and a geometry of the system that is compatible with that of the GPK2-GPK3 wells. In such a way, the forecasting of the areas of higher likelihood for induced seismicity results in a good agreement between Coulomb stress change patterns and induced seismicity.

Key Words: *Heat Transfer, Finite Elements, Natural Convection.*

1. INTRODUCTION

Conventional geothermal resources, such as hot springs, have been effectively exploited in the past century, although their distribution and potential for supplying electricity is somewhat limited [1], [2]. However, geothermal resources span a wider range of heat sources from the Earth, and represent a large, indigenous resource that can provide base-load electric power and heat at a level that can have a major impact on economies [1]. Among these resources, there are enhanced geothermal systems (EGS), which were originally known as ‘hot dry rock’ systems. An EGS system involves drilling of a deep borehole into a layer of non-porous rock that is characterised by high temperature (i.e., usually more than 150 °C). The well is initially stimulated, with the injection of high-pressure fluid, to induce the rock to fracture, and thereby to increase its permeability. At the end, a reservoir for a fluid injected from surface is created, and additional boreholes can be drilled to extract the heat from the rock mass by circulating the fluid through the fracture network. These systems have huge potential for primary energy recovery using heat-mining technology that is designed to extract and use the stored thermal energy of the Earth [3], [4]. There are, however, drawbacks related to the potential for induced seismicity due to the deep borehole water stimulation. This problem is indubitably felt as being an unacceptable price by local communities, as demonstrated by the Deep Heat Mining Project that was started in Basel, Switzerland, in 1996, but is now suspended after a M 3.4 earthquake was recorded on December 7, 2006 [5], [6]. To make this risk acceptable for local communities, the potential for seismicity becomes an environmental

factor in the determination of the economics of EGS project development, and adequate procedures have to be developed for its estimation and mitigation.

We present a procedure for testing the interpretation of the induced seismicity that is based on Coulomb stress changes induced by deep fluid injection during well stimulation [7]. This provides a way to estimate how the potential for seismic failure in different volumes of a geothermal reservoir might change due to the well stimulation. This methodology was successfully applied to reproduce the observations collected during and after the complex stimulation cycle of the GPK2 and GPK3 wells at the Soultz sous Foret EGS site (Alsace, France). It represents a tool for the interpretation and mitigation of induced seismicity that can be used to forecast the areas of higher likelihood for induced seismicity, and also for better planning of oil and gas activities that imply injection and/or withdrawal of fluids in deep wells. To obtain an evaluation of the permeability enhancement obtained during the stimulation process, a conceptual model that links the induced stress tensor and the permeability modifications is considered, with the aim to estimate the permeability change induced during the water injection. In this way, we can adapt the medium behaviour to mechanical changes, in order to evaluate the effectiveness of the stimulation process for the enhancement of the reservoir permeability, while also obtaining the reconstruction of the Coulomb stress change patterns. Numerical tests have been developed that consider a physical medium and a system geometry comparable with the Soultz EGS site.

At the first stage, a continuous injection of cold water in one single well is simulated and the permeability enhancement effects evaluated. Once the procedure has been calibrated for this essential case, the previously mentioned stimulation cycle that involved cold-water injection into the GPK2-GPK3 Soultz system is reproduced.

2. METHOD

Our method of analysis consists of a two-step procedure. In the first step, injection of water is simulated (Pruess, 1991) in a homogeneous medium, approximating a crystalline granite basement compatible with the deep structure of the Soultz-sous-Forets (France) EGS site. The modelled 3D physical domain and the imposed initial conditions are shown (Figure1). Water at ambient condition is injected. In such a way we obtain the pressure and temperature changes at each point in the medium, at the final time. Such P and T changes at any point are subsequently considered as elementary sources, heterogeneously distributed in the whole discretised volume, which generate an incremental stress tensor field estimated by using a finite element code [8], [7]. The incremental changes in the stress tensor due to fluid injection (or withdrawal) are successively summed with background regional tectonic loading, which is assumed to be purely deviatoric and is modelled as stated in [9].

Once the complete field of stress changes is computed, a conceptual model linking induced stress and permeability modification in orthogonally fractured media is adopted, incorporating the influences of both normal strain and shear dilation on the effect of fluid flow. The permeability changes caused by the solid deformation may be expressed as a function of induced stress tensor [10]. An estimate of the permeability change along the whole volume is so obtained.

Due to the anisotropy of the induced stress tensor, permeability changes are, in principle, different in the three orthogonal directions, however, a mean value is assumed as k', the new medium permeability after fluid stimulation. If values of k', are selected exceeding the mean of the enhanced permeability more than 1 standard deviation, the corresponding points in the volume can be considered as the zone where borehole have been effectively stimulated. The procedure can be re-iterated to reconstruct the permeability of the medium as function of the time, during stimulation process composed by different injection rates.

3. RESULTS

Two distinct cases were considered here.

As the first case, ten days of 50 kg/s water continuous injection was simulated in the considered volume, and the induced stress tensor was evaluated at the end of the injection time. Following the procedure previously described, a mean permeability enhancement is obtained, giving a value of $k' = 4.2 \times 10^{-16}$ m^2, which represents a permeability that is about three-fold the starting permeability ($k_0 = 1.8 \times 10^{-16}$ m^2), in a spherical volume of about 0.5 km^3.

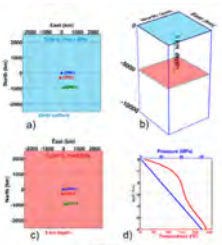
Figure 1

As the second case, the combined stimulation cycle realised in the GPK2-GPK3 wells (Soultz-sous-Forets, France) and descripted in [11] is reproduced. The whole injection cycle has been separated in six contiguous time step, as shown in Figure 2. At the end of each step, the induced stress tensor change was calculated following the proposed procedure, and the permeability enhancement was evaluated. In the following step, the permeability was changed, taking in account this result. Finally, a permeability as an injection function was reconstructed and considered during the stimulation. A final permeability of $k' = 8 \times 10^{-15}$ m^2 is obtained, about fourty-fold the starting permeability, in a volume of about 0.4 km^3. At each time, the Coulomb stress change was also calculated, to have a comparison with the experimentally induced seismicity related to time a and time f, as shown in Figure 3.

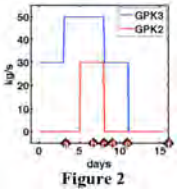

Figure 2

4. CONCLUSIONS

Coulomb stress changes appear to be the main cause for the induced seismicity during the stimulation that is generated by the water injection. These stress changes do not only result from changes in the pore pressure, but also from the whole change in the stress tensor at any point in the medium, which results from the pressure perturbations due to the injection. The numerical procedure presented here takes into account the permeability increase that is due to this induced stress changes.

A marked elongation of the Coulomb stress change patterns in the north direction was retrieved, compatible with the induced seismicity pattern. Furthermore, at the first simulated time step (time a), when the water was continuously injected only into well GPK3, the Coulomb stress changes already showed an elongated behaviour. This behaviour highlights the dependence of the induced seismicity pattern on the pre-existing loading of the regional stress field.

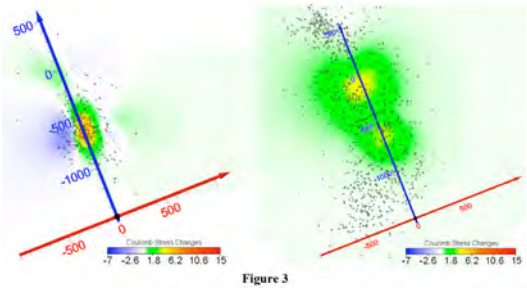
Figure 3

The high correlation between the coulomb stress changes and the induced seismicity distribution supports the reliability and robustness of the main hypothesis of this study of the relationship between the induced stress tensor variation and the permeability enhancement. The use of stress-dependent permeability constitutes an important step towards the theoretical planning of stimulation procedures, and towards interpretation and mitigation of the induced seismicity.

Figure captions

Figure 1. Sketch of the simulation volume. (a) Positions of the GPK1, GPK2 and GPK3 wells projected on the Earth surface. (b) The whole volume analysed. Blue plane, Earth surface; red plane, injection plane. (c) Positions of the GPK1, GPK2 and GPK3 wells projected on the injection plane. The pressure and temperature initial conditions on the plane are also indicated. (d) Initial pressure (blue) and temperature (red) conditions as a function of depth.

Figure 2. Simplified stimulation functions for the GPK2 and GPK3 Soultz- sous-Foreˆts wells, representing the rates of injected water. (a–f) Times of the stimulation cycle shown.

Figure 3. Maximum Coulomb stress changes (bar; projected on horizontal slices at z=-5000 m) at the times a and f indicated in Figure 2. Coulomb stress changes are also compared with seismicity that occurred during these periods. Note the good agreement between positive stress changes and seismic areas. Y axis (blue) of the reference system is along the direction passing between the two wells, with the X (red) and Z (black) axes.

REFERENCES

[1] Massachussetts Institute of Technology. *The Future of Geothermal Energy: Impact of Enhanced Geothermal Systems (EGS) on the United States in the 21st Century: An Assessment*, MIT Press, MA, USA, 2006.

[2] D. Giardini, Geothermal quake risks must be faced, *Nature*, 462, 848–849, 2009.

[3] J.W. Tester and M.C. Smith, Energy Extraction Characteristics of Hot Dry Rock Geothermal Systems, *Proceedings of the Twelfth Intersociety Energy Conversion Engineering Conference, Washington, D.C. American Nuclear Society*, 1, 816, 1977.

[4] S. K. Sanyal and S. J. Butler, An Analysis of Power Generation Prospects From Enhanced Geothermal Systems, *Geothermal Resources Council Transactions*, 29, 2005.

[5] M.O. Haring, U. Schanz, F. Ladner and B.C. Dyer, Characterisation of the Basel 1 enhanced geothermal system, *Geothermics*, 37, 469–495, 2008.

[6] J. Ripperger, P. Kastli, D. Fah and D. Giardini, Ground motion and macroseismic intensities of a seismic event related to geothermal reservoir stimulation below the city of Basel-observations and modelling, *Geophys. J. Int.*, 179, 1757–1771, 2009.

[7] A. Troiano, M. G. Di Giuseppe, C. Troise, A. Tramelli and G. De Natale, A Coulomb stress model for induced seismicity distribution due to fluid injection and withdrawal in deep boreholes, *Geophys. J. Int.*, 2013.

[8] A. Troiano, M. G. Di Giuseppe, Z. Petrillo, C. Troise and G. De Natale, Ground deformation at calderas driven by fluid injection: modelling unrest episodes at Campi Flegrei (Italy), *Geophys. J. Int.*, 187, 833– 847, 2011.

[9] Portier, S. & Vuataz, F.D. (Eds), 2009. *Studies and support for the EGS reser- voirs at Soultz-sous-Foreˆts. Final report April 2004–May 2009*, Project financed by State Secretariat for Education and Research (SER/SBF) and Swiss Federal Office of Energy (OFEN/BFE).

[10] Peng, S., Zhang, J. *Engineering Geology for Underground Rocks*, 207-211. Springer, 2007.

[11] R. Baria et al., *Microseismic monitoring of the world's largest potential HDR reservoir*, in Twenty-Ninth Workshop on Geothermal Reservoir Engineering, Stanford University, Stanford, CA, 2004.

Third International Conference on Computational Methods for Thermal Problems
THERMACOMP2014, June 2-4, 2014, Lake Bled, Slovenia
N. Massarotti, P. Nithiarasu and B. Sarler (Eds.)

NUMERICAL MODELING OF THE THERMAL STRUCTURE AND EVOLUTION OF HYDROTHERMAL SYSTEMS

Samuel Scott, Philipp Weis, Thomas Driesner
Institute of Geochemistry & Petrology, ETH Zurich, Clausiusstrasse 25, 8092 Zurich, Switzerland,
samuel.scott@erdw.ethz.ch

ABSTRACT

This study applies the fluid flow and heat transport code CSMP++ to simulate the cooling of intrusions and the sub-surface structure and evolution of hydrothermal systems. These 2D simulations are focused on characterizing the influence of important factors such as magma chamber depth as well as system-scale permeability. Preliminary results show that the depth of the intrusion plays an important role in system evolution. If the roof of the intrusion is near 2-2.5 km depth, extensive two-phase zones develop above the intrusion and are able to transport heat much more rapidly than for liquid-dominated upflow zones associated with deeper intrusions. Higher host rock permeability results in lower upflow temperatures and thus two-phase zones are more short-lived and confined to shallower depths; however, since the total fluid flux around the intrusion is much greater, higher permeability causes them to cool more rapidly and develop more numerous, narrower upflow zones than develop at lower permeability. In general the thermal and hydraulic structure and system lifetime can vary greatly in response to 'small' changes in heat source depth and system-scale permeability.

Key Words: *Geothermal systems, High enthalpy geothermal resources, finite element method, Natural Convection.*

1. INTRODUCTION

Volcanic geothermal systems represent focused zones of intrusive activity, seismicity, heat transfer, fluid flow and rock alteration of great geologic and economic significance. Due to the difficulty and cost of obtaining high-resolution hydrological, geophysical and geochemical data from active geothermal systems (often not available at all for depths >2.5 km), numerical modeling of fluid flow and heat transfer is an essential method to improving the qualitative and quantitative understanding of these complex systems. In recent decades, modern simulation tools that include the thermodynamic properties of fluid phases in the H_2O(-NaCl) system up to magmatic temperatures and pressures as well as the full physics of two-phase (liquid + vapor) flow including phase separation have been developed. Full incorporation of the non-linear temperature and pressure dependence of fluid properties has been shown to be of critical importance, as hydrothermal systems tend to self-organize in order to optimize energy transfer in response to factors such as fluid density and viscosity (Jupp & Schultz, 2004; Coumou et al., 2008).

The purpose of this study is to perform geologically-constrained numerical simulations exploring the influence of heat source depth and system-scale permeability. The emphasis is not on realistically capturing the complex, dynamic feedbacks between fluid flow, mineral precipitation and rock mechanics, but rather to derive a broad fundament for understanding the sub-surface structure and evolution of natural geothermal systems.

2. MODEL SET-UP

This study was performed using the Complex Systems Modeling Platform CSMP++ (e.g. Matthäi et al., 2007). The governing equations of multi-phase mass and energy conservation are solved using a pressure-enthalpy-based formulation implemented in a Control Volume-Finite

Element (CVFEM) scheme, which has recently been described and benchmarked against HYDROTHERM and TOUGH2 (Weis et al., 2014).

An example of a typical model configuration is given in Figure 1, for an intrusion centered at 3.5 km depth with horizontal and vertical axis lengths of 2 km and 1 km, respectively. The computational domain is 5 km is and 15 km in vertical and horizontal extent, respectively, and consists of roughly 14,000 elements. Initially, the porous medium is saturated with water and thermally equilibrates with a basal heat flux of 100 W m^{-2} (corresponding to thermal gradient of 45°C/km assuming K = 2.25 W m^{-1} C^{-1}). The pressure at the top boundary is fixed to be 1 bar and the temperature 10°C.

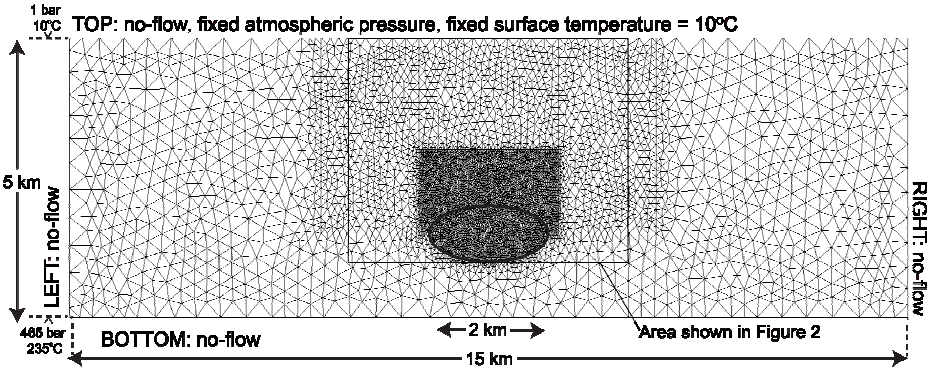

FIGURE 1. Generalized model set-up showing FEM discretization, initial and boundary conditions.

Although relatively little information regarding heat source depth is available from active geothermal systems, this study varies this parameter within a range of 'realistic' values. In these simulations, the top of the intrusion was varied from 3 km depth (i.e. Fig. 1) to 2 km depth. System-scale permeability was varied from 10^{-15} m^2 (intermediate) to 10^{-14} m^2 (relatively high). The most significant assumption that was made involves the temperature dependent permeability model; this study uses the approximation of Hayba and Ingebritsen (1997), where temperature begins to decrease log-linearly from the host-rock value above 360°C and is 10^{-22} m^2 (impermeable) above 500°C.

3. RESULTS

A suite of simulations testing the effect of intrusion depth and system-scale permeability show that the thermal and hydraulic structure and system lifetime can vary greatly in response to 'small' changes in controlling parameters. Systems are highly dynamic and evolve as fluid convection heats the upper crust and the geometry of the heat source changes with progressive cooling from the margins. Snapshots of different types of systems that can develop in response to changes in intrusion depth and system-scale permeability are shown in Figure 2.

The dramatic differences in system style are reflected by different spatial distribution of isotherms and the depth/extent of two-phase zones (shown in red). For a shallow intrusion in an intermediate permeability host rock (Fig. 2a & 3a), a two-phase zone develops directly above the intrusion upon heating due to the fact that the fluid pressure at this depth (~2 km) is less than the critical pressure of pure water. Liquid volumetric saturation in the upflow zones is around 0.5-0.75. The high upward mobility of vapor in the two-phase zone results in a rapid cooling of the intrusion and produces the hottest upflow temperatures, with boiling extending throughout the entire depth.

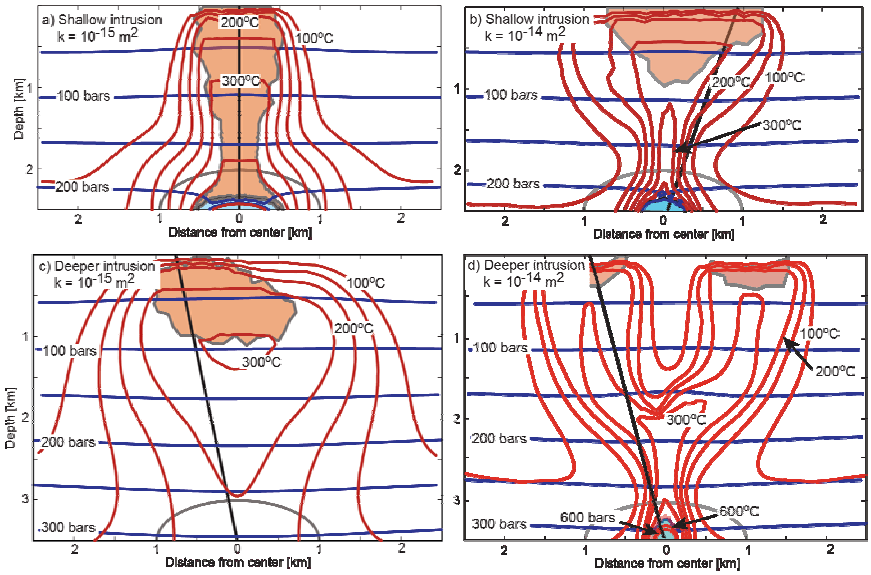

FIGURE 2. Thermal/hydrologic structure of hydrothermal systems at different stages, showing a number of contrasting 'end-member' styles. a) Intrusion depth = 2-3 km, Host rock permeability (k) = 10^{-15} m^2, 3800 years b) 2-3 km, k = 10^{-14} m^2, 2000 years c) 3-4 km, k = 10^{-15} m^2, 12500 years d) 3-4 km, k = 10^{-14} m^2, 2000 years. Black lines show location of temperature profiles shown in Figure 3. Regions of supercritical fluid/superheated steam shown in blue; two-phase zones shown in red.

For a configuration with a shallow intrusion but higher host-rock permeability (Figs. 2b & 3b), the higher permeability causes fluids on the margins of the intrusion to pick up less heat before flowing away, thus resulting in lower upflow temperatures and limiting boiling to the upper 1 km. Additionally, higher permeability allows more efficient recharge of cold, surrounding fluid above the margins of the intrusion, causing the isotherms to be packed more tightly around the central upflow at depth.

For a deeper intrusion with intermediate permeability (Figs. 2c & 3c), the higher fluid pressure above the intrusion prevents phase separation upon heating. In the early stages of cooling, heat is extracted by fluids upflowing along the sides of the intrusion, rather than a single upflow zone located over the center. As the intrusion cools from the margins inward, these two upflow zones eventually merge to form a single one. Boiling begins at depth (~2 km) and gradually moves upward with time. The intrusion cools below 500°C by about 7500 years.

For a deeper intrusion with higher permeability (Figs. 2d & 3d), the lowest upflow temperatures and shallowest depths of boiling zones are observed. Liquid saturation in the boiling zones is >0.9. The 'bifurcated' appearance of the hydrothermal system at 2000 shows that fluid upflow has been centered over the edges of the intrusion. Similar to the case with intermediate permeability (Fig. 2c), the two upflows have merged below 1.5 km as the shape of the intrusion evolved from an oblate to a prolate ellipsoid due to hydrothermal cooling. Despite the lower upflow temperatures, the increased fluid fluxes resulting from higher permeability allow for faster cooling compared to the intermediate permeability.

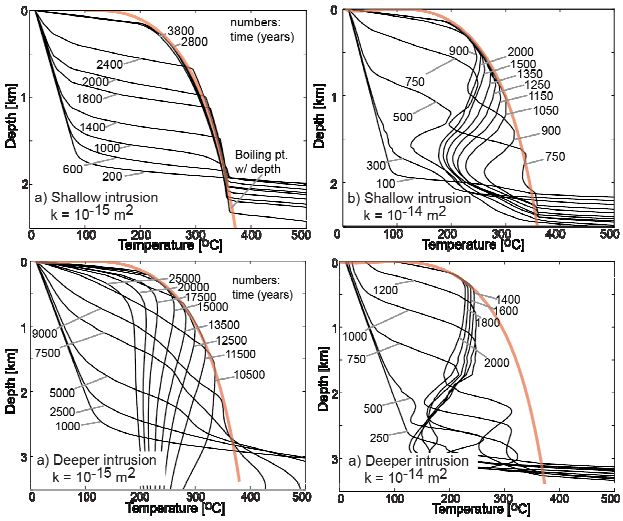

FIGURE 3. Temperature versus depth profiles along black lines shown in Figure 2a-d.

4. CONCLUSIONS

This study reports results for a number of generic numerical simulations carried out to test the main effect of magma chamber depth and system-scale permeability on the thermal and hydrologic structure of volcanic geothermal systems. The results show that relatively 'small' changes in these controlling parameters can result in contrasting styles of hydrothermal systems and different system lifetimes. The differences shown in these geologically simplified numerical models may relate to differences observed between various natural hydrothermal systems. Future simulations will seek to evaluate the influence of a number of other potentially important factors that have been overlooked in the present contribution, such as permeability heterogeneity/anisotropy, topography and fluid salinity.

REFERENCES

[1] T.E. Jupp and A. Schultz, 2004, Physical balances in subseafloor hydrothermal convection cells, *Journal of Geophysical Research: Solid Earth*, 109, B05101

[2] D. Coumou, T. Driesner and C.A. Heinrich, 2008, The structure and dynamics of mid-ocean ridge hydrothermal systems, *Science*, 321, 1825-1828

[3] Matthäi, S. K., Geiger, S., Roberts, S. G., Paluszny, A., Belayneh, M., Burri, A., Mezentsev, A., Lu, H., Coumou, D., Driesner, T., and Heinrich, C. A., 2007, Numerical simulation of multi-phase fluid flow in structurally complex reservoirs: Geological Society, London, Special Publications, 292, 405-429.

[4] Weis, P., Driesner, T., Coumou, D., and Geiger, S., 2014, Hydrothermal, multi-phase convection of H2O-NaCl fluids from ambient to magmatic temperatures: A new numerical scheme and benchmarks for code comparison: Geofluids, (in press), doi: 10.1111/gfl.12080

[5] D.O. Hayba and S.E. Ingebritsen, 1997, Multiphase groundwater flow near cooilng plutons, *J. Geophys. Res.*, 102, 12235-12252

Third International Conference on Computational Methods for Thermal Problems
THERMACOMP2014, June 2-4, 2014, Lake Bled, Slovenia
N. Massarotti, P. Nithiarasu and B. Sarler (Eds.)

ROCK THERMAL BEHAVIOUR – ANALYIS OF DATA FROM A MONITORING PROGRAMME.

Majid Sedighi, Shakil A. Masum, Hywel R. Thomas, Daniel P. Bennett
Geoenvironmental Research Centre, School of Engineering, Cardiff University, The Queen's Buildings, Newport Road, Cardiff, CF24 3AA, UK, SedighiM@cf.ac.uk, MasumSA1@cf.ac.uk, ThomasHR@cf.ac.uk, BennettDP@cf.ac.uk

Erik Johansson
Saanio & Riekkola Oy, 4 Laulukuja, Helsinki, FI-00420, Finland, Erik.Johansson@sroy.fi

Topias Siren
Posiva Oy, Olkiluoto, Eurajoki, FI-27160, Finland, Topias.Siren@posiva.fi

ABSTRACT

This paper presents the results of an investigation into the thermal behaviour of a site proposed for the deep geological disposal of high level radioactive waste in Finland. Temperature data, collected from 57 boreholes at depths of up to 1000m have been studied. The thermal behaviour of the rock at the site, which is based in ONKALO, is discussed. The results achieved provide an improved understanding of in-situ rock thermal conditions at the site; information which is required for the long term safety assessment of the disposal option.

Key Words: *Rock temperature, ONKALO, Olkiluoto, geothermal, data analysis.*

1. INTRODUCTION

This paper considers the results of a thermal monitoring programme carried out at a site in Finland, where a geological repository for the disposal of high level nuclear waste is being considered. The site, which is located in the Gulf of Bothnia, has been selected for the possible disposal of the spent fuel produced by two nuclear power plants on the Olkiluoto island (Figure 1).

An Underground Rock Characterisation Facility (URCF), named ONKALO, has been constructed at the site, which comprises approximately 5km of access tunnel to the 420m disposal depth [1]. Figure 2 presents the ONKALO rock characterisation facilities. The ONKALO URCF allows for the testing of the design concept as the construction is developed and provides on-site information of rock conditions [1].

As part of a multidisciplinary monitoring programme, data related to geological, thermal, rock mechanics, hydrogeological and hydrogeochemical processes have been collected by Posiva Oy [2,3,4]. This paper presents a description of the investigation and analysis carried out on the temperature datasets, with the aim of providing a better understanding of the in-situ temperature of the rock at the site.

FIGURE 1. The Olkiluoto site, ONKALO URCF (hatched area) and investigation boreholes [4]

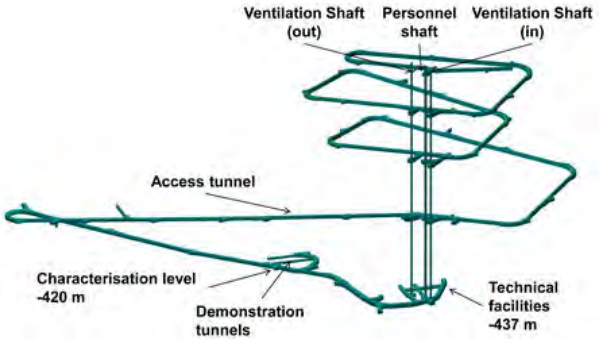

FIGURE 2. The ONKALO Underground Rock Characterization Facility[4]

2. THERMAL MONITORING PROGRAMME AT OLKILUOTO AND ONKALO

Temperature data have been collected at the Olkiluoto site and ONKALO at various locations. Three categories of temperature datasets have been collected as follows: i) data collected from the 57 deep boreholes, ii) measurements in the ONKALO ramp and two investigation rooms located at 140 and 437m depth, iii) surface data obtained from four weather stations and four measurement ditches[4,5].

A series of analyses and visualisations of the data have been performed by the Geoenvironmnetal Research Centre, Cardiff University using techniques relevant to each data series [5]. The time-series data obtained from the measurements during “Posiva Flow Log” (PFL) tests [6] in boreholes OL-KR1 to OL-KR57, shown in Figure 1, have been used to obtain the in-situ rock thermal conditions. The PFL dataset contain two series of information which include information from the PFL measurements, with pumping and without pumping, up to a depth of approximately 1000m [4]. The results of the analysis of the PFL data are presented in this paper.

3. RESULTS OF ROCK THERMAL MONITORING

Data obtained during PFL measurements, without pumping, have been used to retrieve the values of rock temperature with depth. These are presented in Figure 3. The geothermal gradient obtained from the analysis was found to be approximately 1.4 °C/100m with relatively uniform temporal and spatial pattern.

A series of contour plots was prepared based on data recorded in year 2006, based on information from 16 boreholes. The spatial distribution of temperature obtained from various PFL measurements, with pumping, at depths of 50, 100, 200 and 400m was studied. Figure 4 presents a contour plot of temperature distribution at a depth of 400m.

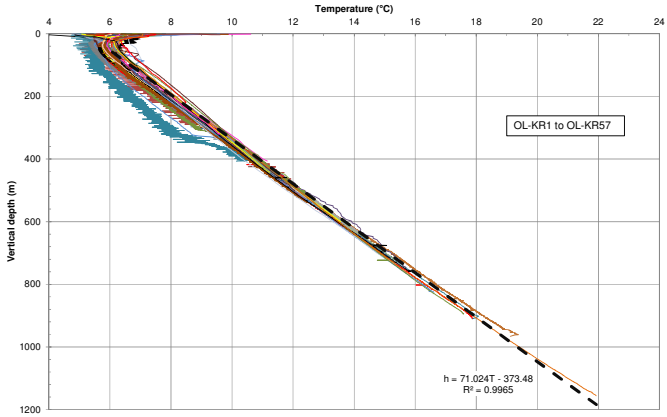

FIGURE 3. Rock temperature with depth obtained from the PFL measurements

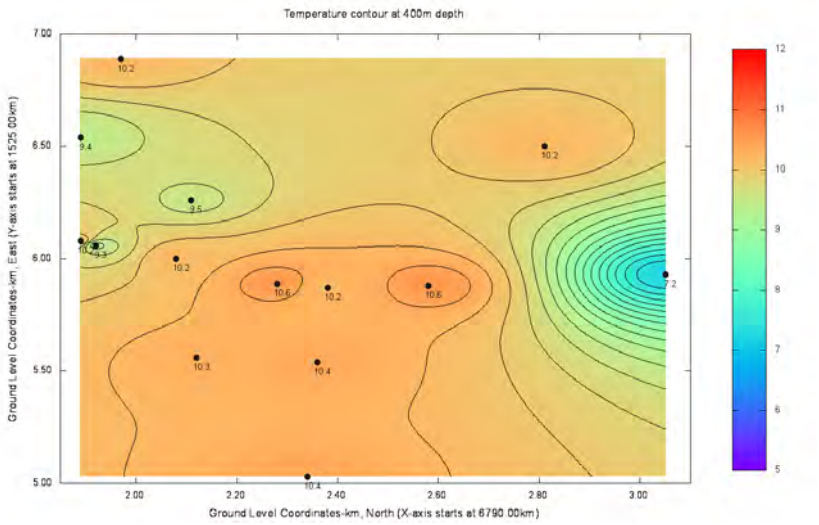

FIGURE 4. Average temperatures at 400m depth calculated from PFL measurements with pumping in year 2006.

As shown in Figure 1 and 2 and from the analysis of rock datasets, a relatively uniform distribution of temperature was observed at all depths across the site. It is anticipated that the proximity to the sea has been effective in relatively higher temperature observed at the depths shallower than 400m in the Southern boundary of the site. The average temperature values observed during the period 2001-2010 for the depth 400m is around 10 – 11 °C.

Analysis of the time series datasets indicated that the variation of temperature with time for all boreholes at depths 50, 100, 200 and 400m, are relatively insignificant, in particular for a period of 5 years between 2005 and 2010. However, more fluctuation in the mean annual temperature can be observed between year 2001 and 2005. The study of data from other boreholes indicated that temperature profile is relatively stable in different yeas.

4. CONCLUSIONS

The results of an investigation into the rock thermal behaviour of a site proposed for the deep geological disposal of high level radioactive waste in Finland have been presented. The results achieved provide an improved understanding of the thermal regime in the rock.

ACKNOWLEDGEMENT

The work presented was performed by the Geoenvironmental Research Centre, Cardiff University under contract to Posiva Oy. The financial support received is acknowledged.

REFERENCES

[1] Posiva, *ONKALO - Main Drawings in 2007*. Working Report 2008-01, Posiva Oy, 2008.

[2] Posiva, *Programme of Monitoring at Olkiluoto During Construction and Operation of the ONKALO*. Report POSIVA 2003-05, Posiva Oy, 2003.

[3] Posiva, *Monitoring at Olkiluoto – A Programme for the Period before Repository Operation.* Olkiluoto, Report POSIVA 2012-01, Posiva Oy, 2012.

[4] E. Johansson and T. Sire, Results *of monitoring at Olkiluoto in 2012, Rock mechanics*. Working Report, 2013-47, Posiva Oy, 2014.

[5] M. Sedighi, D.P. Bennett, S.A. Masum, H.R. Thomas and E. Johansson. *Analysis of temperature data at the Olkiluuto*, Working Report 2013-58, Posiva Oy, 2014.

[6] Öhberg, A. and Rouhiainen, P. 2000. *Posiva groundwater flow measuring techniques*. Report POSIVA 2001-12, Posiva Oy, 2000.

Third International Conference on Computational Methods for Thermal Problems
THERMACOMP2014, June 2-4, 2014, Lake Bled, Slovenia
N. Massarotti, P. Nithiarasu and B. Sarler (Eds.)

Sustainability analysis of geothermal resource for electricity generation: the example of Ischia Island (Southern Italy)

S. Carlino, R. Somma, A. Troiano, M.G. Di Giuseppe, C. Troise and G. De Natale

Istituto Nazionale di Geofisica e Vulcanologia, Sezione di Napoli, Osservatorio Vesuviano
Via Dioclezionao 328, 80124, Naples (Italy), stefano.carlino@ov.ingv.it

ABSTRACT

We analyze the possible disturbance on temperature and pressure filed in the shallow geothermal reservoir of Ischia Island, due to the heat withdrawal for electric production related to small geothermal power plant size (1-5MWe). Such analysis has been performed by using numerical simulations based on a well known thermofluid-dynamical code (TOUGH2®). Obtained results show that such geothermal exploitation generates a perturbation of temperature and pressure field which, however, is confined in a small volume around the well. At shallow level (0-100m) the exploitation does not produce any appreciable disturbance, and can be made compatible with local spa industry, which is the main business of the island. Such results are crucial for the general assessment of geothermal resource sustainability.

Key Words: *geothermal plants, Ischia Island, sustainable energy*

1. INTRODUCTION

The active volcanic island of Ischia has been the site of many hydrogeological, volcanological and geothermal studies since the early XVI century, which provided important data on volcano dynamics and tectonics [1]. The presence of a shallow magma body beneath the island, whose top is located at a depth of about 2km, produced a well developed geothermal system, whit many surface manifestation (fumaroles and hot springs). These features pushed the SAFEN Company to investigate the geothermal system of the island for geothermal exploitation aimed to electric production, since 1939 [2]. The data obtained by the SAFEN researchers highlighted that a large amount of the potential resource is related to vapor dominated systems and that useful temperatures for electric production can be generally found just few hundreds meters below the sea level. In 1950 a 300 kW binary cycle plant, the first one of this kind worldwide, was installed in the Island, on the Forio beach. The endeavor was abandoned later due to practical problems related to incrustations and corrosion, which the adopted technology at that old time was not able to solve [1]. At the present, the geothermal resource is used just for baths and wellness, with more than 180 spa and 130 thermal pools, fed by about 200 shallow wells, and in some cases for house heating. In recent times the interest towards the geothermal-electric exploitation at Ischia is largely increasing, since a number of exploitation leases has been submitted to the Ministry for Economic Development of Italy. In order to understand the possible effect of geothermal fluids extraction, for electric production, on the shallow hydrothermal system of the island, which is exploited for spa industry of the island, we performed a numerical using TOUGH2®. We show that thermal and pressure perturbations, after 30 years of fluids withdrawal, does not affect significantly the shallow hydrothermal system.

2. THE GEOTHERMAL RESERVOIR OF ISCHIA ISLAND

The geothermal system of Ischia Island can be defined from a semi-quantitative point of view by using the literature data [1-2]. The main features of the Ischia geothermal system are accordingly summarized here. The average temperature gradient involves the onset of water critical condition

(374°C, 22MPa) at a maximum depth of about 2km, very close to the top of the cooling magma source. The high average temperature gradient (~180°-220°Ckm^{-1}), which is recorded in the western and southern sector of the island, generates a quickly decreasing of permeability (k), above 370°C [3], thus the expected value of *k* is lower (or equal) than $10^{-17}m^2$ below the brittle-ductile transition, which occurred at about 2km of depth. The permeability from about 150m to about 800m, is calibrated on the temperature-depth curves and is of the order of $10^{-15}m^2$ [1] which promotes the advection of fluids. Above this layer, a less permeable zone of pyroclastic deposits occurs, whose permeability is probably about $10^{-16}m^2$. It should be noted that minimum permeability of magma chamber wall rocks for volatiles escaping is $10^{-20}m^2$ to $10^{-18}m^2$, while above value of $10^{-16}m^2$ advection processes can occur causing fluid mass transfer [3]. Both drilling and geochemical data, provided for the western and south-western sector of the island, allow us to obtain a fairly reliable picture of the geothermal reservoir in this sector. A first shallow geothermal reservoir is located from 150m to at least 500m, with temperature between 150°C and 200°C and pressure of about 4MPa (40bar). A second and deeper reservoir is hypothesized at depth > 900m, with temperature of 270°C to 300°C and pressure of 9MPa (90 bar) [4]. The latter is not well constrained, due to the lack of drilling data, whose maximum depth is about 1000m. The aquifer in the eastern sector of the island is probably deeper than in the western one, and also the isotherms sunk of few hundreds of meters. The depth and the fluid circulation of the geothermal reservoirs are also controlled by the volcano-tectonic of the area. The shallow reservoirs are influenced by the sea and rain water contamination, as testified by the large increase of TDS from the center of the island towards the coast. Isotopic data, actually, show that the main source of H_2O is meteoric water, while the magmatic source supplies most of CO_2 and He. The rising of the deeper geothermal reservoir, which was just inferred from geochemical analysis of gases and thermal waters, is, of course, most enriched in magmatic gases and vapor phases. Periodically, the deeper aquifer can reach the condition for separation of the vapor phase, which rises up along the fracture and faulting of the island[4]. It is also likely that the most of the geothermal reservoir has been developed within the fractured trachitic lavas and welded tuffs, which have a high relative permeability.

3. RESULTS OF NUMERICAL MODELING

The evaluations reported in the previous sections allow us to obtain useful constrains to estimate the thermodynamic effects of fluids withdrawal from geothermal reservoir and reinjection, during production phases. To this aim the numerical code TOUGH2® has been used for numerical evaluations of Temperature and Pressure changes due to geothermal exploitation via a finite Volumes resolution of Mass and Energy balance equations in a region of space, discretized in a mesh grid. The reservoir has been modeled as a porous and fractured medium characterized by volume V=18 km^3, porosity ϕ=0.2 and average rock density ρ=2400kgm^{-3} . A saturated two-phases mixture of water and vapor flows in this interior, due to the fixed porosity, with fluid maintaining thermal equilibrium with surrounding rocks matrix. The simulation takes into account the fluid density variation with temperature. The thermal gradient is comparable with the one experimentally measured and reaches a T=320°C temperature at a depth of 2km; the thermal conductivity is fixed 2.1 $Wm^{-1}K^{-1}$ (the average of upper and lower values generally used in literature) and the pressure gradient is essentially hydrostatic. The considered volume for the simulation is formed by a surface thick layer of 150m with permeability k =$10^{-16}m^2$, where the temperature gradient is roughly purely conductive; an intermediate layer, from 150m to 800m, characterized by permeability k=$10^{-15}m^2$, which represents the advection dominated zone and a deeper layer, below 800m, with k=$10^{-18}m^2$, where the thermal regime is conductive again. The first case simulates the extraction of fluid from a 600m deep well, with flow rate of 22kgs^{-1}, and temperature at well head of about 150°C (it is assumed a production of about 1-2 MWe for each well). The temperature and flow rate data are those related to SAFEN productive test [2]. In such a way, we are firstly simulating a productive well without re-injection. Our simulation ends as soon as the system becomes steady, i.e. when changes of temperature and pressure fields do not occur

anymore; we noted that after about 30 years of fluid withdrawal, the system reaches a roughly steady state. Figure 1 reports temperature changes, indicating that the maximum cooling effects (-6°C) on fluid occur in correspondence to the shallower permeability contrast, over a volume of about 0.02km^3, centred at the vertical well axis. A loss of pressure (less then 10bar) is observed in the whole shallow reservoir, up to a distance of 2km from the well. A more depressurized zone, up to a value of -30bar (3MPa) appears confined within a conic-shaped volume around the well, with radius of 150m, centered at 600m of depth.

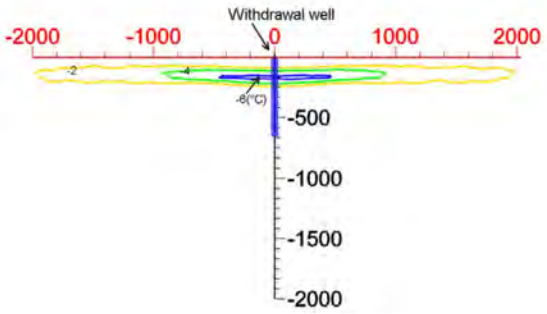

FIGURE 1. Maximum temperature variation after 30 years of heat withdrawal which indicates that maximum cooling effect occurs in correspondence to the shallower permeability contrast.

In a second simulated case a reinjection well, again 600m deep, is also introduced at a distance of 650m from the productive one. Water extracted from the productive well at T=150°C is re-injected with a flow rate of 22kgs^{-1} and a temperature of 90°C. After 30 years of a similar production-reinjection cycle, a substantial thermal perturbation around the reinjection well appears, due to the effect of cooled water on the rocks, resulting in a temperature decrease of more than -35°C (Figure 2). This effect is evidently confined around the bottom of the reinjection well, very close to the well axis (within a ray of 30m the maximum temperature drop is about -50°C). As the distance from the well increases the thermal perturbation decreases, and vanishes at distance of about 300m. Around the productive well, the temperature variation is lower than, and is just of few Celsius degrees. Around the reinjection well, as said before, the effect of cooled water create a strong thermal gradient. Anyway, no significant temperature variations, with respect to the initial conditions, appear close to the surface, where thermal springs are confined. Regarding the pressure changes, the production-reinjection cycle generates a pressure drop of the geothermal system in a roughly spherical volume at the bottom of productive well and a pressure increase at the bottom of the reinjection well. ΔP larger than 2MPa and smaller than -2.5MPa, for injection and production respectively, occurred into a volume of $1.7 \cdot 10^7$m^3 for each well. In general, the pressure drop associated with the fluids withdrawal, can induce a decreasing of hot springs occurrence at the surface, particularly when the geothermal system is water dominated. This effect is mitigated by the presence of reinjection wells, which guarantee the water recharge of the system. The drop of pressure, otherwise, can cause also consistent increment of vapor infusion from vapor dominated zones, towards the surface, which is due to the increment of vapor saturation and mobility [4]. This process, which is considered in our analysis as a part of complex thermo-dynamic processes occurring during fluid withdrawal, produces a slight increment of temperature in the infusion zone due to vapor latent heat releasing. Furthermore, since the drop of pressure is confined around the axis of the well, a slight decrease of water table is expected to occur just in the proximity of the well, while its effect becomes negligible as the distance increases in respect to the perturbation centre. It is important to consider here how the thermodynamic system, during heat extraction, behaves to the variation of fundamental parameters, such as thermal conductivity (λ) and

permeability (k). These parameters are in fact not univocally defined, so that their possible variation ranges have to be considered. In order to get a more reliable picture of the sustainability, a sensitivity study of the system has been done by varying λ and k in the possible range of values inferred from literature and from this study, and observing the response of the system. We considered the upper and lower limit of the values range of λ (1.5 to 2.7 Wm-1K-1) and spanned the permeability of the reservoir (advective zone) over an order of magnitude, considering the limit values of $5 \cdot 10^{-15} m^2$ and $5 \cdot 10^{-16} m^2$ respectively. The results show that the system is low sensitive to variation of thermal conductivity (no appreciable variations occur) and is more sensitive to the variation of the permeability in terms of temperature and pressure field change. The maximum variation of temperature and pressure, for the above values of thermal conductivity is ΔT~1.5K and ΔP~1bar. On the other hand, permeability variation produces a significant drop of pressure and only a minor decrease of temperature (this simulation was performed fixing the average value of λ = 2.1 $Wm^{-1}K^{-1}$.

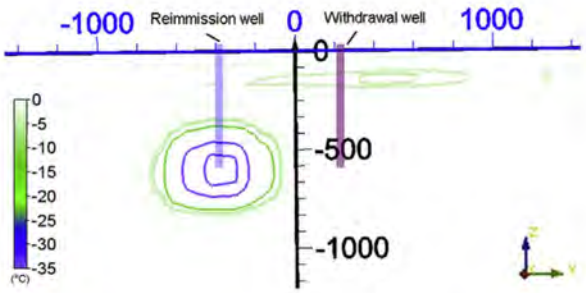

FIGURE 2. Thermal perturbation around the withdrawal and reinjection well after 30 years of fluid extraction. Around the productive well, the temperature variation is negligible. Around the reinjection well the effect of cooled water creates a strong thermal gradient. The effect of cooled water on the rocks results in a temperature variation up to 35 °C. This effect is confined around the bottom of the reinjection well.

REFERENCES

[1] S. Carlino, R. Somma, C. Troise and G. De Natale,. The geothermal exploration of Campanian volcanoes: Historical review and future development, Renewable and Sustainable Energy Reviews, Volume 16, Issue 1, (2012) 1004-1030.

[2] F. Penta, B.Conforto, Risultati di sondaggi e di ricerche geominerarie nell'isola d'Ischia dal 1939 al 1943 nel campo di vapore, delle acque termali e delle forze endogene in generale, Annali di Geofisica 4 (1951) 159-191.

[3] D. O. Hayba, S. E. Ingebritsen, Multiphase groundwater flow near cooling plutons. J. Geoph. Res., 102 (1997)12235-12252.

[4] S. Carlino, R. Somma, A. Troiano, M.G. Di Giuseppe, C. Troise and G. De Natale (2014) The geothermal system of Ischia Island (southern Italy): critical review and sustainability analysis of geothermal resource for electricity generation. Renewable Energy, 62 – 177-196.

MINI-SYMPOSIUM

NUMERICAL SIMULATION OF ENERGY CONVERSION IN WASTE-TO-ENERGY PLANTS

MINI-SYMPOSIUM ORGANISED BY N. MASSAROTTI, P. STEHLIK, J. HÁJEK, M. COSTA AND F. ARPINO

Third International Conference on Computational Methods for Thermal Problems
THERMACOMP2014, June 2-4, 2014, Lake Bled, Slovenia
N. Massarotti, P. Nithiarasu and B. Sarler (Eds.)

CFD ANALYSIS OF TUBE CIRCUMFERENCE HEAT FLUX VARIATION IN RADIANT SECTION OF FIRED HEATER

Jiří Hájek*, Zdeněk Jegla, Jiří Vondál
Brno University of Technology, Faculty of Mechanical Engineering, Institute of Process and Environmental Engineering, Technická 2, Brno 616 69, Czech Republic,
hajek@fme.vutbr.cz, jegla@fme.vutbr.cz, vondal@fme.vutbr.cz

ABSTRACT

Tubular fired heater in vertical cylindrical arrangement operated in crude oil atmospheric distillation unit is simulated numerically to analyse the circumference heat flux variation and distribution of thermal loading on the individual tubes. The complex numerical model describes flow, gas combustion and radiative heat transfer inside the radiation section of the fired heater. Special attention is focused on the degree of non-uniformity of circumferential distribution of heat flux on tube walls. Obtained results show that assumptions invoked in 1D design calculations of fired heaters are significantly underestimating heat flux variability.

Key Words: *Heat Transfer, Tube Circumference Heat Flux Variation, Fired Heater.*

1. INTRODUCTION

American Petroleum Institute Standard 560 [1] can be considered the main fired heater design reference worldwide. Despite regular updates of this standard, the principle of calculation of important operating parameters of the fired heater radiant section remains the same for many decades; it is based on average heat flux to the radiant tubes. The significant variation of the real heat flux distribution around the length and circumference of fired heater tubes was studied in depth over the years by various authors resulting in estimation technique standardized in several updates of API Standard 530, with the latest version in [2]. The calculation using the API Standard 530 [2] yields estimate of maximum tube temperature, which is a critical parameter for the safety and lifetime of the heater. The maximum tube metal temperature is in design calculations estimated dominantly using the product of average radiant heat flux and several empirical correction factors, which can be insufficient for dependable decision support on the lifetime of tube systems under specific operating conditions. One of these parameters that influence uniformity of heat flux on radiant tubes is the so-called tube-circumference heat flux variation factor. Its value is based on empirical correlations and depends on the distance of tubes from furnace wall.

2. BRIEF THEORETICAL BASIS

Allowable average radiant heat flux (q_r) is one of the most closely watched design factors of fired heaters for crude oil atmospheric distillation. For determination of real average radiant heat flux of designed fired heater it is necessary to determine the radiant heat duty (Q_r) first. However, determination of Q_r generally depends on many factors, including the furnace geometry, combustion conditions and heated fluid temperature. Detailed procedure for radiant section duty calculation is beyond the scope of this paper, but there are well-established, 1D quasi-theoretical techniques for determining radiant chamber performance, such as Lobo-Evans, Wimpress [3], etc.

All of existing 1D calculation techniques for radiant heat duty (Q_r) use global parameters of radiant tubular system, such as diameter of tubes and their spacing, distance of tube centre from lining surface etc. The influence of distance between furnace wall and tube centre is usually considered

using so called view factor. In case of vertical cylindrical fired heater with radiant tube coil designed as one single tube row against the lining wall with given distance between wall surface and tubes centreline the view factor can be read (from relevant graph) or calculated as function of a ratio of tube spacing (s) and tube outer diameter (D). Thus obtained total view factor is, however, a sum of direct radiation of flue gas and reradiation from lining wall. Finally, when the radiant heat duty (Q_r) is determined, the average radiant heat flux (q_r) is obtained by dividing Q_r by the total radiant heat transfer area (A_r)

The average radiant heat flux (q_r) is then used for prediction of so-called local-maximum radiant heat flux $q_{m.}$ According to API Standard 530 (API, 2008), the local-maximum radiant heat flux q_m can be calculated from average radiant heat flux q_r using following equation

$$q_m = F_C \, . \, F_L \, . \, F_T \, . \, (q_r - q_{rc}) + q_{rc} \tag{1}$$

where F_C is a tube-circumference heat flux variation factor, F_L is a tube-longitudinal heat flux variation factor, F_T is a tube-surface temperature heat flux variation factor and q_{rc} is the convective component of the average radiant section heat flux q_r.

Because the entire tube circumference is considered also in calculating q_r (as described in text above) tube-circumference heat flux variation factor F_C (varying with tube spacing) tends to be in such 1D calculation somewhat higher.

Prediction of local-maximum radiant heat flux q_m from eq. (1) is sufficient for the purpose of calculation of maximum radiant section tube skin temperature and tube material selection. However, for design of tubular system of radiant section (i.e. sizing of tube coil) and prediction of its thermal behaviour this is rather insufficient, because real heat flux distribution in radiant section strongly influences character of two-phase flow regimes of heated fluid in radiant tubes. Insufficient prediction of real distribution of heat flux in radiation section is then frequently the source of important fired heater operating troubles. These problems stem from the known fact that accurate determination of individual correction factors F_C, F_L and F_T for eq. (1) is very difficult, since they depend on the fuel characteristics, combustion conditions, burner design, shape of flames and their interactions, arrangement and dimensions of radiant section and radiant coils, flue gas flow inside radiant section, etc.

3. METHODOLOGY

The numerically analysed radiant section of fired heater and its tube system have been designed in accordance with the relevant abovementioned API Standards as vertical cylindrical type with nominal firing capacity of 24 MW for the process of atmospheric distillation of crude oil. There are a total of six staged-gas burners vertically oriented and mounted on bottom of radiant section, equipped with guide-vane stabilizers (swirlers), each of nominal firing duty 4 MW. Radiant section's geometry and tube system have been deliberately designed with small imperfections to resemble a used system, where tubes are not in their precise design positions (nominal), but are slightly deformed in various ways. These deformations were inspired by observations in real operated industrial units. This enables to study realistic tube circumference heat flux variation.

Numerical simulation of the reactive flow in the flames is performed using models and methods adequate for industrial applications. It was observed that flue gas flow in the radiant section is unstable; therefore simulation was performed as transient.

Boundary condition on the tube walls assumes a constant inner skin temperature. This assumption is chosen in order to enhance direct comparability of data collected on individual tubes. Conduction in

the tube walls is enabled in all directions (not just radially). Shell conduction is enabled also in the wall of the furnace, the properties of which correspond to fibro-silicate insulation.

4. RESULTS

Tubular system of the radiant section consists of 60 tubes (placed in one row around circular lining wall) with constant outer diameter (D) 194 mm and with tube spacing (s) 350 mm. Nominal distance of tube centre from lining surface is (e) 232 mm. The ratio s/D is then 1.8 and e < s. The height of radiant section is approx. 17 meters. As noted above, some of the tubes are moved from the nominal position closer or farther from the wall and/or to neighbouring tubes.

Results from 1D global heat transfer analysis using the abovementioned method of view factors give the following main data about tube-circumferential heat flux variation. The flame-side maximum local heat flux is predicted at 172% of average heat flux, wall-side minimum local heat flux is predicted at 58% of average heat flux.

The variability of local heat flux predicted by CFD simulation is however much higher. Flame-side peak heat flux is 332 % of average heat flux, while wall-side minimum is 16 % of average heat flux. This means that variability of the heat flux predicted by CFD simulation is about two times bigger than that predicted by a standard 1D model.

Resulting heat loads around the circumference of individual tubes presented below are taken from a level 5 m above the floor of radiant section, which is the height with peak heat loads as documented by Figure 1b. Figure 1a displays a polar plot of typical heat flux profile around tube in nominal location (also neighbours in nominal positions).

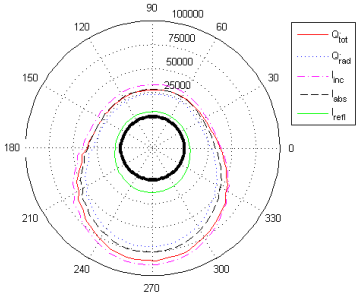

a)

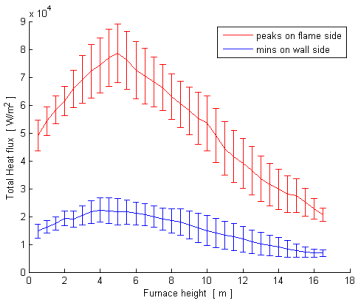

b)

FIGURE 1. Tube circumferential heat flux variation (red solid line) on level 5 m from floor of radiant section (tube in nominal position), b) vertical variation of total heat flux with error bars displaying standard deviation in half-metre horizontal sections

Circumferential tube heat flux profiles predicted by the CFD simulation differ significantly among individual tubes even at the same height, as flow in the furnace is complex, recirculating and non-symmetrical. When we predict local-maximum heat flux (q_m) for analysed radiant section using 1D model by eq. (1) (with $F_C = 1.9$, $F_L = 1.1$ and $F_T = 1.0$, according to [2]) we get a value $q_m = 55.64$ kW/m^2. However, from Fig. 1b it can be seen that CFD analysis gives a value of peak heat flux in radiant section higher by more than 40%. This is a conservative estimate based on average peak values in horizontal sections.

Two examples of tubes that are slightly shifted by D/2 towards the flame and to the wall, respectively, are presented in Figure 2. The figure shows that of the two deformations, the tube which is closer to the furnace wall (Figure 2 b) has a markedly lower heat flux on its wall side. There is also a significant difference of the flame-side heat flux but a detailed inspection of the

results shows this can be attributed rather to overall flow pattern in the furnace than to the flame-tube distance.

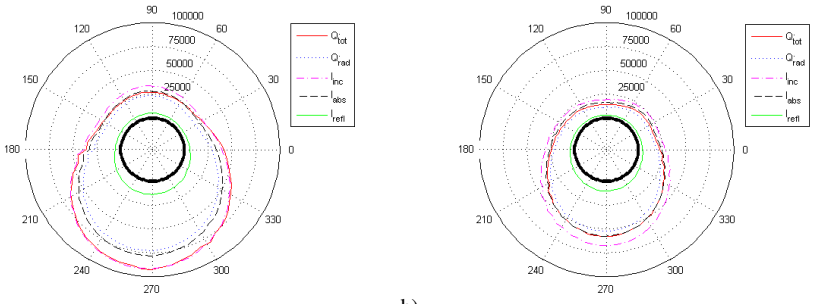

a) b)

FIGURE 2. Tube circumferential heat flux variation (red solid line) on level 5 m from floor of radiant section, a) tube closer to flame than nominal, b) tube closer to wall

5. CONCLUSIONS

Vertical cylindrical fired heater typical for crude oil atmospheric distillation units was simulated numerically to analyse the distribution of thermal loading on the tubes. Predictions were compared with classical design calculations and revealed significantly greater variability. The two different models have been compared with the objective to analyse the circumference heat flux variation of heat flux on tubes. The simple 1D model leads to overly optimistic predictions regarding heat flux uniformity on the tube coil, compared to the detailed CFD model.

ACKNOWLEDGEMENTS

The authors gratefully acknowledge financial support within the framework of Operational Programme “Research and Development for Innovations” – “NETME Centre – New Technologies for Mechanical Engineering”, project registration number CZ.1.05/2.1.00/01.0002. Two of the authors (J. Vondál and J. Hájek) also acknowledge financial support within the framework of Operational Programme “Investment in education development”, project CZ.1.07/2.3.00/30.0039 of Brno University of Technology.

REFERENCES

[1] API Standard 560, Fired Heaters for General Refinery Service, 4th ed., American Petroleum Institute, August 2007.

[2] API Standard 530, Calculation of Heater-tube Thickness in Petroleum Refineries, 6th ed., American Petroleum Institute, September 2008.

[3] Wimpress, N., 1978, Generalized method predicts fired-heater performance, Chemical Engineering (New York), 85(12), 95–102.

Third International Conference on Computational Methods for Thermal Problems
THERMACOMP2014, June 2-4, 2014, Lake Bled, Slovenia
N. Massarotti, P. Nithiarasu and B. Sarler (Eds.)

OPTIMIZATION OF THE NOx EMISSION IN AN INCINERATOR PLANT

M. Costa
Istituto Motori, Consiglio Nazionale delle Ricerche, Viale Marconi 4, 80125, Napoli, Italy
N. Massarotti
Dipartimento per le Tecnologie (DiT), Università di Napoli "Parthenope", Centro Direzionale, Isola C4, Napoli, Italy
V. Indrizzi
Department of Metallurgy and Materials, University of Birmingham, Edgbaston, Birmingham, B15 2TT, United Kingdom

Key Words: Waste to energy, NOx emission

1. INTRODUCTION

Currently, waste-to-energy systems are spreading and improving their potentiality, ranging from small scale local applications, placed close to areas of availability of raw materials, to centralized power generation plants. Nixon *et al.* [1] compared 25 different waste-to-energy plants with different technologies, such as moving grate, fluidized bed and rotary kiln, and finally highlighted that moving grate plants are particularly attractive due to their simplicity, even if they present an high amount of bottom ashes, hydrochloric acid (HCl) and carbon monoxide (CO) emissions. The environmental impact of this kind of energy conversion systems, indeed, is a matter of study, especially as regards chlorine compounds, particulate matter and nitrogen oxides (NOx) [2]. Li *et al.* [3] developed a dynamic model for sludge combustion in order to control NOx formation. Liu *et al.* [4] studied a way to control NOx and CO emission in case of a small boiler. In particular, they used two different feeds and in the both cases they found that the height of the secondary air inlets has an important impact.
Present work aims at optimizing the operation of a waste-to-energy system fed with refuse derived fuel (RDF) by minimizing the NO formation through thermal mechanism and, at the same time, by fulfilling the DIRECTIVE on dioxins formation 2000/76/EC of the European Parliament and of the Council - 4 December 2000 on waste incineration, in particular: "Incineration plants shall be designed, equipped, built and operated in such a way that the gas resulting from the process is raised, after the last injection of combustion air, in a controlled and homogeneous fashion and even under the most unfavorable conditions, to a temperature of 850 °C, as measured near the inner wall or at another representative point of the combustion chamber as authorized by the competent authority, for two seconds.…". The fuel and prompt mechanisms are not considered due to the high uncertainty consequent the variability in the treated fuel composition. A 3D CFD model of the power plant developed by authors [5] within the FLUENT environment is coupled with the MODE-FRONTIER optimization software to achieve the conflicting objectives on the in-chamber temperature field.

2. INVESTIGATION DESCRIPTION

It is well known that the NOx formation in combustion systems follows 3 main routes, thermal, fuel and prompt [6]. Thermal NOx formation is here considered: according to the Zeldovich model:

$$\begin{aligned} N_2 + O &\Leftrightarrow NO + N \\ N + O_2 &\Leftrightarrow NO + O \\ N + OH &\Leftrightarrow NO + H \end{aligned} \tag{1}$$

The RDF indicated as case 2 in the work by Costa *et al.* [5] is considered, whose composition is specified in Table 1. Table 2 reports the main characteristics of the considered plant.

Combustor power	52 MW
Flow rate of produced steam	54 t/h
Exhausts temperature at the chimney	140 °C
Electric power generated	12.5 MW
Secondary air	
Flow rate	4.8 x 10^4 m^3/h
Total relative pressure	0.05 bar
Nominal power	250 kW

TABLE 1-Technical characteristics of the plant

Proximate analysis	**(wt %)**
Moisture	20
Organic Matter	40
Char	30
Ashes	10
Ultimate Analysis	**(wt %)**
C	68.7
H	3.2
O	27
N	0.2
S	0.2
Other	0.7
LHV	18527 (kJ/kg)

TABLE 2- Waste composition

The study is focused on structural and operating parameters. In particular, an equivalent transmittance of the walls and the mass flow rate of the secondary air are considered as input variables for the optimization study. A proper design of experiment (DOE) space is built. The first parameter is given by:

$$h_{eq}(T_{wall} - T_{\infty}) = -k_g \left.\frac{\partial T}{\partial n}\right|_{wall} + \dot{q}_r \tag{2}$$

where T_∞ is the water temperature within the pipes, k_g is the gas thermal conductivity, q_r. is the radiative heat flux. Because walls chamber are partially covered of refractory material, two different equivalent transmittances must be considered in the simulation. Indeed, in the optimization only the equivalent transmittance of refractory covered walls is varied. Regarding the secondary air, it is introduced by three rows of nuzzles above the moving grate, two rows with the same mass flow rate and the other with a higher mass flow rate. Indeed, in the optimization the total mass flow rate varies. It is composed by two rows, which have also the same value, and a third row with a different value.

The results of the FLUENT code are used to obtain the position and temperature of particles 2 seconds after the secondary air injection. In this way, by varying the input parameters, it is possible to both minimize the NOx amount formation and to maximize the temperature of particles at the position they reach 2 seconds after the secondary air injection.

3. RESULTS AND DISCUSSION

Operating conditions, where the equivalent transmittance of refractory covered walls is 180 W/m^{2}K and the total mass flow rate of the secondary air is 4.8 kg/s, are represented in Figure 1 with a green circle. Starting from that conditions, other 24 cases are considered in the DOE space, which has the equivalent transmittance and the total secondary air mass flow rate in the range of 5-400 W/m^{2}K and 2-10 kg/s, respectively.

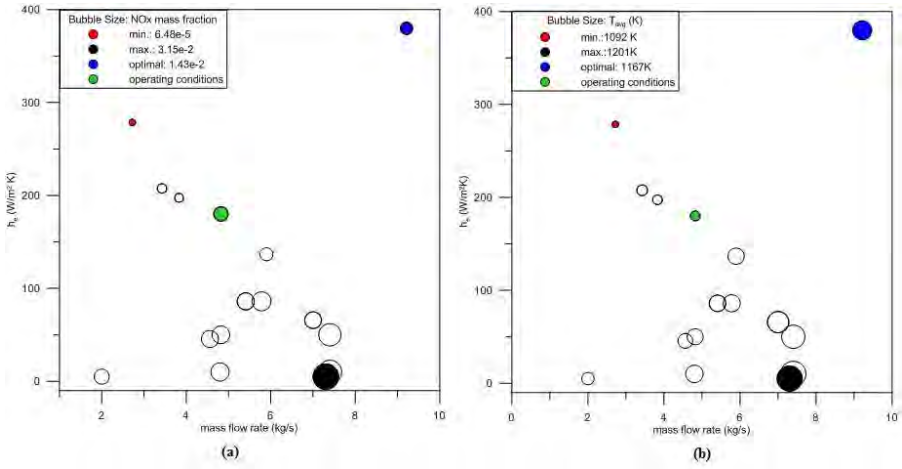

FIGURE 1- NOx mass fraction (a) and average temperature of 200 particles 2 seconds after the last injection of secondary air (b).

The bubble graphs represent the NOx mass fraction in the mass flow rate, transmittance plane and the average particles temperature over 200 considered individuals. These bubble graphs clearly indicate how objectives of the optimization problem are into contrast. In fact, NOx mass fraction increases with higher temperatures, and vice versa. Anyway, the employed optimization algorithm (MOGA-Multi-Objectives Genetic Algorithm) suggests that a compromise solution can be reached when the total mass flow rate of secondary air is 9.21 kg/s (2.855 kg/s for two rows and 3.5 kg/s for the other row), and an equivalent transmittance of 379.74 W/m^{2}K for refractory covered walls. In such conditions (showed in Figure 2) the average temperature (1167 K) is higher than minimum temperature prescribed by regulations, and NOx are minimized with a mass fraction of 1.43E-2.

4. CONCLUSION

Thermo-fluid-dynamical field of an incinerator plant was investigated by mean a multi-objectives algorithm, which vary some design and operating conditions in order to have the optimal situation. In

particular, a compromise between high temperature and low NOx emission. Results indicated that operating conditions, even if some particles have temperature higher than 850 °C, average temperature of 200 particles that has been considered is lower. Anyway, despite there is a contrast between regulations and pollutant emissions, the investigation suggests that it is possible to create some conditions in order to operate in respect of these laws. Produced energy in all these conditions must be better investigated in order to understand if optimal conditions can be really used. Moreover, more information about fuel should be known to better model and understand NOx formation also with prompt and fuel mechanism.

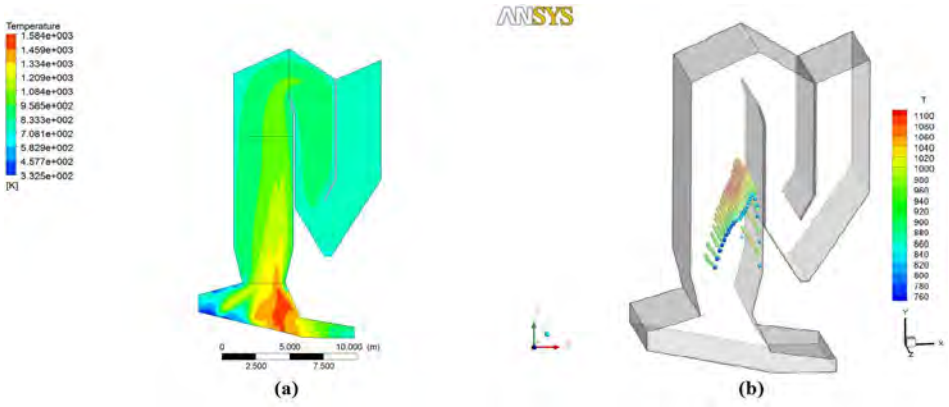

FIGURE 2- Temperature field (a) and temperature of 200 particles after 2 seconds (b) in optimal conditions

REFERENCES

[1] J. D. Nixon, D. G. Wright, P. K. Dey, S. K. Ghosh, P.A. Davies, *A comparativeassessment of waste incinerators in the UK,* Waste Management, Vol. 33, pp. 2234 -2244, 2013.

[2] A. Ranzi, S. Fustinoni, L. Erspamer, L. Campo, M. G. Gatti, P. Bechtold, S. Bonassi, T. Trenti, C. A. Goldoni, P. A. Bertazzi, P. Lauriola, *Biomoniotoring of the general population living near a modern solid waste incinerator: A pilot study in Modena, Italy,* Environment International, Vol. 61, pp. 88 -97, 2013.

[3] S. Li, C. Cadet, P.X. Thivel, F. Delpech, *Towards the modeling and control of NOx emission in a fluidized bed sludge combustor*, Computers and chemical engineering, Vol. 35, pp. 1281-1294, 2011.

[4] H. Liu, J. Chaney, J. Li, C. Sun, *Control of NOx emission of a domestic/small-scale biomass pellet bioler by air staging*, Fuel, Vol. 103, pp. 792-798, 2013

[5] M. Costa, M. Dell'Isola, N. Massarotti, *Numerical analysis of the thermo-fluid-dynamic field in the combustion chamber of an incinerator plant,* Energy, Vol. 34, pp. 2075-2086, 2009.

[6] M.A. Abraham, R.P Hesketh, *Reaction engineering for pollution prevention*, Elsevier Science Ltd, 2000.

Third International Conference on Computational Methods for Thermal Problems
THERMACOMP2014, June 2-4, 2014, Lake Bled, Slovenia
N. Massarotti, P. Nithiarasu and B. Sarler (Eds.)

EFFECTS OF CONVERGENCE CRITERIA ON MASS AND ENERGY BALANCE OF PACKED-BED COMBUSTION MODEL

Tomáš Juřena, Jiří Hájek

Institute of Process and Environmental Engineering, Faculty of Mechanical Engineering, Brno University of Technology, Technická 2, Brno 616 69, Czech Republic, jurena@fme.vutbr.cz

ABSTRACT

The present work is focused on numerical modelling of grate combustion of solid fuels by means of Computational Fluid Dynamics (CFD) methods. A one-dimensional transient numerical model of combustion in an experimental reactor is implemented into a computer program. A method for control of mass and energy balance over the system is developed and applied to a series of simulations of heat-up and pyrolysis of wheat straw in order to evaluate the effect of convergence criteria on total mass and energy imbalance.

Key Words: *Packed Bed, Combustion, Grate, Biomass, Convergence, Balance Equations, CFD.*

1. INTRODUCTION

CFD modelling has become a standard supporting tool for design and optimization of solid fuels utilization systems. This work concerns CFD modelling of grate combustion as widely used technology in biomass and municipal solid waste combustion for heat and power production [1]. A typical model of a grate furnace consists of a grate with primary air inlets, freeboard (an open space area above the fuel layer) with secondary (and possibly tertiary) air inlets and heat exchangers in radiation and convection shafts. Yin et al. [2] summarize main results and findings of both experimental and theoretical works that were conducted on the topic to the date.

One of the key issues in the modelling is the degree of approximation of processes that take place in a fuel layer burning on the grate. Thermal conversion of the bed is initiated by over-bed radiation. As combustion proceeds in the fuel layer, various gaseous products leave the bed entering the freeboard, so the freeboard and in-bed processes are strongly coupled. The effects of coupling have to be taken into account, e.g. in the definition of inlet boundary conditions or additional heat and mass sources. There are three approaches to CFD modelling of grate combustion. If the subject of investigation does not lie in the vicinity of the grate, but sufficiently downstream of the bed, a simplified approach can be applied to model effects of drying, pyrolysis and char oxidation based on calculated or measured profiles of conversion rates along the grate. This approach was used e.g. in one of the authors' previous works [3]. Advanced methods make use of a numerical model of combustion within the bed, which can be either included in the solution domain by means of porous zone as in [4], or separated from it as a standalone model and coupled to the freeboard through boundary conditions, see e.g. [5]. Latter is a promising method for detailed coupled simulation of grate combustion. Since the crucial part of the methodology is the standalone bed combustion numerical model, the attention of researchers has recently been attracted to its development, see e.g. [6], [7].

2. COMPUTATIONAL TOOL FOR FIXED-BED COMBUSTION MODELLING

In order to employ the coupled modelling methodology in CFD analysis of grate-fired boilers, that were previously simulated using the simplified approach as in [3], one-dimensional transient numerical model of combustion in a packed bed of thermally insulated experimental reactor has

been developed based on an experimentally validated model [8]. The fuel bed is treated as porous medium. It consists of gas and solid phases, where solid particles are considered thermally thin. This allows the solid phase to be modelled as continuum. Such an assumption is reasonable for beds of particles with equivalent diameters smaller than 30mm [9] and typically can be applied for biomass fuels such as wheat straw [10]. Governing equations describing heat and mass transfer within the bed are discretized by the finite volume method and solved by an in-house computer program called GRATECAL, which was developed in MATLAB environment. The computer program is capable to predict the drying, devolatilization and char oxidation as individual combustion stages as well as to run a full batch-type simulation including all processes together. Through graphical tools, temperature, concentrations (of both gas and solid species) or flow fields can be viewed along the bed height as well as the propagation of drying, devolatilization and char oxidation reaction fronts. Governing equations are solved iteratively until convergence is reached. The convergence is judged by scaled (non-dimensional) residuals, which can be written for a general transport variable Φ using common CFD notation (see e.g. [11]) as:

$$R_{sc}^{\Phi} = \frac{\sum_{cells\ P} |a_N \Phi_N + a_S \Phi_S + b_P - a_P \Phi_P|}{\sum_{cells\ P} |a_P \Phi_P|}$$

As it is stressed in [2], it is important to ensure, that the model obeys essential physical principles such as conservation laws of mass and energy. Although a natural requirement it may seem, it is not precisely fulfilled in numerical simulations due to various sources of errors [12]. An imperfect conservation implies that the gas does not carry the right amount of mass and energy and therefore such a model cannot improve the estimate of boundary values at the inlet of a freeboard model. This may lead to inaccurate results of freeboard combustion predictions as the accuracy depends, among others, on the quality of input data [13]. Therefore, a method for control of mass and energy balance over the studied system has been developed and implemented within the code. It is based on comparison of total unscaled (dimensional) residuals of governing equations with calculated mass and energy imbalance of the system due to various errors. Details on the method can be found in the authors' previous work [14]. The algorithm is briefly described in the following three steps:

1. Initial mass and energy content of fuel and gas in the reactor is determined prior to the simulation.
2. At the end of each time step, mass and heat entering and leaving the fuel bed are calculated. Unscaled residuals of discretized mass and energy transport equations are stored. The sum of the residuals over simulated time will give total mass and energy residuals as an estimate of the upper bound of the overall error.
3. When the simulation is finished, mass and energy content of gas and fuel left in the reactor is computed. Overall mass and energy imbalances are evaluated and compared to values of total residuals of discretized mass and energy transport equations as a measure of imperfect conservation. If either of imbalances is not covered by the corresponding total residual, then the bed model does not conserve the physical quantity and contains an error.

At the end of the simulation, a log file is generated, which evaluates the heat and mass balance.

3. RESULTS

Since a truncation error is introduced to the calculation, whenever the iterative process is stopped not reaching its limiting value (i.e. each time the convergence criteria are met), the incomplete convergence generates mass and energy imbalance. This effect becomes more important in unsteady simulations, in which truncation errors cumulate at the end of each time step. Therefore, the balance-based method has been used to analyse effects of convergence criteria on mass and energy imbalance of the system. The effect is studied through a series of simulations of heat-up and pyrolysis as essential stages of combustion of dry wheat straw in the reactor. Since straw contains

sizeable amount of volatile matter, which is released during pyrolysis, even a small mass imbalance in the system can lead to large errors in the energy conservation. Values of convergence criteria (scaled residuals) in the series of simulations are varied in the interval (10^{-7}, 10^{-2}) with a step of a half of an order.

The effect of scaled residuals for gas and solid energy equations on the energy imbalance during heat-up of dry wheat straw by primary air (398K) and over-bed radiation is shown on FIGURE 1. The temperature of the radiation heat source in the boundary condition for energy of the solid phase at the bed top is set to 398K. Radiation heat transfer within the bed is modelled using the effective thermal conductivity. The convergence criterion for gas species transport equations is fixed to 10^{-3}. It can be seen that the energy imbalance significantly increases for values of energy scaled residual greater than 10^{-5} and keeps very low for values less than or equal to 10^{-6}. Note that the energy imbalance is not affected by the selected method of evaluation of radiation heat transfer as no additional governing equation for radiation heat transfer is solved.

However, the value 10^{-3} of scaled residuals for gas species transport equations seems to be too low to obtain sufficiently low energy imbalance after volatile matter (approximately 1.1 kg, 79.28wt% on dry basis) is completely pyrolysed as shown on FIGURE 2 (final pyrolysis yields as well as other properties of the fuel are adopted from the work [8]). Temperatures of both primary air and radiation heat source are set to 698K in this case. Although the convergence criterion for energy transport equations is fixed to 10^{-6}, mass imbalance produces relatively large energy imbalance as long as scaled residuals are greater than 10^{-6}. In order to obtain sufficiently accurate results from in-bed simulations in terms of mass and energy conservation within the packed bed, it is, therefore, suggested to require all the scaled residuals to drop to as low as 10^{-6} or lower.

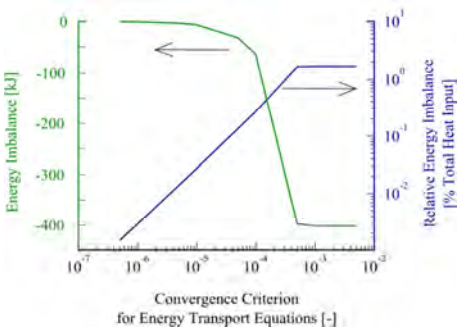

FIGURE 1. Energy imbalances as obtained by simulations of heat-up of dried wheat straw by primary air (398K) and over-bed radiation (398K).

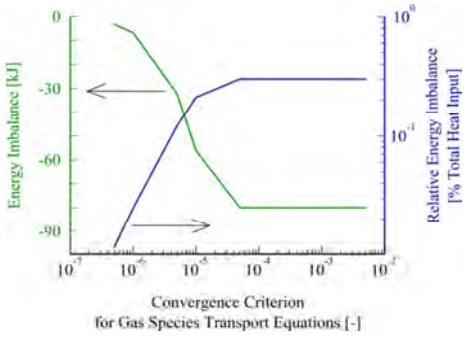

FIGURE 2. Energy imbalances as obtained by simulations of pyrolysis of dried wheat straw by primary air (698K) and over-bed radiation (698K).

4. CONCLUSIONS

Numerical model of packed bed combustion in an experimental reactor has been developed and used to simulate heat-up and pyrolysis of wheat straw. A balance-based method has been applied to evaluate heat and mass imbalance of the system due to incomplete convergence. It is found that all scaled residuals should drop to as low as 10^{-6} or lower in order to obtain sufficiently accurate results from in-bed simulations in terms of mass and energy conservation within the packed bed.

ACKNOWLEDGEMENTS

This work is an output of research and scientific activities of NETME Centre, regional R&D centre built with the financial support from the Operational Programme Research and Development for Innovations within the project NETME Centre (New Technologies for Mechanical Engineering), Reg. No. CZ.1.05/2.1.00/01.0002 and, in the follow-up sustainability stage, supported through NETME CENTRE PLUS (LO1202) by financial means from the Ministry of Education, Youth and Sports under the „National Sustainability Programme I".

The authors gratefully acknowledge financial support within the framework of Operational Programme Investment in education development CZ.1.07/2.3.00/20.0020.

REFERENCES

[1] C. Yin, L. Rosendahl, S. Clausen, and S. L. Hvid, Characterizing and modeling of an 88 MW grate-fired boiler burning wheat straw: Experience and lessons, *Energy*, 41, 473–482, 2012.
[2] C. Yin, L. A. Rosendahl, and S. K. Kær, Grate-firing of biomass for heat and power production, *Prog. Energy Combust. Sci.*, 34, 725–754, 2008.
[3] J. Hájek and T. Juřena, Modelling of 1 MW Solid Biomass Combustor: Simplified Balance-Based Bed Model Coupled with Freeboard CFD Simulation, *Chem. Eng. Trans.*, 29, 745–750, 2012.
[4] M. A. Gómez, J. Porteiro, D. Patiño, and J. L. Míguez, CFD modelling of thermal conversion and packed bed compaction in biomass combustion, *Fuel*, 117, Part A, 716–732, 2014.
[5] Z. Yu, X. Ma, and Y. Liao, Mathematical modeling of combustion in a grate-fired boiler burning straw and effect of operating conditions under air- and oxygen-enriched atmospheres, *Renew. Energy*, 35, 895–903, 2010.
[6] A. Asthana, Y. Ménard, P. Sessiecq, and F. Patisson, Modeling On-Grate MSW Incineration with Experimental Validation in a Batch Incinerator, *Ind. Eng. Chem. Res.*, 49, 7597–7604, 2010.
[7] B. Miljkovic, I. Pesenjanski, and M. Vicevic, Mathematical modelling of straw combustion in a moving bed combustor: A two dimensional approach, *Fuel*, 104, 351–364, 2013.
[8] H. Zhou, A. D. Jensen, P. Glarborg, P. A. Jensen, and A. Kavaliauskas, Numerical modeling of straw combustion in a fixed bed, *Fuel*, 84, 389–403, 2005.
[9] Y. B. Yang, C. Ryu, A. Khor, N. E. Yates, V. N. Sharifi, and J. Swithenbank, Effect of fuel properties on biomass combustion. Part II. Modelling approach--identification of the controlling factors, *Fuel*, 84, 2116–2130, 2005.
[10] Y. B. Yang, R. Newman, V. Sharifi, J. Swithenbank, and J. Ariss, Mathematical modelling of straw combustion in a 38 MWe power plant furnace and effect of operating conditions, *Fuel*, 86, 129–142, 2007.
[11] H. K. Versteeg and W. Malalasekera, *An Introduction to Computational Fluid Dynamics: The Finite Volume Method*. Pearson Education, 2007.
[12] G. Dahlquist and Ä. Björck, *Numerical methods*, 1st ed. Englewood Cliffs, NJ, USA: Prentice-Hall, 1974.
[13] C. Yin, L. Rosendahl, S. K. Kær, S. Clausen, S. L. Hvid, and T. Hille, Mathematical Modeling and Experimental Study of Biomass Combustion in a Thermal 108 MW Grate-Fired Boiler, *Energy Fuels*, 22, 1380–1390, 2008.
[14] T. Jurena and J. Hajek, Energy Considerations in CFD Modelling of Biomass Combustion in an Experimental Fixed-bed Reactor, *Chem. Eng. Trans.*, 25, 803–808, 2011.

Third International Conference on Computational Methods for Thermal Problems
THERMACOMP2014, June 2-4, 2014, Lake Bled, Slovenia
N. Massarotti, P. Nithiarasu, B. Sarler (Eds.)

A DETAILED STUDY OF A MULTI-MW BIOMASS COMBUSTOR BY NUMERICAL ANALYSIS: EVALUATION OF FUEL CHERACTERISTICS IMPACT

Stefano Cordiner,Alessandro Manni,Vincenzo Mulone,Vittorio Rocco

Università di Roma "Tor Vergata" via del Politecnico 1, 00133 Roma, Italy,
cordiner@uniroma2.it , alessandro.manni@uniroma2.it, mulone@uniroma2.it , rocco@uniroma2.it

ABSTRACT

In the recent years the interest toward the use of biomass as a fuel for energy generation, together with the continuous tightening of regulations, has driven the improvement of accurate design techniques which are required to optimize the combustion process and simultaneously control pollutant emissions. In this paper the use of a 3D Computational Fluid Dynamics approach is analysed to this aim by means of an application to an existing 50MWth biomass fixed-bed combustion furnace fuelled by grape marc. This combustor is an interesting example of biomass utilization as it may integrate biomass with organic residual by an industrial process. The numerical approach has used an Eulerian-Lagrangian OpenFOAM solver, which has been properly modified to fit the case. In particular, the fully 3D approach here presented, directly solves fluid and solid evolution in both the combustion bed and the freeboard. Special care has also been devoted to the treatment of radiating fluxes, having a remarkable influence on the bed evolution. Results have been compared to experimental data in terms of temperature showing a good agreement. Further comparisons have been done with literature available data for a similar power size biomass furnace showing reasonable similarities.

Key Words: *Biomass, combustion ,grape marc, OpenFOAM*

1. INTRODUCTION

Computational Fluid Dynamics (CFD) has started to be considered a powerful design tool for the development of bed biomass furnaces with improved performances in terms of pollutant emissions and conversion efficiency. Despite the deep linkage between bed and freeboard, the strategy used in the simulation of this process is generally to separate the solution in two subsystems. State of the art of CFD tools, propose to approach this problem the use of separate [1-3] 1D and 2D models for evaluation of the bed characteristics while the freeboard is usually simulated with standard CFD codes as Fluent, STAR-CD and CFX. The bed and the freeboard are separated by an interface where are exchanged energy and mass in a unidirectional way[4] [5] while only a few authors worked on bidirectional fluxes[6] [7]. In this paper a novel approach is proposed to study directly coupled full 3D bed and freeboard, with the final goal of improving the capabilities of taking into account multi-dimensional issues in both the bed and the freeboard.

2. CASE DESCRIPTION AND MAIN ASSUMPTIONS

The simulation analysis has been applied to a multiMW biomass boiler,8m width for 15m height (Fig 1a), designed to produce steam at the pressure of 54 bar and at the temperature of 420 °C ,used in a CHP plant. The combustion system , realized with an air cooled step-grid(8x8m), is divided into three separated sectors. To respect the limits of NOx SNCR Urea system (sol 40%)is adopted. To simulate this system , the coalChemistryFoam (OF 2.1) solver has been used, modified to modify the injection parameters definition. The computational grid,has been done with SnappyHexMesh via the GUI HelyxOS. The computational domain is divided into about 100M

cells with dimensions in the order of 20cm, and representing only the radiative heat transfer region as the key aspects related to pollutant formation and bed dynamics mainly evolve there.

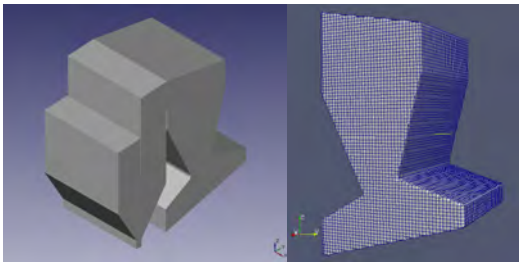

FIGURE 1. (a)Complete steam generator;(b)Simplified Grid

The numerical model has been implemented under the following main assumptions :

- The interaction between primary air and bed has been neglected
- Fuel particles (solid phase) have been injected into the combustion chamber and tracked following a predefined path
- The gas phase has been solved in a Eulerian fashion: the code solves the equations of continuity, momentum and energy of the gas phase taking in account chemical reactions and interactions with the solid phase
- The radiation in the energy equation is taken into account through the P1 model[8][9], convective heat transfer with the Ranz Marshall correlation
- A standard k-epsilon model has been chosen which is state of the art for industrial problems[9]
- A PaSR model has been used to model the turbulence/chemistry interaction in the combustion process.
- A standard Zeldovich mechanism has been chosen to calculate the NOx thermal emissions.
- As the biomass presents a high Moisture Content (MC), up to 50% w.b case, the evaporation process has been treated by a simplified model . A simple Arrhenius equation [10] has been instead used to represent the volatilization of CH4 ,CO and tar.
- Based on particle size, reactions have been considered dominated by oxygen diffusion.

3. FEEDSTOCK CHARACTERISTICS

Fuel proximate and ultimate (CHNS) analyses have been performed at the biomass laboratory of the University of Rome Tor Vergata (TGA and CHNS analysis respectively with a LECO TGA-701 and a vario MACRO cube) on samples of grape marc and wood chips, usually present with a 30% fraction in the mix. A constant biomass particle diameter equal to 0.015 m has been assumed at the inlet of the combustor. The constants used for the volatilization model have been assumed similar to [10].

3. RESULTS ANALYSIS

Temperature, NOx, CO and velocity maps are reported in Figure 2 and qualitatively compared with the results obtained by Yu [6] on a 34MWth power plant. The temperature profile appears qualitatively close, up to the secondary air inlet. In particular, near to the exit section the temperature measured is about 1270K that is close to the temperature obtained at the black spot in Fig 2(a).

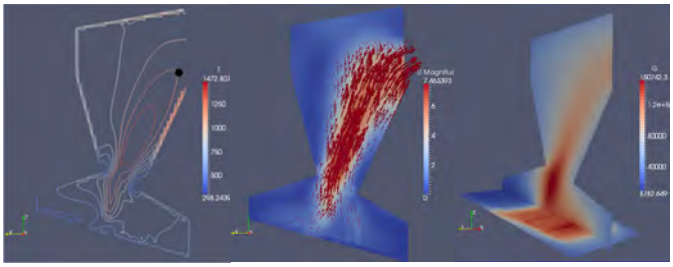

FIGURE. 2. (a) Temperature profile [K]; (b) U field [m/s] ;(c) Incident radiation [W/m2]

The incident radiation (Fig 2c) in a section immediately above the bed and in an axial direction, is in line with this kind of furnace common design criteria (50-150 kW/m2)[11] .The CO concentration is again pretty similar qualitatively to Yu [6], while the NOx field appears different as both residence time and O_2 availability cannot be retained similar. The evolution of the evaporation process is shown in Fig.3c and is reasonable for a 8m long grid designed for high moisture content biomass.

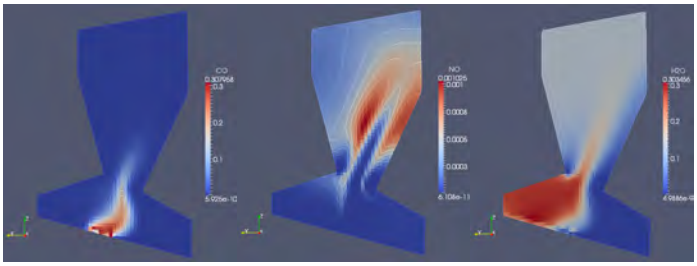

FIGURE. 3. (a) CO mass fraction; (b) NO mass fraction; (c) H2O mass fraction

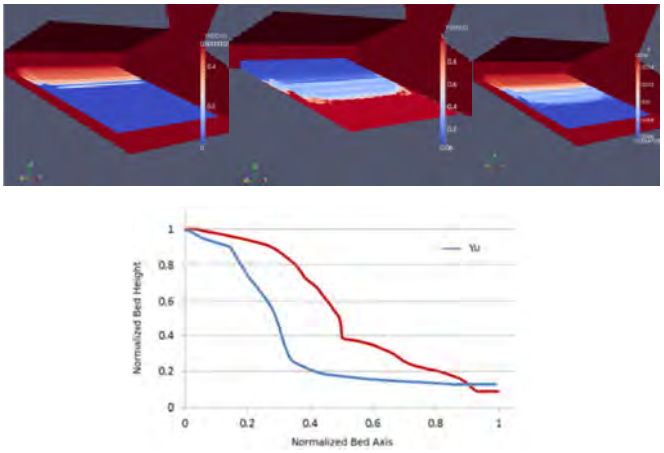

FIGURE. 4. (a) particles H2O fraction; (b) particles ash fraction; (c)particles diameters[m];(d)NBH

In Fig. 4, the influence of 3D representation into bed evolution are clearly visible, in particular in terms of different radiation (side regions with high S/V ratio, H_2O in the primary zone).Results are also qualitatively similar to Yu [6] in terms of non-dimensional height reduction over the non-dimensional bed length (Fig.4d), meaning that the three steps of biomass consumption (namely drying, pyrolysis and char combustion) are well represented. Differences may evidently be due to the already cited residence time and O_2 differences, as well as different assumed moisture content.

3. CONCLUSIONS

A fully 3D model of a biomass furnace has been presented, capable of carefully representing the 3D evolution and coupling of bed and freeboard sections. The model is furthermore capable of tracking the main sub-steps of bed evolution, as well as predicting the pollutant (CO and NOx) concentration evolution over the freeboard. The obtained results present an overall satisfactory behavior, with special regard to the comparison of calculated temperature with the experimentally one as measured closed to the exit section of the furnace. In fact, the correct 3D prediction of temperature profiles, allows to better position the lances of urea in the narrow window temperature's, offered by these systems, thus reducing the impacts of additional NOx formation at high temperature, and urea slip in the coldest zones. All in optical to reduce costs of exercise and environmental impact.

REFERENCES

[1] Yin C, et al. Mathematical modelling and experimental study of biomass combustion in a thermal 108 MW grate- fired boiler. Energy Fuel 2008;22:1380–90.

[2] Shin D, Choi S. The combustion of simulated waste particles in a fixed bed.Combust Flame 2000;121:167–80.

[3] Wang Y, Yan L. CFD studies on biomass thermochemical conversion. Int J MolSci 2008;9:1108–30.

[4] Jordan C, Harasek M. Improvement of a combustion unit based on a grate furnace for granular dry solid biofuels using CFD methods. Heat Transfer Eng 2010;31:774–81.

[5] Scharler R, Obernberger I. Deriving guidelines for the design of biomass grate furnace with CFD analysis – a new multifuel-low-NOx furnace as example. In:6th European conference on industrial furnaces and boilers, vol. III; 2002. p. 24.

[6] Yu Z,et al. Mathematical modeling of combustion in a grate-fired boiler burning straw and effect of operating conditions under air- and oxygen- enriched atmospheres. Renew Energy 2010;35:895–903.

[7] Klason T, Bai XS. Combustion process in a biomass grate fired industry furnace: a CFD study. Prog Comput Fluid Dynam 2006;6:278–82.

[8] Klason, T. et al. Investigation of Radiative Heat Transfer in Fixed Bed Biomass Furnaces, Fuel, vol.87, pp.2143-2153, 2008.

[9] X. Zhang, "Experimental Investigation and Mathematical Modelling of Wood Combustion in a Moving Grate Boiler," Fuel Processing Technology, Vol. 91, No. 11, 2010,pp. 1491-1499.

[10] K. Slopiecka, et al., Thermogravimetric analysis and Kinetic study of poplar wood pyrolysis pages 1687-1698, Third International Conference on Applied Energy, Perugia 2011.

[11] Yang YB, et al. Effect of air flow rate and fuel moisture on the burning behaviours of biomass and simulated municipal solid wastes in packed beds. Fuel2004; 83, 1553–1562.

Third International Conference on Computational Methods for Thermal Problems
THERMACOMP2014, June 2-4, 2014, Lake Bled, Slovenia
N. Massarotti, P. Nithiarasu and B. Sarler (Eds.)

MODELLING OF A TRAVELING BED GASIFIER

F. Marias, P. Bernada, F. Couture
Laboratoire de Thermique Energetique et Procedes
Universite de Pau et des Pays de l'Adour
Rue Jules Ferry, B.P. 7511
64075 Pau cedex (France)
J.P. Robert Arnouil, A. Lamande
Europlasma
21 rue Daugère
33520 Bruges (France)

ABSTRACT

This work deals with the modelling of a travelling bed biomass gasifier. This gasifier is a part of a more general process devoted to the production of electricity from biomass. In a first stage biomass is dried and gasified in a travelling bed gasifier using air with an equivalence ratio of 0.3. This product gas contains light hydrocarbons as well as tars. It is converted into a syngas free from tars in a specific reformer (Turboplasma©) that uses plasma technology in order to raise the temperature of the incoming gas to a value compatible with thermal cracking of tars. The overall process. The model of the travelling bed gasifier is based on the coupling between a software devoted to the description of the chemical and physical processes occurring within the travelling bed, and a CFD package (Fluent™) that allows for the description of the homogenous gas reaction and radiation occurring within the freeboard of the bed. The first software is a "home made" software based on the conservation equations of the solid, liquid and gas phases as well as of the energy. The balance equations are firstly written at the "phase scale", and then, using a homogenisation technique (volume averaging) balance equations are derived at a representative volume scale. In this first work, this model is written using a one dimensional formalism along the axis of the travelling bed. Wood is used as a case study material with a pyrolysis mechanism that uses three parallel reactions leading to the formation of gas, tars and char. The gas and tars produced during the pyrolysis step can be converted within the bed itself but also over the freeboard of the bed. Hence, the free board of the bed is used as a boundary condition of the CFD domain, with known local mass flow-rate, composition and temperature. This study allows for a complete and precise description of the processes occurring within the gasifier under consideration.

Key Words: *Gasification, Biomass, modeling.*

1. INTRODUCTION

The industrial device under study is depicted on **Figure 2**.

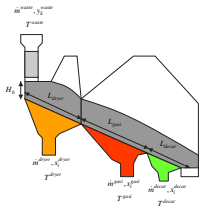

Figure 2: Scheme of the gasifier under study

The process is composed of three stages. The first one is devoted to the drying of the incoming load. It is fed with the incoming waste at a mass. The drying agent is a gas which is fed at the bottom of this stage. The second stage of the overall reactor is the gasifying section, it is fed at its bottom with a gasifying agent which is air. The final stage of the reactor is devoted to the decarbonation of the waste. Indeed, as it will be discussed in the following sections, the waste is expected to decompose into three fractions (permanent gas, condensable gas and char) in the gasifying section. The aim of the decarbonation chamber is to convert the solid residue (char) into gas.

2. MODELLING OF THE TRAVELING BED GASFIER

In order to translate the physical and chemical phenomena occurring within the reactor into mathematical formalism, it is firstly required to list the general assumptions that were used.

The first set of assumption is associated with the description of the travelling bed itself. Indeed, this bed might contain organic material, inorganic material, liquid moisture, gas, solid residue of pyrolysis (referred as phases in what follows). It is quite heterogeneous. A precise and complete description of this reacting bed would include the derivation of the different balances equations (mass, momentum and energy) at the porous scale, and then to integrate this set of equation all over the bed. Even though the computational power has largely increased, the solving of such a model would be highly time consuming. Moreover, it would be necessary to have the knowledge of the exact geometry of the bed and of the geometry of the interfaces between the above mentioned phases. Thus, the choice has been made to use a homogenization method based on the volume averaging theory [1] as it was already performed for the description of slow pyrolysis of wood [2-4].

For our purposes, we introduce the following variables to describe state the bed:

- the intrinsic gas average mass concentration in the bed of chemical species *k*:
- the intrinsic gas average total mass concentration in the bed :
- the volume fraction of the gas phase
- the volume fraction of the organic material phase
- the volume fraction of the inorganic material phase
- the volume fraction of the liquid phase . The liquid phase is supposed to be composed of pure water
- the volume fraction of the char phase
- the average total enthalpy to weight of the bed
- the average temperature of the bed (it is assumed from now that there is a local thermal equilibrium what means that all the phases share the same temperature)
- the average velocity of the gas leaving the bed
- the average vaporization rate of liquid water.

Another phenomenon that has to be discussed here is the thermal degradation of the incoming waste. This degradation is highly associated with the waste itself and with the operational conditions (temperature and heating rate) that this waste undergoes. In this first step of the model, it has been assumed that the organic material (which is the only one that decomposes under heating) could be treated as wood. Several reaction pathways and associated kinetics exist in the literature to describe the thermal degradation of wood [5-7]. In the present work, the data of Thurner and Mann [6] (which assumes three parallel reactions leading to Char, tars and permanent gases)[6] has been used. Dealing with the char conversion, it has been assumes that it was composed of pure carbon and that it could react with available oxygen, steam and carbon dioxide.

3. MODELLING OF THE GASEOUS PHASE

Several researchers have shown that Computational Fluid Dynamics was well suited for the description of processes occurring within the gaseous phase of boilers or incinerators [8-14]. Thus,

in the frame of this study, the commercial software Fluent™ was used for this specific topic. The governing equations of this software will not be developed here. The interested reader should refer to the Fluent User's guide. The following models have been used:

- Turbulence : $k-\varepsilon$ model
- Chemistry: kinetic model with reaction rate computed as the limiting rate between kinetics and turbulent mixing
- Radiation : discrete ordinates model

4. SOLVING

As it has been explained earlier, two sub-models (travelling bed, gaseous phase) allow for specific computation once specific boundary conditions have been yield to each of these sub-models. **Figure 3** illustrates the way the system has been cut, and what information should be exchanged from one sub-model to another.

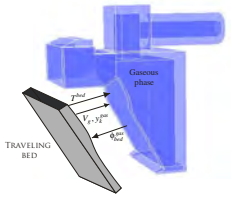

Figure 3: Representation of the coupling between the two softwares

The relevant information yielded by the CFD package is relative to the heat flux to the bed of solids while it receives (from the bed model), the temperature, composition and local velocity of the gas released by the thermal degradation of the bed of solids. Because of the coupling through boundary conditions and exchange variables, the only way to solve the overall problem is iterative. An iteration is composed of one call to the "travelling bed" sub model (Fortran 77), then to the first Matlab™ routine, then to the model describing the phenomena occurring in the gaseous phase (Fluent™) and then to the second Matlab™ routine. Iterations are repeated until convergence which is measured as normalized values of the difference between the values of exchanges variables during iterations. A general Java software was developed to automatically manage the iterations and exchanges of data, and to check for the convergence of the system, as it was done in some previous work [12-14].

5. RESULTS

The results of the overall model are presented for operating conditions at their nominal values. For confidentiality reasons, we are unable to provide further information about these conditions.

Figures 4 represents respectively the evolution of the average mass fraction of each phase in the bed, and of the intrinsic average mass fraction of species contained in the gas leaving the bed along the reactor.

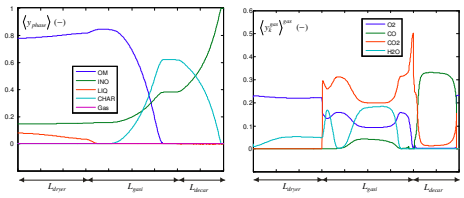

Figure 4: Evolution of the average mass fraction of each phase in the bed along the reactor (left)

and evolution of the intrinsic average mass fraction of species within the gaseous phase along the reactor (right)

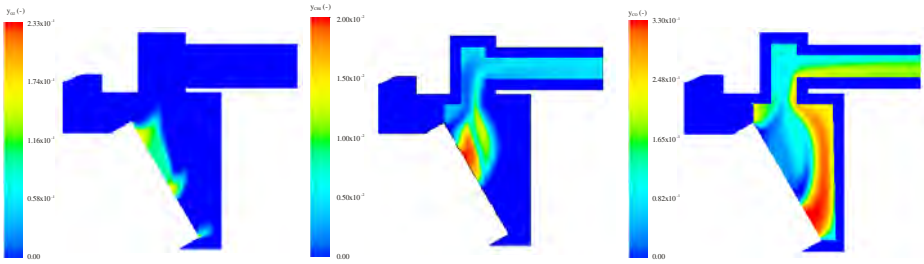

Figure 5: Profile of mass fraction of oxygen (left) methane (centre) and carbon monoxide (right) in the gaseous phase of the reactor

6. CONCLUSIONS

A mathematical model for a travelling bed gasifier has been presented in this study. This model is composed of two main sub-models. The first one is devoted to the description of the physical and chemical phenomena occurring within a bed of waste being gasified. This first model relies on the volume averaging theory which allows for the description of the bed as a continuum with average properties. The second sub-model relies on the use of computational fluid dynamics to describe the aerodynamics, heat transfer and homogeneous combustion occurring at the freeboard of the bed. These models are fully coupled, the upper boundary of one domain being the lowest of the other one.

REFERENCES

[1] S. Whitaker, S.. Simultaneous heat, mass, and momentum transfer in porous media: a theory of drying, *Advances in Heat Transfer*, 13 (1977), 119-203.
[2] MC Melaaen, Numerical analysis of heat and mass transfer in drying and pyrolysis of porous media. *Numerical Heat Transfer Part A*, 29 (1996) 331.
[3] P. Perré, I.W. Turner. A 3-D version of *TransPore*: a comprehensive heat and mass transfer computational model for simulating the drying of porous media. Int. J. Heat Mass Transfer 42 (1999), 4501–4521
[4] J. Ratte, F. Marias, J. Vaxelaire, P. Bernada, Mathematical modelling of slow pyrolysis of a particle of treated wood waste, *Journal of Hazardous Materials* 170 (2009) 1023-1040.
[5] F. Shafizadeh, P.S. Chin, Thermal deterioration of wood, *Wood technology: Chemical Aspects, ACS Symp. Ser.,* 43 (1977), 57-81.
[6] F. Thurner, U. Mann. Kinetic investigation of wood pyrolysis, *Industrial Engineering Chemistry Process Design and Development*, 20 (1981), 482-488
[7] C. Di Blasi, Modeling and simulation of combustion processes of charring and non-charring solid fuels, *Prog. Energy Combust. Sci ,* 19 (1993), 71-104.
[8] Y.B. Yang, R. Newman, V. Sharifi, J. Swithenbank, J. Ariss, Mathematical modelling of straw combustion in a 38 MWe power plant furnace and effect of operating conditions, *Fuel*, 86 (2007) 129-142
[9] Y.B. Yang, C. Ryu, J. Goodfellow, V. Nasserzadeh Sharifi, J. Swithenbank, Modelling Waste Combustion in Grate Furnaces, *Process Safety and Environmental Protection,* 82 (2004) 208-222.
[10] Y. Ménard, A. Asthana, F. Patisson, Ph. Sessiecq, D. Ablitzer, Thermodynamic Study of Heavy Metals Behaviour During Municipal Waste Incineration, *Process Safety and Environmental Protection,*84 (2006) 290-296.
[11] W. Yang, H. Nam, S. Choi., Improvement of operating conditions in waste incinerators using engineering tools, *Waste Management,* 27 (2004) 607-613.
[12] F. Marias**,** A model of a rotary kiln incinerator including processes occurring within the solid and the gaseous phases. *Computers and Chemical Engineering*, 27 (2003) 813-825.
[13] F. Marias, D. Roustan, A. Pichat, Modelling of a rotary kiln for the pyrolysis of Aluminium waste, *Chemical Engineering Science***.** 60 (2005)**,** 4609-4622.
[14] F. Marias, D. Roustan, A. Pichat, Coupling between CFD and a bed model in a rotary kiln. -Aplication to the pyrolysis of Aluminium waste, *Progress in Computational fluid Dynamics,* 7 (2007) 40-50.

MINI-SYMPOSIUM

MESHLESS METHODS FOR THERMOFLUID PROBLEMS

MINI-SYMPOSIUM ORGANISED BY B. ŠARLER, AND M. LI

Third International Conference on Computational Methods for Thermal Problems
THERMACOMP2014, June 2-4, 2014, Lake Bled, Slovenia
N. Massarotti, P. Nithiarasu and B. Sarler (Eds.)

TRANSIENT HEAT TRANSFER IN COMPOSITE MATERIALS

Isa Ahmadi
Department of Mechanical Engineering, University of Zanjan, University Blvd., Zanjan, Iran,
i_ahmadi@znu.ac.ir

ABSTRACT

In this study the transient heat transfer in the composite material is studied from the micromechanical point of view. For modeling of the problem a small part of a fibrous composite includes a fiber surrounded in the matrix in the periodic square arrangement which usually is called the RVE is selected as the solution domain. The selected RVE includes a fiber surrounded in the matrix. The fully bonded interface condition is considered in the fiber-matrix interface. For discretization of the governing equation a numerical technique based on the meshless concept is introduced. By employing the presented meshless method the governing equations of transient heat conduction in the heterogeneous RVE are discretized to ordinary differential equations. Due to fully bonded fiber matrix interface, the interface thermal resistance is not considered in the analysis and so the continuity of temperature is enforce to the fiber-matrix interface. The direct interpolation method is employed for enforcement of the essential boundary conditions to the solution domain. The Euler numerical integration method is used for integration of the discretized governing equations of the problem in the time domain. The numerical results are presented for distribution of steady state and transient temperature and heat flux in the fiber and matrix in the RVE. Comparison of the numerical results shows good agreement with other numerical and analytical methods.

Key Words: *Transient Heat conduction, Fibrous composite, Meshless method, Numerical integration*

1. INTRODUCTION

During the past decade, the idea of using meshless methods for solution of the boundary value problems has received much attention and significant progress were achieved on meshless methods. In the meshless methods, no predefined mesh of elements is needed between the nodes for the construction of trial or test function. Therefore, the one of the main objectives of the meshless methods is to eliminate or alleviate various difficulties related to elements such as meshing and remeshing of entire domain or locking and distortion of elements. In the recent years the meshless methods are used for analysis of heat transfer problems which one could refer to [1-5].

2. MESHLESS FORMULATION

Abstracts should outline the main features, results and conclusions as well as the general significance of the contribution. Relevant references, figures, and tables are welcome. However, please note that extended abstracts

Consider an arbitrary local particle (sub-domain) named. Ω_s^I around node I inside a global material domain Ω. For each sub-domain Ω_s^I with the boundary $\partial\Omega_s^I$, inside the global domain Ω the integral form of energy balance equation in heat conduction problem can be written as;

$$\int_{\Omega_s^I} \rho c \dot{T} d\Omega + \int_{\partial\Omega_s^I} q_i n_i d\Gamma = \int_{\Omega_s^I} g d\Omega \qquad (1)$$

in which ρ is the mass density, c is the specific heat capacity of the medium, $\boldsymbol{n}$ is the outward normal vector of the boundary $\partial\Omega_s^I$ and q_i is the heat flux in the xi direction. g shows the rate of

energy generation per unit volume in the domain. The boundary of the local sub-domain in general consists of three parts, $\partial\Omega_s^I = L_s^I \cup \Gamma_{sq}^I \cup \Gamma_{su}^I$, which $L^I{}_s$, is the local boundary that is totally inside global domain, Γ_{sq}^I and $\Gamma^I{}_{\mathrm{su}}$ are the part of local boundary that coincides with the global Neumann boundary, and global Dirichlet boundary, respectively. Considering these three parts, and using the Fourier's law of heat conduction, Equation (1) can be rewritten as:

$$\int_{\Omega_s^I} \rho c \dot{T} d\Omega - \int_{L_s^I} k_{ik} T_{,k} n_i d\Gamma - \int_{\Gamma_{su}^I} k_{ik} T_{,k} n_i d\Gamma = \int_{\Omega_s^I} g d\Omega - \int_{\Gamma_{sq}^I} \bar{q} d\Gamma \qquad (2)$$

where k_{ik} is the coefficient of thermal conduction for a general anisotropic material and index follow a comma i.e. $,_k$ indicated partial derivative respect to x_k. In this study a meshless method with moving least squares (MLS) approximation is presented for discretization of (2). To obtain the discrete form of (2), the MLS approximation is used to approximate the test function T from the fictitious nodal values $\hat{T}$. Substitution of MLS approximation into (2) for all the nodes that not located on boundaries gives;

$$\int_{\Omega_s^I} \rho c \phi^J \dot{\hat{T}}^J d\Omega - \int_{L_s^I} (k_{ik} \phi^J{}_{,k}) \hat{T}^J n_i d\Gamma - \int_{\Gamma_{su}^I} (k_{ik} \phi^J{}_{,k}) \hat{T}^J n_i d\Gamma = \int_{\Omega_s^I} g d\Omega - \int_{\Gamma_{sq}^I} \bar{q} d\Gamma \qquad (3)$$

where $\phi^J{}_{,k}$ is the partial derivative of $\phi^J(\mathbf{x})$ respect to x_k . Equation (13) may be written in the form of discretized system of linear equations as:

$$C_{IJ} \dot{\hat{T}}^J + K_{IJ} \hat{T}^J = f_I \qquad I, J = 1, \ldots, N \qquad (4)$$

in which

$$\begin{aligned} C_{IJ} &= \int_{\Omega_s^I} \rho c \phi^J d\Omega, \\ K_{IJ} &= \int_{L_s^I} (k_{ik} \phi^J{}_{,k}) n_i d\Gamma + \int_{\Gamma_{su}^I} (k_{ik} \phi^J{}_{,k}) n_i d\Gamma \\ f_I &= \int_{\Gamma_{sq}^I} \bar{q} d\Gamma - \int_{\Omega_s^I} g d\Omega \end{aligned} \qquad (5)$$

After imposing the boundary and interface conditions the Euler integration method is used for time integration of the equations in (4).

3. RESULTS

In the numerical result the transient heat transfer in the fibrous Glass/Epoxy with 35% FVF composite material in micromechanical level is studied. The selected RVE are shown in Figure (1). At t=0 the initial temperature is kept at T=0 and the top, bottom and right edges of the RVE are suddenly subjected to T=1˚C and left side is kept at T=0 and the initial temperature is zero. In this study the dimensionless parameter for the time is defined as $t^*=\alpha_m t/a^2$ in which $2a$ is the length of the RVE and α_m is the thermal diffusivity of matrix. Also the dimensionless heat flux q_i^* is defined as $q_i^* = q_i/(k_m(T_R-T_i)/a)$ in which T_{R} is the temperature of the right side of the RVE. The thermal conductivity of Glass fiber k_f=1.04(W/m ˚C) is bigger than the thermal conductivity of Epoxy matrix k_m=0.2 (W/m C). The time history of temperature and the time history of distribution of dimensionless heat flux $q^*{}_1$ on x_2 axis of RVE at various time are shown in Figures (2) and (3).

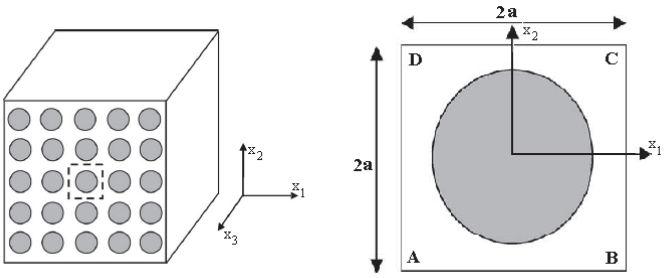

FIGURE (1): The cross section of composite, square array distribution, selected R7E

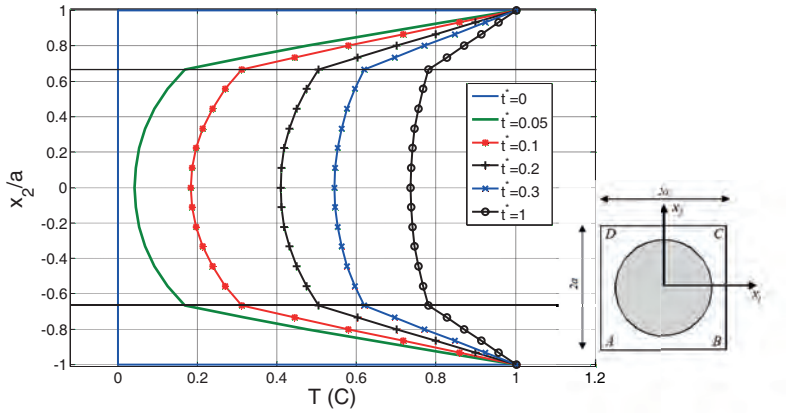

FIGURE (2): Distribution of temperature on x_2 axis of Glass/EpoxY composite

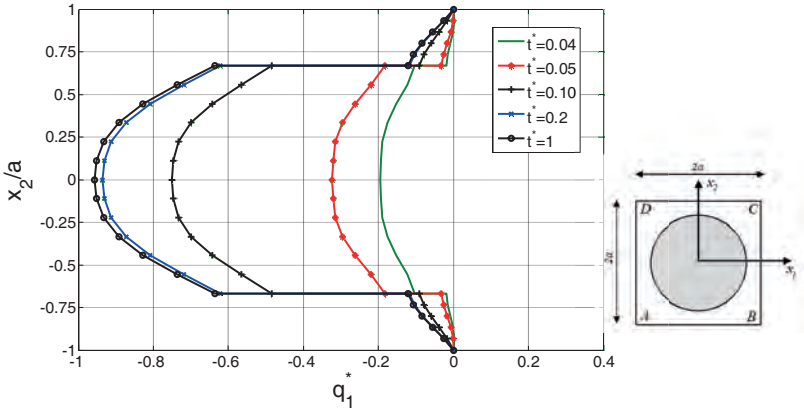

FIGURE (3): Distribution of heat flux q^*_1 on x_2 axis of RVE Glass/Epoxy

The distribution of transient temperature in the RVE, the contour plot of the distribution of temperature in the RVE of Glass/Epoxy composite at t^*=0.05 and t^*=0.1 are shown in Figure (4). These figures show the diffusion of the temperature in the RVE.

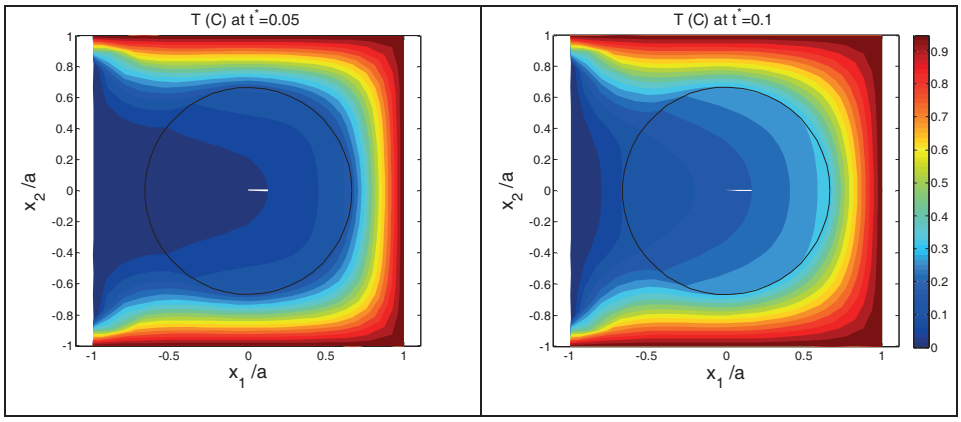

FIGURE (4): Contour plots of distribution of temperature in Glass/Epoxy, at t^*=0.05 and t^*=0.1

4. CONCLUSIONS

The transient heat conduction in the fibrous composite material is studied from the micromechanical point of view. A meshless method based on the integral form of the energy balance equation is presented for the transient conduction heat transfer. The presented method is employed to analysis transient heat conduction in heterogeneous material and as an example the heat conduction in the fiber and matrix of Glass/Epoxy composite is studied. The Euler numerical integration method is used for time integration of the equations. It is seen that the presented meshless method is efficient for analysis of transient conduction heat transfer in heterogeneous materials.

REFERENCES

[1] J. Sladek, V. Sladek, S.N. Atluri, Meshless local Petrov-Galerkin method for heat conduction problem in an anisotropic medium, *CMES,* 6, 477-489, 2004.

[2] J. Sladek, V. Sladek, C.L. Tan, S.N. Atluri, Analysis of transient heat conduction in 3D anisotropic functionally graded solids by the MLPG, *CMES,* 32, 161-174, 2008.

[3] I.V. Singh, A numerical solution of composite heat transfer problems using meshless method, I*nt. J. Heat Mass Transfer*, 47, 2123–2138, 2004.

[4] Isa Ahmadi, N.Sheikhy, M.M. Aghdam, S.S.Nourazar, A new local meshless method for steady-state heat conduction in heterogeneous materials, *Engineering Analysis with Boundary Elements,* 34, 1105–1112, 2010

[5] X.H., Wu, W.Q., Tao, Meshless method based on the local weak-forms for steady-state heat conduction problems, *International Journal of Heat and Mass Transfer*, 51, 3103–3112, 2008.

Third International Conference on Computational Methods for Thermal Problems
THERMACOMP2014, June 2-4, 2014, Lake Bled, Slovenia
N. Massarotti, P. Nithiarasu and B. Sarler (Eds.)

Fast Evaluation of the Method of Fundamental Solutions for Solving Reaction Diffusion Problems

Ji Lin, Wen Chen
College of Mechanics and Materials, Hohai University, Nanjing, China, linji861103@126.com

C. S. Chen
Department of Mathematics, University of Southern Mississippi, Hattiesburg, MS 39406, USA, cschen.math@gmail.com

ABSTRACT

The method of fundamental solutions (MFS) is known as an effective boundary meshless method. However, the formulation of the MFS has resulted in a dense and extremely ill-conditioned matrix. A new approach, based on the exponential decay of the fundamental solution of modified Helmholtz equation, is proposed so that the resultant matrix of the MFS becomes sparse for solving inhomogeneous modified Helmholtz equation. A standard two-step solution process, which consists in evaluating particular solution and homogeneous solution, has been applied. Furthermore, we apply the new scheme to efficiently solving large-scale time-dependent problems. Houbolt method which is a third order time difference scheme is adopted to reduce the time dependent problems to non-homogeneous modified Helmholtz equation. Three benchmark problems in diffusion reaction and wave propagation are considered.

Key Words: *method of fundamental solutions, modified Helmholtz equation, particular solution.*

1. INTRODUCTION

The method of fundamental solution (MFS) [1] is a truly meshless method which has rightfully received a great deal of attention by applied mathematicians and engineers in dealing with a variety of engineering problems. The MFS was combined with the method of particular solution (MPS) [2] for dealing with nonhomogeneous problems. It has been applied to advection-diffusion equations, Burger's equations, advection equations and wave equations. In this paper, we apply the MFS for the solutions of reaction diffusion and wave equations by introducing the Houbolt finite difference scheme [3] to discretize the time-dependent terms, and the coupled MFS-MPS for space discretization. The method of particular solution and the method of fundamental solution satisfy the nonhomogeneous equation and the corresponding homogeneous equation, respectively.

It is known to all that the coefficient matrix resulted from the MFS discretization is dense and the condition number is very large. For large collocation points, it is expensive to solve. Direct solver to such a matrix needs $O(N^3)$ operations and $O(N^2)$ storages. And the ill-conditioned matrix will result in the less accuracy and even the disaster for numerical simulation. As we can see that, the feature of the MFS coefficient matrix is largely depended on the boundary conditions, the choice of the fictitious boundary and the wave-number. Due to the nature exponential decay of the fundamental solutions of the governing equation, we can set most part of the MFS coefficient matrix to be zero which makes it possible for the resultant matrix of the MFS to be sparse to reduce the computational cost and circumvent the ill-conditioned feature. The purpose of this paper is to assess the efficacy of the sparse formulation of the MFS for reaction diffusion and wave problems.

2. PROBLEM DESCRIPTION

We consider the following reaction diffusion equation

$$\Delta u - cu = u_t + f(x) \tag{1}$$

where u = u(x, t) is a state variable at x = (x_1,x_2), c is a constant, Δ is the Laplacian. Our approach is to convert the (1) into the modified Helmholtz equation and then solve the corresponding system by the MFS-MPS. This can be achieved by the Houbolt method which is a three steps implicit and unconditionally stable time-integration scheme based on the third-order interpolation; i.e.,

$$u_t^{n+1} \approx \frac{1}{6\delta t}\left(11u^{n+1} - 18u^n + 9u^{n-1} - 2u^{n-2}\right) \tag{2}$$

where δt is the time interval with $t_n = n*\delta t$ and $u^n = u(x, t_n)$, n denotes the time level. It follows that

$$\Delta u_t^{n+1} - cu^{n+1} - \frac{11u^{n+1}}{6\delta t} = \frac{1}{6\delta t}\left(-18u^n + 9u^{n-1} - 2u^{n-2}\right) + f^{n+1}. \tag{3}$$

Note that in (3) we require u of previous three time steps to carry out the time marching scheme. As a result, the Euler scheme is used to obtain u^{n-1} and u^{n-2} as follows

$$u^{n-1} = u(x,t)|_{t=0} - \delta t * u_t|_{t=0},$$
$$u^{n-2} = u(x,t)|_{t=0} - 2\delta t * u_t|_{t=0}.$$

For each time step, we are solving a nonhomogeneous Helmholtz equation as shown in (3). Hence, let us consider the following modified Helmholtz equation

$$\begin{aligned} &\Delta u - \lambda^2 u = h(x), \quad x \in \Omega, \\ &Bu = g(x), \qquad\quad x \in \partial\Omega, \end{aligned} \tag{4}$$

Where *B* is the boundary operator, *h* and *g* are known functions, and Ω and ∂Ω are domain and its boundary respectively. The solution in (4) can be splitted into two parts $u = u_h + u_p$ where u_p is a particular solution satisfying the governing equation

$$\Delta u_p - \lambda^2 u_p = h(x) \tag{5}$$

without satisfying the boundary conditions. The homogeneous solution u_h satisfies

$$\begin{aligned} &\Delta u_h - \lambda^2 u_h = 0, \qquad x \in \Omega, \\ &Bu_h = g(x) - Bu_p, \quad x \in \partial\Omega, \end{aligned} \tag{6}$$

which can be solved by the MFS. Here we propose an efficient way to solve (6). This allows us to adopt a large number of collocation points using the MFS. We refer readers to [2] for solving (5).

3 THE MFS FOR MODIFIED HELMHOLTZ EQUATION

In the MFS, the approximate solution of (6) can be expressed as a linear combination of fundamental solutions

$$u_h(x) = \sum_{j=1}^{N} a_j G(x, \varepsilon; \lambda), \qquad x \in \Omega, \tag{7}$$

where $G(x,\partial;\lambda) = K_0(\lambda r)$ is the fundamental solution in which K_0 is the modified Bessel function of the second kind of order zero, $r = \|x - \partial\|$ is the Euclidean distance between x and source point ∂.

By collocating the boundary conditions in (6), we obtain the following matrix system

$$\boldsymbol{A}\boldsymbol{a} = \boldsymbol{g} \tag{8}$$

where $\boldsymbol{A} = [BG(x_i, \varepsilon_j)]$, $a = [a_1, a_2, ..., a_N]^T$, **g** is the corresponding boundary conditions. It is known that ***A*** is dense and often severely ill-conditioned. Despite the ill-conditioning, the accuracy of the numerical solution is largely unaffected. And for large collocation points, it is expensive to solve. Direct solver to such a matrix needs $O(N^3$ operations and $O(N^2)$ storages.

As we can see that, the feature of the coefficient matrix ***A*** is largely depended on the boundary conditions, the choice of the fictitious boundary and λ. Due to the nature exponential decaying of the fundamental solutions in (7) for small argument λr, $K_0(\lambda r) \approx -\ln(\lambda r)$, and for large argument,

$$K_0(\lambda r) \approx \frac{\pi}{\sqrt{2\pi\lambda r}} \exp(-\lambda r), \text{ for } \lambda r \gg 1. \tag{9}$$

As a result, most coefficients in ***A*** are very small and the discrepancy between the maximum and minimum values in ***A*** becomes wide apart. For example, for λ=50, the profile of ***A*** can be seen in Figure 1. Hence, a large part of the entries of ***A*** can be neglected and set to zeros. In this way, (8) becomes a sparse matrix system which can be solved efficiently. The trade-off is that the accuracy is slightly decreased. For time-dependent problems, as we shall see, the effect of losing accuracy is negligible.

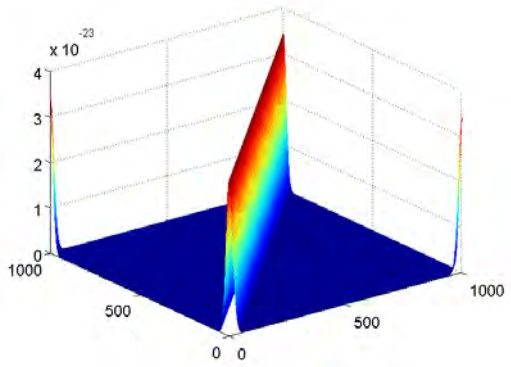

FIGURE 1 The profile of A with λ=50 on the unit circle with 1000 collocation and source points.

4. RESULTS

We consider the following problem

$$\begin{aligned} u_t &= \Delta u + \sin(x_1)\sin(x_2)(2\sin(t) + \cos(t)), \quad (x_1, x_2) \in \Omega, \\ u(x_1, x_2, t) &= g(x_1, x_2), \qquad (x_1, x_2) \in \partial\Omega, \\ u(x_1, x_2, 0) &= 0, \quad (x_1, x_2) \in \Omega, \end{aligned}$$

where $\Omega \cap \partial\Omega = [0,1]^2$. g is given based on the following analytical solution

$$u(x_1, x_2) = \sin(x_1)\sin(x_2)\sin(t).$$

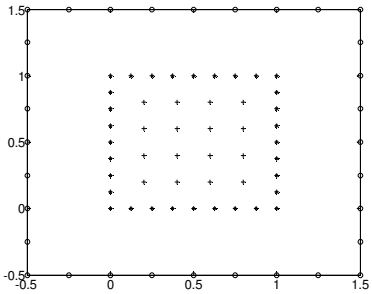

FIGURE 2. '*' boundary points, 'o' source points, '+'interior points

A typical distribution of boundary points, interior points, and source points are shown in Figure 2. To approximate particular solution, we choose $r^6\log(r)$ as the basis function and 244 uniformly distributed interior points. To obtain the homogeneous solution by the MFS, we choose 100 boundary points and the same number of source points which located very close to the boundary; i.e. $\partial_1=(x_1-0.5)\times1.001+0.5$, $\partial_2=(x_2-0.5)\times1.001+0.5$. In Table 1, we show the maximum errors at t=1 with time step $\delta t = 0.01$ and 0.001. Note that the error remains the same even if the sparseness of the matrix is decreasing.

% of nonzero entry	Error ($\delta t=0.01$)	Error ($\delta t=0.001$)
100	1.70E-3	3.28E-5
79	1.70E-3	3.28E-5
47	1.70E-3	3.28E-5
16	1.70E-3	3.28E-5
1	1.60E-3	3.28E-5

TABLE 1. Sparseness of the MFS matrix verses error.

5. CONCLUSIONS

We propose a robust numerical scheme using the MFS, MPS, and Houbolt method for solving reaction diffusion problems. The proposed algorithm allows us to deploy a large number of collocation points to solve the large-scale problems.

REFERENCES

[1] G. Fairweather, A. Karageorghis, the method of fundamental solutions for elliptic boundary value problems, Adv. Comput. Math., 9, 69-95, 1998.

[2] A.S. Muleshkov, M.A. Golberg, and C.S. Chen, Particular solutions of Helmholtz-type operators using higher order polyharmonic splines, Comp. Mech, 23, 411-419, 1999.

[3] C.Y. Lin, M.H. Gu, and K.L. Young, The time-marching method of fundamental solutions for multi-dimensional telegraph equations, CMC, 18 (1), 43-68, 2010.

Third International Conference on Computational Methods for Thermal Problems
THERMACOMP2014, June 2-4, 2014, Lake Bled, Slovenia
N. Massarotti, P. Nithiarasu and B. Sarler (Eds.)

A meshless approach to modelling of solidification: macro- and mesosegragetion issues

Gregor Kosec
Jožef Stefan Institute, Department of Communication Systems, Jamova 39, 1000 Ljubljana, Slovenia, gkosec@ijs.si

Božidar Šarler
University of Nova Gorica, Laboratory for Multiphase Processes, Vipavska 13, 5000 Nova Gorica & Laboratory for Simulation of Materials and Processes, Institute of Metals and Technology, Lepi pot 11, 1000 Ljubljana, Slovenia, bozidar.sarler@ung.si

ABSTRACT

This paper tackles numerical simulation of binary alloy solidification. Coupled volume averaged governing equations for mass, energy, momentum and species transfer are considered by incorporating lever solidification rule and incompressible Newtonian fluid with Darcy limit in the mushy zone. Natural convection in the melt is modelled by the thermal and solutal Boussinesq hypothesis. The physical model is solved by the explicit meshless Local Radial Basis Function Collocation Method (LRBFCM) by using 5-noded influence domains, multiquadrics radial basis functions and explicit time stepping. Local pressure correction is used to couple mass and momentum equations. Adaptive upwind is used for stabilization of the extremely unstable, convection dominated situations. The numerical simulations reveal instabilities during solidification process that introduce anomalies in the final segregation map that scale with the typical cast as well as sub-cast dimensions. The numerical example is based on the SMACS [1] solidification test with Pb-18%Sn alloy with reduced permeability.

Key Words: *Solidification, macrosegregation, mesosegragation, instabilities, adaptive upwinding.*

1. INTRODUCTION

Solidification [2] science and engineering represents an interdisciplinary research field of great interest. Many natural phenomena such as flow of lava in volcano eruptions or modern industrial processes, in particular different types of casting, rely on understanding of solidification. Castings are prone to several types of defects, such as porosities, deformation during solidification, including hot tearing, and chemical inhomogeneities also referred to as segregation. The segregation that scales with the whole casting is called macrosegregation, on the other hand, the segregation, much smaller than the size of the casting and much larger than the typical grain size is called mesosegregation. Recently, substantial efforts and resources were invested [3] to study the behaviour of different numerical methods in the prediction of macrosegregation. This efforts were accelerated through a call for contributions to related numerical benchmark test cases [1]. The related spectra of tests (denoted I-IV) in [1] are gradually complicated from natural convection of a low Prandtl fluid (I), double diffusive natural convection (II), and to solidification of a binary tin based alloy, with 10 (III) or 18wt% (IV) lead. In this work we present a solution towards fourth of these benchmark tests by a novel meshless technique, based on local collocation with radial basis functions (LRBFCM). The present paper follows our previous simulations of test I in [4], test III in [5], based on previous developments of LRBFCM for fluid flow problems [6] and macrosegregation [7]. The main complexities in numerical solution of alloy solidification models are moving interfaces with high gradients of physical properties, strong couplings between the conservation equations, different flow regimes in mushy zone and pure liquid, potentially unstable flow patterns

in low-Pr liquids such as metals, hyperbolic nature of the solute transport due to almost completely advective transport. The problem of strong coupling between the momentum transport and energy and solute transport via the buoyancy force, and between the thermal field and permeability, makes the solution even more complex and less stable.

2. SOLIDIFICATION MODEL

The minimal solidification model, i.e. solidification model, simplified to the largest possible degree, is addressed in the present paper. The set of governing equations is based on continuum conservation laws and related constitutive relations. The model comprises energy transport, solute transport, incompressible Newtonian and porous Darcy fluid flow, and Eutectic phase diagram coupled with the solute transport over the phase front for consideration of the microscopic level. The problem is governed by the following equations

$$\nabla \cdot \mathbf{v} = 0, \tag{1}$$

$$\rho \frac{\partial \mathbf{v}}{\partial t} + \frac{\rho}{f_L}(\nabla \mathbf{v})\mathbf{v} = -f_L \nabla P + \mu \nabla^2 \mathbf{v} - f_L \frac{\mu}{K}\mathbf{v} + f_L \mathbf{b}, \tag{2}$$

$$\rho \frac{\partial h}{\partial t} + \rho \mathbf{v} \cdot \nabla h = \lambda \nabla^2 T, \tag{3}$$

$$\frac{\partial C}{\partial t} + \mathbf{v} \cdot \nabla C_L = 0 \tag{4}$$

$$\mathbf{v} = f_L \mathbf{v}_L, \tag{5}$$

$$K = K_0 f_L^3 / \left(1 - f_L\right)^2, \tag{6}$$

$$\mathbf{b} = \rho_{\text{ref}} \left[1 - \beta_T (T - T_{\text{ref}}) - \beta_C (C_L - C_{\text{ref}})\right]\mathbf{g}, \tag{7}$$

$$h = c_p T + f_L L, \tag{8}$$

$$C = \left[f_L + (1 - f_L)k_p\right]C_L, \tag{9}$$

$$T = T_F + m_L C_L. \tag{10}$$

The coupling between the conservation equations and the phase change is performed by lever rule which permits the closed form solution

$$af_L^2 + bf_L + c = 0; a = \left(k_p - 1\right)L, b = \left(k_p - 1\right)\left(c_p T_F - h\right) - k_p L, c = k_p\left(h - c_p T_F\right) - c_p m_L C. \tag{11}$$

The following quantities are involved in the governing equations: liquid velocity $\mathbf{v}$, intrinsic liquid velocity $\mathbf{v}_L$, enthalpy h, average concentration C, and the pressure P, respectively. The permeability K is defined through a permeability constant K_0 and the liquid fraction f_L. The thermo-physical properties, i.e. viscosity μ, thermal conductivity λ, specific heat c_p and density ρ are assumed to be equal and constant in both phases. The buoyancy term $\mathbf{b}$ depends on the temperature T, the liquid concentration C_L, the thermal expansion coefficient β_T, the concentration expansion coefficient β_C, the reference density ρ_{ref} given at the reference temperature T_{ref} and the reference concentration C_{ref}. The binary phase diagram is defined by the liquidus slope m_L, the equilibrium partition coefficient k_p and fusion temperature of the pure solvent T_F. Symbols t and $\mathbf{g}$ stand for time and gravity acceleration, respectively. We seek the

solution of the temperature, velocity, pressure and concentration fields at time $t = t_0 + \Delta t$, where t_0 represents initial time and Δt a positive time increment. The case is defined for a rectangular domain with dimensions 10x6 cm. However, computational domain can be reduced to 5x6 cm due to the symmetry. The problem is schematically presented in Figure 1. Material properties are taken from Table 1 from [1], except the permeability, chosen as $K_0 = 1.9 \cdot 10^{-11}\ \mathrm{m}^{-2}$.

3. SIMULATIONS

The simulations are performed by LRBFCM. This method and numerical implementation is elaborated in [5]. It is based on explicit time discretisation and on 5-noded influence domains where collocation with multiquadrics radial basis functions is performed locally. Local pressure correction is used to couple mass and momentum equations. Adaptive upwind is used for stabilization of the extremely unstable, convection dominated situations.

The simulation of SMACS test IV starts with stationary over-heated liquid. The heat is extracted from the right side of the domain, described by the Robin boundary conditions. As the initial liquid cools, the thermo-solutal natural convection is set up. It drives the flow anti-clockwise. The solidification process starts when the liquid temperature reaches the liquidus temperature. A negative segregation patch at the bottom of the enclosure and a positive segregation patch in the upper part are clearly visible. Besides the macrosegregation, the formation of mesosegrates starts in the mushy zone as the solidification front advances. The channel-like anomalies in concentration field occur as a consequence of instabilities in the porous mushy zone. Five of them are clearly visible on Figure 1 and two of them can be suggested. The solidification in the channels is slowed down, i.e. the solid fraction in the channels is lower and consequently the hydrodynamic permeability is higher. The lower drag in the channels makes the flow through the channels stronger, and the stronger flow induces stronger segregation.

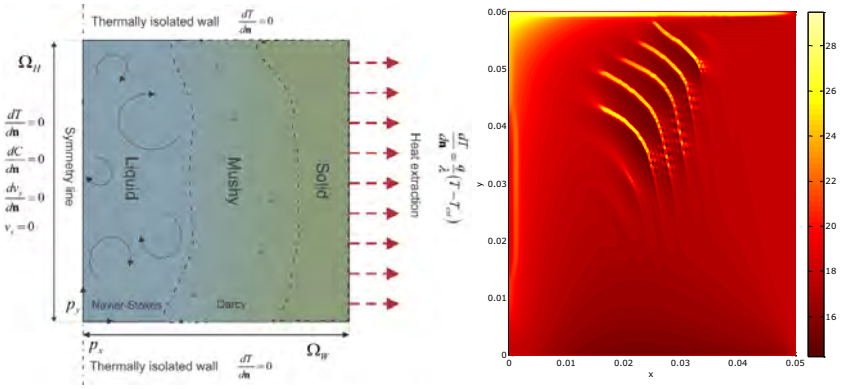

FIGURE 1: The scheme of the problem (right) and simulated concentration of for fully solidified material (left).

4. CONCLUSIONS

A physical model and a meshless solution procedure for calculating macrosegregation with mesosegragates in the cast has been numerically solved in the present paper. The situation tackled is similar to case IV in [1]. Our future work will be focused on a detailed representation of time evolution of the solution with thorough analysis of impact of numerical parameters on results as well as the stability analysis regarding the process parameters. The simulations will be coupled to

mechanical solidification model in order to be able to tackle also possible mechanical issues such as shape changes and hot tearing.

ACKNOWLEDGEMENT: We acknowledge the financial support from the Slovenian Research Agency under the grant J2-4120 and program groups P2-0379 and P2-0095.

REFERENCES

[1] Bellet, M., Combeau, H., Fautrelle, Y., Gobin, D., Rady, M., Arquis, E., Budenkova, O., Dussoubs, B., Duterrail, Y., Kumar, A., Gandin, C. A., Goyeau, B., Mosbah, S. and Zaloznik, M., Call for contributions to a numerical benchmark problem for 2D columnar solidification of binary alloys, *International Journal of Thermal Sciences*, 48, 2013-2016, 2009.

[2] Dantzig, J. and Rappaz, M., *Solidification*, EPFL Press, Laussane, 2009.

[3] Combeau, H., Bellet, M., Fautrelle, Y., Gobin, D., Arquis, E., Budenkova, O., Dussoubs, B., Du Terrail, Y., Kumar, A., Gandin, Ch- A., Goyeau, B., Mosbah, S., Quatravaux, T., Rady, M. and Založnik, M., Analysis of a numerical benchmark for columnar solidification of binary alloys, *IOP Conference Series: Materials Science and Engineering*, 33, doi:10.1088/1757-899X/33/1/012086, 2012.

[4] Kosec, G. and Šarler, B., Solution of a low Prandtl number natural convection benchmark by a local meshless method, *International Journal of Numerical Methods for Heat & Fluid Flow*, 23, 189-204, 2013.

[5] Kosec, G and Šarler, B, Simulation of macrosegregation with mesosegregates in binary metallic casts by a meshless method, *Engineering Analysis with Boundary Elements*, 10.1016/j.enganabound.2014.01.016, 2014.

[6] Kosec, G. and Šarler, B., Solution of thermo-fluid problems by collocation with local pressure correction, *International Journal of Numerical Methods for Heat & Fluid Flow*, 18, 868-882, 2008.

[7] Kosec, G., Založnik, M., Šarler, B. and Combeau, H., A Meshless Approach Towards Solution of Macrosegregation Phenomena, *CMC: Computers, Materials, & Continua*, 22, 1-27, 2011.

Third International Conference on Computational Methods for Thermal Problems
THERMACOMP2014, June 2-4, 2014, Lake Bled, Slovenia
N. Massarotti, P. Nithiarasu and B. Sarler (Eds.)

A LOCAL MESHLESS METHOD FOR SOLVING AN INVERSE HEAT CONDUCTION PROBLEM

Wen Li, Xiaoyan Liu
College of Mathematics, Taiyuan University of Technology, China,
muziwen02@163.com

ABSTRACT

In this paper, we propose a meshless scheme based on compactly supported radial basis functions (CS-RBFs) which are local functions for solving a kind of inverse heat conduction problem in 2D. By assuming the unknown boundary condition to be known as a polynomial function, the inverse problems can be solved by a procedure similar to the process for solving forward problems. We employ Tikhonov regularization technique and L-curve method to obtain a stable numerical solution. Numerical results verify the effectiveness and stability of this method.

Key Words: *Inverse Heat Conduction Problem, Compactly Supported Radial Basis Functions, Local Meshless Method, Tikhonov Regularization, L-curve.*

1. INTRODUCTION

Inverse problems arise in scientific, engineering and even medical fields. As we know, this kind of problems are ill-posed, which means the solutions do not depend continuously on the boundary conditions. Since any small errors caused by the measurement of input data on boundary or interior of the domain can result in highly amplified errors in the numerical solutions, many normal methods for well-posed forward problems are not suitable for solving inverse problems. Therefore, development of effective and stable numerical algorithm is quite necessary.

The meshless method based on the radial basis function (RBF) are of competitive edge, because of its simplicity in selecting points and high adaptability to domain shape and equation type. The main difficulty in designing an algorithm for solving inverse problem stems from the ill-posedness of problem itself and the ill condition of the resultant matrix. However, most of the commonly used globally defined RBFs are not positive-definite and the resulting matrix can be dense and highly ill-conditioned. For this reason, compactly supported RBFs (CS-RBFs) which are positive-definite and can result in a sparse matrix can be used. So far, CS-RBFs were used for solving forward problems [1-2], and not for inverse problems yet.

According to the best of authors' knowledge, a huge majority of methods for solving inverse heat conduction problems are global methods. This paper proposes a kind of stable meshless local numerical method base on CS-RBFs for solving a 2D inverse heat conduction problem with sensors installed at a few of internal points. We devote to determine the Dirichlet boundary data on unreachable boundary.

2. THE LOCAL MESHLESS METHOD FOR AN IHCP

Consider the IHCP as follow:

$$\frac{\partial}{\partial t}u(\mathbf{x},t)=\Delta u(\mathbf{x},t),\quad \mathbf{x}\in\Omega,\quad 0\le t\le T, \tag{1}$$

$$u(\mathbf{x},0)=f(\mathbf{x}),\qquad \mathbf{x}\in\Omega\cup\partial\Omega, \tag{2}$$

$$u(\mathbf{x},t) = g(\mathbf{x},t), \qquad \mathbf{x} \in \partial\Omega_1, \quad 0 \le t \le T, \tag{3}$$

$$u(\mathbf{x},t) = h(\mathbf{x},t), \qquad \mathbf{x} \in \partial\Omega_2, \quad 0 \le t \le T\ . \tag{4}$$

Where $u(\mathbf{x},t)$ is the temperature distribution at time t and T denote the maximum time involved in this problem. $\Omega \subseteq R^2$ is a bounded domain with boundary $\partial\Omega$, and $\partial\Omega = \partial\Omega_1 \cup \partial\Omega_2$, $\partial\Omega_1 \cap \partial\Omega_2 = \varnothing$. f and g are given functions, h is unknown. The additional specification is given as follow:

$$u(\mathbf{x}_i^*,t) = q(\mathbf{x}_i^*,t), \qquad \mathbf{x}_i^* \in \Omega,\ i = 1,2,\mathrm{L}\ ,nk, \tag{5}$$

where $\mathbf{x}_i^*$, $i = 1,2,\mathrm{L}\ ,nk,$ are certain interior points at which sensors are installed in the domain so that the temperature can be measured at every moment. That means $q(\mathbf{x}_i^*,t)$ ($i = 1,2,\mathrm{L}\ ,nk$) are known.

To solve this problem, the standard Euler difference scheme is used to discrete the time variable. u^{m+1} at each time $t = (m+1)\tau$ ($m = 0,1,\mathrm{L}$) on the boundary $\partial\Omega_2$ and in Ω should be determined. Here, we use a polynomial with degree d to approximate the Dirichlet boundary condition at $t = (m+1)\tau$ on $\partial\Omega_2$, which can be expressed as:

$$h^{m+1}(\mathbf{x})\ ;\ \ \hat{h}^{m+1}(\mathbf{x}) = (1 \quad x \quad y \quad x^2 \mathrm{L} \quad y^d) \begin{pmatrix} b_0^{m+1} \\ b_1^{m+1} \\ \mathrm{M} \\ b_{d(d+3)/2}^{m+1} \end{pmatrix} = \mathbf{p}(\mathbf{x})\mathbf{b}^{m+1}, \qquad \mathbf{x} \in \partial\Omega_2. \tag{6}$$

In order to solve problem (1)-(5), we temporarily assume that $h^{m+1}(\mathbf{x})$ is known as expressed in (6), which means $\mathbf{b}^{m+1}$ in (6) is given. Then the problem (1)-(5) can be taken as the well-posed forward problem. We apply Kansa method based on compactly supported RBFs to solve this hypothetical forward problem.

However, in fact the $\mathbf{b}^{m+1}$ in (6) is unknown. Once we get $\mathbf{b}^{m+1}$, the Dirichlet boundary data of any points on $\partial\Omega_2$ can be approximated by (6). By then, we can also get approximate value of u^{m+1} at any node in Ω. It is obvious that the key to the question is how to determine $\mathbf{b}^{m+1}$**.**

We formulate the linear system of equations by fitting the given data set $\{\mathbf{x}_i^*\}_{i=1}^{nk}$ in domain Ω with the imposed conditions (5). Owing to the ill-posedness of original problem, we apply Tikhonov regulation technique with L-curve method [3] to solve the linear system to get $\mathbf{b}^{m+1}$.

3. RESULTS

To validate the efficacy of the proposed method, we choose CS-RBF $(1-r/\alpha)_+^6(35(r/\alpha)^2+18r/\alpha+3)$ in this example. The relative error and the root-mean-square-error (RMSE) defined by the following formula used in this section to demonstrate the accuracy of the solutions:

$$E_r(\mathbf{u}) = \frac{\|\mathbf{u}-\hat{\mathbf{u}}\|}{\|\mathbf{u}\|} \qquad \text{and} \qquad RMSE = \sqrt{\frac{1}{N}\sum_{j=1}^{N}(\hat{u}(\mathbf{x}_j)-u(\mathbf{x}_j))^2}$$

where $\mathbf{u} = (u_1\ u_2 \mathrm{L}\ u_N)^T$ and $\hat{\mathbf{u}} = (\hat{u}_1\ \hat{u}_2 \mathrm{L}\ \hat{u}_N)^T$ denote respectively, the numerical solution and the analytical solution at these points. We use noisy data $g_i = g_i + \sigma \cdot rand(i)$ and $q_i = q_i + \sigma \cdot rand(i)$, where g_i and q_i are the exact data of g and q at point $\mathbf{x}_i$. $rand(i)$ is a random number between [-1, 1].

In this example, the exact solution of problem (1)-(5) is shown as follow:

$$u(x, y, t) = x^2 + y^2 + e^{-t}\sin(x) + e^{-t}\cos(y) + 4t, \quad (x, y) \in \Omega \cup \partial\Omega, \quad \mathbf{0} \le t \le 1.$$

We consider a domain with curved boundaries as shown in Figure 1. $\partial\Omega_2$ is on lower half part of the whole boundary. There are $nk = 13$ sensors fixed in the domain as shown in Figure 1. Let d in (6) equal to 4, time step size $\tau = 0.1$.

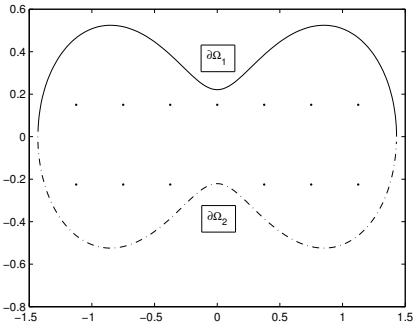

FIGURE 1. Peanut domain boundaries. The nodes inside the domain are for over-specified conditions. $\partial\Omega_2$ is represented by dotted line.

We choose $ni = 5674$ uniformly distributed interpolation points inside the domain and $nb1 + nb2 = 300$ ($nb2 = 150$) points on boundaries. Let $\alpha = 0.35$, so the sparsity of matrix is 87.6%. The relative error and RMSE at every time $t = (m+1)\tau$ ($m = 0, \mathrm{L}\ , 9$) are list in Table 1. Figure 2 shows the approximate temperature and exact temperature on $\partial\Omega_2$ at $t = 0.4$.

t	E_r on $\partial\Omega_2$	RMSE on $\partial\Omega_2$	E_r in Ω	RMSE in Ω
0.1	3.15E − 02	7.68E − 02	1.24E − 02	2.72E − 02
0.2	2.22E − 02	6.03E − 02	7.7E − 03	1.89E − 02
0.3	2.87E − 02	8.66E − 02	9.5E − 03	2.63E − 02
0.4	1.61E − 02	5.38E − 02	5.2E − 03	1.61E − 02
0.5	1.78E − 02	6.50E − 02	7.1E − 03	2.41E − 02
0.6	1.73E − 02	6.91E − 02	6.5E − 03	2.43E − 02
0.7	1.52E − 02	6.58E − 02	5.5E − 03	2.23E − 02
0.8	1.97E − 02	9.22E − 02	6.5E − 03	2.88E − 02
0.9	1.41E − 02	7.11E − 02	4.9E − 03	2.32E − 02
1	2.06E − 02	1.10E − 01	7.5E − 03	3.87E − 02

TABLE 1. Relative error and RMSE with $g_i = g_i + \sigma \cdot rand(i)$, $q_i = q_i + \sigma \cdot rand(i)$, $\sigma = 0.1$.

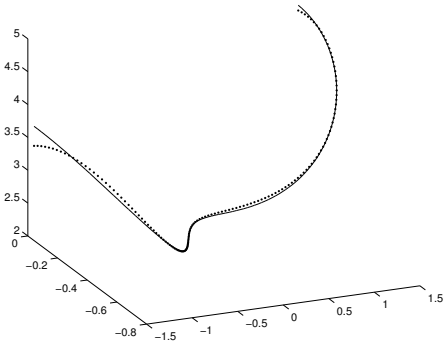

FIGURE 2. Numerical (dots) and exact (curve) temperatures on $\partial\Omega_2$ at $t = 0.4$.

$\tilde{g}_i = g_i + \sigma \cdot rand(i)$, $\tilde{q}_i = q_i + \sigma \cdot rand(i)$, $\sigma = 0.1$.

4. CONCLUSIONS

We present a local meshless algorithm based on CS-RBFs. This algorithm is used to solve a kind of IHCP with certain sensors in the domain. The numerical results show that the method is effective and stable. In solving IHCP, the iteration process did not give rise to increase of error. This method can easily be used to solve problems in curved boundary domain. However, it is difficult for FEM and FDM.

REFERENCES

[1] C. S. Chen, C. A. Brebbia, H. Power, Dual reciprocity method using compactly supported radial basis functions, *Commun. Numer. Meth. Engng*, 15, 137–150, 1999.

[2] C. S. Chen, G. Kuhn, J. Li and G. MishurisRadial basis functions for solving near singular Poisson problems, *Commun. Numer. Meth. Engng*, 19, 333–347, 2003.

[3] Lawson CL, Hanson RJ. Solving least squares problems. *Prentice-Hall*, 1974.

Third International Conference on Computational Methods for Thermal Problems
THERMACOMP2014, June 2-4, 2014, Lake Bled, Slovenia
N. Massarotti, P. Nithiarasu and B. Sarler (Eds.)

Fast Matrix Decomposition Method for Solving Poisson Problems

XiaoYan Liu
School of Mathematics, Taiyuan University of Technology, China, lucyyanxiao@163.com

Wen Li

School of Mathematics, Taiyuan University of Technology, China, muziwen02@163.com

C. S. Chen
Department of Mathematics, University of Southern Mississippi, Hattiesburg, MS 39406, USA, cschen.math@gmail.com

ABSTRACT

In this paper, we propose a fast evaluation using radial basis functions and the idea of circulant matrix to efficiently solve Poisson problems. The circulant matrix formulation and the matrix decomposition method are the central ideas of fast computation. The method of particular solutions is introduced to turn the function interpolation problems into solving partial differential equations.

Key Words: *circulant matrix, matrix decomposition, method of particular solution.*

1. INTRODUCTION

One of the current trends in scientific computing is the development of algorithms for fast computation. In radial basis functions (RBFs), various kinds of fast numerical algorithms for data fitting have been well-developed. Extending these newly-developed, fast algorithms for science and engineering problems, which involve solving PDEs, is important. Using the method of particular solutions (MPS) [4] and the method of fundamental solutions (MFS) [1], there is a strong connection between the surface interpolation and solving PDEs. In this paper, we extend the work of fast algorithm of RBF interpolation using circulant matrix [2], coupled with the MFS-MPS, to solve Poisson problems. The new approach makes it possible to solve large-scale problems efficiently.

2. RBF CENTERS ON CONCENTRIC CIRCLES

We will briefly review the efficient algorithm used in approximating a given function through the use of RBFs and circulant matrix. For more details, we refer the reader to Reference [2].

For efficiently approximate a given function *f*, we cover its domain with the concentric circles of RBF centres $\left\{\left(x_{i,j}, y_{i,j}\right)\right\}_{i=1,j=1}^{m,n}$ where m denotes the number of circles and n the number of points on each circle. The total number of interpolation points is N = *m*×*n*. The collocation equations of RBFs yield a system of the form

$$A_{\varphi} a = b \tag{1}$$

Where $\{a\}$ are the undetermined coefficients, $b = \left\{ f\left(x_{i,j}, y_{i,j}\right)\right\}_{i=1,j=1}^{m,n}$, the *mn*×*mn* matrix A_{φ} has the structure $A_{\varphi} = \left[A_{ij} \right]_{1\le i,j\le m}$ and each n×n submatrix $A_{i,j}$ is circulant. Coupling with Fast Fourier Transform (FFT), a fast algorithm of computing RBF coefficient *a* in (1) can be achieved. Since

$A_{i,j}$ are circulant, they can be diagonalized in the following way: $A_{i,j}$ = U*DU where D = diag(d_1,...,d_n) with $d_j = \sum_{k=1}^{n} c_k \omega^{(k-1)(j-1)}$ and U is the Fourier matrix wich is the conjugate of the matrix

$$U^* = \frac{1}{\sqrt{n}} \begin{bmatrix} 1 & 1 & 1 & \cdots & 1 \\ 1 & \omega & \omega^2 & \cdots & \omega^{(n-1)} \\ 1 & \omega^2 & \omega^4 & \cdots & \omega^{2(n-1)} \\ \vdots & \vdots & \vdots & \ddots & \vdots \\ 1 & \omega^{n-1} & \omega^{2(n-1)} & \cdots & \omega^{(n-1)(n-1)} \end{bmatrix} \tag{2}$$

Where $\omega = e^{2\pi i/n}$. Hence, A can be decomposed as

$$A = \begin{bmatrix} U^* & 0 & \cdots & 0 \\ 0 & U^* & \cdots & 0 \\ \vdots & \vdots & \ddots & \vdots \\ 0 & 0 & \cdots & U^* \end{bmatrix} \begin{bmatrix} D_{11} & D_{12} & \cdots & D_{1m} \\ D_{21} & D_{22} & \cdots & D_{2m} \\ \vdots & \vdots & \ddots & \vdots \\ D_{m1} & D_{m2} & \cdots & D_{mm} \end{bmatrix} \begin{bmatrix} U & 0 & \cdots & 0 \\ 0 & U & \cdots & 0 \\ \vdots & \vdots & \ddots & \vdots \\ 0 & 0 & \cdots & U \end{bmatrix} \tag{3}$$

where $A_{ij} = U^* D_{ij} U$ for $1 \le i, j \le m$.

Let I_m be a m×m identity matrix, and let ⊗ define the tensor product operations of two matrices. The undetermined coefficients *a* in (1) can be obtained in the following way:

1. Compute $\hat{f} = (I_m \otimes U) f$.
2. Compute diagonal elements of submatrices D.
3. Transform D to block diagonal matrix with approximate minimum degree (and) permutation).
4. Solve m linear systems of order n to computer $\hat{a}$.
5. Compute $a = (I_m \otimes U)\hat{a}$.

The efficient MATLAB code (diskBRF.m) of above algorithm can be found in Reference [3].

2 THE MFS FOR POISSON's EQUATION

Consider the following Poisson's equation

$$\begin{aligned} \Delta u &= f(x, y), && (x, y) \in \Omega, \\ Bu &= g(x), && (x, y) \in \partial\Omega, \end{aligned} \tag{4}$$

where *B* is the boundary operator, *h* and *g* are known functions, and Ω and ∂Ω are domain and its boundary respectively. The solution in (4) can be splitted into two parts $u = u_h + u_p$ where u_p is a particular solution satisfying the governing equation

$$\Delta u_p = f(x, y) \tag{5}$$

without satisfying the boundary conditions. The homogeneous solution u_h satisfies

$$\begin{aligned} \Delta u_h &= 0, && (x, y) \in \Omega, \\ Bu_h &= g(x, y) - Bu_p, && (x, y) \in \partial\Omega, \end{aligned} \tag{6}$$

which can be solved by the method of fundamental solutions (MFS). We refer the reader to Reference [1] for further details for the MFS.

Obtaining the particular solution u_p in (5) is the subject of intensive research. Let $\{(x_i, y_i)\}_{i=1}^{N}$ be distinct points on $\Omega \cup \partial\Omega$. In the context of RBFs, the main step in obtaining particular solutions is to approximate the forcing term f(x, y) in (5) by a series of RBFs

$$f(x,y) \approx \hat{f}(x,y) = \sum_{i=1}^{N} a_i \phi\left(\| (x,y) - (x_i, y_i) \|\right) \tag{7}$$

where ||.|| is the Euclidean norm and $\{a_i\}$ are the coefficients to be determined. By RBF collocation method, we have

$$\boldsymbol{A}\boldsymbol{a} = \boldsymbol{b} \tag{8}$$

where $A_{i,j} = \left[\phi\left(\| (x_i, y_i) - (x_j, y_j) \|\right)\right]_{1 \le i,j \le N}$, $\boldsymbol{b} = [f(x_1, y_1), ..., f(x_N, y_N)]^T, \boldsymbol{a} = [a_1, ..., a_N]^T$. Once $\{a_i\}$ is obtained, f in (7) can be established. It follows that an approximate particular solution $\hat{u}_p$ to (5) is given by [4]

$$\hat{u}_p(x,y) = \sum_{i=1}^{N} a_i \Phi_j(r) \tag{9}$$

where $\Delta\Phi = \phi$. In this paper we choose Inverse MQ ($1/\sqrt{1+(\varepsilon r)^2}$) as the basis function. From [5], Φ can be obtained analytically which is

$$\Phi(r) = \frac{1}{\varepsilon^2}\left(\sqrt{1+(\varepsilon r)^2} - \log(1+\sqrt{1+(\varepsilon r)^2}\right). \tag{10}$$

Using the concept of circulant matrix as shown in the previous section, $\{a_i\}$ in (7) can be obtained efficiently. This means $\hat{u}_p$ in (9) can also be evaluated efficiently.

4. NUMERICAL RESULTS

We consider the following problem

$$\Delta u = 2e^{x+y}, \quad (x,y) \in \Omega,$$
$$u = e^{x+y}, \quad (x,y) \in \partial\Omega,$$

where Ω is cardioid as shown in Fig. 1 . The analytical solution is given by $u(x,y) = e^{x+y}$.

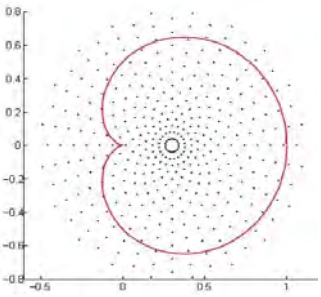

FIGURE 1. Circular interpolation points and the cardioid domain.

For the evaluation of the particular solution, we choose the number of RBF centres to be m × n where m and n represent the number of concentric circles and the number of interpolation points on each circle respectively. For the evaluation of homogeneous solution, we apply the MFS by using 100 boundary collocation points and the same number of source points. The number of random test points is 270. In Table 1, we show the results of absolute maximum error and the optimal shape parameter ∂. We observe the excellent stability and convergence of the proposed approach. Furthermore, we are able to employ 250,000 (m = n = 500) RBF interpolation circular points without any problem. In this case, the CPU time is only 76 seconds which is very fast. This is a significant step for solving large-scale problems.

m = n	Maxerror	∂
100	9.71E-9	1.177
150	1.71E-9	2.740
200	4.53E-7	6.363
320	1.06E-6	22.00
500	5.79E-6	75.99

TABLE 1. Absolute maximum error and shape parameter ∂ for various number of RBF centres.

5. CONCLUSIONS

We propose a fast algorithm to evaluate the particular solution of Poisson's equation using radial basis functions and circulant matrix. For efficiency, the concept of matrix decomposition has been introduced by uniformly distributing the interpolation points in circular form. The proposed approach allows can be extended to solving other elliptic partial differential equations and large-scaled problems.

REFERENCES

[1] G. Fairweather, A. Karageorghis, the method of fundamental solutions for elliptic boundary value problems, Adv. Comput. Math., 9, 69-95, 1998.

[2] A. Karageorghis, C.S. Chen, and Y-S Smyrlis. A matrix decomposition method for solving large scale problems using radial basis functions - approximation of functions and their derivatives. Applied Numerical Mathematics, 57:304–319, 2007.

[3] Alfa R.H. Heryudono and Tobin A. Driscoll. Radial basis function Interpolation on Irregular Domain through Conformal Transplantation. J Sci Comput, 44:286–300, 2010.

[4] A.S. Muleshkov, M.A. Golberg, and C.S. Chen, Particular solutions of Helmholtz-type operators using higher order polyharmonic splines, Comp. Mech, 23, 411-419, 1999.

[5] G. Yao, *Local Radial Basis Function Methods for Solving Partial Differential Equations*, Ph.D. thesis, The University of Southern Mississippi, 2010.

Third International Conference on Computational Methods for Thermal Problems
THERMACOMP2014, June 2-4, 2014, Lake Bled, Slovenia
N. Massarotti, P. Nithiarasu and B. Sarler (Eds.)

A collocation meshless method for linear thermoelasticity in 2D

Boštjan Mavrič
Institute of Metals and Technology, Lepi pot 11, 1000 Ljubljana, Slovenia, bostjan.mavric@imt.si

Božidar Šarler
Institute of Metals and Technology, Lepi pot 11, 1000 Ljubljana, Slovenia, bozidar.sarler@imt.si
University of Nova Gorica, Vipavska 13, 5000 Nova Gorica, Slovenia,
bozidar.sarler@ung.si

ABSTRACT

Multiquadrics based local radial basis function collocation method (LRBFCM) is applied to solve thermoelasticity problem. The convergence rate of the method is estimated for various numbers of collocation points and different values of the shape parameter. The convergence rate is found to be of the second order for 6 and 10 nodes in subdomain and of fourth order for 15 and 21 nodes. The dependence of error on the number of discretization points and on the value of the shape parameter is calculated. It is shown that the performance is limited by the condition number of local collocation matrices.

Key Words: *Thermoelasticity, Radial Basis Functions, Meshless Method, Collocation*

1. INTRODUCTION

The finite element method (FEM) has become de facto standard for solving solid mechanics problems, but in recent years some alternative approaches are being proposed, such as different versions of meshless method [1], that try to remove the need for computationally expensive polygonization needed for FEM. The radial basis functions (RBF) based meshless methods for the strong formulation of solid mechanics have already been implemented by several authors [2, 3, 4], resulting in studies exploring optimal value of shape parameters, local subdomain configuration and stability analysis. The results of the studies indicate that such approach is viable and could result in a stable, flexible numerical method.

The method is in present work implemented for thermoelastic problem with the number of discretization points high enough to demonstrate the industrial applicability of the method. The convergence rate is assessed for various numbers of subdomain nodes and different shape parameters.

2. PHYSICAL MODEL

Consider a thermoelastic problem in domain Ω with boundary Γ. The problem is given by the equilibrium equation written in terms of the displacement field $\vec{u}$

$$G\nabla^2\vec{u}+(\lambda+G)\vec{\nabla}\vec{\nabla}\cdot\vec{u}=\vec{\nabla}\left(\beta(T-T_{ref})\right),\ \beta=E\alpha/(1-2\nu). \tag{1}$$

Here λ and G are the Lame parameters, E Young modulus, ν Poisson ratio and α the coefficient of volumetric expansion. The temperature field is denoted with T and T_{ref} is the reference temperature at which the thermal expansion is zero. We seek the solution for a combination of Dirichlet (deformation) and Neumann (symmetry) boundary conditions as shown in Figure 1.

3. SOLUTION PROCEDURE

The equilibrium equation is solved by the LRBFCM. Firstly a node arrangement is constructed that describes the computational domain. To each node a subdomain consisting of ${}_lN$ neighbouring nodes is assigned. Let us describe the subdomain of a node with index l as the set of neighbouring nodes indices Ω_l. The choice of the subdomain induces the mapping ${}_ls$ from the subdomain index $i \in 1,...,{}_lN$ to the global index $l \in 1,...,N$, where N is the number of the nodes used for discretization. Once appropriate subdomains have been formed, the solution can be approximated by the RBF collocation for point $\vec{r} = (x, y)$ in the subdomain centred on the node l. In the following equations the Greek letters ξ, ζ, χ take the values of Cartesian coordinates (x, y). In this work we use the multiquadrics RBF centred at point $\vec{r}_i$ with the shape parameter c

$$\Phi_i(\vec{r}) = \sqrt{\sum_{\xi}\left(r_\xi - r_{i,\xi}\right)^2 + c^2} \ .$$

To further improve the approximation, the basis is augmented by m monomials $p_i(\vec{r})$. The approximation of displacement on the subdomain l is therefore given by

$$u_\xi(\vec{r}) \approx \sum_{i=1}^{{}_lN} {}_l\alpha_{i,\xi}\Phi_{s(i)}(\vec{r}) + \sum_{i={}_lN+1}^{{}_lN+m} {}_l\alpha_{i,\xi}p_i(\vec{r}) = \sum_{i=1}^{{}_lN+m} {}_l\alpha_{i,\xi}\psi_i(\vec{r}) \ . \tag{2}$$

The coefficients ${}_l\alpha_{i,\mu}$ are determined by collocation of the solution values at each subdomain node. In case a point in a node subdomain lies on the boundary, collocation is replaced by the equation specifying boundary conditions. To account for additional degrees of freedom introduced by the monomials, m augmentation equations must also be included. Let us write the boundary conditions at node j as $B^j_{\xi\zeta}u_\zeta(\vec{r}_j) = b^j_\xi$, where $B^j_{\xi\zeta}$ is the operator specifying boundary conditions. The equations determining ${}_l\alpha_{i,\xi}$ can be written in matrix form

$$\sum_{i,\zeta} {}_lA_{ji,\xi\zeta}\,{}_l\alpha_{i,\zeta} = {}_l\gamma_{j,\xi} \ , \tag{3}$$

with the size $2({}_lN+m)\times 2({}_lN+m)$ of the collocation matrix ${}_lA$. The matrix elements ${}_lA_{ji,\xi\zeta}$ are given by $\Upsilon^D_{{}_ls(j),\xi}\psi_i(\vec{r}_{s(j)})\delta_{\xi\zeta} + \Upsilon^\Gamma_{{}_ls(j),\xi}\sum_\zeta B^{{}_ls(j)}_{\xi\zeta}\psi_i(\vec{r}_{{}_ls(j)})$ if $1 \le j \le n$ and $p_j(\vec{r}_i)\delta_{\xi\zeta}$ otherwise. We have introduced boundary ($\Upsilon^\Gamma_{j,\xi}$) and domain ($\Upsilon^D_{j,\xi}$) indicators, which evaluate to 1 if j-th node lies on the boundary (in the domain) and to 0 otherwise. The element ${}_l\gamma_{j,\xi}$ of the vector γ is given by $\Upsilon^D_{{}_ls(j),\xi}u_{{}_ls(j),\xi} + \Upsilon^\Gamma_{{}_ls(j),\xi}b_{{}_ls(j),\xi}$ if $1 \le j \le n$ and is zero otherwise.

Equation (1) can be written in short form as $D_{\xi\zeta}u_\zeta = g_\xi$. The discretization is performed by using the RBF approximation (2) and subsequent expression of coefficients ${}_l\alpha_{i,\xi}$ in terms of unknown displacement values, achieved by inverting the collocation matrix (3). The terms stemming from augmentation equations vanish by definition. The following sparse system of linear equations with dimension $2N\times 2N$ is obtained for displacement at each node l and direction μ

$$\sum_{k,\kappa} \Upsilon^{D}_{l s(k),\chi} u_{l s(k),\chi} \sum_{i,\zeta} {}_{l}A^{-1}_{ik,\zeta\chi} D_{\xi\zeta} \psi_i(\vec{r}_l) = g_{l,\chi} - \sum_{k,\chi} \Upsilon^{\Gamma}_{l s(k),\chi} b_{l s(k),\chi} \sum_{i,\zeta} {}_{l}A^{-1}_{ik,\zeta\chi} D_{\xi\zeta} \psi_i(\vec{r}_l) \,. \qquad (4)$$

Here index k runs over elements in set Ω_l, while the index i is the local index running over basis functions in RBF expansion (2).

Related double precision Fortran computer code incorporates the Intel MKL implementation of PARDISO solver for solving the differential equation given by (1). The solution of the linear system (3) is performed by the LU decomposition.

5. NUMERICAL TESTS

The method is tested on a 2D domain with boundary conditions shown in Figure 1. The temperature profile is given by $T(\vec{r}) = \sin 2\pi x$. The analytical solution $\hat{\vec{u}}(\vec{r})$ only has non-zero component in x-direction $\hat{u}_x(\vec{r}) = -\alpha(1+\nu)(\cos 2\pi x - 1)/(2\pi(1-\nu))$. The error measure ϵ is calculated by

$$\epsilon = \sqrt{\sum_l \left(\vec{u}_l - \hat{\vec{u}}(\vec{r}_l)\right)^2 / \sum_l \hat{\vec{u}}(\vec{r}_l)^2} \,.$$

The number of subdomain nodes was chosen such that the number of free parameters in collocation problem equals the number of monomials up to a certain order. The number of all monomials up to second order is 6, up to third order 10, up to fourth order 16 and up to fifth order 21.

The dependence of the error on the number of discretization points is shown in Figure 2. We can see that the convergence is of the second order if 6 or 10 nodes are chosen to be in each subdomain and of the fourth order if subdomains consist of 16 or 21 nodes. The errors for the two larger subdomain node counts in each pair are an order of magnitude larger, but the convergence rate stays the same. The performance of the method critically depends on the choice of c. The dependence of the error on c and N is shown in Figure 4. We can see that the optimal value of c depends on the number of discretization points. To obtain the convergence rates shown in Figure 2 we have chosen the best performing c value for the densest node arrangement. The accuracy of multiquadrics collocation is limited by the numerically ill-conditioned calculation of the collocation matrix inverse [5]. This is evident from Figure 4, where the red line, which is the isoline at condition number value of 10^{16}, accurately describes the shape parameter values where the method accuracy starts to deteriorate. Similar behaviour can be observed in Figure 3. We can see that with the

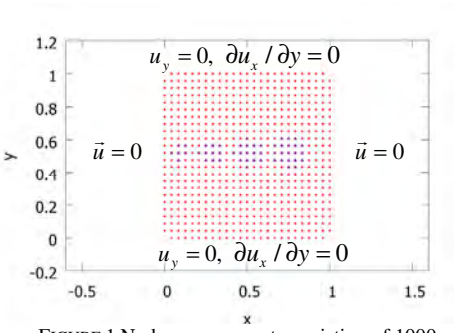

FIGURE 1 Node arrangement consisting of 1000 nodes with indicated boundary conditions. The triangles show examples of 6, 10, 15 and 21 noded subdomains.

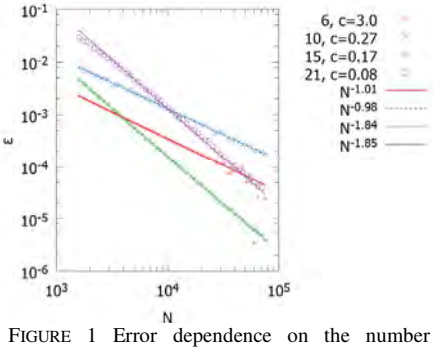

FIGURE 1 Error dependence on the number of discretization points for different numbers of subdomain nodes. The second order convergence can be observed for 6 and 10 nodes in each subdomain and fourth order for 16 and 21 subdomain nodes.

increasing number of subdomain nodes the critical c value, at which the convergence stops, decreases. The cause of this is the fact that the condition number of the collocation matrix increases with increasing the number of the subdomain nodes. This may also explain the order of magnitude difference in accuracy observed in Figure 2. For methods that use larger number of subdomain nodes, the ill-conditioning of the collocation matrix destroys the convergence at smaller values of c. Since the use of smaller c worsens the approximation, such methods show a larger error.

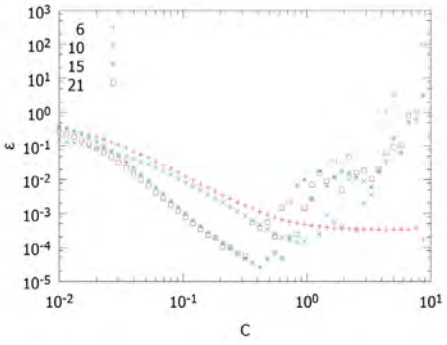

FIGURE 3 Error dependence on the shape parameter for node arrangement with 10 000 nodes.

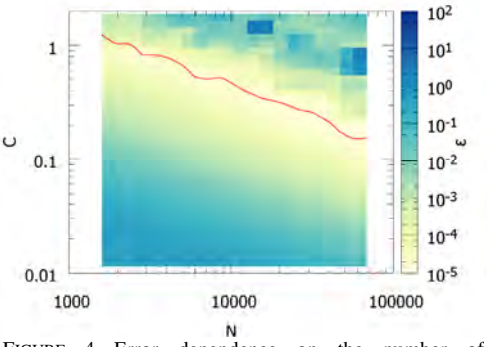

FIGURE 4 Error dependence on the number of discretization points and the value of the shape parameter. The line shows the limit where the condition number of the collocation matrix reaches 10^{16}.

6. CONCLUSIONS

The performance of the LRBFCM method applied to thermoelasticity has been assessed. The convergence rate depends on the number of nodes in each subdomain. It is of the second order in case of 6 and 10 nodes and of fourth order in case of 15 and 21. The performance of the method also depends on the choice of the shape parameter. Accuracy of the method improves with increasing shape parameter as long as the condition number of collocation matrix is small enough. The method appears to be well suited for solutions of thermoelasticity problems.

REFERENCES

[1] G. R. Liu, Mesh Free Methods, CRC Press, 2003.

[2] A. I. Tolstykh and D. A. Shirobokov, On using radial basis functions in a "finite difference mode" with applications to elasticity problems, *Computational Mechanics,* 33(1), 68-79, 2003.

[3] D. Stevens, H. Power and K. Cliffe, A solution to linear elasticity using locally supported RBF collocation in a generalised finite-differrence mode, *Engineering Analysis with Boundary Elements,* 37, 32-41, 2013.

[4] S. Simonenko, V. Bayona and M. Kindelan, Optimal shape parameter for the solution of elastostatic problems with the RBF method, *Journal of Engineering Mathematics,* 85(1), 115-129, 2014.

[5] B. Fornberg, E. Lehto and C. Powell, Stable calculation of Gaussian-based RBF-FD stencils, *Computers and Mathematics with Applications,* 65, 627-637, 2013.

Third International Conference on Computational Methods for Thermal Problems
THERMACOMP2014, June 2-4, 2014, Lake Bled, Slovenia
N. Massarotti, P. Nithiarasu and B. Sarler (Eds.)

SIMULATION OF MACROSEGREGATION INFLUENCED BY MAGNETIC FIELD IN CONTINUOUS CASTING OF STEEL

Katarina Mramor
CO BIK, Tovarniška 26, 5270 Ajdovščina, Slovenia, katarina.mramor@cobik.si

Robert Vertnik
Štore Steel, d.o.o., Železarska 3, 3220 Štore, Slovenia, robert.vertnik@store-steel.si

Božidar Šarler
Institute of Metals and Technology, Lepi pot 11, 1000 Ljubljana, Slovenia, bozidar.sarler@imt.si
University of Nova Gorica, Vipavska 13, 5000 Nova Gorica, Slovenia, bozidar.sarler@ung.si

ABSTRACT

Solution of the transport phenomena in continuous casting of steel, influenced by of a predetermined external magnetic field, typical for electromagnetic flow breaking, is presented. The governing equations stand for a two-dimensional binary (0.8 wt% C) incompressible turbulent solidifying flow. The coupled set of mass, momentum, energy, species, turbulent kinetic energy and dissipation rate are solved by a novel meshless explicit Local Radial Basis Function Collocation Method (LRBFCM), structured with multiquadrics on five-nodded subdomains and non-uniform node arrangement. Abe-Kondoh-Nagano turbulence closure coefficients are used. The solid phase is assumed to move with the casting speed. The mushy zone is modelled with porous media assumption and the microsegregation model relies on the lever rule. The influence of the magnetic field on temperature, streamfunction, velocity components, and carbon concentration is represented.

Key Words: *Continuous casting of steel, Magnetohydrodynamics, Macrosegregation*

1. INTRODUCTION

Continuous casting of steel [1] is nowadays one of the most common processes in the production of semi-finished steel products. Although the process is very efficient it can be further optimised by the application of the external magnetic field. As the processes in the strand are very costly and hard, if not impossible to measure, the process parameters such as the strength and position of the magnetic field are modelled with the help of numerical methods. In the present paper, meshles LRBFCM is chosen to solve the two-dimensional governing equations of mass, momentum, energy, species concentration, turbulent kinetic energy and dissipation rate. The model is based on the benchmark test case for the continuous casting of steel [2], which considers turbulent flow with electromagnetic forces, macrosegregation and solidification, and our recent solution of natural convection subject to magnetic field [3].

2. GOVERNING EQUATIONS

The physical model is established on a set of conservation equations for mass, momentum, energy, species concentration, turbulent kinetic energy and dissipation rate listed below:

$$\nabla \cdot \mathbf{v} = 0, \tag{1}$$

$$\rho\frac{\partial \mathbf{v}}{\partial t}+\rho\nabla\cdot(\mathbf{vv})=-\nabla p+\nabla\cdot\left[(\mu_L+\mu_t)\left[\nabla\mathbf{v}+(\nabla\mathbf{v})^T\right]\right]-\frac{2}{3}\rho\nabla k-\frac{\mu_L(1-f_L)^2}{K_0 f_L^3}(\mathbf{v}-\mathbf{v}_S)$$
$$+\rho\mathbf{g}\left(\beta_T(T-T_{ref})+\beta_C(C-C_{ref})\right)+\mathbf{j}\times\mathbf{B}, \tag{2}$$

$$\rho\frac{\partial h}{\partial t}+\rho\nabla\cdot(\mathbf{v}h)=\nabla\cdot(\lambda\nabla T)+\rho\nabla\cdot\left(\mathbf{v}h-f_S\mathbf{v}_S h_S-f_L\mathbf{v}_L h_L\right)+\nabla\cdot\left(f_L\frac{\rho_L\nu_t}{\sigma_t}\nabla h_L\right), \tag{3}$$

$$\rho\frac{\partial C}{\partial t}+\rho\nabla\cdot(\mathbf{v}C)=\rho\nabla\cdot\left(f_S D_S\nabla C_S+f_L D_L\nabla C_L\right)+\nabla\cdot\left(\rho(\mathbf{v}-\mathbf{v}_S)(C-C_L)\right)+\nabla\cdot\left(\frac{f_L\mu_t}{\sigma_C}\nabla C_L\right), \tag{4}$$

$$\rho\frac{\partial k}{\partial t}+\rho\nabla\cdot(\mathbf{v}k)=\nabla\cdot\left[\left(\mu_L+\frac{\mu_t}{\sigma_k}\right)\nabla k\right]+P_k+G_k-\rho\varepsilon+\rho D-\mu_L\frac{(1-f_L)^2}{K_0 f_L^3}k, \tag{5}$$

$$\rho\frac{\partial \varepsilon}{\partial t}+\rho\nabla\cdot(\mathbf{v}\varepsilon)=\nabla\cdot\left[\left(\mu_L+\frac{\mu_t}{\sigma_\varepsilon}\right)\nabla\varepsilon\right]+\rho E-\mu_L\frac{(1-f_L)^2}{C f_L^3}\varepsilon+\left[c_{1\varepsilon}f_1\left(P_k+c_{3\varepsilon}G_k\right)-c_{2\varepsilon}f_2\rho\varepsilon\right]\frac{\varepsilon}{k}, \tag{6}$$

where $\mathbf{v}$, $\rho=\rho_L$, t, p, μ_t, μ_L, k, K_0, β_T, β_C, $\mathbf{g}$, T, T_{ref}, C, C_{ref}, h, λ, f_S, f_L, $\mathbf{v}_S$, $\mathbf{v}_L$, h_S, h_L, ν_t, ε, $\mathbf{j}$, $\mathbf{B}$, C_L, C_S, D_L, D_S, are velocity, density, time, pressure, turbulent viscosity, viscosity of liquid phase, turbulent kinetic energy, morphology constant, thermal expansion coefficient, solute expansion coefficient, gravitational acceleration, temperature, reference temperature, concentration, reference concentration, enthalpy, thermal conductivity, volume fraction of solid phase, volume fraction of liquid phase, solidus temperature, liquidus temperature, enthalpy of solid phase, enthalpy of liquid phase, turbulent kinetic viscosity, dissipation rate, current density, magnetic field, concentration of liquid phase, concentration of solid phase, diffusion constant of liquid phase and diffusion constant of solid phase. σ_t, σ_k, σ_ε, σ_C, $c_{1\varepsilon}$, f_1, $c_{2\varepsilon}$, and f_2, are closure coefficients. P_k, G_k, D, and E stand for the shear production of turbulent kinetic energy, generation of turbulence due to the buoyancy force, source term for turbulent kinetic energy and source term for dissipation rate. The solidification in the system is treated with the mixture continuum model and the Low-Reynolds-Number $k-\varepsilon$ turbulence model is used to account for the incompressible turbulent flow. The Abe-Kondoh-Nagano closure coefficients and damping functions are applied. The mushy zone is treated as a Darcy porous media and the Kozeny-Carman relation is used to determine the morphology constant. The lever rule is used to account for the microsegregation. The turbulence model details are found in [4].

3. SOLUTION PROCEDURE AND NUMERICAL METHOD

The solution of coupled mass, momentum, energy, turbulent kinetic energy and dissipation rate equations is obtained by explicit time-stepping and LRBFCM. The governing equations are solved with the Fractional Step Method (FSM) on a non-uniform, overlapping, five-nodded subdomains. At every time step the Lorentz force is calculated first and inserted into the intermediate velocity, which is calculated from Equation 2, without the pressure gradient. The Poisson's equation for pressure is then solved by using the sparse matrix. Next, the intermediate velocities are corrected by the calculated pressure gradient. After the solution of the velocity field, Equations 3-6 are solved. The temperature is then calculated from the enthalpy. Finally, the initial values are set to the calculated values and the solution is ready for the next step. The spatial discretization is done through collocation with radial basis functions (RBF) as

$$\theta({}_l\mathbf{p}_n)=\sum_{i=1}^{M}{}_l\psi_i({}_l\mathbf{p}_n)\,{}_l\gamma_i, \tag{7}$$

where M, ${}_l\gamma_i$, θ, and ${}_l\psi_i$ represent a number of shape functions, an expansion coefficient, an approximation function, and RBF shape functions, centred in points ${}_l\mathbf{p}_n$, respectively. Scaled multiquadrics RBFs are selected as trial functions

$$ {}_l\psi_i(\mathbf{p}) = \sqrt{{}_l r_i^2(\mathbf{p}) + c^2}, \qquad {}_l r_i(\mathbf{p}) = \sqrt{\left((x - x_i)/({}_l x_{i\max})\right)^2 + \left((y - y_i)/({}_l y_{i\max})\right)^2}, \tag{8} $$

where the distances in each direction are scaled by ${}_l x_{i\max}$, and ${}_l y_{i\max}$, and c stands for the shape parameter. By implementing the collocation condition ${}_l\theta({}_l\mathbf{p}_n) = \theta_{i(l,n)}$, a linear system of M equations is obtained and the coefficients ${}_l\gamma_i$ are computed by inverting Equation 7. The *j*-th derivatives, that appear in the governing equations, are obtained as

$$ \frac{\partial^j}{\partial \chi^j}\,{}_l\theta(\mathbf{p}) = \sum_{i=1}^{M} \frac{\partial^j}{\partial \chi^j}\,{}_l\psi_i(\mathbf{p})\,{}_l\gamma_i, \qquad \chi = x, y\ . \tag{10} $$

The detailed description of solution procedure can be found in [4].

4. RESULTS

A simplified straight geometry and material properties, suggested in [2], are used in the definition of present numerical example. They are as follows $\rho = 7200\,\mathrm{kg/m^3}$, $\lambda = 30\,\mathrm{W/(mK)}$, $c_p = 700$ J/(kgK), $T_S = 1680\,\mathrm{K}$, $T_L = 1760\,\mathrm{K}$, $h_m = 250000\,\mathrm{J/kg}$, $\mu = 0.006\,\mathrm{Pas}$, $\beta_T = 1\cdot10^{-4}\,\mathrm{1/K}$, $\beta_C = 4\cdot10^{-3}$, $\sigma = 5.9\cdot10^5\ \ 1/(\Omega\mathrm{m})$, $K_0 = 1.6\cdot10^8\,\mathrm{m^{-2}}$ and carbon concentration $C = 0.8\,\%$. The strand is 1.8 m long and 0.14 m wide, with mould reaching to 0.8 m. The magnetic field is generated in a two coil system, placed below the mould, 5 cm from the strand, with 25 x 11 windings and $I = 50$ A. As the calculation domain is symmetric, only half of the domain is used for calculations. The calculations were done on 73940 nodes. The results, presented in Figures 1 and 2, show the effects of the magnetic field on the temperature, velocity and concentration fields. Almost negligible effect on the solid shell is found. The hot region is pushed upwards as well as the stream function maximum. The flow is less intensive when magnetic field is applied. Magnetic field lowers the solid shell carbon concentration.

5. CONCLUSIONS

This paper presents the application of LRBFCM to the problem of macrosegregation in continuous casting of steel, influenced by external magnetic field. It is shown that the magnetic field affects the velocity and temperature fields as well as the concentration field and that the meshless LRBFCM can be used to solve this kind of highly nonlinear problems.

REFERENCES

[1] W. R. Irving, *Continuous Casting of Steel*, The Institute of Materials, London, 1993.

[2] B. Šarler, R. Vertnik and K. Mramor, A numerical benchmark test for continuous casting of steel, *IOP Conference Series: Materials Science and Engineering*, 33, page 012012, IOP Publishing. 2012.

[3] K. Mramor, R.Vertnik and B. Šarler, Simulation of natural convection influenced by magnetic field with explicit local radial basis function collocation method. *CMES: Computer Modeling in Engineering & Sciences*, 94, 327-52, 2013.

[4] R. Vertnik and B. Šarler, Solution of a continuous casting of steel benchmark test by a meshless method, *Engineering Analysis with Boundary Elements*. http://dx.doi.org/10.1016/j.enganabound.2014.01.017iK, 2014.

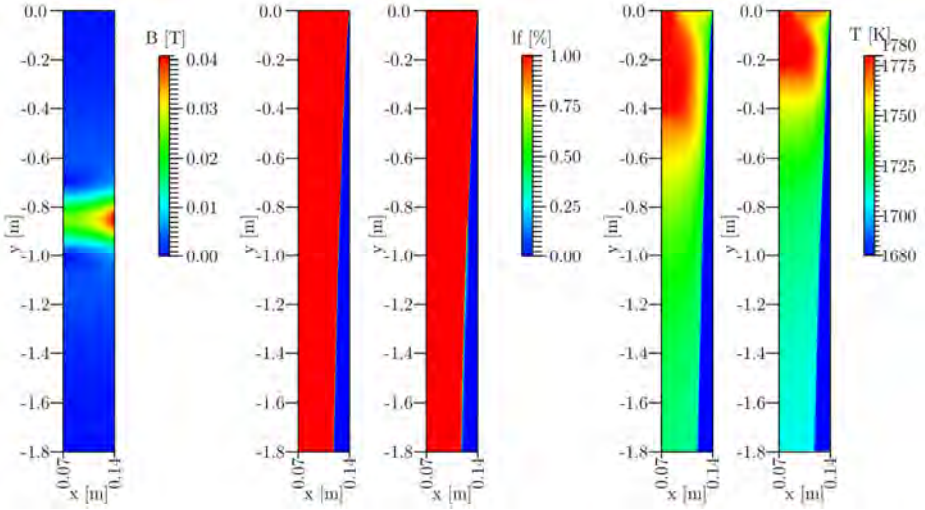

FIGURE 1. Left: magnetic field. Middle: Liquid fraction without/with magnetic field. Right: temperature field without/with magnetic field.

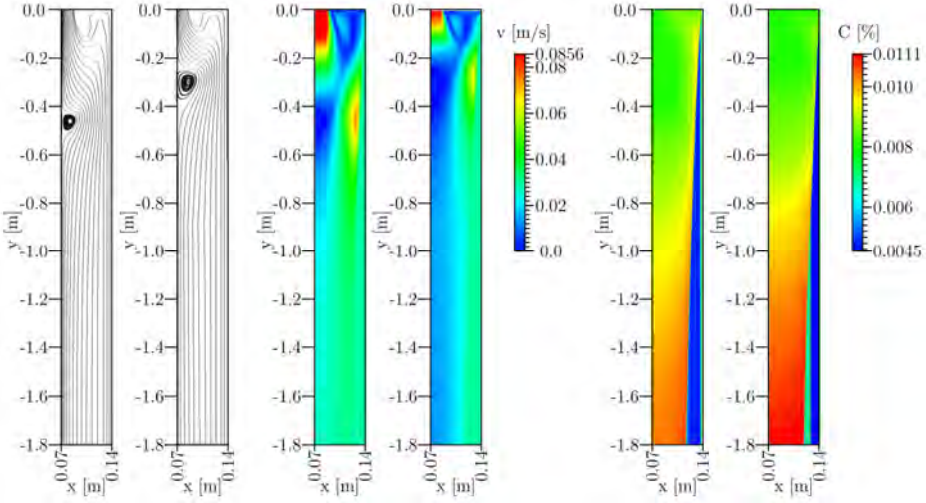

FIGURE 2. Left: Streamlines without/with magnetic field. Middle: Velocity field magnitude without/with magnetic field. Right: Concentration fields without/with magnetic field.

Third International Conference on Computational Methods for Thermal Problems
THERMACOMP2014, June 2-4, 2014, Lake Bled, Slovenia
N. Massarotti, P. Nithiarasu and B. Sarler (Eds.)

NON-SINGULAR METHOD OF FUNDAMENTAL SOLUTIONS FOR THREE DIMENSIONAL STOKES FLOW PROBLEMS

Eva Sincich
University of Nova Gorica, Vipavska 13, SI-5000 Nova Gorica, Slovenia, eva.sincich@ung.si

Božidar Šarler
University of Nova Gorica, Vipavska, 13, SI-5000 Nova Gorica, Slovenia & Institute of Metals and Technology, Lepi pot 11, SI-1000, Ljubljana, Slovenia, bozidar.sarler@ung.si

ABSTRACT

The aim of the present paper is to discuss a Non-Singular Method of Fundamental Solutions (NMFS) for three-dimensional (3D) Stokes flow problems subject to Dirichlet and traction boundary conditions. By following the pioneering approach of Oseen and Lamb is the 3D Stokes equation decomposed into four coupled Laplace problems for modified components of the velocity field and the pressure. The latter are sought in the form of a linear combination of approximation functions obtained by a desingularization procedure of the fundamental solution of the Laplace equation. The solution is subsequently achieved by collocating the pressure and the velocity field boundary condition. In contrary to the classical Method of Fundamental Solution (MFS), the NMFS requires no artificial boundary. Such a simple approach with its meshless character seems to be very suitable also for moving boundary and inverse problems.

Key Words: *Stokes problems, Laplacian decomposition, Non-singular Method of Fundamental Solution.*

1. INTRODUCTION

The underlying idea of the MFS [1] relies on the approximation of the solution of a partial differential equation by a linear combination of fundamental solutions, the expansion coefficients of which are evaluated from boundary conditions. In many situations it happens that the fundamental solution of the discussed partial differential equation has an inherent singularity at the source point, hence the necessity arises to place the source points outside the physical domain in order to be able to match the boundary conditions. Such a method has been already extensively employed for different fluid flow studies. Alves and Silvestre [2], Young et al. used the MFS method for computing the solution to 2D and 3D Stokes flows and Navier-Stokes flows [3]. The main advantage of the method with respect to other boundary methods is due to its simplicity and its meshless character. However, a drawback of this technique is in the fact that in presence of a singular fundamental solution, there is the need to locate the sources on a fictitious boundary outside the physical one in order to determine the expansion coefficients. The satisfactory location of such an artificial boundary is a delicate issue. In general, if the artificial boundary is too close to the physical one, then the accuracy of the problem is poor. On the other hand, if the fictitious boundary is too far, then the problem becomes ill-posed. In order to bridge such a gap, a quite novel approach, known as NMFS, has been recently discussed by Šarler for fluids [4], by Perne et al. for porous media flow with moving boundaries [5] and by Liu et al. for solid mechanics [6,7]. Their approach is based on the smoothing of the fundamental solution by performing an average analytical integration of the chosen singular solution over a ball centred on the source itself. In the present paper we employ the NMFS method for Stokes fluid problems by extending the two-dimensional (2D) Laplace decomposition approach proposed by Curteanu et al. in [8] to the 3D

case. Moreover, we adopt the analogous desingularization strategy introduced by Liu in [9]. First we provide a brief but comprehensive mathematical formulation of our method for both the two and the three dimensional situations. Second, we show the reliability of our technique by presenting a 2D numerical example for a mixed Dirichlet-traction boundary condition.

2. GOVERNING EQUATIONS

Let Ω be a connected domain in the d dimensional space with boundary Γ where $d = 2,3$. We consider Cartesian coordinate system with base vectors $\mathbf{i}_1,...,\mathbf{i}_d$ and coordinates $x_1,...,x_d$. The velocity field $\mathbf{q} = \sum_{k=1}^{d} v_k \mathbf{i}_k$ solves the following Stokes equation (1) and satisfies the incompressibility condition (2)

$$\mu \Delta \mathbf{q}(x_1,...,x_d) = \nabla P(x_1,...,x_d) \text{ in } \Omega, \quad \nabla \cdot \mathbf{q}(x_1,...,x_d) = 0 \text{ in } \Omega \tag{1,2}$$

with μ representing the viscosity and P the pressure. Adapting the argument developed in [8] we proved that (1,2) are equivalent to

$$\Delta f_k(x_1,...,x_d) = 0,\ k = 1,...,d, \quad \Delta P(x_1,...,x_d) = 0, \text{ in } \Omega, \quad \sum_{k=1}^{d} \partial_{x_k} v_k = 0 \text{ in } \partial\Omega \tag{3,4,5}$$

provided

$$\mu v_k(x_1,...,x_d) = f_k(x_1,...,x_d) + \frac{x_k}{2} P(x_1,...,x_d), \quad k = 1,...,d, \tag{6}$$

The boundary is divided in in two not necessarily connected parts $\Gamma = \Gamma_D \cup \Gamma_T$. On the part Γ_D Dirichlet boundary condition are given, while on the possibly empty part Γ_T, the fluid traction boundary condition are prescribed

$$v_k(\mathbf{p}) = v_{\Gamma k}(\mathbf{p});\ \mathbf{p} \in \Gamma_D, \quad k = 1,...,d, \left[\mu(\nabla \mathrm{v}(\mathbf{p}) + \nabla \mathrm{v}^{\mathrm{T}}(\mathbf{p})) - \mathrm{P}(\mathbf{p})\mathbf{I}\right] \cdot \mathbf{n} = \mathbf{t}(\mathbf{p});\ \mathbf{p} \in \Gamma_{\mathrm{T}} \tag{7,8}$$

where $\mathbf{n} = (n_1,...,n_d)$ is the outer unit normal to Γ.

3. SOLUTION PROCEDURE AND NUMERICAL EXAMPLE

The underlying arguments of the MFS and the NMFS methods rely on the representation of the $d+1$ harmonic function f_k, $k = 1,...,d$ and P introduced in (3,4) as a linear combination of N basis functions where the unknown coefficients are fixed by means of a collocation method with the boundary conditions. We chose the fundamental solution of the Laplace equation ϕ as basis functions for the MFS (9,11) and its desingularized version $\tilde{\phi}$ for the NMFS method (10,12)

$$\phi(\mathbf{p},\mathbf{s}) = \frac{1}{2\pi}\log(|\mathbf{p}-\mathbf{s}|^{-1}), \quad \tilde{\phi}(\mathbf{p},\mathbf{s}) = \begin{cases} \phi(\mathbf{p},\mathbf{s}); & |\mathbf{p}-\mathbf{s}| > \mathrm{R} \\ \frac{1}{2\pi}\log\left(\frac{1}{R}\right) + \frac{1}{4\pi} - \frac{|\mathbf{p}-\mathbf{s}|^2}{4\pi R^2}; & |\mathbf{p}-\mathbf{s}| \le \mathrm{R} \end{cases} \tag{9,10}$$

$$\phi(\mathbf{p},\mathbf{s}) = |\mathbf{p}-\mathbf{s}|^{-1}, \quad \tilde{\phi}(\mathbf{p},\mathbf{s}) = \begin{cases} \phi(\mathbf{p},\mathbf{s}); & |\mathbf{p}-\mathbf{s}| > \mathrm{R} \\ \frac{3}{2}\frac{1}{R} - \frac{1}{2}\frac{|\mathbf{p}-\mathbf{s}|^2}{R^3}; & |\mathbf{p}-\mathbf{s}| \le \mathrm{R} \end{cases} \tag{11,12}$$

when $d = 2,3$ respectively and where $\mathbf{p}$ are points on the physical boundary and $\mathbf{s}$ are source points located on a fictitious boundary in case of MFS, and the physical boundary in case of NMFS. We consider N source points $\mathbf{s}_j$, $j = 1,...,N$ and N collocation points $\mathbf{p}_i$, $i = 1,...,N$. We discretize the problem by the superposition

$$f_k(\mathbf{p}_i) = \sum_{j=1}^{N} \alpha^{k,j} \phi(\mathbf{p}_i, \mathbf{s}_j), \; k = 1,...,d, \quad P(\mathbf{p}_i) = \sum_{j=1}^{N} \alpha^{j} \phi(\mathbf{p}_i, \mathbf{s}_j) \tag{13,14}$$

where ϕ has to be replaced by $\tilde{\phi}$ when using the NMFS method. By inserting these special choices into (6), (5) and (7,8) we are able to translate our original problem (1,2,7,8) into the solution of a linear system of $(d+1)\cdot N$ equations $\mathbf{A}\mathbf{x} = \mathbf{b}$ where the $(d+1)\cdot N \times (d+1)\cdot N$ matrix $\mathbf{A}$ collects the information about the underlying partial differential equations and the considered boundary condition, the $(d+1)\cdot N \times 1$ vector $\mathbf{x}$ gather the unknown coefficients $\alpha^{k,j}$, $k = 1,...,d$ and α^{j}, $j = 1,...,N$ in (13,14) and the $(d+1)\cdot N \times 1$ vector $\mathbf{b}$ contains the Dirichlet and the traction data v_k and t_k, $k = 1,...,d$ appearing in (7,8). We solve the Stokes problem (1,2) in the rectangular domain $\Omega = (-2,2)\times(-0.5,0)$ and we consider the following analytical solution $v_1(p_1,p_2) = 24p_2{}^2 - 3$, $v_2(p_1,p_2) = 0$, $P(p_1,p_2) = 24p_1$. We impose traction boundary condition on $(-2,2)\times\{0\}$ and Dirichlet condition on the remaining portion of the boundary. Both are derived directly from the analytical solution. We employed 1728 equidistant boundary nodes both for the MFS and the NMFS method. We fixed the source points at a distance 5d from the physical boundary when dealing with the MFS method while we chose R in (10) equal to d/4 when dealing with the NMFS method where d represents the distance between two consecutive nodes. In Fig.1 the profile of v_1 at $p_1 = 0$ along the p_2 axis and the profile of v_2 at $p_2 = -0.25$ along the p_1 axis respectively are presented (-: analytical solution, +: MFS, o: NMFS).

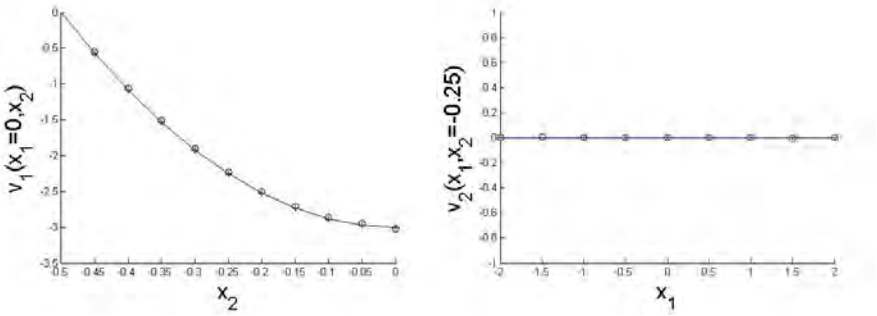

Fig.1 Profiles of v_1 at $p_1 = 0$ along p_2 axis and profiles of v_2 at $p_2 = -0.25$ along p_1 axis respectively.

4. CONCLUSIONS

In this paper we extended the formulation of the authors [10] in a two dimensional setting to to the three dimensional case where the Laplace decomposition technique is combined with the NMFS method for solving a simple Stokes problem.. We show the accuracy and the efficiency of our

method by providing a two dimensional numerical example for which a mixed Dirichlet-traction boundary condition applied on the domain boundary. Indeed it can be observed that the MFS and the NMFS solutions are in good agreement with the available analytical one. The three dimensional numerical examples will be the object of our future study and will be presented at the conference. The new approach, with its meshless feature, could be applied in the analysis of large scale problems in fluid mechanics such as realistic 3D biomedical or geophysical flows.

ACKNOWLEDGEMENT: This work was partially performed within the Creative Core program (AHA-MOMENT) contract no. 3330-13-500031, co-supported by RS-MIZS and European Regional Development Fund Research; project J2-4093 Development and application of advanced experimental and numerical methods in Karst processes, and program group P2-0379 Modelling and simulation of materials and processes, sponsored by Slovenian Grant Agency (ARRS).

REFERENCES

[1] C.S. Chen, A. Karageorghis, Y.S. Smyrlis, *The Method of Fundamental Solutions- A Meshless Method* , Dynamic publishers, Atlanta, 2008.

[2] C.J.S. Alves, A.L. Silvestre, Density results using Stokeslet and a method of fundamental solution for Stokes equation, *Engineering Analysis with Boundary Elements,* 28, 1348-61, 2004.

[3] D.L. Young, S.J. Jane, C.M. Fan, K. Murgesan, C.C. Tsai, The method of fundamental solutions for 2D and 3D stokes problems, *Journal of Computational Physics*, 211, 1-8, 2006.

[4] B. Šarler, Solution of potential flow problems by the modified method of fundamental solutions: Formulations with single layer and the double layer fundamental solution, E*ngineering Analysis with Boundary Elements*, 33, 1374-82, 2009.

[5] M.Perne, B. Šarler , F. Gabrovšek, Calculating transport of water from conduit to the porous matrix by boundary distributed source method, E*ngineering Analysis with Boundary Elements*, 36, 1649-59, 2012.

[6] Q. Liu, B. Šarler, Non singular method of fundamental solutions for two-dimensional isotropic elasticity, *Computer Modeling in Engineering and Sciences,* 91, 253-66, 2013.

[7] Q. Liu, B. Šarler, Non singular method of fundamental solutions for anisotropic elasticity, E*ngineering Analysis with Boundary Elements*, http://dx.doi.org/10.1016./j.enganbound.2014.01.020.

[8] A.E. Curteanu, L. Elliot, D.B. Ingham, D. Lesnic, Laplacian decomposition and the boundary element method for solving Stokes problems, *Engineering Analysis with Boundary Elements*, 31, 501-513, 2007.

[9] Y.L. Liu, A new boundary meshfree method with distributed sources, E*ngineering Analysis with Boundary Elements*, 34, 914-9, 2010.

[10] E. Sincich, B. Šarler, Non-singular method of fundamental solutions for biomedical Stokes flow problems*, CMBE Proceeding series in print (ISSN 2227-3085) format*.

Third International Conference on Computational Methods for Thermal Problems
THERMACOMP2014, June 2-4, 2014, Lake Bled, Slovenia
N. Massarotti, P. Nithiarasu and B. Sarler (Eds.)

ADAPTIVE FINITE INTERGRATION METHOD FOR SINGULAR PERTURBATION PROBLEMS WITH MULTIPLE BOUNDARY LAYERS

Zhi-Hua Wen, Ming Li
College of Mathematics, Taiyuan University of Technology, Taiyuan, China
tyfaith@163.com
Yiu-Chung Hon
Department of Mathematics, City University of Hong Kong, Hong Kong SAR, China
maychon@cityu.edu.hk

ABSTRACT

Based on the recently developed finite integration method for solving partial differential equations, we extend in this paper the advantages of the method in tackling singular perturbation problems with multiple boundary layers. Numerical results indicate that, even with the most simple numerical trapezoidal integration rule, the method provides very stable, efficient, and highly accurate solutions to the singular perturbation problems. Convergence error estimate of the method is derived. An adaptive refinement of integration points is also proposed for further improvement of the method in locating multiple boundary layers. Illustrative examples are given to compare with other existing numerical methods.

Key Words: *Finite Integration, Singular perturbation, Boundary layer*

1. INTRODUCTION

Singular perturbation problems arise in many physical modelling processes of fluid flows. Due to the stiffness and complexity of the boundary layers exerted by the singularly perturbed equations, it is very difficult to obtain exact solutions for these equations. The rapid advancement of computing technology allows the simulation of the boundary layers through seeking numerical approximate solutions to the mathematical models. During the last decades, these singular perturbation problems have been extensively studied by many researchers using various kinds of numerical methods among which the finite difference method (FDM) and finite element method (FEM) are mostly well established. Despite their many attractive features, the FDM and FEM are mesh-dependent in the sense that accurate approximation of the solution requires the generation of uniform grid/mesh in the discretization process. For problems defined in regular domain, the generation of these uniform meshes is usually not difficult. However, the uniform meshing usually does not work well. Recently, Hon [1] adopted a Multiquadric Collocation Method (MQCM), which is a kind of kernel-based approximation methods, to solve a singular perturbation problem with one boundary layer.

In this paper, we extend the recently developed Finite Integration Method (FIM) [2,3]for solving the singularly perturbed equations with multiple boundary layers. Unlike the finite difference method FDM which uses finite quotient formula, the FIM uses numerical quadratic integration rule and hence avoids the wellknown roundoff-discretization error problem in using FDM. In this paper we observe that, even with the most simple numerical trapezoidal integration formula, the FIM provides a very stable, efficient, and highly accurate solutions for solving these singular perturbation problems. Numerical comparisons with the Multiquadric Collocation Method MQCM and FDM with Shishkin grids show that the FIM achieves better accuracy at a lower computational usage.

2. MAIN BODY

Finite integration method with composite quadrature rule:

Define $U(x)$ to be the integration of an integrable function $u(x)$

$$U(x) = \int_0^x u(\xi) d\xi \tag{1}$$

and applying linear interpolation technique for integral function $f(x)$, we have

$$U(x_k) = \int_0^{x_k} u(\xi)\, d\xi = \sum_{i=1}^{k} a_{ki} u(x_i) \tag{2}$$

We can write integrations in a matrix form as

$$U^{(1)} = \mathbf{A}^{(1)} u \tag{3}$$

Applying the composite quadrature rule to the above integration at x_k gives:

$$U^{(m)}(x) = \int_0^x \ldots \int_0^{\zeta} u(\xi) d\xi \ldots d\zeta = \sum_{i=0}^{k} \ldots \sum_{j=0}^{i} a_{ki}^{(1)} \ldots a_{ij}^{(1)} u(x_i) = \sum_{i=0}^{k} a_{ki}^{(m)} u(x_i) \tag{4}$$

whose matrix form is given by

$$U^{(m)} = \mathbf{A}^{(m)} u = \mathbf{A}^m u \tag{5}$$

FIM for solving boundary layer problem

To demonstrate the advantage of the FIM for solving singular perturbation problems, we consider the following two-point boundary value problem (BVP):

$$\begin{aligned} &-\varepsilon u''(x) + p(x)u'(x) + q(x)u(x) = f(x) \qquad x \in (a,b) \\ &u(a) = \alpha \qquad u(b) = \beta \end{aligned} \tag{6}$$

We consider the following singular perturbation problem:

$$\begin{aligned} &\varepsilon u''(x) + u'(x) = 0 \qquad x \in (0,1) \\ &u(0) = 0 \qquad u(1) = 1 \end{aligned} \tag{7}$$

Applying the integration operation twice on both sides of equation (7), we have

$$\varepsilon u + Au = c_0 x + c_1 i$$
$$u_1 = 0 \qquad u_N = 1 \tag{8}$$

We then recompute the solution of the boundary layer problem (7) by using FIM on these Shishkin points and he numerical results are much improved. The result is compared with the solutions given by upwind central difference FDM and the Multiquadric Collocation Method (MQCM) in the recent paper of Hon [3] where the total number of points are chosen to be 40 and 160 respectively. The superior advantage of FIM over MQCM is further illustrate in Table 2, where the comparisons between MQCM and FIM is made under different number of points and accuracies.

	N = 40			N = 160		
ε	FDM	MQCM	FIM	FDM	MQCM	FIM
0.1	$1.89E-02$	$8.16E-05$	$2.87E-04$	$1.47E-03$	$1.86E-08$	$1.11E-05$
0.05	$3.48E-02$	$1.43E-04$	$2.90E-04$	$2.39E-03$	$7.08E-06$	$1.09E-05$
0.025	$6.48E-02$	$4.08E-03$	$2.90E-04$	$4.20E-03$	$7.31E-06$	$1.09E-05$
0.0125	$1.19E-01$	$1.29E-02$	$2.90E-04$	$7.78E-03$	$3.41E-05$	$1.09E-05$
0.00625	$2.11E-01$	$2.90E-02$	$2.90E-04$	$1.49E-02$	$1.07E-04$	$1.09E-05$
0.003125	$3.45E-01$	$5.91E-02$	$4.39E-04$	$2.88E-02$	$4.27E-04$	$1.09E-05$
0.0015625	$5.10E-01$	$8.13E-02$	$2.24E-03$	$5.54E-02$	$8.81E-04$	$1.09E-05$
0.00078125	$6.69E-01$	$1.38E-01$	$7.22E-03$	$1.04E-01$	$2.62E-03$	$1.09E-05$
0.000390625	$7.94E-01$	$3.12E-01$	$1.33E-02$	$1.89E-01$	$4.58E-03$	$1.12E-05$

Table 1: Comparison errors at point $x_{\frac{N}{2}}$ on Shishkin points

	MQCM			FIM		
N	50	100	150	100	200	300
Error at $x_{\frac{N}{2}}$	$1.32E-02$	$3.40E-03$	$6.66E-04$	$3.68E-03$	$9.71E-03$	$2.73E-06$
Time (s)	$4.76E-03$	$1.69E-02$	$3.74E-02$	$3.93E-03$	$8.37E-03$	$2.18E-02$

Table 2: Comparison between results by MQCM and FIM when $\varepsilon = 10^{-4}$

3. RESULTS

Numerical comparison results displayed in Table 1 indicate that the MQCM gives much better

approximation than the FDM for all different values of ε and slightly better than the FIM when ε is large. This is due to the spectral convergence of the MQCM. However, when ε is small, the FIM gives superior results than the MQCM because the MQCM suffers from the well known problems of ill-conditioning due to its full matrix and optimal choice of shape parameter.

The computations are implemented on Shishkin points when $\varepsilon = 10^{-4}$. It can be observed from Table 2 that the FIM require less CPU time than MQCM for the same accuracy. This verifies that FIM provide a stable, efficient and accurate approximationof solution of PDEs including these kinds of singularly perturbed problems.

Although the numerical results have shown to be much improved by using Shishkin points, the construction of these points requires a good priori knowledge on the location and width of the boundary layer, which in general are not known.

4. CONCLUSIONS

In this paper we apply the recently developed Finite Integration Method (FIM) with composite Trapezoidal rule to solve a singular perturbation problem with multiple boundary layers. An adaptive FIM (AFIM) is also devised to better approximate the solution without a priori knowledge on the location and width of the boundary layer. Numerical comparisons with the exact solution and several numerical methods (FDM, FEM, MQCM) are made and the numerical results verify that both the FIM and AFIM schemes offer a very stable, accurate, and efficient method for solving the singularly perturbed problems with boundary layers. The FIM is similar to the mesh-dependent FDM with the difference in approximating the solution and its derivatives by integration, whereas the FDM uses finite quotient formula. This completely eliminates the well-known optimal roundoff and discretization errors problem in using FDM. The use of higher quadrature rule will give a better convergent FIM scheme but the use of the simplest composite Trapezoidal rule in this paper already demonstrates its superior advantage over the traditional FDM and FEM. Furthermore, the use of radial basis functions (RBFs) in the FIM will result into a meshless computational method but then the resultant matrix will be full instead of lower triangular. The open problem in choosing optimal shape parameter in using the radial basis functions will still hinder the development of FIM(RBF) method. Our future work is to extend the FIM to solve higher dimensional problems.

REFERENCES

[1] Hon Y. C., *Multiquadric collocation method with adaptive technique for problems with boundary layer*, Internat. J. Appl. Sci. Comput. 1999;6 (3): 173-184.

[2] Li M., Hon Y. C., Korakianitis T., Wen P. H., *Finite integration method for nonlocal elastic bar under static and dynamic loads*, Engineering,Analysis with Boundary Elements. 2013; 37(5): 842-849.

[3] Wen P. H., Hon Y. C., Li M., Korakianitis T., *Finite integration method for partial differential equations*, Applied Mathematical Modelling, InPress.

MINI-SYMPOSIUM

MULTI-STREAM HEAT EXCHANGERS

MINI-SYMPOSIUM ORGANISED BY K.N. SEETHARAMU, V. KRISHNA, K.H. JYOTHIPRAKASH AND C. RANGANAYAKULU

Third International Conference on Computational Methods for Thermal Problems
THERMACOMP2014, June 2-4, 2014, Lake Bled, Slovenia
N. Massarotti, P. Nithiarasu and B. Sarler (Eds.)

STEADY STATE AND TRANSIENT ANALYSIS OF COMPACT PLATE-FIN HEAT EXCHANGER FINS FOR GENERATION OF DESIGN DATA USING CFD

Dr. C. Ranganayakulu
P.B. 1718, Vimanapura Post. Aeronautical Development Agency, Bangalore – 560017 India.
Email: chennu_r@rediffmail.com

ABSTRACT

Thermo-hydraulic performances of Compact Heat Exchangers is strongly depending upon the prediction of performance of various types of heat transfer surfaces such as Offset Strip fins, Wavy fins, Rectangular fins, Triangular fins, Triangular and Rectangular perforated fins in terms of Colburn '*j*' and Fanning friction '*f*' factors. A Computational Fluid Dynamics (CFD) program FLUENT has been used to predict the design data in terms of '*j*' & '*f*' factors for plate-fin heat exchanger fins. Also transient analysis has been carried out using CFD for generation of '*j*' factors for Offset fins for validation of single flow transient technique experimental data. The suitable design data is generated using CFD analysis covering the laminar, transition and turbulent flow regimes for various types of fins.

Key Words: *Heat Transfer, CFD, Compact Heat Exchanger fins, Colburn 'j' and friction 'f' factors.*

1. INTRODUCTION

Compact heat exchangers are widely used in aerospace, cryogenic and automobile industries due to its high compactness (i.e., high heat transfer area-to-volume ratio) and higher thermal performance. Depends upon the usage of the heat exchanger, various types of augmented heat transfer surfaces such as plain fins, wavy fins, and Offset strip fins, perforated fins and Louvered fins are used. They have a high degree of surface compactness and substantial heat transfer enhancement obtained as a result of the periodic starting and development of laminar boundary layers over uninterrupted channels formed by the fins and their dissipation in the fin wakes. There is, of course, an associated increase in pressure drop due to increased friction and a form-drag contribution from the finite thickness of the fins. In common, the surface geometry of both the fins is described by the fin height (h), transverse spacing (s) and thickness (t). Uninterrupted flow length of offset strip fin is described by offset length (l) and that of wavy fin by pitch of the wave (l_w).

2. MAIN BODY

To generate the '*j*' and '*f*' data numerically for the fins, the entry effects into the fin play predominant role. In order to overcome this difficulty, S.V. Patankar [1] introduced the concept of periodic fully developed flow and heat transfer. The underlying concept was that for a constant property flow in a duct of constant cross section, the velocity temperature distribution becomes independent of the stream wise coordinate at sufficiently large distances from the inlet and such velocity distribution is said to be fully developed. It is not easy to define for complex geometries like offset fins etc. In the above analysis, the concept of periodic flow and constant wall boundary conditions were introduced. Finally, the variations of '*j*' and '*f*' in both cases have been highlighted for the Reynolds number ranging from 300 to 15,000.The '*j*' and '*f*' characteristic curves were also drawn with respect to Reynolds numbers and compared with other correlations available in the open literature.

3. RESULTS

For a duct of constant cross section, the range of Reynolds numbers for laminar, transition and turbulent regions is well recognized and presented in many heat transfer book. But, in the case of complex geometry, the range of Reynolds numbers for various regions is not defined clearly. In this paper, one of the wavy was analyzed using both laminar as well as κ-ε turbulent 2-equation model for the Reynolds number ranging from 300 to 7000 and the variations in '*j*' and '*f*' was compared [2] as shown in sample Figure 1. At the low Reynolds number region (Re<3500), the variation in '*j'* and '*f*' are minimum and at the same time it is quiet significant in the high Reynolds number region (Re>3500). Above Re 3500, the use of Laminar equation is not acceptable.

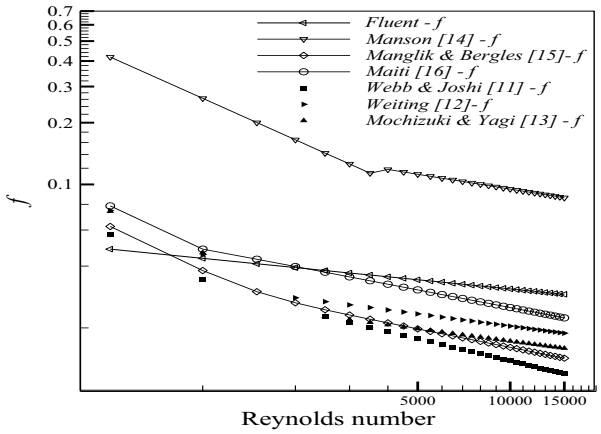

(a)

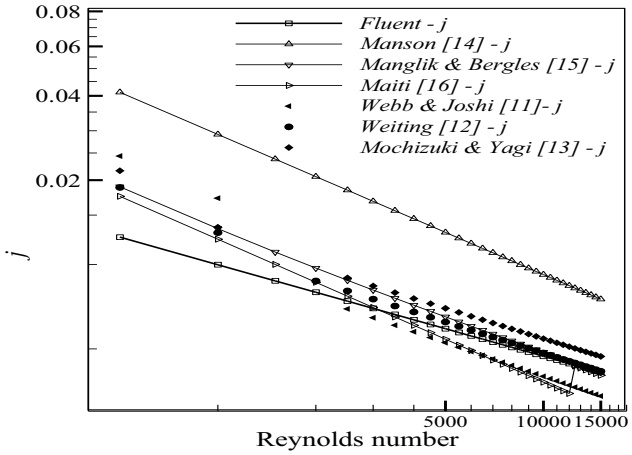

(b)

FIGURE 1. Comparison with the open literature for the Offset fin (3.0S-28.5-0.0762).

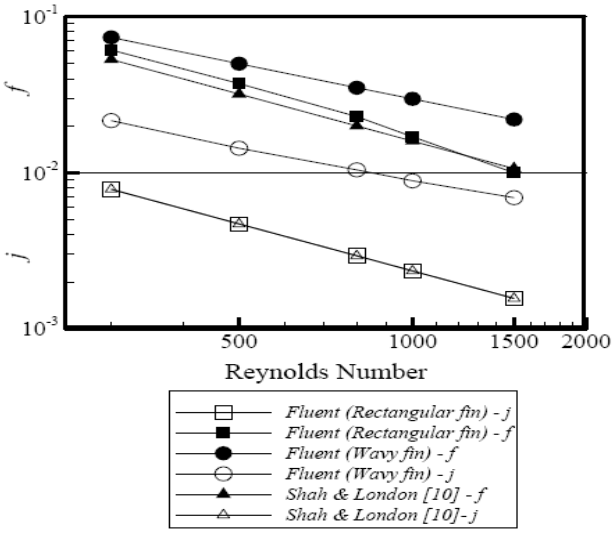

FIGURE 2. Comparison of wavy and rectangular fin data

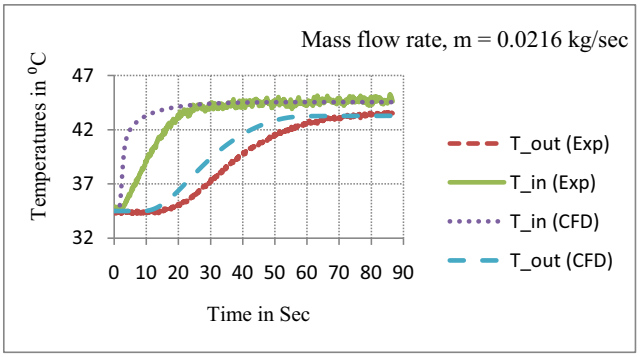

FIGURE 3. Inlet and outlet Temperature transient responses of test section for Offset fin(5.0S-28-0.125)

Also, in the validation point of view, a rectangular channel was analyzed in the similar lines as mentioned above and the results were compared with wavy fin of same dimensions as well as with correlation for ducts given by R.K. Shah and A.L. London[3] as shown in Figure 2. Finally, the Fluent results have been validated with experimental data of heat exchanger fins and single blow transient testing data effectively as shown in Figure 3. Using CFD, heat exchanger design data in terms of '*j*' and '*f*' is presented for wavy fins in references [4, 5]. Similarly the '*j*' and '*f*' data correlations for Rectangular plain fins are presented in reference [6] and for Offset fins are presented in reference [7].

The power law expressions have been used for determining the Colburn factor '*j*' and Friction factor '*f*' as a function of the Reynolds Number and dimensionless fin parameters. Two separate equations have been proposed for Rectangular perforated fins for the low and high Reynolds Numbers versus '*f*' and '*j*' as follows:

$f = 0.7127(\mathrm{Re})^{-1.8858}(\mathrm{h/s})^{0.4196}(\mathrm{t/s})^{-1.4826}$ for Laminar Range ($100 \le \mathrm{Re} \le 1000$) (1)

$f = 0.4345(\mathrm{Re})^{-1.3029}(\mathrm{h/s})^{0.3725}(\mathrm{t/s})^{-1.3178}$ for Turbulent Range ($1000 \le \mathrm{Re} \le 7500$) (2)

$j = 0.121\ (\mathrm{Re})^{-2.2920}(\mathrm{h/s})^{2.75}(\mathrm{t/s})^{-1.830}$ for Laminar Range ($100 \le \mathrm{Re} \le 1000$) (3)

$j = 11.71\ (\mathrm{Re})^{-2.3111}(\mathrm{h/s})^{2.144}(\mathrm{t/s})^{-1.9237}$ for Turbulent Range ($1000 \le \mathrm{Re} \le 7500$) (4)

4. CONCLUSIONS

The design data in terms of '*j*' & '*f*' factors for various types of plate-fin heat exchanger fins (Wavy,Offset, Rectangular Plain, Triangular plain, Rectangular perforated and triangular perforated fins) is generated using CFD package FLUENT.

Nomenclature:

h	Fin height, m
f	Fanning friction factor, dimensionless
j	Colburn factor ($\mathrm{StPr}^{2/3}$), dimensionless
Pr	Prandtl number, dimensionless
d_h	hydraulic diameter, mm
Re	Reynolds number = ($\rho v d_h$)/ , dimensionless
St	Stanton number, dimensionless flow velocity, m/s
s	Fin spacing, m
t	Fin thickness, m

Greek Symbols:

μ	dynamic viscosity, $\mathrm{Ns/m^2}$
ρ	density of the air, $\mathrm{kg/m^3}$

REFERENCES

[1] S.V. Patankar, C.H. Liu, E.M. Sparrow, Fully Developed Flow and Heat Transfer in Ducts Having Stream wise Periodic Variations of Cross Sectional Area, ASME, *International Journal of Heat Transfer* 99 (1977)180-186.

[2] A.L. London, R.K. Shah, Offset Rectangular Plate Fin Surfaces – Heat Transfer and Flow Friction Characteristics, *ASME Journal of Eng. Power* 90 (Series A) (1968) 218-228.

[3] R.K Shah, A.L London, Laminar Forced Convection in Ducts, *Supplement I to Advances in Heat Transfer*, Academic Press, New York, NY, 1978.

[4] Ranganayakulu C., Ismail L. S., Vasudeva Rao V., Rajeshwar S., *Optimization of Wavy Fin Parameters in Compact Heat Exchangers, P*roceedings of XIX National Heat and Mass Transfer & VIII ISHMT-ASME Heat and Mass Transfer Conference, held at JNTU, Hyderabad, India, January 2008.

[5] L. Sheik Ismail, C. Ranganayakulu and Ramesh K. Shah, Numerical study of flow patterns of compact plate-fin heat exchangers and generation of design data for offset and wavy fins, *International J of Heat and Mass Transfer*, 52, 3972-3983, 2009.

[6] R. Bala Sundar Rao, G. Ranganath & C. Ranganaykulu, Development of colburn '*j*' factor and fanning friction factor '*f*' correlations for compact heat exchangers plain fins by using CFD, International Journal of Heat and Mass Transfer, Volume 49, No. 4, April 2013.

[7] Pallavi P., Ranganayakulu C., Development of Heat Transfer coefficient and Friction factor correlations for Offset fins using CFD, *Int. Journal of Numerical Methods for Heat and Fluid Flow*, Volume 21, No. 8, 2011.

Third International Conference on Computational Methods for Thermal Problems
THERMACOMP2014, June2-4, 2014, Lake Bled, Slovenia
N. Massarotti, P.Nithiarasuand B. Sarler(Eds.)

DYNAMIC BEHAVIOUR OF THREE FLUID HEAT EXCHANGERS SUBJECT TO STEP CHANGE IN THE HOT FLUID INLET TEMPERATURE

Vinayakaraddy , Meghana H. Chaturvedi,V. Krishna,K. N. Seetharamu
Department of Mechanical Engineering, P.E.S. Institute of Technology, Bangalore - 560085, India
vinayakapesit@gmail.com,meghana.chaturvedi@gmail.com;vkrishna@pes.edu;
knseetharamu@yahoo.com.

K.Veerabhadrappa
Department of Mechanical Engineering, B.M.S. College of Engineering, Bangalore - 560019, India.
kavadiki@yahoo.com;

ABSTRACT

Three-fluid heat exchangers find wide usage in chemical processes and cryogenics. Knowledge of dynamic behaviour of heat exchangers is necessary for designing control and regulation systems of different industrial processes and operations, such as in nuclear reactors, cryogenic and petrochemical process plants. In the current paper, dynamic behaviour of three-fluid heat exchangers is analyzed using the finite element method. The solution is obtained for a parallel-flow three-fluid heat exchanger with two thermal communications for step change in temperature at the inlet hot fluid. The variation of fluids' exit temperatures, temperature profiles, and effectiveness with time, and the time to reach steady state, are discussed.

Keywords: three-fluid heat exchangers, finite element method, dynamic model, transient analysis.

1. Introduction

Systems that deal with ammonia gas synthesis, purification and liquefaction of hydrogen, air separation systems and helium-air separation units are typical applications which make use of three-fluid heat exchangers. In the general design process of multi-fluid heat exchangers, the stationary operating conditions are of decisive importance; however, in reality heat exchangers frequently undergo transients resulting from external load variations and regulations. Knowledge of dynamic behaviour of heat exchangers is necessary for designing control and regulation systems of different industrial processes and operations, such as in nuclear reactors, cryogenic and petrochemical process plants. In case of the three fluid heat exchangers there is a lot of literature available to describe the steady state behaviour of heat exchangers [1, 2, 3]. There are very less papers published regarding the transient behaviour of three fluid heat exchangers. Sekulic and Herman [6] solved numerically the set of partial differential equations describing temperature field in a counter-flow three-fluid heat exchanger. They used the Wendroff implicit finite-difference approximation and steady state initial conditions. Sekulic et al [7] studied experimentally and numerically transient temperature fields in a three-fluid heat exchanger with two thermal connections. The experiments confirmed the accuracy of the method used in [6]. A semi-analytical solution for a three-fluid parallel-flow heat exchanger with two thermal communications and the steady-state initial conditions was formulated by Bielski and Malinowski [8]. Theyapplied the Laplace transform technique with numerical inversion. Bielski and Malinowski [9] derived fully analytical expressions for temperatures in a parallel-flow three-fluid heat exchanger with two heat connections between the fluids, constant temperature in one channel, the uniform temperature initial conditions, and a step increase in the inlet temperature of one fluid . As per the best knowledge of the authors none of the papers have discussed the effect of the change in the inlet temperature on outlet temperatures, effectiveness,time to reach steady state are not discussed.In the present paper, finite element

method has been used to analyse the transient behaviour of three-fluid heat exchanger, subject to a step change in the temperature hot fluids at the inlet. The fluids' exit temperatures,effectiveness and time to reach steady state, are discussed for various cases.

2. Mathematical Model

The solution is obtained for a three fluid heat exchanger with two thermal communications with pipe configuration as shown in the Fig (1). Channels 1, 2 and 3 represent the paths for the intermediate, hot and the cold fluids respectively. The following assumptions are used: (a) All properties are constant with time and space. (b) There is no axial conduction in the pipes or the fluids (c) Within a stream the temperature distribution is uniform in the transverse direction and equal to the average temperature of the fluid. (d) There is no heat source or sink in the heat exchanger or in any of the fluids (e) There is no phase change in the fluid streams (f) The heat transfer area is constant along the length of the heat exchanger (g) There is no heat transfer with the ambient i.e., the heat exchanger is adiabatic (i) The flow is assumed to be turbulent in all the channels and fully developed.

Heat exchanger is divided into number of elements and governing equations of each of element in the heat exchanger are based on the above assumptions,

Intermediate Fluid $$\frac{\partial T_i}{\partial t} + P_{i,e}\frac{\partial T_i}{\partial X} = b_{ih}\,(T_h - T_i) \quad (1)$$

Hot Fluid $$\frac{\partial T_h}{\partial t} + P_{h.e}\frac{\partial T_h}{\partial X} = b_{hi}\,(T_1 - T_2) + b_{hc}\,(T_c - T_h) \quad (2)$$

Cold Fluid $$\frac{\partial T_c}{\partial t} + P_{c,e}\frac{\partial T_c}{\partial X} = b_{ch}\,(T_h - T_c) \quad (3)$$

Non- Dimensional parameters used are

$$L_e = \frac{L}{n},\quad X = \frac{x}{L_e},\quad P_{n,e} = \frac{V_n}{L_e},\quad b_{nj} = \frac{k_{nj}}{\rho_n\, c_{pn}\, A_n} \quad (4)$$

3. Finite Element Method

The heat exchanger is divided in to a number of elements. For all fluids a linear variation of temperature in each of the element is assumed as the differential equations are first order. The fluid temperature at any point in each of the element is given by,

$T_i(x,t) = N_1 T_{i,in}(x,t) + N_2 T_{i,out}(x,t)$ (5)

$T_h(x,t) = N_1 T_{h,in}(x,t) + N_2 T_{h,out}(x,t)$ (6)

$T_c(x,t) = N_1 T_{c,in}(x,t) + N_2 T_{c,out}(x,t)$ (7)

Where N_1 and N_1 are the shape functions defined by

$N_1 = 1-X \qquad N_2 = X$ (8)

The differential equations Eqs. (1) – (3) are solved using the Galerkin's method of minimising weighted residuals [10]. The governing equations are reduced to a set of algebraic equations. The discretised governing equations are written in matrix form for each element

$[K]\{T\} + [C]\{\partial T/\partial t\} = \{f\}$ (9)

We apply implicit method [10], to equation (9) and it reduces to

$([K] + ([C]/\Delta t))\{T\}_{t+\Delta t} - ([C]/\Delta t)\{T\}_t = \{f\}$ (10)

[K}is stiffness matrix, [C] capacitance matrix, [T] temperature matrix; {f} is load vector The elemental matrices are assembled to give the global stiffness, capacitance, load matrix and the boundary conditions are re-enforced to get the temperatures along the heat exchanger .The system of equations are solved by using the MATLAB tool.

3.1 Boundary and initial conditions

3.1.1 Step change in inlet temperature Initial conditions: (11)

$T_i(x, 0) = T_{is}(x)$

$T_h(x, 0) = T_{hs}(x)$

$T_c(x, 0) = T_{cs}(x)$
Boundary conditions : (12)
$T_i(0,t)= T_{i,in} +\Delta T_{i,in}$
$T_h(0,t)= T_{h,in} +\Delta T_{h,in}$
$T_c(0,t)= T_{c,in}+\Delta T_{c,in}$

4.Effectiveness

Cooling of the hot fluid has been identified as the objective of the three fluid heat exchanger adopted for analysis. Cooling effectiveness of hot fluid for a three-fluid heat exchanger can be based on its temperature effectiveness or thermal effectiveness [2, 4].

$$\varepsilon_h = \frac{\dot{Q}_{h,actual}}{\dot{Q}_{h,max}} \quad (13)$$

The expressions for $\dot{Q}_{h,actual}$and $\dot{Q}_{h,max}$,for various combinations have been presented earlier in [2, 4]. When the thermal capacity of hot fluid is greater than the thermal capacity of the other two fluids then $\dot{Q}_{h,max}$given by

$$\dot{Q}_{h,max}= C_h(T_{h,in}- T_{c,in}) \quad (14)$$

5. Results and discussion

Solution is obtained for a particular case when k_{ih}= 17.361 W/mK ,k_{hc}= 50.001 W/mK, V_i=0.5ms^{-1}, V_h=1ms^{-1}, V_c=0.6ms^{-1}, D_i=0.008m, D_h=0.02m, D_c=0.03m, L=2m. Thermo physical properties correspond with that of water. The following values for initial steady state are used: $T^0_{i,in}$= 30^{0}C; $T^0_{h,in}$= 70^{0}C; $T^0_{c,in}$= 10^{0}C. The transient behaviour is studied when the hot fluid undergoes a step change in temperature by ΔT.The solution was mesh independent at N=256 and 256 and Δt = 0.001s.The effect of step changes in the inlet temperature of hot fluid are shown in the Figs.(2a) – (2d). The step changes in the hot fluid inlet temperature do not reflect in an immediate response in terms of the fluid exit temperatures. All the fluids take almost 2 seconds (approx.) to show a change in their exit temperatures. While the cold and intermediate fluids show a relatively more gradual response, the hot fluid shows an abrupt response. An increase in hot fluid inlet temperature results in more heat transfer between the hot and cold fluids leading to an increase in the exit temperatures of the cold and intermediate fluid as shown in Figs.(2a) &(2c). The hot fluid exit temperature is more influenced by the increase in its inlet temperature than the increased heat transfer and as such its exit temperature is enhanced as shown in Fig.(2b). This leads to reduced effectiveness as shown in Fig.(2d). Conversely, a decrease in the inlet temperature of the hot fluid decreases its exit temperatures leading to an increase in its effectiveness with respect to time as shown in Figs. (2b) and (2d). For any step change in inlet temperature of the hot fluid the effectiveness converges to a single value. The time to reach steady state for the hot, intermediate and cold fluids is 2.99 seconds, 4.07seconds, and 3.39 seconds respectively for all the cases and is independent of the step change in inlet temperature of the hot fluid.

6. Conclusions

The effect of step change in inlet temperatures on outlet temperatures, temperature profiles, effectiveness, time to reach steady state is analysed using the finite element method. Due to (increase/decrease) in hot fluid inlet temperature there is (increase/decrease) in the outlet temperatures of all fluids, (decrease/increase) in effectiveness. Time to reach steady stateremained same. The results presented give valuable inputs towards better understanding of the behaviour of three fluid heat exchangers under dynamic behaviour.

References

[1] D. Shrivastava, T.A. Ameel, Three-fluid heat exchangers with three thermal communications. Part B: Effectiveness evaluation, Int. J. Heat Mass Transfer 47 (2004) 3867–3875.

[2] V. Krishna, Pradeep, G. Hegde, N. Subramanian, K.N. Seetharamu, Effect of ambient heat-in-leak on the performance of a three fluid heat exchanger, for cryogenic

applications, using finite element method, Int. J. Heat and Mass Transfer 55 (2012) 5459–5470.

[3] V. Krishna ,S.Spoorthi , PradeepG.Hegde , K.N.Seetharamu Effect of longitudinal wall conduction on the performance of a three-fluid cryogenic heat exchanger with three thermal communications , Int. J. Heat and Mass Transfer 62 (2013) 567–577.

[4] D.P. Sekulic, C.V. Herman, Transient temperature fields in a three fluid heat exchanger, in: Proceedings of the XVIIth International Congress of Refrigeration B, IIF, Vienna, Austria, 1987, pp. 833–837.

[5] D.P. Sekulic, M. Dzolev, I. Kmecko, Dynamic behaviour of a three fluid heat exchanger: the experimental study, in: J.F. Keffer, R.K. Shah, E.N. Ganic (Eds.), Experimental Heat Transfer, Fluid Mechanics, and Thermodynamics, Elsevier, New York, 1991, pp. 1338–1343.

[6] S. Bielski, L. Malinowski, A semi-analytical method for determining unsteady temperature field in a parallel-flow three-fluid heat exchanger, International Communications in Heat and Mass Transfer 30 (2003) 1071–1080.

[7] S. Bielski, L. Malinowski, An analytical method for determining transient temperature field in a parallel-flow three-fluid heat exchanger, International Communications in Heat and Mass Transfer 32 (2005) 1034–1044.

[8] Roland W. Lewis, PerumalNithiarasu, Kankanhalli N. Seetharamu, 'Fundamentals of Finite Element Method for Heat and Fluid Flow', John Wiley and Sons, 2004.

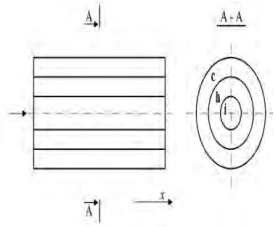

Fig. (1): Schematic representation of three-fluid heat exchanger under consideration

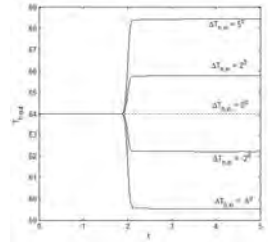

Fig.(2b). Variation of hot fluid exit temperature with time due to change in inlet temperature of hot fluid ($T^0_{h,in}$= 70^{0}C).

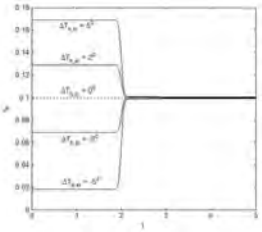

Fig.(2d).Variation of hot fluid effectiveness with time due to change in inlet temperature of hot fluid ($T^0_{h,in}$= 70^{0}C).

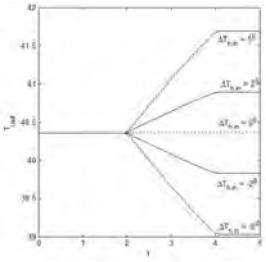

Fig.(2a). Variation of intermediate fluid exit temperature with time due to change in inlet temperature of hot fluid ($T^0_{h,in}$= 70^{0}C).

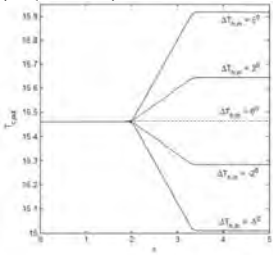

Fig.(2c). Variation of cold fluid exit temperature with time due to change in inlet temperature of hot fluid ($T^0_{h,in}$= 70^{0}C).

Third International Conference on Computational Methods for Thermal Problems
THERMACOMP2014, June 2-4, 2014, Lake Bled, Slovenia
N. Massarotti, P. Nithiarasu and B. Sarler (Eds.)

ANALYSIS OF MULTIFLUID COMPACT HEAT EXCHANGER USING FINITE ELEMENT METHOD

Jyothiprakash K H, Teoh Wah Chung
P.E.S. Institute of Technology, Bangalore - 560085, Karnataka, India, email: jpuvce@gmail.com
Y T Krishnegowda
Maharaja Institute of Technology, Mysore, Karnataka, India, email:ytkrishnegowda@gmail.com
V.Krishna, K.N.Seetharamu
P.E.S. Institute of Technology, Bangalore - 560085, Karnataka, India
email: knseetharamu@yahoo.com; vkrishna@pes.edu.com

ABSTRACT

The engineering applications of multi fluid heat exchangers are found in petrochemical industries, aerospace, cryogenics, etc. In this paper, thermal analysis of a cross-flow three-fluid heat exchanger is carried out using the finite element method. The hot stream is assumed to exchange heat with two cross-flow cold streams. This study investigates the effect of inlet flow maldistribution and ambient interaction. The governing equations are derived based on the conservation of energy principle. The results are presented in terms of effectiveness versus number of transfer units for different values of governing parameters. The results indicate that when there is flow maldistribution, the thermal performance of the heat exchanger is enhanced.

Key Words: *multifluids, cross flow heat exchangers, heat leak.*

1. INTRODUCTION

Heat exchangers are devices that facilitate heat transfer between two or more heat fluids at different temperatures. In this work, thermal analysis of a three fluid heat exchanger both co-current & counter-current cross flow heat exchanger are carried out using the finite element method. The engineering applications of multi fluid heat exchangers are found in petrochemical industries, aerospace, cryogenics, etc [1]. Many micro-scale heat exchangers with two working fluids can be treated as three fluid heat exchangers where the ambient is treated as the third fluid with infinite thermal capacity. In a cross-flow, three-fluid heat exchanger, one fluid flows perpendicular to the other two. Thus, it is a two dimensional temperature field and it is the most seen situation in practical applications. The dimensionless governing equations are derived based on the conservation of energy principle and solved using weighted residual method for both cross-countercurrent C1 and cross-cocurrent flow arrangements C2 shown in fig(1). The effectiveness is calculated for different values of transfer units and fixed value of heat capacity ratio parameter. Once the effectiveness values at various transfer units are calculated the graph of effectiveness verses transfer units are obtained using MATLAB software. A similar analysis can be carried out for finding the effect of ambient on the three fluid heat exchangers.

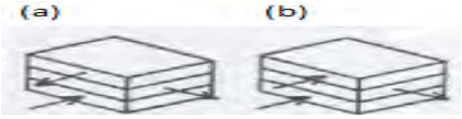

Figure (1): (a) C1, cross-countercurrent flow (b) C2, cross-cocurrent flow.

2. GOVERNING EQUATIONS

Using the energy balance equation for a differential element, the governing equations for the C2 arrangement are written as follows:

Fluid 1:
$$\alpha_1 \frac{dT_{f1}}{dx} + \frac{U_{1,2}L}{\left(\dot{m}c_p\right)_1}\left(T_{f1} - T_{f2}\right) = 0 \tag{1}$$

Fluid 2:
$$\alpha_2 \frac{dT_{f2}}{dy} - \frac{U_{1,2}W}{\left(\dot{m}c_p\right)_2}\left(T_{f1} - T_{f2}\right) + \frac{U_{2,3}W}{\left(\dot{m}c_p\right)_2}\left(T_{f2} - T_{f3}\right) = 0 \tag{2}$$

Fluid3:
$$\alpha_3 \frac{dT_{f3}}{dx} - \frac{U_{2,3}L}{\left(\dot{m}c_p\right)_3}\left(T_{f2} - T_{f3}\right) = 0 \tag{3}$$

where
$$\Theta_i = \frac{T_i - T_{1,in}}{T_{2,in} - T_{1,in}};\ \xi = \frac{x}{W};\ \eta = \frac{y}{L};\ C_{1,2} = \frac{\left(\dot{m}c_p\right)_1}{\left(\dot{m}c_p\right)_2};\ C_{3,2} = \frac{\left(\dot{m}c_p\right)_3}{\left(\dot{m}c_p\right)_2};\ NTU_1 = \frac{(UA)_{1,2}}{\left(\dot{m}c_p\right)_1};\ R = \frac{(UA)_{3,2}}{(UA)_{1,2}},\ H = \frac{(UP)_{23}}{(UP)},\ \alpha_i = \frac{\dot{m}_{local}}{\dot{m}_{average}}\ i = 1,2,3 \tag{4}$$

Similarly governing equations for C1 arrangement are written and the governing equations for the effect of heat in leak to the cross cocurrent arrangement are

$$\frac{d\Theta_3}{d\xi} + R \cdot NTU_1 \cdot \frac{C_{1,2}}{C_{3,2}}(\Theta_3 - \Theta_2) + NTU_1 \cdot \frac{C_{1,2}}{C_{3,2}} \cdot H \cdot (\Theta_3 - \Theta_{amb}) = 0 \tag{5}$$

(When the ambient temperature is lower than cold fluid)

$$\frac{d\Theta_3}{d\xi} + R \cdot NTU_1 \cdot \frac{C_{1,2}}{C_{3,2}}(\Theta_3 - \Theta_2) + NTU_1 \cdot \frac{C_{1,2}}{C_{3,2}} \cdot H \cdot (\Theta_{amb} - \Theta_3) = 0 \tag{6}$$

(When the ambient temperature is higher than cold fluid)

Boundary conditions

	Fluid flow arrangements					
	C2			C1		
i	ξ	η	Θ	ξ	η	Θ
1	0	-	0	1	-	0
2	-	0	1	-	0	1
3	0	-	$\Theta_{3,in}$	0	-	$\Theta_{3,in}$

Table 1: Dimensionless Boundary Conditions for Cross-flow Arrangements [1].

Finite Element Method

The heat exchanger is discretized into a number of elements. The method of minimizing the weighted residual (Lewis et.al [4]) is used to solve equations (1)-(5) as follows

$$\int_0^1 W\left\{\frac{d\Theta_1}{d\xi} - NTU_1(\Theta_2 - \Theta_1)\right\} d\zeta = 0 \tag{7}$$

$$\int_0^1 W\left\{\frac{d\Theta_2}{d\eta} + C_{1,2} \cdot NTU_1(\Theta_2 - \Theta_1) + C_{1,2} \cdot R \cdot NTU_1(\Theta_2 - \Theta_3)\right\} d\zeta = 0 \tag{8}$$

$$\int_0^1 W\left\{\frac{d\Theta_3}{d\xi} + R \cdot NTU_1 \cdot \frac{C_{1,2}}{C_{3,2}}(\Theta_3 - \Theta_2)\right\} d\zeta = 0 \tag{9}$$

A linear variation of the hot and cold fluids is assumed in every single element for cross flow as: $\Theta_1 = N_1\Theta_{1,in} + N_2\Theta_{1,out}; \Theta_2 = N_1\Theta_{2,in} + N_2\Theta_{2,out}; \Theta_3 = N_1\Theta_{3,in} + N_2\Theta_{3,out}$
where the shape functions N_1 and N_2 are given by $N_1 = 1- X$ and $N_2 = X$ in the flow direction . Substitution of these approximations in equations (1) – (9) the set of algebraic equations can be obtained if the weighted parameter W is defined. In the present analysis the Galerkin's method is used, in which the weights are taken to be the shape functions N_1 and N_2. The discretized governing equations are written in matrix form for each element as: $[K]\{\ \Theta\ \} = \{f\}$ (10)
Assembling the element matrix form of the governing equations for all the elements in the solution domain leads to the global matrix form of the governing equations in the whole solution domain. The resultant global matrix form is modified by the forcing boundary conditions chosen and solved by MATLAB for the dimensionless temperatures along the heat exchanger.

3. RESULTS

In order to determine the validity of the present method and the number of elements used for further analysis, the present numerical scheme is tested for a classical cross-flow two-fluid heat exchanger. The results of the present method for the classical cross-flow two-fluid heat exchanger are listed in Table 2 using different number of elements together with the solution for equation defined by J. P. Holman [3]

$$\varepsilon = 1 - \exp\left[\left(\frac{1}{C}\right)(NTU)^{0.22}\left\{\exp\left[-C(NTU)^{0.78}\right]-1\right\}\right] \quad (11)$$

It can be seen that from Table 2, the present method gives results which are closer to the analytical solutions, with a maximum of 2.13 % for an 8 element solution. All further analysis is made using 8-elements. In the study of uniform inlet flow effect for the C2 arrangement involving mixed flows of all three fluids, the effectiveness increases with the increase of governing parameters ($C_{1,2}$,$C_{3,2}$,R, $\Theta_{3,in}$) while effectiveness decreases with increase in $C_{3,2}$. For the unmixed flows of the three fluids, the effectiveness decrease with the increase of $C_{1,2}$ and $C_{3,2}$ as shown in the figs (3a),(3b). The effectiveness increase with a decrease in R and $\Theta_{3,in}$ as shown in the figs (4a),4(b). It is observed that C1 arrangement also exhibits the same result trends in the cases studied. In the study of the inlet flow maldistribution effect, the C2 and C1 arrangements have the same trend of results. In order to discuss about the maldistribution effect, a deterioration factor α is used as defined in Eq (4). As observed in fig (5c), the deterioration factor for C2 arrangement decreases with the number of transfer units. This means that the effect of maldistribution promotes thermal performance of a three-fluid heat exchanger. The effect of ambient is to reduce the effectiveness at low values of transfer units as seen in Figs. (2a) and (2b).

4. CONCLUSIONS

- The effectiveness values are found to increase with maldistribution factor.
- The effect of ambient is to decrease the effectiveness of heat exchanger for variation in heat capacity ratio.

REFERENCES

[1] Sekulik, D.P. and Shah, R.K, "Thermal Design Theory of Three-fluid Heat Exchangers", *Advances in Hat Transfer*, Vol. 26, 1995, pp 219-328.
[2] J. P. Holman, Heat Transfer Eight metric Edition, McGraw Hill, New York, 2001.
[3] V.Krishna, Pradeep ,K.N. Seetharamu, "Effect of ambient heat in leak on the performance of three fluid heat exchanger, for cryogenic applications, using finite element method", IJHMT (2012)
[4] "Fundamentals of Finite Element Method foerHeat and Fluid Flow" Ronald W.Lewis,Perumal Nithiarasu, Kankanhalli N. Seetharamu, John Wiley and Sons, 2004

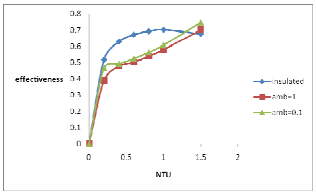

Figure(2a): effectiveness study for H=0.1 with $\Theta_{3,in}$=0.4 and R = C_{12} = C_{32} = 0.5, Θ_{amb}=1,0.1 and insulated

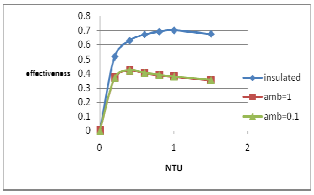

Figure(2b): effectiveness study for H=0.01 with $\Theta_{3,in}$=0.4 and R = C_{12} = C_{32} = 0.5, Θ_{amb}=1, 0.1 and insulated

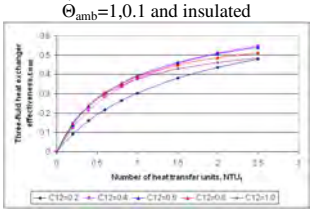

Figure (3a): Study of $C_{1,2}$, for C2 with $C_{3,2}$ =R=0.5, $\Theta_{3,in}$=0.4. Mixed, mixed, mixed flows

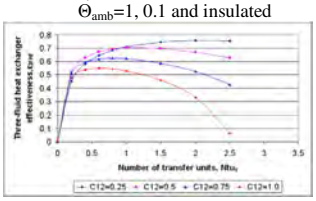

Figure (3b): Study of $C_{1,2}$, for C2 with $C_{3,2}$ =R=0.5, $\Theta_{3,in}$=0.4. Unmixed, unmixed, unmixed flows.

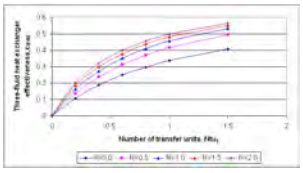

Figure (4a): Study of R for C1 with $C_{1,2}$ = $C_{3,2}$ =0.5, $\Theta_{3,in}$=0.4.Mixed, mixed, mixed flows.

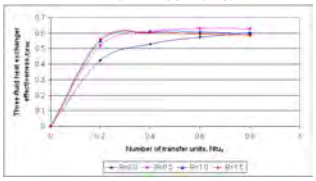

Figure (4b): Study of R for C1 with $C_{1,2}$ = $C_{3,2}$ =0.5, $\Theta_{3,in}$=0.4. Unmixed, unmixed, unmixed flows.

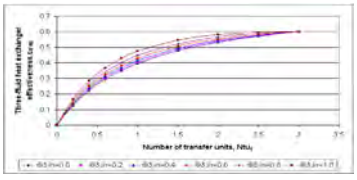

Figure (5a): Study of $\Theta_{3,in}$ C1 with $C_{1,2}$ = $C_{3,2}$ =R=0.5. Mixed, mixed, mixed flows

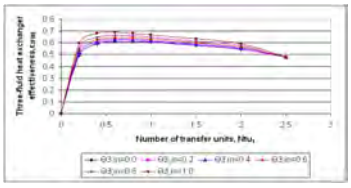

Figure (5b): Study of $\Theta_{3,in}$ C1 with $C_{1,2}$ = $C_{3,2}$ =R=0.5. Unmixed, unmixed, unmixed flows.

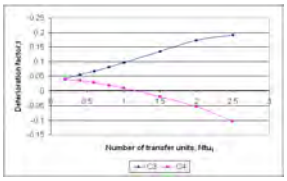

Figure (5c): Study of detoriation factor for C3,C4

NTU	Eq.(11)	2 elements		4 elements		8 elements		16 elements	
	ε (analytical)	E	Error (%)	E	Error (%)	E	Error (%)	E	Error (%)
0.2	0.1686	0.172	2.02	0.1721	2.08	0.1722	2.13	0.1722	2.13
0.5	0.3467	0.3511	1.27	0.3518	1.47	0.3525	1.67	0.3529	1.79
1	0.5337	0.5299	-0.71	0.5316	-0.39	0.5341	0.07	0.5356	0.36
2	0.7213	0.6991	-3.08	0.7009	-2.83	0.7071	-1.96	0.7111	-1.42
3	0.8088	0.7776	-3.86	0.778	-3.81	0.7873	-2.65	0.7937	-1.87

Table 2: Comparison of the results of effectiveness of the classical cross-flow two-fluid heat exchanger using different number of elements for U_{12}=0

Third International Conference on Computational Methods for Thermal Problems
THERMACOMP2014, June 2-4, 2014, Lake Bled, Slovenia
N. Massarotti, P. Nithiarasu and B. Sarler (Eds.)

EFFECT OF AMBIENT HEAT-IN-LEAK AND LONGITUDINAL WALL CONDUCTION ON A THREE-FLUID CRYOGENIC HEAT EXCHANGER WITH TWO COMMUNICATIONS

V. Krishna, S. Spoorthi, K. N. Seetharamu
Department of Mechanical Engineering, P.E.S. Institute of Technology, Bangalore - 560085, India
vkrishna@pes.edu; spoorthi333@gmail.com; knseetharamu@yahoo.com

Pradeep G. Hegde
Department of Mechanical Engineering, Higher Colleges of Technology, Dubai,
pghegde@gmail.com;

ABSTRACT

In addition to operating and design parameters, the thermal performance of heat exchangers, working in cryogenic temperature range, is strongly governed by losses such as longitudinal conduction through the wall, heat-in-leak from the surroundings, flow maldistribution, etc. In this paper, a three-fluid cryogenic heat exchanger, involving two thermal interactions, is investigated for the effect of ambient heat-in-leak and longitudinal conduction in the separating walls on the perfromance, using FEM. Further the effect of the capacity ratio has also been explored for its effect on the hot fluid temperature profile.

Keywords: *Heat exchangers; Heat-in-Leak; Finite Element Method; Longitudinal Wall Conduction*

1. INTRODUCTION

Three fluid heat exchangers find wide usage in chemical processes and cryogenics [1]. Systems that deal with ammonia gas synthesis, purification and liquefaction of hydrogen, air separation systems, helium-air separation units are typical applications which make use of three-fluid heat exchangers. A three-fluid heat exchanger may be desirable or even necessary due to space constraints, (as in the aerospace industry) and/or overall system thermal balance considerations (as in cryogenics and low-temperature refrigeration processes)**.** In most cryogenic applications, heat in leak from the ambient is a significant factor for the degradation in the performance of heat exchangers. The assumption of negligible longitudinal heat conduction along the separating walls between the streams is generally valid except when the heat exchanger effectiveness is expected to be high (above 0.9) or when the length of the flow passage is short. Aulds and Barron [2] mention that this aspect of the problem is one which deserves further investigation, since heat exchanger effectiveness of 0.95 and above are not uncommon in cryogenic systems. The effect of heat-inleak and longitudinal wall conduction has been analysed for two-fluid heat exchangers [3,4] and three fluid heat exchangers with three communications [5,6]. In the present paper, the effect of heat-inleak and longitudinal wall conduction has not been analysed separately and together for three-fluid heat exchanger with two thermal communications.

2. MODEL FORMULATION

In the present paper, a three-fluid parallel flow heat exchanger, involving two thermal interactions, of the type shown in Fig (1), is investigated for the effect of ambient heat-in-leak and longitudinal wall conduction. The flow arrangement for the heat exchanger is shown in Fig (2) and involves the hot fluid flowing counter to the cold and intermediate fluids. The following assumptions are made for the analysis: (a) The heat exchanger is in a steady state (b) All properties are constant with time and space. (c) Within a stream the temperature distribution is uniform in the transverse direction

and equal to the average temperature of the fluid. (d) There is no heat source or sink in the heat exchanger or in any of the fluids (e) There is no phase change in the fluid streams (f) The heat transfer area is constant along the length of the heat exchanger.

The non-dimensional governing equations, obtained by energy balance, are as follows:-

Hot Fluid: $$i_H \frac{d\theta_H}{dX} + n_{H-W1}(\theta_H - \theta_{W1}) + n_{H-W3}(\theta_H - \theta_{W3}) = 0 \quad (1)$$

Intermediate Fluid: $$i_I \frac{d\theta_I}{dX} - n_{W3-I}(\theta_{W3} - \theta_I) = 0 \quad (2)$$

Cold Fluid: $$i_C \frac{d\theta_C}{dX} - n_{W1-C}(\theta_{W1} - \theta_C) - n_4(\theta_a - \theta_C) = 0 \quad (3)$$

Wall-1: $$\frac{\lambda_1}{R_2}\frac{d^2\theta_{W1}}{dX^2} + n_{H-W1}(\theta_H - \theta_{W1}) - \frac{n_{W1-C}}{R_2}(\theta_{W1} - \theta_C) = 0 \quad (4)$$

Wall-3: $$\frac{\lambda_3}{R_2}\frac{d^2\theta_{W3}}{dX^2} + n_{H-W3}(\theta_H - \theta_{W3}) - \frac{n_{W3-I}}{R_1}(\theta_{W3} - \theta_I) = 0 \quad (5)$$

In the above expressions θ_h, θ_i and θ_c represent the dimensionless temperatures of the hot fluid, intermediate fluid and the cold fluid respectively, while θ_{w1} and θ_{w3} represent the dimensionless temperatures of the two walls as defined in Eqs. (4)-(5). Directional constants - $i_{h,}\ i_i \text{ and } i_c$ - are introduced to the governing equations to make them applicable for all four flow arrangements. Their values are +1 for the positive x direction and -1 for negative x direction. The different non-dimensional terms used in the analysis are defined below:-

$$\theta = \frac{T - T_{C,in}}{T_{H,in} - T_{C,in}}, \quad X = \frac{x}{L}, \quad R_1 = \frac{C_H}{C_I}, \quad R_2 = \frac{C_H}{C_C}, \quad \lambda = \frac{kA_c}{C_c L_e},$$

$$H_2 = \frac{U_3 A_3}{U_1 A_1}, \quad H_3 = \frac{U_4 A_4}{U_1 A_1}, \quad NTU_c = \frac{U_1 A_1}{C_c} \quad (6)$$

$$n_{H-W1} = \left(\frac{hA_1}{C_H}\right)_{H-W1}, \quad n_{W1-C} = \left(\frac{hA_1}{C_C}\right)_{W1-C}, \quad n_{H-W3} = \left(\frac{hA_3}{C_H}\right)_{H-W3}$$

$$n_{W3-I} = \left(\frac{hA_3}{C_I}\right)_{W3-I} \quad (7)$$

The notations for the four walls are seen in Fig (1) and are as follows:
W1 - Wall 1 - wall between the hot and the cold fluid
W3 - Wall 3 - wall between the hot and the intermediate fluids

In the non-dimensional analysis, it is assumed that the local Ntu of each pair of fluids across a given wall is same [7], i.e.,

Across wall 1: $n_{H-W1} = n_{W1-C} = n_1$
Across wall 2: $n_{I-W2} = n_{W2-C} = n_2$
Across wall 3: $n_{3h} = n_{3i} = n_3$ (8)
The local Ntu of each fluid is related to the overall NTU_c as given below:-

$$NTU_c = n_1\left[\frac{R_2}{1+R_2}\right] = n_3\left[\frac{R_2}{H_2(1+R_1)}\right] = \frac{n_4}{H_3} \quad (9)$$

3. FINITE ELEMENT METHOD

The heat exchanger is discretized into a number of elements. A linear variation is assumed for the hot, intermediate and the cold fluids in a single element. The fluid temperature at any point, for the flow arrangement of Fig. 2, is given by the following equations:

$$\theta_h = N_1\theta_{h\,out} + N_2\theta_{h\,in} \quad (10)$$

$$\theta_i = N_1\theta_{i\,in} + N_2\theta_{i\,out} \quad (11)$$

$$\theta_c = N_1\theta_{c\,in} + N_2\theta_{c\,out} \quad (12)$$

where N_1 and N_2 are the shape functions and given by

$N_1 = 1 - X$ and $N_2 = X$. (13)

Using the Galerkin's method of minimizing the weighted residual (Lewis et al, [8]), the governing equations are reduced to a set of algebraic equations. The discretized governing equations are written in matrix form for each element as:

$[K]\{\theta\} = \{f\}$ (14)

where [K] is known as the stiffness matrix $\{\theta\}$ is the non-dimensional temperature vector and $\{f\}$ gives the loading terms. The stiffness matrix is assembled for all the elements in the solution domain to get the global stiffness matrix. The boundary conditions are enforced and the system of equations is solved by MATLAB to get the dimensionless temperatures along the heat exchanger.

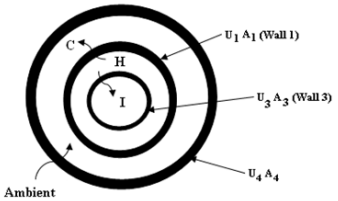

Fig. 1: Tubular arrangement of a three-fluid heat exchanger with two thermal communications with heat-in-leak from the ambient and longitudinal wall conduction.

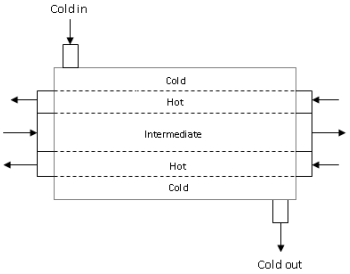

Fig. 2: Flow arrangement involving hot fluid flowing counter to the other two.

4. RESULTS

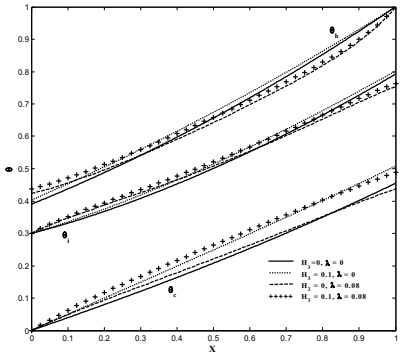

Fig. 3: Three-fluid heat exchanger with two thermal communications: Temperature profiles for P2 arrangement – Effect of Heat-in-leak and Longitudinal Wall Conduction. Values of non-dimensional parameters: H_2=2, R_1=2, R_2=1.25, NTU_c=1, $\theta_{i,in}$ = 0.3, θ_a=1, H_3 = 0.1, λ=0.08

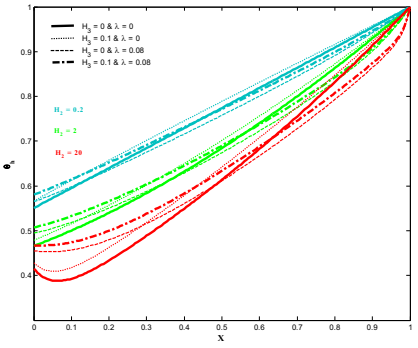

Fig. 4: Three-fluid heat exchanger with two thermal communications: Effect of H_2 on the hot fluid temperature profile - P2 arrangement. Values of other non-dimensional parameters: NTU_c =1, R_1=2, R_2=1.25, $\theta_{i\,in}$= 0.5, θ_a=1, H_3 = 0.1, λ=0.08

A three-fluid parallel flow heat exchanger, involving two thermal interactionsis investigated for the effect of ambient heat-in-leak and longitudinal wall conduction. The ambient temperature is taken θ_a=1, and the intermediate fluid inlet temperature is taken as 0.3 and 0.5 for different situations, however this could be any value between 0 and 1. The values of the other constants have been taken from the literature [5,6].

It is noticed that ambient heat-in-leak enhances the temperature distributions for all fluids. Longitudinal wall conduction alters the gradients of all the fluid temperature profiles at the heat exchanger ends leading to the profiles crossing with and without wall conduction. An increase in H_2 increases the thermal interaction between the hot and the intermediate fluids and/or reduces that between the hot and the cold fluids. Thus an increase in H_2 results in the reducing temperature difference between the hot and the intermediate fluids. It also experiences increasing temperature gradients at the inlet with increase in H_2 and enhanced temperatures at the exit. The hot fluid experiences increasing temperature difference between their inlet and exit with increase in H_2. Ambient heat-in-leak increases the temperatures of all the fluids leading to increased values of $\theta_{h,out}$. Longitudinal wall conduction alters the gradients of all fluid profiles at the inlet and exit, enhancing $\theta_{h,out}$. The combined effect is found to enhance $\theta_{h,out}$.

5. CONCLUSIONS

The salient conclusions are:-

a) Ambient heat-in-leak enhances the temperature distributions for all fluids leading to enhanced hot fluid exit temperatures.
b) Longitudinal wall conduction alters the gradients of all the fluid temperature profiles at the heat exchanger ends resulting in enhanced hot fluid exit temperatures.
c) An increase in the capacity ratio H_2 results in reducing hot fluid exit temperatures.
d) The combined effect of ambient heat-in-leak and longitudinal wall conduction is found to enhance hot fluid exit temperatures.

REFERENCES

[1] D.P. Sekulic, R.K. Shah, 1995. “Thermal design theory of three-fluid heat exchangers”. Advances in Heat Transfer (26), pp. 219–329.
[2] D.D. Aulds, R.F. Barron, 1967. “Three-fluid heat exchanger effectiveness”. International Journal of Heat and Mass Transfer (10), pp. 1457–1462.
[3] S.P. Narayanan, G. Venkatarathnam, 1999. “Performance of counter flow heat exchanger with heat loss through the wall at the cold end”. Cryogenics (39), pp. 43–52.
[4] Prabhat Gupta, M.D. Atrey, 2000. “Performance evaluation of counter flow heat exchangers considering the effect of heat in leak and longitudinal conduction for low temperature applications”, Cryogenics (40), pp. 469–474.
[5] V.Krishna, Pradeep G. Hegde, N. Subramanian, K.N. Seetharamu, 2012. “Effect of ambient heat-in-leak on the performance of a three fluid heat exchanger, for cryogenic applications, using finite element method”. Int. J. Heat Mass Transfer, (55), pp. 5459–5470
[6] V.Krishna, Spoorthi S, Pradeep G. Hegde, K.N. Seetharamu, 2013. “Effect of longitudinal wall conduction on the performance of a three-fluid cryogenic heat exchanger with three thermal communications”. International Journal of Heat and Mass Transfer (62), pp. 567–577
[7] P.G. Kroger, 1967. “Performance deterioration in high effectiveness heat exchangers due to axial conduction effects”. Adv. Cryog. Eng. (12) pp. 363–372.
[8] Roland W. Lewis, Perumal Nithiarasu, Kankanhalli N. Seetharamu, ‘Fundamentals of Finite Element Method for Heat and Fluid Flow’, John Wiley and Sons, 2004.

PARALLEL SESSIONS

PARALLEL SESSION

CONDUCTION, CONVECTION AND RADIATION

Third International Conference on Computational Methods for Thermal Problems
THERMACOMP2014, June 2-4, 2014, Lake Bled, Slovenia
N. Massarotti, P. Nithiarasu and B. Sarler (Eds.)

EQUIVALENT THERMAL DIFFUSIVITY OF FIBROUS COMPOSITE MATERIALS

Isa Ahmadi
Department of Mechanical Engineering, University of Zanjan, University Blvd., Zanjan, Iran,
i_ahmadi@znu.ac.ir

ABSTRACT

The aim of present study is investigation of the equivalent thermal properties of composite material as a heterogeneous material from properties of fiber and matrix. These properties mainly include the thermal diffusion and thermal conductivity of the composite. For this aim a micromechanical model based on the representative volume element (RVE) is presented for modeling the heat transfer in fibrous composite materials. The problem of heat transfer in the RVE is defined so that by analogy of results the overall property of the RVE could be estimated. The thermal diffusion of the composite is defined based on transient heat transfer in the RVE. A numerical method is presented for solution of heat transfer in the RVE. The numerical results for transient heat flux and temperature in the RVE is presented. The equivalent properties for composite are then obtained for fibrous composites with various fiber volume fractions. Some of the obtained results are compared with other available results in the literature.

Key Words: *Equivalent Thermal Diffusivity, Numerical Modelling, Transient Heat Conduction, Fibrous Composite*

1. INTRODUCTION

The utilization of fiber reinforced composite (FRC) materials is increasing in the various fields of application and over past decades significant progresses are achieved in modeling and analysis the behavior of these materials. Due to the advantages of fiber reinforced composites (FRC) such as higher specific stiffness and strength, low thermal expansion, excellent fatigue strength and improved corrosion-resistance compared to conventional materials, composite materials are becoming an essential part of present engineering materials. With the increasing utilization of composite materials in various industries, prediction of the effective thermal properties of these materials is necessary for design purpose. Numerous works are done on estimation the equivalent thermal conductivity of composite materials. Thermal transport properties of composite materials are very important in the performance of practical components especially at high (elevated) temperature. In design of many non-isothermal engineering components a detailed knowledge of temperature distribution, temperature gradient and heat flux through the component is necessary. From the earliest contributions in prediction of thermal conductivity of composite materials one can refer to [1-9].

2. FORMULATION

As we know the thermal diffusivity controls the rate of diffusion of energy into the material in a transient heat transfer. Now consider a transient heat transfer in which the temperature of the RVE increases from initial value to final steady state value by diffusion of energy to the RVE from one side of the RVE. The speed of diffusion of energy and increasing the temperature to the final value is controlled by the thermal diffusivity of the material. In this study the equivalent thermal

diffusivity of a composite material is defined based on the rate of diffusion of energy to the material. So the diffusion in the real heterogeneous RVE is compared with diffusion in the RVE with homogeneous material properties. For this aim, at first a heat diffusion problem must be defined for the RVE.

Suppose the RVE of a composite which consists of fiber and matrix Suppose transient heat diffusion in the transverse direction of the RVE and so the RVE is isothermal in the fiber direction i.e. x_3, direction and so the heat transfer in the RVE is 2D x_1x_2 plane. The RVE is in uniform initial temperature T_i, and the top, bottom and left sides of the RVE is isolated and the RVE is in the steady state conditions. Now the right side of the RVE suddenly is subjected to T_1. Because the top, bottom and left sides is isolated if $T_1>T_i$ the heat transfer only from the right side to the RVE and finally in the steady state conditions the temperature of the RVE increase from T_i to T_1. Because other sides of the RVE are isolated, the total energy which is transferred from the right side to the RVE is stored in it. The total heat transferred energy into the RVE from initial conditions to final steady state conditions is called Q_{total} and could be obtained from the thermodynamic lows. Theoretically Q_{total} will transfer to RVE at $t=\infty$. Now $Q(t)$ is defined the heat energy which transfer from right side to the RVE and stored in it from initial conditions $t=0$ to time t. It is clear that $Q(t=\infty)=Q_{total}$. Now in order to eliminate some physical parameters and dimensions from the problem, the dimensionless heat $Q^*(t)$ is defined the ratio of $Q(t)$ to Q_{total} as $Q^*(t)= Q(t)/Q_{total}$. It is clear that $Q^*(t=0)=0$ and $Q^*(t=\infty)=1$. It is clear that for greater value for thermal diffusivity, Q^* increase rapider from 0 to 1. Now for $0<\beta<1$, t_β is defined the time that $Q(t_\beta)=\beta Q_{total}$ and so $Q^*(t_\beta)=\beta$. It could be shown that for homogeneous isotropic material, for a known value for β, the value of t_β is depend only on the thermal diffusivity of the material and greater value for thermal diffusivity of the material leads to smaller value for t_β. So for a composite material the equivalent thermal diffusivity of the composite could be defined based on t_β. In this study the equivalent thermal diffusivity for a composite (RVE) is defined as follows.

A real RVE is equivalent in thermal diffusivity with a homogenized RVE if for a predefined value for β ($0<\beta<1$), t_β for real RVE (composite) be equal with t_β for homogenous RVE with same heat transfer problem i.e. $t_{\beta nh}=t_{\beta h}$ which subscript nh refers to non-homogeneous RVE and h refers to homogenized RVE. So for the defined transient problem $Q(t)$ must be calculated for real non-homogeneous RVE and for homogeneous RVE. For a homogeneous RVE with thermal diffusivity α, the solution of the defined problem is obtained analytically as a series solution and for a given value for β the value of t_β could be obtained by the analytical solution.

For a real RVE of composite with fiber surrounded in the matrix the analytical solution could not be found and so numerical method is used for solution of the transient heat transfer problem. In this study the dimensionless time parameter is defined as $t^*=\alpha t/a^2$ in which 2a is the length of the RVE and α is the thermal diffusivity of the material. As said before in this study thermal diffusivity of a real RVE is equivalent with homogeneous RVE if $t_{\beta nh}=t_{\beta h}$, so the equivalent diffusivity could be obtained.

In the prediction $t_{\beta h}$ is obtained from the analytical series solution of homogeneous RVE and $t_{\beta nh}$ is obtained from the numerical solution of the transient heat transfer in the real non-homogeneous RVE. In this study a meshless method is used for solution of the problem in non-homogeneous RVE [9]. As we know $t^*_{\beta h}$ is a dimensionless parameter and is not depends on the dimensions and the properties of the RVE and for a given value for β it could be obtained by the analytical solution of the homogeneous RVE. Now for real non-homogeneous RVE the $t_{\beta nh}$ is obtained by numerical solution and thermal diffusivity is obtained.

3. RESULTS

A square RVE with a fiber which is located in the center of REE is considered as the representative volume element of the composite. The initial temperature of the RVE is taken T_i=0 and the bottom, top, front, back and left sides of the RVE are isolated and the right side is suddenly subjected to a constant temperature T_1=1˚C. For this problem the heat diffuses to the RVE from the right side of the RVE and stores in it and the temperature of the RVE rises from T_i=0 to 1˚C. For Glass/Epoxy composite for various Fiber volume fraction V_f the transient heat transfer problem are solved. Figure (1) shows the time history of the dimensionless heat Q^* for a homogeneous composite. A meshless method is used for numerical solution of the problem. It is seen that a good agreement is seen between the numerical and analytical method. Figure (2) shows the time history of the distribution of the temperature on the x_2 axis of the RVE. It is seen that the temperature is increased from zero to the final values at t^*=4. Table (1) shows the predicted value for equivalent thermal diffusion $\bar{\alpha}_\beta$ of the Glass/Epoxy composite in the transverse (normal to fiber) direction. As seen in the Table (1) the predicted value for $\bar{\alpha}_\beta$ slightly depends on the selected value for β. In this table α_m is the thermal diffusivity of the matrix (Epoxy).

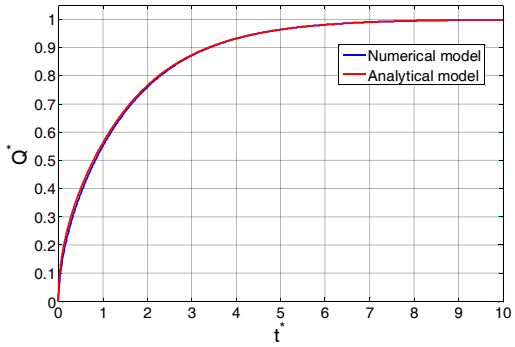

FIGURE (1): Time history of dimensionless transferred heat $Q^*(t^*)$

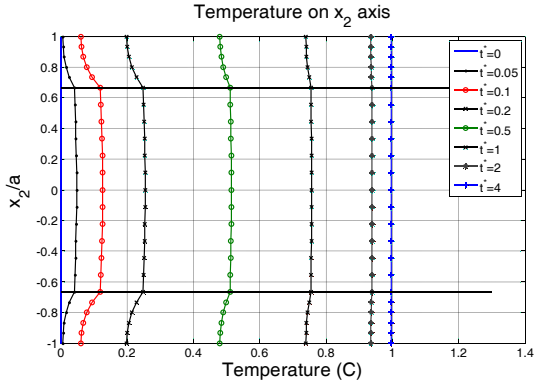

FIGURE (2): The distribution of temperature on the x_2 axis (x_1=*0*) of the RVE.

		β=0.5	β=0.75	β=0.80	β=0.85	β=0.90	β=0.95	β=0.99
	$t^*_{\beta h}$ (Series solution)	0.7871	1.9072	2.2690	2.7355	3.3930	4.5173	7.1317
V_f=0.35	$\alpha \times 10^6$ (m^2/s)	**0.1532**	**0.1730**	**0.1755**	**0.1778**	**0.1799**	**0.1816**	**0.1793**
	α/α_m	1.1951	1.8652	1.3691	1.3870	1.4032	1.4168	1.3988
V_f=0.4	$\alpha \times 10^6$ (m^2/s)	**0.1615**	**0.1840**	**0.1869**	**0.1895**	**0.1919**	**0.1940**	**0.1916**
	α/α_m	1.2600	1.4350	1.4578	1.4783	1.4971	1.5130	1.4945

Table (1): The predicted thermal diffusivity of Glass/Epoxy composite

4. CONCLUSIONS

In this study a concept is introduced for estimation of the thermal diffusivity of a heterogeneous material such as a fibrous composite material from the properties of its constituents. This concept is based on the rate of the diffusion of the energy to the material in a transient heat conduction problem. The rate of heat transfer to a non-homogeneous material in transient heat conduction is compared with the same heat transfer in a homogeneous material and the equivalent property is defined based on this comparison. The numerical value for equivalent thermal diffusivity for Glass/Epoxy composite with various fiber volume fractions is obtained in this study.

REFERENCES

[1] G.S. Springer, S.W. Tsai, Thermal Conductivities of Unidirectional Materials, *Journal of Composite Materials*, 1, 166-173, 1967.

[2] W. Gogo, P. Furmanski, Some Investigations of Effective Thermal Conductivity of Unidirectional Fiber-Reinforced Composites, *Journal of Composite Materials,* 14, 167-176, 1980.

[3] R.C. Progelhof, J.L. Throne, R.R. Ruetsch, Methods for prediction the thermal conductivity of composite systems, *Polymer Engineering and Science*, 9, 615-625, 1976.

[4] L.S. Han, A.A. Cosner, Effective thermal conductivities of fibrous composites, ASME Transactions, *Journal of Heat Transfer*,103, 387–392, 1981.

[5] F.H. Gordon, S.P. Turner, R. Taylor, T.W. Clyne, The effect of the interface on the thermal conductivity of titanium-based composites, *Composites*, 25, 583-592, 1994.

[6] G.W. Milton, *Mechanics of Composites*, Cambridge University Press, Cambridge, 2000.

[7] I. Sevostianov, M. Kachanov, Connection between elastic moduli and thermal conductivities of anisotropic short fiber reinforced thermoplastics: theory and experimental verification, *Materials Science and Engineering A*, 360, 339-344, 2003.

[8] H. Zhou, S. Zhang, M. Yang, The effect of heat-transfer passages on the effective thermal conductivity of high filler loading composite materials, *Composites Science and Technology*, 67, 1035–1040, 2007.

[9] Isa Ahmadi, Transient heat transfer in composite materials, *Third International Conference on Computational Methods for Thermal Problems*, THERMACOMP2014, June 2-4, 2014, Lake Bled, Slovenia, (accepted for publication)

Third International Conference on Computational Methods for Thermal Problems
THERMACOMP2014, June 2-4, 2014, Lake Bled, Slovenia
N. Massarotti, P. Nithiarasu and B. Sarler (Eds.)

EXPERIMENTAL INVESTIGATION AND MODELLING OF MINERAL WOOL MELT ADHESION ON A SPINNER WHEEL

Benjamin Bizjan, Brane Širok
Faculty of Mechanical Engineering Ljubljana, Aškerčeva 6, 1000 Ljubljana,
benjamin.bizjan@abelium.eu, brane.sirok@fs.uni-lj.si

ABSTRACT

In this paper, melt film adhesion was studied on an industrial spinning machine. Parametric dependence of melt film structural dynamics on the spinner wheel rotational speed and film width was investigated by measurements of film velocity and gray level. A temperature estimation algorithm was developed to convert gray level from images recorded in visible light spectrum to absolute temperature fields. Spatial fluctuations in melt film temperature are significant, indicating a highly non-uniform melt viscosity along the wheel perimeter. Based on the results, phenomenological models for melt film adhesion were formed, showing a characteristic influence of the film Reynolds number and width on its temperature and consequently, also on the properties of forming fibers.

Key Words: *Spinning wheel, Mineral wool, Melt film, Adhesion, Flow visualization, Temperature estimation*

1. INTRODUCTION

Mineral wool is an inorganic fibrous insulation material with excellent sound and heat insulation properties. It is most commonly produced on a spinner [1] where melt is fed on fast-spinning wheels, forming a thin radial film from which the fibers are formed. Initial fiber formation is governed by centrifugal force, viscous resistance and surface tension [2] and is one of the most important phases in mineral wool production, determining the end product quality.

To attain optimal and reasonably uniform fiber properties (i.e., thickness and length), it is important that the melt film adheres well to the spinner wheel, with minimum spatial and temporal fluctuations in thickness, temperature and velocity [1]. While melt film velocity determines the effect of centrifugal force which drives fiber growth, melt temperature affects its surface tension and viscosity that dampen the growth. Surface tension changes little with temperature [1], but viscosity increases exponentially as the melt temperature decreases [3]. Due to the complex hydrodynamics of the melt film and a large number of operating parameters that must be taken in consideration, it is necessary to improve the understanding of the melt film adhesion mechanism by developing proper adhesion models.

In the present study, melt film adhesion on an industrial spinner wheel was investigated experimentally by visualization methods. Analysis of the melt film flow characteristics on the spinner wheel was based on the film velocity calculation by our image velocimetry method [4] implemented in the *ADMflow* software and by temperature estimation from the image gray level. Phenomenological models for characterization of melt film adhesion are proposed.

2. METHODOLOGY

Experiment was conducted on the first wheel of an industrial spinner. Melt film that forms on the wheel surface and from which fiberization occurs was visualized using a high speed CCD camera at 18660frames/s. Experimental setup is shown in Fig. 1.

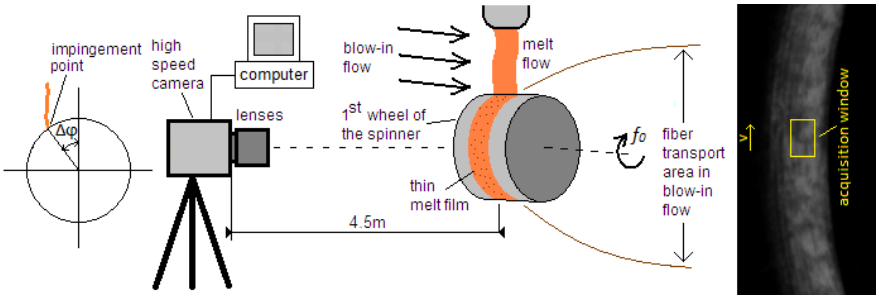

FIGURE 1. Experimental setup for visualization of the fiberization process and a sample image with data acquisition window

A 2500-image sequence was recorded for each of the 10 operating points used. Spinner wheel rotational speed was varied between f_0 = 100Hz and 117Hz. We also used 3 different melt stream impingement positions, $\Delta\phi$ (0.5rad, 0.7rad and 1.0rad, which corresponds to high, normal and low position, respectively) and 3 different wheel cooling water flow rates, Q_C (normal, normal+80%, normal+160%).

Then, melt film circumferential velocity was calculated in a window shown in Fig. 1. For the purpose of velocity calculation, an advection-diffusion equation-based, computer-aided visualization method developed by Bajcar et al. [4] and implemented in the *ADMflow* software (http://admflow.net) was used.

Next step was to estimate melt temperatures from images recorded in visible light spectrum. Hot melt film on the spinner can be assumed to radiate as a black body (Stefan-Boltzmann law 1879, 1884), hence melt absolute temperature (T) is (nonlinearly) proportional to the image gray level $0 \leq G \leq 255$. Temperature was calculated by Eq. (1):

$$T = C\sqrt[4]{\frac{G}{k \cdot \eta(T) \cdot t_E \cdot \sigma_S}} \;\; ; \;\; C(t_E = 6\mu s) = 0.3409 \;\; ; \;\; \sigma_S = 5.67 \cdot 10^{-8} Wm^{-2}K^{-4} \qquad (1)$$

In eq. (1), $\eta(T)$ is the light efficacy, i.e. the ratio between luminous flux and total radiation power incident on the camera sensor. It changes with the temperature, thus Eq. (1) must be solved iteratively. Camera exposure time is given by t_E while k = 388.6(gray levels)/lux·s is the CCD sensor sensitivity. Constant C changes with t_E and is determined by calibration to a surface with a known temperature.

Using Eq. (1), melt film temperature fields can be obtained from recorded images. In Fig. 2, a typical grayscale process image is shown along with the temperature field calculated by Eq. (1) and a binary image that shows regions of melt film with T > 1500K. From Fig. 2 it is evident that melt surface temperature field can be highly non-homogenous with fluctuations in excess of 100K. Also, there are well visible voids within the melt film where little or no melt is present, indicating a poor melt adhesion and wheel surface wetting. For this reason, a study of melt film gray level and temperature can provide valuable information about the quality of film adhesion.

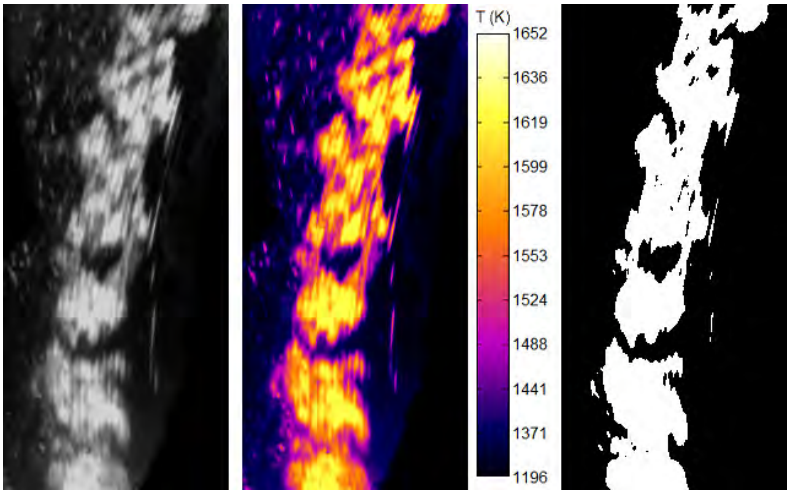

FIGURE 2. Left: input grayscale image. Center: estimated temperature field image. Right: binary image with melt film areas that exceed T = 1500K colored white

3. RESULTS

Time series of film gray levels ($G(t)$), velocities ($v(t)$) and temperatures ($T(t)$) were obtained from instantaneous spatially averaged values within the acquisition window (Fig. 1). Then, the temporal averages of these time series (i.e., $|v|$, $|G|$ and $|T|$) were calculated. Mean melt film temperature $|T|$ was chosen as the most characteristic measure of film adhesion as it significantly affects melt viscosity and also reflects non-homogeneities in the topological structure of the film.

We propose a following phenomenological model for $|T|$ with c_0, c_1 and c_2 as fitting constants:

$$|T| = c_0 \cdot Re^{c1} \cdot q^{c2} \tag{2}$$

In Eq. (2), Re is the Reynolds number (Eq. (3)) and q is the flow number (Eq. (4)):

$$Re = \frac{2vR\rho}{\mu} \tag{3}$$

$$q = \frac{Q}{W}\frac{\rho}{\sqrt{R\sigma}} \tag{4}$$

In Eqs. (3) and (4), R is spinner wheel radius, Q melt flow rate and W mean film width on the wheel. ρ, μ and σ denote melt density, dynamic viscosity and surface tension, respectively, and depend on $|T|$.

By least-squares fitting the model from Eq. (2) to the calculated Re, We and $|T|$ we get

$$|T| = 1123 \cdot Re^{0.0427} \cdot q^{0.0175} \tag{12b}$$

There is a good agreement between modeled and measured temperatures (r^2 = 0.995, Fig. 3). Higher Reynolds numbers seem to occur at higher temperatures, which can be explained by the fact that at higher $|T|$, melt viscosity is reduced. Faster wheel rotation may increase Re if velocity increase has a predominant effect, or decrease it if the effect of increased viscosity due to increased film heat rejection rate is more pronounced. Mean temperature also grows slightly if flow number is increased. If Q remains unchanged and W is reduced, melt film becomes thicker, thus increasing both temperature and q.

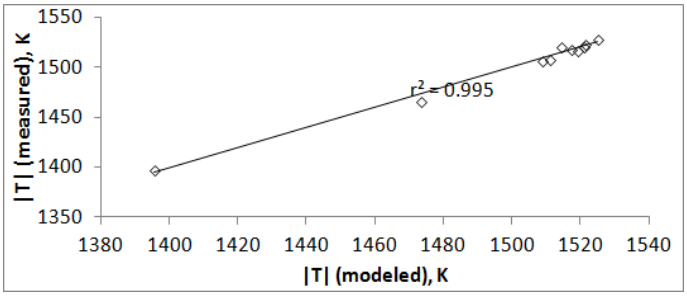

FIGURE 3. Comparison between measured and phenomenological model-predicted |*T*|

Apart from the mean melt film temperature, temperature fluctuations are also an important measure of film adhesion. Larger fluctuations mean more non-uniform melt viscosity along the wheel perimeter. A good measure for temperature oscillations is the standard deviation, std(*T*). Using data fit analogous to Eq. (2), we obtain a following relation for std(*T*) with a good r² value of 0.944:

$$std(T) = 5.29 \cdot Re^{-0.277} \cdot q^{0.356} \tag{5}$$

Model given by Eq. (5) suggests that melt film temperature field is more uniform at lower flow numbers (i.e., higher film width) and higher Reynolds numbers. Again, the Reynolds number may either rise or drop with rising spinner wheel rotational speed.

4. CONCLUSIONS

Mineral wool melt adhesion to the wheel of an industrial spinning machine was studied using high-speed camera visualization. Recorded images were analyzed numerically to determine the structural dynamics and velocities of the melt film and a model for temperature field estimation from image gray level was developed. Data was then combined to form phenomenological models for temperature average and standard deviation as key parameters for evaluation of melt film adhesion. Presented models can be used to estimate temperature field non-homogeneity caused by a non-homogenous melt film topological structure on spinner wheels. By proper variation of spinner operating parameters considering the obtained phenomenological models, tearing of the melt film can be minimized. This way, more uniform fiberization conditions (e.g. melt velocity, viscosity and thickness) can be attained in an industrial mineral wool production line, leading to improvements in the end product quality. However, presented phenomenological models are also valuable for subsequent numerical modeling of the process that will further improve the understanding of melt film formation and disintegration.

REFERENCES

[1] B. Širok, B. Blagojević and P. Bullen, *Mineral Wool: Production and Properties*; Woodhead Publishing Limited, Cambridge, 2008.

[2] J. Liu, Q. Yu, P. Li, and W. Du, Cold experiments on ligament formation for blast furnace slag granulation, *Applied Thermal Engineering*, 40(1), 351–357, 2012.

[3] T. Lakatos, L.G. Johannson, and B. Simmingsköld, Viscosity and liquids temperature relations in the mineral-wool part of the system SiO_2-Al_2O_3-CaO-MgO-Alkalies-FeO-Fe_2O_3, *Glasteknisk Tidskrift*, Vol. 36, No. 4, pp. 51-55, 1981.

[4] T. Bajcar, B. Širok, and M. Eberlinc, Quantification of flow kinematics using computer-aided visualization. *Strojniški vestnik – Journal of mechanical engineering*, 55(4), 215-223, 2009.

Third International Conference on Computational Methods for Thermal Problems
THERMACOMP2014, June 2-4, 2014, Lake Bled, Slovenia
N. Massarotti, P. Nithiarasu and B. Sarler (Eds.)

EXTERNAL FLOW CONJUGATED PROBLEM ANALYSIS VIA INTEGRAL TRANSFORMS AND SINGLE DOMAIN FORMULATION

Kleber M. Lisbôa and Renato M. Cotta*
Federal University of Rio de Janeiro, UFRJ
Laboratory of Transmission and Technology of Heat - LTTC
Department of Mechanical Engineering, POLI/COPPE, Rio de Janeiro, Caixa Postal 68503,
Cidade Universitária, 21941-972, Brazil
(*Corresponding author: cotta@mecanica.coppe.ufrj.br)

ABSTRACT

This work advances a hybrid integral transforms methodology for the solution of conjugated heat transfer problems involving the thermal interaction between a solid wall and an external flow. A single domain formulation strategy is employed, coupling the two regions (solid and fluid) by accounting for the transition of the materials through space variable thermophysical properties and source terms with abrupt variations at the interface. The resulting energy equation is solved using a hybrid numerical-analytical technique known as the Generalized Integral Transform Technique (GITT). Illustrative results of the converged eigenfunction expansions for the temperature field are presented, for the test case of a flat plate subjected to an internal uniform heat generation.

Key Words: *Conjugated Heat Transfer, External Forced Convection, Single Domain Formulation, Hybrid Methods, Integral Transforms.*

1. INTRODUCTION

Conjugated heat transfer problems were first identified as such by Perelman (1961) and Luikov et al. (1971), and further studied by many others along more than fifty years. They can be easily spotted in almost every process or equipment in thermal engineering applications, and are in fact avoided in many practical situations due to their inherent mathematical complexity, by adopting simplified boundary conditions that decouple the heat transfer processes in the fluid and solid regions, but eventually leading to significant error in thermal analysis or design. Normally, when considered in full coupled formulation, this class of heat transfer problem is treated using the same number of energy balance differential equations as the number of regions (solids and fluids) and coupling them using continuity conditions at the interfaces. It is then necessary to solve all such energy equations simultaneously, which may be extremely difficult in some cases, even leading to the need of a time consuming iterative technique.

In this context, the present work is aimed at advancing a robust, accurate and fast analytical approach for solving conjugated heat transfer problems, based on combining integral transforms and a single domain formulation strategy, first introduced in the context of internal flows (Knupp et al., 2012), but here extended to consider a solid body immersed in a flow. A key aspect in this technique is that instead of establishing one energy equation for each domain, a single domain formulation is written that accounts for the thermophysics of the various regions and incorporates the transitions between them through abrupt variations of space variable thermophysical properties, drastically diminishing the complexity and the computational time required to simulate such situations. Then, the auxiliary eigenvalue problem that offers the basis for the temperature eigenfunction expansion, accounts for the space variations of the energy equation coefficients. A simple test case of a flat plate subjected to an air flow and an uniform heat generation within the wall is more closely considered to demonstrate the suitability of the proposed approach.

2. ANALYSIS

The physical illustration of the test case is presented in Figure 1. It consists of a 0.1 m long flat plate with 7 mm thickness, exposed to an external boundary layer and an uniform internal heat source such as one generated by an electrical current. The plate is insulated at the bottom and the right edges, and has a prescribed temperature at the left edge, equal to the free stream temperature. The two different regions (solid and fluid) across the single domain are represented by abrupt variations in the thermophysical properties yielding the formulation in equations (1.a-f), including the advection terms in order to account for the external convection, which vanish in the solid region. For this simple case these velocities fields can be readily obtained by the Blasius solution (Schlichting, 1979), or in more general cases the boundary layer equations can be solved using the Generalized Integral Transform Technique itself. The longitudinal diffusion term, that is usually neglected within boundary layer models, is here retained for consistency with the heat conduction model for the solid region.

$$w(y)\frac{\partial T}{\partial t} + w_f u(s,y)\frac{\partial T}{\partial s} + w_f v(s,y)\frac{\partial T}{\partial y} = k(y)\frac{\partial^2 T}{\partial s^2} + \frac{\partial}{\partial y}\left[k(y)\frac{\partial T}{\partial y}\right] + g(y,t) \tag{1.a}$$

$$T(s,y,0) = T_\infty \tag{1.b}$$

$$T(0,y,t) = T_\infty;\ \left.\frac{\partial T}{\partial s}\right|_{s=L} = 0 \tag{1.c,d}$$

$$\left.\frac{\partial T}{\partial y}\right|_{y=0} = 0; T(s,\delta_c,t) = T_\infty \tag{1.e,f}$$

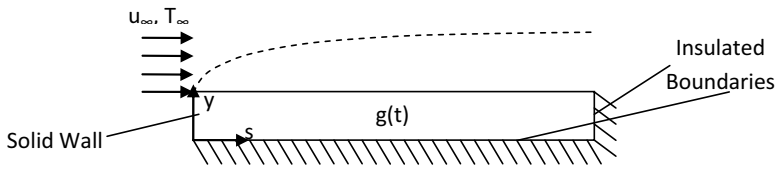

FIGURE 1. Conjugated heat transfer representation for a flat plate exposed to an external boundary layer and an uniform internal heat source

The adopted dimensionless groups and the resulting dimensionless model are presented in equations (2.a-i) and (3.a-h), respectively:

$$S = \frac{s}{L};\ \eta = \frac{y}{\delta_c};\ \tau = \frac{\alpha_f t}{L^2};\ \theta = \frac{T-T_\infty}{\Delta T_c};\ U = \frac{u}{u_\infty};\ V = \frac{v\sqrt{Re_\infty}}{u_\infty};\ W = \frac{w}{w_f};\ K = \frac{k}{k_f};\ F = \frac{L}{\delta_c} \tag{2.a-i}$$

$$W(\eta)\frac{\partial \theta}{\partial \tau} + Pe_\infty U(S,\eta)\frac{\partial \theta}{\partial S} + \frac{Pe_\infty F}{\sqrt{Re_\infty}}V(S,\eta)\frac{\partial \theta}{\partial \eta} = K(\eta)\frac{\partial^2 \theta}{\partial S^2} + F^2\frac{\partial}{\partial \eta}\left[K(\eta)\frac{\partial \theta}{\partial \eta}\right] + G(\eta,\tau) \tag{3.a}$$

$$\theta(S,\eta,0) = 0 \tag{3.b}$$

$$\theta(0,\eta,\tau) = 0;\ \left.\frac{\partial \theta}{\partial S}\right|_{S=1} = 0 \tag{3.c-d}$$

$$\left.\frac{\partial \theta}{\partial \eta}\right|_{\eta=0} = 0;\quad \theta(S,1,\tau) = 0 \tag{3.e-f}$$

$$\text{with } K(\eta) = \begin{cases} K_1, \eta \le \eta_i \\ K_2, \eta > \eta_i \end{cases};\ W(\eta) = \begin{cases} W_1, \eta \le \eta_i \\ W_2, \eta > \eta_i \end{cases} \tag{3.g,h}$$

The Generalized Integral Transform Technique (GITT) (Cotta, 1993) is now employed in the hybrid numerical-analytical solution of problem (3). It consists in the proposition of an eigenfunction expansion for the temperarture field, which is based on the eigenvalue problem with space variable

coefficients, which carries the information on the transition of the solid and fluid regions. Thus, a multilayer Sturm-Liouville eigenvalue problem as shown in equations (4.a-g) is here proposed, and the abrupt space variations of thermophysical properties are naturally included in the eigenfunction expansion, as follows:

$$K_m\left(\frac{\partial^2\Psi_{m,i}}{\partial S^2}+F^2\frac{\partial^2\Psi_{m,i}}{\partial\eta^2}\right)+{\lambda_i}^2 W_m\Psi_{m,i}(S,\eta)=0, m=1,2 \tag{4.a}$$

$$\Psi_{m,i}(0,\eta)=0;\ \left.\frac{\partial\Psi_{m,i}}{\partial S}\right|_{S=1}=0 \tag{4.b,c}$$

$$\left.\frac{\partial\Psi_{1,i}}{\partial\eta}\right|_{\eta=0}=0;\Psi_{1,i}(S,\eta_i)=\Psi_{2,i}(S,\eta_i);-K_1\left.\frac{\partial\Psi_{1,i}}{\partial\eta}\right|_{\eta=\eta_i}=-K_2\left.\frac{\partial\Psi_{2,i}}{\partial\eta}\right|_{\eta=\eta_i};\ \Psi_{2,i}(S,1)=0 \tag{4.d-g}$$

The transform-inverse pair is then given as in equations (5.a,b), which allow for the transformation to reduce the original partial differential equation to a system of ordinary differential equations.

$$\bar{\theta}_i(\tau)=\int_0^1\int_0^{\eta_i}W_1\widetilde{\Psi}_{1,i}(S,\eta)\theta(S,\eta,\tau)d\eta dS+\int_0^1\int_{\eta_i}^1 W_2\widetilde{\Psi}_{2,i}(S,\eta)\theta(S,\eta,\tau)d\eta dS \tag{5.a}$$

$$\theta(S,\eta,\tau)=\sum_{i=1}^{\infty}\bar{\theta}_i(\tau)\begin{cases}\widetilde{\Psi}_{1,i}(S,\eta),\eta\le\eta_i\\ \widetilde{\Psi}_{2,i}(S,\eta),\eta>\eta_i\end{cases} \tag{5.b}$$

Once one applies the integral transformation $\int_0^1\int_0^{\eta_i}W_1\widetilde{\Psi}_{1,i}(S,\eta)\_d\eta dS+\int_0^1\int_{\eta_i}^1 W_2\widetilde{\Psi}_{2,i}(S,\eta)\_d\eta dS$ to the partial differential model of equation (3.a), equations (6.a-c) are obtained, which form a finite system of coupled linear ordinary differential equations upon truncation of the series that represents the inverse formula to a sufficiently large finite order N.

$$\frac{d\bar{\theta}_i}{d\tau}+\sum_{j=1}^{N}\Omega_{i,j}\bar{\theta}_j(\tau)=\bar{g}_i(\tau),i,j=1,2,\dots,N \tag{6.a}$$

$$\bar{\theta}_i(0)=0 \tag{6.b}$$

$$\text{where }\Omega_{i,j}={\lambda_i}^2\delta_{i,j}+\int_0^1\int_{\eta_i}^1 Pe_\infty W_2\widetilde{\Psi}_{2,i}(S,\eta)\left\{U(S,\eta)\frac{\partial\widetilde{\Psi}_{2,j}}{\partial S}+\frac{F}{\sqrt{Re_\infty}}V(S,\eta)\frac{\partial\widetilde{\Psi}_{2,j}}{\partial\eta}\right\}d\eta dS \tag{6.c}$$

$$\bar{g}_i(\tau)=\int_0^1\int_0^1 G(\eta,\tau)\widetilde{\Psi}_{1,i}(S,\eta)d\eta\,dS \tag{6.d}$$

The truncated transformed system can be analytically solved through matrix exponentials, and the final solution to the transformed potential is obtained as in equation (7).

$$\bar{\theta}_i(\tau)=e^{-[\Omega_{i,j}]\tau}\int_0^\tau e^{[\Omega_{i,j}]\tau'}\bar{g}_i(\tau')d\tau' \tag{7}$$

3. RESULTS

Results are now reported for the considered test case and as an example the following heat source term was used:

$$G(\eta,\tau)=\begin{cases}K_1F^2(1-e^{-10\tau}),\eta\le\eta_i\\ 0,\eta>\eta_i\end{cases} \tag{8}$$

Results for an air free stream velocity of 1 m/s were obtained, with the following dimensionless input data W_1=0.604719, W_2=1, K_1=4.61538, K_2=1, Re=5950.58, Pe=4165.41, and F=5.7568. The position which corresponds to the solid-fluid interface is η_i=0.402976. The dimensionless temperature transversal profiles are presented in Figures 2a,b, for two different longitudinal positions, S=1/2 and 1. In each figure, four different curves are shown, corresponding

to different time values, in order to show the time evolution of the temperature field along the transversal coordinate, covering the whole solid and fluid regions.

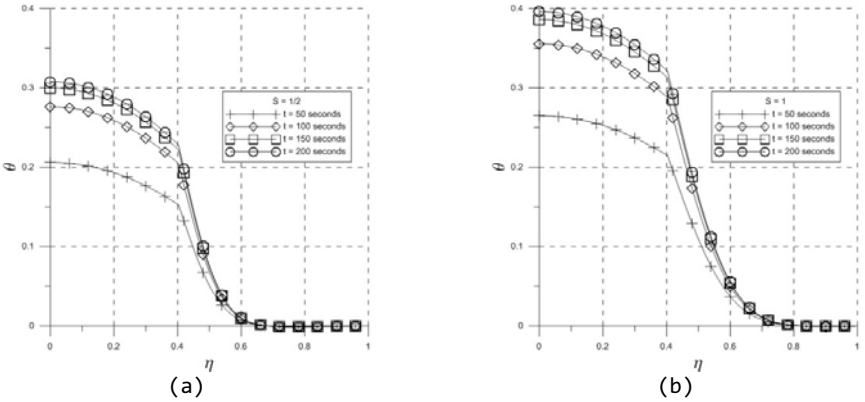

FIGURE 2. Dimensionless temperature field for two longitudinal positions: (a) S=1/2; (b) S=1

4. CONCLUSIONS

An integral transforms solution to conduction-external convection conjugated problems has been presented, in combination with a single domain formulation that gathers the solid and fluid regions in just one energy equation with space variable coefficients. The required analytical and computational steps in the solution methodology are then markedly simplified. Aside from the truncation of the transformed system, the present approach is formal and exact, being a fully analytical procedure, which brings enormous advantages in both computational cost and robustness. The proposed methodology may also be extended to more involved problems, including irregular geometries, complex configurations and simultaneous solution of the flow problem.

REFERENCES

[1] Cotta, R.M., *Integral Transforms in Computational Heat and Fluid Flow*, CRC Press, Boca Raton, 1993.

[2] Knupp, D. C., C. P. Naveira-Cotta, and R. M. Cotta, "Theoretical Analysis of Conjugated Heat Transfer with a Single Domain Formulation and Integral Transforms", *Int. Comm. Heat & Mass Transfer*, V.39, no.3, pp.355-362, 2012.

[3] Luikov, A.V., Aleksashenko, V.A., and Aleksashenko, A.A., *Analytical Methods of Solution of Conjugated Problems in Convective Heat Transfer*, Int. J. Heat and Mass Transfer, Vol. 14, pp. 1047-1056, 1971.

[4] Perelman, Y.L., *On Conjugate Problems of Heat Transfer*, Int. J. Heat and Mass Transfer, Vol. 3, pp.293-303, 1961.

[5] Schlichting, H., *Boundary Layer Theory*, 7th edition, McGraw-Hill, New York, 1979.

Third International Conference on Computational Methods for Thermal Problems
THERMACOMP2014, June 2-4, 2014, Lake Bled, Slovenia
N. Massarotti, P. Nithiarasu and B. Sarler (Eds.)

DEVELOPMENT OF AN OPTIMUM REFLECTIVE METAL INSULATION USING COMPUTATIONAL FLUID DYNAMICS

M. H. Eo, S. M. Lee, W.S. Kim
R&D Center BHI CO., LTD., Gyeongnam, South Korea, mheu@bhi.co.kr, smlee@bhi.co.kr, wskim@bhi.co.kr

ABSTRACT

Generally, materials of low thermal conductivity are used for thermal insulation. But it is necessary to build up a safety-enhanced Reflective metal insulation (RMI) of high thermal conductivity in nuclear power plant. RMI is made of thin stainless plate with low emissivity and closed air space. Thermal radiation is blocked by stainless steel with low emissivity. Thermal conductivity and thermal convection are blocked by closed air space. Analysis of the conjugate heat transfer in RMI including an air layer, using computational fluid dynamics (CFD), is presented. The analysis consisted of the study of heat transfer in the air layer to determine the heat flow that passed through RMI. Especially, different combinations of air layer thickness with parallel partitions were analyzed to improve the insulating capacity of RMI. Computational analysis showed that the radiation heat was dramatically reduced, when there was an increase in the number of thin plates. However the number of thin plates of RMI is limited by the production costs and RMI with 7 partitions (thickness of air layer: 0.85cm) can perfectly prevent the generation of the convection of air.

Key Words: *CFX, Reflective Metal Insulation, Radiation Heat Transfer, Air Layer Thickness.*

1. INTRODUCTION

The recent Fukushima accident in Japan is increasing concerns about safety in nuclear power plants. Existing insulation used to minimize thermal losses is difficult to apply for a nuclear reactor, steam generator, pressurizer and recirculation pump in nuclear power plants where the high level of safety is required. Especially, the conservative insulation is difficult to apply for the NPP facilities for the operator's safety because it has unstable chemical and structural property, is easy to degrade, and causes the harmful gases in the accident and the high temperature. Therefore, a safety-enhanced reflective metal insulation (RMI) is needed to overcome this weakness. RMI is made of stainless thin plate with low emissivity and closed air space. Thermal radiation is blocked by stainless steel with low emissivity. Thermal conductivity and thermal convection are blocked by closed air space. In this study, we analyzed for the air layer thickness which is the most important factor for the RMI design by using computational fluid dynamics.

2. EXPERIMENTAL & SIMULATION

2.1 Experimental of the reflective metal insulation

The thermal conductivity of RMI was measured for comparison with the simulation result. The test method of ASTM C 518 was utilized for this measurement. [1] Figure 1 shows the configuration of the RMI and the sample. Table 1 shows sample information. Thermal resistance of the sample can be obtained by utilizing HFM436 (thermal conductivity measuring equipment). At this time, the direction of heat flow is downward. In the experiment, the thermal conductivity of RMI is 0.037W/m·K and the thickness of RMI is 0.075m. Therefore the thermal resistance of RMI is calculated as 2.027m^2K/W by division thickness to thermal conductivity.

2.2 Model of the reflective metal insulation

The analysis of the RMI considers the solution of the conjugate heat transfer (radiation, conduction, convection) between the solid and the air layer which was obtained by CFD with CFX-code. The temperature used in hot surface is 303K (30°C) and the temperature of the cold surface is 283K (10°C). Then, the boundary conditions are: left and right adiabatic boundary, bottom and top isothermal boundary and no-slip condition in the walls (including the partitions). [2] In the solid-gas interface, the temperature and the heat flux must be continuous. Shear stress transport model was used for the turbulence analysis and discrete transfer model was used for the radiation analysis. In this study, different combinations of air layer thickness with vertical, horizontal partitions were analyzed by using the CFD.

Sample dimension	Material	Thermal conductivity	Emissivity	Surface thickness	Layer thickness	Layer numbers
300(w) x 300(l) 75(h)	SUS304	15.2(w/m·K)	0.2	1(mm)	0.1(mm)	8(#)

TABLE 1. Reflective metal insulation sample information

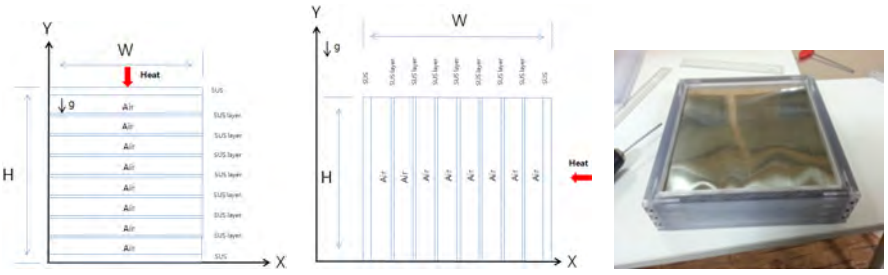

FIGURE 1. Reflective metal insulation sample
(a) Vertical direction of heat flow, (b) Horizontal direction of heat flow, (c) RMI

3. RESULTS

In the case of an air layer with 0.85cm of thickness and 7 parallel partitions, the thermal resistance of RMI is calculated as 2.350m^2K/W by CFD analysis. The computational result is validated by the experimental result. The computational and experimental results (2.027m^2K/W) show fairly good agreement. Therefore, the computational analysis can be applied for the expectation of the additional RMI experiment. The computational analysis is performed by the cases for 1, 3, 7 and 15 partitions in the vertical and the horizontal direction of the heat flow. The result of the analysis shows that the heat transfer is caused by the convection of air in case of 1 and 3 partitions. The convection of air is generated more actively in the horizontal direction because of the influence of gravity such as Figure 3. For insulation efficiency, prevention of the convection is required. The thickness of air is influenced by the convection of air and increase of the thickness cause the generation of the convection of air such as Figure 2(a). Therefore, number of partitions can be used for the prevention of convection of air. The computational analysis shows 7 partitions can perfectly prevent the generation of the convection of air such as Figure 2(b). Therefore, in the case of more than 7 partitions, heat transfer is caused by radiation and conduction of air. Direction of the heat flow does not affect heat transfer of the conduction and radiation. And in case of more than 7

partitions, computational analysis shows almost the same heat flux in the vertical and the horizontal direction of the heat flow such as Figure 4(a) and 4(b).

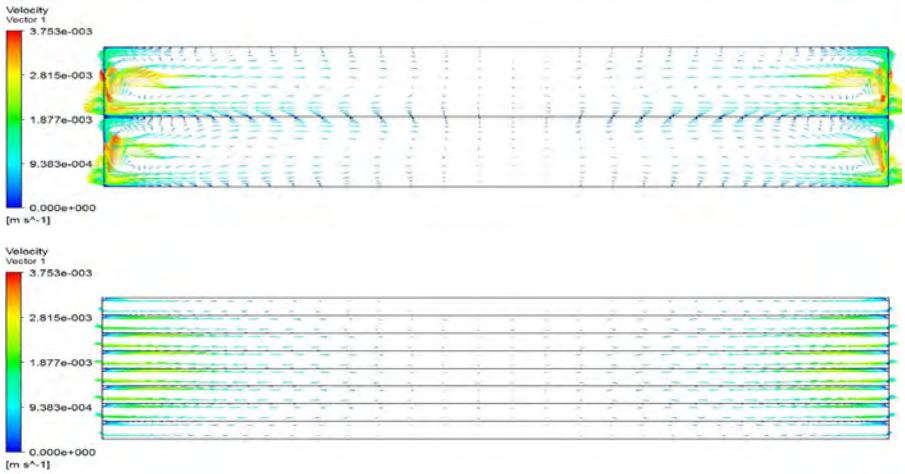

FIGURE 2. Velocity profile of RMI with vertical direction of heat flow
(a) 1 partition, (c) 7 partitions

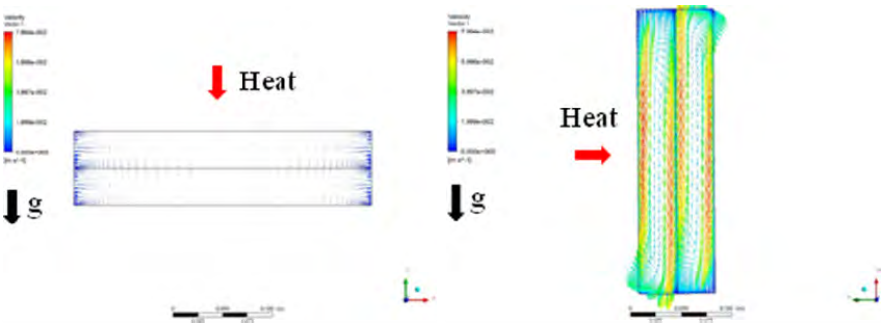

FIGURE 3. Velocity profile of RMI with 1 partition
(a) Vertical direction of heat flow, (b) Horizontal direction of heat flow

Radiation heat transfer is determined by surface property of materials and temperature difference of objects. [3] When the number of partitions increases, the radiation heat loss is dramatically reduced. Because the stainless thin plates act as a radiation shield. When the number of the thin film doubles, heat transfer by radiation decreases to about half such as Figure 4(a) and 4(b). When the number of partitions increase from 7 partitions to 15 partitions, heat flux by conduction of air slightly increases, because RMI is considered as the thermal resistance network for heat transfer through an eight-layer plane wall. The total heat resistance of air is reduced by reduction of air space.

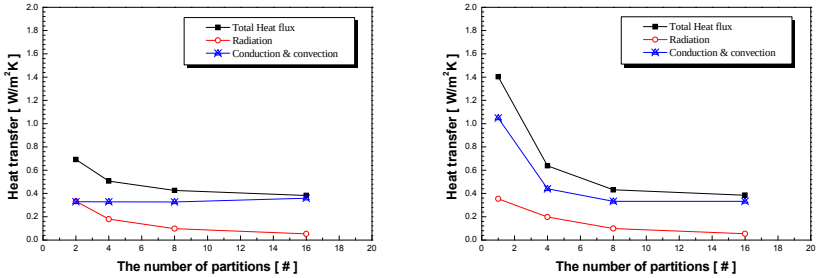

FIGURE 4. Heat flux of RMI with other direction of heat flow (a) Verticality, (b) Horizontality

4. CONCLUSIONS

Insulating capacity of the RMI according to the thickness of the air layer was analyzed by Computational fluid dynamics. The results are as follows.

1. In case of an air layer with 0.85cm of thickness and 7 parallel partitions, Heat transfer by convection is completely blocked. Therefore, the number of partitions is seven or more, the heat transfer by convection does not occur.
2. The number of the stainless thin plates must be minimized, because it can reduce thermal resistance of air.
3. When the number of partitions increases, radiation heat loss is dramatically reduced. Because the stainless thin plates act as a radiation shield. However the number of thin plates of RMI is limited by the production costs. Therefore, the number of thin plates should be determined by considering the economic efficiency.

ACKNOWLEDGEMENT

This study was performed as a part of “Development of the Safety-enhanced Reflective Metal Insulation” project sponsored by Ministry of Knowledge Economy Department.

REFERENCES

[1] Y.C. Kwon, J.G Joo, A Study on the thermal resistance of the Air Space according to the Surface Emissivity of Reflective Insulation, KIAEBS (2011) 89-95.

[2] G.M. Armando, B.B. J. Armando, Analysis of the conjugate heat transfer in a multi-layer wall including an air layer, Applied Thermal Engineering 30 (2010) 599–604.

[3] Richard T. Bynum. Jr. , “INSULATION HANDBOOK”, McGraw-Hill, 2001.

Third International Conference on Computational Methods for Thermal Problems
THERMACOMP2014, June 2-4, 2014, Lake Bled, Slovenia
N. Massarotti, P. Nithiarasu and B. Sarler (Eds.)

INFLUENCE OF INJECTION RATE AND THE NUMBER OF ROWS OF HOLES ON THE EFFECTIVENESS OF FILM COOLING OF GAS TURBINE BLADES

Mahfoud Kadja, Zakarya Tifraten, Bilal Guechi
Laboratory of Applied Energetics and Pollution, University Constantine 1, Route d'Ain El Bey, Constantine 25000, Algeria, E-mail: jegm.cirta@caramail.com

ABSTRACT

The present work aims to study the film cooling of gas turbine blades. The turbulence model k- ε has been applied and the governing equations were solved using a software based on finite volume and finite difference methods. The results obtained during the validation of the code have been found in good agreement with the numerical or experimental data already published in the literature. Two studies were then performed following the validation process: The first study focused on the effect of injection rate on the cooling effectiveness and the second study examined the effect of increasing the number of rows of cooling holes. For each study, the profiles of effectiveness and cooling temperature were plotted as a function of the position along the flow field. The results showed that both parameters are equally important in film cooling.

Key Words: *Film Cooling, Cooling Effectiveness, Injection Rate, Turbulence Model, Number of Rows Of Holes.*

1. INTRODUCTION

Several research studies have been made on film cooling. All were designed to improve the effectiveness of this type of cooling in general and for specific configurations to find optimal cooling. According to Bunker [1] there have been over 2700 articles on the subject during the last forty years. Goldstein et al [2] have studied the characteristics of the lateral injection hole using an angle of inclination between 15 and 35 degrees. Mehendale and Han [3] have studied the influence of high mainstream turbulence on the cooling coefficient at the leading edges of the blades. The orientation angle was 90 degrees and the results indicated that the effectiveness of the film decreases with the increase of the injection rate, but the opposite was true for the heat transfer coefficient. Honami et al [4] made an experimental study of the behavior of a laterally injected jet over a flat surface using a jet holes orientation angle of 90 degrees. They measured the temperature of the surface as well as the dynamic and thermal fields above the surface. Schmidt et al [5] measured the film cooling effectiveness of using a row of compound angle holes inclined at 60 degrees. Ekkad et al [6] studied the cooling effectiveness over a flat surface with air and CO_2 injection through compound angle holes using a transient liquid crystal image method. The tests yielded the heat transfer coefficients and the distributions of the film effectiveness for compound angles ranging from 0 to 90 deg.

2. GEOMETRY, MESH AND CONDITIONS OF THE TWO STREAMS INVOLVED IN THE COOLING

Figure 1a shows a film cooled blade. The air escapes through the holes on the leading edge in order to cool the blade surface. A row of holes disposed on each side of the leading edge serves to cool the lower and upper surfaces by covering them with a film of fresh air. Figure 1b shows the symmetric calculation area which is selected to model film cooling in the case of a single row of

holes. This model was considered experimentally by Sinha et al. [7] for the case where the hot gas is at a temperature of T_∞ = 300 K and wherein the cold air stream is at the temperature T_C = 150 K.

The central vertical plane through the hole and the wall creates a symmetrical calculation field. The hole diameter is D = 12.7 mm and a length-to-diameter ratio L/D=1.75 was used in the computations. The cooling fluid is injected at an angle of 35°. An unstructured mesh of this geometry was determined using the Gambit code. A step of 2 mm was used on all domain boundaries, which gave a high-quality mesh with 453,000 cells. Figure 2 shows the mesh in the region around the hole. The Reynolds number based on the diameter of the hole is Re = 16000, and the injection rate is M = 0.5. M is the ratio of the mass flow through the two flow sections (cold fluid / hot fluid). The temperatures ratio of hot and cold fluids was taken equal to T_∞ / T_c = 1.97 where T_c is the temperature of the coolant and T_∞ is the temperature of the hot gas T_∞ = 300 K.

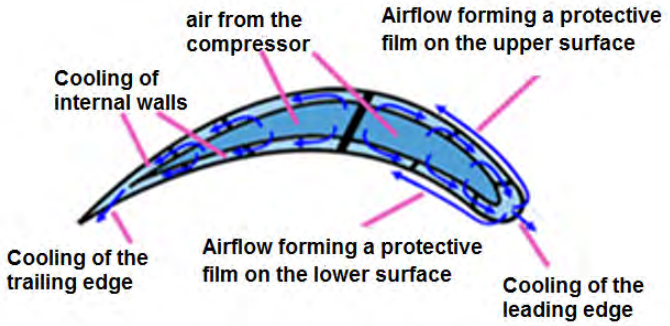

(a)

(b)

FIGURE 1. Computational domain

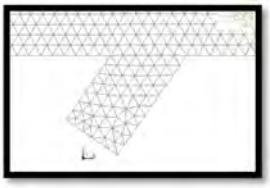

FIGURE 2. Mesh of the computational domain near the exit hole of the cooling jet

3. RESULTS AND DISCUSSION

In this section, we present the results obtained in the present aerothermal study of film cooling of the leading edge of a gas turbine blade. The contours of the static temperature for an injection rate of M = 0.5 is shown in Figure 3.

It is noted from this figure that the temperature of the fluid gradually increases downstream of the hole. This can be attributed to the process of mixing between the hot gas and the mainstream of the injected cooling air. The temperature along the hole is maintained at 153 K up to the intersection region of the flows.

The local film cooling effectiveness η in this work is taken as a function of the temperature of the main current T_∞, the wall temperature T_w and the temperature T_c of the coolant, using the following formula:

$$\eta = \frac{T_\infty - T_w}{T_\infty - T_c}$$

The cooling effectiveness is dimensionless and is used to interpret the decline of the temperature distribution in the transverse direction z along the wall. One can see in Figure 4 the effect of increasing the injection rate of 0.5 to 1.5 on the variation curves of the film cooling effectiveness. We notice an increase of the cooling effectiveness for z <8mm and a decrease of η beyond this value.

Figure 5 shows the effect of the number of holes on the cooling effectiveness. It is very evident from the figure that increasing the number of rows of holes leads to a greater value of η, that is to say to lower wall temperatures at which the hot gas flows.

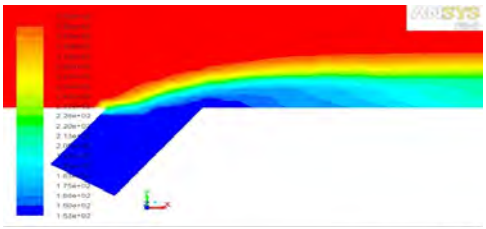

FIGURE 3. Isotherms around the jet exit

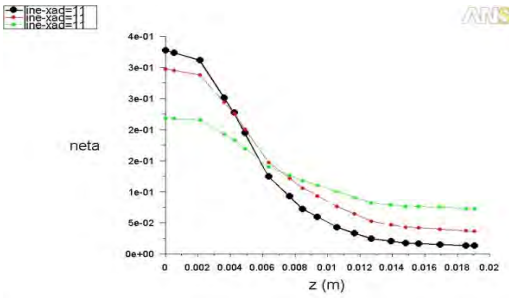

FIGURE 4. Effect of M (M=0.5, 1.0 and 1.5) on the cooling effectiveness: Profiles of effectiveness as a function of Z, in Y=-4.1 mm, in X/D=11 (• M=0.5, • M=1.0, • M=1.5)

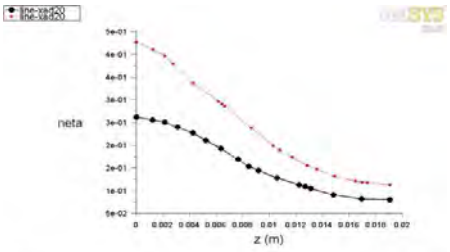

FIGURE 5. Effect of the number of hole rows on the cooling effectiveness. Profiles of effectiveness as a function of Z, in Y=-4.1 mm, in X/D=20 (• 1row, • 2 rows)

4. CONCLUSIONS

The main findings of this investigation of the performance of film cooling for the case of a single row of holes and for the case of two rows of holes with three injection rates are as follows :

(1) The method of film cooling is an effective method to protect the material of the blade from the hot main flow . This is due to the combination of internal convective cooling and outer surface cooling of the blade .

(2) This simulation shows a very good agreement with the results of previous numerical and experimental studies of turbulent film cooling of plates .

(3) There is a decreased film cooling effectiveness when the rate of injection M increases from 0.5 to 1.5. This is due to the cold jet penetration of the upstream flow, which enlarges the film cooling layer. Cooling fluid is therefore blown farther from the wall.

(4)The results of this study led us to recommend the use of small injection ratios in order to maintain the presence of the coolant close to the wall .

REFERENCES

[1] B.S.Bunker, A review of shaped hole turbine film cooling technology, *Journal of Heat Transfer,* 127, 441-453, 2005.

[2] R.J.Goldstein, E.R.G.Eckert, V.L.Eriksen, and J.W.Ramsey, Film cooling following injection through inclined circular tubes, *Israel Journal of Technology*, 8 No. 1–2,145–154, 1970.

[3] A.B.Mehendale, J.C.Han, and S.Ou, Influence of high mainstream turbulence on leading edge heat transfer, *ASME Journal of Heat Transfer*, 113, 843-850, 1991.

[4] S.Honami, T.Shizawa, and A.Uchiyama, Behavior of the laterally injected jet in film cooling: measurements of surface temperature and velocity/temperature field within the jet, *ASME Journal of Turbomachinery*, 116, 106–112, 1994.

[5] D.L.Schmidt, B.Sen, Film cooling with compound angle holes: adiabatic effectiveness, *ASME Journal of Turbomachinery*, 118, 807–813,1996.

[6] S.V.Ekkad, D.Zapata, and J.C.Han, Film effectiveness over a flat surface with air and CO_2 injection through compound angle holes using a transient liquid crystal image method, *ASME Journal of Turbomachinery*, 119, 587–593, 1997.

[7] A.K.Sinha, D.G.Bogard and M.E.Crawford, Film cooling effectiveness downstream of a single row of holes with variable density ratio, *ASME J. Turbomachinery*, 113, 442-449, 1999.

PARALLEL SESSION

REACTIVE HEAT AND MASS TRANSPORT

Third International Conference on Computational Methods for Thermal Problems
ThermaComp2014, June 2-4, 2014, Lake Bled, Slovenia
N. Massarotti, P. Nithiarasu and B. Sarler (Eds.)

Lattice Boltzmann method for thermomechanics of fluid flow with chemical reactions

Arkadiusz Grucelski, **Jacek Pozorski**

Institute of Fluid-Flow Machinery, Polish Academy of Sciences
Fiszera 14, 80-952 Gdańsk, Poland, {agrucelski, jp}@imp.gda.pl

ABSTRACT

A detailed description of thermomechanics of fluid flow through porous media with a release of chemical compounds from grains of solid fuel particles (biomass, coal, etc.) is presented together with first simulation results of a simplified model for degasification process. Following our earlier Lattice Boltzmann benchmark computations for fluid flow and heat transfer, an additional distribution function was used to model the evolution of chemical species. A simulation of the pyrolysis process with the use of a simple reference model of coal devolatilisation, known in the literature, gives first quantitative results along with a notable increase of computational cost. We account here for fluid flow with heat transfer through reactive granular media at the level of a representative element of volume (REV) including also mechanical interactions of solid grains due to their thermal expansion.

Key Words: *porous media flow, heat transfer, LBM, chemical kinetics of pyrolysis.*

1. INTRODUCTION

Coking plants are widely used in coal processing industry to obtain chemically cleaner coal (coke), benzene, ammonium hydroxide and other chemical species (generally known as coal gas) as well as tar. From the fluid thermomechanics point of view, coking occurs in a bed of granular material (coal grains) that upon heating becomes a uniform porous medium. During the coking process, complex phenomena occur at the level of a single grain (pore). They include fluid flow through the bed, thermal conduction, chemical reactions, plastic deformation of medium coupled with the temperature increase, and others.

2. GOVERNING EQUATIONS FOR LBM AND IMPLEMENTATION ISSUES

In the present work we use the Lattice Boltzmann method (LBM), where the flow density and velocity are solved for in terms of the density distribution function, cf. [1], the temperature field is found from the internal energy density distribution function (IEDDF), cf. [2,3], and the evolution of chemical species is governed by a separate distribution function, cf. [4], the form of all these LB equations being similar [2]. An exhaustive description of LBM for fluid flow is available in cited works and references therein. Mechanical stresses between particles (in contact) will be calculated with use of the Discrete Element Method (DEM), which is widely used in practical applications involving granular media. Recently a number of works have been presented that considered a coupled use of LBM (for modelling of fluid flow) and DEM (for solid-solid interactions), cf. [5]. Also, for mechanical interactions of grains, the DEM method can be applied to model plastic deformations in the system [6].

The Lattice Boltzmann equation, discretized in time, space (on a regular square lattice), and velocity (on a set of directions $\mathbf{e}_i$), describes the evolution of a relevant physical field in terms of its distribution function. In our case, we proceed with the simulation of fluid flow, heat transfer and chemical species evolution:

$$f_i(\mathbf{x}+\mathbf{e}_i, t+\delta t) - f_i(\mathbf{x},t) = -\tau_\nu^{-1}(f_i(\mathbf{x},t) - f_i^{eq}(\mathbf{x},t)), \tag{1}$$

where f_i^{eq} represents the equilibrium state of distribution function corresponding to the averaged field at $(\mathbf{x}, t)$; it has the following form:

$$f_i^{eq} = \alpha\Omega_i \left(A_i + B_i \mathbf{e}_i \cdot \mathbf{u} + C_i (\mathbf{e}_i \cdot \mathbf{u})^2 - D_i (\mathbf{u})^2 \right), \tag{2}$$

where $\mathbf{u}$ is the local fluid velocity and the coefficients A_i through D_i depend only on direction i and the discretization scheme (D2Q9, D3Q15, etc.). The complete description of equations (with exact arrays of coefficients in Eq. 2 for fluid flow and heat transfer) in 2D and 3D can be found in [2,7] with references therein. It is worth to mention that Eq. (2) shows the same polynomial form in the case of the evolution equations for the density, internal energy and chemical species but their coefficients A, B, C, D may or may not depend on direction (cf. [2,5,8]), and the respective evolution equation has a form analogous form to Eq. (1).

The relaxation times depend on physically relevant variables for modelled phenomena; for example, the thermal relaxation time in phase m has the following form, cf. [3,5,7]:

$$\tau_i = 0.5 + \frac{3}{2} \frac{\lambda_m}{\rho_m C_{pm} \delta t} \tag{3}$$

written both for fluid f (gas) and solid s (coal grains) in the computational domain, so $m \in \{s, f\}$ and $\delta t = 1$, C_{pm} is the heat capacity for m and λ_m the heat conductivity of m.

The averaged values of macroscopic fields at every node (temperature, fluid density, stresses at the surface of grains, chemical species concentration, etc.) are obtained by integration of the distribution functions (summation over discretized velocity directions).

Because curvilinear solid-fluid interfaces are present in case of the modelled geometry, a boundary scheme has to be used in LBM. Description of the used scheme with some benchmark results can be found in [1]; the method (for curvilinear interface) was also developed for IEDDF [9]. For both density and internal energy distribution functions at the flow outlet, unknown distribution functions were calculated with use the Gradd condition [1]; whereas at the inlet we use the nonequilibrium distribution function in the form: $f_i(\mathbf{x}, t) = 2f_i(\mathbf{x} - \mathbf{e}_i \delta t, t) - f_i(\mathbf{x} - 2\mathbf{e}_i \delta t, t)$.

The chemical species evolution in case of released gases is modelled in LBM with additional distribution functions for every chemical compound k considered. In case of modelled phenomena, large ratios of concentration occur; the initial concentration of the chemical species is set to zero in the fluid when it is released from the surface of grains. Because of observed numerical instabilities, we use a scheme proposed by Di Rienzo *et al.* (cf. [4] for a detailed description). The modified equilibrium distribution function for D2Q9 scheme of LBM can be presented in the form:

$$\phi_{0,k}^{eq} = \frac{\rho Y_k}{9}(9 - 5\psi), \phi_{i=1,..,4;k}^{eq} = \frac{\rho Y_k}{9}(\psi + 3\mathbf{e}_i \cdot \mathbf{u}), \phi_{i=5,..,9;k}^{eq} = \frac{\rho Y_k}{36}(\psi + 3\mathbf{e}_i \cdot \mathbf{u})$$

and can be easily modified for D3Q15:

$$\phi_{0,k}^{eq} = \frac{\rho Y_k}{9}(9 - 7\psi), \phi_{i=1,..,6;k}^{eq} = \frac{\rho Y_k}{9}(\psi + 3\mathbf{e}_i \cdot \mathbf{u}), \phi_{i=7,..,15;k}^{eq} = \frac{\rho Y_k}{72}(\psi + 3\mathbf{e}_i \cdot \mathbf{u})$$

where $\phi_{i,k}^{eq}$ is the distribution function corresponding to a species k in direction i, $\psi = \rho^*/\rho$ is the ratio of the minimum density in the entire domain and the density at a given lattice node. Di Rienzo *et al.* also assume that $\tau \sim (D_k/\psi)$ where D_k is the diffusivity coefficient of species k.

3. RESULTS

As a benchmark case for fluid flow and heat transport we taken a simple geometry of flow past a single circular cylinder (cf. [1,3]). In the present work we also use a simplified geometry for modelling heat transfer with an extended solid-fluid boundary scheme for IEDDF and the geometry of a flow in a granular medium with chemical species release. Figure 1 presents two benchmark results for flow past a single obstacle. Left plots (flow is from the bottom to top) show isolines of constant temperature for a few Prandtl numbers. A qualitative agreement with experimental data is readily noticed; a detailed study is in preparation [9]. The temperature gradients at the front of the cylinder (where the nodes tagged as solid are kept at a constant temperature) increase with increasing Prandtl number. The right plot in Fig. 1 presents a zoomed part around a circular cylinder showing creation of vortices.

Figures 2 and 3 illustrate some of our recent results obtained with LBM for the simulation of heat transfer (Fig. 2) and degassing process (pyrolysis) of the granular deposit (Fig. 3). Figure 2 shows a comparison of the LBM results for flow past a regular array of square obstacles (the Kuwahara experiment) compared with an empirical correlation for the average Nusselt number proposed in [8]; we use a modified LBM boundary scheme for IEDDF at curvilinear solid-fluid interfaces (grain boundaries). We observe good conformity, especially for lower porosities in a wide range of Re and Pr numbers.

Regarding the modelling of pyrolysis, a simple model of Solomon *et al.* [10] has been applied for the present work. The model is based on the functional groups concept for hydrocarbons. Unfortunately, it amounts to solve for a considerable number of species: nine in the present study, meaning nine additional distribution functions which is costly in LBM. Figure 3(a1,a2) shows a single time stamp for the simulation of pyrolysis phenomena in a simple (high porosity) granular media. Figure 3(b) shows that the degree of the degassing depends on the heating rate by the observed dispersion of results; the graph shows averaged results with respect to chemical component (green line, here: methane) inside of the volume of solid grains.

4. CONCLUSIONS AND PERSPECTIVE

The Lattice Boltzmann method, earlier validated for fluid flow and heat transport, has been extended to account for chemical reactions during pyrolysis processes observed as a release of compounds from the surface of fuel grains into the flow. This has been done by the use of the LBM boundary scheme developed for curvilinear interface for both density and internal energy distribution functions. For modelling the evolution of species emitted from grains, a reduction model of chemical kinetics has been adopted. The first results presented here are encouraging. Aside of detailed description of thermomechanics of the flow, work is under way to develop solid-solid mechanical interactions. The numerical tool for the coupled phenomena after implementing the chemical species evolution functions has become quite costly (in terms of CPU time), especially for the complex geometry of the granular bed. For this reason, a further simplification of pyrolysis is under development. For a higher accuracy together with a reasonable computational complexity, we will apply a reduced model of chemical kinetics of the thermal break of coal molecules and reactions within solid fuel particles.

REFERENCES

[1] A. Grucelski and J. Pozorski (2013). Lattice Boltzmann simulations of flow past an obstacle and in simple porous media, *Comp. Fluids* **71** 406–416.

[2] S. Succi (2001). The Lattice Boltzmann Method for Fluid Dynamics and Beyond, *Clarendon Press, Oxford*.

[3] A. Grucelski and J. Pozorski (2012). Lattice Boltzmann simulation of fluid flow in porous media of temperature-affected geometry, *J. Theor. Appl. Mech. (Pol.)* **50** 193–214.

[4] A.F. Di Rienzo, P. Asinari, E. Chiavazzo, N.I. Prasianakis and J. Mantzaras (2012). Lattice Boltzmann model for reactive flow simulations, *Eur. Phys. Lett.* **98**, 34001

[5] K. Han, Y.T. Feng, D.R.J. Owen (2007). Numerical simulations of irregular particle transport in turbulent flows using coupled LBM-DEM, *Comp. Modelling in Eng. & Sci.* **18**, 87–100

[6] A.A. Pena, P.G. Lind and H.J. Herrmann (2008). Modeling slow deformation of polygonal particles using DEM, *Particuology* **6**, 506–514

[7] J. Wang, M. Wang and Z. Li (2007). A lattice Boltzmann algorithm for fluid-solid conjugate heat transfer, *Int. J. Thermal Sci.* **46**, 228–234

[8] F. Kuwahara, M. Shirota and A. Nakayama (2001). A numerical study of interfacial convection heat transfer coefficient in two-equation model for convection in porous media, *Int. J. Heat Mass Transfer* **44** 1153

[9] A. Grucelski and J. Pozorski (2014). Lattice Boltzmann simulations of heat transfer in flow past a cylinder and in simple porous media *Int. J. Heat Mass Transfer* [IN PREPARATION].

[10] P.R. Solomon, D.G. Hamblen, R.M. Carangelo, M.A. Serio and G.V. Deshpande (1988). General Model of Coal Devolatilization, *Energy and Fuels* **4**, 405-422

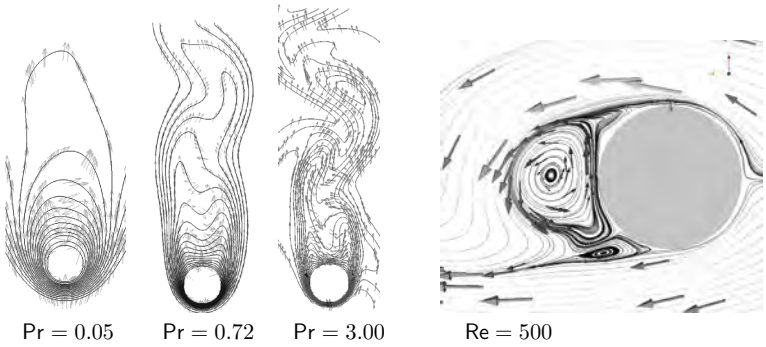

FIGURE 1. Lines of constant temperature for flow of heated fluid past an obstacle (with vectors of fluid velocity, gray). Left plots: results at $\mathrm{Re} = 100$ with use of the OSIF scheme for IEDDF. Right plot: stream lines near obstacle

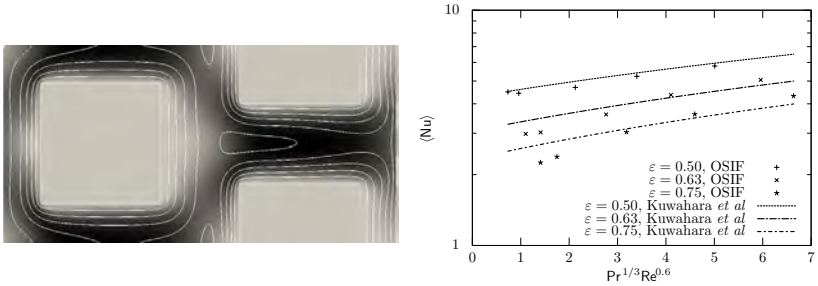

FIGURE 2. Forced convection in a bank of square rods. Left: the velocity magnitude (in grayscale: darker for higher velocity), and the lines of constant temperature; the flow is from left to right; Right: the LBM results for the average Nusselt number compared with the correlation of Kuwahara [10].

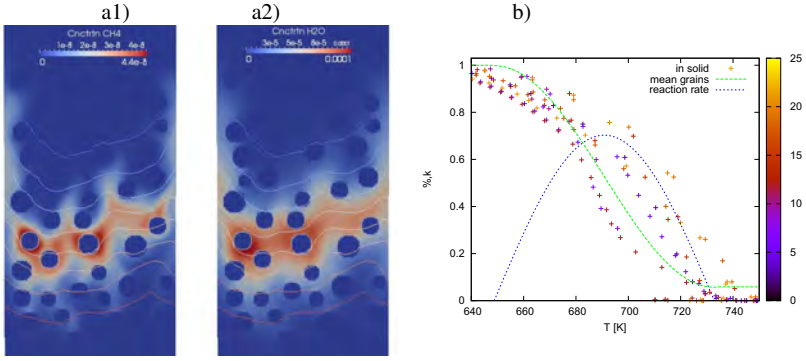

FIGURE 3. The concentration maps of chemical components (left) for methane (a1) and water vapour (a2) with the isolines of temperature. The graph on the right shows the mass fraction of methane corresponding to the fuel particle (point in the appropriate color) with respect to the average temperature (Grucelski 2013, unpublished).

Third International Conference on Computational Methods for Thermal Problems
THERMACOMP2014, June 2-4, 2014, Lake Bled, Slovenia
N. Massarotti, P. Nithiarasu and B. Sarler (Eds.)

AN EVALUATION OF PLANCK MEAN COEFFICIENTS FOR PARTICLE RADIATIVE PROPERTIES IN COMBUSTION ENVIRONMENTS

Henrik Hofgren, Bengt Sundén
Lund University, Department of Energy Sciences, Box 118, 221 00 Lund, Sweden
henrik.hofgren@energy.lth.se

ABSTRACT

Thermal radiation is the dominating form of heat transfer in several combustion technologies that combust solid fuels, such as pulverized coal combustion and fixed bed combustion. The thermal radiation originates from the hot combustion gases and particles such as soot, fly ash, char and unburned fuel. For accurate modelling of thermal radiation in these environments the selection of the radiative transport model and radiative property model is important. Radiative property models for gases have received large attention and several well documented models exists. For particles, soot has received large attention whereas the other particles have not. The radiative properties of fly ash, char and unburned fuel have a strong coupling with the prevailing combustion technology. Mass load of particles, size distribution and complex index of refraction is needed to describe the particles radiative properties. The Planck mean coefficients are most commonly used to describe the radiative properties of the particles. For gases the Planck mean absorption coefficient is known to give large deviations from recognized exact models in predicting the radiative heat transfer. In this study the use of Planck mean coefficients for particles are investigated and compared to spectral models. Two particle mass size distributions of fly ash are used, representing biomass and coal combustion. The evaluation is conducted in several combustion-like test cases with both gases and particles in plane parallel environments. The evaluation show that using Planck mean coefficients for particles can give large errors in predicting both the radiative heat flux and the source term. A new weighted sum of grey gas approach is tested that includes both the particles and gases to better account for the non-greyness of the fly ash absorption coefficient. This approach decreases the errors compared to the Planck mean approach in almost all cases but can still give large errors and is less generic.

Key Words: *Heat Transfer, Thermal Radiation, Particles, Gases*

1. INTRODUCTION

The particle radiation properties determines their contribution to the radiative transport. The radiative properties of the particle depend on the size, shape and its constituent species. Several studies have investigated the effects of these factors on the properties and on the overall radiative heat transfer in coal and grate fired combustion technologies [1-6]. Fly ash have been the sole investigated particle in several of the studies and will also be the particle investigated in this study. The fly ash particle exist throughout the whole furnace, in both combustion technologies, as the ash does not combust like the other mentioned particles. To simplify the treatment of particle radiation spectrally averaged black body weighted radiation properties have been investigated and used in several of the studies. Gupta et al. [1] investigated the effects of fly ash particles on thermal radiation in a pulverized coal fired furnace. They concluded that with a spectrally independent optical constant and their range of parameters the spectrally averaged properties gave adequate results. Goodwin and Mitchner [2] investigated the effect of spectrally dependent optical constants. They concluded that spectrally dependent optical constants gave significant difference for the radiative properties and heat flux compared to the spectrally independent optical constants. The Planck mean coefficients were used in the evaluation. Liu and Swithenbank [3] also investigates the spectrally dependent, compared to the

spectrally independent, optical constants and came to the conclusion that spectrally independent optical constants yields unacceptable results of the Planck mean coefficients. They also state that uncertainties in the size distribution also have a large effect on the Planck mean coefficients. In the studies [4-6] the Planck mean coefficients are used for particle radiation in a grate fired furnace, the prediction of radiative fluxes from an experimental coal fired furnace and a parametric study of radiative heat transfer in a pulverized coal fired furnace.

The Planck mean absorption coefficient should be used with great care as it is useful for considering emission and only radiative heat transfer in some special cases [7]. In the development of a new effective absorption coefficient Patch [8] showed in several different cases that the error that follows with the use of the Planck mean absorption coefficient can be high. Even though the Planck mean coefficients have been proven to give large errors, and most often abandoned when gas absorption/emission is considered, it is still used for particle radiation properties. This study will investigate the effect of using Planck mean coefficients for the fly ash particle properties in a number of cases, resembling the conditions in a combustion environment. Also an alternative to the Planck mean absorption coefficient is suggested.

The absorption coefficient of soot have been included by extra gray gases in the weighted sum of gray gas model (WSGG) [9, 10]. With this approach two extra gray gases are introduced to represent the soot which doubles the computational demand for solving a radiative problem. This study instead suggest a new set of coefficients for the WSGG model that includes both the gases and the fly ash. For the varying particle load case a correlation method is suggested. The gas spectral calculations are based on the latest spectral database that includes the so called hotlines, HITEMP2010 [11].

Produced WSGG coefficients are highly connected to the ash particle size distribution. The purpose of this work is not to produce sets of coefficients for a variety of particles and distributions. The purpose is to investigate the errors connected to the use of Planck mean coefficient and an alternative to the Planck mean absorption coefficient for particles.

THEORY

Thermal radiative transport through a media with combustion gases and ash particles are accurately described by the spectral radiative transport equation (RTE) that includes emission, absorption and scattering. In this study the RTE is solved with the discrete ordinates method (DOM), also known as the S_N-method [12]. For gases the absorption coefficient is the only relevant thermal radiative property in combustion environments. For benchmarking in this study the absorption coefficient for gases are taken from line-by-line (LBL) calculations using the HITEMP2010 spectral database [11]. The LBL calculations in this study follows the work of [13]. For the fly ash particles the absorption coefficient, scattering coefficient and scattering phase function are the relevant properties. Having the particle mass size distribution and complex index of refraction one can with Mie theory calculate the relevant spectral particle properties. Mie theory analysis the interaction between a particle and an electromagnetic wave. From the spectral output from Mie theory one can calculate the Planck mean coefficients for the particles. The WSGG coefficients are fitted against emissivity charts produced from the LBL calculations for temperatures between 400-2500K and 0.01-10 bar m. When fly ash is included in the WSGG, a new set of WSGG coefficients are produced for that specific particle load and distribution. To account for a varying load of fly ash in the combustion environment a polynomial fitting, similar to [13], is used.

3. RESULTS

Four combustion-like cases are used in this study. The model named LBL is the reference model, the model named WSGG incl. part. is the model where particle absorption/emission is incorporated in

the WSGG model and the model named WSGG+Planck is the model where all particle properties are described by a Planck mean coefficient. All cases are plane parallel with 20 percent H_2O, 10 percent CO_2 and 70 percent N_2 at 1 bar total pressure. The two distributions taken from coal and biomass are used in all cases with an equal mass load of 6.5 g/Nm^3.

Case 1 is for an isothermal homogeneous path with cold black walls investigated at three temperatures, 700, 1400 and 2100K, and three path lengths, 0.2, 1.0 and 10 m. The deviation of the heat flux, error(q_w), the average absolute source term, error(∇q_{avg}), and half width source term, error(∇q_{half}) are investigated between the LBL model and the WSGG+Planck, WSGG incl. part models. The setup of the case produced 18 subcases were the three deviations are evaluated for each sub model. The WSGG incl part. model is more accurate in almost all cases.

Case 2 and 3 are non-isothermal cases with a sinusoidal temperature distributions. Case 2 have colder walls than the gas and case 3 the other way around. The wall emissivity was also investigated in case 2. Figure 1 presents the source term and the wall heat flux for the three models in case 2, having a black wall, for the coal and the biomass distribution. An overall evaluation of the results from case 2 shows that the WSGG incl. part. performs better though looking only at the heat flux the WSGG+Planck performs best. The change of wall emissivity worked in favor for WSGG incl. part.

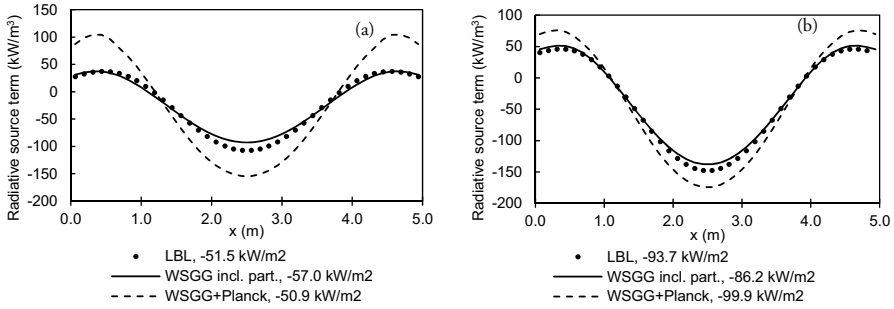

FIGURE 1. Radiative heat source and heat flux for the LBL, WSGG incl. part. and WSGG+Planck according to set up of case 2 for (a) Coal and (b) Biomass.

The results of case 3 are presented together with the results for case 4 in table 1. The error for the WSGG+Planck is much higher than for the WSGG incl. part on all investigated deviations in case 3. The last investigated case is case 4. It has the same setup as case 2 except with a sinusoidal load between 10 percent and 200 percent of the fly ash load 6.5 g/Nm^3, having the lowest load close to the walls. The WSGG incl part. performs best out of the two models but an increased overall error can be seen compared to the previous results.

	error(q_w)		error(∇q_{avg})		error(∇q_{half})	
	W	WP	W	WP	W	WP
Case 3						
Biomass	0.01	**-0.65**	0.07	**0.65**	-0.05	**-0.91**
Coal	0.01	**-0.72**	0.10	**0.75**	-0.14	**-0.32**
Case 4						
Biomass	**0.32**	-0.18	0.21	**0.27**	0.14	**-0.28**
Coal	0.16	**-0.30**	0.23	**0.53**	0.26	**-0.57**

TABLE 1. Errors for WSGG incl. part, W in table, and WSGG+Planck, WP in table, compared to LBL in case 3, 4.

4. CONCLUSIONS

Planck mean coefficients have been used for a long time to describe the radiative properties of particles in combustion environments. In this study the use of Planck mean coefficients for particles and WSGG for gases in combustion-like environments are compared to spectral, exact models, for particles and gases. The conclusion is that when predicting the radiative transfer the error in using the Planck mean coefficient for particles is large. This study shows that errors close to 100 percent can be found in source term and more than 70 percent error in the wall heat flux. A new WSGG model which includes the absorption/emission of particles is suggested. With such a model the error in both the source term and wall heat flux was at the most around 30 percent. The WSGG model is less generic and more cumbersome to apply as new WSGG coefficients have to be produced. More effort is needed in developing fast, general and accurate radiative properties models for particles.

REFERENCES

[1] Gupta, R.P., T.F. Wall, and J.S. Truelove, Radiative scatter by fly ash in pulverized-coal-fired furnaces: Application of the Monte Carlo method to anisotropic scatter*, International Journal of Heat and Mass Transfer*, 26, pp. 1649-1660, 1983

[2] Goodwin, D.G. and M. Mitchner, Flyash radiative properties and effects on radiative heat transfer in coal-fired systems*, International Journal of Heat and Mass Transfer*, 32, pp. 627-638, 1989

[3] Liu, F. and J. Swithenbank, The effects of particle size distribution and refractive index on fly-ash radiative properties using a simplified approach*, International Journal of Heat and Mass Transfer*, 36, pp. 1905-1912, 1993

[4] Butler, B., M. Denison, and B. Webb, Radiation heat transfer in a laboratory-scale, pulverized coal-fired reactor*, Experimental thermal and fluid science*, 9, pp. 69-79, 1994

[5] Marakis, J.G., C. Papapavlou, and E. Kakaras, A parametric study of radiative heat transfer in pulverised coal furnaces*, International Journal of Heat and Mass Transfer*, 43, pp. 2961-2971, 2000

[6] Klason, T., et al., Investigation of radiative heat transfer in fixed bed biomass furnaces*, Fuel*, 87, pp. 2141-2153, 2008

[7] Siegel, R. and J.R. Howell, *Thermal radiation heat transfer*, 1 1, New York: McGraw-Hill, 1972

[8] Patch, R.W., Effective absorption coefficients for radiant energy transport in nongrey, nonscattering gases*, Journal of Quantitative Spectroscopy and Radiative Transfer*, 7, pp. 611-637, 1967

[9] Truelove, J.S., The zone method for radiative heat transfer calculations in cylindrical geometries*, HTFS DR33, AERE-R8167, Harwell, Oxon, England*, 1975

[10] Felske, J.D. and T.T. Charalampopoulos, Gray gas weighting coefficients for arbitrary gas-soot mixtures*, International Journal Heat Mass Transfer*, 25, pp. 1849-1855, 1982

[11] Rothman, L.S., et al., HITEMP, the high-temperature molecular spectroscopic database*, Journal of Quantitative Spectroscopy and Radiative Transfer*, 111, pp. 2139-2150, 2010

[12] Chandrasekhar, S., *Radiative transfer*, New York: Dover Pubns, 1960

[13] Kangwanpongpan, T., et al., New correlations for the weighted-sum-of-gray-gases model in oxy-fuel conditions based on HITEMP 2010 database*, International Journal of Heat and Mass Transfer*, 55, pp. 7419-7433, 2012

Third International Conference on Computational Methods for Thermal Problems
THERMACOMP2014, June 2-4, 2014, Lake Bled, Slovenia
N. Massarotti, P. Nithiarasu and B. Sarler (Eds.)

QUENCHING IN NONLOCAL REACTIVE-DIFFUSIVE MEDIA

J. I. Ramos
Escuela de Ingenierías, Universidad de Málaga, Doctor Ortiz Ramos, s/n, 29071 Málaga, Spain
jirs@lcc.uma.es

ABSTRACT

A system of two two-dimensional reaction-diffusion equations with nonlocal reaction terms is studied numerically by means of an iterative, time-linearized, approximate factorization, second-order accurate, finite difference method. It is shown that, for local reaction terms, the dependent variables are characterized by counter-rotating spiral waves that preserve their integrity upon variations of the parameters that characterize the reaction terms. When the reaction terms are nonlocal, local quenching is found if the kernel of these terms is sufficiently nonlocal; however, the spiral waves preserve their integrity although their arms may be locally quenched in both space and time, and reconnection between two previously broken parts of the spiral wave's arm may occur.

Key Words: *Nonlocal Reaction-Diffusion Equations, Heat and Mass Transfer, Time Linearization.*

1. INTRODUCTION

Nonlocal heat and mass transfer phenomena occur in a variety of disciplines and engineering problems, e.g., conductive-radiative heat exchanges [1,2], and are governed by nonlinear, nonlocal boundary-value problems of the integro-differential type. Nonlocal phenomena in heat transfer have also been observed in nanosystems, electron transport in laser plasmas, materials with cracks and dislocations, fibrous materials, etc.

Most of the research performed to date on heat transfer at nanoscales has been based on solutions of the Boltzmann equation, kinetic theory [3], phenomenological models, etc. Some nanoscale heat transfer studies performed with the Boltzmann equation predict that Fourier's law is only valid if the nano-particle radius is much larger than the heat-carrier mean free path of the host medium, while studies based on kinetic theory result in a (nonlocal) heat flux which is the sum of the classical Fourier's flux, a second term proportional to the Laplacian of the heat flux, and a third one which contains the time derivative of the heat flux; the second term includes nonlocal effects, whereas the third one accounts for the time-history of the heat flux [3]. On the other hand, in materials science and composite materials, the microstructure often results in couplings between different temporal and spatial scales which, in turn, affect the dynamic, diffusive and thermal characteristics of these materials. Such couplings can be modelled by nonlocal effects that connect and correlate the micro- to the macro-scales. Nonlocal theories that do not include spatial gradients may be used to tackle problems with discontinuities, e.g., cracks, dislocations, granular media, etc., and can be used for the development of multiscale models. An example of such theories is the peridynamic one [4] that was initially developed for modelling fracture and damage, and was extended to analyze nonlocal heat transfer phenomena. In this theory, the heat flux is given by a convolution that depends on the temperature difference and a kernel that usually only depends on the spatial coordinates and results in a heat flux which depends on the temperature differences and not on the gradient of temperature as in classical heat transfer, and such a formulation has been used to study heat transfer at the nanoscale, e.g., [3].

As stated above, most of the studies peformed to-date on nonlocal heat transfer have dealt with the modelling of the heat flux. Here, it is assumed that the heat and mass fluxes are governed by the classical Fourier's and Fick's laws, whereas the reaction terms are nonlocal.

The paper has been arranged as follows. In the next section, a brief description of both the model and numerical method employed in this study is presented. This section is followed by the presentation of some sample results and a summary of the most important findings of the paper.

2. FORMULATION AND NUMERICAL METHOD

We consider the following system of two-dimensional reaction-diffusion equations

$$\boldsymbol{U}_t = \mathbf{D}\,\nabla^2\,\mathbf{U} + \mathbf{S}(\mathrm{t},\mathbf{x},\mathbf{U}), \tag{1}$$

where the subscripts denote differentiation, t is time, $\mathbf{x}=(x,y)$ denotes the two-dimensional Cartesian coordinates, $\mathbf{U} = (u,v)$ denote the (nondimensional) dependent variables, $\mathbf{D}$ is a diagonal constant matrix whose entries are the dimensionless diffusion coefficients of $\mathbf{U}$, and $\boldsymbol{S} = (S_u, S_v)$ are the reaction/source terms of $\mathbf{U}$ which can be written as

$$\boldsymbol{S}(\mathrm{t},\mathbf{x},\mathbf{U}) \;=\; \iint \boldsymbol{K}(t,\boldsymbol{x}-\boldsymbol{\rho})\;\boldsymbol{F}(\boldsymbol{U}(t,\boldsymbol{\rho}))\,d\boldsymbol{\rho},\, \boldsymbol{\rho} \in\; \boldsymbol{\omega} \;\in \boldsymbol{\Omega}, \tag{2}$$

where $\boldsymbol{F}$ is the source term given by the (local) law of mass action, $\boldsymbol{K}$ is a kernel that may depend on time if the time history or memory is included and/or on space if nonlocal effects are considered, and $\boldsymbol{\omega}$ is a subset of the domain of interest $\boldsymbol{\Omega}$. In this paper, we shall asume that $\boldsymbol{K}(t,\boldsymbol{x}-\boldsymbol{\rho}) = \boldsymbol{K}(\boldsymbol{x}-\boldsymbol{\rho})$, and, therefore, we shall only be concerned with nonlocal effects. Note that, if $\boldsymbol{K}(t,\boldsymbol{x}-\boldsymbol{\rho}) = \boldsymbol{\delta}(\boldsymbol{x}-\boldsymbol{\rho})$, where $\boldsymbol{\delta}(\boldsymbol{x}-\boldsymbol{\rho})$ is the two-dimensional Dirac's delta function, $\boldsymbol{S}(t,\boldsymbol{x},\boldsymbol{U}) = \boldsymbol{F}(\boldsymbol{U}(t,\boldsymbol{\rho}))$, i.e., the local law of mass action is recovered.

Equation (2) is a nonlinear equation of the integro-differential type and may include the whole domain if $\boldsymbol{\omega} = \boldsymbol{\Omega}$, or part of it if $\boldsymbol{\omega} \neq \boldsymbol{\Omega}$; in either case, Eq. (2) indicates that the solution at $\boldsymbol{x_P}$ depends on this location and all the points in $\boldsymbol{\omega}$. Equation (1) was first discretized in time by means of the second-order accurate trapezoidal rule and then the nonlinear terms at time level $(n+1)$ were linearized with respect to time to obtain

$$(\boldsymbol{I} - \mathbf{D}\,\Delta t\,\nabla^2 - \boldsymbol{J}(t^n,\mathbf{x},\boldsymbol{U^n})\,\Delta t/2)\,\Delta\boldsymbol{U} = \boldsymbol{R^n}, \tag{3}$$

where $\boldsymbol{I}$ is the 2x2 identity matrix, $\boldsymbol{R^n} = \mathbf{D}\,\Delta t\,\nabla^2\boldsymbol{U^n} + \Delta t\,\mathbf{S}(t^n,\,\mathbf{x},\,\boldsymbol{U^n})$, Δt is the time step, the superscript n denotes the n-th time level, i.e., $t^n = n\Delta t$, $\boldsymbol{J} \equiv \boldsymbol{S_t} + \boldsymbol{S_U}\,\Delta\boldsymbol{U}$, and $\Delta\boldsymbol{U} = \boldsymbol{U^{n+1}} - \boldsymbol{U^n}$, and is a linear integro-differential equation. Equation (3) can be factorized into a sequence of one-dimensional two-point, linear boundary-value problems in each spatial coordinate, but these problems are nonlocal and, upon spatial discretization, result in dense matrices in the domain $\boldsymbol{\omega}$ due to the nonlocality of the reaction terms (cf. Eq. (2)). In order to obtain sparse matrices after discretization, Eq. (3) was written as

$$(\boldsymbol{I} - \mathbf{D}\,\Delta t\,\partial_x^2)\big(\boldsymbol{I} - \mathbf{D}\,\Delta t\,\partial_y^2\big)\Delta\,\boldsymbol{U} = \boldsymbol{R^n} + \boldsymbol{AFE^n} + \Delta\mathrm{t}\,\boldsymbol{J^n}\,\Delta\,\boldsymbol{U}/2, \tag{4}$$

where $\boldsymbol{J^n} = \boldsymbol{J}(t^n,\mathbf{x},\boldsymbol{U^n})$, the second-order approximate-factorization errors $\boldsymbol{AFE^n}$ can be easily deduced by expanding the operator on the left-hand side of Eq. (4) and comparing the resulting equation with Eq. (3). Equation (4) was solved iteratively by first solving the linear one-dimensional equations $\big(\boldsymbol{I} - \mathbf{D}\,\Delta t\,\partial_y^2\big)\Delta\,\boldsymbol{U} = \Delta\,\boldsymbol{V}$ and then $(\boldsymbol{I} - \mathbf{D}\,\Delta t\,\partial_x^2)\,\Delta\,\boldsymbol{K} = \boldsymbol{R^n} + \boldsymbol{AFE^n} + \Delta\mathbf{t}\,\boldsymbol{J^n}\,\Delta\,\boldsymbol{U/2}$ after discretizing the second-order spatial derivatives by means of second-order

accurate central finite difference formulae. Such a discretization results in block-tridiagonal matrices which were solved by means of the method of Thomas.

3. RESULTS

Equation (1) was solved with $d_u = 1$, $d_v = 0.6$, $F_u = (u(1-u) - p\,v\,(u-q)/(u+q))/\varepsilon$, and $F_v = u - v$, where $p = 1.4$, $q = 0.002$, $\varepsilon = 0.01$, $S_u = F_u$, and $S_v = C(u) - v$, $u - C(v)$ or $C(u) - C(v)$, and C denotes the convolution operator defined in Eq. (2). The kernel of such a convolution was considered to be equal to one in $\boldsymbol{\omega}$ and zero in $\boldsymbol{\Omega} - \boldsymbol{\omega}$

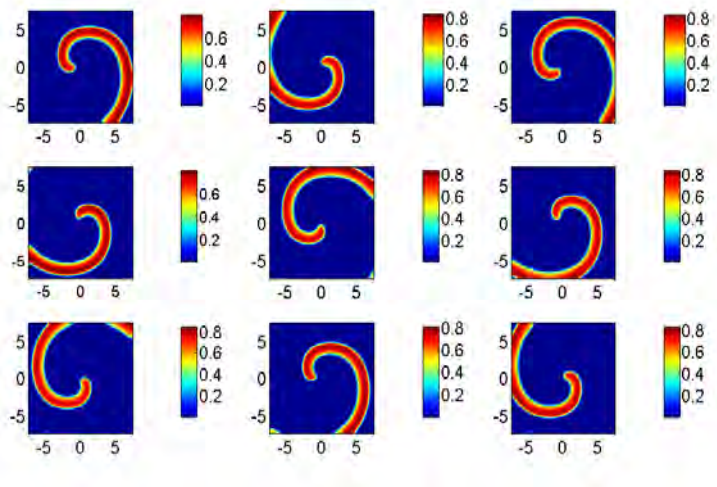

FIGURE 1. *u* as a function of *x* and *y* at (from left to right; from top to bottom) *t* = 77.5 (2.5) 97.5 for local reaction of both *u* and *v*.

Figure 1 shows the contours of *u* for the case that the kernel in Eq. (2) is the Dirac's delta function, i.e., when reaction terms are local, and exhibits a counter-rotating spiral wave that preserves its integrity. A similar behaviour is exhibited by *v*, and the time histories of *u* and *v* at any point within the domain are periodic functions of time. On the other hand, Figure 2 shows u for the case that there are only nonlocal effects on S_v only and these are caused only by the convolution of *v*, the kernel for *u* is the Dirac's delta function, the same initial conditions as for Figure 1, and $|\boldsymbol{\omega}| = 0.46\,|\boldsymbol{\Omega}|$, where $|\boldsymbol{\omega}|$ denotes the size of $\boldsymbol{\omega}$. This figure clearly illustrates that there is a spiral wave as can be seen in the three frames of the last row of Figure 2; this spiral wave does not have a uniform thickness, is strongly affected by the nonlocal reaction terms and its arm may be quenched as shown in the second to the fifth frames of Figure 2. The sixth frame shows the thinning of the spiral wave's arm just before local quenching occurs, while the third and fifth frames show some islands that have resulted from the quenching; these islands are quenched at later times, as illustrated in, for example, the seventh and eighth frames of Figure 2. Despite the local quenching phenomena observed in Figure 2 and others not presented here, it was found that there is reconnection between two previously broken parts of the wave's arm. The time required for such as a reconnection and the quenching time and location have been found to depend strongly on the dimensions of the nonlocality domain $\boldsymbol{\omega}$.

For the same initial and boundary conditions as those of Figures 1 and 2, local reaction terms for *u*, and nonlocal sources for *v* with $|\boldsymbol{\omega}| = 0.24\,|\boldsymbol{\Omega}|$, i.e., nonlocal effects smaller than those of Figure 2,

it has been found that the spiral wave has a longer arm than and quenching/extinction is not so frequent as in Figure 2.

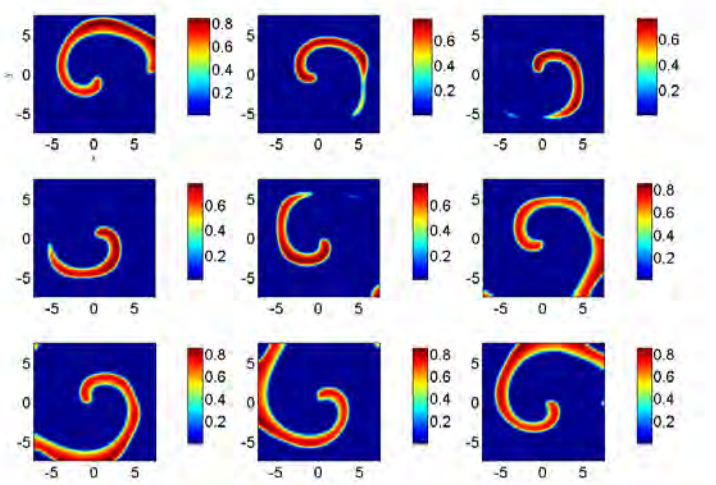

FIGURE 2. *u* as a function of *x* and *y* at (from left to right; from top to bottom) *t* = 77.5 (2.5) 97.5 for local reaction of *u* and nonlocal reaction of *v*.

4. CONCLUSIONS

The local quenching of reactive-diffusive systems characterized by nonlocal reaction terms has been studied numerically as a function of the domain of the nonlocality and it has been found that, if this domain exceeds a threshold that depends on the reactive-diffusive system, local quenching and the formation of islands may occur. For the system considered in this study, reconnection phenomena have also been observed.

ACKNOWLEDGEMENTS

The research reported here was financially supported by Project FIS2012-38430 from the Ministerio de Economía y Competitividad of Spain and FEDER funds.

REFERENCES

[1] D.D. Joseph and L. Preziosi, Heat waves, *Reviews of Modern Physics,* 61, 41–73, 1989.

[2] A. A. Amosov, Stationary nonlinear nonlocal problem of radiative-conductive heat transfer in a system of opaque bodies with properties depending on the radiation frequency, *Problems in Mathematical Analysis,* 164, 3-34 2009.

[3] A. Sellitto, D. Jou and J. Bafaluy, Non-local effects in radial transport in silicon thin layers and graphene sheets, *Proceedings of The Royal Society. Series A Mathematical Physical and Engineering Sciences,* 468, 1217-1229, 2012.

[4] F. Bobaru and M. Duangpanya, The peridynamic formulation for transient heat conduction, *International Journal of Heat and Mass Transfer,* 53, 4047–4059, 2010.

Third International Conference on Computational Methods for Thermal Problems
THERMACOMP2014, June 2-4, 2014, Lake Bled, Slovenia
N. Massarotti, P. Nithiarasu and B. Sarler (Eds.)

A SIMPLIFIED MODEL TO SIMULATE AP1000 CONTAINMENT PRESSURIZATION UNDER DESIGN BASIS ACCIDENTS

Guodong WANG*, Weijian TANG
Department of Reactor Core Design, Shanghai Nuclear Engineering Research and Design Institute, Shanghai 200233, P.R. China, wangguodong@snerdi.com.cn

ABSTRACT

The passive containment cooling system (PCS) is one of the main passive safety systems in AP1000. A simplified model is developed to simulate the AP1000 containment pressurization under design basis accidents (DBAs). The containment response has been performed by WGOTHIC code for comparison proposes. A good agreement between the model and code prediction confirms that the applicability of the simplified model to simulate AP1000 containment pressurization under DBAs.

Key Words: *passive containment cooling system, WGOTHIC, AP1000, heat and mass transfer*

1. INTRODUCTION

The AP1000 system, which was designed by Westinghouse, is one of the most advanced nuclear power units among the generation III nuclear power plant [1]. As a generation III reactor that received final design approval by U.S. NRC, AP1000 adopts a series of passive safety system which rely only on natural driving forces, such as pressurized gas, gravity force, natural circulation flow, and convection. The passive containment cooling system (PCS) is one of the main passive safety systems to remove heat from containment under design basis accidents (DBAs), such as loss of coolant accident (LOCA) and main steamline break (MSLB) accident. A schematic sketch of the PCS is shown in Fig. 1a. Under DBAs, heat removal process is accomplished primarily by absorption of energy by the gas volume and structures inside containment, by condensation of steam on the inside shell surface, by heat conduction through the steel shell, and by evaporation of water film covered on the outer containment shell surface. Air flow is forced into downcomer in shield building, and then turns the flow upward the riser. Air flows upwards in the riser to the top of the containment vessel and exhausts through the shield building chimney.

In the past several decades, many researches about the PCS have been analyzed with commercial code based on lumped parameter methods, such as CONTAIN, MELCOR and WGOTHIC. Especially, the WGOTHIC code was used as an analysis tool in the AP1000 design. In this paper, a simplified in-house developed model is developed to simulate the AP1000 containment pressurization under DBAs. The containment response calculated by this model is compared with that by WGOTHIC code. It shows good agreements under DBAs, which validates the application and qualification of the model on the analysis of PCS performance.

2. MAIN BODY

The simplified model to simulate the AP1000 containment pressurization requires consideration of mass, momentum, and energy transport, as well as state equation and constitutive relationships. Essentially the model is developed for a single control volume, based on the assumption that the control volume is well-mixed, which is schematically described in Fig. 2b. A containment gas pressure relationship is developed that couples the gas volume to the heat source and heat sinks. It should be noted that the objective of the model is to develop a containment pressure simulation to the dominant phenomenon. Thus the contribution of pool water to containment pressurization is not an important factor, which is neglected in the model.

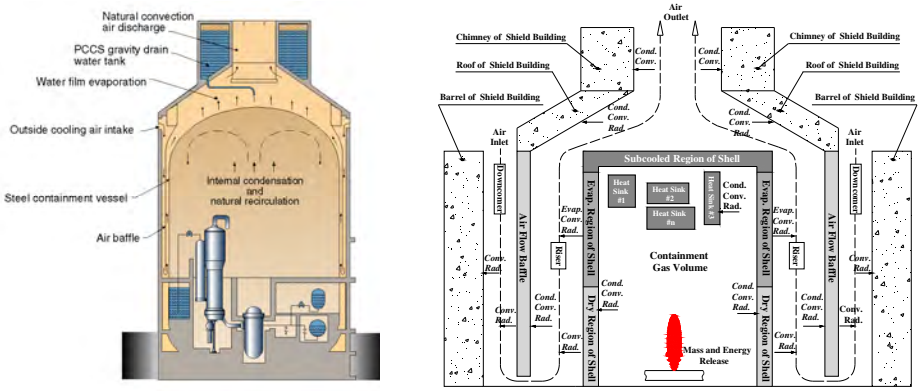

(a) The schematic PCS (b) The simplified model of heat removal

FIGURE 1. AP1000 Passive Containment Cooling System

2.1 Conservation equations inside containment

The conservation equations inside containment system are written for a gas control volume with a single steam source and multiple heat sinks. The gas mixture mass and energy equation is given by:

$$\frac{dm}{dt} = \dot{m}_{g,brk} + \sum \dot{m}_{stm,j} \tag{1}$$

$$\frac{d(mu)_g}{dt} = \dot{m}_{g,brk} h_{g,brk} + \sum (\dot{m}_{stm,j} h_{stm,j} + q_j) + \frac{P}{\rho_f} \dot{m}_f \tag{2}$$

Expressions for the rate of change of internal energy are used in the control volume equations for energy and pressure rates of change. The expressions below are developed from thermodynamics and calculus, which is not presented in detail here.

$$d(mu) = \left(\frac{C_p}{ZR} + m_{stm} \left.\frac{\partial h_{stm}}{\partial P_{stm}}\right|_T - 1\right) V dP + \left(\frac{C_p}{ZR} - 1\right) P dV - \frac{C_p}{ZR}\left(\frac{P_{air}}{\rho_{air}} dm_{air} + \frac{P_{stm}}{\rho_{stm}} dm_{stm}\right) + h_{air} dm_{air} + h_{stm} dm_{stm} \tag{3}$$

A rate of pressure change equation can be written by combining equations (1) to (3), and is given by:

$$\chi V \frac{dP}{dt} = \dot{m}_{g,brk}\left(h_{g,brk} - h_{stm}\right) + \Lambda \dot{m}_{g,brk} + \sum [\dot{m}_{stm,j}(h_{stm,j} - h_{stm})] + \Lambda \sum \dot{m}_{stm,j} + \sum q_j + \Lambda \dot{m}_f \frac{\rho_{stm}}{P_{stm}} \frac{P}{\rho_f} \tag{4}$$

The symbol $\chi = \frac{C_p}{ZR} + \rho_{stm} \left.\frac{\partial h_{stm}}{\partial P_{stm}}\right|_T - 1$ is used to represent compliance and the symbol $\Lambda = \frac{C_p}{ZR} \frac{P_{stm}}{\rho_{stm}}$ represents the pressure response to mass injection. It should be noted that equation (4) is only used in condition where steam is saturated or superheated in gas mixture. If steam is in subcooled state, steam would turn into liquid with latent heat release. Thus, equation (4) is modified to

$$\chi V \frac{dP}{dt} = \dot{m}_{g,brk}\left(h_{g,brk} - h_{stm}\right) + \Lambda \dot{m}_{g,brk} + \sum [\dot{m}_{stm,j}(h_{stm,j} - h_{stm})] + \Lambda\left(\sum \dot{m}_{stm,j} - \Gamma\right) + \sum q_j + \Lambda \dot{m}_f \frac{\rho_{stm}}{P_{stm}} \frac{P}{\rho_f} + \Gamma(h_{stm} - h_{sliquid}) \tag{5}$$

2.2 Heat and mass transfer in heat sinks

2.2.1 Heat sinks inside containment

Internal solid heat sinks include steel, concrete, and steel-jacketed concrete based on AP1000 design. These heat sinks are assumed to be slabs or plates with two parallel sides. The heat conducted into the solid couple the containment atmosphere with convection, radiation, and condensation heat transfer as well as conduction through condensed film, which are given by

$$q_{conv} = h_{c,hs}\Delta T = 0.13\frac{k}{L}(Gr\,Pr)^{1/3}(T_{cont} - T_{surf}) \tag{6}$$

$$q_r = \sigma\varepsilon(T_{cont}^4 - T_{surf}^4) \tag{7}$$

$$\dot{m} = k_g M_{stm}\left(P_{stm,bulk} - P_{stm,surf}\right) = \frac{h_{c,hs}PD_v}{RTP_{lm,air}k}\left(\frac{Sc}{Pr}\right)^{1/3} M_{stm}\left(P_{stm,cont} - P_{stm,surf}\right) \tag{8}$$

The mass transfer coefficient, k_g, is determined from the heat and mass transfer analogy, $Sh/Nu=(Sc/Pr)^{1/3}$, defined by Kreith. The heat conduction in heat sinks are described as

$$\rho c\frac{dT}{dt} = \frac{d}{dx}\left(k\frac{dT}{dx}\right) \tag{9}$$

2.2.2 Containment shell

The containment shell is assumed to be dry at the initiation of containment high pressure signal that actuates the PCS flow. After a time delay, it is assumed that the containment shell outside instantly establishes steady-state water film with certain water coverage (e.g. 90%). Thus, the containment shell is modeled considering three independent regions defined by external film: the relatively small area covered by subcooled film (subcooled region), the area covered by evaporating film (evaporating region), and the dry area covered no film (dry region).

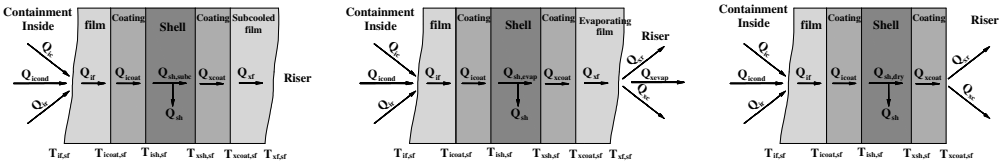

(a) Subcooled region (b) Evaporating region (c) Dry region

FIGURE 2. Sketch of energy transfer of containment shell with different regions

The heat transfer process couples the containment atmosphere to shell, and the shell to the riser shown in Fig. 2. The tota1 energy flux out of the containment gas is first reduced by the liquid entha1py of the condensed film. The shell has such a high heat capacity that its heat capacity can not be neglected until several thousand seconds into the transient. The heat flux in the shell can be related to convection, radiation, condensation, film/coating/shell conduction and evaporation. The heat and mass transfer correlations are similar to heat sinks inside containment in section 2.2.1, except heat convection and mass evaporation in riser, which are listed below:

$$q_{conv} = h_{c,xsh}\Delta T = 0.023\frac{k}{d_h}Re^{0.8}\,Pr^{1/3}(T_{xf,sf} - T_{ri}) \tag{10}$$

$$\dot{m} = \frac{h_{c,xsh}PD_v}{RTP_{lm,air}k}\left(\frac{Sc}{Pr}\right)^{1/3} M_{stm}\left(P_{stm,xf,sft} - P_{stm,ri}\right) \tag{11}$$

The areas of the subcooled and evaporating regions change with time. The area of the subcooled region is determined from an energy balance on the subcooled liquid in which the heat conducted from the shell heats the liquid to temperature of the evaporating film with no evaporation, radiation, and convection to riser. The evaporating area is the difference between the wet area and the subcooled area. The dry area is the difference between the total area and the wet area.

2.2.3 Air flow baffle and shield build

The baffle receives heat by radiation from the shell and loses heat by radiation to the shield building and by convection to the riser as well as downcomer. Since the baffle is a thin steel plate with low Biot number, baffle is well-represented as a lumped parameter with identical bulk temperatures.

The shield building is divided into three parts based on its design character, which are barrel heat sink, roof heat sink, and chimney heat sink. The heat and mass transfer correlations of shield building are similar to heat sinks inside containment in section 2.2.1, and is not represented here.

2.2.4 PCS air flow path

The PCS air flow is modelled as only buoyancy-driven. The positive buoyancy is provided by air heating and the evaporation of low density steam into the riser. A small amount of negative buoyancy is provided by heating from the baffle and shield walls in the downcomer, and chimney at the outlet. The system of momentum equation for air flow path is given to

$$\sum_i [(\rho_i - \rho_{envi}) g L_i] = \frac{1}{2} \sum_i \left(\frac{k_i}{A_i^2} \frac{\dot{m}_i^2}{\rho_i} \right) \tag{12}$$

3. RESULTS

The simplified model is performed to simulate the AP1000 containment response under LOCA and MSLB accidents. And WGOTHIC code is also used for comparison purpose. Fig. 3a to 3c present the containment pressure, and Fig. 3d to 3f present the steam condensation rate on containment shell inside, film evaporation rate on containment shell outside, as well as air flow mass in annulus of shield building. The good agreement between the model and WGOTHIC prediction of containment response, especially pressure response, confirms that the simplified model in this paper is applicable to simulate AP1000 containment pressurization under DBAs.

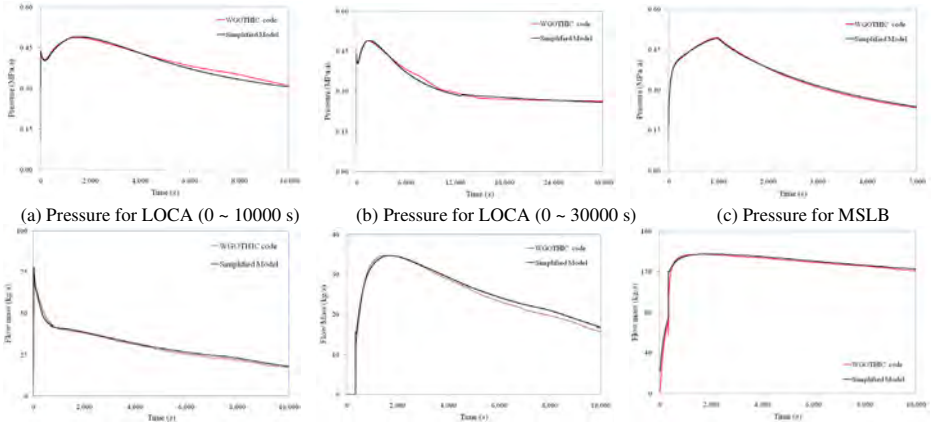

(a) Pressure for LOCA (0 ~ 10000 s) (b) Pressure for LOCA (0 ~ 30000 s) (c) Pressure for MSLB

(d) Condensation for LOCA (e) Evaporation for LOCA (f) Air flow rate for LOCA

FIGURE 3. Comparison of containment response with simplified model and WGOTHIC code

4. CONCLUSIONS

In this paper, a simplified model has been developed to simulate the AP1000 containment response under DBAs and compared with WGOTHIC code prediction. The good agreement between the model and code predictions confirms that the applicability of the simplified model to simulate AP1000 containment pressurization under DBAs.

REFERENCES

[1] T.L. Schulz, Westinghouse AP1000 advanced passive plant, *Nuclear Engineering and Design,* 236, 1547-1557, 2006.

PARALLEL SESSION

HEAT AND MASS TRANSFER IN POROUS MEDIA

Third International Conference on Computational Methods for Thermal Problems
THERMACOMP2014, June 2-4, 2014, Lake Bled, Slovenia
N. Massarotti, P. Nithiarasu and B. Sarler (Eds.)

TRANSIENT THERMAL ANALYSIS OF POROUS CAVITIES

F. Arpino, G. Cortellessa

Dipartimento di Ingegneria Civile e Meccanica, Università degli Studi di Cassino e del Lazio Meridionale, Via G. Di Biasio 43, 03043 Cassino (FR), Italy. f.arpino@unicas.it; g.cortellessa@unicas.it.

N. Massarotti, A. Mauro

Dipartimento di Ingegneria, Università degli Studi di Napoli "Parthenope", Isola C4, Centro Direzionale, 80143 Napoli, Italy. massarotti@uniparthenope.it; alessandro.mauro@uniparthenope.it

ABSTRACT

In this paper the authors numerically investigate dynamic heat transfer in porous and partially porous cavities, paying particular attention to the dependence of velocity and temperature fields on Rayleigh (Ra) number, porous layer permeability, and cavity aspect ratio (AR). Heat and fluid flow are described by using the generalized porous medium model and the governing equations have been numerically solved using the Artificial Compressibility (AC) version of the Characteristic Based Split (CBS) scheme.

Key Words: *Finite element method, Time-periodic oscillating flow field, Heat transfer coefficient calculation.*

1. INTRODUCTION

In the scientific literature, few works are available about heat transfer analysis in tall, partly porous cavities in presence of natural convection [1]. The main objective of the present paper consists in a better insight of the transient buoyancy driven heat and fluid flow phenomenon in porous and partly porous tall cavities. To this purpose, the transient pressure, velocity and temperature fields have been calculated by employing the AC-CBS algorithm for the resolution of the generalized model for heat and fluid flow through saturated porous media. To the authors knowledge, numerical procedures adopted in the scientific literature for the resolution of transient buoyant flows in porous or partly porous tall cavities are only implicit or semi-implicit. In order to obtain a transient explicit solution, a dual time stepping approach is employed [2], consisting in the splitting of a transient problem into several instantaneous steady state successive steps, by adding the so called true transient term to the governing partial differential equations. This term is discretized to get a third order of approximation over the real time step size. The stabilized AC-CBS algorithm is here applied for the first time to the simulation of transient buoyancy driven flows in porous and partly porous tall cavities. In this paper, the effects caused by the presence of a porous layer in a buoyancy driven cavity are analysed in detail. In particular, the influence of parameters such as the Ra and the Darcy (Da) numbers, and the geometrical AR on the flow characteristics has been investigated. The proposed model has been first validated against data available in the scientific literature showing an excellent agreement. Then, the transient AC-CBS algorithm has been employed to investigate the dependence of Nu number on Ra and Da numbers for a 4:1 and 8:1 partly porous cavity. The Ra and Da numbers ranges of variation are $10^1 \div 3.4 \cdot 10^6$ and $10^{-5} \div 10^2$, respectively.

2. MATHEMATICAL AND NUMERICAL MODEL

The generalized model describing flow and energy transport in a saturated porous medium with constant porosity, filled with a single phase incompressible fluid consists of a set of conservation equations. It can be derived by averaging the Navier-Stokes equations over a representative

elementary volume, using the well-known volume averaging procedure [3]. The PDEs constituting the generalized porous medium model have been numerically solved by the transient AC-CBS algorithm. The governing equations have been discretized in time along the characteristics, and in space using the standard Galerkin procedure [4]. Transient problems are modelled using a dual time-stepping technique and adding a true transient term to the first or the third step of the AC-CBS algorithm. The true transient term is discretized over the real time to the third order of approximation, using the following relation:

$$\Delta u_i^n = \frac{11u_i^n - 18u_i^{n-\Delta\tau} + 9u_i^{n-2\Delta\tau} - 2u_i^{n-3\Delta\tau}}{6} \tag{1}$$

The explicit nature of the true transient term introduces a limitation on the pseudo time step size to ensure the required stability of the method. On the basis of the order of magnitude analysis [5] it has been derived that $\Delta t \leq 3\Delta\tau/20$ for a third order of approximation.

3. RESULTS

Transient incompressible flow in a square buoyancy driven porous cavity

In the present section, transient heat and fluid flow in a square porous cavity is numerically investigated. In order to validate the proposed numerical method, the obtained results have been compared with the analytical and numerical data available in reference [6]. The initial condition employed to perform transient simulations consists of an isothermal fluid at rest, with a non-dimensional temperature equal to zero. The gravity vector is directed in the negative y-coordinate direction. As concerns the boundary conditions, it is assumed that the left and right vertical walls are maintained at a constant dimensionless temperature of +0.5, and -0.5, respectively. The top and bottom walls are considered adiabatic.

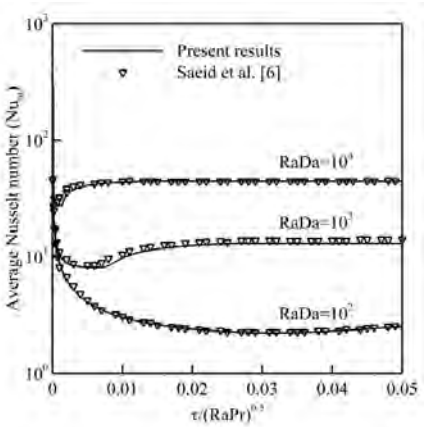

Figure 1. Variation with time of the average Nusselt number at the hot wall. Comparison with the numerical solution proposed by Saeid *et al.* [6]

Data in reference [6] are produced for the following three values of the porous Rayleigh number, $Ra_p = g\beta K\Delta TL/\nu\alpha = RaDa$: 10^2, 10^3 and 10^4. Saeid and Pop [23] neglected the viscous drag and inertia terms in the governing equations, given the low values of Darcy and porous Reynolds numbers considered. For this reason, in order to reproduce the flow conditions indicated by Saeid and Pop [6], simulations have been conducted employing a Darcy number equal to 10^{-8} and for the following three values of the Rayleigh number: 10^{10}, 10^{11}, 10^{12}. Porosity in equations has been set to 1. The transient behaviour of the proposed numerical scheme for the description of heat and fluid

flow in a porous square cavity has been assessed by comparing the variation with time of the average Nusselt number at the hot wall with numerical results available in [6]. This comparison is available in Figure 1 for $RaDa = 10^2$, $RaDa = 10^3$, and $RaDa = 10^4$. The decreasing trend of the average Nusselt number during the first time interval indicates that heat transfer by conduction dominates the problem, while the following positive trend evidences that the amount of heat transferred by convection is increasing. The proposed results are in good agreement with the reference data from the scientific literature, and represent a further assessment of the effectiveness of the proposed numerical scheme.

Transient incompressible flow in a partially porous buoyancy driven tall cavity
In this section, the numerical results obtained for transient natural convection in a partly porous tall cavity with an Aspect Ratio (AR) of 8:1 and 4:1 are presented. The computational domain and the boundary conditions employed are reported in Figure 2.

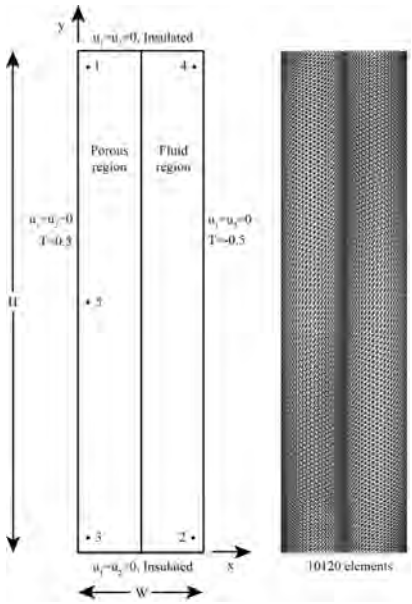

Figure 2. Natural convection in a partially porous vertical cavity. Problem definition with boundary conditions employed (left); 4:1 computational grid, composed by 5717 nodes and 10120 triangular elements (right).

The initial condition employed to perform transient simulations consists of an isothermal fluid at rest, with a non-dimensional temperature equal to zero. The fluid is assumed to be incompressible and Newtonian. The porous medium is assumed to be isotropic and homogeneous. The numerical investigations have been carried out assuming: Prandtl (Pr) number equal to 0.71; Rayleigh number (Ra) ranging between 10 and the value at which oscillations start in absence of the porous layer inside the cavity (3.4×10^6 for the 4:1 cavity and 3.4×10^5 for the 8:1 cavity); porosity uniform and constant equal to 0.5; Darcy (Da) number ranging between 10^{-5} and 10^2. Figure 3 shows, for the two investigated cavities, the variation of Nu_m with Ra and Da. The obtained results showed that Nu number is an increasing function of both Ra and Da numbers. The Nu_m decreases as the Ra decreases and becomes independent on the Ra number when Ra is lower than about 10^3, indicating

that conductive heat transfer mechanism dominates. Such aspect has been observed for both 4:1 and 8:1 cases. In fact, Nu_m is in practice constant and about equal to 0.9 when $Ra \leq 10^3$ regardless of the Da considered. As regards the dependence of Nu_m on the Da number, it increases as the Da increases, even though it can be observed that Nu_m becomes independent on the considered Darcy number if Da is larger than about 10^{-1}. Results coincide to the fluid cavity case when $Da \geq 10^2$ for both the considered ARs.

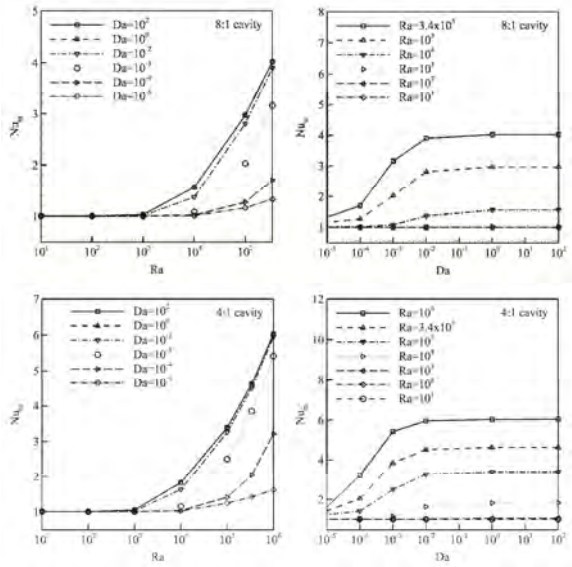

Figure 3. Variations of Nu_m with Ra (a-c) and Da (b-d) for a 8:1 and for a 4:1 partially filled porous cavity.

4. CONCLUSIONS

In the present paper, the AC-CBS algorithm has been employed to solve transient natural convection in porous and partially porous rectangular cavities. The obtained results have shown that the Nu number is an increasing function of Ra and Da numbers for both the ARs considered.

REFERENCES

1. J.F. Mercier, C. Weisman, M. Firdaouss and P. Le Quéré, Heat Transfer Associated to Natural Convection Flow in a Partly Porous Cavity, Journal of Heat Transfer, vol. 124, pp. 130-143, 2002.
2. A.G. Malan, R.W. Lewis and P. Nithiarasu, An improved unsteady, unsctructured, artificial compressibility, finite volume scheme for viscous incompressible flows: part II. Application International Journal for Numerical Methods in Engineering, vol. 54, pp. 715-729, 2002.
3. S. Whitaker, Diffusion and dispersion in porous media, AIChE J., vol. 13, pp. 420-427, 1961.
4. R.W. Lewis, P. Nithiarasu and K.N. Seetharamu, Fundamentals of the finite element method for heat and fluid flow, John Wiley & Sons, Chichester, 2004.
5. F. Arpino, N. Massarotti and A. Mauro, High Rayleigh Number Laminar-Free Convection in Cavities: New Benchmark Solutions, Numerical Heat Transfer, Part B: Fundamentals, vol. 58(2), pp. 73-97, 2010.
6. S. Saeid and I. Pop, Transient free convection in a square cavity filled with a porous medium, International Journal of Heat an Mass Transfer, vol. 47, pp. 1917-1924, 2004.

Third International Conference on Computational Methods for Thermal Problems
THERMACOMP2014, June 2-4, 2014, Lake Bled, Slovenia
N. Massarotti, P. Nithiarasu and B. Sarler (Eds.)

THERMAL HYDRAULIC ANALYSIS FOR SFP OF 300MW NPP USING POROUS MEDIA MODEL

Gan Fujun, Jia Hongyi, Zhu Libing
Shanghai Nuclear Engineering Research & Design Institute, 200233, ganfujun@snerdi.com.cn

ABSTRACT

A thermal-hydraulic analysis for SFP of 300MW NPP is carried out to validate that no local coolant boiling occurs in accident conditions. The bounding cladding surface temperature is a conservative summation of CFD calculated peak local coolant temperature and cladding superheat based on laminar flow heat transfer theory. The storage racks and SFAs are modelled as porous media, and the permeability and inertial resistance factor are closely related to the geometrical parameters. Results show that no local coolant boiling will occur when the full-core is off-loaded.

Key Words: *SFP, CFD, porous media model, local coolant boiling, cladding superheat.*

1. INTRODUCTION

In Spent Fuel Pool (SFP) of Nuclear Power Plant (NPP), the buoyancy-driven flow is induced by the decay heat generated by Spent Fuel Assemblies (SFAs). The heated coolant goes upwind through the storage racks, removing the decay heat, with the cooler water supplied to the bottom of racks meanwhile. The SFP is designed to provide a forced cooling and circulation system to maintain the pool water at acceptable temperatures for SFAs handling for all heat load conditions, including full-core offload during refuelling. One of SFP design requirements addressed in Regulatory Guide 1.13[1] is that the structures, systems and components in SFP should be designed to provide adequate cooling ability to remove residual heat. This guide considers a thermal-hydraulic analysis of coolant flow through the storage racks and prevention of nuclear boiling under all anticipated operating conditions. In order to prevent the local boiling, the cladding surface temperature should below the saturation temperature of coolant.

The objective of this paper is to present a thermal-hydraulic evaluation for SFP of 300 MW NPP, to ensure that the decay heat removal system is reliable so that the temperature on the cladding surfaces remains within the allowable limits under accident conditions. Qualification of coupled flow and temperature fields in the SFP is accomplished using a Computational Fluid Dynamics (CFD) code, FLUENT. The cladding superheat is calculated from the principles of laminar flow heat transfer, and is added to the CFD calculated peak local coolant temperature to obtain a conservative cladding surface temperature. When carrying out the CFD simulation, the storage racks and SPAs are modelled as porous media, which consists of several parts, with or without heat source. The permeability and inertial resistance factor of porous media model are closely related to the geometrical parameters of storage racks and SFAs.

2. DESCRIPTION OF 300MW SFP MODEL

There are two SFPs in 300MW NPP, named FX202 and FX203, with same dimensions about 11800mm length, 4850mm width and 11800mm height. The top views of each SFP are shown in Fig.1. There are 5 storage racks in FX202, and 8 in FX203. The gray region is full of coolant. These two SFPs share a maximum total heat load of 1.308MW in normal refuelling conditions (40 SFAs refuelling per circle), and 3.766MW in accident conditions (full-core off-loading). In following calculations, a main conservative input assumption is that the heat load of selected SFP is equivalent to the total value. In normal conditions, the forced cooling flow rate and maximum

design bulk coolant temperature is 167m^3/h and 323.15K, respectively. While in accident conditions, there are two strategies. One keeps cooling flow rate unchanged and the design bulk coolant temperature goes up to 353.15K. The other strategy is that the flow rate and design bulk temperature are 334m^3/h and 338.15K, respectively. The liquid level in SFP also has different design values in different conditions. To make our calculation conservative when forced cooling is available, we choose the lowest liquid level, i.e., 12m.

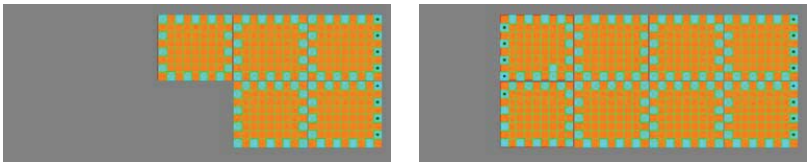

Fig. 1 Top view of SFPs of 300MW NPP, FX202 (left) and FX203 (right)

SFA in storage rack consists of a 15×15 array of fuel rods, with about 2.9m active length. For the storage racks and fuel assemblies is numerous and the geometry is very complex, it is necessary to get a simplified model for following high-efficiency calculations. Therefore, SFP FX203 with 8 storage racks is selected for following calculations with its heat load ability equals to that of total heat load of two SFPs. The simplified SFP is divided into coolant region and porous region. The later models the storage racks and SFAs, and is further divided into high heat source region, low heat source region and no heat source region. In our simplified model, the off-loaded full-core during accident conditions is positioned in a square region in the centre of porous region as high heat source region, to maximize the calculated local coolant temperature. The rest part in active region is low heat source region. Other part in porous region is without heat source. The final simplified model for CFD simulation is shown in Fig. 2. The forced cooling flow is induced by injection flow which is far above the top of storage rack.

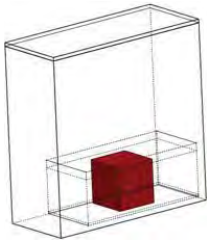

Fig. 2 Simplified model of SFP FX203.

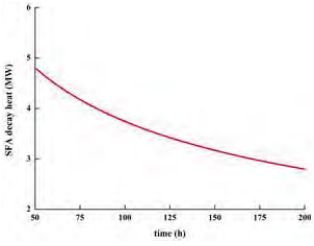

Fig. 3 Time variation of decay heat of 300MW SFA.

3. SIMULATION PARAMETERS

The thermal-hydraulic flow analysis in SPF is simulated using CFD code, FLUENT. It has the ability to solve problems with a variety of turbulence, buoyancy-driven circulation, porous media and heat transfer models, including flows in complex geometries. The governing equations are continuity, momentum and energy equations. The *k-* turbulence model with standard wall function is employed. Gravity and full buoyancy effects are adopted for the density of coolant is a function of temperature. The properties, such as density, viscosity and thermal conductivity, are defined as piecewise-linear functions of temperature. FLUENT uses the SIMPLE algorithm to solve the pressure, momentum, turbulence and convective heat transfer equations with a finite volume algorithm. The total decay heat of the offloaded full-core is obtained via summation of 121 SFAs. Time variation of decay heat generated by each SFA is shown in Fig. 3, which is assumed

that each SFA experiences three circles and the burn-up reaches a maximal value. HZP is selected as the beginning of calculation of decay heat of each SFA. The volume heat source is 144542.6W/m^3 in the off-loaded full-core region, and 7344.2W/m^3 in low heat source region when decay heat of SFA at 150h is selected.

Two key parameters of porous media model are permeability and inertial resistance factor, which are included in momentum sink terms added to the momentum equations. Each source term consists of two parts, a viscous loss term (the first part) and an inertial loss term (the second part), as is shown in Eq. 1, in which, is coolant density and coolant viscous factor. The permeability is calculated from Eq. 2, in which, A_{act} is the actual area, A_{super} the gross or superficial area, and D_h the hydraulic diameter based on the actual flow area. C_2 is obtained using Eq. 3, in which, L_{flow} is the flow path length and K_n the nth loss coefficient for the blockage. Loss coefficient is calculated using standard hydraulic calculations. An additional 10% reduction of permeability and a 10% increase of inertial resistance are imposed in the analysis for conservative results. During the calculation of above parameters, the geometrical dimensions of storage racks and SFAs are considered. Final viscous resistance and inertial resistance are 559336 m^{-2} and 68 m^{-1}, respectively.

$$S_i = -\mu \times \overline{v}_i / k_{perm} - C_2 \times \rho \times |v_i| v_i \tag{1}$$

$$k_{perm} = A_{act} / A_{super} \times D_h^2 / 32 \tag{2}$$

$$C2 = 1 / L_{flow} \times \sum K_n \tag{3}$$

4. RESULTS

Three sets of grids are used in our calculations, i.e., case 1 with 480 millions grids, case 2 with 1360 millions grids and case 3 with 1880 millions grids. To speed up the convergence, the obtained field of case 1 is set as the initial solution of case 2, and the resultant field of case 2 is set as the initial field of case 3. The temperature contours of above three cases in section $y = 0$ are shown in Fig. 4, from which it can be seen that temperature distribution is already grid-independent.

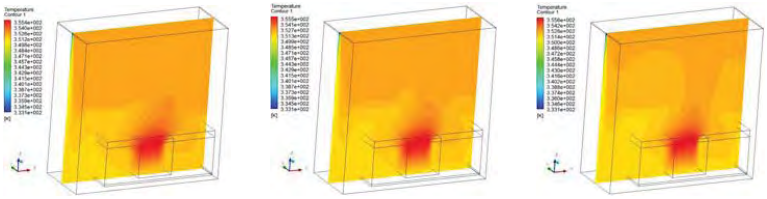

Fig. 4 Temperature distribution of case1 (left), case 2(middle) and case 3 (right) in plane $y = 0$.

For the decay heat of each SFA varies a lot as time goes by, which affects the peak local coolant temperature and cladding superheat, four different decay heat of SFA at 120h, 150h, 180h and 200h are selected to carry out heat source sensitivity analysis. The resultant temperature contours in section $y = 0$ are shown in Fig. 5. The qualitative distribution of temperature hardly changes, while the peak local coolant temperature slightly decreases as time goes by, as shown in Fig. 6 (left). The cladding superheat is obtained from the principles of standard flow heat theory giving the following relationship for constant heat flux laminar flow , as is shown in Eq. 4[2], in which, *Nu* is Nusselt number, h convective heat transfer coefficient, k_w coolant thermal conductivity. This equation is used to solve for h. A thin crud layer on the outside of fuel rods provides an additional heat transfer coefficient, R_c = t/k_c, in which, R_c is crud heat transfer resistance, t crud thickness and k_c crud thermal conductivity. The overall heat transfer coefficient, including both convective heat transfer coefficient and crud resistance is determined by Eq. 5, in which, U is overall heat transfer coefficient. The peak rod heat flux is divided by this quantity to obtain the cladding superheat, as is shown in Eq. 6. The variation of superheat is presented in Fig. 6 (right), and is finally added to the

CFD calculated peak local coolant temperature to obtain a bounding cladding surface temperature, which is shown in Fig. 6.

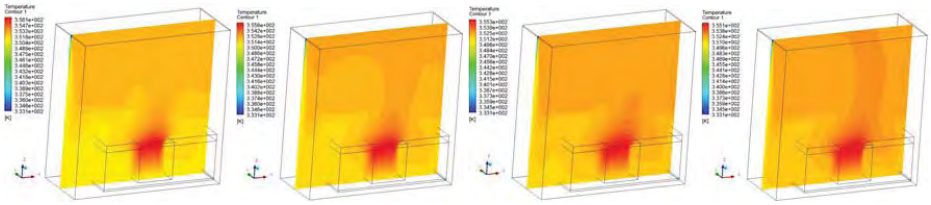

Fig. 5 Temperature distribution in plane $y = 0$ for decay heat at 120h (left), 150h (2th), 180h (3th) and 200h (right).

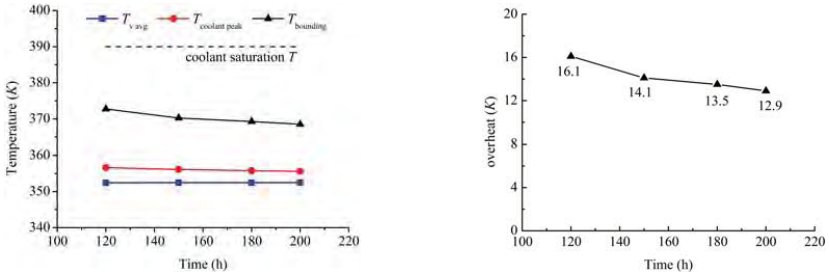

Fig. 6 Time variation of peak local coolant temperature, cladding surface temperature (left) and cladding superheat (right).

In fact, the calculated cladding surface temperature is conservative. It is due to the reason that the CFD calculated peak local coolant temperature usually occurs in the top nozzle region, while the cladding overheat usually appears in the middle of SFA. Nevertheless, their summation is still below the saturation temperature of coolant, validating that no local boiling occurs in SFP.

$$Nu = h \times D_h / k_w = 4.364 \tag{4}$$

$$1/U = 1/h + R_c \tag{5}$$

$$\Delta T = q_{\max} / U \tag{6}$$

5. CONCLUSIONS

A thermal-hydraulic analysis for SFP of 300MW NPP is conducted to validate that no local coolant boiling occurs in accident conditions. The SPF is simplified into coolant region, high heat source region, low heat source region and no heat source region further. The permeability and inertial resistance factor are calculated based on the geometrical parameters. In order to ensure that no local boiling occurs, the cladding surface temperature is obtained by the summation of CFD calculated peak local coolant temperature and cladding superheat based on laminar flow heat transfer theory conservatively. Results based on different values of decay heat of SFA show the cladding surface temperature is well below the coolant saturation temperature, proving that no local coolant boiling will occur when full-core is offloaded.

REFERENCES

[1] U.S. Nuclear Regulatory Commission, Regulatory Guide 1.13, Spend fuel storage facility design basis, March 2007, Revision 2.

[2] J.P. Holman, Heat transfer, 10th Edition, McGraw Hill, 2010.

Third International Conference on Computational Methods for Thermal Problems
THERMACOMP2014, June 2-4, 2014, Lake Bled, Slovenia
N. Massarotti, P. Nithiarasu and B. Sarler (Eds.)

INFILTRATION OF A POROUS MATRIX BY A SOLIDIFYING LIQUID METAL : A LOCAL MODEL

Nadine Moussa, Dominique Gobin, Benoît Goyeau

CNRS – EM2C – Ecole Centrale Paris, Grande Voie des Vignes,
92295 Châtenay-Malabry Cedex, France
dominique.gobin@ecp.fr

ABSTRACT

This paper describes the first step of a study dedicated to the development of a macroscopic numerical model simulating the casting of a metallic foam by infiltration and solidification of a liquid metal in a porous mould. The first stage presented here describes a local model of injection of the metallic melt in a capillary tube and subsequent solidification of the metal by heat exchange with the walls of the duct.

The model is intended to account for the air/liquid interface during the infiltration phase, for the heat transfer to the wall and for liquid-solid phase change in the presence of the fluid flow. The objective is to determine the influence of the operating conditions on the penetration depth and on the solidification time in a simplified geometry before using this local information in a macroscopic homogenized model presently under development.

Key Words: Solidification – Phase change – Capillary tube – Infiltration - Interface.

1. INTRODUCTION

A metallic foam is a porous structure whose solid matrix has a large fraction of interconnected cells. One possible way to elaborate such foams is to inject a liquid metal in a porous mould consisting of a regular arrangement of sand or salt beads which are destroyed after solidification of the metallic structure. The competitiveness in the metal industry results of severe products specifications in order to reduce the cost of the manufacturing process. Thus, metal foams present a promising solution since it retains the high mechanical properties of the metal while reducing the weight up to 90%.

The objective of this study is to develop a model able to simulate the infiltration and solidification process in order to study the influence of the operating parameters of this manufacturing technique and to monitor the production of homogenous open cell metal foams.

The metal foams are characterized by their high porosity and permeability values (Figure 1) ; thus, the size of the mould pore is small enough to be considered as a capillary tube. The modelling approach consists of two major steps. First the infiltration and solidification mechanisms are studied at the pore level, namely in a capillary tube cooled by its lateral wall. This is to characterize the filling and cooling process at the local level. In a second step, a macroscopic model is developed to simulate the process at the scale of a porous mould.

FIGURE 1. An example of metallic foam

2. INFILTRATION AND SOLIDIFICATION MODEL

The problem under consideration considers a capillary tube whose internal diameter d is small compared to its length L. A liquid metal is injected at the entrance of the duct and a pressure difference is applied between the inlet and the outlet of the tube. In a first phase of the process the infiltration of the liquid flow pushes the air phase out of the tube. The liquid metal progressively solidifies at the walls of the mould up to a certain point where the solid phase blocks up the capillary tube and stops the liquid flow. Then solidification proceeds in the liquid trapped upstream.

FIGURE 2. Schematic description of the infiltration problem

Model. The model assumes that the fluid flow is laminar and incompressible, both in the liquid metal and in the air initially present in the tube and natural convection inside the tube is assumed to be negligible. The mathematical model makes use of a one-domain formulation where the four phases (liquid + solid metal, mould and air) are considered as one effective medium throughout the domain, with physical properties weighted as functions of the phase fractions. Let us call α the local volume fraction of metal in the tube (1 for the metal ; 0 for the air) ; we also introduce the duct indicator ϕ (= 1 inside the tube (air or metal) ; = 0 in the mould) and γ_T the solid-liquid indicator (= 1 in the liquid $T \geq T_{melt}$ and = 0 in the solid phase $T < T_{melt}$). These effective properties are obtained by linear combination of the physical properties of each phase at the different interfaces, except for the effective conductivity due to strong conductivity contrasts between the phases.

The fluid flow is governed by the modified Navier-Stokes equation for an incompressible fluid and therefore the continuity and the momentum equations are given by:

$$\frac{\partial \rho}{\partial t} + \nabla.(\rho \mathrm{v}) = 0 \tag{2}$$

$$\frac{\partial \rho \mathrm{v}}{\partial t} + \nabla.(\rho \mathrm{vv}) = -\nabla p + \nabla.(\mu \nabla \mathrm{v}) + \sigma K \nabla \alpha - A\,\mathrm{v} - B\,\mathrm{v} \tag{3}$$

where K is the curvature of the liquid metal-gas interface. The momentum equation (3) contains an additional source term which is the pressure jump at the liquid-air interface arising from the surface tension between the two fluids. Using the volume-of-fluid (VOF) method [1]

this term (the third term in the RHS) is evaluated by solving a transport equation of the metal volumetric fraction α:

$$\frac{\partial \alpha}{\partial t} + \nabla.(\mathbf{v}\alpha) + \nabla.[\mathbf{v}_r \alpha(1-\alpha)] = 0 \tag{4}$$

where $\mathrm{v}_r = \mathrm{v}_L - \mathrm{v}_g$ is the relative velocity of the two fluids. The fourth and fifth terms in the RHS of (3) are penalty terms: the first one depends on the solid-liquid phase indicator and imposes a zero velocity field in the metal once solidified and the other one depending on the duct indicator imposes a zero velocity in the mould : $A = \alpha \phi \mathrm{P}_1 (1-\gamma_T)$ and $B = (1-\phi)P_2$, where P_1 and P_2 take large values.

The phase change model for the solidifying pure metal uses a procedure adapted from the enthalpy-porosity method [2] proposed by Voller. The general energy conservation equation :

$$\frac{\partial H}{\partial t} + \nabla.(\mathbf{v}H) = \nabla(k\nabla T)\cdot \tag{5}$$

is transformed by deriving the relationship between the enthalpy and the temperature with respect to time and space in eq. (5), and we obtain a formulation where temperature is the depending variable :

$$\rho c_P \frac{\partial T}{\partial t} + \rho c_P \nabla.(\mathrm{v}T) = \nabla(k\nabla T) - \phi\ \alpha\ \rho_L\ L_F \frac{\partial \gamma_T}{\partial t}. \tag{6}$$

Numerical solution. The set of equations resulting from the mathematical model presented above is implemented in the open source software OpenFOAM [3]. The basic source code, which contains the essential modules for solving flow and heat transfer problems, uses the finite volume method [4]. The solution procedure can be summarized as follows: first the mesh is generated and the variable fields are initialized. Then, the time step is calculated in order to satisfy the Courant-Friedrichs-Lewy (CFL) condition. The transport equation for the metal volume fraction is solved, which enables us to calculate the surface tension force. Subsequently, the metal-gas interface is built-up and the physical properties are updated as functions of the phase fractions. Next, the pressure-velocity coupling is solved using the PIMPLE (PISO-SIMPLE) scheme of OpenFOAM for the continuity and the momentum equations (1, 2). The convergence of the solution is monitored by calculating the error on the velocity divergence. At this stage, the pressure and velocity fields as well as the metal fraction distribution are known for the current time step. Using the velocity field solution, the energy equation can be solved to obtain the temperature field and the metal liquid fraction, which is used to update the penalty source term of the momentum equation.

Numerical validation tests have been performed separately to validate the fluid flow and the phase change problems and to verify grid convergence. The simulations presented hereafter have been performed with the 2D axisymmetric version of the code, which originally exists in 3D.

3. RESULTS

Fluid flow in the capillary tube and diffusive phase change tests have been performed first to check the ability of the code. In this section, we present a first simulation test where a uniform heat flux is extracted from the tube wall in order to observe the solidification phenomena of the liquid flowing inside the tube (no mould). The tube is initially filled with liquid aluminium at a temperature of 1073 K (initial superheat of 140 K) and the flow is driven by a pressure difference of 300 Pa between the inlet and outlet of the duct. The progression of the solid phase is described in Figure 3 below.

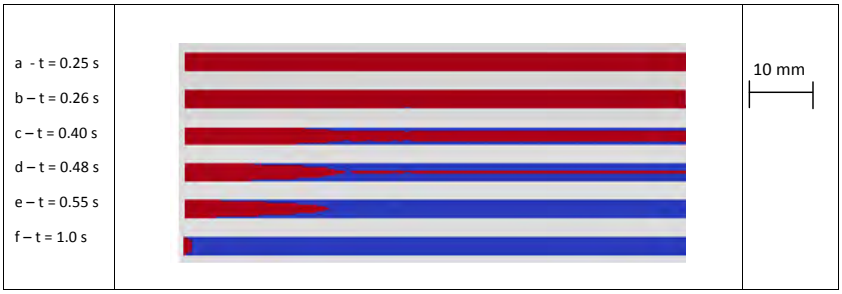

FIGURE 3. Solidification process of liquid aluminium (liquid phase : red – solid phase : blue)

a –tube initially filled with liquid aluminium, b – aluminium solidification starts at the tube wall, c – solidification progresses in the radial direction, d – solidified metal closes the tube and blocks up the fluid flow, e – solidification proceeds towards the inlet of the tube, f –complete aluminium solidification.

Our interest is to observe the solidification process during the infiltration of a cylindrical mould by liquid aluminium. In the simulations being presently performed, we consider a 200 mm long capillary tube with an annular cross section of 1.2 mm and 2 mm inner and outer radius, respectively. The external wall of the mould is adiabatic (zero thermal flux) and the mould and the air are initially at the ambient temperature. The liquid aluminium flow is driven by a constant pressure difference of 1500 Pa, sufficient to overcome the Laplace pressure at the metal-air interface. We consider that the liquid metal is initially overheated at different temperatures between 50 K and 200 K above the the solidification point of the metal. This allows the metal to flow on a certain distance in the mould before solidification takes place.

5. CONCLUSIONS

The code allows us to study the relationship between the infiltrated length and the solidification time as a function of the operating parameters such as the initial superheat, the imposed pressure difference between the tube inlet and outlet and the initial mould temperature.

ACKNOWLEDGEMENT

The authors wish to gratefully acknowledge the financial support of the French National Research Agency (ANR) in the frame of the MATEPRO Program under grant ANR-10-RNMP-018 (FOAM project).

REFERENCES

[1] H. Rusche, Computational Fluid Dynamics of Dispersed Two-Phase Flows at High Phase Fractions, 2002.

[2] V. R. Voller, An overview of numerical methods for solving phase-change problems, *in Advances in. Numerical Heat Transfer*, 1997, 341-380.

[3] www.openfoam.com

[4] S. V. Patankar, Numerical Heat Transfer and Fluid Flow. *Hemisphere*, 1980.

Third International Conference on Computational Methods for Thermal Problems
THERMACOMP2014, June 2-4, 2014, Lake Bled, Slovenia
N. Massarotti, P. Nithiarasu and B. Sarler (Eds.)

NON-ISOTHERMAL DIFFUSION OF CHEMICALS IN SEMI-INFINITE POROUS MEDIA

Haijian Xie
College of Civil Engineering and Architecture, Zhejiang University, 866, Yuhangtang Road, Hangzhou, 310058, China, xiehaijian@zju.edu.cn

Majid Sedighi
Geoenvironmental Research Centre, School of Engineering, Cardiff University
The Queen's Buildings, Newport Road, Cardiff, CF24 3AA, UK, sedighim@cf.ac.uk

Hywel R. Thomas
Geoenvironmental Research Centre, School of Engineering, Cardiff University
The Queen's Buildings, The Parade, Cardiff, CF24 3AA, UK, thomashr@cf.ac.uk

Yunmin Chen
College of Civil Engineering and Architecture, Zhejiang University, 866, Yuhangtang Road, Hangzhou, 310058, China, chenyunmin@zju.edu.cn

ABSTRACT

This paper presents an analytical solution for one-dimensional diffusion of chemicals under coupled chemical and thermal potentials. The theoretical formulation considered includes heat conduction and chemical diffusion due to both molecular and thermal processes. A Laplace transformation has been used to derive the analytical solution of the problem in a semi infinite domain. The results of a verification test which deals with non-isothermal diffusion of a chemical in water are presented. An application of the model to study the effects of thermal diffusion on chemical transport in a landfill clay liner is presented.

Key Words: *Thermal Diffusion, Chemical Transport, Heat Conduction, Analytical Model.*

1. INTRODUCTION

A temperature gradient can induce mass flow due to thermal diffusion, also known as the Soret-Ludwig effect or Soret effect [1]. The ratio of the thermal diffusion coefficient to the molecular diffusion coefficient, i.e. the Soret coefficient, has been reported to be of the order of 10^{-2} to 10^{-3} K^{-1} [1]. Experimental studies have also shown the importance of thermal effects on the diffusion of chemicals in electrolyte solutions e.g. [2], and in compacted clays e.g. [3].

This paper presents an analytical solution for non-isothermal diffusion of chemicals in a semi-infinite porous medium. The analytical solution developed considers steady state heat transfer via conduction and chemical transport due to both molecular and thermal diffusion processes. The analytical solution is tested against a coupled heat, moisture and chemical numerical model [4]. The theoretical formulation of the numerical model applied for the verification of the analytical solution includes a coupled formulation for the diffusion of multicomponent ions under electrochemical and thermal potentials [4].

The model developed is used to study the long term diffusion of a non-reactive chemical in a compacted clay liner, used to contain contaminants in landfills. The application example demonstrates the impact of thermal diffusion on the transport process.

2. THEORETICAL FORMULATION AND ANALYTICAL SOLUTION

A coupled theoretical formulation of heat conduction and chemical diffusion in saturated porous media is considered in the analytical solution. Heat conduction is assumed to be under steady-state condition whilst transient chemical diffusion under chemical and thermal potentials is considered. The assumption of steady state heat conduction is based on the fact that the temperature profile in the domain reaches equilibrium more quickly than is the case for chemical transport. This has been observed both in experimental studies of thermal diffusion in aqueous solution [2] and also shown using numerical simulations [4].

The governing equation for chemical diffusion in a multicomponent chemical system under coupled electrochemical and thermal potentials, as presented by Thomas et al. [4], can be simplified for the one dimensional diffusion of a single chemical, as:

$$R_d \frac{\partial C}{\partial t} = D^* \frac{\partial^2 C}{\partial z^2} + S_T D^* \frac{\partial}{\partial z}\left(C \frac{\partial T}{\partial z} \right) \tag{1}$$

where C is the chemical concentration, R_d is the retardation factor and t represents the time. D^* is the effective diffusion coefficient which is assumed to be constant in the development of the solution. z represents the distance, S_T is the Soret coefficient and T is temperature.

The solution to the governing equation of one-dimensional heat conduction under steady state conditions can be expressed as:

$$T = Az + B \tag{2}$$

where A and B are constants, dependent only on the boundary conditions of the problem.

By substituting Eq. 1 into Eq. 2, coupled molecular and thermal diffusion can be presented as:

$$R_d \frac{\partial C}{\partial t} = D^* \frac{\partial^2 C}{\partial z^2} + AS_T D^* \frac{\partial C}{\partial z} \tag{3}$$

For a semi-infinite domain in which the initial concentration is $C(z,0) = C_i$, and the chemical concentration at one boundary is constant, i.e. $C(0,t) = C_0$ with the other boundary assumed to be impermeable, i.e. $\frac{\partial C(\infty,t)}{\partial z} = 0$, the analytical solution to Eq. 3 can be obtained using a Laplace transformation technique. Using this approach and under the conditions described, the analytical solution can be expressed as:

$$\frac{C(z,t) - C_i}{C_0 - C_i} = \frac{1}{2} erfc\left[\frac{AD^* S_T t + R_d z}{2\sqrt{D^* R_d t}} \right] + \frac{1}{2}\left[\exp(-AS_T z)\right] erfc\left[\frac{-AD^* S_T t + R_d z}{2\sqrt{D^* R_d t}} \right] \tag{4}$$

where, *erfc* denotes the complementary error function.

3. MODEL VERIFICATION

The results of a verification exercise on the analytical solution against a numerical model of coupled thermal, hydraulic and chemical behaviour of multicomponent chemicals [4] are presented. The problem considered includes a 10m domain in which the diffusion of a non-reactive ion in water, under a thermal and chemical gradient is studied. The ion considered is chloride. The diffusion coefficient and the Soret coefficient were considered to be 10^{-9} m^2/s and 5×10^{-3} K^{-1}, respectively [1]. The domain, initial and boundary conditions of the problem are shown in Figure 1.

The results of the analytical solution and those obtained from the numerical model for chemical distribution in the domain at 5.6 and 11.1 years are presented in Figure 2.

$$T(0,t)=333 \qquad C(0,t)=1000\ \text{mol/m}^3$$

$$T(x,0)=293\ \text{K} \qquad C(x,0)=0.1\ \text{mol/m}^3$$

$$T(\infty,t)=293 \qquad \frac{\partial C(\infty,t)}{\partial x}=0$$

FIGURE 1. The initial and boundary conditions of the verification exercise

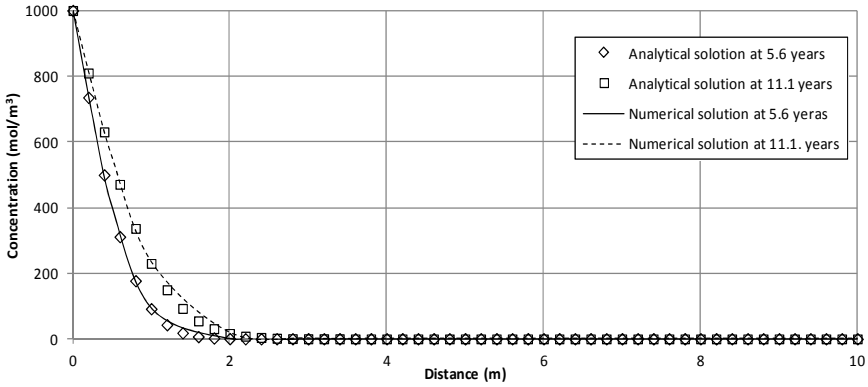

FIGURE 2. The results of the analytical solution and numerical model

These provide confidence in the accuracy of the analytical solution developed under the conditions considered in this verification exercise.

4. MODEL APPLICATION

The analytical solution presented was applied to study the long term diffusion of a non-reactive chemical in a compacted clay liner used as the bottom barrier in landfills. Waste degradation may induce a considerable amount of heat at the base of the landfill [5]. High values of temperature have been reported e.g. temperatures up to 80 ^{o}C in semi-aerobic landfills [6]. It was also assumed that groundwater percolation below the clay liner maintains the temperature of the ground at a constant value.

Under the conditions described the effects of the thermal diffusion on transport rate were studied. The problem studied is a 0.6m compacted clay liner in which a constant temperature is applied at the top and bottom of the domain, i.e. 353 K and 283 K, respectively. A constant concentration of the chemical compound was considered at the top of the liner, i.e.100 mol/m^3. The diffusion coefficient was assumed to be 2.8×10^{-10} m^2/s which is in the range of values reported for clay barriers in landfill applications [5]. The effect of thermal diffusion was studied using a value for the Soret coefficient based in the range reported in the literature for compacted clays i.e. 10^{-2} (K^{-1}) [2].

Two sets of calculations were carried out which consider the diffusion of the chemical due to i) molecular diffusion and ii) coupled molecular and thermal diffusion. The results obtained, for a duration of 100 years, are presented in Figure 3. A larger rate of diffusion is observed from the simulation which considers thermal diffusion. The concentration of the chemical at the bottom of the liner shows an increase of approximately 24% due to thermal diffusion. The results indicate the importance of thermal diffusion when considering chemical movement in these cases.

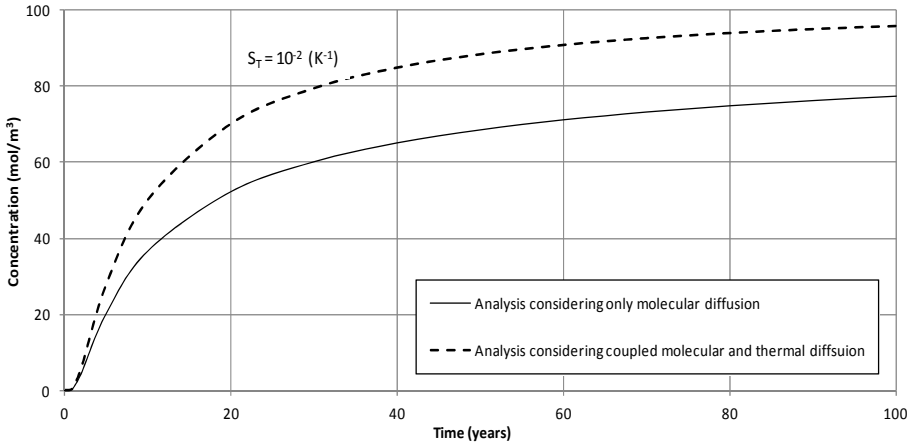

FIGURE 3. Results of non-isothermal chemical diffusion in a compacted clay.

5. CONCLUSIONS

A new analytical solution for chemical diffusion under coupled chemical and thermal potentials has been presented. The Laplace transformation approach was successfully adopted to derive the solution for a semi-infinite domain, considering steady state heat conduction. Confidence in the approach developed was obtained from the results of a verification test. An application for the diffusion of a non-reactive chemical in a compacted clay liner highlighted the importance of thermal diffusion in the process of chemical transport. The model developed can be applied in the verification of numerical solutions and to obtain a better understanding of thermal impacts on the diffusion process and chemical transport.

REFERENCES

[1] A.C. Lasaga, *Kinetic Theory in the Earth Sciences*. Princeton Series in Geochemistry, Princeton University Press. 1998.

[2] D.G. Leaist, and L. Hui, Conductometric determination of the Soret coefficients of a ternary mixed electrolyte, Reversed thermal diffusion of sodium chloride in aqueous sodium hydroxide solutions. *Journal of Physical Chemistry*, 94, 447-451, 1990.

[3] M. Rosanne, M. Paszkuta, M. and P.M. Adler, Thermodiffusional transport of electrolytes in compact clays. *Journal of Colloid Interface Science*, 299, 797-805, 2006.

[4] H.R. Thomas, M. Sedighi, and P.J. Vardon, Diffusive reactive transport of multicomponent chemicals under coupled thermal, hydraulic, chemical and mechanical conditions, *Journal of Geotechnical and Geological Engineering*, 30, 4, 841-857, 2012.

[5] R.K. Rowe, Long-term performance of contaminant barrier systems, 45th Rankine Lecture. *Géotechnique*, 55, 631-678, 2005.

[6] F. Li, Q. Huang, Z. Zhang, and Q. Wang. Spatial variability of temperature in semi-aerobic landfilling structure. *Chinese Journal of Applied Ecology*, 17, 7, 1291-1294, 2006.

Third International Conference on Computational Methods for Thermal Problems
THERMACOMP2014, June2-4, 2014, Lake Bled, Slovenia
N. Massarotti, P. Nithiarasu and B. Sarler(Eds.)

Effect of domain size on grid convergence in numerical models of alloy solidification

Igor Vušanović
University of Montenegro, George Washington St. bb, 81000 Podgorica, Montenegro,
igor.vusanovic@ac.me

Vaughan R. Voller
Department of Civil Engineering, University of Minnesota, Minneapolis, MN 55455, USA,
vole001@umn.edu

ABSTRACT

When a multi-component alloy solidifies the redistribution of solute components leads to the formation of segregation patterns. One common form of patterns is the formation of high solute segregation channels, which can have thickness dimensions from several to tens of mm. Many numerical casting models have the ability to predict the formation of these channels. The problem, however, is that the grid size in such calculations can have a significant influence on the shape, size, number, and location of these channels. With this lack of grid convergence results it is not possible to formulate a phenomenological understanding of the segregation processes. Recently, working with an Al - 4.5%Cu binary alloy solidifying in a small side cooled cavity 40x40 mm we have shown that it is possible to arrive at grid independent predictions of channels once the grid size falls below ~ 0.3 mm. Clearly, however, such a cavity size is well below that that might be used in industrial and even laboratory settings. Here our task is to see if similar grid independent results can be obtained with simulations on a larger grid size of 76x76mm. Our results indicate that although grid resolution is approached with a grid size of ~0.3 mm it has still not been fully achieved. Thus indicating that the expected increase in fluid flow in the larger cavity produces more and finer channels which are harder to numerically resolve.

Key Words: *Macrosegregation, Al-Cu alloys, Darcy law, Enthalpy model, Explicit scheme*

1. INTRODUCTION

The study of macro-segregation patterns in solidified metals has been a keen research area for many decades. A common pattern, which is still not fully understood is the appearance of high solute channel segregates adjacent to solute poor zones. Open questions center on knowing what process factors control the shape, size, number and location of the channels [1-2]. Clearly numerical simulations of the governing flow, heat transfer, and solute conservations equations have the potential to make significant advances on these issues. Such efforts, however, are hampered by the fact that many of the current simulation models do not achieved full grid independence. In particular as the grid is refined new channels can appear and existing channels can move or vanish. A counter to this is the recent two-dimensional simulation of the solidification of an Al-4.5%Cu alloy in a side cooled square (40x40mm) cavity by Vušanović et al. [3]; Fig. 1 shows the predicted horizontal midline copper concentrations on full solidification using three grid size. It is obvious from these profiles that the macro-segregation predictions are converging as the grid is refined. To eliminate sources of numerical and physical noise that could seed the formation of spurious numerical channels a number of simplifying assumptions were made in these calculations; in particular, a simple porosity model, constant properties, laminar flow and a lever rule for the thermodynamic coupling between temperature and temperature fields. In addition, to quench noise from iterative solvers, explicit time stepping was used to solve the thermal and solutal fields. The

main finding from the work of Vušanović et al. [3] is that in a cavity of 40x40mm a grid size of ~ 0.3 mm is required to reach grid independent results. Our objective here is simple. We would like to see if a similar treatment and grid size will also give grid independent results when the cavity size is increased to 76x76mm. Our suspicion is that the increased fluid flow intensity will lead to more channels which in turn may require a finer grid refinement.

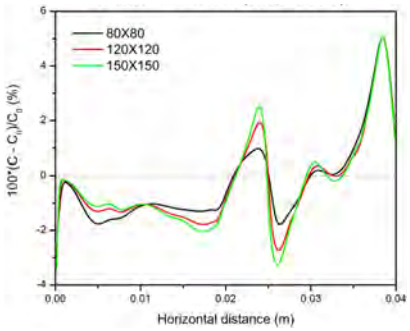

FIGURE 1. Midline horizontal segregation profiles for 40x40mm domain(after [3])

2. PHYSICAL AND MATHEMATICAL MODEL

The initial condition is a Al-4.5wt%Cu alloy superheated by 20K over the liquidus temperature. Solidification occurs via heat convection on the left vertical wall; a constant heat transfer coefficient (h_{tc}=1000W/m^{2}K) and a constant ambient temperature (T_0=300K) are assumed. The mathematical model for solidifications is based on mixture continuum theory originally proposed by Bennon and Incropera [4]. A simple version of the model is used in which (i) the solid velocity is fixed to zero, (ii) properties of alloy are the same within and across phases, (iii) there is no air voids, (iv) solute diffusion is neglected, (v) a linear liquidus line in the phase diagram (vi) there is isotropic permeability and (vii) a lever rule couples the thermal and solutal fields. The model equations are as follows:

$$\frac{\partial \rho}{\partial \tau} + \nabla \cdot (\rho \mathbf{u}) = 0 \tag{1}$$

$$\frac{\partial}{\partial t}(\rho u) + \nabla \cdot (\rho \mathbf{u} u) = \nabla \cdot (\mu \nabla u) - \frac{\partial p}{\partial x} - \mu K^{-1} u \tag{2}$$

$$\frac{\partial}{\partial t}(\rho v) + \nabla \cdot (\rho \mathbf{u} v) = \nabla \cdot (\mu \nabla v) - \frac{\partial p}{\partial y} - \rho g[\beta_T (T - T^{rerf}) + \beta_C (C_L - C_L^{ref})] - \mu K^{-1} v \tag{3}$$

$$K = \kappa_0 \frac{f^3}{(1-f)^2}, \ \kappa_0 = 1.0x10^{-10} m^2 \tag{4}$$

$$\frac{\partial}{\partial t}(\rho C) + \nabla \cdot [(\rho C_L)\mathbf{u}\ ] = 0 \tag{5}$$

$$\frac{\partial}{\partial t}(\rho H) + \nabla \cdot [(\rho c T + \rho L)\mathbf{u}\ ] = \nabla \cdot (k \nabla T) \tag{6}$$

Where $\boldsymbol{u_L}=(u_L,v_L)$is the liquid velocity, $\boldsymbol{u}=f\boldsymbol{u_L}$ is the mixture velocity, f is the liquid fraction, ρ is the density (a constant here), p is pressure, μ is the dynamic viscosity, g=9.81 ms^{-2} is the acceleration of gravity, $H=cT+fL$ is the enthalpy, c the specific heat, k thermal conductivity, and the temperature T is related to the liquid solute concentration C_L through $T=T_m+m_LC_L$, where T_m is the fusion temperature of Al and m_L is the slope of the liquidus line. Numerical solution is obtained

using a square grid of control volumes. The fluid flow equations are solved using a pressure correction approach [5]. As noted above, however, the thermal and solutal conservation terms are solved with the time explicit scheme suggested in [6]. As noted in our recent similar study [3] although such a scheme may be computationally inefficient it is exact and does not induce numerical noise that might lead to the formation of spurious channels.

3. RESULTS

Figure 3 shows the predicted macro-segregation field in 76x76mm cavity size, in particular the formation of channel segregates, for three levels of grid size: 150x150 ($\Delta t = 2.22 \times 10^{-4}$sec.), 250x250 ($\Delta t = 8.0 \times 10^{-5}$sec.) and 300x300 ($\Delta t = 5.0 \times 10^{-5}$sec.). On comparing with the 40x40mm case, Fig. 2, although there are broad similarities there are also some important differences. In the first place more channels with a wider range of length scales appear. Secondly, even when we go below a grid size of ~0.3mm, it quite clear that a grid independent result has not been achieved.

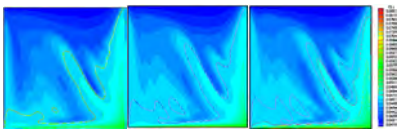

80x80 120x120 150x150

FIGURE 2. Final macro-segregation patterns for 40x40mm domain (after [3])

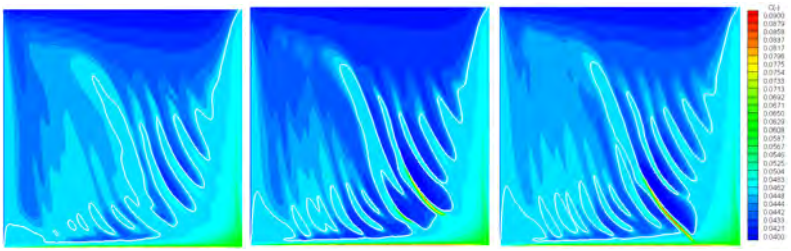

150x150 250x250 300x300

FIGURE 3. Final macro-segregation patterns for 76x76mm domain. The superimposed white line indicates the initial alloy composition and thereby separates low and high concentration regions in the final solidified casting

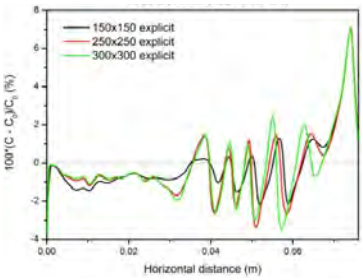

FIGURE 4. Midline profiles of concentration for 76x76mm domain. The peaks and valleys in the results, presented as relative to the nominal concentrations, indicate the locations and size of the channel segregates.

An observation, reinforced by looking at the prediction of mid-line concentration, see Fig. 4, which indicate a sharpening and shifting of the channels as the grid is refined. Thus, the grid size of ~0.3mm obtained in our previous work cannot be regarded as a size that will guarantee grid convergence in a macro-segregation calculation. Clearly, as we suspected, the increased intensity in the natural convection flow in the larger domain seems to lead to more and finer channel segregates, which in turn requires a finer grid for numerical resolution.

4. CONCLUSIONS

The formation of channel segregates in alloy casting is an industrial problem. The use of high-end numerical simulation may be able to shed important light on their formation and ultimately on their mitigation from the process. In achieving this goal it is necessary to have grid independent results. The work in this paper indicates that even when investigating small domains with simplifying assumptions it is possible but difficult to arrive at grid independent results. However, our results also indicate that when moving toward industrial castings, that will be larger, three-dimensional and require more complex thermodynamic and fluid flow modeling, the task of obtaining grid independent predictions may be well beyond our current computational power [7]. In determining a specific answer to this question our next step will be aimed at trying to find an a-priori means of calculating the grid size requirement for a given simulation; perhaps through relating this size to appropriate dimensionless groups.

REFERENCES

[1] H. Combeau, M. Bellet, Y. Fautrelle, D. Gobin, E. Arquis, O. Budenkova, B. Dussoubs, Y.Du. Terrail, A. Kumar, Ch-A. Gandin, B. Goyeau, S. Mosbah, T. Quatravaux, M. Rady and M. Založnik, Analysis of a numerical benchmark for columnar solidification of binary alloys, *IOP Conf. Series: Materials Science and Engineering*, 33 (012086), 2012.

[2] A. Kumar, B. Dussoubs, M. Založnik, H. Combeau, Effect of discretization of permeability term and mesh size on macro and meso-segregation predictions, *Journal of Physics. D: Appl. Phys.*42,105503 (13pp),2009.

[3] I. Vušanović and V. R. Voller, Understanding channel segregates in numerical models of alloy solidification: A case of converge first and ask questions later, *The 6th International Conference on Solidification and Gravity*, Miskolc Lillafured, Hungary,2013.

[4] W. D. Bennon, F. P. Incropera, A continuum model for momentum, heat and species transport in binary solid-liquid phase change system - I. Model formulation, *Int. J. Heat Mass Transfer,* 30, 2161 - 2170, 1987.

[5] S. Patankar, *Numerical Heat Transfer and Fluid Flow*, Hemisphere, New York, 1980.

[6] V. R. Voller, A. Mouchmov, M. Cross, An explicit scheme for coupling temperature and concentration fields in solidification models, *App. Math. Model*. 28, 79 - 94, 2004.

[7] V.R. Voller, and F. Porte-Agel, Moore's law and numerical modeling, *J. Comp. Phys.*, 179, 698-703, 2002.

PARALLEL SESSION

NUMERICAL METHODS

Third International Conference on Computational Methods for Thermal Problems
THERMACOMP2014, June 2-4, 2014, Lake Bled, Slovenia
N. Massarotti, P. Nithiarasu and B. Sarler (Eds.)

GENERALIZED TRANSFER FUNCTIONS FOR REAL TIME MONITORING OF THERMAL PROCESSES

Jose V. Aguado
Institut GeM, UMR CNRS 6183, at Ecole Centrale Nantes, 1 rue de la Noë 44321 Nantes (France),
jose.aguado-lopez@ec-nantes.fr

Antonio Huerta
LaCaN at Universitat Politècnica de Catalunya, BarcelonaTech 08034 Barcelona (Spain),
antonio.huerta@upc.es

Francisco Chinesta, Adrien Leygue
Institut GeM, UMR CNRS 6183, at Ecole Centrale Nantes, 1 rue de la Noë 44321 Nantes (France),
francisco.chinesta@ec-nantes.fr, adrien.leygue@ec-nantes.fr

Elias Cueto
I3A at Universidad de Zaragoza, Maria de Luna 3 50018 Zaragoza (Spain),
ecueto@unizar.es

ABSTRACT

This work is concerned with the real-time temperature monitoring of a part under a forced excitation translating on its boundary. In practice, monitoring is usually carried out by performing few measures at some specific points in order to ensure the correct management of a thermal process, to identify model and process parameters, or even to perform non-destructive inspection by comparing measures to the numerical prediction, for instance. To these purposes, we propose a simple methodology that provides, in real time, the long-term forced response at the monitored point from the only knowledge of a pre-computed *generalized transfer function* (GTF) and the imposed excitation up to the monitored instant. In addition, it allows solving the inverse problem, i.e. from the measured temperature identify the shape of the translating forcing excitation. The methodology is based on reciprocity and model reduction, and thus it is only applicable to linear problems. For reciprocity to be applicable to heat transfer, we provide an appropriate setting of the problem. This approach is combined with the Proper Generalized Decomposition (PGD), a model reduction technique, in order to compute efficiently and offline the GTF. The PGD also offers the possibility to further extend the GTF concept by considering the explicit dependence on material or process parameters, for instance. Such GTF constitutes a quite general tool that allows monitoring temperature at the point of interest for an arbitrary excitation following an arbitrary path on the part with non-fixed (eligible) material or process parameters.

Key Words: *Monitoring, Heat Transfer, Reciprocity, Real Time, Generalized Transfer Function, Model Reduction, Proper Generalized Decomposition, Harmonic Analysis.*

1. INTRODUCTION

From research to industry, many scientific experiments and manufacturing processes involve thermal processes that need of measuring temperature. Several techniques are available to measure temperature. The most extended practice consists in performing few measures at some specific points, although other techniques allow measuring the temperature field. The collected information can be used with many purposes. Among the classic ones, we can cite material or process parameters identification, model validation, detection of process malfunction, quality assessment and process control, for instance. First two applications try to fit the measured temperature, assumed as the *reference*. Last three applications, however, assume that a trustworthy model is

available. Thus, the model is considered as *reference*, and deviations are used to detect if the process operates under abnormal conditions, to perform non-destructive inspection or to control the process by adjusting the process parameters. In any case, a model has to be solved, and for thermal processes that model is usually the heat transfer equation.

In general, as monitoring is performed at few points, only the temperature at those points needs to be computed. Therefore, classic numerical methods (e.g. finite element discretization and time integration scheme) [1] are inefficient to our purposes, as they compute the entire *reference* temperature field. Moreover, that field is related to a particular process configuration, i.e. a certain forced excitation following a pre-defined path on the boundary of the part. If the process configuration changes new predictions have to be computed, and of course, they can hardly be attained in real time because computing the entire temperature field is relatively costly. Instead, simplified or even phenomenological models are derived very frequently for real time applications, such process control. For all these reasons, other approaches are needed.

Ideally, the approach should provide the temperature at the monitored point, and it should be easy to compute. Green's functions [2] fulfil, at least theoretically, those requirements. In particular, if the adjoint Green's function were known, the temperature at the monitoring point could be readily evaluated. However, this is by no means a trivial task, viz. for an arbitrary domain.

This work presents a simple methodology that provides, in real time, the long-term forced response at the monitored point from the only knowledge of a pre-computed *generalized transfer function* (GTF) and the imposed excitation up to the monitored instant. The methodology is based on reciprocity [3] and model reduction. It is well-established that reciprocity does not hold for heat transfer in the time domain because the operator is not self-adjoint. But in the frequency domain the operator becomes symmetric, although not hermitian, and symmetry reveals sufficient for reciprocity to hold. This approach is combined with the Proper Generalized Decomposition (PGD) [4,5], a model reduction technique, in order to compute efficiently and offline the GTF. The PGD also offers the possibility to further extend the GTF concept by considering the explicit dependence on material or process parameters, for instance [6]. Such GTF constitutes a quite general tool that allows monitoring temperature at the point of interest for an arbitrary excitation following an arbitrary path on the part with non-fixed (eligible) material or process parameters.

In addition, it allows solving the inverse problem, i.e. from the measured temperature identify the shape of the translating forcing excitation.

2. USING RECIPROCITY TO MONITOR TEMPERATURE

As it has been explained in the previous section, for reciprocity to apply for the heat transfer problem, it must be solved in the frequency domain. For the sake of brevity, we shall omit the proof. Thus we consider the Fourier transform of the canonical dimensionless form of the heat equation, with isotropic and homogeneous linear material, and homogeneous Dirichlet boundary conditions. The transfer function $\hat{h}(x \in \Omega)$ can be computed from solving such complex-valued problem with a Dirac function centred on the monitored point, x_0, i.e.

$$\begin{cases} i\omega\hat{h} - \nabla^2\hat{h} = 0 & in \quad \Omega, \\ \hat{h} = 0 & on \quad \Gamma_D, \\ n \cdot \nabla\hat{h} = \delta(x - x_0) & on \quad \Gamma_N, \end{cases} \tag{1}$$

Γ_D and Γ_N represent Dirichlet and Neumann boundaries, respectively, and n is the exterior unit normal to Γ_N. Notice that having to solve eq. (1) for all frequency, even if this can be done offline, is potentially expensive. A major contribution of the PGD is to view parameters as new coordinates [6], and then, we shall consider that the transfer function explicitly depends on ω. This is called *generalized transfer function* (GTF). The n-rank approximation of the GTF is computed under the form:

$$\hat{h}(x,\omega) \approx \hat{h}^n(x,\omega) = \sum_{i=1}^{n} X^i(x) W^i(\omega). \quad (2)$$

GTF concept can be further generalized by considering the explicit dependence on material parameters such as diffusivity, although this topic is not discussed for the sake of brevity. Thanks to reciprocity, it can be shown that temperature can be monitored at a given point and instant by solving the following simple expression:

$$u(x_0,t_0) = \int_0^{t_0} \int_{\Gamma_N} h(x,\tau) q(x, t_0 - \tau) d\Gamma_N d\tau. \quad (3)$$

Eq. (3) only needs the Fourier inversed GTF and the forcing excitation up to t_0.

3. SPATIAL IDENTIFICATION OF EXCITATION

It consists in determining the actual spatial distribution of the imposed flux that travels at a constant velocity. Assuming that the shape can be approximated as a linear combination of m known basis functions (finite element shape functions, for instance), the coefficients of the linear combination must be found. From eq. (3), provided that $\ell \geq m$ measures are available, the coefficients can be computed by solving a least square problem, in general.

4. RESULTS

We consider a quarter of cylinder with the geometry and mesh depicted in the Fig. 1 (left), submitted to a forced excitation following a parallel trajectory to the exterior face. Constant velocity of 1 m/s is considered. The monitoring point is placed in the middle of the internal face, indicated in red. The forced excitation is a laser producing a flux that follows a Gaussian of zero mean and standard deviation of 0.05. All material properties are taken equal to unity, and convective heat exchanges are not considered, although it could be possible. Homogeneous Dirichlet boundary conditions are imposed at both ends of the piece. The propriety of these conditions for realistic applications is not discussed here as the objective is to demonstrate the performance of the methodology. The GTF involves 11 terms, $n = 11$ in eq. (2), for a L^2 residual error of 0.01%. The frequency range considered goes from 0 to 250 Hz, i.e. $\omega \in [0,500\pi]$.

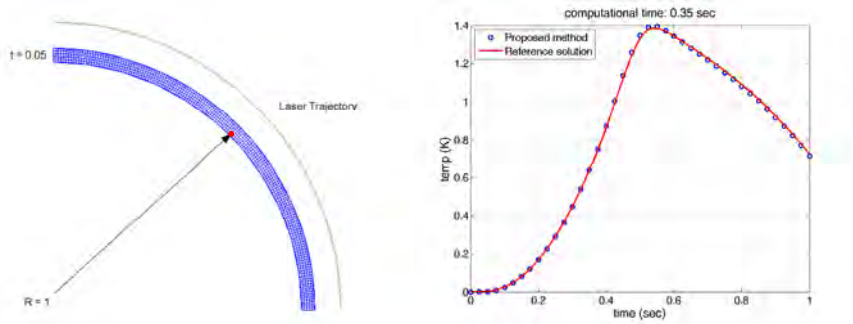

FIGURE 1. Left: geometry and discretization. Right: verification of monitoring results

Fig. 1 (right) shows in red the temperature evolution at the monitored point during the excitation path. It was obtained with a finite element discretization and a Crank-Nicolson integration scheme. Blue marker symbols are used for the temperature predicted by the proposed methodology. Good agreement is observed. In addition, 1 second of simulation is achieved in 0.35 seconds of

computational, meaning that real time applications are feasible even using an interpreted language such MATLAB in this case. Fig. 2 shows a sequence of four snapshots at different times: 0.25, 0.50, 0.75 and 1.00 seconds. Each one shows in the left the temperature field computed with the reference method, and in the right the prediction computed with the proposed methodology.

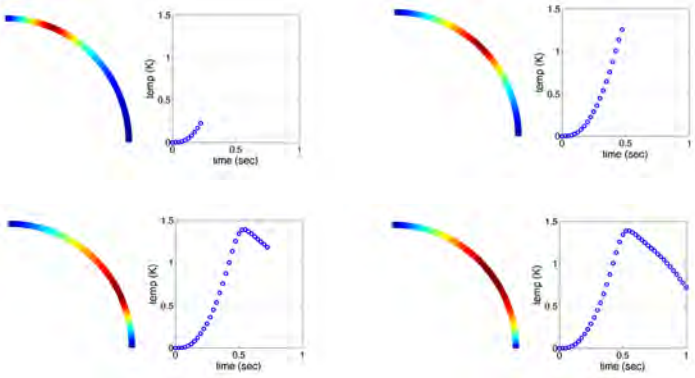

FIGURE 2. Temperature field and monitored temperature at: 0.25, 0.50, 0.75 and 1.00 sec

5. CONCLUSIONS

A simple methodology that provides in real time the long-term forced temperature of a linear problem at the monitored point has been presented and verified against standard numerical methods. This methodology operates from the only knowledge of a pre-computed *generalized transfer function* (GTF) and the imposed excitation up to the monitored instant. Moreover, it allows solving the inverse problem, i.e. from the measured temperature the shape of the translating forcing excitation can be identified.

REFERENCES

[1] O.C. Zienkiewicz and R.L. Taylor, *The Finite Element Method*, 5th Edition, Vol. I, Butterworth Heinemann, 2000.

[2] S. Bayin, *Mathematical Methods in Science and Engineering*, 3rd Edition, Wiley, 2006.

[3] J.D. Achenbach, *Reciprocity in Elastodynamics*, Cambridge University Press, 2003.

[4] A. Ammar, B. Mokdad, F. Chinesta and R. Keunings, A new family of solvers for some classes of multidimensional partial differential equations encountered in kinetic theory modeling of complex fluids. Part II: transient simulation using space-time separated representations, *Journal of Non-Newtonian Fluid Mechanics*, 144(2-3), 98-121, 2007.

[5] F. Chinesta, P. Ladeveze and E. Cueto, A short review on model order reduction based on Proper Generalized Decomposition, *Archives of Computational Methods in Engineering. State of the Art Reviews*, 18(4), 395-404, 2011.

[6] F. Chinesta, A. Leygue, F. Bordeu, J.V. Aguado, E. Cueto, D. Gonzalez, I. Alfaro, A. Ammar and A. Huerta, PGD-based computational vademecum for efficient design, optimization and control, *Archives of Computational Methods in Engineering. State of the Art Reviews*, 20(1), 31-59, 2013.

Third International Conference on Computational Methods for Thermal Problems
THERMACOMP2014, June 2-4, 2014, Lake Bled, Slovenia
N. Massarotti, P. Nithiarasu and B. Sarler (Eds.)

An improved wavelet collocation method for numerical solution of two-dimensional elliptic partial differential equations

Imran Aziz,
Department of Mathematics, University of Peshawar, Pakistan.
Email: imran_aziz@upesh.edu.pk

Siraj-ul-Islam
Department of Basic Sciences, University of Engineering and Technology, Peshawar, Pakistan.

Abstract

A new collocation method based on Haar wavelet is presented for the numerical solution of two-dimensional elliptic partial differential equations. The method is applicable to both linear and nonlinear problems. The proposed method is an improved form of the method [1] and is more efficient. A distinguishing feature of the method is that it can be applied to a variety of boundary conditions with a little modification. The method is tested on several benchmark problems from the literature. The numerical results show convergence, simple applicability and efficiency of the method.

Keywords: Haar wavelets, Elliptic partial differential equations

1 Introduction

In this paper an improved wavelet collocation method based on Haar wavelet is proposed in order to obtain numerical solution of the following Elliptic Partial Differential Equations (EPDEs):

$$a_1(x,y)\frac{\partial^2 u}{\partial x^2} + a_2(x,y)\frac{\partial^2 u}{\partial y^2} + a_3(x,y)\frac{\partial u}{\partial x} + a_4(x,y)\frac{\partial u}{\partial y} + a_5(x,y)u = f(x,y) \tag{1}$$

where $a_1, a_2, \ldots, a_5$ and f are any functions of x and y or constants. The computation domain for the given EPDEs (1) is $[0,1]\times[0,1]$. The method is applicable to nonlinear problems as well.

2 Numerical method

For Haar wavelet approximation we use the following collocation points:

$$x_k = \frac{k-0.5}{n}, \quad k = 1, 2, \ldots, n, \tag{2}$$

$$y_l = \frac{l-0.5}{n}, \quad l = 1, 2, \ldots, n, \tag{3}$$

where $n = 2M$ and M is the maximum level of resolution of the Haar wavelet. The elliptic PDE of the following type will be considered:

$$a_1(x,y)\frac{\partial^2 u}{\partial x^2} + a_2(x,y)\frac{\partial^2 u}{\partial y^2} + a_3(x,y)\frac{\partial u}{\partial x} + a_4(x,y)\frac{\partial u}{\partial y} + a_5(x,y)u = f(x,y), \tag{4}$$

where $a_1, a_2, \ldots, a_5$ and f are any functions of x and y or constants. The computation domain for the given EPDEs (4) is $[0,1] \times [0,1]$. Assume the following Haar wavelet approximation:

$$\frac{\partial^4 u}{\partial x^2 \partial y^2} = \sum_{i=1}^{N}\sum_{j=1}^{n} \lambda_{ij} h_i(x) h_j(y). \tag{5}$$

Integrating Eq. (5) partially w.r.t. y using the limits 0 to y we obtain the following:

$$\frac{\partial^3 u}{\partial x^2 \partial y} = \frac{\partial^4 u}{\partial x^2 \partial y}(x,0) + \sum_{i=1}^{n}\sum_{j=1}^{n} \lambda_{ij} h_i(x) p_{j,1}(y), \tag{6}$$

$$\frac{\partial^2 u}{\partial x^2} = \frac{\partial^4 u}{\partial x^2}(x,0) + y\frac{\partial^4 u}{\partial x^2 \partial y}(x,0) + \sum_{i=1}^{n}\sum_{j=1}^{n} \lambda_{ij} h_i(x) p_{j,2}(y). \tag{7}$$

Using Haar approximations for the single-valued functions $\frac{\partial^4 u}{\partial x^2}(x,0)$ and $\frac{\partial^4 u}{\partial x^2 \partial y}(x,0)$, the following is obtained:

$$\frac{\partial^2 u}{\partial x^2} = \sum_{i=1}^{n} \alpha_i h_i(x) + y\sum_{i=1}^{n} \beta_i h_i(x) + \sum_{i=1}^{n}\sum_{j=1}^{n} \lambda_{ij} h_i(x) p_{j,2}(y). \tag{8}$$

Substituting the collocation points defined in Eqs. (2) and (3), we have the following:

$$\frac{\partial^2 u}{\partial x^2}(x_k, y_l) = \sum_{i=1}^{n} \alpha_i h_i(x_k) + y_l \sum_{i=1}^{n} \beta_i h_i(x_l) + \sum_{i=1}^{n}\sum_{j=1}^{n} \lambda_{ij} h_i(x_k) p_{j,2}(y_l), \quad k, l = 1, 2, \ldots, 2M. \tag{9}$$

In matrix notation this can be written as:

$$\mathbf{u_{xx}} = (\mathbf{H} \otimes \mathbf{1}_n)\boldsymbol{\alpha} + (\mathbf{H} \otimes \mathbf{y})\boldsymbol{\beta} + (\mathbf{H} \otimes \mathbf{P_2})\boldsymbol{\lambda}, \tag{10}$$

where

$$\begin{aligned}
&\mathbf{u_{xx}} = \left[\frac{\partial^2 u}{\partial x^2}(x_1,y_1), \ldots, \frac{\partial^2 u}{\partial x^2}(x_1,y_n), \frac{\partial^2 u}{\partial x^2}(x_2,y_1), \ldots, \frac{\partial^2 u}{\partial x^2}(x_2,y_n), \ldots, \frac{\partial^2 u}{\partial x^2}(x_n,y_1), \ldots, \frac{\partial^2 u}{\partial x^2}(x_n,y_n)\right]^T, \\
&\mathbf{1}_n = [1,1,\ldots,1]^T, \quad \boldsymbol{\alpha} = [\alpha_1, \alpha_2, \ldots, \alpha_n]^T, \quad \boldsymbol{\beta} = [\beta_1, \beta_2, \ldots, \beta_n]^T, \quad \mathbf{y} = [y_1, y_2, \ldots, y_n]^T, \\
&\boldsymbol{\lambda} = [\lambda_{11}, \lambda_{12}, \ldots, \lambda_{1n}, \lambda_{21}, \lambda_{22}, \ldots, \lambda_{2n}, \ldots, \lambda_{n1}, \lambda_{n,2}, \ldots, \lambda_{nn}]^T.
\end{aligned} \tag{11}$$

Similarly, integrating Eq. (5) w.r.t. we obtain the following similar expression:

$$\mathbf{u_{yy}} = (\mathbf{1}_n \otimes \mathbf{H})\boldsymbol{\gamma} + (\mathbf{x} \otimes \mathbf{H})\boldsymbol{\delta} + (\mathbf{P_2} \otimes \mathbf{H})\boldsymbol{\lambda}, \tag{12}$$

where

$$\boldsymbol{\gamma} = [\gamma_1, \gamma_2, \ldots, \gamma_n]^T, \quad \boldsymbol{\delta} = [\delta_1, \delta_2, \ldots, \delta_n]^T, \quad \mathbf{x} = [x_1, x_2, \ldots, x_n]^T. \tag{13}$$

2.1 Dirichlet boundary conditions

Integrating Eq. (9) and using boundary conditions, we obtain the following expressions:

$$\mathbf{u_x} = \mathbf{1}_n \otimes (g(1,\mathbf{y}) - g(0,\mathbf{y})) + ((\mathbf{P_1} - \mathbf{1}_n\mathbf{p^T}) \otimes \mathbf{1}_n)\boldsymbol{\alpha} + ((\mathbf{P_1} - \mathbf{1}_n\mathbf{p^T}) \otimes \mathbf{y})\boldsymbol{\beta} + ((\mathbf{P_1} - \mathbf{1}_n\mathbf{p^T}) \otimes \mathbf{P_2})\boldsymbol{\lambda}, \tag{14}$$

$$\mathbf{u} = \mathbf{1}_n \otimes g(0,\mathbf{y}) + \mathbf{x} \otimes (g(1,\mathbf{y}) - g(0,\mathbf{y})) + ((\mathbf{P_2} - \mathbf{x}\mathbf{p^T}) \otimes \mathbf{1}_n)\boldsymbol{\alpha} + ((\mathbf{P_2} - \mathbf{x}\mathbf{p^T}) \otimes \mathbf{y})\boldsymbol{\beta} + ((\mathbf{P_2} - \mathbf{x}\mathbf{p^T}) \otimes \mathbf{P_2})\boldsymbol{\lambda}, \tag{15}$$

where

$$\mathbf{p} = [p_{1,2}(1), p_{2,2}(1), \ldots, p_{n,2}(1)]^T. \tag{16}$$

Similarly,

$$\mathbf{u_y} = (g(\mathbf{x},1) - g(\mathbf{x},0)) \otimes \mathbf{1}_n + (\mathbf{1}_n \otimes (\mathbf{P_1} - \mathbf{1}_n\mathbf{p^T}))\boldsymbol{\gamma} + (\mathbf{x} \otimes (\mathbf{P_1} - \mathbf{1}_n\mathbf{p^T}))\boldsymbol{\delta} + (\mathbf{P_2} \otimes (\mathbf{P_1} - \mathbf{1}_n\mathbf{p^T}))\boldsymbol{\lambda}, \tag{17}$$

$$\mathbf{u} = g(\mathbf{x},0) \otimes \mathbf{1}_n + (g(\mathbf{x},1) - g(\mathbf{x},0)) \otimes \mathbf{y} + (\mathbf{1}_n \otimes (\mathbf{P_2} - \mathbf{y}\mathbf{p^T}))\boldsymbol{\gamma} + (\mathbf{x} \otimes (\mathbf{P_2} - \mathbf{y}\mathbf{p^T}))\boldsymbol{\delta} + (\mathbf{P_2} \otimes (\mathbf{P_2} - \mathbf{y}\mathbf{p^T}))\boldsymbol{\lambda}. \tag{18}$$

Discretizing Eq. (4) and substituting the expressions of $\mathbf{u}$ and its partial derivatives, a system of equations is obtained having n^2 equations and $n^2 + 4n$ unknowns is obtained. In order to obtain additional $4n$ equations the two expressions of u given in Eq. (15) and Eq. (18) respectively are compared and the values $x = 0$, $x = 1$, $y = 0$ and $y = 1$ are substituted one by one. The additional $4n$ equations are given as follows:

$$(\mathbf{P_2} - \mathbf{y}\mathbf{p^T})\boldsymbol{\gamma} = g(0,\mathbf{y}) - g(0,0)\mathbf{1}_n - (g(0,1) - g(0,0))\mathbf{y},$$
$$(\mathbf{P_2} - \mathbf{y}\mathbf{p^T})\boldsymbol{\gamma} + (\mathbf{P_2} - \mathbf{y}\mathbf{p^T})\boldsymbol{\delta} + (\mathbf{p^T} \otimes (\mathbf{P_2} - \mathbf{y}\mathbf{p^T}))\boldsymbol{\lambda} = g(1,\mathbf{y}) - g(1,0)\mathbf{1}_n - (g(1,1) - g(1,0))\mathbf{y},$$
$$(\mathbf{P_2} - \mathbf{x}\mathbf{p^T})\boldsymbol{\alpha} = g(\mathbf{x},0) - g(0,0)\mathbf{1}_n - (g(1,0) - g(0,0))\mathbf{x},$$
$$(\mathbf{P_2} - \mathbf{x}\mathbf{p^T})\boldsymbol{\alpha} + (\mathbf{P_2} - \mathbf{x}\mathbf{p^T})\boldsymbol{\beta} + ((\mathbf{P_2} - \mathbf{x}\mathbf{p^T}) \otimes \mathbf{p^T})\boldsymbol{\lambda} = g(\mathbf{x},1) - g(0,1)\mathbf{1}_n - (g(1,1) - g(0,1))\mathbf{x}.$$

Combining all these equations results in a $(n^2 + 4n) \times (n^2 + 4n)$ linear system. Solution of this system yields the unknowns $\boldsymbol{\lambda}, \boldsymbol{\alpha}, \boldsymbol{\beta}, \boldsymbol{\gamma}$ and $\boldsymbol{\delta}$. The approximate solution $u(x, y)$ and its derivatives at any point of the domain can be calculated using these values.

3 Numerical Experiments

Test Problem 1. (Constant source) Consider the Poisson equation:

$$\frac{\partial^2 u}{\partial x^2} + \frac{\partial^2 u}{\partial y^2} = Q, \quad -a \le x \le a, \ -b \le y \le b, \tag{19}$$

where Q is a constant, subject to the dirichlet boundary conditions:

$$\begin{aligned} u(-a,y) = 0, u(a,y) = 0, \quad & -b \le y \le b, \\ u(x,-b) = 0, u(x,b) = 0, \quad & -a \le x \le a. \end{aligned} \tag{20}$$

Eq. (19) describes the steady-state two-dimensional diffusion (cross-wind integrated) of a pollutant in the absence of wind with constant source strength Q in a finite domain [2]. It also describes the steady-state transport of oxygen in a slab of tissue with a constant oxygen consumption rate [3]. In addition to this, it also represents the steady-state temperature distribution in a rectangular region with heat loss (production) at a constant rate Q [4].

Table 1: **Maximum absolute errors and CPU time for Test Problem 1**

N	L_∞	$CPUtime$ (in secs)
2×2	5.9×10^{-3}	0.002
4×4	1.7×10^{-3}	0.002
8×8	4.5×10^{-4}	0.003
16×16	1.1×10^{-4}	0.01
32×32	2.8×10^{-5}	0.1
64×64	7.1×10^{-6}	2.2
128×128	1.8×10^{-6}	86

The solution of Eq. (19) with boundary conditions (20) is symmetric with respect to both x- and y-axis. Due to this reason Eq. (19) is solved in the region $(0 < x < a,\ 0 < y < b)$ subject to the following boundary conditions [2]:

$$\begin{aligned} u(a,y) = 0, \frac{\partial u}{\partial x}(0,y) = 0, \quad 0 \le y \le b \\ u(x,b) = 0, \frac{\partial u}{\partial y}(x,0) = 0, \quad 0 \le x \le a. \end{aligned} \tag{21}$$

The exact solution of the problem is given as follows [2]:

$$u(x,y) = \frac{2Q}{a} \sum_{k=0}^{\infty} \frac{(-1)^k}{(\lambda_k)^{3/2}} \left(\frac{\cosh \sqrt{\lambda_k} y}{\cosh \sqrt{\lambda_k} b} - 1 \right) \cos\left(\sqrt{\lambda_k} x \right), \tag{22}$$

where $\sqrt{\lambda_k} = \frac{(2k+1)\pi}{2a}$.

Maximum absolute errors for different number of collocation points are shown in Table 1.

4 Conclusion

An improved form of the Haar wavelet collocation method [1] is presented. The proposed method improves the efficiency of the method [1]. A distinguishing feature of the method is that it can be applicable to both linear and nonlinear problems.

References

[1] I. Aziz, S. ul Islam, B. Sarler, Wavelets collocation methods for the numerical solution of elliptic bv problems, Appl. Math. Modell. 37 (2013) 676–694.

[2] M. Modani, M. Sharan, S. Rao, Numerical solution of elliptic partial differential equations on parallel systems, Appl. Math. Comp. 195 (2008) 162–182.

[3] M. Sharan, M. Singh, I. Sud, Mathematical modeling of oxygen transport in the systemic circulation in hyperbaric environment, Fron. Med. Bio. Eng. 3 (1991) 27–44.

[4] M. Sharan, E. Kansa, S. Gupta, Application of the multiquadratic method for numerical solution of elliptic partial differential equations, Appl. Math. Comp. 84 (1997) 275–302.

Third International Conference on Computational Methods for Thermal Problems
THERMACOMP2014, June 2-4, 2014, Lake Bled, Slovenia
N. Massarotti, P. Nithiarasu and B. Sarler (Eds.)

PARAMETRIC SOLUTION OF THE RAYLEIGH-BENARD CONVECTION MODEL BY USING THE PGD

Saeid Aghighi, Amine Ammar
Arts et Métiers ParisTech, 2 Boulevard du Ronceray, F-49035 Angers, France
Amine.Ammar@ensam.eu E-mail addresses

Francisco Chinesta
GeM, Ecole Centrale Nantes, 1 rue de la Noe, F-44300 Nantes, France
Francisco.Chinesta@ec-nantes.fr

ABSTRACT

This work focuses on the advanced solution of the parametric non-linear model related to the Rayleigh-Bénard laminar flow involved in the modeling of natural thermal convection. This flow is fully determined by the dimensionless Prandtl P_r and Rayleigh R_a numbers. Thus, if one could precompute (off-line) the model solution for any possible choice of P_r and R_a, then the analysis of many possible scenarios could be performed on-line and in real time. Moreover, one could explore the whole parametric domain and evaluate the impact of any change in the fluid and process conditions. Such parametric solution could be viewed as a sort of abacus, but despite its inherent interest such calculation is at present unaffordable for nowadays computing availabilities because one must solve too many problems and of course store all the solutions related to each choice of both parameters. In this paper we propose an alternative route: P_r and R_a numbers will be introduced as model extra-coordinates, and then the resulting multidimensional problem solved thanks to the space-parameters separated representation involved in the PGD - Proper Generalized Decomposition - that allows circumventing the curse of dimensionality. Thus the parametric solution will be available fast and easily.

Key Words: *Rayleigh-Bénard model, Nanofluids, Model reduction, Parametric solutions, Proper Generalized Decomposition, PGD*

1. INTRODUCTION

Several systems and industrial processes are based on natural convection, justifying the impressive volume of work devoted to its understanding and efficient solution during more than one century. These problems, quite simple in appearance, deserve many surprises related to its intricate nature and many issues concerning its numerical solution.

In [1] we addressed the transient solution of the Rayleigh-Bénard flow model within a non-incremental framework. For that purpose the different fields involved in the model (the components of the velocity $\mathbf{v}(\mathbf{x},t)$ and temperature $\theta(\mathbf{x},t)$ fields) where approximated by using a space-time separated representation:

$$\begin{cases} u(\mathsf{x},t) \approx \sum_{i=1}^{N} X_i^u(\mathbf{x}) \cdot T_i^u(t) \\ v(\mathsf{x},t) \approx \sum_{i=1}^{N} X_i^v(\mathbf{x}) \cdot T_i^v(t) \end{cases} \tag{1}$$

and

$$\theta(\mathrm{x},t) \approx \sum_{i=1}^{N} X_i^{\theta}(\mathbf{x}) \cdot T_i^{\theta}(t)$$

Functions X_i^u, X_i^v and X_i^θ were calculated by solving a series of 2D BVP problems and functions T_i^u, T_i^v and T_i^θ by solving a series of IVP problems (see [1] for additional details on the solution procedure). Separated representations are involved in the so-called Proper Generalized Decomposition - PGD - methods. The interested reader can refer to [2] and the references therein. This non-incremental strategy allowed significant CPU time savings.

The present work constitutes a step forward towards an efficient solution of such coupled non-linear models that govern many systems of industrial interest. The Rayleigh-Bénard flow problem is completely determined by the dimensionless Prandtl P_r and Rayleigh R_a numbers. Thus, if one could precompute (off-line) the model solution for any possible choice of P_r and R_a, then the analysis of many possible scenarios could be performed on-line and in real time. Moreover, one could explore the entire parametric domain and evaluate the impact of any change in the fluid and process conditions. Such parametric solution could be viewed as a sort of abacus, but despite its inherent interest such calculation is at present unaffordable for nowadays computing availabilities because one must solve too many problems and of course store all the solutions related to each parameters choice.

2. PARAMETRIC RAYLEIGH-BERNARD MODEL SOLUTION

We consider the dimensionless form of the Rayleigh-Bénard model [1]:

$$\begin{cases} \nabla \cdot \mathbf{v} = 0 \\ \dfrac{\partial \mathbf{v}}{\partial t} + \mathbf{v} \cdot \nabla \mathbf{v} = -\nabla p + \left(\dfrac{P_r}{R_a} \right)^{\frac{1}{2}} \nabla \cdot \mathbf{D} + \theta \, \mathbf{e}_y \\ \dfrac{\partial \theta}{\partial t} + \mathbf{v} \cdot \nabla \theta = \left(P_r \cdot R_a \right)^{-\frac{1}{2}} \nabla^2 \theta \end{cases} \tag{2}$$

where $\mathbf{v}$ is the dimensionless velocity, p is the dimensionless pressure, θ the dimensionless temperature, $\mathbf{D}$ the dimensionless strain rate tensor (symmetric component of the dimensionless velocity gradient) and $\mathbf{e}_y$ the unit vector defining the direction along which gravity force applies (the y-direction in our case).

The model is defined in the unit square domain $\Omega = (0,1) \times (0,1)$ (related to the square domain of size H depicted in Fig. 1) fulfilled by a fluid initially at rest. A dimensionless temperature $\theta(x, y = 0) = \theta_H = 0.5$ is enforced at the bottom boundary $y = 0$ whereas a low dimensionless temperature $\theta(x, y = 1) = \theta_C = -0.5$ is applied on the upper boundary. The dimensionless temperature θ is defined by:

$$\theta = \frac{T - T_r}{T_H - T_C} \tag{3}$$

where T_H and T_C ($T_H > T_C$) are the temperatures enforced at the top and bottom cavity boundaries respectively and T_r is a reference temperature $T_r = 0.5 \cdot (T_H + T_C)$.

The heat flux is assumed vanishing on the left and right domain boundaries. The initial temperature distribution compatible with a thermal conduction regime in a fluid at rest evolves linearly in the y-direction: $\theta(x,y,t=0)=\theta_H - y$. In what follows we are focusing in the steady state solutions.

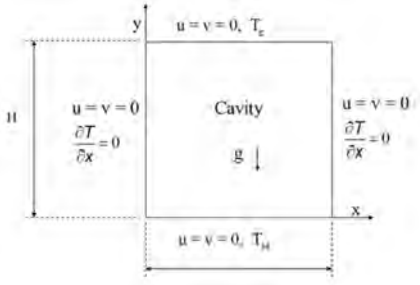

FIGURE 1. Square domain and boundary conditions

3. RESULTS

In the previous model the coefficients $\left(P_r/R_a\right)^{\frac{1}{2}}$ and $\left(P_r \cdot R_a\right)^{-\frac{1}{2}}$ will be from now on denoted by η and α. In order to compute a quite general parametric solution we consider the separated representation [3]:

$$\begin{cases} u(\mathrm{x},\eta,\alpha) \approx \sum_{i=1}^{N} X_i^u(\mathbf{x}) \cdot T_i^u(\eta,\alpha) \\ v(\mathrm{x},\eta,\alpha) \approx \sum_{i=1}^{N} X_i^v(\mathbf{x}) \cdot T_i^v(\eta,\alpha) \end{cases} \tag{4}$$

and

$$\theta(\mathrm{x},\eta,\alpha) \approx \sum_{i=1}^{N} X_i^\theta(\mathbf{x}) \cdot T_i^\theta(\eta,\alpha) \tag{5}$$

The previous model is non-linear because the advective terms $\mathbf{v}\cdot\nabla\mathbf{v}$ and $\mathbf{v}\cdot\nabla\theta$, and coupled. The simplest linearization consists of linearizing at iteration $m+1$ the non-linear terms around the solution at the previous iteration m. Thus, we can write at iteration $m+1$:

$$\begin{cases} \mathbf{v}^{m+1}\cdot\nabla\mathbf{v}^{m+1} \approx \mathbf{v}^{m}\cdot\nabla\mathbf{v}^{m+1} \\ \mathbf{v}^{m+1}\cdot\nabla\theta^{m+1} \approx \mathbf{v}^{m}\cdot\nabla\theta^{m+1} \end{cases} \tag{6}$$

4. RESULTS

In what follows we are applying the technique just described to the solution of the Rayleigh-Bénard problem in the case of a Newtonian fluid. For approximating functions depending on the physical space $\mathbf{x}$ we use standard 8-nodes quadrilateral C^0 finite elements. The considered computational

meshes of the square cavity involve 1160 and 2296 nodes. The finer mesh was used to conclude on the convergence of the results computed on the coarser one.

The parametric domain where η and α vary was chosen in order to cover the domain of variation of both the Prandtl and the Rayleigh numbers, that we considered taking values in the intervals $P_r \in [0.7, 7]$ and $R_a \in [10^3, 10^5]$. The mesh considered in the parametric domain involves 30×30 nodes.

After solving the model just presented both parametric solutions, the ones related to the velocity and temperature fields, are available and can be particularized easily and in real time at each position $\mathbf{x}$ and for each couple (η, α) that can be obtained from the values of the dimensionless Prandtl and Rayleigh numbers.

Figure 2 compares the evolution of the maximum value of the x-component of the velocity vector with the Prandtl number for three different values of the Rayleigh number (on the left) and its evolution with the Rayleigh's number for three values of the Prandtl's number (on the right).

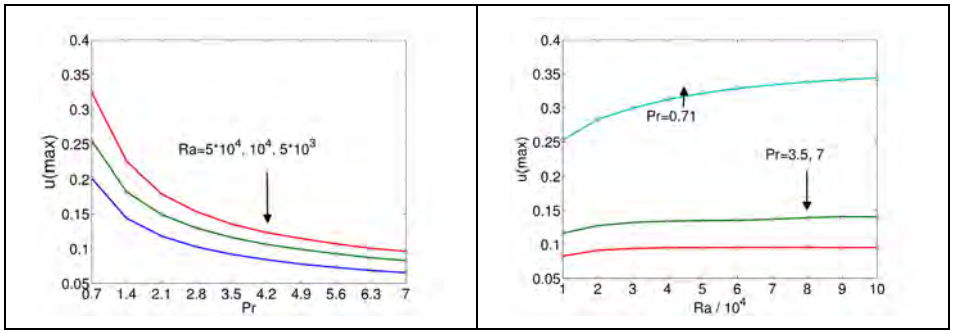

FIGURE 2. Evolution of the maximum value of the x-component versus R_a (left) and P_r (right)

5. RESULTS

In this work we proposed a novel solution procedure of the Rayleigh-Bénard coupled problem, involving several nonlinearities, the ones related to the couplings, the inertia term in the momentum balance equation and finally the ones related to the fluid constitutive law. We proved that in all cases an efficient solution can be obtained by assuming the different parameters involved in the dimensionless model as extra-coordinates within the PGD framework, opening many perspectives.

REFERENCES

[1] M.S. Aghighi, A. Ammar, C. Metivier, M. Normandin, F. Chinesta, Non-incremental transient solution of the Rayleigh-Bénard convection model by using the PGD, *J. Non-Newtonian Fluid Mech.*, 200, 65-78, 2013.

[2] F. Chinesta, R. Keunings, A. Leygue. The Proper Generalized Decomposition for Advanced Numerical Simulations. A primer. *Springerbriefs*, Springer, 2014.

[3] F. Chinesta, A. Leygue, F. Bordeu, J.V. Aguado, E. Cueto, D. Gonzalez, I. Alfaro, A. Ammar, A. Huerta. Parametric PGD based computational vademecum for efficient design, optimization and control. *Archives of Computational Methods in Engineering*, 20/1, 31-59 2013.

Third International Conference on Computational Methods for Thermal Problems
THERMACOMP2014, June 2-4, 2014, Lake Bled, Slovenia
N. Massarotti, P. Nithiarasu and B. Sarler (Eds.)

SOME LES RESULTS OF LOW MACH NUMBER FLOWS USING DYNAMIC AND NONLINEAR SUGBRID SCALES

Ramon Codina
Universitat Politècnica de Catalunya, Jordi Girona 1, Barcelona, ramon.codina@upc.edu

Matías Ávila
Barcelona Supercomputing Center, Jordi Girona 1, Barcelona, mavila@gmail.com

Javier Principe
Universitat Politècnica de Catalunya, Jordi Girona 1, Barcelona, principe@cimne.upc.edu

ABSTRACT

In this work we present some numerical results of turbulent low Mach number flows obtained with a numerical model that is able to simulate turbulence by purely numerical means. It is based on a variational multiscale (VMS) approximation to the Navier-Stokes equations, but considering the subscales as transient and accounting for their nonlinear couplings. Thus, the model falls within the class of implicit Large Eddy Simulation (ILES) models. The examples chosen are the thermally coupled flow in a channel and in a cubic cavity.

Key Words: *Low Mach number flows, turbulence, Variational Multiscale, dynamic subscales, nonlinear subscales.*

1. INTRODUCTION

In the present work we study the approximation to thermal turbulence from a strictly numerical point of view, without the use of any physical model. The main goal is to analyze the behavior of our numerical method in the large eddy simulation (LES) of thermally coupled turbulent flows at low Mach number.

Our numerical method is a stabilized finite element approximation based on the variational multi-scale method, introduced in [1], in which the functional space of the solution Y is split as $Y = Y_h + Y'$, where Y_h is the finite element space (coarse scale resolvable part), and Y' is the subgrid space (fine scale subgrid part), that can be in principle any space to complete Y_h in Y. Modeling the subscale and taking its effect on the coarse scale problem into account results in a stable formulation. The quality of the final approximation (accuracy, efficiency as LES model) depends on the particular subscale model.

Approximation of the subscales. The equations for the subgrid scales are obtained by projecting the original equations onto their corresponding spaces Y'. The distinctive features of our approach are to consider the subscales as transient and to keep the scale splitting in all the nonlinear terms in the finite element and subgrid equations, considering the nonlinear nature of the problem. For a detailed description, see [2].

The space of subscales can be chosen to be as that of the residuals, obtaining the dynamic algebraic subgrid scale method (DASGS), described in [2]. Another possibility is to use a density-weighted L2 product to define the orthogonality of the subscales and the finite element spaces, obtaining the extension of the orthogonal subgrid scale method (DOSS) ([3]), widely tested and initially developed for incompressible flows, to variable density flows.

We stress that the formulation we propose is the same as in laminar regimes, where the

improvement with respect to classical stabilized finite element methods is notorious. Having a unique formulation for all regimes. We first present a laminar test-case validation, where it is observed that DOSS method is less dissipative and gives more accurate results than DASGS method for transient and non turbulent problems.

2. NUMERICAL RESULTS

The turbulent channel flow. The turbulent channel flow is considered within two isothermal walls, at temperature ratios of TH /TC = 1.01 and TH /TC = 2.0. While the former problem is useful to test the method in the nearly incompressible case, in the latter problem thermal effects are relevant. The turbulent channel flow is investigated at Reτ =180 using noslip boundary conditions and at Reτ = 1500 using wall law boundary conditions.

For the lower Reynolds number problem the ability of the numerical methods to predict the correct turbulent behavior close to the wall is analyzed, by comparison of the obtained results against direct numerical simulation (DNS) results of [4]. For the higher Reynolds number problem different wall boundary conditions are implemented, and the obtained numerical results are compared against those obtained using modern LES methods, as sigma method described in [5]. The obtained solutions are stable and convergent to DNS values, as shown in Figure 1 for mean and RMS profiles.

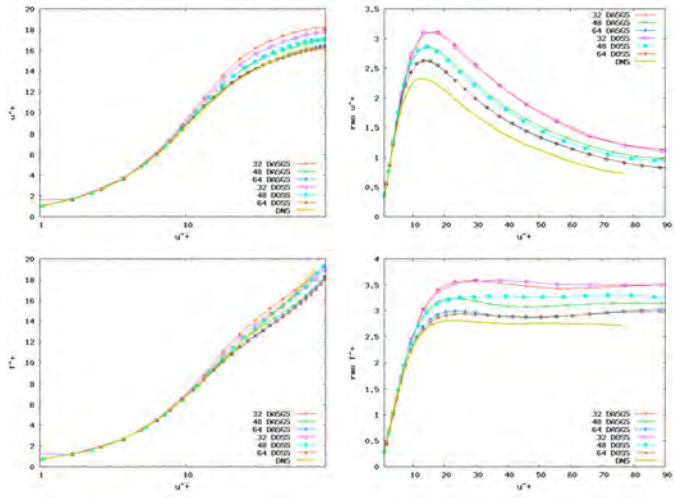

Figure 1. Left: Profiles of mean velocity (a), mean temperature (b) for the case TH /TC = 2 using the DASGS and DOSS methods against DNS (Hot wall) using meshes of 32^3, 48^3 and 64^3 elements. Right: Profiles of rms velocity (c) and rms temperature (d) for the case TH /TC = 2 using the DASGS and DOSS methods against DNS (Hot wall) using meshes of 32^3, 48^3 and 64^3 elements.

Thermal driven cavity. The present turbulent example consists in a differentially heated cavity of aspect ratio 4 with adiabatic horizontal walls. This problem has been solved in [6] using DNS, and [7] using LES models. The problem domain is Ω=[0,Lx]×[0,Ly]×[0,Lz] with Lx =Lz =1m, and Ly

= 0.25 m. The gravity force g points in −z direction. Two vertical walls are maintained at a fixed hot temperature TH (y = 0) and cold temperature TC (y = Ly), adiabatic boundary conditions are prescribed for upper (z = Lz) and lower walls (z = 0), and periodic boundary conditions are imposed in x-direction. No slip velocity is imposed over all walls. The cavity is evaluated at three different Rayleigh numbers Ra = $6.4 \cdot 10^8$, Ra = $2 \cdot 10^9$ and Ra = 10^{10}.

Turbulent flows driven by temperature differences are characterized by a high degree of spatial and temporal intermittency. The upstream part of the boundary layer is almost laminar and most downstream boundary layers become turbulent. Then, the small-scale structures associated with turbulence are concentrated in the downstream regions of vertical boundary layers. Thus, LES of buoyant turbulent flows require accurate SGS models, which dynamically adjust in time and space to local instantaneous flow conditions. The present example is useful to test the ability of the present numerical methods to adapt from laminar to transitional and turbulent flows. The behavior of the method is evaluated by comparison against results available in the literature obtained using LES in [7] and DNS in [6]. The accuracy of the obtained results using only numerical techniques is even better than that obtained using modern LES methods. In Figure 2 are shown mean profiles of vertical velocity and temperature for Ra = $2 \cdot 10^9$ against DNS. It is observed that the obtained profiles match DNS results almost exactly. In Figure 2 (right) are shown profiles of the obtained turbulent statistics for Ra = $2 \cdot 10^9$. The DASGS and DOSS methods give similar results, being excellent at predicting the turbulent statistics over the entire width of the cavity.

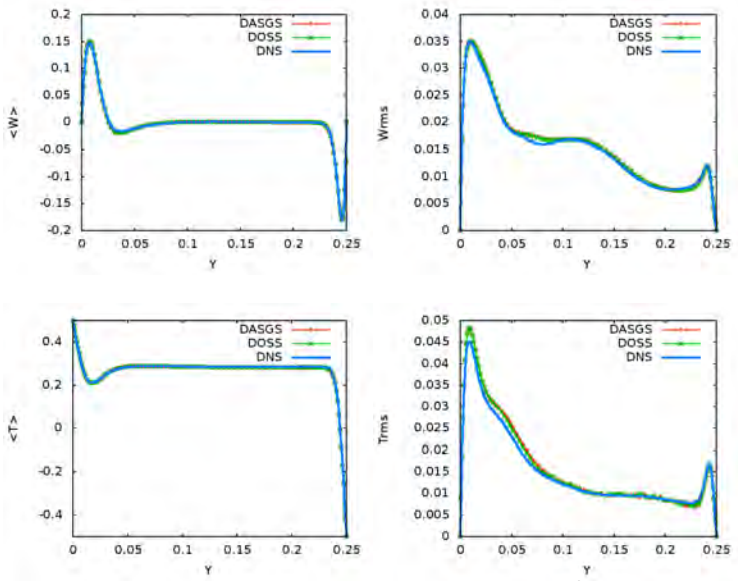

Figure 2. Left: Mean vertical velocity and temperature profiles for Ra = $2.0 \cdot 10^9$, at off center location z = 0.8 m using the DASGS and DOSS methods against DNS results. Right: RMS for Ra = $2.0 \cdot 10^9$ at off center location z = 0.9 m using the DASGS and DOSS methods against DNS results.

3. CONCLUSIONS

The turbulent channel flow and the thermal driven cavity have been solved using only numerical techniques, without introducing any additional turbulence model. For both turbulent problems it is observed that DOSS and DASGS methods introduce similar amount of numerical dissipation and solutions have similar level of accuracy. The obtained solutions are stable and convergent to DNS values. The accuracy of the obtained results for the thermal driven cavity is even better than that obtained when using modern LES methods. However, for the turbulent channel flow results are not as precise as that obtained using modern LES models with a proper damping close to the wall. Turbulent results are explained based on analysis of the dissipative structure of the method. We believe that the material presented here is a clear indication of the potential of the method to model all kinds of thermally coupled flows.

REFERENCES

[1] T. J. R. Hughes, G. R. Feijóo, L. Mazzei, J. Quincy, The variational multiscale method– A paradigm for computational mechanics, Computer Methods in Applied Mechanics and Engineering 166 (1998) 3–24

[2] M. Avila, J. Principe, R. Codina, A finite element dynamical nonlinear subscale approximation for the low Mach number flow equations, Journal of Computational Physics 230 (2011) 7988–8009.

[3] R. Codina, Stabilized finite element approximation of transient incompressible flows using orthogonal sub-scales. Computer Methods in Applied Mechanics and Engineering 191 (2002) 4295–4321.

[4] F. Nicoud, T. Poinsot, DNS of a channel flow with variable properties, in: Int. Symp. On Turbulence and Shear Flow Phenomena, 1999, pp. 12–15.

[5] F. Nicoud, H. B. Toda, O. Cabrit, S. Bose, J. Lee, Using singular values to build a subgrid-scale model for large eddy simulations, Physics of Fluids 23 (8) (2011) 085– 106.

[6] F. Trias, A. Gorobets, M. Soria, A. Oliva, Direct numerical simulation of a differentially heated cavity of aspect ratio 4 with Rayleigh numbers up to 1011. Part 1: Numerical methods and time-averaged flow, International Journal of Heat and Mass Transfer 53 (4) (2010) 665 – 673.

[7] S. Ghaisas, D. A. Shetty, S. H. Frankel, Large eddy simulation of thermal driven cavity: Evaluation of sub-grid scale models and flow physics, International Journal of Heat and Mass Transfer 56 (12) (2013) 606 – 624.

Third International Conference on Computational Methods for Thermal Problems
THERMACOMP2014, June 2-4, 2014, Lake Bled, Slovenia
N. Massarotti, P. Nithiarasu and B. Sarler (Eds.)

POINT AUTOMATA METHOD FOR MODELLING OF DENDRITIC GROWTH IN MULTICOMPONENT ALUMINIUM ALLOYS WITH MELT CONVECTION

Agnieszka Zuzanna Guštin
Institute of Metals and Technology, Lepi pot 11, 1000 Ljubljana, Slovenia
agnieszkazuzanna.gustin@imt.si

Božidar Šarler
Institute of Metals and Technology, Lepi pot 11, 1000 Ljubljana, Slovenia, bozidar.sarler@imt.si
University of Nova Gorica, Vipavska 13, 5000 Nova Gorica, Slovenia, bozidar.sarler@ung.si

ABSTRACT

We consider a two-dimensional computational model of growth and movement of an aluminium alloy dendrite from multicomponent melt with convection. The dynamics of the interface is controlled by convective-diffusive heat and species transfer. The flow around the dendrite is assumed to be potential and estimated from analytical solution for a circle. The phase change kinetics is based on KGT growth model with liquid flow. The heat and species transfer models are solved on a regular grid by the standard explicit Finite Difference Method (FDM) while the growth model is solved by the classical Cellular Automata (CA) or a Novel Point Automata (PA) approach. The CA/PA model receives temperatures, concentrations and velocities from the transfer models and the transfer models receive the solid fraction from the CA/PA model. The solid fraction calculations are performed on regular CA or random PA nodes and then interpolated back to the FDM nodes. The CA/PA model involves calculations of undercooling, curvature, kinetic and thermodynamic anisotropy. The undercooling is modified by the fluid boundary layer correlation. The movement of the dendrite requires the coupling scheme which transfers all set of quantities calculated at macro and micro scale in front of the dendrite to position after the dendrite. Simulations have been carried out for a ternary aluminium alloy Al-5.3 wt% Zn-2.35 wt% Mg-1.35 wt% Cu-0.5 wt% Cr. A numerical example with movement of the dendrite upwards in counter flow velocity downwards is presented.

Key Words: *Cellular Automata Technique, Point Automata Technique, Dendritic Structures, Multicomponent Alloy, Fluid Flow, Grain Movement*

1. INTRODUCTION

Numerical simulation is a powerful tool for studying microstructure formation during solidification of alloys. Various models for simulating dendritic structures have been proposed. The most common models apply the CA technique or Phase Fields (PH) approach. However, simple CA models are not capable of reproducing the typical growth features of dendrites when the primary branches do not coincide with the preferential mesh orientations [1]. The reason for that is that a simple CA model suffers from the strong impact of the mesh orientation. In order to resolve this problem, a novel PA method was developed [2]. Most of the dendritic growth models focus on the binary alloys and very little attention is focused on multicomponent alloys. The aim of the present contribution is to provide a comprehensive computational model based on the classical CA and the novel PA approach for multicomponent systems by taking into account the fluid flow and dendrite movement calculations.

2. GOVERNING EQUATIONS

Temperature and solute transfer calculations

Consider a system with solid and liquid phase, composed of I different alloying elements. All material properties are assumed constant for simplicity of formulation. The governing equation for transient heat conduction is described in mixture continuum approach as

$$c_p \frac{\partial T}{\partial t} + L\frac{\partial f_l}{\partial t} + \mathbf{v}\cdot\nabla\left[\left(L + c_p T\right) f_l\right] = \frac{\lambda}{\rho}\nabla^2 T, \tag{1}$$

where T, $\mathbf{v}$, c_p, ρ, L, λ, f_l stand for temperature, fluid velocity, specific heat, density, latent heat, thermal conductivity and liquid fraction. The governing equation for diffusion in liquid and solid is formulated in terms of mixture concentration c_i for each of the species i

$$\frac{\partial c_i}{\partial t} + \left(f_l \mathbf{v}\right)\nabla c_i = \nabla\cdot\left(D_i \nabla c_i\right) + c_i\left(1-k_i\right)\frac{\partial f_s}{\partial t}, \quad c_i = f_s c_i^s + \left(1-f_s\right)c_i^l \quad \text{for } i = 1,2,...,I-1 \tag{2}$$

where $D_i = f_s D_i^s + \left(1-f_s\right)D_i^l$, D_i^s, D_i^l, f_s stand for mixture, solid and liquid diffusivities of species i, and solid fraction, respectively. The concentrations of solid and liquid at the interface are assumed to be in equilibrium i.e. $c_i^s = k_i c_i^l$, where k_i, c_i^s, c_i^l stand for partition coefficient and concentration of species i in solid and liquid phase, respectively. The velocity is in the present paper calculated from the assumption of potential flow.

Phase Change Kinetics

In order to calculate the dendritic growth velocity V for a given undercooling temperature ΔT, the equations (1) and (2) are solved first for each species i. The growth process is driven by the local undercooling, defined as

$$\Delta T = T_m + \sum_{i=1}^{n} m_i c_i^l\left(t\right) - T\left(t\right) - \Gamma K, \tag{3}$$

by taking into account the thermodynamic anisotropy related to the crystal orientation and type as follows [2]

$$\Gamma = \overline{\Gamma}\left[1 - \delta_t \cos\left[S\left(\theta - \theta_{def}\right)\right]\right], \tag{4}$$

where T_m, m_i, Γ, $\overline{\Gamma}$, K, S, θ, θ_{def}, δ_t stand for the melting temperature, liquidus slope of species i, Gibbs-Thomson coefficient, average Gibbs-Thomson coefficient, curvature, factors which control the number of preferential directions of the material's anisotropy ($S = 4$ for four fold anisotropy), growth angle (angle between the y coordinate and the line that connects the center of the mass of the dendrite), preferential crystallographic orientation and thermodynamic anisotropy coefficient, respectively. The crystal growth velocity is calculated according to the crystal orientation by taking into the consideration the crystal growth direction and preferred orientation following equation [3]

$$V = V_p\left(\Delta T\right)\left[1 + \delta_k \cos\left(S\left(\theta - \theta_{def}\right)\right)\right], \tag{5}$$

where V_p, δ_k stand for growth velocity and degree of the kinetic anisotropy, respectively. Following the model proposed by Kurz et al. [4] the marginal stability criterion is used to relate the radius of curvature at the dendrite tip

$$\frac{\Gamma}{r_i^2\sigma^*}=\sum_{i=1}^{n}m_iG_{ci}-G;\quad G_{ci}=\frac{-V_pc_i^l\left(1-k_i\right)}{D_i^l}. \tag{6}$$

The total dendrite tip undercooling is

$$\Delta T=\sum_{i=1}^{n}m_ic_i^0\left(1-\frac{1}{1-\left(1-k_i\right)\Omega_i\left(\mathrm{Pe}_{V_p},\mathrm{Pe}_{V^*}\right)}\right), \tag{7}$$

where c_i^0 G_{ci}, G, σ^* stand for initial concentration of species i, interface concentration gradient in the liquid of species i, interface mean temperature gradient and marginal stability constant considered as $\sigma^*=1/4\pi^2$. The solution relates the non-dimensional supersaturations Ω_i for each alloying element i following equation $\Omega_i\left(\mathrm{Pe}_{V_p},\mathrm{Pe}_{V^*}\right)$. The supersaturation can be expressed as a boundary layer correlation as a function of the dimensionless number [5]

$$\Omega_i\left(\mathrm{Pe}_{V_p},\mathrm{Pe}_{V^*}\right)\mathrm{Pe}_{V^*}=\mathrm{Pe}_{V_p}\exp\left(\mathrm{Pe}_{V_p}\right)\left[E_1\left(\mathrm{Pe}_{V_p}\right)-E_1\left(\mathrm{Pe}_{V_p}\left(1+4/\zeta_1\,\mathrm{Re}^{\zeta_2}\,\mathrm{Sc}^{\zeta_3}\sin\left(\theta_{V^*}/2\right)\right)\right)\right], \tag{8}$$

$$\mathrm{Pe}_{V_p}=\frac{r_iV_p}{2D_i^l},\ \mathrm{Pe}_{V^*}=\frac{r_iV^*}{2D_i^l},\ \mathrm{Sc}=\frac{\nu}{D_i^l},\ \mathrm{Re}=\frac{4\mathrm{Pe}_{V^*}}{\mathrm{Sc}}, \tag{9}$$

where Pe_{V_p}, Pe_{V^*}, Sc, Re, E_1, V^*, θ_{V^*}, ν stand for the growth Péclet number, flow Péclet number, Schmidt number, Reynolds number, integral exponential function, fluid flow velocity far from the interface ($V^*=\left|\mathbf{v}^*-\mathbf{v}_{mov}\right|$ by taking into account the movement of the dendrite), angle between the dendrite tip and fluid velocity far from the interface, kinematic viscosity, and $\zeta_1, \zeta_2, \zeta_3$ are the coefficients [5].

3. NUMERICAL EXAMPLE

We simulate a dendritite of Al-5.3 wt% Zn-2.35 wt% Mg-1.35 wt% Cu- 0.5 wt% Cr alloy with respect to the described set of equations. Upon simulation start, one solid seed with assigned preferred growth orientations θ_{def} is placed at the predetermined location of the domain with $T_m=933.45\,\mathrm{K}$. All liquid is assumed to have temperature $T=770.23\,\mathrm{K}$. The movement of the dendrite is assumed upwards with the velocity $\mathbf{v}_{mov}=0.06$ µm/µs in counter flow velocity $\mathbf{v}^*=0.1$ µm/µs downwards. The stochastic model receives temperature, concentration and fluid flow information from the deterministic model and the deterministic heat and species diffusion equations receive the solid fraction information from the stochastic model. The grain starts to grow with respect to the Nastac's neighbourhood configuration in the CA method and with the neighbourhood which is associated with the position of the neighboring PA nodes which fall into a circle with assumed radius $R=0.5\,\mu\mathrm{m}$ for the PA method [2]. For given values of the physical and thermodynamic properties m_i, k_i, D_i of each alloy element $i\in$ Zn, Mg, Cr, Cu, the variable V_p for a specified undercooling temperature can be calculated. This requires to provide the KGT model with values for ΔT, c_i^l and V^*. Independent calculations of the growth velocity for a given set of these values are carried out in each time step by using an iterative method. The rejected solute amount is added to all left liquid points in the domain in each time step. The fluid flow $\mathbf{v}^*$ is currently calculated from the potential flow assumption around the circle [6] and will be replaced in

the future calculations by the Stokes flow on the realistic shape of the dendrite [7]. The velocity components for each cell (or point) located at the border of the dendritic envelope are calculated by simple trigonometric equations. Dendrite starts to move from location (350 μm, 350 μm) to the top of the domain with the velocity $\mathbf{v}_{mov} = 0.06$ μm/μs. This movement requires the shift of all calculated quantities (temperature, concentration, fluid flow and the coordinates of random PA nodes) from position in front of the dendrite to a new position behind the dendrite. The calculation domain is in CA method divided into 700 x 700 mesh points with a size of 0.5 μm.

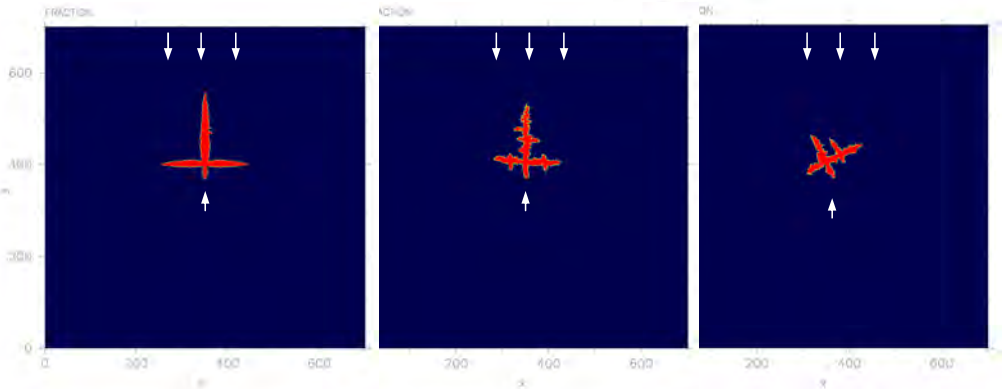

FIGURE 1. Dendritic growth of Al-5.3 wt% Zn-2.35 wt% Mg-1.35 wt% Cu- 0.5 wt% alloy including fluid flow and dendrite movement with the CA method (left), PA method for $\theta_{def} = 0^{\circ}$ (middle) and $\theta_{def} = 30^{\circ}$ (right). The white arrows at top depict the flow direction and the white arrow at the bottom the dendrite velocity.

REFERENCES

[1] J. A. Dantzig, M. Rappaz, *Solidification*, EPFL Press, Lausanne, 2009.

[2] A. Z. Lorbiecka, B. Šarler, Simulation of dendritic growth with different orientation by using the point automata method, *Computers, Materials & Continua*, 18, 63-103, 2010.

[3] Y. H. Shin, C.P. Hong, Modelling of dendritic growth with convection using a modified cellular automata model with a diffuse interface, *ISIJ International*, 42, 359-367, 2002.

[4] W. Kurz, G. Giovanola, R. Trivedi, Theory of microstructural development during rapid solidification, *Acta Metallurgica*, 34, 823-830, 1986.

[5] G. Guillemot, Ch. A. Gandin, H. Combeau, Modeling of macrosegregation and solidification grain structures with coupled cellular automaton - finite element model, *ISIJ International*, 46, 880-895, 2006.

[6] B. Šarler, Solution of a two dimensional bubble shape in potencial flow by the method of fundamentals solutions, *Engineering Analysis with Boundary Elements*, 30, 227-235, 2006.

[7] E. Sincich, B. Šarler, Non-singular method of fundamental solutions for biomedical Stokes flow problems, P. Nithiarasu (Ed.), *CMBE13 Hong Kong*, 429-432, 2013.

Third International Conference on Computational Methods for Thermal Problems
THERMACOMP2014, June 2-4, 2014, Lake Bled, Slovenia
N. Massarotti, P. Nithiarasu and B. Sarler (Eds.)

RAY TRACING ENHANCEMENT FOR SPACE THERMAL ANALYSIS: ISOCELL METHOD

Lionel Jacques, Luc Masset, Gaetan Kerschen
University of Liège, Space Structure and System Laboratory, ljacques@ulg.ac.be

ABSTRACT

The finite element method (FEM) is widely used in mechanical engineering, especially for space structure design. However, FEM is not yet often used for thermal engineering of space structures where the lumped parameter method is still dominant. Radiative exchange factors (REFs) are usually computed through Monte Carlo ray-tracing. Due to the large number of elements composing a FE model, the computation of the REFs is prohibitively expensive. The developments of the new Isocell quasi-Monte Carlo ray tracing method are presented. The Isocell method enhances the uniformity of the generated quasi-random sequence of ray directions and leads to faster convergence. It is associated with different surface sampling to derive the REFs. The method is benchmarked against ESARAD, the standard ray-tracing engine for thermal analysis used in the European aerospace industry. Various geometries are used. In particular, one entrance baffle of the Extreme Ultraviolet Imager (EUI) instrument developed at the Centre Spatial de Liège in Belgium is used. The EUI instrument of the Solar Orbiter European Space Agency mission and will be launched in a Sun-centered 0.28 perihelion orbit in 2018.

Key Words: *Heat Transfer, radiation, Monte Carlo Ray-tracing, Isocell.*

1. INTRODUCTION

The finite element method (FEM) is widely used in mechanical engineering, especially for space structure design. However, FEM is not yet often used for thermal engineering of space structures where the lumped parameter method is still dominant [1,2]. Able to deal with mixed specular and diffuse surface properties, the most general and efficient method to compute the radiative exchange factors (REFs) is Monte Carlo ray tracing [2-4]. This method is however computationally expensive due to the large number of elements composing a FE model and the large number of rays to be fired to have meaningful REF values. Two main approaches may be considered to alleviate this problem:

- First, reduce the number of rays to be fired from each face to achieve a given accuracy with a given confidence level. This is the purpose of the new Isocell quasi-Monte Carlo ray tracing method presented here.
- The second approach focuses on decreasing the number of faces between which the radiative exchange factors must be computed. Since the temperature field usually varies much more smoothly than the stress field, the thermal model does not need a mesh as fine as the one required for structural analysis. Adjacent FE external facets can therefore be grouped into *super-faces* between which the REFs are computed.

2. THE ISOCELL QUASI-MONTE CARLO RAY-TRACING METHOD

Because of wide versatility and scalability, Monte Carlo ray-tracing is the preferred choice to compute the radiative exchange factors. However, following the central limit theorem, crude Monte Carlo ray-tracing converges rather slowly. The error being inversely proportional to the square root of the number of rays traced.

The REF computation between two faces by ray-tracing involves the spatial sampling of the ray origins over the surface and the direction sampling of the rays over the hemisphere. Direction sampling can be done following Nusselt's analogy. Nusselt's analogy states that the point-wise view factor between a point P on surface i and a surface j is equal to the area of its orthographic projection divided by π (ratio of the projected area to the area of the unit disc as shown in Figure 2). Based on that, Malley proposed a method to generate the ray directions by sampling the unit disc with uniformly distributed random numbers. Each point defines a direction by projecting it back to the unit hemisphere (Figure 2, left).

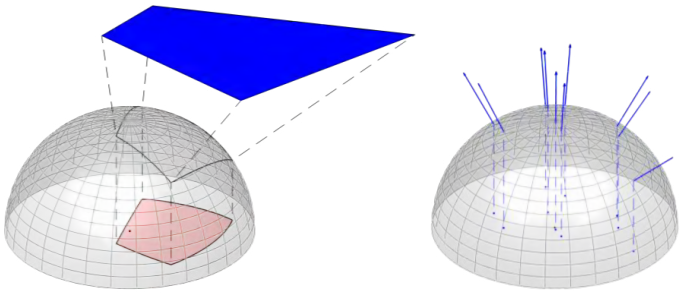

FIGURE 2. Nusselt's analogy (left) and Malley's method (right)

For a crude Monte Carlo process, the sampling of the unit disc is done randomly. However, quasi-Monte Carlo techniques such as stratified sampling and low discrepancy sequences [5-7] have proven to be more efficient than crude Monte Carlo. Stratified sampling consists in dividing the integration domain into *strata* that are randomly sampled independently. The stratified sampling method developed in [8] shows However, Masset *et al*. have shown in [9] that because the cells of the unit disc in the stratified hemisphere method have very different shapes and aspect ratios, the method behaves poorly in some particular configurations. This is the origins for the development of the Isocell method [10]. The generation of cells with more uniform aspect ratio (Figure 3.) enhances the uniformity of the ray directions and leads to faster convergence.

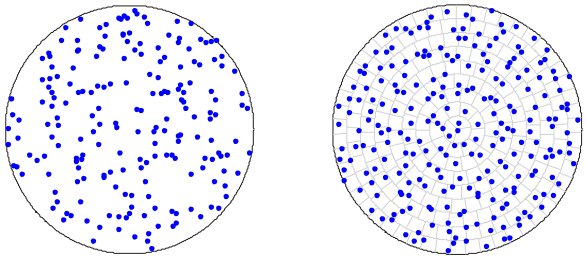

FIGURE 3. Random unit disc sampling (left) and Isocell sampling (right)

3. RESULTS

The direction sampling is used directly to compute the point-wise view factor with a rectangle. Figure 4 compares the results obtained with ESARAD (the European Space Agency ray-tracing engine for thermal analysis), an implementation of crude Monte Carlo ray-tracing and the Isocell method. In addition to a reduction of the error, the Isocell method provides a higher convergence rate τ as expected and demonstrated in [8].

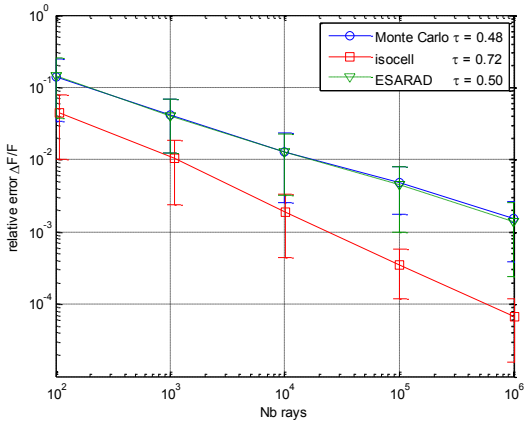

FIGURE 4. Point-wise view factor convergence in function of the number of rays traced: comparison between ESARAD, crude Monte Carlo and Isocell methods.

The Isocell direction sampling was associated with different surface sampling strategies to derive the REFs between finite faces. The method is benchmarked on various geometries. In particular, one entrance baffle of the Extreme Ultraviolet Imager (EUI) instrument developed at the Centre Spatial de Liège in Belgium is used. The EUI instrument is part of the Solar Orbiter European Space Agency mission and will be launched in a Sun-centered 0.28 perihelion orbit. It is therefore subjected to a high solar flux (17.5kW/m²) and is a critical item for the thermal design of the instrument. Figure 5 shows the geometry of the entrance baffle and the convergence the temperatures based on a pure radiative case for two surface sampling strategies: Gauss-Legendre integration points as ray origins with a local direction sampling for each origin gives very good results. The robustness of the global direction sampling strategy for which the number of origins equal to the number of rays does not need the user to choose the number of origins and still allows a 50% reduction of the number of ray compared to ESARAD to achieve the same level of accuracy on the temperature.

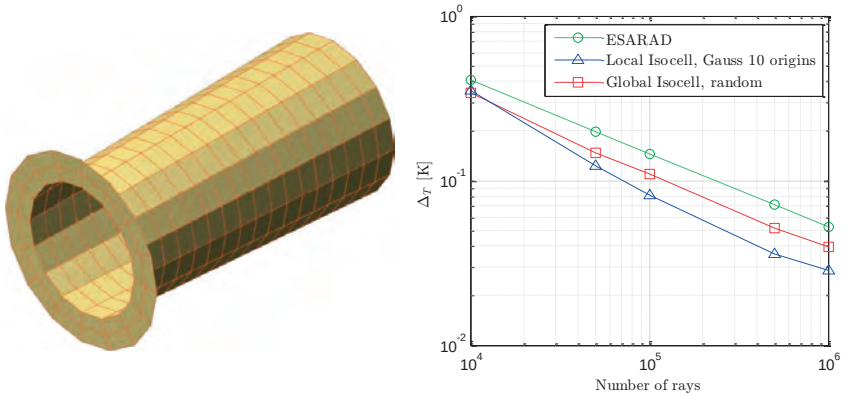

FIGURE 5. EUI entrance baffle geometry and mesh (left) and error convergence on temperature in a pure radiative equilibrium case for two surface sampling strategies (right)

4. CONCLUSIONS

Isocell direction sampling enhances the ray-tracing convergence for the computation of the radiative exchange factors. Different surface sampling strategies are considered and compared. The global direction sampling strategy reduces the number of rays to be traced for a given accuracy and the random distribution of the origins of the face makes it a promising strategy for the super-face concept.

REFERENCES

[1] T. D. Panczak, The Failure of Finite Element Codes for Spacecraft Thermal Analysis. in International Conference On Environmental Systems (SAE International, 1996).

[2] D. Gilmore, *Spacecraft Thermal Control Handbook: Fundamental Technologies*, 2nd Edition, Aerospace Press, 2002.

[3] J. R. Howell, The Monte Carlo method in radiative heat transfer. *Transactions - American Society of Mechanical Engineers Journal of Heat Transfer*, 120 (3):547–560, 1998.

[4] M. F. Modest, *Radiative heat transfer*, Academic Press, 3rd Edition, 2013.

[5] C. Lemieux, *Monte Carlo and Quasi-Monte-Carlo Sampling*, Springer, 2009.

[6] J. Arvo, P. Hanrahan, H. W. Jensen, D. Mitchell, M. Pharr, P. Shirley, J. Arvo, and M. Fajardo, *State of the Art in Monte Carlo Ray Tracing for Realistic Image Synthesis*, ACM SIGGRAPH 2001 Course 29. New York: ACM Press, 2001.

[7] P. S. Cumber, Accelerating ray convergence in incident heat flux calculations using Sobol sequences, *International Journal of Thermal Sciences*, vol. 48, no. 7, pp. 1338–1347, 2009.

[8] P. Vueghs, *Innovative Ray Tracing Algorithms for Space Thermal Analysis*, Ph.D. Thesis, University of Liège, 2009.

[9] L. Masset, O. Brüls, and G. Kerschen. *Partition of the circle in cells of equal area and shape*. Technical report, University of Liège, 2012.

[10] B. Beckers and P. Beckers, A general rule for disk and hemisphere partition into equal-area cells. *Computational Geometry*, 45(7):275–283, August 2012.

Third International Conference on Computational Methods for Thermal Problems
THERMACOMP2014, June 2-4, 2014, Lake Bled, Slovenia
N. Massarotti, P. Nithiarasu and B. Sarler (Eds.)

High-order Interpolation Schemes for Capturing Flow Discontinuities

S. Karimpour Ghannadi, Vincent H. Chu
Department of Civil Engineering, McGill University, Montreal, Canada,
shooka.karimpourghannadi@mail.mcgill.ca,vincent.chu@mcgill.ca

ABSTRACT

The performance of a numerical scheme developed for the shallow-water equations on a staggered grid is evaluated based on grid refinement study for a series of simulations conducted for the nonlinear instabilities of a shallow mixing layer over a range of convective Froude numbers. Several flux limiting schemes has been employed to capture the shock waves and manage the spurious numerical oscillations. These include MINMOD, ULTIMATE and WENO schemes. The computational error is systematically evaluated using progressively smaller grid sizes. Calculations are conducted for the number of nodes over a wave length that are $\lambda/\Delta x = \lambda/\Delta y$ = 16, 32, 64, 128, 256, and 512. The results are analyzed for the order of convergence for each scheme and for the sensitivity of the wave radiation and energy dissipation on grid size.

Key Words: *Shallow Water Equations, Finite Volume Method, High-Order Interpolation, Shock Capturing Schemes, MINMOD, ULTIMATE, WENO.*

1. INTRODUCTION

The numerical solution of the shallow water equations has application to a wide range of problems including hydraulic simulation of free-surface flow in open channel and the simulation of density currents in the atmosphere and oceans. Radiation of gravity wave and formation of shock waves plays a significantly role in the mass and momentum exchanges across shear flow of different velocity. Analogous effect due to radiation of sound is known in the study shear flow in gas-dynamics [2][3][6]. The spurious numerical oscillation is managed using a minimal intervention strategy [4]. High-order interpolation for the fluxes in the solver is developed for rotational invariant. Time integration is by a fourth order Runge-Kutta scheme. Simulations are conducted for temporal development of a transverse mixing layer on a staggered grid using a periodic boundary condition.

2. MAIN BODY

The simulations for the shear instabilities start with a based flow of TANH velocity profile. Figure 1 shows the vorticity contours of the shear instabilities for two convective Froude number $Fr_c = (U_1-U_2)/(c_1+c_2)$ = 0.1 and 0.8. The radiation of gravity wave and the local energy dissipation during the transition from linear instability to fully developed shear flow depend on the value of the convective Froude number Fr_c. Several flux limiting strategies are employed to manage the spurious numerical oscillations. These include the fifth-order WENO (Weighted Essentially Non-Oscillatory) [5], the third-order ULTIMATE [1], and the second-order MINMOD schemes [4]. Figure 2 shows the vorticity contours for the development of the shear instabilities of two convective Froude numbers.

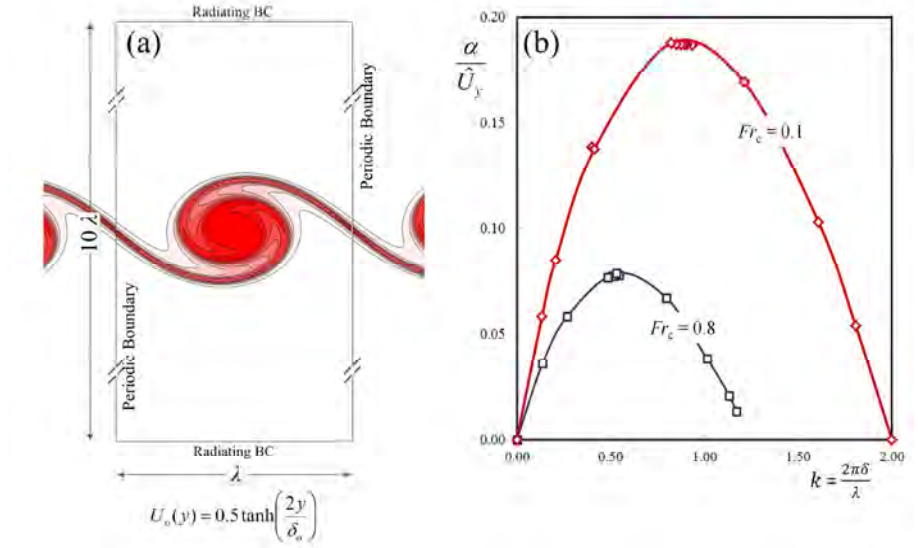

FIGURE 1. (a) Computational domain defined over one wave length (λ) in the *x*-direction and 10 wave lengths (10λ) in the *y*-direction. Periodic boundary condition at $x = 0$ and λ, and radiating boundary condition at $y = \pm 5\lambda$. (b) Dimensionless linear growth rate with wave number for convective Froude numbers of $Fr_c = 0.1$ and 0.8. The linear growth rate $\alpha / \hat{U}_y$ for the shallow-water shear flow of wave number *k* matches the data produced by Sandham and Reynolds [6] for compressible gas flow of the same convective Mach number.

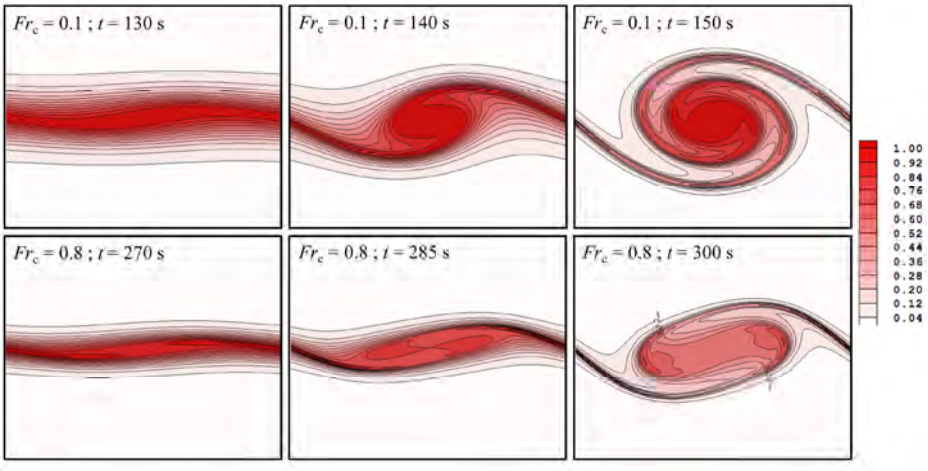

FIGURE 2. The vorticity contours showing the development of shear instabilities into eddies and shocklets in shallow waters for convective Froude numbers $Fr_c = 0.1$ (upper 3) and convective Froude number $Fr_c = 0.8$ (lower 3 images).

Figure 3 shows the convergence of the vorticity thickness δ_ω toward its true solution $\delta_{\omega\text{-exact}}$ for shear flows of two convective Froude numbers. The 2nd-order TVD schemes such as MINMOD follow a lower order of convergence in compare with ULTIMATE-QUICK and WENO. The most accurate fifth-order WENO has the highest order of convergence. The ULTIMATE-QUICK is in between of the TVD schemes and the 5th-order WENO. The 2nd-order TVD schemes (MINMOD) have the lower order of convergence compared with the 5th-order WENO. A nearly 5th-order of convergence has been achieved by the simulation using the WENO scheme when the grid is sufficiently refined. The orders of convergence are 4.42 and 4.20 for WENO, 2.73 and 2.95 for ULTIMATE-QUICK, and 1.65 and 2.00 for MINMOD, respectively. These orders of accuracy of the numerical simulations are only slightly reduced from the theoretical order of the numerical scheme. Full details of the numerical simulation including sensitivity of energy dissipation on grid size are to be presented in the conference.

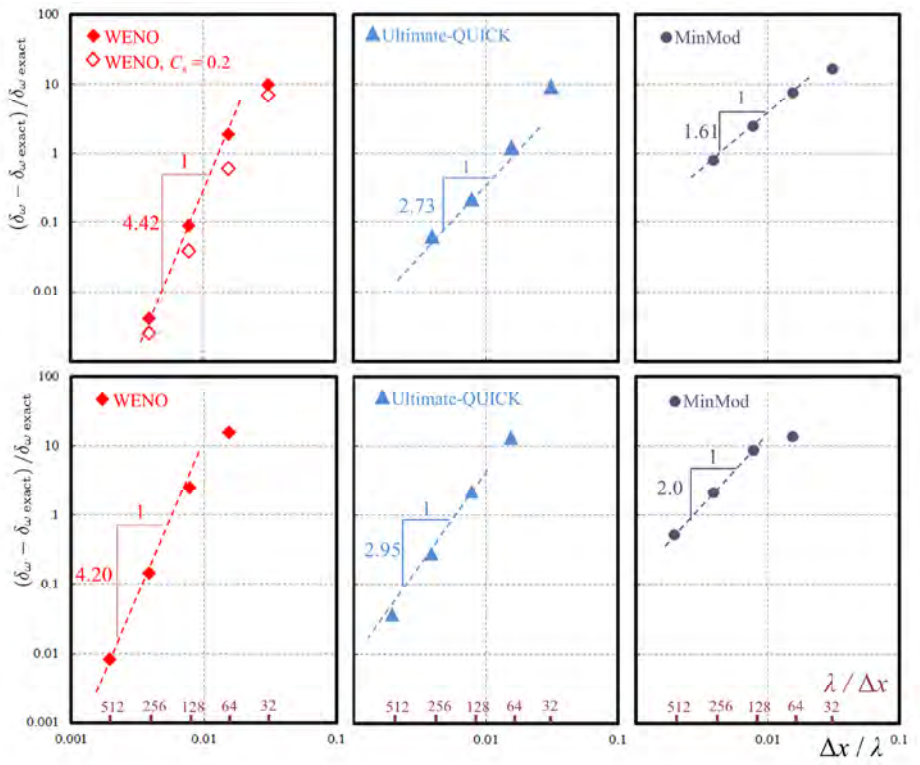

FIGURE 3. Fractional computational error for vorticity thickness, $(\delta_\omega - \delta_{\omega\text{-exact}}) / \delta_{\omega\text{-exact}}$, obtained by WENO (left), ULTIMATE-QUICK (centre) and MINMOD (right). The order of convergence for each scheme are determined using the grid size of $\Delta x / \lambda$ = 1/512, 1/256, 1/128, 1/46 and 1/32. The top three figures are the results for the convective Froude number of $Fr_c = (U_1 - U_2)/(c_1 - c_2)$ = 0.1. The lower three figures for the convective Froude number of Fr_c = 0.8.

4. CONCLUSIONS

Nonlinear shear instability is the precursor to turbulence. To capture flow discontinuities, false numerical diffusion error can be significant as accuracy of the numerical scheme is reduced to first order. The sub-grid viscosity is second order [7][8]. Therefore, false numerical diffusion can potentially exceed the magnitude of the sub-grid scale viscosity. The nonlinear simulations and the errors evaluated from the five levels of grid refinement are presented in this paper as a guide for the selection of grid in numerical simulation. With correct interpolation and minimal intervention, the actual order of accuracy of the numerical simulations is only slightly reduced from the order of the base scheme. The present study of the shear instability is part of a comprehensive investigation on the relative role and the interference between the false numerical diffusion error and the sub-grid scale viscosity in the modelling of turbulent flow.

REFERENCES

[1] B.P. Leonard. Universal Limiter for Transient Interpolation Modeling of the Advective Transport Equations: The ULTIMATE Conservative Difference Scheme. *NASA Technical Memorandum 1009 16*, 1988.

[2] C.C. Lin. On the stability of the laminar mixing region between two parallel streams in a gas, National Advisory Committee for Aeronautics (NACA) Technical Report, 1953.

[3] P. Papamoschou. Evidence of shocklets in a counterflow supersonic shear layer. *Phys. Fluids*, v. 7, pp. 233-236, 1995.

[4] C. Pinilla, S. Bouhairie, L.W. Tan and V.H. Chu. Minimal intervention to simulations using the shallow-water equation. *J. Hydro-Environ. Res.*, v. 4:201-207, 2010.

[5] C.W. Shu. High Order Weighted Essentially Non-oscillatory Schemes for Convection Dominated Problems. *SIAM Review*, v. 51, pp. 82-126, 2009.

[6] N.D. Sandham and W.C. Reynolds. Compressible mixing layer: linear theory and direct simulation. *AIAA Journal*, v. 28, n. 4, pp. 618-624, 1990.

[7] Smagorinsky, J., General circulation experiments with the primitive equations. I: the basic experiment, Monthly Weather Review, Vol. 91, 1963, pp 99-164.

[8] Vreman, A.W., An eddy-viscosity subgrid-scale model for turbulent shear flow: Algebraic theory and applications. Physics of Fluids. 16 (10), 2004, 3670-3681.

Third International Conference on Computational Methods for Thermal Problems
THERMACOMP2014, June 2-4, 2014, Lake Bled, Slovenia
N. Massarotti, P. Nithiarasu and B. Sarler (Eds.)

Inverse Problems in Heat Transfer with Applications to Detection of Subsurface Flaws and Cavities

Alain Kassab, Marcus Ni
Mechanical and Aerospace Engineering. 12760 Pegasus Drive, PO Box 162450, University of Central Florida, Orlando, Florida, 32816-2450, Alain.kassab@ucf.edu

Eduardo Divo
Mechanical Engineering Department, Embry-Riddle Aeronautical University, DB Campus, M-130, 386-226-7987, DivoE@erau.edu

ABSTRACT

The inverse geometric problem finds application to nondestructive evaluation of subsurface flaws and cavities. The governing equation, thermophysical properties, initial condition, boundary conditions, and portion of the geometry which is exposed, are all known, however, the subsurface geometry is to be determined using an overspecified Cauchy condition at the exposed surface. The geometry of the cavity(ies) that generated the measured temperature footprint is to be determined. A boundary condition at the cavity side is specified. Successful detection of subsurface cavities by thermal methods for thre solution of the inverse geometric problem is achieved by (1) a steady approach based on a hybrid BEM singularity superposition methodology or (2) a transient approach based on a meshless method/volume of fluid methodology.

Key Words: *Heat Transfer, Inverse Problems, Cavity Detection.*

1. INTRODUCTION

Within the family of inverse heat transfer problems, the inverse geometric problem (IGP) finds its application in the nondestructive evaluation of subsurface flaws and cavities. The governing equation, thermophysical properties, initial condition, boundary conditions, and exposed portion of the geometry, are all known. The portion of the geometry that is hidden from view is unknown. The surface temperature and heat flux are given at the exposed surface and the geometry of the cavity(ies) that generated the measured temperature footprint is to be determined, see Figure 1. The boundary condition at the cavity side is specified as either homogeneous or nonhomogeneous 1st, 2nd, or 3rd kind of boundary condition. The IGP can be solved with either the transient (thermal wave imaging methods[1,2]) or steady-state thermal response(IR CAT methods [3]) of the system subjected to a thermal load. Ramm [4] demonstrates mathematically that the steady state IGP has a unique solution for media with constant thermal conductivity. The IGP has been solved by a variety of methods [5] and its closely related shape optimization problem [6] are arguably the most computationally intensive of all inverse heat transfer problems and this is due to the need to solve the associated direct problem, which requires a complete regeneration of the mesh as the geometry evolves. Moreover, the continous evolution of the geometry itself poses certain difficulties analytical or numerical sensitivity coefficient determination for gradient-based optimization approaches and in the updates of the subsurface geometry(ies) and associated mesh(es), particularly

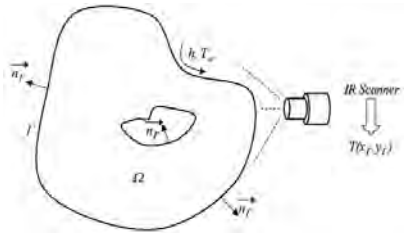

Figure 1. Problem setup using IR scanner to measure thermal footprint at the exposed boundary.

in three dimensions, whether using domain-meshing methods. An efficient BEM-based approach was introduced by Divo and Kassab [7] where singularity clusters were employed in a boundary element method (BEM) heat conduction formulation to simulate the presence of subsurface cavities in 2D and 3D geometries. Here, the problem geometry does not need to be regenerated during the search process. Instead, the search is performed for the location, distribution, and strength of singularity clusters that act as voids within the medium efficiently identifying subsurface cavities without the need of regenerating geometries or BEM matrices. This technique was later extended by Ojeda, Divo, and Kassab [8] for biomechanical applications of cavity detection in cortical bones. In the transient case, a localized meshless method [9,10] along with the Volume of Fluid (VOF) method is introduced to effectively solve for the termperature in the process of searching for the cavity. This approach avoids the implicit requirement of performing completely new solutions as the geometry is sought while offering the possibility for automation for predicting the location, size, and shape of cavities, voids, inclusions, defects, or de-attachments within the conducting media.

2. MAIN BODY

The governing heat conduction problem is solved by the BEM in the steady state and a localized collocation meshless method (LCMM) in the transient case. The IGP of determining the location, size, and shape of the cavity is formulated as an optimization problem whose objective is to minimize a function that computes the standard deviation between the LRC-VoF-computed temperatures T_i at the exposed boundaries and the temperatures acquired through IR measurements $\hat{T}_i$. This can be expressed as a least-squares function over a finite number of measurement locations N_m, or:

$$S(z)=\sqrt{\frac{1}{N_m}\sum_{i=1}^{N_m}\left[T_i(z)-\hat{T}_i\right]^2} \tag{1}$$

This objective function S depends on a number of geometric parameters z that define the location, size, and shape of the cluster of LRC Meshless points that are imposed with a VoF value $s=0$, i.e. a simulated cavity. For instance, in 2D, the cluster may be generally defined by an anchored Cubic spline (ACS) set centered at (x_o, y_o) with a number of rays N_r each extending a distance r_i from the center, expressed in polar coordinates as:

$$r(\theta)=M_{i-1}\frac{(\theta_i-\theta)^3}{6\Delta\theta_i}+M_i\frac{(\theta-\theta_{i-1})^3}{6\Delta\theta_i}+\left(r_{i-1}-\frac{M_{i-1}\Delta\theta_i^2}{6}\right)\frac{\theta_i-\theta}{\Delta\theta_i}+\left(r_i-\frac{M_i\Delta\theta_i^2}{6}\right)\frac{\theta-\theta_{i-1}}{\Delta\theta_i} \tag{2}$$

Where M_i is the value of the second derivative of the spline at the node i, and $\Delta\theta_i$ is the angular spread of each spline, i.e. $\Delta\theta_i = \pi/4$ for $N_r = 8$. Requiring that the first and second derivatives are continuous at all nodes of the spline set results in a simple 8-dof tri-diagonal system for the values of M_i A sample anchored Cubic spline set is shown in Figure 2 for $N_r = 8$. The LCMM points that lie within the resulting ACS set will then be imposed with a VoF parameter value of $s = 0$.

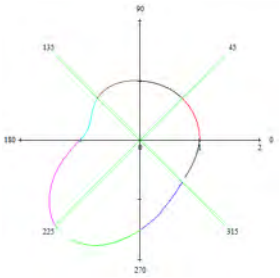

Figure 2. Anchored Cubic spline set for $N_r = 8$

The parameters z in the objective function are the coordinates of the center and the size r_i of the N rays of the cubic (in 2D) or bi-Cubic (in 3D) spline set. The minimization of the objective function $S(z)$ may be accomplished by a non-gradient based method such as Nelder and Mead's non-linear Simplex search method. The Simplex search process may be aided by a good initial guess provided by the classical 1D temperature distribution solution. The Volume-of-Fluid (VoF) method introduced by Hirt and Nichols [11] implicitly traces the interface between the two dissimilar evolving media through the transport of a continuous variable s that quantifies the absolute content of one of the fluids $(s = 1)$ or the absolute absence of it $(s = 0)$ as:

$$\frac{\partial s}{\partial t} + \left(\vec{V} \cdot \nabla\right) s = 0 \tag{3}$$

Therefore, the VoF parameter s is used to post-determine the location of the interface between the two phases, $(s = 0.5)$. This approach offers the great advantage that a two-phase flow problem can be modeled in a single domain through a single set of governing equations while the VoF parameter s is used as a weighting factor for the thermo-physical properties of the two fluids as, for instance, in the case of the thermal conductivities k^1 and k^2: $k = (1-s)k^1 + sk^2$. One of the premises of this research is that the presence of a cavity within a thermally conducting medium can be simulated and approximated using a static version of the VoF method, where the parameter s is not transported through the static field $\vec{V} = 0$ but simply fixed at a value $s = 0$ at the hypothetical location of the cavity and $s = 1$ elsewhere. And, therefore, there is no need to model the actual geometry of the cavity.

3. RESULTS

An example of detection of multiple subsurface cavities is illustrate for two cavities placed inside an arbitrarily shaped object, see Figure 3. Boundary conditions were then applied, and the remaining boundary conditions were found using BEM. Since the internal cavities do not provide much conductivity, the heat flow through the cavity can be closely approximated to zero. These particular boundary conditions are chosen to create a temperature field that will show large

differentiations on the boundaries due to interior cavities. The internal cavities are found using the simplex method. The calculated cavities are a closely matched. The convergence criterion for this case was set to 10^{-6} and the final solution was found in 623 iterations using the Simplex method.

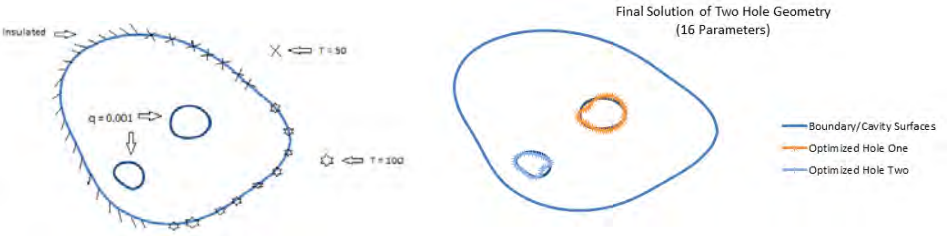

Figure 3. Imposed boundary conditions and final detected cavities within an irregular domain.

4. CONCLUSIONS

The IGP can effectively be solved by steady or transient methods. The hybrid BEM/singularity superposition method is most effective in steady state does not lend itself to the transient case, while the LCMM/VOF approach is most effective in the transient case.

REFERENCES

[1] Krapez, J.C. and Cielo, P., Thermographic Nondestructive Evaluation: Data Inversion Procedures, Part I: 1-D Analysis, *Res. Nondestr. Eval*., vol. 3, pp. 81–100, 1991.
[2] Mandelis, A., Nondestructive Evaluation, Prentice-Hall, Englewood Cliffs, NJ, 1994.
[3] Kassab, A.J. and Hsieh, C.K., "Application of Infrared Scanners and Inverse Heat Conduction Problems to Infrared Computerized Axial Tomography," *Review of Scientific Instruments*, Vol. 58, No. 1, 1987, pp. 89-95.
[4] Ramm, A.G., A Geometrical Inverse Problem, *Inverse Problems*, vol. 2, pp. L19–L21, 1986.
[5] Kassab, A.J. and Pollard, J., "Automated Cubic Spline Anchored Grid Pattern Algorithm for the High Resolution Detection of Subsurface Cavities by the IR-CAT Method," Numerical Heat Transfer, Part B: Fundamentals, Vol. 26, No.1, 1994, pp. 63-78.
[6] Dulikravich, G.S. and Martin, J.M., Geometrical Inverse Analysis Problems in Three-Dimensional Non-linear Steady Heat Conduction, *Eng. Anal. Boundary Elements*, vol. 15, pp. 161–169, 1995.
[7] Divo, E, Kassab, A.J., and Rodriguez, F., An Efficient Singular Superposition Technique for Cavity Detection and Shape Optimization, *Numerical Heat Transfer B*, vol. 46, pp. 1-30, 2004.
[8] Ojeda, D., Divo, E., and Kassab, A.J., Cavity Detection in Biomechanics by an Inverse Evolutionary Point Load BEM Technique, *Inverse Problems in Science and Engineering*, vol. 16, no. 8, pp. 981-993, 2008.
[9] Divo, E. and Kassab, A.J., "An Efficient Localized RBF Meshless Method for Fluid Flow and Conjugate Heat Transfer," *ASME Journal of Heat Transfer*, 2007, Vol. 129, pp. 124-136.
[10] Divo, E. and Kassab, A.J., "Localized Meshless Modeling of Natural Convective Viscous Flows," *Numerical Heat Transfer, Part A: Fundamentals*, Volume 53, Issue 6, June 2008, pages 487-509.
[11] Hirt, C.W. and Nichols, B.D., Volume of Fluid (VOF) Method for the Dynamics of Free Boundaries, *Journal of Computational Fluids*, 1981, Vol. 39, pp. 201-225.

Third International Conference on Computational Methods for Thermal Problems
THERMACOMP2014, June 2-4, 2014, Lake Bled, Slovenia
N. Massarotti, P. Nithiarasu and B. Sarler (Eds.)

TOWARDS REAL TIME THERMAL CONDUCTIVITY HOMOGENIZATION OF HETEROGENEOUS MICROSTRUCTURES

E. Lopez, E. Abisset-Chavanne, C. Ghnatios, C. Binetruy, F. Chinesta
GeM Institute, UMR CNRS
Ecole Centrale de Nantes, 1 rue de la Noe, BP 92101, F-44321 Nantes cedex 3, France
elena.lopez-tomas@ec-nantes.fr, emmanuelle.abisset-chavanne@ec-nantes.fr,
chady.ghnatios@ec-nantes.fr, christophe.binetruy@ec-nantes.fr, francisco.chinesta@ec-nantes.fr

ABSTRACT

In the numerical modeling of composite materials and structures, microscopic heterogeneities introduce the need for defining homogenized thermal conductivities that depend on microscopic details.

There are many techniques for performing computational homogenization. However image-based simulation introduces a new constraint, that of real time image-based calculations in the frame of the on-line control of manufacturing processes. We have to predict the local homogenized properties of a heterogeneous material at different scanning scales, as fast as possible for a given acceptable error.

Therefore, model reduction techniques open new routes for performing such kinds of efficient high-resolution homogenization. Depending on the acceptable level of error, richer reduced bases can be used, but the price to pay in this case is the increase of the computation time.

As microstructures cannot be reduced, we explore different routes that combine reduced bases of the thermal fields and hyper-reduction strategies able to avoid the construction of the whole discrete matrices involved in finite elements discretizations.

In this work we are describing, analyzing and comparing different reduced order models of thermal conductivities of heterogeneous microstructures.

Key Words: *Image-based simulation, Homogenization, Reduced Order Model, Hyper-reduction.*

1. INTRODUCTION

For processes and part performance, we want to know the macrostructure's behaviour and for that we need to predict first what happens locally. We can obtain data from image with computer tomography or 3D scanners.

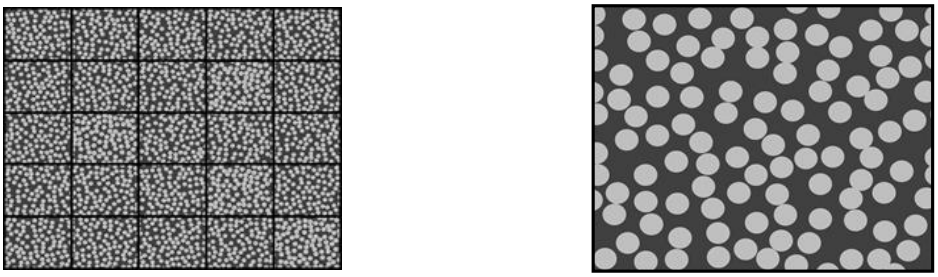

FIGURE 1. Macro-Scale and Micro-Scale

The set of synthetic microstructures that we are generating as our data, can be considered as a sampling defined in a bigger macrostructure. By this way we can deal with complex and random media, and we will be able to replace one only big scale computing by a certain number of computings in smaller areas.

In our image-based simulation, we generate a set of 100 heterogeneous microstructures like the one showed in FIGURE 1, with circular inclusions representing the fibers, placed randomly in the Representative Volume Element. We only change the position of the fibers, being its number fixed, and we allow contacts between them, forbidding the overlapping.

2. THERMAL HOMOGENIZATION

Hereafter, the objective is to use mode reduction methods in order to compute "in real time" the effect the microstructure has on the global material thermal behaviour. To do so, as we are in 2D, for each one of the 100 microstructures generated, we consider and solve by Finite Element Method the two following thermal problems with their respective boundary conditions:

$$\begin{cases} \nabla \cdot \left(\boldsymbol{k}(\mathbf{x}) \cdot \nabla T_1(\mathbf{x}) \right) = 0 \\ T_1(\mathbf{x}) = x \end{cases} \qquad \begin{cases} \nabla \cdot \left(\boldsymbol{k}(\mathbf{x}) \cdot \nabla T_2(\mathbf{x}) \right) = 0 \\ T_2(\mathbf{x}) = y \end{cases}$$

The first step is to obtain the reduced bases of the temperature fields. The application of the Singular Value Decomposition (SVD) to all temperature fields allows us to extract the N first modes, ϕ_i, having the higher amplitude (in the following we will investigate the effect of the N value choice).

To perform the model reduction and the homogenization process, we then generate a new microstructure with the same characteristics as the previous ones. Now we want to compute the relative error between the eigenvalues of the Exact and the Reduced Homogenized Thermal Conductivity matrices. To do so we use this relation:

$$\boldsymbol{K} = \left\langle \, \boldsymbol{k} \cdot \boldsymbol{M} \, \right\rangle$$

being $\boldsymbol{k}$ the Local Thermal Conductivity Matrix and $\boldsymbol{M}$ is the Localization Matrix:

$$\boldsymbol{M} = \begin{bmatrix} \vdots & \vdots \\ \nabla \mathrm{T}_1 & \nabla \mathrm{T}_2 \\ \vdots & \vdots \end{bmatrix}$$

The temperature field used to compute $\boldsymbol{M}$ can be the exact or the reduced one, being the reduced the one computed with the N modes coming from the SVD:

$$T_i^{RED} \approx \boldsymbol{B_i} \cdot \alpha_i$$

being α_i the projection coefficients and $\boldsymbol{B_i}$:

$$\boldsymbol{B_i} = \begin{bmatrix} \vdots & & \vdots \\ \phi_1 & \cdots\cdots & \phi_{\mathrm{N}} \\ \vdots & & \vdots \end{bmatrix}$$

being i = 1,2 for both thermal problems.

And so, we can compute both matrices and the relative error between them:

$$\boldsymbol{K} = \left\langle \boldsymbol{k} \cdot \boldsymbol{M} \right\rangle \qquad \boldsymbol{K}^{\boldsymbol{RED}} = \left\langle \boldsymbol{k} \cdot \boldsymbol{M}^{\boldsymbol{RED}} \right\rangle$$

$$\text{Relative error} = \sqrt{\frac{(\lambda_{\max} - \lambda^{RED}{}_{\max})^2}{(\lambda_{\max})^2}}$$

being λ_{max} the maximum exact eigenvalue and $\lambda^{RED}{}_{max}$ the maximum reduced eigenvalue.

With this methodology we have to compute, at each time step, the full finite element matrix at each time. Then, even if the use of the reduced matrix M to compute it allows time saving, the process is still relatively slow and expensive. It is possible to go one step further by using the Hyper-reduction strategy.

3. HYPER-REDUCTION

If we have a microstructure in which we have local conductivity $\mathbf{k_1}$ in the polymer matrix and local conductivity $\mathbf{k_2}$ inside the fibers, instead of computing its FEM matrix, we can decompose that microstructure in the sum of two microstructures:

- One where we only have local conductivity $\mathbf{k_1}$ everywhere, corresponding to the polymer. In this one we compute the FEM matrix, $\mathbf{G_1}$, what is expensive but we only do it once, and this matrix is valid for all microstructures' decompositions.
- Another one where we only have the fibers, being local conductivity ($\mathbf{k_2}$- $\mathbf{k_1}$) inside the fibers and zero outside. Now we compute the FEM matrix, $\mathbf{G_2}$, what is really cheap, because we only have to select the elements inside the inclusions (fibers).

Combining now the reduced bases of the temperature fields and the hyper-reduction matrices in the FEM formulation, we can compute the α_i coefficients that allow us to compute the Hyper-reduced Homogenized Thermal Conductivity Matrix.

$$\boldsymbol{B}_i^{\boldsymbol{T}} \cdot (G_1 + G_2) \cdot (\boldsymbol{B}_i \cdot \alpha_i) = \boldsymbol{B}_i^{\boldsymbol{T}} \cdot F_i$$

being i = 1,2 for both thermal problems.

But we do not want to select all the elements inside each inclusion, we want to be faster, so first we select one random element per inclusion, and only with the first two modes coming from the reduced model, we obtain the relative error. Then we do the same but selecting the center of gravity of each inclusion, and finally, we select four contour elements per inclusion.

$$\text{Relative error} = \sqrt{\frac{(\lambda^{RED}{}_{\max} - \lambda^{HYP-RED}{}_{\max})^2}{(\lambda^{RED}{}_{\max})^2}}$$

being $\lambda^{RED}{}_{max}$ the maximum reduced eigenvalue and $\lambda^{HYP-RED}{}_{max}$ the maximum hyper-reduced eigenvalue.

4. RESULTS

The results of applying the Singular Value Decomposition to both thermal problems indicate that the most important amount of information is contained in the first two modes.

In TABLE 1 we present the results for the relative error, computed with different number of modes coming from the SVD, between the Exact and the Reduced Homogenized Thermal Conductivity matrices.

Number of Modes	Relative Error
20	0.0409
15	0.0413
10	0.0415
5	0.0427
2	0.0433

TABLE 1. Relative Error with different number of modes

With this methodology we obtain good results, as the relative error is really low and we can only take the first two modes for representing the solution.

The results for the relative error, computed with the two first modes coming from the SVD, between the Reduced and the Hyper-reduced Homogenized Thermal Conductivity Matrices are presented in TABLE 2.

Case	Relative Error
One random element per inclusion	0.00488
Center of gravity element per inclusion	0.00487
Four contour elements per inclusion	0.00514

TABLE 2. Relative Error depending on the Hyper-reduction case

The relative error is very similar and low, what means we can perform the hyper-reduction method with important computing time-savings.

5. CONCLUSIONS

In this work we have performed computational homogenization, combining the reduced bases of the thermal fields coming from the reduced order modeling and hyper-reduction technique. The Homogenized Thermal Conductivity Matrix in an exact or in a reduced way exhibits a low relative error between both matrices, what means that we can apply reduced order modeling to computational homogenization. We can improve the reduced computational homogenization applying the hyper-reduction strategy, because this technique allows us to be faster and cheaper from the computational point of view.

REFERENCES

[1] F. Chinesta, A. Ammar, F. Lemarchand, P. Beauchene, F. Boust, Alleviating mesh constraints: Model reduction, parallel time integration and high resolution homogenization, *Comput. Methods Appl. Mech. Engrg.*, 400–413, 2008.

[2] H. Lamari, A. Ammar, P. Cartraud, G. Legrain, F. Chinesta, F. Jacquemin, Routes for Efficient Computational Homogenization of Nonlinear Materials Using the Proper Generalized Decompositions, *Arch. Comput. Methods Engrg.*, 373–391, 17 (2010).

Third International Conference on Computational Methods for Thermal Problems
THERMACOMP2014, June 2-4, 2014, Lake Bled, Slovenia
N. Massarotti, P. Nithiarasu and B. Sarler (Eds.)

CONVECTIVE-PRESSURE SPLIT ALGORITHM FOR INCOMPRESSIBLE FLOW COMPUTATION

Shainath Kalamkar, J. C. Mandal
Aerospace Engineering Department, Indian Institute of Technology Bombay, Mumbai, India

ABSTRACT

A simple low diffusive convective-pressure split finite volume algorithm for solving incompressible flows in artificial compressibility formulations is presented. The convective part is discretized by upwind differencing and the pressure part by central differencing. The viscous fluxes are discretized in a central differencing manner. A few benchmark problems are solved in order to demonstrate the efficacy of the present method.

Key Words: *Artificial compressibility, Finite volume method, Convective-pressure splitting.*

1. INTRODUCTION

Over the years, many methods have been developed to compute incompressible flows for variety of engineering applications. Among them, artificial compressibility (AC) method of Chorin [1] has drawn considerable attention because of it's attractive properties over the others such as the possibility of solving the system in a closely coupled manner, superior convergence, automatic satisfaction of divergence free condition to the level of residual error at steady state and its ability to adapt advanced numerical techniques developed for compressible flow. Flux difference splitting methods for AC formulation, like Roe and HLLC methods are found to be comparatively very robust and accurate. These methods use upwind discretization for the whole inviscid terms, which adds sufficient stability for flow involving shock waves arising in compressible flow. So much of diffusion may not be necessary for incompressible flow computations for stability. In case of incompressible flows, the amount of diffusion can be reduced by discretizing only a part of inviscid terms in upwind manner. With this in mind, (inviscid) flux split method similar to AUSM[2] is considered in the present approach. Here, the inviscid flux is split into convective and pressure parts. The convective part is discretized by upwind method and the pressure part in central difference manner. Above discretization can be justified from a linear analysis of flux split equations in AC formulation. A very similar approach is used by Vierendels et al [3] without providing any justification and analysis. To the best of authors knowledge, no study about the performance of such a method is reported in literature. The aim of this paper is to study this method in detail to establish its efficacy. The numerical results of a few test cases show great promise of the present method.

2. GOVERNING EQUATIONS

Two dimensional artificial compressibility formulation for incompressible flow can be written as

$$\frac{\partial U}{\partial t}+\frac{\partial F}{\partial x}+\frac{\partial G}{\partial y}=S$$

Where $U=\left[p,u,v,T\right]^T$, $F=F^c-F^v$, $G=G^c-G^v$ and $S=\left[0,0,g_t\beta_t\left(T-T_{ref}\right),0\right]^T$.

Superscripts c, v denotes the inviscid and viscous flux respectively. Superscript T denotes transpose of a matrix.

where $F^c = \left[\beta u, u^2 + p, uv, Tu\right]^T$, $G^c = \left[\beta v, uv, v^2 + p, Tv\right]^T$,

$$F^v = \left[0, 2\nu\left(\frac{\partial u}{\partial x}\right), \nu\left(\frac{\partial v}{\partial x} + \frac{\partial u}{\partial y}\right), \alpha\left(\frac{\partial T}{\partial x}\right)\right]^T,\ F^v = \left[0, \nu\left(\frac{\partial v}{\partial x} + \frac{\partial u}{\partial y}\right), 2\nu\left(\frac{\partial v}{\partial y}\right), \alpha\left(\frac{\partial T}{\partial y}\right)\right]^T.$$

Here u and v are the Cartesian components of velocity, p, ν and T are normalised pressure (with density), dynamic viscosity and temperature respectively. g_t and β_t are acceleration due to gravity and coefficient of thermal expansion respectively, T_{ref} and β are reference temperature and artificial compressibility parameter respectively.

3. FORMULATION

Finite volume formulation of governing equations can be obtained by integrating governing equations over an arbitrary finite volume by changing the volume integral over the flux vectors to surface integral is given as,

$$\iint_\Omega \frac{\partial U}{\partial t} + \oint_A \left[Fn_x + Gn_y\right] dA = \iint_\Omega S$$

where n_x and n_y are the components unit normal vector of the surface of area A enclosing volume Ω. Above equation applying to a volume in $2D$ form can be written as

$$\Omega_i \frac{\Delta U}{\Delta t} + \sum_{k=1}^{K} \left[Fn_x + Gn_y\right]_k \Delta s = \Omega_i S$$

Where summation is taken over K faces of cell i and Δs is the length of the edge.

3.1 *Inviscid flux computation*

Inviscid flux normal to any cell interface between left cell L and right cell R can be written as $\mathbf{F} = F^c n_x + G^c n_y$. Face normal flux in convective-pressure split can be written as $\mathbf{F} = u_n \left[\beta, u, v, T\right]^T_{L/R} + p\left[0, n_x, n_y, 0\right]^T$, where $u_n = \left[\left(u_L n_x + v_L n_y\right) + \left(u_R n_x + v_R n_y\right)\right]/2$ and $p = \left(p_L + p_R\right)/2$. Selection of L or R in convective term is as follows

$$\left[\cdot\right]_{L/R} = \begin{cases} \left[\cdot\right]_L \text{ if } u_n \geq 0 \\ \left[\cdot\right]_R \text{ if } u_n < 0 \end{cases}$$

Since pressure evolution equation is discretized in a central differencing manner, a diffusion term $\left(p_L - p_R/2\beta_x\right)n_x + \left(p_L - p_R/2\beta_y\right)n_y$ is added to continuity equation for stability. Where $\beta_x = \tilde{V} + 2\nu/\Delta x$ and $\beta_y = \tilde{V} + 2\nu/\Delta y$ has dimension of the velocity in which $\tilde{V}$ is the maximum velocity of the domain. Left and right states for unwind discretization of convective term are obtained using linear solution dependent weighted least squares (SDWLS) [6] reconstruction.

3.2 *Viscous flux computation*

Viscous flux is calculated in a central differencing way. Green Gauss theorem is applied over Courier diamond path [5] to calculate the spatial derivatives of velocity and temperature at cell interfaces.

4. RESULTS AND DISCUSSION

Three test cases are considered to validate the present method with benchmark solutions, namely lid driven cavity [4], backward facing step [7] and natural convection [8] problems. Second order accuracy is achieved using SDWLS for the present and the Roe's method. No slip boundary condition is applied on solid walls. In all the cases, the accuracy of the present results is compared with the Roe's methods, which is considered to one of the most accurate method.

4.1 *Lid driven cavity flow*

A square cavity is discretized into uniform grid of size 129×129 for the simulation. Lid velocity is taken as unity. Flow is computed for $\mathrm{Re}=5000$ and compared with the results in reference [4]. Figure 4.1 clearly shows the ability of the present method to capture more accurate solution as compare to Roe's method.

4.2 *Flow over backward facing step*

Laminar incompressible flow over a backward facing step at $\mathrm{Re}=800$ is simulated on the 300×70 non-uniform grid. Figure 4.2 shows the schematic of the domain and inlet velocity profile used for the computation. Pressure is extrapolated at the outer boundary. Figure 4.3 shows that peak value of velocity is captured close to the experimental value [7] by the present method. Roe's method is found to produce marginally better results in this case.

4.3 *Natural convection flow*

A unit square cavity with unit dimension heated differentially on left and right walls is considered. Non uniform grid of size 41×41 of quadrilateral cells is used for the simulation for Rayleigh number 10^3 and Prandtl number 0.71. Hot and cold side walls are considered isothermal and other two adiabatic. Differential heating of the cavity leads to buoyancy-driven recirculation. Figure 4.4 shows that the non dimensional velocities (where thermal diffusivity α is taken as 0.0375) computed by both the methods match well with the experimental results [8].

4. CONCLUSION

A simple inexpensive convection-pressure split method presented here is found to be quite accurate in computing incompressible flow with or without heat transfer.

REFERENCES

[1] A.J. Chorin, A numerical method for solving incompressible viscous flow problems, *Journal of Computational Physics*, 135, 118-125, 1997.

[2] M. Liou and C.J. Steffen, Jr, A new flux splitting scheme, *Journal of Computational Physics*, 107, 23-39, 1993.

[3] J. Vierendeels, K. Riemslagh and E. Dick, A multigrid semi-implicit line method for viscous incompressible and low Mach number flows on high aspect ratio grids, *Journal of Computational Physics*, 154, 310-341, 1999.

[4] K. N. Ghia, U. Ghia and C.T. Shin, High-Re solutions for incompressible flow using Navier-Stokes equations and multigrid method *Journal of Computational Physics*,48, 387-411,1982.

[5] W. Coirier and K. Powell, Solution-adaptive Cartesian cell approach for viscous and inviscid flows, *AIAA Journal,* 34, 938-945, 1996.

[6] J.C. Mandal and Sundeep P. Rao, High Resolution Finite Volume Computations on Unstructured Grids using Solution Dependent Weighted Least Squares Gradients, *Computers & fluids*, 44,23-31, 2011.

[7] T. Lee and Mateescu D., Experimental and numerical investigation 2-D backward-facing step flow, *Journal of Fluids and Structures*, 12, 706-713, 1998.

[8] de Vahl Davis and Jones, I.P., Natural convection in a square cavity-a comparison exercise, *International Journal of Numerical Methods in Fluids*,3,227-248, 1983.

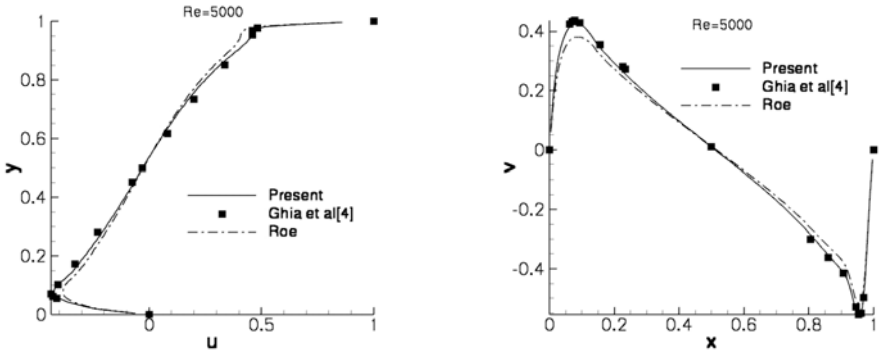

Figure 4.1 Variation of u along vertical midline and v along horizontal midline of lid driven cavity.

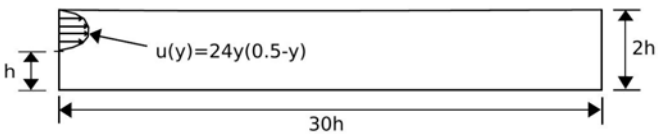

Figure 4.2 Schematic of backward facing step with dimensions and inlet velocity profile.

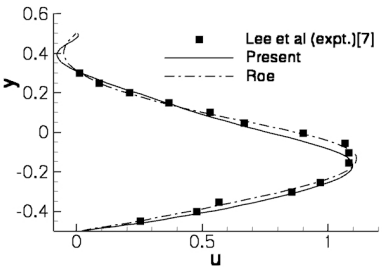

Figure 4.3 Variation of u at $x = 7$.

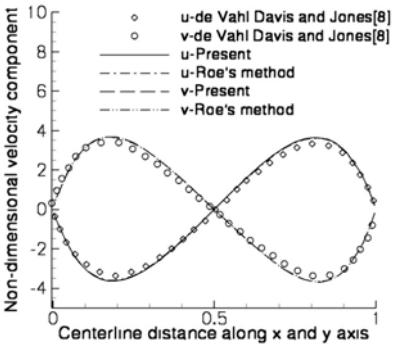

Figure 4.4 Variations of u and v.

Third International Conference on Computational Methods for Thermal Problems
THERMACOMP2014, June 2-4, 2014, Lake Bled, Slovenia
N. Massarotti, P. Nithiarasu and B. Sarler (Eds.)

SIMULATING PHASE TRANSFORMATIONS WITH POINT AUTOMATA AND FRONT TRACKING

Markus Rettenmayr, Klemens Reuther
Friedrich Schiller University Jena, Otto Schott Institute of Materials Research, Löbdergraben 32, 07743 Jena, Germany

ABSTRACT

Dendritic solidification is simulated with a newly developed meshless front tracking method. The method uses a random grid that does not contain any preferred orientation, suppressing artificial grid anisotropy that tends to obscure the (relatively weak) effects of interfacial anisotropy on the evolution of the dendritic morphology. The position of the solidification front is tracked with the help of particles that are placed on the interface between liquid and solid nodes of the grid. Special features concerning the growth of secondary arms that are not found by conventional methods are captured by the meshless front tracking method.

Key Words: *Solidification, Dendritic Growth, Meshless Method.*

1. INTRODUCTION

Dendritic growth is a form of unstable growth where the instabilities form due to concentration or temperature gradients or a combination thereof. The first dendritic growth theories were restricted to describing the large scale energetics that arise from such gradients [1] by solving the heat flow equation around a dendrite tip of the shape of a paraboloid of revolution. These solutions are not entirely complete, because interface thermodynamics plays an important role with respect to formation of instabilities and directionality of growth and thus also needs to be included. It is nowadays well accepted that the earlier assumption of an isothermal solid/liquid interface is inadequate and that the subtle changes of interface temperature or interface concentration along a growing dendrite tip cannot be neglected in an up-to-date model.

Analytical models of dendrite growth include the effects of interface energy since the late 1970ies [2]. In numerical models of dendritic growth, it appears to be straightforward to also include the physical effects that slightly change interface temperature / concentration due to the local curvature and determine the local growth direction. However, in the vast majority of dendrite growth models a spatial discretization with a rectangular grid is used that introduces its own anisotropy - this can lead to deviations from interface concentrations or growth directions that are orders of magnitude larger than those caused by the physical effect and thus generate unacceptable artefacts. The problem of grid artefacts is particularly pronounced for Cellular Automaton (CA) models, but has also not been completely solved in Phase Field (PF) models. Even though not always openly discussed, the main effort in improving CA models for dendritic growth has in the last decade been on reducing the numerical anisotropy.

Meshless methods offer the potential for simulations that are completely free of artificial anisotropy. First models applying this method have been published in recent years [3], where grid points are attributed a state of ’liquid’ or ’solid’ that is changed when the solid/liquid interface (which is not tracked explicitely) passes the position of the grid point. In the present work, a meshless model with front tracking for alloy solidification is presented. The model includes diffusion in the liquid and solid phases, respectively, the dependence of the interface concentration on the local curvature and interface anisotropy.

2. THE MODEL

The dendrite growth model is installed using a meshless method where the spatial domain is discretized by nodes on random positions, with a minimum distance between the nodes as an additional condition. The minimum distance between the nodes helps to avoid stability issues of the numerical solution routine. Each node is attributed either a liquid or solid state. The solid/liquid interface is not restricted to be situated on node positions, it is represented by ”particles” that migrate between nodes towards the liquid (see Fig. 1). A node with state ”liquid” state becomes solid when it is reached or passed by the particle.

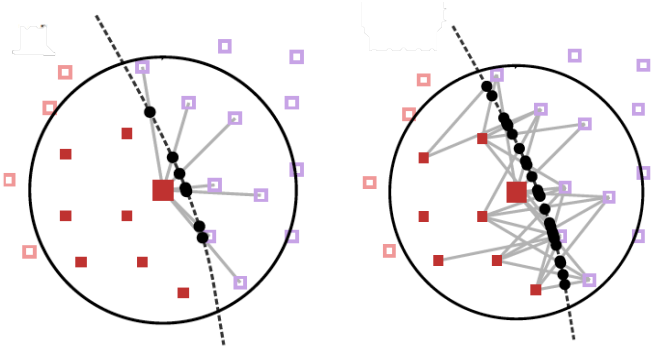

FIGURE 1. Position of nodes (red: solid, purple: liquid) and particles (black) defining the neighbourhood of a particular node (large square); only solid symbols and particles are part of the neighbourhood; an earlier model for plane front solidification [4], left hand side, and the present model for dendrite growth, right hand side, are compared.

The diffusion equation is solved in both the liquid and solid phases, where the interface particles take part in the calculation in both phases, respectively. As opposed to an earlier model that was proposed for solidification with a plane front [4], the number of particles that represent the interface has been increased to include the case of (strongly) curved interfaces: not only the connection of the central point of the neighbourhood to the nodes in the other phase accommodate a particle, but more of the nodes inside the neighbourhood are included in the front tracking procedure (see Figure 1). The methodology for solving the diffusion equation is the Diffuse Approximation Method [5,6] with additional stability handling for the reduction of numerical noise [7]. Integration of the diffusion equation is done using an explicit time-forward scheme. The solidification front velocity v_F is determined by the mass balance as

$$v_F = (J_\ell - J_s) / (C_\ell - C_s) \tag{1}$$

where J_ℓ and J_s are the solute fluxes normal to the interface in the liquid and solid phase, respectively, and C_ℓ and C_s are the interface concentrations. The effect of curvature is included by introducing the capillary undercooling $\Delta T_c = \kappa \cdot \gamma$, where κ is the curvature and γ is the sum of the interfacial energy and its stiffness (i.e. its second derivative with respect to the angle). In two dimensions γ is defined by

$$\gamma = \gamma^0 [1\text{-}15\varepsilon \cos(4\langle\Theta_0\text{-}\arccos n_x\rangle] \quad (2)$$

where γ^0 is the Gibbs-Thomson coefficient, ε is the anisotropy parameter (here chosen to be 0.01), and Θ_0 is the angle of the maximum of the anisotropic interfacial energy with respect to the coordinate system in which the normal direction and its component n_x in x-direction are noted.

The model does not contain any adjustable parameters. We simulate for the case of growth velocities of several mm/s, for which local equilibrium is still a valid assumption. The interface concentrations C_ℓ and C_s in eq. (1) can therefore be safely taken from a linearized phase diagram with curvature correction according to eq. (2).

3. RESULTS

Dendritic solidification was simulated using the parameters and physical constants for an Al-2.1wt.%Cu alloy. The simulation domain is quadratic with a side length of 100μm. Periodic boundary conditions were used. Overall there were 2.7×10^6 nodes with a minimum distance of 0.05μm to their respective next neighbour in the domain. The radius defining a local neighbourhood was set to 0.25μm, the time step to Δt=0.2μs, and the total time of the simulation extended over 50 000steps, i.e. 10ms. The circular solid nucleus at the beginning of the calculation was placed in the center of the domain and had a diameter of 1μm and an initial concentration of 2.1wt.%Cu, the liquid concentration at the interface was calculated from the solid concentration using a linear equilibrium phase diagram (partition coefficient k = 0.14 and slope of the liquidus line m_L = -2.6K/wt.%) and the curvature correction (eq. 2). The domain temperature was set to 920K, i.e. an undercooling of 8K with respect to a plane front was chosen, leading to swift development of a dendritic morphology.

FIGURE 2. Simulated dendrite, grown for 10ms from a melt that is undercooled by 8K; the total length of the dendrite in horizontal and vertical direction, respectively, is 40μm.

The shape of the simulated dendrite is shown in Fig. 2. The basic known features of dendritic growth are well captured by the meshless front tracking method. It is interesting to note that the preferred growth directions of the primary arms (i.e. the ⟨1 0⟩ directions) are not the growth directions of the secondary arms that are in close vicinity to the root in the centre. The solute distribution around the growing seed forces the innermost secondary arms to grow in a ⟨1 1⟩

direction. As soon as the growth is not influenced by solute rejection of the neighbouring primary arm (e.g. for the secondary arms close to the tip), growth occurs in the ⟨1 0⟩ directions as expected for a cubic crystal system. It can also be seen at the tips of the longer secondary arms that at a larger distance from their root are subject to splitting and start growing in the ⟨1 0⟩ directions. These growth features are generally not reproduced by PF and CA models, since the growth of secondary arms is delayed or even suppressed in these models and requires stimulation by the introduction of artificial noise into the diffusion or solidification front velocity part of the simulation. A recently published anisotropy free model [8] yields similar shapes as our model, confirming the suitability of our model for describing the formation of instabilities with good accuracy.

4. CONCLUSIONS

The meshless front tracking method allows for simulating the formation of complex morphologies. The most important feature of the meshless method, in particular the absence of a preferred grid direction, makes it most suitable for the simulation of processes where the anisotropy of the interfacial energy plays a pronounced role, which certainly is the case for crystal growth.

REFERENCES

[1] G.P. Ivantsov, The temperature field around cylindrical, spherical and needle-shaped crystals which grow in supercooled melts, *Doklady Akademii Nauk SSSR*, 58, 567-569, 1947.

[2] J.S. Langer and H. Müller-Krumbhaar, Theory of dendritic growth, *Acta Metallurgica*, 26, 1681-87, 1978.

[3] A. Lorbiecka and B. Sarler, Simulation of dendritic growth with different orientation by using the point automata method, *Computers, Materials and Continua*, 18, 69-103, 2010.

[4] K. Reuther and M. Rettenmayr, A meshless front tracking method for simulating phase transformations, *Acta Materialia*, 60, 2128-34, 2012.

[5] B. Nayroles, G. Touzot and P. Villon, The diffuse approximation, *Comptes rendues de l'Academie des Sciences Serie II*, 313, 293-6, 1991.

[6] C. Prax, H. Sadat, and E. Dabboura, Evaluation of high order versions of the diffuse approximate meshless method, *Applied Mathematics and Computation*, 186, 1040-53, 2007.

[7] K. Reuther B. Sarler and M. Rettenmayr, Solving diffusion problems on an unstructured, amorphous grid by a meshless method, *International Journal of Thermal Sciences*, 51, 16-22, 2012.

[8] M.E. Glicksman, J.S. Lowengrub, S.W. Li, and X.R. Li, A deterministic mechanism for dendritic solidification kinetics, *Journal of Metals*, 59, 27-34, 2007.

Third International Conference on Computational Methods for Thermal Problems
THERMACOMP2014, June 2-4, 2014, Lake Bled, Slovenia
N. Massarotti, P. Nithiarasu and B. Sarler (Eds.)

An Immersed Boundary Method and a Ghost Cell Method for the Simulation of Heat Transfer Problems

Claudio Santarelli, Tobias Kempe, Jochen Fröhlich
Institut für Strömungsmechanik, Technische Universität Dresden, 01062 Dresden, Germany

claudio.santarelli@tu.dresden.de

ABSTRACT

In the framework of heat transfer problems in multiphase flows, it is essential to correctly impose adequate boundary conditions on the phase boundary. To this end, an Immersed Boundary Method (IBM) and a Ghost Cell Method (GCM) are described and validated when imposing both Dirichlet and Neumann boundary conditions on the phase boundary.

Key Words: *Heat Transfer, Multiphase Flows, Immersed Boundary Method, Ghost Cell Method.*

1. INTRODUCTION

Multiphase flows play an important role in many industrial and environmental applications and one of the most important aspects is the heat transfer between the different phases. It is therefore fundamental to provide numerical methods that correctly simulate such phenomena and that can handle various types of boundary conditions (BC) on the phase boundary, depending on the problem considered. In this work two different methods are described for the simulation of heat transfer problems where both Dirichlet and Neumann BCs are taken into account.

2. COMPUTATIONAL METHODS

Direct numerical simulations of unsteady Navier-Stokes equations and thermal energy equation (1) for incompressible two-phase flows with constant fluid properties are performed, where the disperse phase is introduced via an IBM described in [1]. It is based on a continuous forcing approach and on a three-point regularized Dirac function for the phase coupling. The required forces $\mathbf{f}_{\mathrm{IBM}}$ at the phase boundary Γ are computed by a direct forcing method.

$$\frac{\partial \mathbf{u}}{\partial t} + \nabla \cdot (\mathbf{u}\mathbf{u}) = \nabla \cdot \boldsymbol{\tau} + \mathbf{f}_{\mathrm{IBM}} \quad , \qquad \frac{\partial T}{\partial t} + \nabla \cdot (\mathbf{u}T) = \alpha \nabla T + q_{\mathrm{IBM}} \qquad (1a,b)$$

2.1 Dirichlet condition with IBM

The direct heating approach, i.e. the IBM for the temperature field, is the counterpart of the direct forcing approach for the velocity, which has been extensively described and validated in [1]. The common procedure will therefore only be recalled briefly here. As for $(1a)$, the time advancement of $(1b)$ is based on a three-step Runge-Kutta scheme for the convective term and on a semi-implicit Crank-Nicholson scheme for the diffusive term. First, an intermediate temperature field is evaluated with $q_{\mathrm{IBM}} = 0$ and fully explicit evaluation of the diffusive terms. Afterwards, the temperature at the Eulerian grid points is interpolated to the heating points, $\mathbf{X}_{\mathrm{L}}$, by means of a regularized Dirac function yielding $T_{\mathrm{L}}(\mathbf{X}_{\mathrm{L}})$, Fig. (1a). The heat source Q at the Lagrangian points is directly computed

$$Q(\mathbf{X}_{\mathrm{L}}) = -\frac{T_{\mathrm{L}}(\mathbf{X}_{\mathrm{L}}) - T_{\Gamma}(\mathbf{X}_{\mathrm{L}})}{\Delta t} \quad , \qquad (2)$$

where $T_\Gamma(\mathbf{X}_L)$ is the desired temperature on Γ. The heat source Q is then spread to the Eulerian points and is introduced as q_{IBM} in the solution of a Helmholtz equation, required for the implicit treatment of the diffusive term of $(1b)$. With an IBM, interpolation and successive spreading do not yield identical values [2], so that $T_L(\mathbf{X}_L) \neq T_\Gamma(\mathbf{X}_L)$. As used for the momentum equation in [1], additional heating loops are hence introduced after solving the Helmholtz equation as follows:

1. The temperature is interpolated at the heating point, yielding ${T_L}^{(m)}(\mathbf{X}_L)$, where m is the loop index.
2. $Q^{(m)}(\mathbf{X}_L)$ is evaluated, as the difference between ${T_L}^{(m)}(\mathbf{X}_L)$ and $T_\Gamma(\mathbf{X}_L)$, as in (2).
3. ${q_{IBM}}^{(m)}(\mathbf{x})$ is evaluated and used to correct the temperature field according to

$$T(\mathbf{x})^{(m)} = T(\mathbf{x})^{(m-1)} + \Delta t \, {q_{IBM}}^{(m)}(\mathbf{x}) \ .$$

The correction is supposed to be small enough so that a repeated evaluation of the other terms of $(1b)$ is not performed in the same Runge-Kutta sub-step.

2.2 Neumann condition with IBM

To impose a constant heat flux $K = (\partial T/\partial n)_\Gamma$ on Γ, an additional layer of Lagrangian points, called help points $\mathbf{X}_H$, is introduced at a distance δ normal to Γ, Fig. 1(a). The method described above for a Dirichlet condition is then modified as follows. First, the temperature $T_H(\mathbf{X}_H)$ at the help points and the temperature $T_L(\mathbf{X}_L)$ at the Lagrangian points are evaluated via Dirac interpolation, then $T_\Gamma(\mathbf{X}_L)$ is evaluated by a first order approximation of the temperature gradient i.e.

$$T_\Gamma(\mathbf{X}_L) = \ T_H(\mathbf{X}_H) - K\,\delta \quad , \tag{3}$$

and then used in (2). The parameter δ is set equal to the mesh width h, identical in all Cartesian directions. This approach is been inspired by [3] and [4].

2.3 Dirichlet condition with GCM

The Ghost Cell Method considered here has been proposed by [3] and is now extended to three-dimensional problems. First, a number of Eulerian points, so-called ghost points, are detected inside the body, fulfilling the criterion that their normal distance from Γ is below h. Then, two additional points are defined on the straight line normal to Γ passing through a ghost point: a projection point located on Γ, and an image point at a distance δ from Γ, Fig. 1(b). The temperature at the image point $T_I(\mathbf{X}_I)$ is evaluated from the eight surrounding points (in 3D) by tri-linear interpolation. Then, the temperature at the ghost point is linearly extrapolated from the temperature at the image point and the projection point according to

$$T_G(\mathbf{X}_G) = T_P(\mathbf{X}_P) - \frac{T_I(\mathbf{X}_I) - T_P(\mathbf{X}_P)}{\delta} \ |\mathbf{X}_G - \mathbf{X}_P| \ . \tag{4}$$

In the CGM, q_{IBM} is set equal to 0 during all computation steps. After the evaluation of the intermediate temperature and after the solution of the Helmholtz equation, the temperature at the ghost points is finally overwritten by the value from (4). The time-advection scheme and the treatment of the diffusive terms is not modified with respect to Sec 2.1. The distance δ is equal $\sqrt{3}\Delta$ so that no ghost point contributes to the computation of $T_I(\mathbf{X}_I)$.

2.4 Neumann condition with GCM

To apply a Neumann BC in the framework of the CGM, the temperature at the ghost point is determined by the temperature at the image point and by the temperature gradient on Γ, i.e. K:

$$T_G(\mathbf{X}_G) = T_I(\mathbf{X}_I) - K\ |\mathbf{X}_G - \mathbf{X}_I| \qquad (5)$$

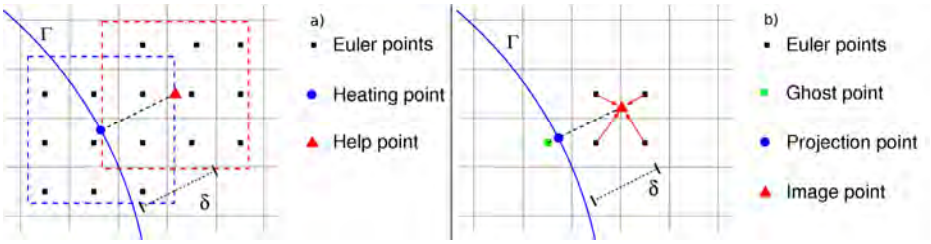

FIGURE 1: Points involved in the definition of the boundary condition: a) IBM and b) GCM. The dashed squares identify the support of the smoothed delta function for Lagrangian and help points.

3. RESULTS

The same configuration is used for all simulations presented: a cubic box $L \times L \times L$ discretized by 128^3 mesh points. A fixed sphere of diameter $d_p = 0.24L$ is located at $(L/2, L/2, L/2)$, with around 30 mesh point across the diameter. An inflow BC with constant velocity $\mathbf{u}_{\mathrm{ref}}$ and temperature $T = 0$ is applied at the inlet boundary. At the outlet, $\mathbf{u}_{\mathrm{ref}}$ is imposed and a convective BC is applied for the temperature. A homogeneous Neumann condition is applied at the other four boundaries for both quantities. On the sphere, a zero velocity is imposed by means of the IBM of [1]. The Reynolds number based on the inflow velocity and on the diameter is 10 and the Prandlt number is 0.71. The CFL number $(\mathbf{u}_{\mathrm{ref}}\Delta t)/h$ is around 0.74. Below, the computed results are compared to simulations performed with ANSYS Fluent using a body-fitted mesh of around 4.7 Million cells. This mesh is fine enough, so that further refinement does not change the solution. A very good agreement for the velocity field was found between the body-fitted mesh and the IBM (not presented here).

The first problem investigated (*Case 1*) is an isothermal sphere, so that an inhomogeneous Dirichlet condition is applied, $T_\Gamma = T_{ref}$. The resulting temperature with the GCM is very close to the reference in the internal of the flow field and about 10% lower in the stagnation point, Fig. 2.

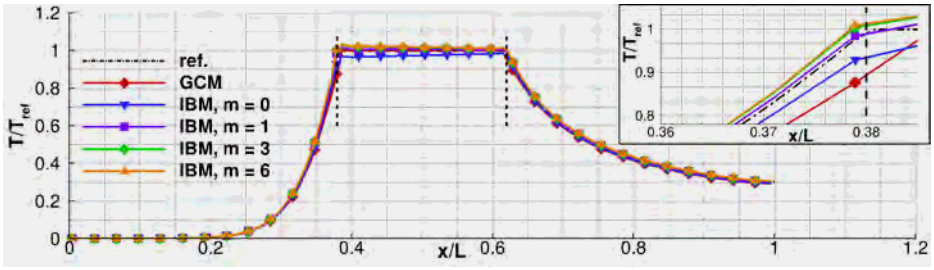

FIGURE 2: Temperature profile along the line $(x; y = L/2)$ for *Case 1*.
Symbols correspond to grid points coarsened by a factor of 4.

With the IBM, this difference is smaller and the improvement achieved by the additional heating loops can be appreciated in the zoomed region. Up to 10 loops have been performed, but after $m = 6$ the solution is only slightly modified (not shown).

Case 2 is defined by $K = 0$ on the surface of the sphere, by a homogeneous Neumann condition for the temperature at the inlet and outlet boundaries, and by a Dirichlet conditions at the two horizontal walls, $T(y = 0) = 0$ and $T(y = L) = 2\,T_{ref}$. With the GCM, the temperature at the stagnation point is very close to the reference, about 0.3% higher. The IBM solution without heating loops is slightly further off (~5%) and improves with increasing number of heating loops: with $m = 3$ the temperature is around 0.5% lower than the reference. Results for *Case 2* are not shown here for lack of space.

Case 3 is similar to *Case 1*, but with a constant heat flux imposed on the sphere surface, setting $K = 29.16$ and $T_{ref} = K\alpha$. Also for this problem, the agreement using the GCM is very good, Fig. 3. For the IBM additional loops are essential to obtain good agreement. The solution for $m = 0$ is not satisfying, while three loops are enough to remarkably improve the solution.

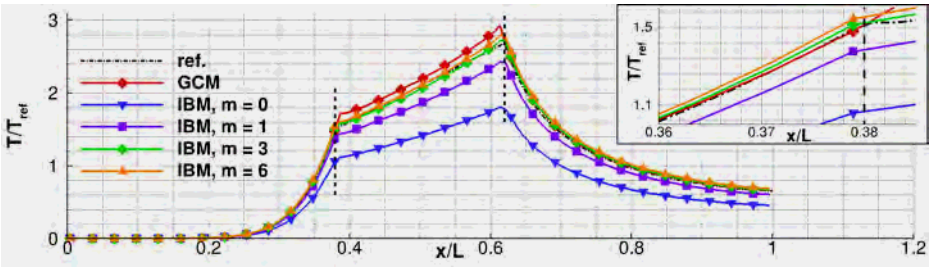

FIGURE 3: Temperature profile along the line $(x; y = L/2)$ for *Case 3*.
Symbol coarsening factor as in Fig. 2.

ACKNOWLDEGMENTS

The present work was sponsored by the German Federal Ministry of Education and Research (BMBF) under the contract number 02NUK010B. Computational time was provided by the Center for Information Services and High Performance Computing (ZIH) in Dresden.

REFERENCES

[1] T. Kempe and J. Fröhlich, An improved immersed boundary method with direct forcing for the simulation of particle laden flow, *Journal of Computational Physics*, 231,3663-3684, 2012.

[2] Z. Wang, J. Fan, K. Luo, and K. Cen, Immersed Boundary Method for the simulation of flows with heat transfer, *International Journal of Heat and Mass Transfer*, 52(19),4510-4518, 2009.

[3] D. Pan, A Simple and Accurate Ghost Cell Method for the Computation of Incompressible Flows Over Immersed Bodies with Heat Transfer, *Numerical Heat Transfer Part B*: *Fundamentals*, 58(1):17-39, 2010.

[4] N. Zhang, Z. Zheng, and S. Eckels, Study of heat-transfer on the surface of a circular cylinder in flow using an immersed-boundary method, *International Journal of Heat and Fluid Flow*, 29(6),1558-1566, 2008.

Third International Conference on Computational Methods for Thermal Problems
THERMACOMP2014, June 2-4, 2014, Lake Bled, Slovenia
N. Massarotti, P. Nithiarasu and B. Sarler (Eds.)

Fracture analysis in piezoelectric semiconductors under a thermal load

Jan Sladek, Vladimir Sladek
Institute of Construction and Architecture, Slovak Academy of Sciences, 84503 Bratislava, Slovakia, Jan.sladek@savba.sk

Ernian Pan
Computer Modeling and Simulation Group, Department of Civil Engineering, University of Akron, Akron, OH 44325-3905, pan2@uakron.edu

Michael Wünsche
Department of Civil Engineering, University of Siegen, D-57068 Siegen, Germany, wuensche@bauwesen.uni-siegen.de

ABSTRACT

This paper presents in-plane crack problem in piezoelectric semiconductors under a transient thermal load. General boundary conditions and sample geometry are allowed in the proposed formulation. The governing partial differential equations for stresses, electric displacement field and current are satisfied in a local weak-form on small fictitious subdomains. All field quantities are approximated by the moving least-squares (MLS) scheme. After performing the spatial integrations, one obtains a system of ordinary differential equations for certain nodal unknowns. The influence of initial electron density on the intensity factors and energy release rate is investigated.

Key Words: *Heat Conduction, Meshless Local Petrov-Galerkin Method, Moving Least-Squares Approximation, Intensity Factors, Uncoupled Thermoelasticity, Impermeable Conditions*

1. INTRODUCTION

Piezoelectric materials (PZ) have wide range of engineering applications in smart structures and devices. Certain piezoelectric materials are also temperature sensitive, i.e. an electric charge or voltage is generated when temperature variations are exposed. This effect is called the pyroelectric effect. The physical laws for thermo-piezoelectric materials have been explored by Nowacki [1]. Dynamic thermoelasticity is relevant for many engineering problems since thermal stresses play an important role in the integrity of structures. The uncoupled thermoelasticity is considered here, since there is no heat production due to the strain rate, i.e. no thermoelastic dissipation. Then, the temperature field is not influenced by mechanical deformation and the heat conduction equation can be solved first to obtain the temperature distribution. Recently, the authors have analyzed non-conducting piezoelectric materials under a thermal load [2].

However, piezoelectric materials can be either dielectrics or semiconductors. Up to date dielectric materials are more intensively investigated than semiconductors. The analyzed problem for non-conducting PZ is simpler than for semiconductors. In piezoelectric semiconductors the induced electric field produces also the electric current. The interaction between mechanical fields and mobile charges in piezoelectric semiconductors is called the acoustoelectric effect [3].

Piezoelectric ceramics are brittle and susceptible to fracture during service. To improve the performance and to predict the reliable service lifetime of ceramic piezoelectric components, it is necessary to analyze theoretically the damage and fracture processes taking place in piezoelectric materials with consideration of the coupled effects of mechanics and electrics. There are only few papers devoted to crack problems in piezoelectric semiconductor materials. All papers concern the anti-plane crack problem in unbounded domain with a semi-infinite crack [4] and a finite crack [5]

under stationary conditions. In the present paper the meshless Petrov-Galerkin (MLPG) method is applied to a crack problem for piezoelectric semiconductor under a thermal load. The coupled governing partial differential equations for stresses, electric displacement field and current are satisfied in a weak-form on small fictitious subdomains. The heat conduction equation is solved separately in the uncoupled thermoelasticity. Nodal points are introduced and spread on the analyzed domain and each node is surrounded by a small circle for simplicity, but without loss of generality. The spatial variations of the displacement, electric potential and electron density are approximated by the Moving Least-Squares (MLS) scheme [6].

2. LOCAL INTEGRAL EQUATIONS FOR PIEZOELECTRIC SEMICONDUCTOR

Consider a homogeneous n-type piezoelectric semiconductor with m_0 being the electron density in unloaded state with vanishing initial electric field E_0 . Supposing the frequency of external loadings to be close to characteristic frequency of elastic waves, one can assume quasi-static approximation for electromagnetic fields. Then, the effect of Faraday's induction is neglected even if there is a magnetic field induced by the electric current according to the Ampere's law. Eventually, the governing equations within the linear theory are given by the balance of momentum, Gauss`s law and conservation of charge [3]

$$\sigma_{ij,j}(\mathbf{x},\tau)=\rho\ddot{u}_i(\mathbf{x},\tau)\,,\qquad D_{i,i}(\mathbf{x},\tau)=qm(\mathbf{x},\tau)\,,\qquad q\dot{m}(\mathbf{x},\tau)+J_{i,i}=0\ , \tag{1}$$

where $\ddot{u}_i$, σ_{ij} , D_i , and q are the acceleration of displacements, stress tensor, electric displacement field, and electric charge of electron, respectively. The electron density and electric current are denoted by m and J_i , respectively. Symbol ρ is used for the mass density. A comma followed by an index denotes partial differentiation with respect to the coordinate associated with the index. We shall consider plane strain problems with $i,j\in\{1,3\}$.

In uncoupled thermo-elastic theory the temperature distribution is independent on mechanical and electrical fields. The governing equations (1) have to be supplemented by the heat conduction equation

$$\left[k_{ij}(\mathbf{x})\theta_{,j}(\mathbf{x},\tau)\right]_{,i}-\rho(\mathbf{x})c(\mathbf{x})\dot{\theta}(\mathbf{x},\tau)=0\,, \tag{2}$$

where $k_{ij}=k\delta_{ij}$ and c are the thermal conductivity tensor and specific heat, respectively.

The constitutive equations [3] have to be supplied by thermal terms [2]

$$\begin{aligned}
&\sigma_{ij}(\mathbf{x},\tau)=c_{ijkl}(\mathbf{x})\varepsilon_{kl}(\mathbf{x},\tau)-e_{kij}(\mathbf{x})E_k(\mathbf{x},\tau)-\lambda_{ij}(\mathbf{x})\theta(\mathbf{x},\tau)\,,\\
&D_j(\mathbf{x},\tau)=e_{ijk}(\mathbf{x})\varepsilon_{jk}(\mathbf{x},\tau)+h_{ij}(\mathbf{x})E_i(\mathbf{x},\tau)+p_j(\mathbf{x})\theta(\mathbf{x},\tau)\,,\\
&J_i(\mathbf{x},\tau)=qm_0(\mathbf{x})\mu_{ij}(\mathbf{x})E_j(\mathbf{x},\tau)-qd_{ij}(\mathbf{x})m_{,j}(\mathbf{x},\tau)\,,
\end{aligned} \tag{3}$$

where $c_{ijkl}(\mathbf{x})$, $e_{ijk}(\mathbf{x})$, $h_{ij}(\mathbf{x})$, $\mu_{ij}(\mathbf{x})$, $d_{ij}(\mathbf{x})$ and $p_j(\mathbf{x})$ are the elastic, piezoelectric, dielectric, electron mobility, carrier diffusion and pyroelectric material coefficients, respectively. The stress-temperature modulus $\lambda_{ij}(\mathbf{x})$ can be expressed through the stiffness coefficients and the coefficients of linear thermal expansion β_{kl} as $\lambda_{ij}=c_{ijkl}\beta_{kl}$.

The strain tensor ε_{ij} and the electric field vector E_j are related to the displacements u_i and the electric potential ϕ by

$$\varepsilon_{ij}=\frac{1}{2}\left(u_{i,j}+u_{j,i}\right)\,,\qquad E_j=-\phi_{,j}\ . \tag{4}$$

For the solution of governing equations (1) these will be considered in weak sense on artificial subdomains[3,7]. By choosing a Heaviside step function as the test function, the local integral equations can be derived

$$\int_{L_s+\Gamma_{su}} t_i(\mathbf{x},\tau)d\Gamma - \int_{\Omega_s} \rho\ddot{u}_i(\mathbf{x},\tau)d\Omega = -\int_{\Gamma_{st}} \tilde{t}_i(\mathbf{x},\tau)d\Gamma\,, \qquad t_i(\mathbf{x},\tau) = n_j(\mathbf{x})\sigma_{ij}(\mathbf{x},\tau) \tag{5}$$

$$\int_{L_s+\Gamma_{sp}} Q(\mathbf{x},\tau)d\Gamma - \int_{\Omega_s} qm(\mathbf{x},\tau)d\Omega = -\int_{\Gamma_{sq}} \tilde{Q}(\mathbf{x},\tau)d\Gamma\,, \qquad Q(\mathbf{x},\tau) = D_j(\mathbf{x},\tau)n_j(\mathbf{x}) \tag{6}$$

$$\int_{L_s+\Gamma_{sa}} S(\mathbf{x},\tau)d\Gamma + \int_{\Omega_s} q\dot{m}(\mathbf{x},\tau)d\Omega = -\int_{\Gamma_{sb}} \tilde{S}(\mathbf{x},\tau)d\Gamma\,, \qquad S(\mathbf{x},\tau) = J_j(\mathbf{x},\tau)n_j(\mathbf{x}) \tag{7}$$

$$\int_{L_s+\Gamma_{se}} \zeta(\mathbf{x},\tau)d\Gamma - \int_{\Omega_s} \rho(\mathbf{x})c(\mathbf{x})\dot{\theta}(\mathbf{x},\tau)d\Omega = -\int_{\Gamma_{sf}} \tilde{\zeta}(\mathbf{x},\tau)d\Gamma\,, \qquad \zeta(\mathbf{x},\tau) = k_{ij}\theta_{,j}(\mathbf{x},\tau)n_i(\mathbf{x}) \tag{8}$$

where $\partial\Omega_s$ is the boundary of the local subdomain.

The approximations for the primary field variables $f(\mathbf{x},\tau) \in \{u_i(\mathbf{x},\tau), \phi(\mathbf{x},\tau), m(\mathbf{x},\tau), \theta(\mathbf{x},\tau)\}$ can be written as [2,6]

$$f^h(\mathbf{x},\tau) = \sum_{a=1}^{n} N^a(\mathbf{x})\hat{f}^a(\tau) \tag{9}$$

where the nodal values $\hat{f}^a(\tau)$ are fictitious parameters for corresponding quantities, and $N^a(\mathbf{x})$ is the shape function associated with the node *a*. The number of nodes *n* used for the approximation is determined by the weight function $w^a(\mathbf{x})$.

Substituting spatial approximations (9) into the local boundary-domain integral equations (5) - (8), we obtain a system of ordinary differential equations in time, which is solved numerically by the Houbolt finite-difference scheme and backward difference method.

3. RESULTS

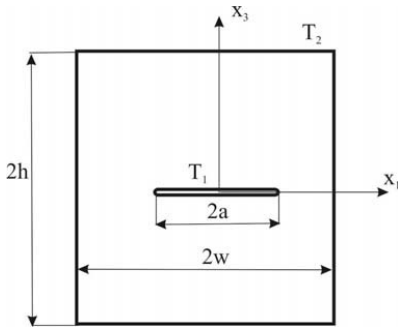

FIGURE 1. Central crack in a finite strip with prescribed temperatures

A straight central crack in a finite strip under a thermal load is analyzed. The geometry of the strip is given in Fig. 1 with the following values: $a = 0.5$, $a/w = 0.4$ and $h/w = 1.2$. On the outer boundary of the strip $\tilde{t}_i = 0$, $\tilde{Q} = 0$ and $\tilde{T}_2 = \theta_0 = 1\text{deg}$, while on the crack surface $\tilde{t}_i = 0$, $\tilde{T}_1 = 0$, $\tilde{S} = 0$ and electrically impermeable boundary conditions are assumed. The material properties correspond to Aluminium Nitride (AlN).

In the first example, the influence of the stationary electric current $J_0 = \tilde{S}(x_2 = \pm h/2)$ on the energy release rate is shown in Fig. 2. Two different initial electron densities are considered in the numerical analyses. One can observe that the energy release rate is less sensitive on the electric current for PZ semiconductor as for almost non-conducting PZ solid.

The influence of non-stationary boundary conditions on the physical quantities is investigated too. The strip is subjected to a thermal shock with Heaviside time variation on the outer boundary $\tilde{T}_2 = H(\tau)\theta_0$, $\theta_0 = 1\text{deg}$, with keeping $\tilde{S} = 0$. The initial electron density has vanishing influence on the SIF. One can observe finite value of the electric displacement intensity factor (EDIF) for a pure thermal load in Fig. 3. For non-conducting PZ the character of the EDIF curve is similar to the SIF. The EDIF evolution is exponentially growing for the conducting material. It is

due to strong influence of m_0 on K_D as observed for electric potential at stationary boundary conditions.

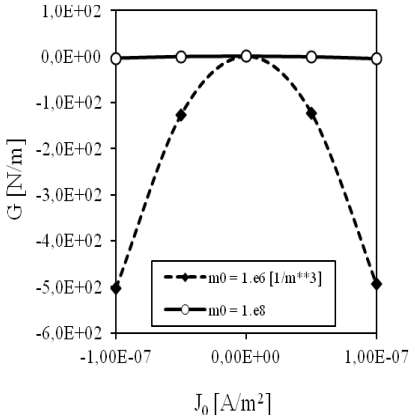

FIGURE 2. Influence of the electric current on the energy release rate for a mixed load

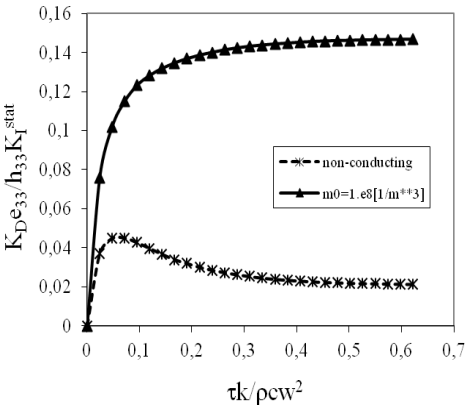

FIGURE 3. Time evolution of the electric displacement intensity factor

4. CONCLUSIONS

The MLPG has been successfully applied for 2-D crack problems in piezoelectric semiconductors subjected to a thermal loading. Stationary and transient thermal conditions are considered in the heat conduction equation. The numerical results revealed that initial density of electrons (carriers of electric charge in n-type PZ semiconductors) has a small influence on the crack displacement. However, the induced electric potential is strongly dependent on the initial electron density. The largest value of the induced potential is for a non-conducting PZ material. One can observe that the energy release rate is less sensitive on the electric current for PZ semiconductor as for almost non-conducting PZ solid.

REFERENCES

[1] W. Nowacki, Some general theorems of thermo-piezoelectricity, *Journal of Thermal Stresses*, 1, 171-182, 1978.

[2] J. Sladek, V. Sladek, Ch. Zhang, and P. Solek, Application of the MLPG to thermo-piezoelectricity, *CMES-Computer Modeling in Engineering & Sciences*, 22, 217-233, 2007.

[3] A.R. Hutson, and D.L. White, Elastic wave propagation in piezoelectric semiconductors, *Journal of Applied Physics*, 33, 40-47, 1962.

[4] J. Yang, An anti-plane crack in a piezoelectric semiconductor, *International Journal of Fracture*, 136, L27-L32, 2005.

[5] Y. Hu, Y. Zeng, and J. Yang, A mode III crack in a piezoelectric semiconductor of crystals with 6mm symmetry, *International Journal of Solids and Structures*, 44, 3928-3938, 2007.

[6] S.N. Atluri, *The Meshless Method, (MLPG) for Domain & BIE Discretizations*, Tech Science Press, 2004.

Third International Conference on Computational Methods for Thermal Problems
THERMACOMP2014, June 2-4, 2014, Lake Bled, Slovenia
N. Massarotti, P. Nithiarasu and B. Sarler (Eds.)

A Hybrid Computational Method for Dynamic Thermal Analysis of Structures Including Thin Layers

Israel Tuval[a], Prof. Dan Givoli[b]

The Faculty of Aerospace Engineering, Technion City, Haifa 3200003, Israel
[a]israel.tu@gmail.com , [b]givolid@technion.ac.il

ABSTRACT

Thin layers in the context of transient phenomenon appear in many applications in the field of aeronautics and space. Examples for such applications include external thin coatings of bare panels which are exposed to the periodic solar radiation, and the thin glue layer that connects the complex parts in a plane or satellites.

Usually there are two different and extreme approaches to handle the modelling and analysis of such thin layer. The first is to ignore this layer and the second is to fully model it using FEM for example. The first can suffer from severe inaccuracy, and the latter is time consuming and expensive.

Among other methods, unique asymptotic models were developed to deal with thin layer modelling. In which the thin layer is replaced by an interface with zero thickness, and special jump conditions are being dictated on this interface in order to express the special effect of the layer.

The present work shows how the first-order asymptotic interface model proposed by Bövik P. in 1994, and later generalized by Benveniste Y., can be incorporated in a FE formulation, to yield an accurate and efficient computational scheme for problems involving thin layers. This is done here for linear scalar parabolic problems in two dimensions, prototyped by transient heat conduction, using numerical examples to show that the proposed scheme is more cost-effective than fully modelling the layer.

Key Words: *Heat Transfer, Finite Elements, Numerical Analysis, Numerical Methods*

1. INTRODUCTION

Thin layers or interphases refer to structural zones which have different material properties that significantly differ from those of its surroundings and are generally smaller in size by an order of magnitude. The thin layer may appear in various geometries, it may be flat or curved, and it plays a structural role depending on the physical context. Thin layers appear in variety of applications in applied mechanics and in different engineering disciplines, and include both internal and external structures. Thin layers in the context of transient phenomenon appear in many applications in the field of aeronautics and space, and their influence on the thermo-mechanic design can often be quite challenging.

Thin layers are not only challenging the design itself, but also burden the thermal and mechanical analysis by means of the proper way to treat it in finite element (FE) computations. There are basically two different and extreme approaches to handle the modelling and analysis of such thin layer. The first approach is to ignore this layer under the assumption that its effect on the solution is negligible, based on prior knowledge of the contribution of the layer or a conclusion from some kind of sensitivity test. The second is to fully model it, using FEM for example. The first can suffer from severe inaccuracy, especially in transient analysis which also includes significant deviation in material properties of the layer compared to its surroundings, while the latter is time consuming and expensive due to the fact that the mesh inside the thin layer needs to be adequately fine in order to satisfy the proper solution. Furthermore, the latter might force the use of needle like mesh with poor aspect ratio.

The thin layer problem was vastly investigated in different contexts in the past, and few numerical methods were suggested in order to handle its modelling and simplify the analytic solution. Among other methods were unique asymptotic models that have been created precisely for that matter, in the field of linear heat transfer and elasticity. In these models the thin layer is replaced by an interface with zero thickness, and special jump conditions are being dictated on this interface in order to express the special effect of the layer. The idea above is illustrated in Fig. 1, where three phase problem with a thin layer with thickness 'τ' is approximated by two phase 'Interface problem' which is formulated that its solution is approaching the original three phase problem in the asymptotic limit when 't' goes to zero.

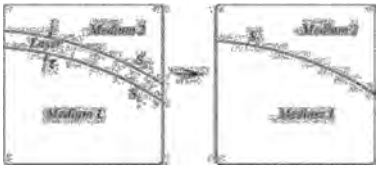

Fig. 1-Approximating a thin layer problem by an interface problem

As a result, the mathematical and the FE formulation of the 'Interface problem' needs to take into account the discontinuity in the physical fields. That is being done by the use of special jump conditions derived from first order asymptotic based interface mathematical model for 3D curved thin anisotropic interphase which was introduced in the work of Benveniste Y.[1] which generalized the work initiated by Bövik P.[2].

The present work is an expansion of the work done by Sussmann C. et al [3], which focused on steady state analysis. By adopting the Bövik-Benveniste mathematical interface model and combining it with a FE formulation, we yield an accurate and efficient computational scheme for transient heat conduction of the thin-layer problem. In order to enlighten the proposed method we will make use of simple test case of 2D transient heat conduction in a cylinder made of composite material with a circular layer. Though we focus on rather simple geometry, the method can be extended to any "closed" arbitrary shaped layer.

2. THE PROPOSED METHOD

As a prototype for scalar parabolic problems, we consider 2D transient heat conduction problem in a composite material. Fig. 2 illustrates the assumed geometrical setup. The left panel shows the original 'Layer problem' geometry, a cylinder composed of 3 layers which comprises the whole domain Ω. The material properties in these three regions generally differ, but we assume that in each region separately the material is homogeneous and isotropic. The layer thickness can change, but in terms of simplicity we will assume that the thickness of the layer $'\tau'$ is constant. On the right panel one can see the new geometry configuration of the 'Interface' modified problem, which is mainly the two domains Ω_1 and Ω_2 which are being extended on the account of domain 0, but the total size of the problem remains unchanged. The layer separating the two domains is now modelled as an interface S_0 which is located in the midline of domain Ω_0.

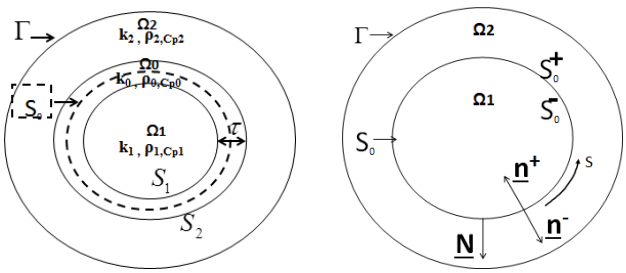

Fig. 2-LEFT SIDE: Original 3 Phase Problem configuration, RIGHT SIDE: Interface Problem modified new configuration

We denote $u(x,y,t)$ the unknown temperature field in Ω. We also use $u^{(1)}$, $u^{(2)}$ and $u^{(0)}$ to denote the restriction of the solution u to Ω_1, Ω_2 and Ω_0 respectively. Similarly, the unknown heat flux $\mathbf{q(x)}$ and also $\mathbf{q}^{(1)}, \mathbf{q}^{(2)}$ and $\mathbf{q}^{(0)}$ in the three regions. At t=0 [Sec] the layers of the material are held at constant possibly distributed initial temperature, and at t>0 the boundaries are subjected to different constraints which can be changed during the time of the problem T, and continuity condition for the heat flux and temperature are applied on the common boundaries S_1 and S_2.

The original heat equation for the 'Layer problem' is stated as follows:

$$\nabla \cdot \mathbf{q}^{(j)} + \rho_j C_{p\_j} \frac{\partial u^{(j)}}{\partial t} = f^{(j)} \text{ in } \Omega_j, \text{ where } \mathbf{q}^{(j)} = -k_j \nabla u^{(j)}, \text{ j=0,1,2, } 0 \le t \le T \qquad (1)$$

Our goal is to derive boundary conditions on the artificial interface S_0 for the interface configuration in order to describe the connection between the temperature and the heat flux from both sides of S_0 .

$$\left.\begin{array}{l} u^+ - u^- = f \\ q_N^+ - q_N^- = g \end{array}\right\} \text{goal: finding } f \text{ and } g \rightarrow \left.\begin{array}{l} u^+ - u^- = Aq_N^+ + Bq_N^- \quad \text{on } S_o \\ q_N^+ - q_N^- = Cu_{ss}^+ + Du_{ss}^- + E\dot{u}^+ + F\dot{u}^- \quad \text{on } S_o \end{array}\right\} \qquad (2)$$

The temperature and heat flux jump conditions (2) are derived in two steps: first we develop first-order asymptotic relations based on the continuity conditions on S_1 and S_2, in the layer configuration combined with Fourier law, and the 2D unsteady heat equation in radial coordinates. Second we enforce the relations in the new interface configuration, and express them as jump Conditions. A-F are constants depending on the heat conductivities and volumetric heat capacities of the three layers, and the thickness of the mid layer (τ).

The next step is to incorporate the jump condition in the FE formulation. After extracting the terms for q_N^+ and q_N^-, the interface conditions are now in the form suitable for variational treatment and are ready to be substituted in the weak form of the interface problem. The result after doing the common practice of developing the weak form for the heat conduction problem for the interface configuration and substitution of the jump condition expressions yields (3)

$$\mathbf{b}(\mathbf{w},\dot{\mathbf{u}}) + \mathbf{b}^*(\mathbf{w},\dot{\mathbf{u}}) + \mathbf{a}(\mathbf{w},\mathbf{u}) + \mathbf{a}^*(\mathbf{w},\mathbf{u}) = \mathbf{l}(\mathbf{w}) \qquad (3)$$

which is the familiar weak form for the heat conduction problem in addition to two new terms which are indicated by asterisk and are associated to the contribution of the interface. After approximation using Galerkin FE-method the discrete system is:

$$(\overline{\mathbf{M}} + \mathbf{M}^*)\dot{\mathbf{d}}(t) + (\overline{\mathbf{K}} + \mathbf{K}^*)\mathbf{d} = \mathbf{F}(t) \qquad (4)$$

where the interface mass, and stiffness matrices are $\mathbf{M}^*$ and $\mathbf{K}^*$ respectively. The way to construct the interface matrices is using a collection of 1D interface elements which lay on top of the sides of the 2D elements that belong to the meshes on the two sides of S_0 (See Fig. 3). This special interface element occupies the domain S_0^e and has N_{en} nodes and $2 \cdot N_{en}$ degrees of freedom (DOFs), namely DOFs on each side of the interface.

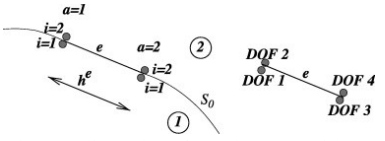

Fig. 3-A linear interface element- with two-nodes (a, b), having 2 DOF's on each side of S_0 corresponding to '-' and '+'

3. RESULTS

Test case: Transient heat conduction in a 3 phase cylinder with constant initial temperature (0°C) suddenly subjected to axisymmetric constant temperature constraints in its boundaries (100°C @ $r = R_{in}$ [2 m], 0°C @ $r = R_{out}$ [4 m]) up to steady- state (2000 sec).

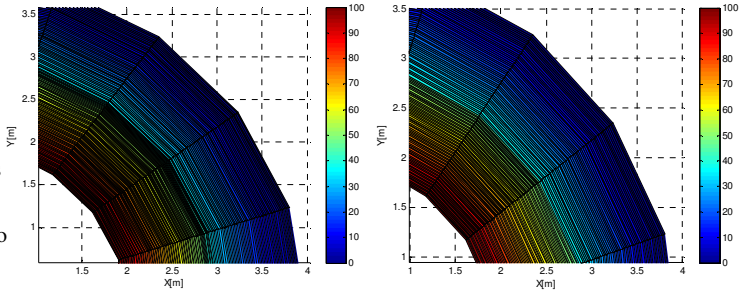

Fig. 4-Spatial Temperature distribution [℃] @ 2000 Sec: LEFT SIDE: Layer Problem, RIGHT SIDE: Interface Problem

The layer Ω_0 has insulation thermal properties compared to its enclosure domains Ω_1, Ω_2 . τ=0.1[m], $r = R_{interface}$ =3[m]. Equal mesh is used in both problems outside the mid layer, and inside the layer, 10- 2D elements in the radial direction for the 'Layer problem' vs. one 1D interface element, for the 'Interface problem'. From the comparison between the original 3-phase 'Layer problem' to the suitable approx. 'Interface problem', for the spatial (Fig. 4) and radial (Fig. 5) temperature distribution in specific time, one can see a very good agreement (also to steady state analytical solution).

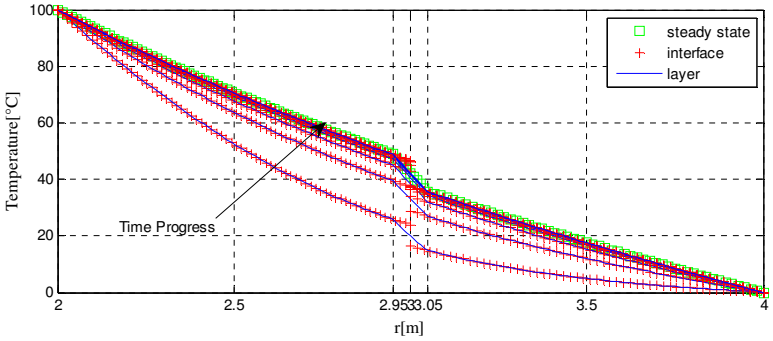

Fig. 5-Radial temperature distribution comparison between the models in different time steps (every 200 sec)

From comparison in time (Fig. 6): There is also good agreement through time.

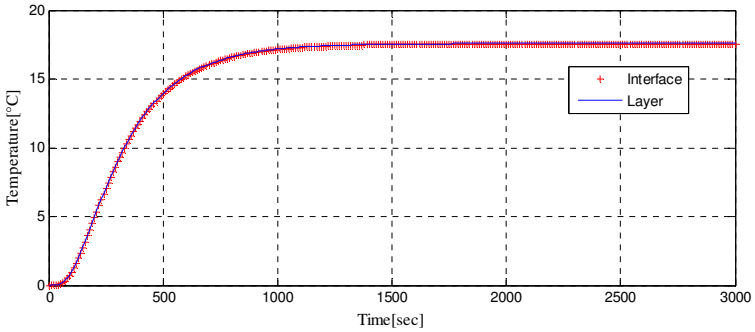

Fig. 6- Temperature comparison in time for specific location (@ 3.5 m)

4. CONCLUSIONS

The proposed asymptotic interface model method showed very good agreement to the compared results of the original 'Layer problem' within less computational effort compared to the full model approach.

REFERENCES

[1] Benveniste Y. A general interface model for a three-dimensional curved thin anisotropic interphase between two anisotropic media. *J Mech Phys Solids*, 54, 708-734, 2006

[2] Bövik P. On the modelling of thin interface layers in elastic and acoustic scattering problems. *Q J Mech Appl Math*, 47, 17-42, 1994

[3] Sussmann C, Givoli D, and Benveniste Y. Combined asymptotic finite-element modeling of thin layers for scalar elliptic problems. *Comput Methods Appl Mech Eng*,200, 3255-3269, 2011

PARALLEL SESSION

POWER PLANTS AND EQUIPMENT

Third International Conference on Computational Methods for Thermal Problems
THERMACOMP2014, June 2-4, 2014, Lake Bled, Slovenia
N. Massarotti, P. Nithiarasu and B. Sarler (Eds.)

INFLUENCE PARAMETERS ON THE PHOTOVOLTAIC MODULES PERFORMANCE

F. Arpino, G. Cortellessa, A. Frattolillo
Dipartimento di Ingegneria Civile e Meccanica, Università degli Studi di Cassino e del Lazio Meridionale, Via G. Di Biasio 43, 03043 Cassino (FR), Italy

ABSTRACT

In this work the authors propose an experimental and numerical investigation of the dependence of temperature and efficiency of photovoltaic modules on main design parameters (thickness of the aluminium frame, etc.), installation technique (distance between photovoltaic panel and supporting panel, tilt angle of the module), and environmental operating conditions, with particular reference to the wind velocity. The main objective of the present paper is to provide installation and operating indications in order to maximize efficiency. From the conducted investigations it has been evidenced that an optimal distance of the panel from the support can be found, in correspondence of which the efficiency is maximized.

Key Words: *Finite Elements, module efficiency, aluminium frame, distance supporting panel.*

1. INTRODUCTION

A better efficiency of the PV panels [1] can be obtained by ensuring operating conditions that avoid modules overheating. In fact, PV panels electric efficiency is inversely proportional to their operating temperature. In the authors' opinion, from the analysis of the scientific literature emerges that there is a lack of information about modules design optimization and installation indications. Therefore, in this paper the authors propose an experimental and numerical investigation of two PV modules assembly aimed at providing installation and operating indications that allow efficiency optimization. A detailed numerical simulation of the actual PV testing configuration has been conducted employing the commercial CFD code Comsol Multiphysics®, validated against the collected experimental data. On the basis of findings in the scientific literature, turbulence was modelled using the RANS approach and the $RNG\, k-\varepsilon$ and standard $k-\omega$ two-equations models. In particular, the work consists in a study of the effects induced by the main design parameters of a PV module (thickness and type of glass, thickness of the aluminum frame) and by the installation techniques (distance panel-supporting panel, tilt angle of the module), on the temperature and efficiency. On the basis of the obtained results, indications about PV modules installation and frame optimal dimensions are obtained in order to optimize operating conditions and efficiency.

2. EXPERIMENTS

Experimental investigations have been conducted on a two PV modules assembly installed on the roof of the faculty of Engineering of the University of Cassino. In particular, it consists of a pair of solar panels arranged horizontally and mounted on a frame structure, able to simulate different tilt angles of installation, from 0° to 90°. Two model of PV module have been experimentally investigated: i) the model 1, with a size of 1675x1000 mm and an aluminium frame of 30 mm thick, is characterized by a nominal power of 245 W; ii) the model 2, that presents the same size of model 1, but with an aluminium frame thickness of 50 mm, is characterized by a nominal power of 260 W. Experiments have been conducted with a tilt angle of 18° and an azimuth angle equal to zero. The temperatures of the PV panels and supporting plate, were constantly monitored through n. 10 thermocouples positioned on the back surface of the modules and n. 4 thermocouples positioned on

the supporting insulating panel. The wind was monitored using an anemometer able to measure the wind velocity and direction. It has been observed that a significant temperature difference is present between the leading edge and the center of the PV panel, probably due to the chimney effect in correspondence of the gap between the module and the supporting insulating panel. Such effect is more pronounced for the bottom panel, where a temperature difference of about 25 °C was measured in a distance of 335 mm. Looking at the collected data, it seems that the wind velocity does not significantly affect the PV panels temperature if it is below 2 m/s.

3. NUMERICAL MODEL AND VALIDATION

Experiments were accompanied by numerical simulations that allowed to calculate local temperature and velocity values in correspondence of the two PV panels. In particular, the experimental apparatus has been numerically investigated by means of two-dimensional steady-state simulations. The computational domain and the boundary conditions employed are available in Figure 1, where the fluid domain is represented in blue, the PV bottom module and part of the top module are red in the enlargement of Figure **1**, whilst the aluminium frame together with the supporting insulating plate are green.

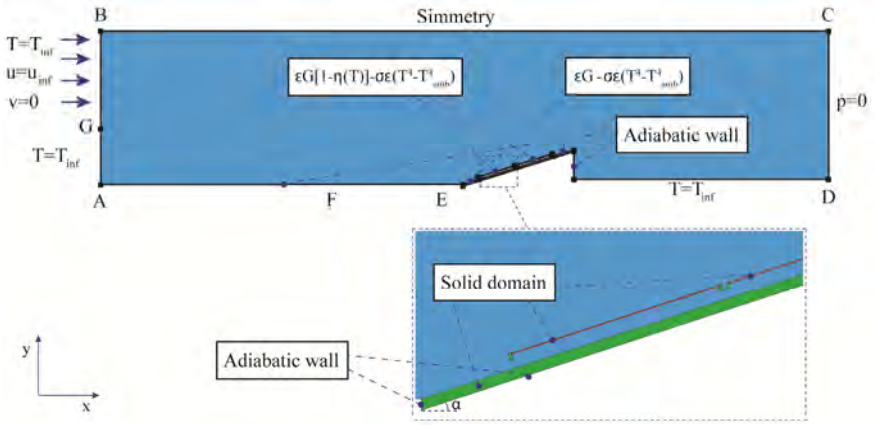

Figure 1. Numerical modelling of photovoltaic panels: computational domain and employed boundary conditions.

Simulations have been conducted assuming a steady, two-dimensional, incompressible fluid that behaves as an ideal gas. The solid surfaces were assumed to be grey for the radiation. The buoyant forces have been modelled invoking the Boussinnesq approximation. The well-known mass, momentum and energy conservation equations [2] were solved using the numerical commercial code Comsol Multiphysics®. The turbulence was modelled using the RANS (Reynolds Averaged Navier Stokes) approach and the quantities were averaged variables in the domain. In particular, in the present work, the $RNG\ k-\varepsilon$ turbulence model together with the buoyancy terms, were implemented by readjusting the default equations. The $RNG\ k-\varepsilon$ allows to consider the smallest scales of motion. In particular, whereas in the standard $k-\varepsilon$ model, the turbulent kinematic viscosity calculation is made considering a single spatial scale, into the $RNG\ k-\varepsilon$ model different spatial scales contribute to the calculation of the turbulent viscosity. In addition, the $k-\omega$ turbulence model, that allows an accurate prediction of velocity field in the proximity of solid walls, was employed [3, 4] and compared with the first one. All the simulations were performed using a computational grid composed by 418818 quadratic triangular elements, chosen on the basis of a proper grid sensitivity analysis. The simulated test conditions provide an irradiance G=980.7 W/m^2,

an air temperature equal to Ta=23.5 °C and a wind velocity u=0.5 m/s, with front direction (from the South). The comparison between numerical and experimental data is reported in Figure 2. In particular, the Figure 2(a) on the left hand side shows, with reference to the analysed test conditions, the average temperature of the upper surface of the bottom module with respect to the panel length, while in Figure 2(b) the same quantity is reported for the upper surface of the top module. In these figures the experimental results were compared with that obtained by the two considered turbulence models: $RNG\ k-\varepsilon$ and $k-\Omega$.

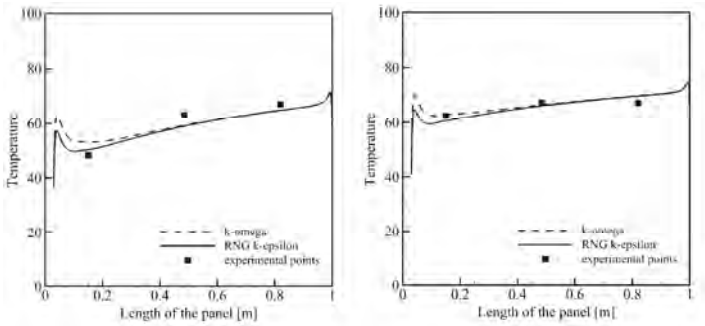

Figure 2. Temperature profile on the upper surface of the bottom module (a) and the top one (b), obtained for G=980.7 W/m^2, Ta=23.5°C and u=0.5 m/s.

From the analysis of Figure 2 it is possible to underline that, in the case of the top module, the temperature difference between simulations and experiments is lower than 3 °C on the whole panel for both the used turbulence models. Regarding the bottom module, the temperature differences between the numerical $RNG\ k-\varepsilon$ and experimental data are about 5 °C in correspondence of the centre of the module, while such difference is about 2 °C at the two panel ends. The results obtained using the $k-\Omega$ model are the same except for the left end of the bottom panel for which the greatest deviations from the measured temperature data were found (about 5 °C). The $RNG\ k-\varepsilon$ had the best agreement in predicting the temperature profile on the photovoltaic modules, for this reason it was selected for the parametric numerical analysis reported in the next section.

3. RESULTS

In this section a parametric analysis was carried out in order to understand the effects of the selected geometrical and fluid-dynamics parameters on the photovoltaic modules temperature profiles. The input parameters used for the numerical model validation were chosen as a reference configuration. Starting from these default parameters, a sensitivity analysis was performed by changing the modules tilt angle, the panels installation height, the frame height and the wind velocity. Ranging the tilt angles from 15 to 30 degree, the change in the average temperature was of about 4 °C on the bottom panel and about 6 °C on the top panel, for both the considered frame heights. Consequently, the efficiency of the panel was almost constant reaching a value of about 0.12 for all the tilt angle considered. The numerical results in Figure 3 correspond to the model with frame height h=30 mm and with different installation height: d=0 mm, d=20 mm, d=40 mm, d=60 mm, d=80 mm. The critical conditions were reached in the case of total absence of the fixing bar (panels directly mounted on the support: d=0), with average temperatures constantly above 90 °C. Ranging the installation height from d=0mm to d=80mm the average temperature on the modules is always decreasing. In particular, under these test conditions, the average temperatures differences between the lower and the higher considered installation height are of 35 °C on the bottom panel and of 26

°C on the top panel. It is important to notice that, the panel efficiency increase of 2% on both the modules in the considered installation heights range.

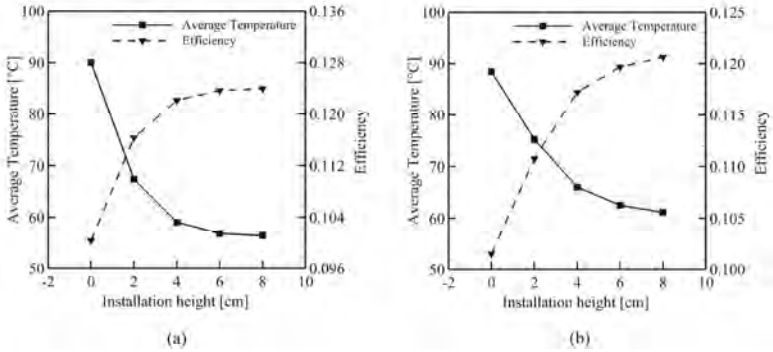

Figure 3. Average temperature variation with the installation height on the upper surface of the bottom module (a) and the top one (b), obtained with the frame height of 3 cm.

The effect is more pronounced for lower values of the installation heights. From a qualitative point of view, the considerations made for the couple of panels with 30 mm frame are still valid for the frame height h=50 mm. However it is possible to note that, a higher frame of the panels, and the consequent wider cavity subtended between the same panels and the support, involves an increase of the average temperature compared with the lower frame (about 5 °C for panels directly mounted on the support and about 2 °C for an installation height major then d=0). From the analysis of such results, it is possible to observe that, as expected, the lowest temperature (and consequently the largest efficiency) has been obtained for an installation height of 6.0 cm with frame height h=30 mm. Finally the average temperature variations on both the panels are of about 1°C in the considered wind velocity range, for the two considered frame height of 30 cm and 50 cm. The wind velocity change does not cause excessive cooling since the presence of a wall in proximity of the panels makes them non directly invested by the air flow.

4. CONCLUSIONS

In this paper the authors propose an experimental and numerical investigation of two PV modules assembly aimed at providing installation and operating indications that allow efficiency increasing. From the conducted investigations, it has been evidenced that an optimal distance of the panel from the support can be found, in correspondence of which the efficiency is maximized.

REFERENCES

1. Y. Tripanagnostopoulos, T. Nousia, M. Souliotis and P. Yianoulis, Hybrid photovoltaic/thermal solar system., Solar Energy, vol. 72, pp. 217–234, 2002.

2. R.W. Lewis, P. Nithiarasu and K.N. Seetharamu, Fundamentals of the finite element method for heat and fluid flow, John Wiley & Sons, Chichester, 2004.

3. H. Zaïdi, S. Fohanno, R. Taïar and G. Polidori, Turbulence model choice for the calculation of drag forces when using the CFD method, Journal of Biomechanics, vol. 43 pp. 405-411, 2010.

4. H.K. Versteeg and W. Malalasekera, An introduction to computational fluid dynamics. The finite volume method, Essex, England, 1995.

Third International Conference on Computational Methods for Thermal Problems
THERMACOMP2014, June 2-4, 2014, Lake Bled, Slovenia
N. Massarotti, P. Nithiarasu and B. Sarler (Eds.)

A SIMPLIFIED GENERAL MODEL FOR A WASTE-TO-ENERGY PLANT

F. Arpino, A. Frattolillo

Dipartimento di Ingegneria Civile e Meccanica, Università degli Studi di Cassino e del Lazio Meridionale, Via G. Di Biasio 43, 03043 Cassino (FR), Italy

M. Costa

CNR Istituto Motori, Viale Marconi, 4, 80125, Naples, Italy

N. Massarotti

Dipartimento di Ingegneria, Università di Napoli "Parthenope", Isola C4, Centro Direzionale di Napoli, 80143 Napoli, Italy

S. Ghetti, T. Lombardi

HERAmbiente S.p.a., Via dell'Energia, 86077, Pozzilli (IS), Italy

ABSTRACT

In this paper the authors present a simplified thermodynamic model able to predict the operating conditions of a waste-to-energy plant. Unlike simplified models typically used to monitor a plant operation, the proposed model does not employ correlations based on empiric observations or on experimental data regressions. The developed numerical tool, being phenomenological, is generally applicable to any waste-to-energy plant, and is here applied to the HERAmbiente S.p.A. plant in Pozzilli, Italy. Input parameters are determined from measurements and the obtained results are validated against experiments, showing a good agreement. The model allows verifying the constraints imposed by the European legislation on temperature and residence time of the combustion products in the plant chamber.

Key Words: *Thermodynamic model, waste-to-energy plant, residence time.*

1. INTRODUCTION

Energy recovery from incineration is an important part of waste management, although attention is to be devoted to the environmental impact of waste-to-energy plants. In order to avoid the formation of pollutants a proper combustion control is needed. In fact, in the last decades research activity showed that particulate carbon act as major carbon source for dioxins, that inorganic chlorides act as chlorine source, and that the presence of oxygen is essential for the process [1]. Favoured precursors for dioxins formation are the products of incomplete combustion. Their reduction by a proper combustion control significantly reduces dioxin formation. To this aim, European legislation 2000/76/CE prescribes that, for non hazardous wastes, the temperature of the gaseous combustion products, referred in the following as T_{2S}, must be kept above 850 °C for at least 2 seconds after the last air injection in the combustion chamber. In theory, the T_{2S} definition by legislation would require a measurement technique able to follow any fluid particle in the combustion chamber for at least 2 seconds. Such a measurement is unfeasible in the practice. The respect of the imposed temperature constraint, therefore, is usually verified *in situ* by employing simplified 0D models. The main disadvantages of such simplified models consists in the use of empiric correlations obtained from measurements performed on similar plants. Besides, calculation are performed assuming a reference biomass with fixed composition.

Authors conducted both an experimental and a numerical analysis on a waste-to-energy plant located in Pozzilli, Italy, fed by Refused Derived Fuel (RDF). The plant produces an electric power of about 11 MW and a thermal power of about 47 MW. The combustion chamber is composed of a grate fired boiler, with three vertical channels for energy recovery, able to produce about 60 t/h of water vapour at a pressure of about 60 bar. The main aim of this work is the evaluation of the T_{2S}. To this purpose, referring to an operating period of one week: i) all operating parameters from the plant instrumentation were collected; ii) a detailed composition analysis of the RDF was conducted; iii) additional temperature measurements were performed in the first channel of the combustion chamber; iv) a general simplified thermodynamic model for waste-to-energy plants was formulated; v) a detailed CFD analysis was performed.

In the present paper, the general simplified thermodynamic model formulated by authors is presented. The proposed model describes the RDF gasification, the gaseous combustion process ant the heat exchange within the first vertical channel. Obtained results were validated against collected experimental data.

2. THE THERMODYNAMIC MODEL

The first channel of the combustion chamber is subdivided in the following 4 control volumes (Figure 1): i) RDF gasification control volume; i) heat exchange volume placed upstream the gaseous combustion; iii) combustion of gaseous products; iv) heat exchange volume placed downstream the gaseous combustion region.

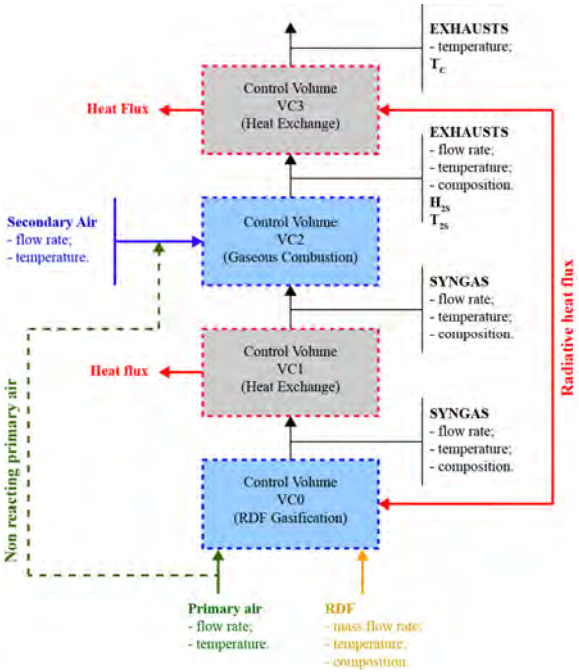

Figure 1. Schematic representation of the proposed general thermodynamic model.

The RDF gasification process is modelled assuming thermodynamic equilibrium, according to the following global reaction:

$$CH_xO_yN_z + wH_2O + m\left(O_2 + 3.76N_2\right) = n_{H_2}H_2 + n_{CO}CO + n_{CO_2}CO_2 + n_{CH_4}CH_4 + \left(\frac{z}{2} + 3.76m\right)N_2 \qquad (1)$$

where $CH_xO_xN_z$ represents the equivalent chemical formula of the feedstock. Mass balance for carbon, hydrogen and oxygen are solved. Besides, thermodynamic equilibrium equation is solved for the Boudouard reaction, water-shift and methane oxidation [2]. Finally, the gasification temperature is calculated by solving the energy conservation equation, taking into account heat from reactions and radiation to the surrounding combustion chamber. The heat transferred between gaseous products and the working fluid (water vapour) is calculated using the heat exchangers equation, numerically estimating the global heat transfer coefficient, U ($Wm^{-2}K^{-1}$), on the basis of the characteristics of the solid walls of the combustion chamber. Finally, the combustion of gaseous products (control volume VC2) is considered, allowing the calculation of exhaust composition and of the heat power released.

3. RESULTS

As previously introduced, a 5-days experimental campaign, from 17th to 21st of December 2012, was conducted aimed at collecting information about operating temperatures, reactants and products flow rates, and RDF composition. An additional silicon carbide bar equipped with four thermocouples was also introduced within the combustion chamber at a distance of about 6 m form the secondary air injection zone.

The collected experimental data allows the complete definition of the input parameters for the thermodynamic model, with related measurement uncertainty. Obtained results are validated in terms of averaged temperature in correspondence of instruments installed in the combustion chamber, and of the oxygen and water vapour content in the exhausts. In particular, a detailed parametric analysis is conducted and the results are compared with experiments in terms of data compatibility, taking into account measurements uncertainty. Figure 2, as an example, shows the dependence of some model results from the carbon mass fraction composition of the dry RDF. In particular, Figure 2(a) reports the syngas composition, while Figure 2(b) describes the variation of the temperature T_{2S}, the averaged temperature in correspondence of the instrumented bar, T_B, the mean temperature at the chamber top, T_C, the gasification temperature, T_{RDF}, and the distance, H_{2S}, travelled by the combustion products two seconds after the last air injection in the chamber.

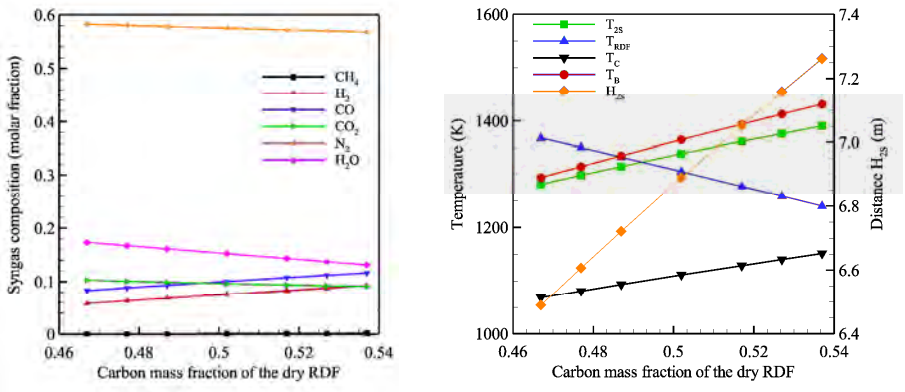

(a) (b)

Figure 2. Schematic representation of the proposed general thermodynamic model.

The thermodynamic model validation is shown in Figure 3. In particular, the obtained results are compared with the experimental data in terms of mean temperature at the top of the combustion chamber (left) and oxygen content at the exhaust (right). The error bars in the figure represent the estimated uncertainty. Numerical and experimental data are compatible for all the considered plant operating conditions.

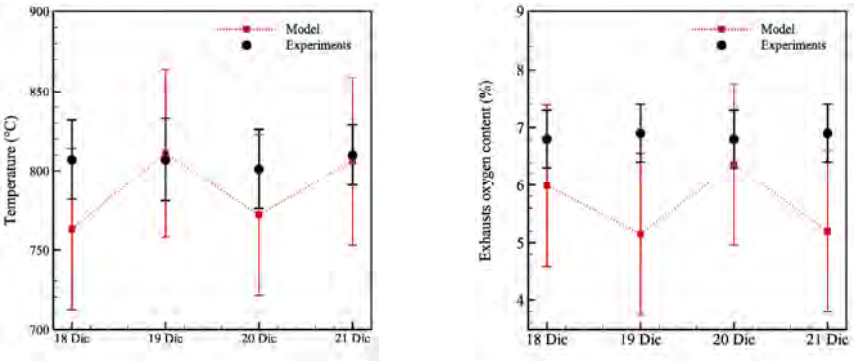

(a) (b)

Figure 3. Thermodynamic model validation.

The application of the proposed thermodynamic model confirms the respect of the constraint, imposed by the European directive, on the exhausts average temperature at a distance of H_{2S} from the secondary air injection zone. As a further development, the thermodynamic model also allows the definition of the input parameters for a detailed non reacting 3D CFD simulation of the first vertical channel of the combustion chamber. 3D CFD simulations allows the determination of the particles path into the combustion chamber, that gives a T_{2S} calculation in accordance with the actual definition of the European legislation 2000/76/CE [3, 4]. Results of the 3D CFD calculations are in good agreement with those derived from the simplified model, that proves being a good compromise solution between results reliability, flexibility and computational time.

4. CONCLUSIONS

The paper presents a simplified general thermodynamic model for the description of waste-to-energy plants fed by RDF. The model is part of a wider research activity aimed at a complete description of the thermo-fluid-dynamic field in an operating waste-to-energy plant. A detailed experimental campaign was conducted, which allowed the authors to validate the model. The proposed simplified model is not based on empirical or semi-empirical correlation, but is of phenomenological type, since it is based on balance equations for the thermodynamic variables and the chemical equilibrium hypothesis between participating species.. The comparison of results with detailed CFD simulations showed that the model presents a good reliability and flexibility, with a very low computational cost.

REFERENCES

[1] Vehlow, J., Reduction of dioxin emissions from thermal waste treatment plants: a brief survey. *Reviews in Environmental Science and Bio/Technology*, 11 (2012), 393-405.
[2] S.Jarungthammachote, A. Dutta, Thermodynamic equilibrium model and second law analysis of a downdraft waste gasifier. *Energy*, 32 (2007), 1660-1669.
[3] M. Costa, M. Dell'Isola, N. Massarotti, Numerical analysis of the thermo-fluid-dynamic field in the combustion chamber of an incinerator plant. *Energy*, 34 (2009), 2075-2086.
[4] EuropeanCommission, *Integrated Pollution Prevention and Control. Reference Document on the Best Available Techniques for Waste Incineration*, 2006.

Third International Conference on Computational Methods for Thermal Problems
THERMACOMP2014, June 2-4, 2014, Lake Bled, Slovenia
N. Massarotti, P. Nithiarasu and B. Sarler (Eds.)

CFD ANALYSIS OF THE COMBUSTION CHAMBER OF A WASTE-TO-ENERGY PLANT

M. Costa
Istituto Motori, Consiglio Nazionale delle Ricerche, Viale Marconi 4, 80125, Napoli, Italy

N. Massarotti
Dipartimento per le Tecnologie (DiT), Università di Napoli "Parthenope", Centro Direzionale, Isola C4, Napoli, Italy

F. Arpino, G. Cortellessa
Dipartimento di Ingegneria Civile e Meccanica, Università degli Studi di Cassino e del Lazio Meridionale, Via G. Di Biasio 43, 03043 Cassino (FR), Italy

S. Ghetti, T. Lombardi
HERAmbiente S.p.a., Via dell'Energia, 86077, Pozzilli (IS), Italy

Key Words: Refuse derived fuels, waste to energy, grate fired combustion chambers

1. INTRODUCTION

The operation of waste to energy plants based on incineration inevitably implies the production of greenhouse gases and the emission of harmful species to the human health. Post-combustion technologies are often used to reduce pollutants. Alternatively, it is possible to act directly on the combustion process to reduce emissions at the source, while also maximizing energy conversion efficiency. This is the reason why the European Directive on the construction and operation of incineration plants fixes strict rules concerning both the temperature and the residence time of the combustion products within the combustion chamber [1, 2]. The peculiar characteristics of the treated waste or Refuse Derived Fuel (RDF) may also cause problems to the burner long term operation. One of these is related to deposits formation, due to the presence of ash, which may have a slow melting temperature consequent the relatively high alkali content. Ash particles in the in-chamber flow may be sticky even at relatively low temperatures and deposit over the walls. Ash deposition modifies the heat transfer coefficient, reduces the systems efficiency and requires frequent stops for overhauling [3]. Therefore, the characterization of the phenomena occurring in a combustor through experimental and numerical techniques is strongly demanded for both identifying the kind of RDF most suitable for certain system and assisting its optimal maintenance.

Present work introduces a CFD (computational fluid dynamics) model for the numerical simulation of a real scale waste to energy plant operating in Italy, which allows investigating the turbulent reacting flow within the combustion chamber and, in particular, studying the temperature and residence time of the combustion products, or the effects deriving from any change in the heat transfer coefficient of the refractory covered surfaces.

2. DESCRIPTION OF THE CFD APPROACH

In this work, the incineration plant run by Herambiente S.p.A. in Pozzilli, Italy is analysed [4]. The plant produces 11 MW of electric power and 47 MW of thermal power. It treats 12 tons/hour of RDF and produces 60 tons/hour of vapour at a pressure of 60 bar. The combustion chamber has a moving grate furnace with continuous feeding and three vertical channels. In order to correctly validate the

hereafter presented numerical model, a proper experimental campaign was realised on the plant to both derive the actual composition of the treated RDF, and measure temperature at the ceiling of the combustion chamber and at about half the first vertical channel, as described in [5]. The RDF composition measured during a whole operational day was assumed as representative of the experimental campaign, and it is given in Table I.

3. Table I. Average RDF composition measured during the representative operating day

Proximate Analysis		Ultimate Analysis	
Component	(wt%)	Component	(wt%)
Volatile matter	69.73	C	58.84
Humidity	19.20	H	8.21
Ashes	11.07	O	30.71
		N	1.99
		S	0.25

Grate combustion is a well developed technology for the thermal treatment of municipal solid waste with energy recovery [6]. In moving grate furnaces, a stack of waste is supplied on a grate, possibly preceded by a mechanical treatment. Primary air is supplied below the grate, secondary air is introduced through nozzles above the layer of solid material in the so-called freeboard. The primary air is generally preheated, so that the heat transfer from the gas to the fuel increases temperature and determines the evaporation of the moisture content. When fuel is dried, the temperature of the solid particles further increases and volatiles start to release. All the available oxygen is assumed to be consumed in the reaction zone and combustible gases are released from the fuel layer. With the introduction of secondary air, these gases are burnt in the freeboard. Primary fuel conversion to the so-called syngas, therefore, has to be distinguished from secondary conversion in the freeboard [2, 6]. The two processes are anyway interdependent, since the composition and flow rate of the released syngas obviously affects the freeboard combustion, but also because the radiative heating from the freeboard to the solid fuel contributes to its drying and conversion process, thus affecting the syngas release.

The RDF conversion to syngas is here simulated through an in-house model developed, where the fuel bed on the solid grate is schematised as compounded by two open and sequential sub-systems, one for drying, the other for conversion, as schematised in Figure 1.a. The approach is analogous to the one by Deydier et al. [7], but chemical reactions follows the simplified scheme of Jarungthammachote and Dutta [8]. Steady conditions and constant operating atmospheric pressure are assumed. Gaseous species are modelled as ideal gases, with species outgoing the conversion section being in thermo-chemical equilibrium. Conservation equations are written for the number of moles of each chemical element (C, H, O and N), together with the equilibrium equations of the chemical reactions of the gasification process. Energy conservation is also properly formulated. The heating of the inorganic matter and the correct distribution of the net heat flux on the fuel bed are accounted for in the energy balance. The bed length is divided into 4 parts, as shown in Figure 1.b. Inlet 1 is the drying section. The solution of the resulting algebraic equation system is obtained through an iterative procedure. The model, properly validated on the basis of literature data, allowed to perform a sensitivity analysis with respect to the variation of RDF composition.

The 3D simulation of the syngas combustion within the freeboard is obtained through a properly developed model employing the SST (shear stress transport) k-ω sub-model for turbulence [9] and

the EDC (eddy dissipation concept) approach for combustion [10]. This is assumed as following the reduced kinetic scheme:

$$H_2 + \tfrac{1}{2}O_2 \Rightarrow H_2O \quad (1)$$

$$CO + \tfrac{1}{2}O_2 \Rightarrow CO_2. \quad (2)$$

Particular attention was devoted to the evaluation of the heat transfer coefficient at the walls in the two zones covered and uncovered by refractory material. The global heat transfer coefficient, U ($Wm^{-2}K^{-1}$), was estimated from additional numerical simulations, taking into account the actual geometric and thermal characteristics of the walls of the combustion chamber. In particular, assuming an internal average temperature of 1000 °C, it was determined that the value of the wall transmittance is U=15.8 W/m^2K for the areas that are covered with refractory material, while this values in equal to U=1844 W/m^2K for the areas of the chamber that are uncovered buy refractory material.

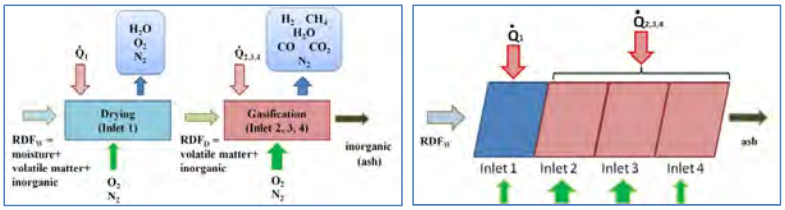

(a)……..(b)

FIGURE 1 – Scheme of the followed approach for the solid phase modeling

4. RESULTS AND DISCUSSION

The simulation of the coupled problem for the solid phase and the freeboard was made through an iterative process in order to verify the energy balance over the whole system. The validation of the model, here not discussed for the sake of brevity, was realised by comparing the temperature of the combustion products with the measurements collected at the plant in the day chosen as representative of its operation. Some computed results are reported in Figure 2. Figure 2.a represents the temperature field on the longitudinal symmetry plane of the computational domain, chosen as made of the first and the second vertical channel. This last is cut at a distance from the ceiling that allows the flow field not suffering of numerical reflection errors deriving from the imposition of the outlet boundary condition. The flame position in the zone placed in correspondence of the secondary air nozzles is evident. Figure 2.b represents the distribution of the oxygen mass fraction on the same plane. Oxygen enters only from Inlet 1 of Figure 1.b and through the secondary air nozzles. A value of 5.4 % at the exhaust is found, which is in good agreement with the measured value. Figure 2.c represents the flow path-lines within the combustion chamber that may give an idea of the barrier role played by the secondary air in this incineration plant.

5. CONCLUSIONS

A coupled solid-gaseous model for the simulation of the thermal conversion of RDF in a full scale plant is formulated. The model allows both characterising the temperature field and the residence time within the combustion chamber of the plant, for the fulfilment of the European Directive.

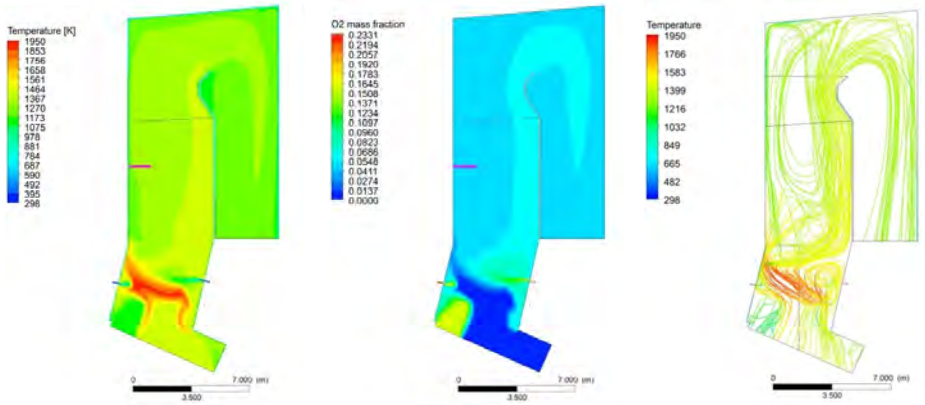

(a) (b) (c)

FIGURE 2 – Temperature field (a) and oxygen mass fraction on the symmetry plane of the combustion chamber (b) and path-lines (c)

REFERENCES

[1] European Directive n. 133 of 03/05/2005, "Directive 2002/96/EC of the European Parliament and of the Council on waste electrical and electronic equipment"

[2] M. Costa, M. Dell'Isola, N. Massarotti, Temperature and residence time of the combustion products in a waste to energy plant, *Fuel*, Vol. 102, 92-105, 2012

[3] T. R. Miles, T. M. Miles Jr., L. L. Baxter, B. M. Jenkis, L. L. Olden, Furnace deposits from firing biomass fuels, *Biomass and Bioenergy*, Vol. 10, pp. 125-138, 1996

[4] http://www.energonut.it/visita_virtuale.php

[5] F. Arpino, A. Frattolillo, M. Costa, N. Massarotti, S. Ghetti, T. Lombardi, A simplified general model for a waste-to-energy plant, Third International Conference on Computational Methods for Thermal Problems, June 2-4, 2014, Lake Bled, Slovenia

[6] P. Stehlik, Up-to-date technologies in waste to energy field, *Rev. Chem. Eng.*, Vol. 8 (4-6), 2012

[7] A. Deydier, F. Marias, P. Bernada. F. Couture, U. Michon, Equilibrium model for a travelling bed gasifier, *Biomass and Bioenergy*, Vol. 35, pp. 133-145, 2011

[8] Jarungthammachote, A. Dutta, Thermodynamic equilibrium model and second law analysis of a downdraft waste gasifier, *Energy*, Vol. 32, pp. 1600-1669, 2007

[9] Menter, F. R., Zonal Two Equation k-ω Turbulence Models for Aerodynamic Flows, AIAA Paper 93-2906, 1993

[10] Magnussen B.F., On the Structure of Turbulence and a Generalized Eddy Dissipation Concept for Chemical Reaction in Turbulent Flow, Proc. 19th AIAA Meeting, St. Louis, 1981

Third International Conference on Computational Methods for Thermal Problems
THERMACOMP2014, June 2-4, 2014, Lake Bled, Slovenia
N. Massarotti, P. Nithiarasu, B. Sarler (Eds.)

CFD MODEL OF AN INDUSTRIAL CIRCULATING FLUIDIZED BED BOILER

Wojciech Adamczyk[1], Gabriel Węcel[1], Adam Klimanek[1], Ryszard Białecki[1], Paweł Kozołub[1], Marcin Klajny[2]

[1]Institute of Thermal Technology, Silesian University of Technology, Konarskiego 22, 44-100 Gliwice, Poland, e-mail: wojciech.adamczyk@polsl.pl

[2]Foster Wheeler Energia Polska Sp. z o.o., Staszica 31, 41-200 Sosnowiec, Poland

ABSTRACT

Circulating Fluidized Bed (CFB) coal fired steam boilers, due to their low sensitivity to fuel quality, robustness and simple desulphurization become a competitive technology to the conventional Pulverized Coal (PC) units. Recent years have seen significant growth in the number of placed into service new CFB units. The aim of this paper is to develop and validate CFD simulation technique applied to large industrial CFB boilers.

Despite their importance, the simulation techniques of large scale CFB boilers lags behind the needs of engineering community. The reason for this seems to the complexity of the physical and chemical phenomena taking place in the fluidized bed, specifically the hydrodynamic of the dense particular matter and multistage combustion. Moreover, even significantly simplified simulation models lead to prohibitive usage of computing resources. An additional difficulty encountered in the computational process is the poor convergence of the procedure. Thus, the contemporary designing process of large industrial CFB plants bases mainly on experience of the engineers rather than on in depth mathematical description of the process.

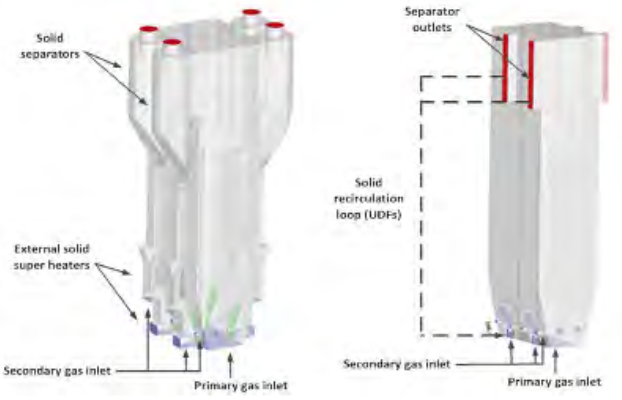

Fig. 1. CFB boiler geometries: complete (left) and simplified (right).

The European regulations concerning carbon tax impose strong limitations on CO2 emission of all combustion processes. As a result, coal fired units need to be equipped with carbon separation plants. Cost of CO2 separation via absorption can be reduced by switching to oxycombustion, a process where the flue gases are composed of almost pure carbon dioxide. This is achieved by using as an oxidizer a mixture of pure oxygen and recirculated flue gases. Presence of such oxidizer introduces additional aspect in the simulation of CFB units, as the radiative properties of the flue gases significantly differ from the standard air combustion case.

The computational tool applied to simulate a large scale CFB boiler (see Fig. 1 left) was Ansys FLUENT 14.0 commercial CFD package, whose functionality has been extended by in house set of user defined functions, specifically those modeling radiation and drag. The numerical simulations were carried out using a simplified boiler geometry (Fig 1. right) and combustion of coal. Advantage has been taken from the symmetry of the boiler, thus the computational domain was limited to one half of the unit. Moreover, the domain has been limited to the combustion chamber, with the external solid separators and solid heat exchangers were replaced by the set of UDFs used for recirculation procedure, see Fig. 1.

The set of numerical simulations was performed for 100% of the nominal boiler thermal load. The particle transport within the boiler was simulated applying the hybrid Euler-Lagrange (*Dense Discrete Phase Model* - DDPM) approach. Evaluated results have been compared against measured data collected during normal boiler operating conditions [1].

MODELING PARTICLE TRANSPORT

The gas and solid particle flow in the CFBs is frequently modeled by two fluid model, Euler-Euler. In this approach, the gas and particulate matter are treated as two interpenetrating phases. Detailed description of this method, its advantages, disadvantages and limitations can be found in [2, 3, 4, 5, 6]. The main drawback of that approach is the long calculation time required for evaluating the time averaged solution. The problem becomes much more involved when the Particle Size Distribution (PSD) is taken into account, in which case, several fluids describing the behavior of a given diameter range of the solid phase needs to be introduced. This not only increases the dimensionality of the governing equations set, but also reduces the convergence of the equation solver. To reduce the curse of dimensionality various population balance techniques are introduced [7].

An alternative of the Euler-Euler approach, used in this study is the hybrid Euler-Lagrange DDPM technique where the PSD is accounted for in a natural way, by tracking groups of particles of various sizes. It should be stressed, that standard Lagrange tracking of particles neglects the interaction between particles and thus, should not be applied in fluidized bed context where the four-way coupling between solid and fluid phase [8] is of importance. DDPM accounts for particles collisions by resorting to the Kinetic Theory of Granular Flow (KTGF) [9].

Tab. 1: Closure models for the Euler-Euler and hybrid DDPM approaches

Solid pressure	Lun et al. [13]
Solid viscosity	Gidaspow [9]
Bulk viscosity	Lun et al. [13]
Friction viscosity	Schaeffer [14]
Friction pressure	Based on KTGF
Granular temperature	Algebraic [2]
Wall spec. coeff. Euler-Euler	0.1
Restitution coeff.	0.9

The influence of the particle movement and energy transfer between particles and the fluid carrier in the hybrid Euler-Lagrange model are embedded in the conservation equations of the continuous phase by additional source terms. These terms result from the solution of KTGF equations defined in Euler frame. The data transfer between the Eulerian grid and particle position is modeled by the use of interpolation (projection) operators [10, 11].

The radiation equations have been solved using an enhanced Discrete Ordinate (DO) solver. The novelty of this approach is twofold. First, the coefficients of the Weighted Sum of Gray Gases (WSGG) have been evaluated directly from the HITEMP base. Second, the solution strategy has

been modified to account for the real WSGG by solving the DO set for a set of absorption coefficients and weighted summation of the results. The weights of the model were made temperature and flue gas composition dependent. Details of this approach are described in [12].

NUMERICAL MODEL

The cross section of the upper part of the combustion chamber is a 27.6x10.6 m rectangle of 48m height. The gas and fuel injection ports, as well as the solid internal circulation opening are located below this zone. The one half of the boiler geometry was equipped with 16 secondary gas inlets and 7 fuel feeding ports distributed at both boiler side walls. At the left wall two solid injection ports were located. It was assumed that the primary gas enters the combustion chamber through its whole bottom wall.

The CFB geometry was meshed using a combination of tetrahedral and hexahedral elements. The total number of grid elements for simplified geometry was 1.3 M. The average size of the grid element was 0.2 m. In order to obtain time average solution the wall clock simulation time 3 months needs to be used. The presented simulations have been carried using 2 PCs, each equipped with 2x4 core processors and 16~GB operating memory.

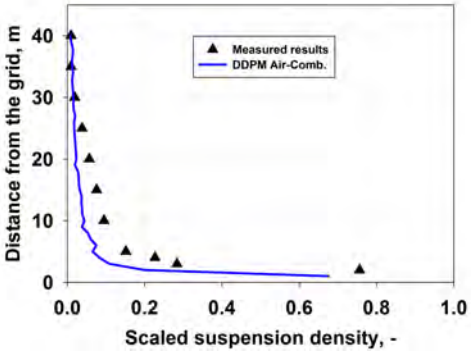

Fig. 2: Time average distribution of material in the combustion chamber carried out for air-fuel combustion

The set of used closure models by both used approaches are summarized in Tab. 1. The interphase exchange coefficient was modeled applying the modified version of the Wen&Yu/Ergun drag correlation [9]. That drag correlation has been implemented to the solution procedure using the UDF mechanism.

The turbulence was modeled using a standard k-epsilon model with enabled dispersed option. The node based averaging procedure was used for distributing of the solid material over the nodes of the computational grid. Owing to this technique, longer time steps could be used and the convergence of the scheme was enhanced. The QUICK interpolation scheme was used for the mass conservation equation, whereas the second order upwind scheme was selected for the remaining equations. The velocity boundary condition (BC) was applied for all gas, and solid inlets. At the outlets the atmospheric pressure boundary condition was used. The no-slip BC was used for the gaseous phase at the boiler walls.

RESULTS

Figure 2 shows the comparison of the calculated and measured scaled temperature profiles for air-fuel combustion process. The results for air-fuel combustion have been evaluated for 560 s of physical time where averaging time was 60 s. Figure 3 illustrates the dimensionless distribution of the solid material along the boiler high. The measured suspension density profile was calculated using measured pressure profile over the boiler height applying simple relation

$$\rho_{sus} = \varepsilon_s \rho_s = \Delta p / (g \Delta h)$$

where g is the gravitational acceleration, Δp is the pressure drop in the gaseous phase, h is the boiler height, ε_s is the volume fraction of the solid material, and ρ_s denotes the solid phase

density. The pressure distribution was measured using 11 ports located within the combustion chamber.

The calculated particle size distribution within the boiler is illustrated in Fig. 3. The results show that the particles larger than 300 μm have been mainly collected at the bottom of the combustion chamber, which is in line with the measured particle size distribution. Numerical results are in reasonable agreement with the measurements.

Another set of simulations has been carried out for the oxycombustion case. Due to space limitations, these results will be shown during the presentation at the conference.

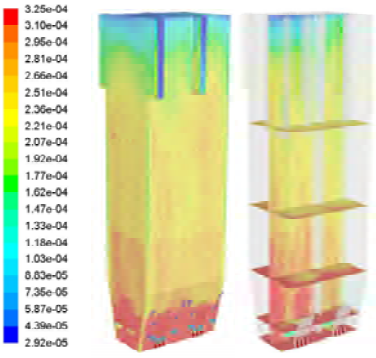

Fig. 3: Simulated time averaged solids volume fraction distributions on the external boiler walls (left) and within the boiler (right): air-fuel combustion

CONCLUSIONS

The main objective of this work was to find, develop and test a CFD model capable for solving the complex particle transport and combustion process in a dense fluidized bed of a large scale industrial CFB boiler, both for air and oxy combustion. The hybrid Euler-Lagrange DDPM approach implemented in ANSYS Fluent equipped with several UDFs, seems to be an optimal tool for simulation of CFB boilers. Evaluated results were validated using the measured data.

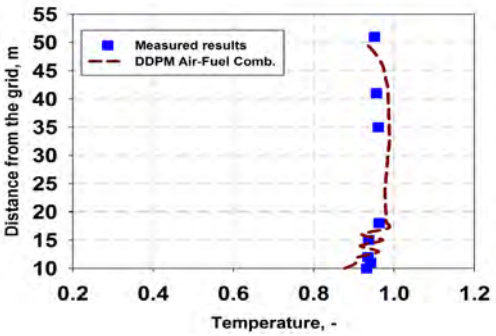

Fig. 4: Time averaged scaled temperature profile compared with measured data: air-fuel combustion

As the simplifications behind the implemented model have been quite severe, substantial differences between the measured and simulated fields could be expected. The performed calculations shown, however, good agreement between the calculated and measured parameters.

ACKNOWLEDGMENTS

The work of WA, GW, RB and PK was supported by the National Centre for Research and Development, within the confines of Research and Development Strategic Program Advanced Technologies for Energy Generation Project no. 2 Oxy-combustion technology for PC and FBC boilers with CO2 capture, agreement no. SP/E/2/66420/10. The research of AK has been supported by Project no. 3 Development of coal gasification technology for high production of fuels and energy of the same Strategic Program.

REFERENCES

[1] Blaszczuk, A., Komorowski, A., Nowak, W., Distribution of solids concentration and temperature in the combustion chamber of the SC-OTU CFB boiler. *Journal of Power Technologies* 92 (1), 27-33, 2012.

[2] Syamlal, M., Rogers, W., O'Brien, T., MFIX Documentation. *National Technical Information Service 1*, 5540-5551, Theory Guide, 1993.

[3] Gidaspow, D., Multiphase flow and fluidization. *Academic Press*, Boston, MA, 1994.

[4] Zhang, N., Lu, B., Wang, W., Li, J., 3D CFD simulation of hydrodynamics of a 150MWe circulating fluidized bed boiler. *Chemical Engineering Journal* 162, 821-828, 2010.

[5] Myohanen, K., Hyppanen, T., A three-dimensional model frame for modelling combustion and gasification in circulating fluidized bed furnaces. *International Journal of Chemical Reactor Engineering* 9 (A25), 2011.

[6] Adamczyk, W., Klimanek, A., Bialecki, R., Wecel, G., Kozolub, P., Czakiert, T., Comparison of the standard Euler-Euler and hybrid Euler-Lagrange approaches for modelling particle transport in a pilot-scale circulating fluidized bed experimental test-rig. Particuology. http://dx.doi.org/10.1016/j.partic.2013.06.008, 2013.

[7] Fan, R., Marchisio, D.L., Fox, R.O., Application of the direct quadrature method of moments to polydisperse gas–solid fluidized beds, *Powder Technology* 139, 7– 20, 2004.

[8] Crowe, C., Schwarzkopf, J., Sommerfeld, M., Tsuji, Y., Multiphase flows with droplets and particles, 2012.

[9] Huilin, L., Gidaspow, D., Hydrodynamics of binary fluidization in a riser: CFD simulation using two granular temperatures. *Chemical Engineering Science* 58, 3777-3792, 2003.

[10] Andrews, M., O'Rourke, P., The Multi fluid Particle-in-Cell (MP-PIC) Method for dense particulate flows. *International Journal of Multiphase Flow* 22 (2), 379-402, 1996.

[11] Snider, D., An incompressible three-dimensional Multiphase Particle-in-Cell Model for dense particle flows. *Journal of Computational Physics* 170, 523-549, 2001.

[12] Węcel, G., Ostrowski, Z., Białecki, R., A novel approach of evaluating absorption line black body distribution function employing proper orthogonal decomposition, *Journal for Quantitative Spectroscopy and Radiative Transfer*, 111, 309-317, 2010.

[13] Lun, C., Savage, S., Jerey, D., Chepurnly, N., Kinetic theories for granular flow: inelastic particles in coquette flow and slightly inelastic particles in a general flow field. *Journal of Fluid Mechanics* 140, 223-256, 1984.

[14] Schaeffer, D., Instability in the evolution equations describing incompressible granular flow. *Journal of Differential Equations* 66, 19-55, 1987.

[15] Chapman S. and Cowling T.G., The mathematical theory of non-uniform gases. *Cambridge Univ. Press, Cambridge*, 3 edition, 1970.

[16] Cloete, S., Johansen, S., Braun, M., Popo , B., Amini, S., May, Evaluation of a Lagrangian discrete phase modeling approach for resolving cluster formation in CFB riser. *7-th International Conference on Multiphase Flow*, ICMF 2010 Tampa, Florida USA, 2010.

[17] Jenkin, J., Savage, S., A theory for the rapid flow of identical, smooth, nearly elastic, spherical particles. *Journal of Fluid Mechanics* 130, 187-202, 1983.

[18] Wang X.Y., Jiang F., Xu X., Fan B.G., Lei J., Xiao Y.H., Experiment and CFD simulation of gas solid flow in the riser of dense fluidized bed at high gas velocity. *Powder Technology* 199, 203-212, 2010.

Third International Conference on Computational Methods for Thermal Problems
THERMACOMP2014, June 2-4, 2014, Lake Bled, Slovenia
N. Massarotti, P. Nithiarasu and B. Sarler (Eds.)

A COMPARISON OF TWO MODELS FOR THE NUMERICAL SIMULATION OF A WALKING BEAM REHEATING FURNACE

Tiago Morgado, Pedro J. Coelho
Mechanical Engineering Department, Instituto Superior Técnico/IDMEC, Universidade de Lisboa, Av. Rovisco Pais 1049-001 Lisboa, Portugal,
tiago.morgado.07@hotmail.com, pedro.coelho@tecnico.ulisboa.pt

Prabal Talukdar
Department of Mechanical Engineering, Indian Institute of Technology Delhi, New Delhi 110016, India, prabal@mech.iitd.ac.in

ABSTRACT

The numerical simulation of the heating process of steel slabs in a walking beam reheating furnace is reported using two different models. In one model, the turbulent reactive flow in the furnace is simulated together with the heat conduction in the slabs. The calculations are performed using a commercial code and a user-defined function is used to simulate the periodic movement of the slabs by the walking beams in the furnace. Unsteady calculations are performed until a periodic transient solution is achieved. In the second model, the furnace is divided into a small number of zones and the average temperature and chemical composition are prescribed in every zone. The unsteady heating process of the slabs is modelled using the same software and accounting for radiative transfer in the furnace and heat conduction in the slabs. The second model is computationally more economical. The results show that the two models yield mean volume average temperatures of the slabs leaving the furnace that differ by less than 3%, provided that accurate values of the temperature of the gases and walls are used.

Key Words: *Reheating Furnace, Walking Beam Furnace, Slab heating.*

1. INTRODUCTION

The present work deals with the numerical simulation of a walking beam type reheating furnace, which is used in the steel industry to heat steel slabs and increase their temperature above the recrystallization temperature for the subsequent plastic deformation in the rolling mill. The temperature distribution in the slabs, which plays a major role in the quality of the final product, and the heating efficiency of the furnace are of major importance, and have been widely investigated [1-6] due to the economical and environmental benefits of improvement in the design and operating conditions. The mathematical models employed to simulate these furnaces may be divided into two groups, namely models that prescribe the temperature and gas composition in the furnace or use a simplified approach to obtain those data [3, 5, 6], and models that solve the governing equations for the reactive flow field [1, 2, 4]. No comparison is available in the literature between the models of the two groups mentioned above. However, the solution of the governing equations for a reactive flow is time consuming, and therefore it would be better to rely on models of the first group whenever possible. The main purpose of the present work is to compare two similar models, which differ only in the way the gas temperature and composition are obtained. In one of the models, referred to below as model A, these quantities are calculated using CFD, while in the other model, which will referred to as model B, the furnace is divided into a small number of zones and the average temperature and gas composition are prescribed for every zone using the average values obtained from the CFD calculations.

2. MATHEMATICAL MODEL

Model A solves the unsteady time-averaged equations that govern the mass, momentum and energy conservation for turbulent reactive flows. The realizable k-ε model is used for turbulence closure, and the laminar flamelet model is employed for combustion modelling. The mean composition of the medium is obtained using the conserved scalar and prescribed pdf formalism. A β function is assumed for the pdf of mixture fraction, which is completely defined from the mean and variance of mixture fraction that are obtained from the solution of their transport equations. The mean temperature is determined in a similar way, but uses the enthalpy defect concept to relate instantaneous values of mixture fraction to temperature while accounting for radiative heat losses. Radiative transfer in the medium is calculated using the discrete ordinates method, and the radiative properties of the combustion gases are determined using the weighted-sum-of-grey-gases method. Heat conduction in the slabs is also modelled. The coupled reactive fluid flow and slab heat conduction calculations were performed using the commercial software Ansys–Fluent. A hybrid mesh with about 1.5×10^6 control volumes was employed.

The walking beams periodically move the slabs in the furnace towards the exit to the rolling mill. A new slab at 300 K enters into the furnace every 256 s. During this time period the slabs are held fixed in their positions on the static beams. A user defined function was used to simulate the periodic movement of the slabs. This function copies the temperature field in the region occupied by every slab to the region occupied by the neighbouring downstream slab. Unsteady calculations were performed using a time step of 8 s until a transient periodic solution was achieved.

In the case of model B, the furnace is divided into eight zones [3, 5, 6]. A volume averaged gas temperature is calculated for each zone based on the predicted solution from model A obtained at the end of the transient simulation. The temperature of the walls of the furnace in each zone is evaluated as an area averaged temperature using again the results from model A. The gas composition is taken as uniform over the furnace and set equal to the composition of the mixture resulting from complete combustion of the fuel, while maintaining the excess air. Radiative transfer in the interior of the furnace and heat conduction in the slabs are coupled in a transient simulation using the same time step employed in model A.

All the calculations were performed in a personal computer with an Intel® Core™ i7-2600K processor, 3.40 GHz. The computational times for models A and B were about 62 h and 51 h, respectively, when radiation is calculated in every time step. However, this time may be significantly reduced for model B with no impact on the computed solution if radiation is computed with a time step of 256 s, i.e., only when the slabs move.

3. RESULTS AND DISCUSSION

The studied walking beam reheating furnace, whose dimensions are 36.0 m × 5.4 m × 10.7 m, is identical to that described in [5, 6] and is schematically shown in Fig. 1. Three zones may be distinguished in the furnace: preheating, heating and soaking zones. The slabs are mostly heated in the first two zones, the purpose of the soaking zone being to reduce the temperature differences in every slab before they leave the furnace. The geometrical dimensions, the operating conditions and the boundary conditions employed in the simulations are given in [5, 6], and are similar to those reported in [1-4]. The furnace accommodates 27 slabs, 11 of them in the preheating zone, 8 slabs in heating zone and 8 slabs in the soaking zone. The size of the slabs is 1.0 m × 0.25 m × 9.6 m, and they are placed on static beams at a height of 2.4 m above the bottom of the furnace, with a distance of about 0.3 m between two neighbouring slabs. The fuel composition is given in [1-2], and the furnace operates with an excess air of 10%.

The predicted mean radiative heat fluxes on the top and bottom surfaces of the slabs are shown in Fig. 2 and compared with other values reported in the literature [3, 4]. This comparison

should be mainly qualitative, since the models and the input data are not exactly the same in the different works, e.g., 29 slabs were considered in [3, 4]. The radiative fluxes on the top surface predicted by model A increase in the preheating zone up to the 9th slab, remain relatively high in the heating zone of the furnace, and then decrease in the soaking zone, since in this last zone there is less heat released from combustion and the temperature of the slabs is closer to the temperature of the combustion gases. There are two regions where the radiative heat fluxes drop and rise again further downstream, namely for slabs 11–15, and 19–22, which are due to the necks of the furnace roof. This trend is similar to that shown in [4], even though the dips in the present work are more pronounced, and have also been predicted by other authors, e.g. [1, 2]. However, the predictions from model B show a significant decrease of the radiative fluxes in the heating region, and no dips are present, as also observed in [3, 6]. This is probably due to the different models employed. In fact, model B, as well as the models in [3, 6], belong to the first group mentioned in the introduction, which do not simulate the turbulent reactive flow, in contrast with model A and with the models employed in [1, 2, 4]. The radiative heat fluxes on the bottom surface of the slabs (see Fig. 2b) are a little lower than on the top surface, except in the region where dips are present, and change relatively smoothly along the furnace. This trend is consistent in all the works.

The predicted area averaged temperatures of the top and bottom surfaces and the volume averaged temperature of the slabs are shown in Fig. 3, along with predictions taken from [3, 4]. All temperatures increase continuously as the slabs approach the exit to the rolling mill, but the temperature variation is smaller in the soaking zone, where the lower heat release contributes to reduce the temperature gradients inside the slabs. The area averaged temperatures on the top and bottom surfaces of the slabs are close to each other, and exceed a little the volume averaged temperature. In fact, the surfaces are exposed to radiation, while the interior of the slabs is only heated by conduction, and is cooler than the surface, even though the temperature differences become smaller towards the exit. Model B consistently predicts lower average temperatures than model A, as a result of the lower radiative heat fluxes. However, the differences between the two models are relatively small, and do not exceed 14%. At the outlet, where the temperatures are most important due to their impact on the quality of the final product, the difference between the mean volume average temperatures is below 3%, while the differences between the mean temperatures on the top surface and on the bottom surface are even smaller.

A comparison of the predicted temperatures with the results reported in [3, 4] shows qualitative agreement, although the temperature increase in the soaking zone is marginal in [3]. The higher temperatures predicted in [3, 4] are due to the longer residence time, the higher emissivity of the slabs for temperatures above 1073 K, and the use of a fuel with higher heating value in the simulations reported in [4].

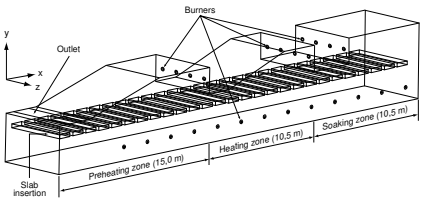

FIGURE 1. Configuration of the walking beam reheating furnace.

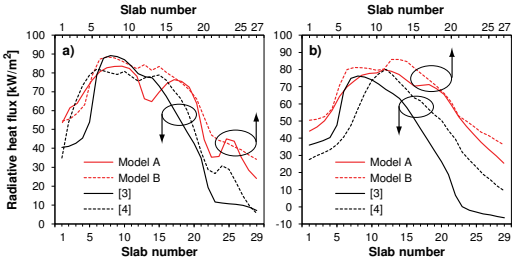

FIGURE 2. Average radiative heat fluxes on the top (a) and bottom (b) surfaces of the slabs.

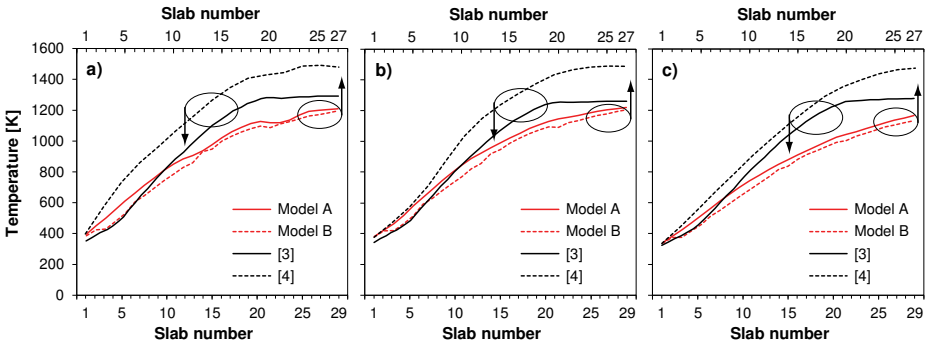

FIGURE 3. Average temperatures of the slabs, (a) Top surface, (b) Bottom surface, (c) Volume averaged temperature.

Hence, we can conclude that model B is able to simulate the heating process of the slabs in the furnace with a reduction in the computational requirements and a minor impact on the accuracy of the predictions. However, in order to obtain this level of agreement between the two models, a very good estimation of the mean gas and wall temperatures in each zone is required, due to the sensitivity of the results to these data. These are difficult to estimate if there are little or no experimental data available, unless another reliable model is used for that purpose.

4. CONCLUSIONS

The results obtained using the two different models are consistent with previous results reported in the literature. The observed differences can be explained by the slightly different conditions considered in the simulations. Model A, which solves the governing equations for the turbulent reactive flow in the furnace, is computationally more expensive. Model B does not predict the details of the radiative heat flux distribution on the slabs, but yields rather satisfactory predictions of the average temperatures on the slabs. The difference between the mean volume average temperatures of the slabs leaving the furnace is below 3%. However, in order to achieve this level of agreement between the two models, a good estimation of the average temperature of the gases and walls is needed, and this may be difficult to obtain without experimental data or the use of a more detailed model, like model A.

REFERENCES

[1] J.G. Kim, K.Y. Huh, and I.T. Kim, Three-dimensional analysis of the walking-beam-type slab reheating furnace in hot strip mills, *Numerical Heat Transfer, Part A*, 38, 589–609, 2000.

[2] J.G. Kim and K.Y. Huh, Prediction of transient slab temperature distribution in the re-heating furnace of a walking-beam type for rolling of steel slabs, *ISIJ Int.*, 40, 1115-1123, 2000.

[3] S.H. Han, S.W. Baek, and M.Y. Kim, Transient radiative heating characteristics of slabs in a walking beam type reheating furnace, *Int. J. Heat and Mass Transfer*, 52, 1005–1011, 2009.

[4] S.H. Han, D. Chang, and C.Y. Kim, A numerical analysis of slab heating characteristics in a walking beam type reheating furnace, *Int. J. Heat and Mass Transfer*,53, 3855–3861, 2010.

[5] V.K. Singh and P. Talukdar, Comparison of different heat transfer models of a walking beam type reheat furnace, *Int. Communications in Heat and Mass Transfer,* 47, 20–26, 2013.

[6] V.K. Singh, P. Talukdar, and P.J. Coelho, Performance evaluation of two heat transfer models of a walking beam type reheat furnace, accepted for publication in *Heat Transfer Engineering*.

Third International Conference on Computational Methods for Thermal Problems
THERMACOMP2014, June 2-4, 2014, Lake Bled, Slovenia
N. Massarotti, P. Nithiarasu and B. Sarler (Eds.)

COMPUTATIONAL EVALUATION OF DIFFERENT CONSTRUCTION MATERIALS PERFORMANCE IN THERMAL ENERGY STORAGE SYSTEMS

D. Frattini, C. Ferone, F. Colangelo, M. de Pertis, R. Cioffi
Department of Engineering University of Naples 'Parthenope', Centro Direzionale Is. C4 80143 Naples Italy, domenico.frattini@uniparthenope.it, claudio.ferone@uniparthenope.it, francesco.colangelo@uniparthenope.it, marco.depertis@uniparthenope.it, raffaele.cioffi@uniparthenope.it

R. di Maggio
Department of Civil, Environmental and Mechanical Engineering University of Trento, Via Belenzani 12 38122 Trento Italy, rosa.dimaggio@unitn.it

ABSTRACT

This paper is focused on sensible heat thermal energy storage in solid media and its numerical analysis of transient behaviour during charging/discharging phase. The thermal performance of different storage materials has been investigated using the finite element method through modelling a differential element. Its parameters such as: volume, total weight and thermal capacity have been used in the analysis. In this work the thermal behaviour of a cement-graphite composite, a fibre reinforced concrete, an high temperature concrete and a castable ceramic, selected in the literature, has been modelled and simulated in order to provide useful information for development of novel energy storage materials and sensible heat thermal energy storage system design.

Key Words: *Modelling, Storage Materials, Thermal Properties, Thermal Storage.*

1. INTRODUCTION

The overall efficiency of a solar power plant has been recognized to highly increase when a Thermal Energy Storage (TES) system is fully integrated to the plant [1]. To this regard one of the most suitable and economically feasible, among all the TES options, is represented by a Sensible Heat Thermal Energy Storage (SHTES) in solid media [2]. The components of the SHTES module considered in this study are: a tube register heat exchanger, embedded in the storage material, and a thermal insulation jacket adopted to reduce heat loss. Thermal storage cycle is composed essentially by three phases: charge, break (the effective storage phase) and discharge [3]. Storage system response to dynamic conditions and unsteady heat transfer is a critical issue for SHTES and a numerical modelling of transient thermal behaviour of the modules is of fundamental importance for performance evaluation.

2. STORAGE MATERIALS AND SHTES SIMULATION

The evaluation of thermal performance for a differential storage element has been based on the following hypothesis, as suggested in [2,4]: the materials are considered homogeneous and isotropic; for the length L, the variation of temperature in axial direction can be neglected; the steel pipes, due to their very high thermal conductivity, have an ignorable effect on heat transfer to the solid media; the operating temperature range is 350-390°C; thermal properties are assumed to be constant; the charging period lasts 3600 s, the following break period lasts 3600 s, without thermal losses. According to these conditions, the simplified equations considered for the calculation of thermal performance are:

$$\frac{\partial T_{sol}}{\partial t} = \alpha_{sol} \nabla^2 T_{sol} \quad (1)$$

$$Q = \int_{T_i}^{T_f} \rho_{sol} V_{sol} c_{sol} \Delta T(T_{sol}) dT_{sol} \quad (2)$$

$$\alpha_{sol} = \frac{k_{sol}}{\rho_{sol} \cdot c_{sol}} \quad (3)$$

Thermal performance of SHTES module is essentially governed by the density, ρ_{sol}, the specific heat capacity, c_{sol}, and the thermal conductivity, k_{sol}, of the solid media employed. A selection of solid thermal storage materials, available in the literature, has been carried out. The thermal properties of selected materials, retrieved from literature, are reported in Table 1.

Storage Material	ρ_{sol} [kg/m^3]	c_{sol} [J/kg·K]	k_{sol} [W/m·K]	$\alpha_{sol} \cdot 10^7$ [m^2/s]	Ref.
Plain Concrete (PC)	2451	810	1.02	5.14	[5]
Fibre-Reinforced Concrete (FC)	2440	630	1.16	7.55	[5]
High-Temperature Concrete (HT)	2750	916	1.00	3.97	[6]
Castable Ceramic (CC)	3500	866	1.35	4.45	[6]
Graphite Concrete (A4)	2680	950	2.43	9.54	[7]

TABLE 1. Thermal properties and references for selected storage materials

The differential storage element is a square prism with a centered hollow channel, representing the channel for the Heat Transfer Fluid (HTF). The total length L is fixed to 1 m, the inner diameter d_i for the pipe is 0.02 m and, the width of the prism is 0.08 m [4]. The mesh employed is composed by triangular prism elements and is shown in Figure 1.

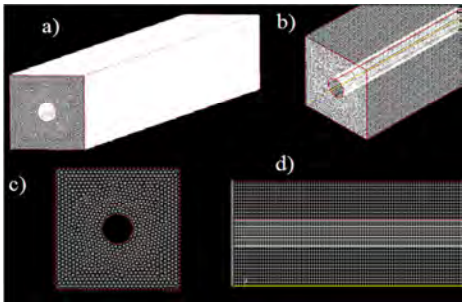

FIGURE 1. Differential storage element with mesh.
a) Overall view; b) Isometric view; c) Frontal view; d) Lateral view

From equation (2), two different approaches have been used for the evaluation of thermal performance: in the first one the volume of the storage element, V_{tot}, is kept constant, in the second approach nominal thermal storage capacity, Q_{nom}, is kept constant. In this case, for each material employed, the width has been adjusted to keep total thermal capacity constant.

3. RESULTS AND DISCUSSION

The calculation of the effective thermal energy stored, Q_{eff}, requires the knowledge of the temperature profile at the wall to obtain the effective temperature difference (ΔT_{eff}) experienced by the storage element because it takes into consideration the non-uniform temperature distribution in the solid media. In fact Q_{nom} is defined as the asymptotic thermal capacity when the temperature is equal to that of hot HTF throughout the solid media. At the beginning of the charging phase, the storage material has been considered at the constant and uniform temperature of 350°C. The

thermal cycle starts with a sudden increase of HTF temperature to 390°C; after 1 h of break, the hot storage material experiences a rapid change of HTF temperature from 390°C to 350°C that represents the initial condition of the discharging phase. The simulation results obtained for the five selected materials for the case of constant V_{tot} are reported in Figure 2a.

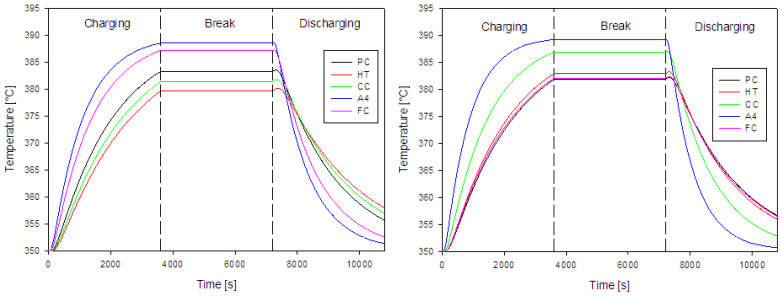

FIGURE 2. Temperature profile at the wall for the differential storage element (a) constant V_{tot}; (b) constant Q_{nom};

In Figure 2a the temperature profiles showed are ordered for increasing thermal diffusivity, α_{sol} reported in Table 1, of the storage material, which is the governing thermal property in unsteady heat transfer phenomena. Simulation results are summarized in Table 2.

Material	Storage weight m_{tot} [kg]	Eff. temp. diff. ΔT_{eff} [°C]	Storage vol. V_{tot} [dm^3]	Eff. storage cap. Q_{eff} [kWh_{th}]	Nom. storage cap. Q_{nom} [kWh_{th}]
PC	14.92	33.32	6.40	0.112	0.134
HT	16.74	29.69	6.40	0.126	0.170
CC	21.30	31.39	6.40	0.161	0.205
A4	16.31	38.56	6.40	0.166	0.172
FC	14.85	37.23	6.40	0.097	0.104

TABLE 2. Simulation results at constant V_{tot} for selected materials

At constant V_{tot}, CC has the higher weight, while PC and FC present the lower weight due to their density. Q_{eff} and Q_{nom} are influenced by the value of specific heat capacity and even if FC was characterized by a limited c_{sol}, its thermal properties, combined and resumed in α_{sol}, for the given geometry and thermal cycle, seem to offer remarkable dynamic performance, comparable with the best benchmark, the A4 graphite concrete. In fact, A4 concrete resulted to have the best profile in this case and a significant storage capacity, very close to the nominal capacity value. On the other hand, to obtain similar performances from remaining materials, the only way is to accept extended charging time or changing module geometry.

For the case of constant Q_{nom}, temperature profiles obtained from simulations are shown in Figure 2b, while Table 3 summarizes the thermal performance results obtained for this analysis. The temperature profile showed in Figure 2b are ordered for increasing Q_{eff} and from Table 3 it can be seen that it is also related to the value of ΔT_{eff}, as envisaged from equation (2). The performance evaluation at constant Q_{nom} revealed that A4 concrete resulted to have the best profile even in this case, CC performed very well, if compared to previous analysis, while HT slightly improved its thermal behaviour. A terrific decrement in dynamic behaviour, respect to previous results, has been experienced by FC, which showed the worst profile in Figure 2b.

Material	Storage weight m_{tot} [kg]	Eff. temp. diff. ΔT_{eff} [°C]	Storage vol. V_{tot} [dm^3]	Eff. storage cap. Q_{eff} [kWh_{th}]	Nom. storage cap. Q_{nom} [kWh_{th}]
PC	16.11	31.87	6.88	0.116	0.145
HT	14.25	32.96	5.50	0.120	0.145
CC	15.07	36.93	4.62	0.134	0.145
A4	13.74	39.30	5.44	0.142	0.145
FC	20.71	32.13	8.80	0.116	0.145

TABLE 3. Simulation results at constant Q_{nom} for selected materials

These evidences can be explained in the following way: during unsteady simulations Q_{eff}, is not only a function of c_{vol}, but also a function of the average temperature difference ΔT_{eff}, and the latter is also governed by thermal conductivity k_{sol}, so that this combined effect influences the observed behaviour. At last, from Table 3 graphite concrete A4 grants for the lower total weight and so the highest energy density in addition to its excellent transient behaviour in terms of ΔT_{eff} and Q_{eff}.

4. CONCLUSIONS

The adopted numerical model allowed to effectively compare the thermal performance of several solid materials used in a thermal energy storage module. The two employed approaches, based on keeping constant the volume or the nominal thermal capacity of a single storage element, revealed some differences. In fact, in both cases the graphite concrete showed the best performances, but the other tested materials performed very differently. In conclusion, we can say that the adopted model and the obtained results can be very useful in order to properly design a SHTES module.

REFERENCES

[1] M. Medrano, A. Gil, I. Martorell, X. Potau, and L.F. Cabeza, State of the art on high temperature thermal energy storage for power generation. Part 2–Case Studies, *Renewable & Sustainable Energy Reviews*, 14, 56-72, 2010.

[2] D. Laing, C. Bahl, T. Bauer, M. Fiss, N. Breidenbach, and M. Hempel, High-temperature solid-media thermal energy storage for solar thermal power plants, *Proceedings of IEEE*, 100, 516-24, 2012.

[3] A. Gil, M. Medrano, I. Martorell, A. Làzaro, P. Dolado, B. Zalba, and L.F. Cabeza, State of the art on high temperature thermal energy storage for power generation. Part 1–Concepts, materials and modellization, *Renewable & Sustainable Energy Reviews*, 14, 31-55, 2010.

[4] R. Tamme, D. Laing, W.D. Steinmann, Advanced thermal energy storage technology for parabolic trough, *Journal of Solar Energy Engineering*, 126, 794-800, 2004.

[5] O.B. Ozger, F. Girardi, G.M. Giannuzzi, V.A. Salomoni, C.E. Majorana, L. Fambri, N. Baldassino, and R. Di Maggio, Effect of nylon fibres on mechanical and thermal properties of hardened concrete for energy storage systems, *Materials & Design*, 51, 989-97, 2013.

[6] D. Laing, W.D. Steinmann, R. Tamme, and C. Richter, Solid media thermal storage for parabolic trough power plants, *Solar Energy*, 80, 1283-89, 2006

[7] C. Guo, J. Zhu, W. Zhou, W. Chen, Fabrication and thermal properties of a new heat storage concrete material. *Journal of Wuhan University of Technology-Mater. Sci. Ed.,* 25, 628-30, 2010.

Third International Conference on Computational Methods for Thermal Problems
THERMACOMP2014, June 2-4, 2014, Lake Bled, Slovenia
N. Massarotti, P. Nithiarasu and B. Sarler (Eds.)

NUMERICAL SIMULATION OF IMMERSION QUENCHING COOLING PROCESS FOR SIMPLIFIED CYLINDER HEAD STRUCTURE

Kopun R., Kovačič Z.,
AVL-AST d.o.o., Ul. kneza Koclja 22, 2000 Maribor, rok.kopun@avl.com

Škerget L., Hriberšek M.
Faculty of Mechanical engineering, University of Maribor, Smetanova ul.17, 2000 Maribor.

ABSTRACT

In this paper, a recently improved Computational Fluid Dynamics (CFD) methodology for virtual experimental investigation of the heat treatment characteristic for cast aluminium parts is presented. The objective of the current study was to predict the cooling of the simplified cylinder head structure, by using a commercial CFD code AVL FIRE®. The boiling phase change process between the heated part and a sub-cooled liquid domain is handled by using the Eulerian multi-fluid modelling approach with additional interfacial forces and the Leidenfrost temperature prediction, where instead of constant, variable temperature is applied. Numerically predicted temperatures histories at various positions are discussed and compared with the available measured data, where an excellent agreement at different monitoring points was achieved.

Key Words: *Heat Transfer, Immersion quenching, Leidenfrost temperature, FEA stress analysis.*

1. INTRODUCTION

Efficient heat treatment techniques, such as immersion quenching, are introduced in order to replace heavier metals with lower weight alloys, which results in vehicle weight reduction and consequently improved fuel consumption and lower emission values. Immersion quenching cooling process, among all other heat treatment techniques, has been long identified as one of the most useful techniques to prevent component failure and provide even temperature distribution during the cooling process. An accurate prediction and optimization of the thermal treatment process is important in order to achieve low residual stress levels resulting from even temperature distribution during cooling process. In order to achieve the desirable microstructure and mechanical properties of the metal piece, solid is heated to a very high temperature and then immediately submerged into a sub-cooled liquid [1],[2].

The paper outlines the recently improved Eulerian multi-fluid modelling approach implemented within the commercial CFD code AVL FIRE, where the additional interfacial forces and the variable Leidenfrost temperature are used. Simulation results of a simplified cylinder head structure in a real-time quenching process are compared and discussed with the available measurement data. The temperature gradients predicted by the presented model correlate very well with the provided measurement data and represent a reliable spatially resolved temperature input for later Finite Element Analysis (FEA) of thermal stresses.

2. MATHEMATICAL MODEL AND SIMULATION SET UP

Eulerian multi-fluid model considers each phase as interpenetrating continua coexisting in the flow domain, with inter-phase transfer terms accounting for phase interactions where conservation laws apply [3]. Governing equations and multiphase boiling models are well described and can be observed in the work of Srinivasan *et al*. [4]. Many researchers reported that the drag force is the most important force affecting the vapour bubbles [4], although there are some other forces as well.

Ustinenko *et al.* [5] reported that the lift and wall lubrication forces are important in obtaining correct two-phase radial distribution and flow characteristics, therefore those forces were implemented in the commercial CFD code. The wall lubrication force is introduced in order to push the bubbles away from the wall to assure the experimentally found zero void condition near vertical walls [6]. It is described by

$$F_{WL} = \alpha_g \rho_l C_{WL} \left\{ \left(\vec{v}_g - \vec{v}_l \right) - \left[\left(\vec{v}_g - \vec{v}_l \right) \cdot \vec{n}_w \right] \vec{n}_w \right\}^2 \vec{n}_w \tag{1}$$

where $\vec{n}_w$ is the unit wall normal vector (pointing from the wall into the fluid), C_{WL} stands for wall lubrication coefficient and v for velocity vector of a gas or liquid phase. Based on Tomiyama`s work, an extended generalized wall lubrication force model can be observed in the work of Frank *et al.* [6]. When the continuous phase field is non-uniform or rotational, the bubbles experience the lift force perpendicular to the relative velocity. The lift force F_L is derived by:

$$F_L = -\alpha_g \rho_l C_L \left(\vec{v}_g - \vec{v}_l \right) \times \left(\nabla \times \vec{v}_l \right) \tag{2}$$

Tomiyama's lift model is employed to determine the lift coefficient as described in reference [7], where the effect of the aforementioned forces can be obtained from Kopun *et al.* [2].

A new approach for modelling the variable Leidenfrost temperature threshold is presented in this work. As long as the surface temperature is above the Leidenfrost threshold, film boiling regime is applied, while transition boiling occurs, when the surface temperature drops below the Leidenfrost temperature. Thus, the Leidenfrost threshold is a very important parameter for the numerical simulation of the quenching process, since it determines which regime is responsible for the calculation of the heat transfer coefficient. Due to the higher vapour concentration at the top of the quenched piece, transition boiling occurs there at a lower temperature level due to vapour arriving from the bottom areas and accumulating at the top, thereby slowing down heat removal. Linear interpolation of a Leidenfrost temperature is described as:

$$T_{Leid,\max} = T_{Leid,mean} + \frac{\Delta T_{Leid,range}}{z_{\max} - z_{\min}} (z - z_{mean}), \qquad T_{Leid,\min} = T_{Leid,mean} - \frac{\Delta T_{Leid,range}}{z_{\max} - z_{\min}} (z - z_{mean}) \tag{3}$$

where detailed information concerning the variable Leidenfrost temperature treatment is provided by Kopun *et al.* [8].

Fig. 1 left, displays the physical domain and the boundary conditions applied in the CFD simulation. Fixed atmospheric pressure was applied at the outlet boundary (green surface at the top), whereas the inlet section was treated with the velocity boundary condition (black part at the bottom). The dipping velocity was set to a constant value of 0.14 m/s until the final submerging depth has been reached.

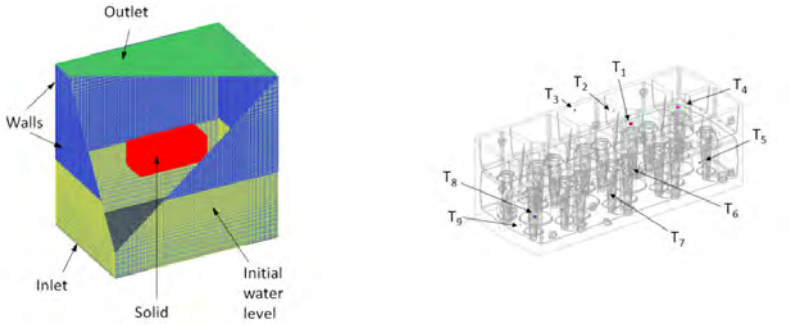

FIGURE 1: Computational domain and detailed positions of the monitoring points.

Temperature measurements were performed at nine different locations along the test piece and are referred to as T_1, T_2, T_3, T_4, T_5, T_6, T_7, T_8 and T_9 respectively (Fig. 1 right).

3. SIMULATION RESULTS

The model capability to predict quench rates was tested on the simplified cylinder head, where the comparison between measured and numerically predicted temperature history immersed inside the water pool temperature of 353K, at three different monitoring locations along the solid piece are presented, see Fig. 2. From all monitoring points it can be seen, that the simulated film and transition boiling regime are well described and that the variable Leidenfrost temperature approximation are in very good agreement with the available measurement data.

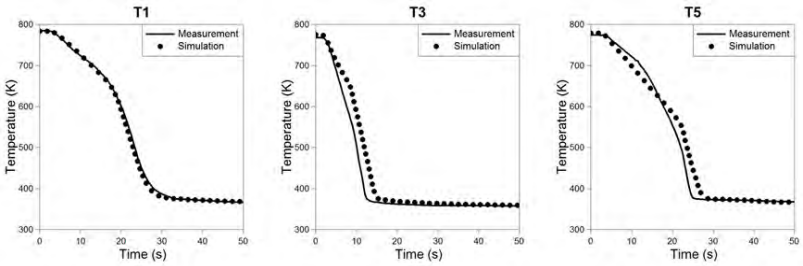

FIGURE 2: Comparison of measured (full line) and numerically predicted (dotted line) solid part temperature quenched with water temperature of 353K at monitoring points T_1 (a), T_3 (b) and T_5 (c).

Fig. 3 shows the liquid volume fraction distribution at different time instants, where the red colour represents 100% water, and blue colour 100% gas. It can be seen in Fig. 3a that after 1 second quenched surface is still not completely submerged and that the liquid phase is still entering the heated surface. Rapid boiling appears between the time of 5 and 20 seconds (see Fig. 3b and 3c), where film boiling is the dominant regime. After 50 seconds, homogeneous temperature is established and no more vapour is produced, as shown in Fig. 3d.

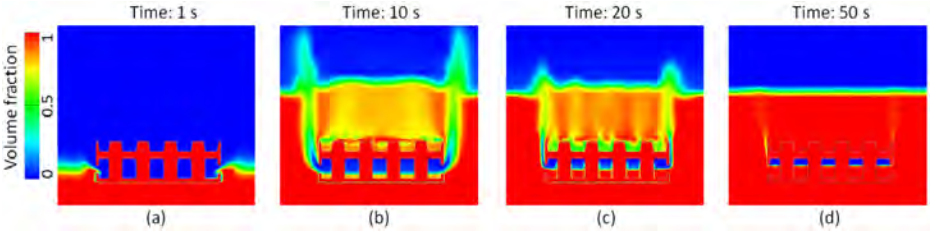

FIGURE 3: Liquid volume fraction distribution at different time steps: (a) 1sec, (b) 10sec, (c) 20sec and (d) 50 sec.

Development of temperature (results of CFD part) and deformations (results of FEA part) during the immersion quenching submerged within the water are presented in Fig. 4. The principal mechanism of deformation development is contraction at the bottom which is immersed first, accompanied by a mostly tensile stress state at warm conditions and ductile response of the material (see Fig. 4b and Fig. 4c). After the time of 20 seconds, tensile reaction begins to turn, because the initially cooled material has to follow the contraction of the still warmer side, see Fig. 4d).

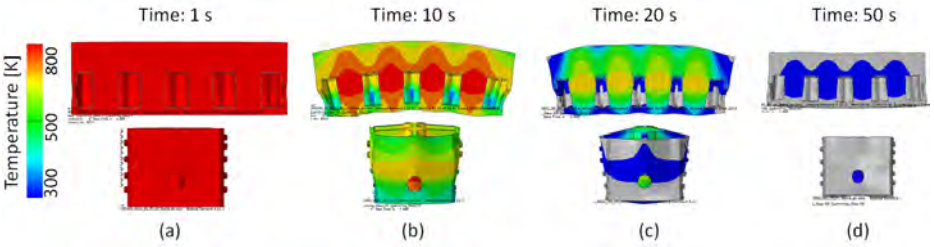

FIGURE 4: Temperature and deformation distribution scale of 50 during the water quenching at different time steps: (a) 1sec, (b) 10sec, (c) 20sec and (d) 50 sec.

4. CONCLUSIONS

The applied CFD code AVL FIRE® with combination of interfacial forced and variable Leidenfrost temperature is capable to predict real time quenching effects for simplified cylinder head structure. Very good agreement between the numerical and available measured data has been achieved, where the variable Leidenfrost temperature approximation has a significant effect on the solid temperature histories. The improved CFD model represents a solid basis for future research in the field of real-time cylinder head immersion quenching application and FEA stress and deformation analysis.

ACKNOWLEDGMENTS

This research work was partly funded by the European Union, European Social Fund and SPIRIT Slovenia, Slovenian Public Agency for Entrepreneurship, Innovation, Development, Investment and Tourism. Parts of the results presented in this paper were obtained within the FFG funded project QUENCH-IT, project number 828697.

REFERENCES

[1] N.A.F. Campbell, S.J. Charlton, L. Wong, Designing towards nucleate boiling in combustion engines*, IMechE* vol. 496/092, pp. 587-595, 1995.

[2] R. Kopun, D. Greif, W. Edelbauer, D. Zhang, R. Tatschl, B. Stauder, Advances in Numerical Investigation of Immersion Quenching at Different Pool Temperatures. *22th International Conference SAE Brasil*, 7-9 Okrober 2013, Sao Paulo, Brasil, pp.369, 2013.

[3] AVL LIST GmbH, FIRE CFD Solver, Eulerian Multi-fluid model. *Solver Theory Guide*. 2013, Graz, Austria.

[4] V. Srinivasan, K. Moon, D. Greif, D.M. Wang, M. Kim, (2010). Numerical simulation of immersion quench cooling process using an Eulerian multi-fluid approach. *Appl. Thermal Eng.*, vol. 30(5): 499-509, 2010.

[5] V. Ustinenko, M. Samigulin, A. Loilev, S. Lo, A. Tentner A, A. Lychagin, A. Razin, V. Girin, Ye. Vanyukov, Validation of CFD-BWR, a new two-phase computational fluid dynamics model for boiling water reactor analysis, *Nucleate Engineering and Design* Vol. 238, (2008), pp. 660-670.

[6] T. Frank, J.M. Shi, A.D. Burns, Validation of Eulerian Multiphase Flow Models for Nuclear Safety Applications, *3rd International Symposium on Two-Phase Flow Modelling and Experimentation*, Pisa, Italy, 2004.

[7] A. Tomiyama, Struggle with computational bubble dynamics, ICMF'98*, 3rd Int.Conf.Mph Flow*, pp. 1-18V, 1998.

[8] R. Kopun, L. Škerget, M. Hriberšek, D. Zhang, B. Stauder, D. Greif, Numerical simulation of immersion quenching process for cast aluminium part at different pool temperatures. *Appl. Thermal Eng*., vol. 65, pp 74-84, 2014.

Third International Conference on Computational Methods for Thermal Problems
THERMACOMP2014, June 2-4, 2014, Lake Bled, Slovenia
N. Massarotti, P. Nithiarasu and B. Sarler (Eds.)

MODELING OF THERMAL ENERGY STORAGE: A REVIEW OF DIFFERENT SYSTEMS

F. Arpino
Dipartimento di Ingegneria Civile e Meccanica, Università degli Studi di Cassino e del Lazio Meridionale, Via G. Di Biasio 43, 03043 Cassino (FR), Italy, f.arpino@unicas.it

N. Massarotti, A. Mauro, R. Muoio, L. Vanoli
Dipartimento di Ingegneria, Università degli Studi di Napoli "Parthenope", Centro Direzionale, Isola C4, Napoli, Italy, massarotti@uniparthenope.it, alessandro.mauro@uniparthenope.it, raffaella.muoio@uniparthenope.it, laura.vanoli@uniparthenope.it

ABSTRACT

In this paper, different types of Thermal Energy Storage (TES) systems are reviewed and discussed, including sensible heat storage, latent heat storage and aquifer thermal storage. Design criteria, materials selection and numerical models employed have been analysed. The TES systems taken into account are: two types of concentric-tube latent heat systems with Phase Change Material (PCM), a latent heat system employing PCM and metal foam, a packed-bed molten salt thermocline system and an aquifer.

Key Words: *Numerical Analysis, PCM, Thermal Properties, Thermal Storage.*

1. INTRODUCTION

The integration of a TES system inside a power plant makes the overall efficiency to increase. This study analyses five different types of TES systems: a) Triple concentric-tube latent heat thermal energy storage (LHTES) system, based on Phase Change Material (PCM); b) Shell-and-tube latent heat storage unit using PCM; c) latent heat system employing PCM and metal foam; d) packed-bed molten salt thermocline sensible heat system; and e) Thermal Energy Storage in an Aquifer (ATES). The systems described above are illustrated in Figure 1. Thermal storage cycle is composed essentially by three phases: charge, break (the effective storage phase) and discharge. The analysis of storage system response to dynamic conditions by numerical modelling of transient thermal behaviour of the specific system assumes a fundamental importance for performance evaluation.

2. DESCRIPTION OF THE DIFFERENT TES SYSTEMS

In sensible TES systems, energy is stored by changing the temperature of the storage material. The amount of heat stored depends on density, specific heat, volume and variation of temperature of the storage material. This kind of storage systems is characterized by large size and temperature swing created from the charge and discharge phase based on sensible heat.

In latent TES systems, during the energy storage process, the thermal medium changes its phase. The latent heat is generally higher than sensible heat for a given substance. Temperature variation during operation is restrained due to phase change occurring at nearly constant temperature. As a consequence, smaller storage volumes are required.

Aquifers are geological formations containing water, offering a potential way of storing heat for long periods of time (seasonal storage). The storage medium in aquifers consists of water saturated gravel rock or sand. This type of storage is well suited for seasonal storage, i.e. transferring heat from the summer to the cooling season, but also for daily operation.

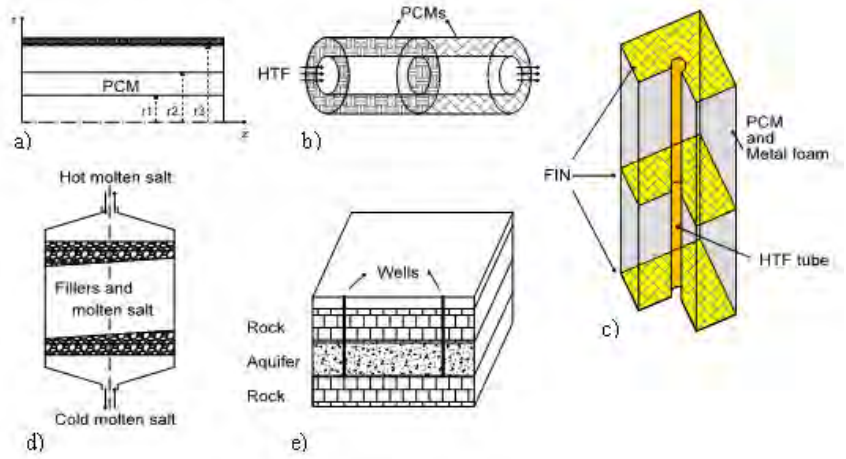

FIGURE 1. TES systems: a) triple concentric-tube with PCM, b) shell-and-tube with PCM, c) PCM and metal foam storage, d) packed-bed and e) aquifer storage

For the storage configuration a), a triple concentric-tube arrangement inside a cylindrical shell with a 200 cm length and a 10 cm diameter is considered. Numerical calculations are carried out by considering RT 52 as PCM (a product by RUBITHERM) and water as Heat Transfer Fluid (HTF). The temperature operating range is below 100 °C [1].

The storage system b) consists of two concentric tubes, with the shell space filled with two PCMs, P116 and n-octadecane, with different melting temperatures (50 °C and 27.7 °C, respectively). The outer tube is insulated. The HTF is water, which flows by forced convection through the inner tube. The temperature operating range is below 100 °C [2].

Figure 1(c) shows the third TES system. Metal foam and PCM (sodium nitrate) composite medium are installed between fins. Water vapor is employed as HTF, flowing through the circular tube. If temperature is below 100°C, the HTF is liquid, otherwise is vapor. The metal foam and fins (both made of copper) are used to overcome the low thermal conductivity limitation of the PCM. Sodium nitrate has an excellent storage capacity in temperature range from 300 °C to 350 °C [3].

The thermocline storage system, Figure 1(d), is composed of a vertically standing cylindrical tank with molten salt (mixture of 60 wt% $NaNO_3$ and 40 wt% KNO_3) and solid fillers. The tank has inlet/exit ports on the top and bottom, to let hot and cold molten salt (quartz rocks and sand) to flow in and out the tank. The temperature varies between 290 °C and 390°C [4].

In Aquifer Thermal Energy Storage (ATES) systems, as shown in Figure 1(e), two or more wells are employed, half of which are for injection and the other half for withdrawal of water. The extracted water goes through a heat exchanger to meet the energy needs of the building. It is then re-injected into the aquifer through the injection well(s). Warm water, during the cold months, and cold water, during the hot months, is withdrawn from the aquifer. The temperature operating range is below 100 °C [5]. The numerical models employed to simulate transient behaviour of different TES system are reported in Table 1, while Table 2 reports the classification of the TES systems in terms of working temperature, kind of storage and possible final use.

[Ref.]	EQUATIONS	
a)-d) [1-4]	Continuity Equation	$\nabla \cdot \mathbf{U} = 0$
a) [1]	Energy Equation for HTF *(Inner and annulus tube)*	$(\rho c_p)_f \frac{\partial T_{f,i}}{\partial t} + (\rho c_p) u_i \frac{\partial T_{f,i}}{\partial z} = k_f \left(\frac{\partial^2 T_{f,i}}{\partial z_i^2}\right) + \frac{4h_i}{D_1}(T_{p,i} - T_{f,i})$ $(\rho c_p)_f \frac{\partial T_{f,a}}{\partial t} + (\rho c_p) u_a \frac{\partial T_{f,a}}{\partial z} = k_f \left(\frac{\partial^2 T_{f,a}}{\partial z^2}\right) + \frac{4h_a D_2}{D_3^2 - D_2^2}(T_{p,a} - T_{f,a})$
	Energy Equation for PCM	$(\rho c_p)_p \frac{\partial T_p}{\partial t} = \frac{1}{r}\frac{\partial}{\partial r}\left(r k_p \frac{\partial T_p}{\partial r}\right) + \frac{\partial}{\partial z}\left(k_p \frac{\partial T_p}{\partial z}\right) - \rho_p \Delta H \frac{\partial f}{\partial t}$
b) [2]	Energy Equation for HTF	$(\rho c_p)_f \frac{\partial \Theta_f}{\partial t} + (\rho c_p) \frac{\dot{m}_f}{\pi R_i^2} \frac{\partial \Theta_f}{\partial x} = \frac{4h_i}{D_1}(T_p - T_f); \qquad \Theta_f = T_f - T_{m2}$
	Energy Equation for PCMs	$(\rho c_p)_p \frac{\partial \Theta}{\partial t} = \frac{1}{r}\frac{\partial}{\partial r}\left(r k_p \frac{\partial \Theta}{\partial r}\right) + \frac{\partial}{\partial z}\left(k_p \frac{\partial \Theta}{\partial z}\right) - \rho_p \Delta H \frac{\partial f}{\partial t}; \qquad \Theta = T_p - T_m$
c) [3]	Momentum Equation	$\frac{1}{Pr}\left(\frac{1}{f}\frac{\partial U}{\partial t^*} + \frac{1}{f^2}(U \cdot \nabla)U\right) = -\nabla P + \frac{1}{f}\nabla^2 U - \left(\frac{1}{Da^2}U + \frac{c_f}{Pr \cdot Da}\lvert U\rvert\right)U + RaT^* \frac{g}{\lvert g\rvert} + SU$
	Energy Equation for PCM	$\sigma \frac{\partial T^*}{\partial t^*} + (U \cdot \nabla)T^* = k^* \nabla^2 T^* - \frac{\varepsilon}{Ste}\frac{\partial f_l}{\partial t^*}; \qquad Ste = \frac{c_{pf}(T_H - T_C)}{\Delta H}$
	Energy Equation for Fin	$\frac{(\rho c_p)_m}{(\rho c_p)_f}\frac{\partial T^*}{\partial t^*} = k^* \nabla^2 T^*_{fin}; \qquad \sigma = \frac{\varepsilon(\rho c_p)_f + (1-\varepsilon)(\rho c_p)_s}{(\rho c_p)_f}$
d) [4]	Momentum Equation *(x,r)*	$\frac{\partial(\rho_l u_x)}{\partial(\varepsilon t)} + \frac{1}{\varepsilon^2}\frac{\partial(\rho_l u_x u_r)}{\partial r} + \frac{1}{\varepsilon^2}\frac{\partial(\rho_l u_x^2)}{\partial x} = -\frac{\partial p}{\partial x} + \mu\left(\frac{1}{r}\frac{\partial}{\partial r}\left(r\frac{\partial u_x}{\partial r}\right) + \frac{\partial^2 u_x}{\partial x^2}\right) + \rho_l g \gamma_i - \frac{\mu u_x}{K} - \frac{C_F \rho}{\sqrt{K}}\lvert u_x\rvert u_x$ $\frac{\partial(\rho_l u_r)}{\partial(\varepsilon t)} + \frac{1}{\varepsilon^2}\frac{\partial(\rho_l u_x u_r)}{\partial x} + \frac{1}{\varepsilon^2}\frac{\partial(\rho_l u_r^2)}{\partial r} = -\frac{\partial p}{\partial r} + \mu\left(\frac{\partial^2 u_r}{\partial x^2} + \frac{1}{r}\frac{\partial}{\partial r}\left(r\frac{\partial u_r}{\partial r}\right) - \frac{u_r}{r^2}\right) + \rho_l g \gamma_i - \frac{\mu u_r}{K} - \frac{C_F \rho}{\sqrt{K}}\lvert u_r\rvert u_r$
	Energy Equation for molten salt and solid fillers	$\frac{\partial}{\partial t}\left(\varepsilon \rho_l c_{p,l} T_l + (1-\varepsilon)\rho_S c_{p,S} T_S\right) + u_x \frac{\partial(\rho_l c_{p,l} T_l)}{\partial x} + u_r \frac{\partial(\rho_l c_{p,l} T_l)}{\partial r} = \Gamma_{l,eff}\left(\frac{\partial^2 T_l}{\partial x^2} + \frac{1}{r}\frac{\partial}{\partial r}\left(r\frac{\partial T_l}{\partial r}\right)\right) + \Gamma_{s,eff}\left(\frac{\partial^2 T_s}{\partial x^2} + \frac{1}{r}\frac{\partial}{\partial r}\left(r\frac{\partial T_S}{\partial r}\right)\right)$
	Energy Equation for insulation layers and tank steel wall	$\frac{\partial(\rho_i c_{p,i} T_i)}{\partial t} = \Gamma_i\left(\frac{\partial^2 T_i}{\partial x^2} + \frac{\partial^2 T_i}{\partial r^2}\right)$
e) [5]	Continuity Equation	$\frac{\partial(\varepsilon \rho_l)}{\partial t} + \frac{\partial(\rho_l u_x)}{\partial x} + \frac{\partial(\rho_l u_y)}{\partial y} + \frac{\partial(\rho_l u_z)}{\partial z} = \frac{S_f}{\partial V}$
	Momentum Equation	$\frac{\partial^2 q}{\partial x^2} + \frac{\partial^2 q}{\partial y^2} + \frac{\partial^2 q}{\partial z^2} = \frac{S_f(x,y,z)}{K \rho \partial V}$
	Energy Equation	$(\rho c_p)_s \frac{\partial T}{\partial t} + (\rho c_p)_f \left[-K_f\left(\frac{\partial q}{\partial x}\frac{\partial T}{\partial x} + \frac{\partial q}{\partial y}\frac{\partial T}{\partial y} + \frac{\partial q}{\partial z}\frac{\partial T}{\partial z}\right)\right] = k\left(\frac{\partial^2 T}{\partial x^2} + \frac{\partial^2 T}{\partial y^2} + \frac{\partial^2 T}{\partial z^2}\right) + S_H$
	Heat transfer in upper/lower rock layers	$\frac{\partial T}{\partial t} = \alpha\left(\frac{\partial^2 T}{\partial x^2} + \frac{\partial^2 T}{\partial y^2} + \frac{\partial^2 T}{\partial z^2}\right)$

TABLE 1. Numerical models of TES systems.

In Table 1, ρ is density, c_P specific heat, h heat transfer coefficient, k thermal conductivity, Γ_{eff} effective thermal conductivity, K permeability of porous material, μ viscosity, α diffusivity, ΔH latent heat, T_m melting temperature, f liquid fraction, f_l liquid fraction in the pore, ε porosity, U is the velocity in the dimensionless form, q the hydraulic head, S is flow the source term and heat source term. The subscripts *f, P, l, S, s* and *m* represent fluid, PCM, liquid, molten salt or cold fluid, solid filler, solid and melting, respectively.

When solving the energy equation for the PCM, the liquid fraction f can be calculated at each time step (k) of the numerical procedure using the relation below, proposed by Voller and reported in [1].

$$f = 0\,; \quad if \quad T_p < T_m \quad in\ the\ solid\ region$$
$$0 < f < 1; \quad if \quad T_p = T_m \quad at\ the\ solid - liquid\ interface$$
$$f = 1; \quad if \quad T_p > T_m \quad in\ the\ liquid\ region$$
$$f_{k+1} = f_k + \frac{a_p h_p}{\rho_p \Delta H}; \quad a_p = 1 + \frac{\alpha_p \Delta t}{r_p \Delta r}; \quad f = \begin{pmatrix} 0, & se & f_{k+1} < 0 \\ 1, & se & f_{k+1} > 1 \end{pmatrix}; \quad h_p = sensible\ enthalpy = \int_{T_m}^{T_p} \rho_p c_p dT$$

Ref.	TES technology	Working temperature [°C]	Possible final use
a) [1]	Latent Heat Storage	50-60	Domestic hot water
b) [2]	Latent Heat Storage	50-60	Domestic hot water
c) [3]	Latent Heat Storage	300-350	Cogeneration, cooling, drying
d) [4]	Sensible Heat Storage	290-390	Cogeneration, cooling, drying
e) [5]	Sensible Heat Storage	50-60	Domestic hot water

TABLE 2. Classification of TES systems.

3. CONCLUSIONS

In the scientific literature, a number of works dealing with experimental and numerical activity of TES systems are available. Many literature models neglect fluid motion or consider fully developed flow, as seen in a) and b) systems. Concerning LHTES systems a), b) and c), a dual equation approach for energy conservation in PCM and HTF is employed. In the energy conservation equation for PCM, an additional term is necessary to consider the latent heat energetic contribution. In c) and d) systems, heat and fluid flow equations for porous medium are considered. On the basis of this overview on numerical modelling of TES systems, the relevance of the subject is evident. However, a comparison of the performance of different systems, employed for a specific final use, should be carried out.

ACKNOWLEDGEMENTS

The authors gratefully acknowledge the financial support of Poligrid “Smart Grid con Sistemi di Poligenerazione Distribuita” and FC Smartgen “Fuel Cell and Smart Hybrid Generation from fossil and renewable sources” projects.

REFERENCES

[1] B. Basal, A. Unal, Numerical evaluation of a triple concentric-tube latent heat thermal energy storage, *Solar Energy*, 92, 196-205, 2013.

[2] H.A. Adine, H. El Qarnia, Numerical analysis of the thermal behaviour of a shell-and-tube heat storage unit using phase change materials, *Applied Mathematical Modelling*, 33, 2132-2144, 2009.

[3] J. Yang, X. Du, L. Yang, Y. Yang, Numerical analysis on the thermal behaviour of high temperature latent heat thermal energy storage system, *Solar Energy*, 98, 543-552, 2013.

[4] C. Xu, Z. Wang, Y. He, X. Li, F. Bai, Sensitivity analysis of the numerical study on the thermal performance of a packed-bed molten salt thermocline thermal storage system, *Applied Energy*, 92, 65-75, 2012.

[5] H. Ghaebi, M.N. Bahadori, M.H. Saidi, Performance analysis and parametric study of thermal energy storage in an aquifer coupled with a heat pump and solar collectors, for a residential complex in Tehran, Iran, *Applied Thermal Engineering*, 62, 156-170, 2014.

Third International Conference on Computational Methods for Thermal Problems
THERMACOMP2014, June 2-4, 2014, Lake Bled, Slovenia
N. Massarotti, P. Nithiarasu, B. Sarler (Eds.)

NUMERICAL SIMULATION AND DESIGN OF EJECTOR FOR SOLAR AIR CONDITIONING SYSTEMS

Prana Fistianduta[(a)], Lih Wu Hourng[(b)]
Department of Mechanical Engineering, National Central University of Taiwan,
[(a)]prana_fistianduta@yahoo.com,[(b)]lwhong@cc.ncu.edu.tw

ABSTRACT

In this paper a generalized ejector for solar air conditioning system was successfully developed by using FLUENT. The primary nozzle geometries parameter was varied as 2.90 mm^2, 2.93 mm^2 and 2.96 mm^2. The best performance was obtained by operating condition P_g = 0.4 MPa, T_g = 100 ^oC, P_e = 0.04 MPa, T_e = 4 ^oC, P_c = 0.06 Mpa, and T_c = 28 ^oC with primary nozzle geometry of 2.90 mm^2.

A 2D axisymmetric, ideal gas model was developed to calculate the flow in the ejector air conditioning system. Predictions at the operating conditions in the ejector air conditioning system were discussed to obtain the ejector performance in the double choking or critical mode condition.

Key Words: *Ejector Design, Numerical Simulation.*

1. INTRODUCTION

A solar cooling / refrigeration system which converts the solar thermal energy into cooling effect has long been an interesting subject for scientists and engineers. Firstly, a solar collector is used to absorb the solar energy and then the heat is used to drive a heat driven cooling machine to produce a cooling effect. The solar cooling system consists solar collector (generator), ejector, condenser / regenerator, and evaporator. The solar collector acts as the generator of the ejector cooling system in which the working fluid is heated and evaporated. The mixing ejector is used here with the separator to recirculate the liquid working fluid through the solar collector to enhance the boiling heat transfer. An ejector is also known as jet, injector or jet pump in different literatures. The main components of an ejector include a primary nozzle (motive nozzle), the suction chamber, the mixing chamber (including a convergent chamber if available and a constant area throat tube which is named as secondary throat) and the diffuser (Figure 1) [1].

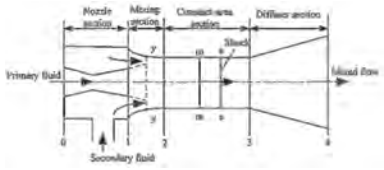

Figure 1 Principle Structure of Ejector [1]

2. EJECTOR AIR CONDITIONING SYSTEMS

Based on Munday and Bagster's theory [2], it is assumed that the primary fluid flows out without mixing with the secondary fluid immediately. It expands and forms a converging duct for the secondary fluid. At a certain cross section along this duct, the speed of the secondary fluid increases to sonic value and chokes, where it was named as "hypothetical throat" (or "fictive throat" or "aerodynamic throat" in some literatures). Then the mixing process begins after secondary flow chokes (double choking, critical mode operation). By the end of the mixing chamber, the two

streams are completely mixed and the static pressure is assumed to remain constant until it reaches the constant area tube section.

3. CFD MODEL

3.1 EJECTOR MODEL

The ejector was modeled as a 2D axisymmetric model in a commercial CFD software package (Ansys Fluent R14.5). Figure 2 shows the configuration of two dimensional axisymmetric quadrilateral grid structure of the ejector (all size in millimeters) with close up mesh elements near the primary nozzle and around it. The entire computational domain is a region ranging from the inlet of the primary nozzle to the end of diffuser, including the nozzle. The size of the computational domain is 242.52 mm in the axial direction, and 26.35 mm in the radial direction. The grid was created based on the structural quadrilateral elements. The total mesh size was 3664 cells number, 7640 faces number, 3977 nodes number to confirm that the results are grid independent. The grid density was concentrated on the areas where significant phenomena were expected.

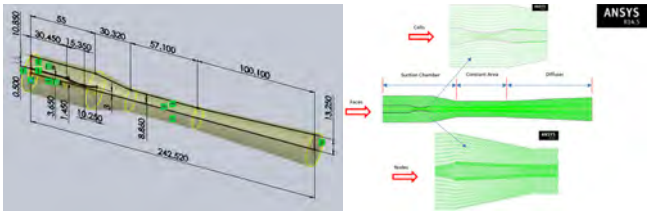

Figure 2 Two Dimensional Axisymmetric Quadrilateral Grid Structure (Overall Length is 242.52 mm and Throat Area is 2.90 mm^2)

3.2 GOVERNING EQUATION

Modeling ejector flow is based on the conservation equations; namely, the continuity, momentum, and energy equation. Because of the nature of flow in the ejector, those equations need to be written in the compressible, steady state, and axisymmetric form. For variable density flows, the Favre averaged Navier Stokes equations are the most suitable. The governing equations refer to the commercial code (Ansys Fluent R14.5) [3]. The compressible, steady state, and axisymmetric form of the fluid flow governing equations are shown below together with ideal gas equation.

Conservation of mass :
$$\frac{\partial \rho}{\partial t} + \frac{\partial}{\partial x_i}(\rho u_i) = 0 \quad (1)$$

Conservation of momentum :
$$\frac{\partial}{\partial t}(\rho u_i) + \frac{\partial}{\partial x_j}(\rho u_i u_j) = -\frac{\partial p}{\partial x_i} + \frac{\partial \tau_{ij}}{\partial x_j} \quad (2)$$

Conservation of Energy :
$$\frac{\partial}{\partial t}(\rho E) + \frac{\partial}{\partial x_i}[u_i(\rho E + p)] = \vec{\nabla} \cdot \left(\alpha_{eff} \frac{\partial T}{\partial x_i}\right) + \vec{\nabla} \cdot [u_i(\tau_{ij})] \quad (3)$$

3.3 FLUID PROPERTIES

Ammonia vapour is used as the working fluid of the model by employing the assumption of an ideal gas. Even though the ideal gas relation seemed to be a unrealistic assumption to the model, for the ejector application where the operating pressure is relatively low, it was proved by some researchers that it provides similar results to a real gas model [4].

3.4 BOUNDARY CONDITIONS

Pressure at primary inlet boundary conditions are 0.4 MPa, 0.5 MPa and 0.6 MPa. Pressure at secondary inlet boundary condition is 0.04 MPa. Temperature at primary inlet boundary conditions

are 80 °C, 90 °C, and 100 °C. Temperature at secondary inlet boundary conditions are 4 °C, 8 °C, and 12 °C. Pressure at outlet boundary conditions are 0.04 MPa, 0.06 MPa, 0.08 MPa, and 0.1 MPa. Temperature at outlet boundary conditions are 28 °C, 32 °C, and 36 °C.

4. RESULTS AND DISCUSSION

4.1 EFFECT OF FLOW PRESSURE

When the nozzle is under expanded, the supersonic flow outgoing from the primary nozzle forms a combination of oblique shocks and expansion waves called "diamond wave" pattern or "shock train" [5]. The direct effect of such phenomenon on the static pressure is the formation of some pressure fluctuations along the centerline which can be observed in Figure 3.

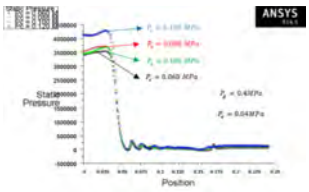

Figure 3 Comparison of Static Pressure Distributions for Various Discharge Pressure; (a) 0.060 MPa, (b) 0.088 MPa, (c) 0.100 MPa, and (d) 0.120 MPa Along The Axial Direction of The Ejector

4.2 EFFECT OF FLOW MACH NUMBER

It is of interest to note that even though the local Mach Number is greater than unity and flow is supersonic, the shock wave has occurred (according to pressure rise location in Figure 4 and the flow after the shock is still remaining supersonic.

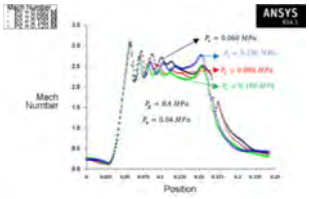

Figure 4 Comparison of Contour Mach Number Distributions for Various Discharge Pressure; (a) 0.060 MPa, (b) 0.088 MPa, (c) 0.100 MPa, and (d) 0.120 MPa Along The Axial Direction of The Ejector

Figure 5 illustrates the Mach contour for various primary inlet pressures at constant secondary inlet pressure and constant discharge pressure of 0.04 MPa and 0.06 MPa, respectively.

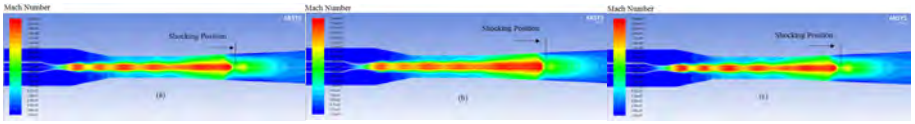

Figure 5 Contour of Mach for Various Primary Inlet Pressure; (a) 0.4 MPa, (b) 0.5 MPa, and (c) 0.6 Mpa

4.3 EFFECT OF CONVERGING DUCT

The simulation is conducted at constant primary and discharge pressure at 0.4 Mpa and 0.06 Mpa, respectively. The secondary pressures are varied at 0.04 Mpa, 0.05 Mpa, and 0.06 Mpa.

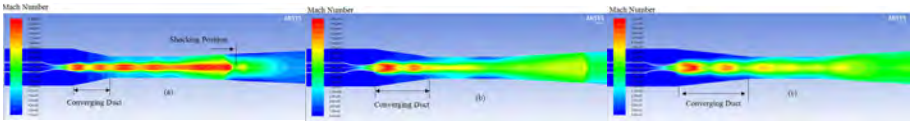

Figure 6 Effect of Converging Duct on The Contour of Mach Number; for Various Secondary Inlet Pressure; (a) 0.04 MPa, (b) 0.05 MPa, and (c) 0.06 MPa

Figure 6 demonstrates the influence of converging duct angle on the Mach number of ejector, respectively. Concerning the flow structure, the models of ejector from the converging duct mixing (constant pressure mixing) ejector are different with each other (Model A, Model B, and Model C).

5. CONCLUSIONS

The effect of various operating pressures on the ejector performance have been investigated. Ejector shapes or geometries, i.e., converging duct angle, are also varied and the ejector performance is simulated. We conclude that the ejector with operating condition P_g = 0.4 Mpa, T_g = 100 ^oC, P_c = 0.06 Mpa, T_c = 28 ^oC, $\dot{m}_p$ = 0.1039, $\dot{m}_s$ = 0.0852 and the converging duct angle at P_e = 0.04 Mpa and T_e = 4 ^oC gives the best performance. However, the ejector does not exceed the critical point or within the double choke flow region ($P_c < P_c^*$). For better performance of an ejector cooling system, the ejector should be designed and operated in the double-choking or critical mode.

REFERENCES

[1] S. He, Y. Li, and R.Z. Wang, Progress of Mathematical Modeling on Ejectors, *Renewable and Sustainable Energy Reviews*, Vol. 13, Issues 8, Pages 1760-1780, October 2009.

[2] J.T. Munday, and D.F. Bagster, A New Theory Applied to Steam Jet Refrigeration, *Ind. Eng. Chem.*, Proc. Res. Dev, Vol. 16, Pages 442-449, 1977.

[3] *Ansys Fluent Theory Guide Release 14.5*, Ansys Inc., October 2012.

[4] T. Sriveerakul, S. Aphornratana, and K. Chunnanond, Performance Prediction of Steam Ejector Using Computational Fluid Dynamics: Part 1. Validation of The CFD Results, *International Journal of Thermal Sciences*, Vol. 46, Pages 812-822, 2007.

[5] K. Matsuo, Y. Miyazato, H.D. Kim, Shock Train and Pseudo Shock Phenomena in Internal Gas Flows, *Prog. Aerosp. Sci.*, Vol. 35, Pages 33-100, 1999.

PARALLEL SESSION

CHEMICAL PROCESSES AND HEAT TRANSFER

Third International Conference on Computational Methods for Thermal Problems
THERMACOMP2014, June 2-4, 2014, Lake Bled, Slovenia
N. Massarotti, P. Nithiarasu and B. Sarler (Eds.)

MODULATION OF SOOT RESIDENCE TIME IN A FLAME SYSTEM

Stefano di Stasio(*), Maddalena Auriemma
Istituto Motori CNR, Nanostructures and X-ray Lab, via Marconi 8, 80125 Napoli, Italy

ABSTRACT

The aim of this communication is to show how a very simple stagnation plate positioned transversally to the of an air-ethylene premixed flame ([C]/[O]=1.38) does introduce significant changes in both flame temperature, soot 2D distribution and, moreover, does produces a dramatic increase of the soot particle residence time **about a factor 6-8** with respect to the identical flame without the stagnation plate. This has crucial effect of the possibility to modulate the permanence time of the carbon particle in the high-reactive flow according to the design of the burner system.

Key Words: *Ethylene-air Flame, Porous Plug, Stagnation Plate, residence time, FLUENT.*

1. INTRODUCTION

Stable flames can be regarded as attractive reactor for synthesis of nanostructured materials owing to the facts that they realize remarkably high temperature conditions, are free from ambient contamination and simple to implement and their spatial confinement is relatively easy to localize with infrared detectors. In a flames study by Small-Angle and Wide-Angle synchrotron X-ray scattering previously reported [1] we referred to a system composed by a porous plug ethylene-air flame with a stagnation plate. In this paper, we decided to use FLUENT to simulate a system identical to the one used in the experiments [1]in order to try retrieving the physical reasons of those SAXS results.

2. SIMULATIONS AND EXPERIMENTS

The combustion system described elsewhere [1] and here studied by numerical simulations by FLUENT 14.0 code and PDF technique, is composed by premixed ethylene-air flame obtained with a porous frit 20 mm dia burner in which a total flux ethylene-air of 250 cm^3/min is supplied plus a stagnation plate positioned horizontally above the burner at a certain distance (12.5 mm in our examplary case). The working model used in this work is obtained by coupling a reduced kinetic mechanism with the fluid dynamics solver available in commercial ANSYS Fluent 14.0. Boundary conditions include the cold-gas inlet velocity and temperature (300 K) at the burner mouth (burner inner diameter 20 mm) and ambient air at atmospheric pressure around the flame. Soot mass concentration (kg m^{-3}) is evaluated according to the Moss-Brookes equations [3]. The convergence is tracked within 8 significant digits accuracy. A reduced kinetic mechanism of 19-Species for C2H4 Oxidationis implemented as available at web site of Princeton University [4]. The PDF model [5], is implemented for soot evaluation through a hybrid mesh–particle technique with a finite difference flow solver, plus Lagrangian particle numerical methods. PDF methods allows to implement finite-rate chemistry and the turbulence-chemistry interactions without any a-priori assumption, according to a *bluff-body* stabilized premixed turbulent flame scheme (settings reported in Appendix). With concern to experiments we refer here to the SAXS results previously published [1]. Burner inner diameter in the SAXS experiments was 2 cm. Ethylene gas was supplied as the fuel at a flow rate 250 cm^3/s. The experimental system was identical to the system

(*) Corresponding Author: stefano.distasio1600@gmail.com

burner-plate used here in the FLUENT simulations. The analysis of the scattering data returns the presence of three particle size modes said *sub-primary*, *primary* and nanoparticle *aggregates* referring to a *hierarchical aggregation* scheme, in which the constituting bricks of the larger particles are, in turns, constituted by smaller sub-units, as previously found out by di Stasio in the pioneering papers [2,6] by TEM and SAXS.

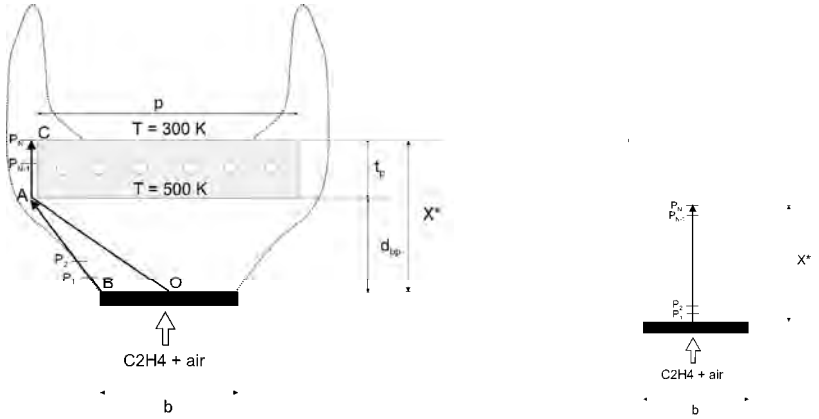

FIGURE 1. Left: Premixed ethylene air flame ([C]/[O]) burning without (right) and with (left) the stagnation plate. For the latter we refer to the experimental flame system by Ossler et al. (2013), Fig.1 therein reported. The boundary conditions at the cooled plate lower surface and burner exit are 300 K and 690 K, respectively. Geometrical parameters: b=20 mm; p=36 mm; d_{bp}=12.5 mm; t_p=10 mm; X*=22.5 mm.

3. RESIDENCE TIMES EVALUATION AND FLUENT SIMULATION RESULTS

The evaluation of the soot residence time is the focus in this paper. Residence time is defined as the time spent by a new born carbon nanoparticles by travelling inside the flame. This task in general case consists in two subtasks, the first is the finding out of the particle trajectory and the second the evaluation of the transit time. In the case of free flame (see Fig. 1 right) this evaluation is significantly simpler with respect to the case of flame coupled with stagnation plate (Figure 1 left). In fact, the path in the flame is basically vertical as the local component of radial velocity is a few percent of the axial component. Thus, the domain inside the flame can be represented by N slices ("pie" of variable diameter) with thickness Δx_i (i=1, 2,…, N) with $\sum_{i=1}^{N} \Delta x_i = X^*$. The position of the particle at the slice j is given by the velocity and position at the slice j-1 by recursive equation $\mathbf{P}_j = \mathbf{P}_{j-1} + \Delta\mathbf{x}_j$, j = 1, 2, …, N, where $\Delta\mathbf{x}_j = \Delta t_{j-1} \cdot \mathbf{v}_{x,j-1} + \mathbf{x}_{j-1}$, $\mathbf{v}_{x,0} = v_{cold-gas}\,\hat{\mathbf{x}}$ and $\Delta t_0 = \Delta_{grid} / v_{x,0}$. The velocity $v_{cold\text{-}gas}$ is evaluated by the total flux at **x**=0, that is 4.1667 cm^3 s^{-1}, and $v_{cold\text{-}gas}$ = 1.326 cm s^{-1}. We can write: $\Delta t_j = \Delta x_j / v_j$ with $v_j^2 = v_{x,j}^2 + v_{y,j}^2$. The total transit time, namely the residence time, will be $\tau_f = \sum_{j=1}^{N} \Delta t_{j,f}$ where the deponent "*f*" indicates the free flame. In the case of flame coupled with the stagnation plate, we must evaluate first the trajectory, which can be done with the recursive equations $\mathbf{P}_j = \mathbf{P}_{j-1} + \Delta\mathbf{x}_j + \Delta\mathbf{y}_j$, where $\Delta\mathbf{x}_j = \Delta t_{j-1} \cdot \mathbf{v}_{x,j-1} + \mathbf{x}_{j-1}$ and $\Delta\mathbf{y}_j = \Delta t_{j-1} \cdot \mathbf{v}_{y,j-1} + \mathbf{y}_{j-1}$. This procedure will allow to find out the positions $\mathbf{P}_1$, $\mathbf{P}_2$, …, $\mathbf{P}_N$ of the generic particle which follows the fluid flow. Thus, the particles that nucleate in the proximity of flame axis (along the path OA, Fig.1 left) will probably impact under the plate being accelerated by the thermophoresis force, but, vice versa, the particles which nucleate at a position more off axis

(along the path BA, Fig. 1 left) will escape the impact onto the plate and will floe aside the plate upwards (BA-AC). For these particles the partial residence times spent by crossing the slice j will be $\Delta t_j = \Delta t_{j-1}\ T(P_{j-1}) / T(P_j)$ or $\Delta s_j / v_j$ where s_j is the curvilinear abscissa along the trajectory (x_j, y_j), with the initial transit time given by the same equation above $\Delta t_0 = \Delta_{grid} / v_{x,0}$. We consider as reference height in both the configurations $X^* = d_{bp} + t$ that is, in the considered example, $X^* = 22.5$ mm. The total transit time is the residence time $\tau_p = \sum_{j=1}^{N^*} \Delta t_{j,p}$ where "p" is plate and N* is the number of steps considered along the trajectory BA-AC up to $X^* = 22.5$ mm (see Figure 1 right).
Figure 2 shows the temperature and the soot weight concentration (kg m^{-3}) distributions obtained for the free flame (without any plate). The reference length scale is the inner burner wall distance, 2.0 cm in the experimental arrangement.

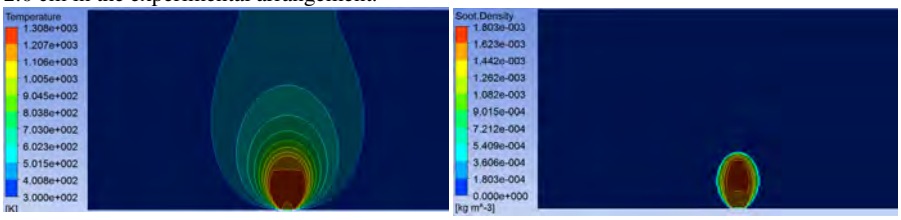

FIGURE 2. Free flame arrangement. Left: temperature distribution; right: soot distribution. Ethylene-air premixed flame with total flux 250 cm^3/min, cold gas velocity 1.33 cm/s, [C]/[O]=1.38. Scale length is the inner diameter of the burner (20 mm).

The vertical dimension of the Figure 2 left is about 41 cm. The limits of format here prevent us from a detailed discussion. However, we observe that the flame apparent length (evaluated considering the heigths where temperature is above 1000 K (pseudo-colors green turning to yellow), is about 14 cm. Moreover, the maximum flame temperature is about 1300 K and the hottest zone is relative to heights 1.7 to 8.6 cm. Concerning the soot, Figure 2 right reveals that maximum soot weight density (1.8 g/m^3) is on the axis at heights 4.0 to 9.0 cm and decrease down to about 0.4 g/m^3 at 10.5 cm height on flame axis and soot starts to nucleate preferentially off axis near the border of the flame, where soot concentration is maximum already at about 2.7 cm height. The results of simulation for the combustion system composed by flame burner and plate positioned at height 12.5 mm are shown in Figure 3. The temperature is quenched to lower values both below and above the plate boundary owing to cooling inside it with flowing cold water at 300K. This has two major effects. On one side, it enforces the thermophoretic deposition onto a circular annular region near the plate border, as effectively observed in the experiments. On the other side, the temperature decreasing does act as a brake on the motion of particles which are escaping from below to outside the confinement. A decreasing of temperature from about 1100 (red pseudo-color) to 870 (green) and to 540 K (light blue) yields a total overall reduction of temperature of a factor 2, i.e., at parity of length travelled by the generical soot particles, τ_p increases a factor 2. However, the path as evaluated in the free flame configuration at distance burner-plate X=12.5 mm is about a factor $\sqrt{2}$ shorter with respect to the path in the flame burner plus stagnation plate, i.e., at parity of temperature, τ_p should be 1.5 times larger for the flame with plate vs. the free flame τ_f. Last and more important, the flame distribution at heights below 12.5 mm, is *not the same* with respect to the free flame, owing to the fact that the plate is considered to be cooled by water and the boundary condition imposed at its upper surface is 300 K. This yield a further increasing of τ_p under the plate of a factor about 2. In total, the residence time τ_p of particle which escape the plate is expected about a factor $F_\tau = 2 \times 1.5 \times 2 = 6$ longer with respect to $\tau_f = 604$ ms=0.604 s (as evaluated through the computational scheme described above in Figure 1 left). A home made algorithm designed to evaluate the residence time accounting for the exact values output from Fluent simulation returned a prediction for the increase of the residence time about 8 as evaluated for the trajectory BA-A'C' (see Figure 1).

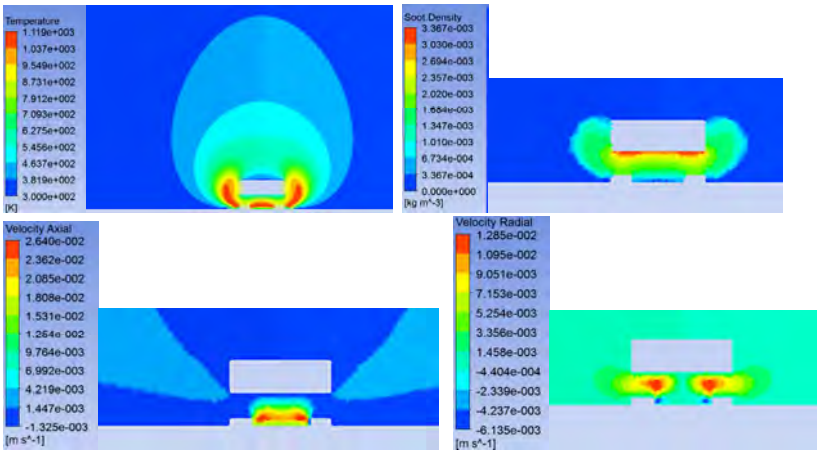

FIGURE 3. Premixed flame plus stagnation plate arrangement (Figure 1 right). Top) left: temperature; right: soot weight concentration. Bottom) left: velocity component along the axial coordinate x, coincident with the burner axis; right: velocity component along the radial coordinate y. Scale lengths are the inner diameter of the burner (20 mm) and the distance burner-plate d_{bp} = 12.5 mm.

In conclusion, at the hight X*=22.5 mm and radial coordinate Y=19 mm, the soot escaping from the region in between burner and plate, has experienced a residence time $\tau_p \approx 5$ s that is a factor between 6 to 8 times longer (depending on the particular particle trajectory off flame axis below the plate) with respect to the soot observed at the height X*=22.5 mm and radial coordinate Y=0 in the configuration of the free flame (without plate) at parity of burner geometry and ethylene-air flow. Further detailed results and the crucial consequences of this result will be given in the mother paper.

APPENDIX. FLUENT SETTINGS

Domain axisymmetric. Solver Pressure-based, time steady. Computational domain: 25840 cells and 26197 nodes. Error tolerance ISAT . Turbulence model Standard k–E with Cμ = 0.09, Ce1 = 1.6, Ce2 = 1.92, rk = 1.0, re = 1.3, energy Prandtl number 0.85, turbulent Schmidt number 0.7. Mixing model = PDF Transport Lagrangian solves the composition PDF transport equation by stochastically tracking Lagrangian particles through the domain with EMTS (*Euclidean Minimum Spanning Tree Mixing model.* Thermodynamic Database for pdf mixture 19-Species. Reduced Kinetics Mechanism for C2H4. Wall treatment Low Reynolds number model. Discretization schemes Standard for pressure. SIMPLE for pressure–velocity coupling; second order upwind for all the quantities. Material Incompressible ideal gas. Mixing law for Cp. Mass weighted mixing law for thermal conductivity and viscosity; kinetic theory for mass diffusivities. Axial velocity 13.82 cm/s with turbulent intensity 10% and a hydraulic diameter of 1.1c m.

REFERENCES

[1] F. Ossler, Linda Vallenhag, Sophie E. Canton, J. B. A. Mitchell, J-L Le Garrec, M. Sztuck, S. di Stasio, Dynamics of incipient carbon particle formation in a stabilized ethylene flame by in situ extended-small-angle and wide-angle X-ray scattering, Carbon 51, 1-19, 2013

[2] S. di Stasio, et al, Synchrotron SAXS (in situ) identification of three different size modes for soot nanoparticles in a diffusion flame, *Carbon* 44, 1267-1279, 2006

[3] S J Brookes, JB Moss, Predictions of soot and thermal radiation properties in confined turbulent jet diffusion flames. *Combustion and Flame* 116, 486, 1999

[4] http://lcg.princeton.edu/research/chemical-kinetic-mechanisms/19-species-reduced-mechanism-for-c2h4-oxidation.aspx

[5] http://aerojet.engr.ucdavis.edu/fluenthelp/html/ug/node722.htm

[6] S di Stasio, Electron microscopy evidence of aggregation under three different size scales for soot nanoparticles in flame, *Carbon* 39, 109-118, 2001

Third International Conference on Computational Methods for Thermal Problems
THERMACOMP2014, June 2-4, 2014, Lake Bled, Slovenia
N. Massarotti, P. Nithiarasu and B. Sarler (Eds.)

Multiphase numerical model of spray drying of zeolite-water suspension

Gregor Sagadin
Silkem, d.o.o., Tovarniška cesta 10, 2325 Kidričevo; gregor.sagadin@silkem.si
Matjaž Hriberšek
University of Maribor, Faculty of mechanical engineering, Smetanova ulica 17, 2000 Maribor; matjaz.hribersek@um.si
Leopold Škerget
University of Maribor, Faculty of mechanical engineering, Smetanova ulica 17, 2000 Maribor; leopold.skerget@um.si

ABSTRACT

The contribution deals with advanced numerical model of spray drying of zeolite 4A suspension. The model is based on upgrading the classical one-stage spray drying model to a two-stage drying model, suitable for the implementation in a multiphase Lagrange-Euler CFD code. The model considers the bounded moisture, which in the drying process diffuses through the dried outer core of the particle and is governed by the Stefan diffusion model. The results obtained from the numerical model are compared with experimental results, obtained from the test dryer, and confirm the applicability and physical correctness of the proposed model.

Key Words: *Heat and Mass Transfer, Spray drying, CFD, Multiphase flow, Particle Transport*

1. INTRODUCTION

Spray drying is the process where a transformation of slurry droplets, obtained by using a nozzle or rotary atomizers, into dried particles takes place. The process is characterised by large energy demands, arising mainly from evaporation of the liquid phase in the slurry droplet. Although the process of spray drying is becoming reliable, additional research has to be invested in lowering its energy demands. During the last decade, the drying efficiency was intensively studied by means of computational fluid dynamics (CFD), as it allows evaluation of drying gas conditions and particulate phase conditions within the drying chamber, especially in the case of the Lagrange-Euler multiphase CFD models [3]. One of the main challenges with this technique is that spray drying models do not considered specific material properties, as well as a fact that particle moisture is considered as a surface moisture only (single stage drying), and particle porosity and its influence on drying characteristics is neglected. Since drying of zeolite suspensions, consisting of micro porous crystalline solids with well-defined structure, is influenced by porosity of half dried droplets as well as porosity of the zeolite, it is necessary to upgrade the established drying models with second stage drying model, taking into account the specific properties of zeolite material.

2. HEAT AND MASS TRANSFER IN DRYING OF ZEOLITE SUSPENSIONS

The zeolite 4A suspension contains water as the solvent, which means that the adsorption characteristics of zeolite-water system also play an important role in the drying kinetics of particles. Dependence of particle moisture fraction or water contents vs. temperature can be determined by a thermo gravimetric analysis, which is for the case of zeolite 4A show in the Fig. 1.

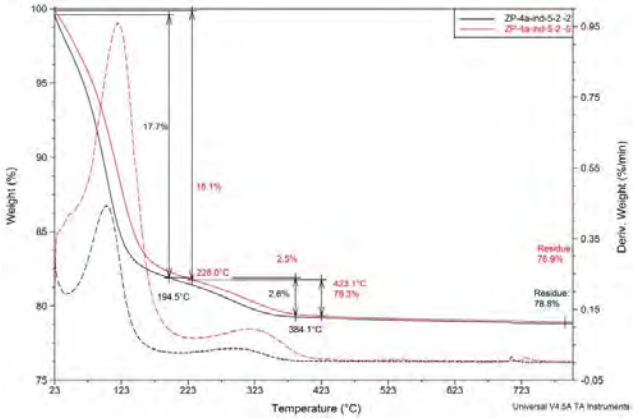

FIGURE 1. Thermo gravimetric analysis of zeolite 4A [4].

The drying starts when the partial pressure of water vapour at the surface of the particle is larger than the partial water vapour pressure in the surrounding gas. The first drying stage is characterised by the evaporation process at the outer diameter of the particle, which is considered spherical. Mass flow of evaporated water from the surface of radius R_d by convection is

$$\dot{m}_v = h_D\left(\rho_{v,s} - \rho_{v,\infty}\right)4\pi(R_d)^2 \qquad 2.1$$

The difference in partial densities of water vapor on the surface and in the surroundings depends on temperature of the droplet, and the heat and mass transfer coefficients are determined from the Ranz-Marshall correlation for a sphere:

$$Nu_d = \left(2 + 0{,}6Re_d^{1/2}Pr^{1/3}\right)(1+B)^{-0{,}7} \qquad 2.2$$
$$Sh_d = \left(2 + 0{,}6Re_d^{1/2}Sc^{1/3}\right)(1+B)^{-0{,}7}$$

Considering also the influence of heat radiation by applying the radiation heat transfer coefficient, $h=h_d + h_R$, the energy conservation for the droplet reads as

$$c_{p,d}m_d\frac{dT_d}{dt} = h\left(T_g - T_d\right)4\pi R_d^2 - h_{fg}\dot{m}_v \qquad 2.3$$

Evaporation of water results in the decrease of the particle radius,

$$\frac{dR_d}{dt} = -\frac{1}{\rho_{d,w}4\pi(R_d)^2}\dot{m}_v \qquad 2.4$$

At the end of the each time step the remaining particle moisture is calculated. If the moisture is higher than critical particle moisture, the calculation returns to the start of first drying stage. In the second drying stage the drying front (interface) is moved inside the particle, and simple evaporation model 2.1 is no longer valid. The diffusion of water vapor through the pores from the interface of the wet core to the outer surface of dry crust is now the main resistance to drying [1,2]. By considering that the diffusion process is governing the mass transfer inside the porous crust the Stefan model for one sided diffusion is applied:

$$\dot{m}_v = -\frac{8\pi\varepsilon^{\beta} D_{v,cr} M_w p_g}{\kappa\left(T_{cr,s} + T_{wc,s}\right)} \frac{R_p R_i}{R_p - R_i} * \ln\left[\frac{p_g - p_{v,i}}{p_g - \left(\frac{\kappa}{4\pi M_w h_d R_p^2}\dot{m}_v + \frac{p_{v,\infty}}{T_g}\right) T_{p,s}}\right] \quad 2.5$$

In the model ε is the porosity of the dry crust, consisting of a system of zeolite particles. The p_g, $p_{v,i}$ and $p_{v,\infty}$ are partial water vapor pressures at the interface of wet core, dry crust, and in the surrounding air, respectively. The water vapor saturation is calculated with the Antoine model, where A,B and C are component specific constants (for water from 0 to 100°C is A=8.07, B=1730.6 and C=233.43). Calculation of mass flux of evaporated water is iterative. When convergence criteria (relative error of 1e-6) is achieved calculation continues with determination of the new interface radius of the wet core based on the modified mass conservation equation,

$$\frac{dR_i}{dt} = -\frac{1}{\varepsilon\rho_{d,w} 4\pi (R_d)^2}\dot{m}_v \quad 2.6$$

In this stage the outer diameter of the particle remains constant, but the radius of the interface is decreasing. The conservation of energy in the second drying stage is calculated separately for the dry crust region,

$$\rho_{wc} C_{p,wc} \frac{\partial T_{wc}}{\partial t} = \frac{1}{r^2}\frac{\partial}{\partial r}\left(k_{wc} r^2 \frac{\partial T_{wc}}{\partial r}\right), 0 \le r \le R_i(t) \quad 2.7$$

and for the wet core,

$$\frac{\partial T_{cr}}{\partial t} = \frac{\alpha_{cr}}{r^2}\frac{\partial}{\partial r}\left(r^2 \frac{\partial T_{cr}}{\partial r}\right), R_i(t) \le r \le R_p \quad 2.8$$

Both equations are linked by the following boundary and initial conditions:

$$\begin{aligned} \frac{\partial T_{wc}}{\partial r} &= 0, \qquad r = 0; \\ T_{wc} &= T_{cr}, \qquad r = R_i(t); \\ k_{cr}\frac{\partial T_{cr}}{\partial r} &= k_{wc}\frac{\partial T_{wc}}{\partial r} + h_{fg}\frac{\dot{m}_v}{A_i}, \qquad r = R_i(t); \\ h\left(T_g - T_{cr}\right) &= k_{cr}\frac{\partial T_{cr}}{\partial r}, \qquad r = R_p; \end{aligned} \quad 2.9$$

3. RESULTS

The developed numerical model was solved by applying the Finite Difference Method. The drying gas was hot air with temperature 300°C and initial absolute humidity of 8 g/kg water. Since only one particle was considered in the calculation, the applied mass flow of air was 4.2 e-5 kg for a single particle. The suspension droplets were formed by a spray nozzle, and had initial temperature of 45°C, absolute humidity of 1.4 and initial diameter of the particle of 0.5 mm. A transition region encompassing 10% of the interface radius was used to account for the non-spherical shape of the interphase, and mixing rule was applied for evaluation of parameters in calculating the moisture evaporation. As is seen in Fig. 2, the duration of first drying phase was about 2.5s. Intensity of

evaporation in the second drying stage decreases, because of additional resistance in diffusivity of water vapor through the pores. The energy equation in the dry crust and the wet core was discretized with 9 mesh points in the particle (numbered 0-3 in the dry crust, 4 at the interface and 4-8 in the wet core), so one can also see the time history of the temperature distribution in the interior of the particle, Fig. 2 right. The results were qualitatively compared with experimental data, available from the laboratory spray dryer Anhydro LAB S1. A good agreement was observed, where comparing residence time with computed drying time and measured outlet moisture contents of dried particles, with computed values. However a more detailed experimental analysis is needed in order to optimize model parameters.

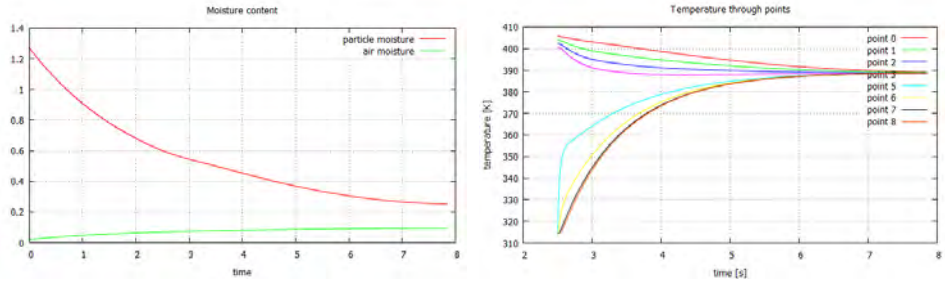

FIGURE 2. Left: Particle and air moisture contents. Right: Temperature at mesh points in the second drying phase.

4. CONCLUSIONS

Spray drying of zeolite 4A-water suspension was studied by a numerical model. The developed two-stage spray drying numerical model takes into account the additional heat and mass transfer resistance, when the drying front is moved inside a particle. As the porous inner structure of the dried particle determines the heat and mass transfer conditions, its inclusion into the numerical model allows to compute a more realistic drying kinetics. In order to further improve the model, equilibrium characteristics of zeolite should be included in the form of the third drying stage, which is the scope of the current research.

REFERENCES

[1] David Levi-Hevroni, Avi Levy, Irene Borde; *Mathematical modelling of drying of liquid/solid slurries in steady state one-dimensional flow*, Drying technology, 13 (5-7): 1187-1201,1995.

[2] M. Mezhericher, A. Levy, I. Borde; *Theoretical Drying model of single droplet containing insoluble or dissolved solids*, Drying technology, 25: 1035-1042, 2007.

[3] D.J.E. Harvie, D.F. Fletcher, T.A.G. Langrish: *A computational fluid dynamics study of a tall-form spray dryer*. Trans IChemE, Vol 80, Part C, September 2002, 163-175.

[4] National institute of Chemistry, Thermo gravimetric analysis, Ljubljana, 2014.

Third International Conference on Computational Methods for Thermal Problems
THERMACOMP2014, June 2-4, 2014, Lake Bled, Slovenia
N. Massarotti, P. Nithiarasu and B. Sarler (Eds.)

A NEW APPROACH TO MODELLING HEAT TRANSFER IN A FIXED BED BY COUPLING CHARACTERISTIC PACKING INFORMATION FROM DEM TO CFD

Nan Zhang, Xiaoxing Liu, Cun Zhang, Guangwen Xu
State Key Laboratory of Multiphase Complex System, Institute of Process Engineering, Chinese Academy of Sciences, Beijing, China, 100190, nzhang@home.ipe.ac.cn

ABSTRACT

A DEM-CFD coupled approach were proposed to joint the advantage of discrete models of providing detailed packing information and continuous models of realizing macro-scale simulations. DEM simulation of particle packing in a small-scale fixed bed was first validated, then the model was used on particle packing in a lab-scale fixed bed with internals, statistics voidage distribution was obtained and coupled with Eulerian Granular Multiphase Model, realized the maro-scale simulation of fixed beds of considering the meso-scale packing structure .

Key Words: *Heat Transfer, CFD, DEM, Fixed Bed.*

1. INTRODUCTION

Although fixed beds (FB) have found wide applications in coal gasification, coal pyrolysis, residue hydrodesulphurization, steam-methane reforming, biomass gasification and drying, detailed understanding of their complex hydrodynamic behaviour, heat transfer and reactions are still lacking, thus making the design and scale-up difficult. With the development of computational fluid dynamics (CFD), numerical simulations on FB can provide certain understanding not easily obtained through experiment. Currently most of the models at the macro scale are based on simplifying assumptions, such as uniform voidage, pseudo-homogeneous phases, effective heat transfer parameters, thus ignoring the important meso-scale packing heterogeneity effect on flow, heat transfer and reactions. While with the development of discrete models, simulations done at the meso-scale are developing rapidly, but they are still far from simulations on industrial reactors, because of a large number of particles in the reactor.

A new approach is proposed to modelling heat transfer in a fixed bed by coupling discrete models of providing detailed packing information to continuous models of realizing simulations on the reactor scale. The strategy for this approach is illustrated in Figure 1. First, the DEM model is validated by comparing packing characteristics with experiment data, good agreement were achieved and the relative error were less than 5%, then simulations of particle packing in a lab-scale fixed bed are done, and voidage distribution are analysed and statistics information were obtained, at last the characteristic voidage information is coupled with continuous models, and the maro-scale simulations considering the meso-scale packing structure are realized.

This is the first step we tried to couple discrete models to continuous models on fixed beds modelling, right now only characteristics voidage are coupled, the work of coupling other important transfer parameters to continuous models are still on-going. The preliminary work done provides an integrated study over FB and shows a fresh possibility to design and scale-up FB better optimized.

2. MODEL DESCRIPTION

Dynamic particle packing can be simulated by conventional discrete element method (DEM) or molecular dynamics (MD) methods, here we tried a new digital approach through the DigiPac^{TM} software, which digitalize particles and packing vessels as a collection of pixels, and collision and

overlap detection of pixels are realized through different packing modules. Here we want to stress that particle packing can be done by different models, and we will try other packing models in the future, but as a first step right now, DigiPac were used. More information about DigiPac can be found in [1][2].

Particle packing information from Experimental and simulation were analysed and the characteristics voidage distribution show reasonable agreement. Then the simulation of particle packing in a packed bed with internals were done, and the characteristics voidage were coupled with CFD through UDF. The Eulerian Granular Multiphase Model in Fluent® 6.3.26 were chosen to simulate the heat transfer in packing beds with internals, so that more phase-transfer parameters could be coupled in the future.

The conservation of mass (continuity) equations are

$$\frac{\partial}{\partial t}\left(\alpha_g \rho_g\right) + \nabla \cdot (\alpha_g \rho_g \mathbf{v}_g) = 0$$

$$\frac{\partial}{\partial t}(\alpha_s \rho_s) + \nabla \cdot (\alpha_s \rho_s \mathbf{v}_s) = 0$$

Where α is the volume fraction , ρ is the density, $\mathbf{v}$ is the velocity, subscripts *g* and *s* denote gas and solid phase.

The equations of momentum are

$$\frac{\partial}{\partial t}(\alpha_g \rho_g \mathbf{v}_g) + \nabla \cdot (\alpha_g \rho_g \mathbf{v}_g \mathbf{v}_g) = -\alpha_g \nabla p + \nabla \cdot \boldsymbol{\tau}_g + \alpha_g \rho_g \mathbf{g} + K_{gs}(\mathbf{v}_s - \mathbf{v}_g)$$

$$\frac{\partial}{\partial t}(\alpha_s \rho_s \mathbf{v}_s) + \nabla \cdot (\alpha_s \rho_s \mathbf{v}_s \mathbf{v}_s) = -\alpha_s \nabla p - \nabla p_s + \nabla \cdot \boldsymbol{\tau}_s + \alpha_s \rho_s \mathbf{g} + K_{gs}(\mathbf{v}_g - \mathbf{v}_s)$$

Where $\mathbf{g}$ is gravitational acceleration, p is the pressure shared by all phases, $\boldsymbol{\tau}$ is the stress tensor, and K is the interphase momentum exchange coefficient.

The energy equations are

$$\frac{\partial}{\partial t}(\alpha_g \rho_g c_{p,g} T_g) + \nabla \cdot (\alpha_g \rho_g \mathbf{v}_g c_{p,g} T_g) = \nabla \cdot (\alpha_g \kappa_g \nabla T_g) + h_{gs}(T_s - T_g)$$

$$\frac{\partial}{\partial t}(\alpha_s \rho_s c_{p,s} T_s) + \nabla \cdot (\alpha_s \rho_s \mathbf{v}_s c_{p,s} T_s) = \nabla \cdot (\alpha_s \kappa_g \nabla T_s) + h_{gs}(T_g - T_s)$$

Where c_p is the specific heat, T is the temperature, κ is the thermal conductivity, and h is the interphase heat transfer coefficient.

More detailed information can be found in in [3]. Mesh independent test were done through 2D and 3D simulation of heat transfer in the beds with internals were performed and the results were showed below.

3. RESULTS

A small scale study of particle packing in a fixed bed was performed. Experimental and simulated results were shown in Figure 1. The cross-section of the bed is a square of edge length 92 mm, the height of the bed is 128 mm. The diameter of the glass beads is around 5 mm. The measurement of packing voidage were performed by micro-CT. The simulation domain was set in consistent with the experimental bed.

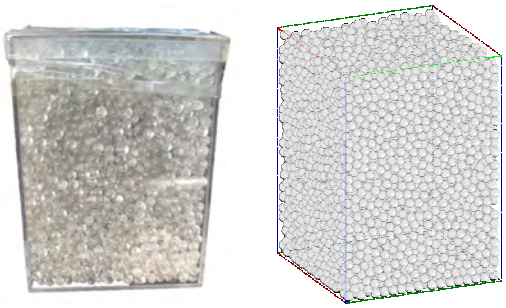

FIGURE 1. Particle packing in a cubic fixed bed: (Left) experimental packing, (Right), simulated packing

The length averaged voidage distribution is showed in Figure 2. The simulation is able to capture the trend that the fluctuation of the voidage is large near the wall and small in the core region. The averaged voidage of the experiment is 0.628, while the simulated voidage is 0.607, the relative error is 3.34%, showing that the simulation is acceptable, and thus the model is used for the following packing.

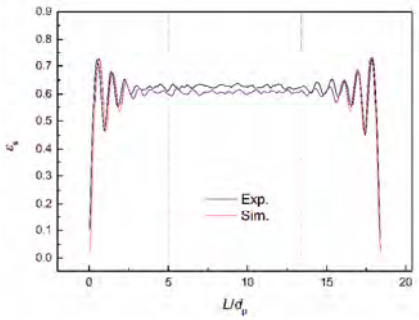

FIGURE 2. Voidage distribution in a cubic fixed bed between experiment and simulation

The validated DEM Packing model was used on the particle packing in lab-scale fixed beds with internals(shown in Figure 3). Here the new bed has a central gas collection pipe[4], while the conventional bed has a top outlet . The statistics voidages from DEM packing were then coupled with CFD simulations through UDF.

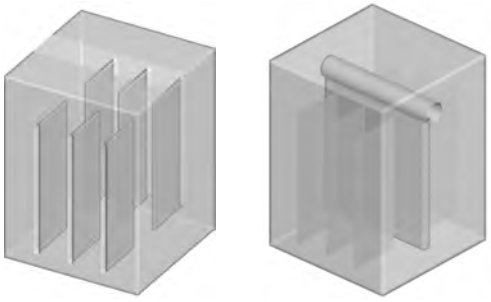

FIGURE 3. Lab-scale fixed beds with internals: (Left) Conventional bed, (Right) New bed

The simulated dynamic temperature change in the two beds were showed in Figure 4. It can be seen that the particularly designed central gas collection pipe can raise the reactor temperature, and thus increasing the heating efficiency of the bed.

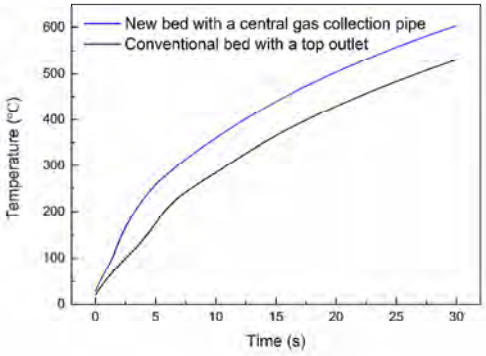

FIGURE 4. Simulated dynamic temperature change in the bed

4. CONCLUSIONS

The main object of this work was to demonstrate the capability of modelling heat transfer in fixed beds with coupling characteristic packing information from DEM to CFD. This work is a first step in simulations of macro-scale fixed beds by coupling detailed packing information. It provides a fresh possibility to realize more detailed simulations on fixed beds.

5. ACKNOWLEDGEMENTS

The financial support from NSFC under Grant No. 2014CB744304, CAS under No. XDA07080405, and MPCS under No. MPCS-2012-A-04 are greatly acknowledged.

REFERENCES

[1] X. Jia, and R.A. Williams, A packing algorithm for particles of arbitrary shapes, *Powder Technology*, 120(3), 175-186, 2001.

[2] X. Jia, M. Gan, R.A. Williams, D. Rhodes, Validation of a digital packing algorithm in predicting powder packing densities, *Powder Technology*, 174(1–2), 10-13, 2007.

[3] N. Zhang, B. Lu, W. Wang, J. Li, Virtual experimentation through 3D full-loop simulation of a circulating fluidized bed, *Particuology*, 6(6), 529-539, 2008.

[4] C. Zhang, R. Wu, G. Xu, Coal Pyrolysis for High-Quality Tar in a Fixed-Bed Pyrolyzer Enhanced with Internals, *Energy & Fuels*, 28(1), 236-244, 2014.

PARALLEL SESSION

MICRO- AND NANO- HEAT TRANSPORT

Third International Conference on Computational Methods for Thermal Problems
THERMACOMP2014, June 2-4, 2014, Lake Bled, Slovenia
N. Massarotti, P. Nithiarasu and B. Sarler (Eds.)

1D-METAL OXIDE NANOSTRUCTURES via CVD ROUTE: a STUDY by PHONON HEAT TRANSFER SIMULATIONS

Stefano di Stasio[(*)], **Aniello Iazzetta**
Istituto Motori CNR, Nanostructures, Light Scattering and X-ray (NLSX) Lab,
via Marconi 8, 80125 Napoli, Italy

ABSTRACT

A Monte Carlo model is here considered to account for phonon heat transfer in 1D nanostructures (nanowires and nanorods) based on the Boltzmann equation, Bose-Einstein statistics and Debye parameters. We focus attention on metal oxide nanostructures obtained in our NLSX lab via CVD experiments and demonstrate by the simulations that the heat conductivity is expected to be size-depending upon the dimension of the transverse size of these nanomaterials. The model is tested for silicon to compare with previous literature and, therafter, applied to zinc oxide 1D nanostructures, which were reported in previous experimental work [1]. The role of *boundary scattering* is discussed. Thermal conductivity λ_T is found out to be lower by a factor 2-3, with respect to the bulk ZnO, depending on transverse size of the 1D nanopillar.

Key Words: *Phonon Heat Transfer, Monte Carlo, Metal 1D Nanostructures, Dispersion Models.*

1. INTRODUCTION

The relevance of heat transfer in nanostructures is evident in a number of fields of science and technology including electronics, energy production and storage, space and automobile racing. In a previous paper [2] we demonstrate that a simple Monte Carlo model of phonon heat transfer as derived from Boltzmann equation, which neglected either dispersion or scattering, was able to return the transient temperature distribution in a one dimensional (1D) nanostructure. When one studies the mechanisms of transferring heat energy flux through domains with dimensions smaller than 100 nm, Fourier law looses its applicability, owing to the fact that scattering events of dual nature do obstacle the transferring of heat power with strictly proportionality law between the temperature gradient and the heat flux, which is observed in the bulk materials. Scattering events can occur as effect of interaction *phonon-boundary* or *phonon-phonon*. Such an effect is more severe in the cases when small transient times are considered (about 100 ps). The objective of this study is the comparison of the results obtained for transient temperatures and heat conductivity when the above modeling is applied to 1D nanomaterials of different metal oxide species. The geometry of the nanostructures here considered is mutuated on a number of experimental TEM analysis on different metals [1,3], metal oxide [4,5]. Without loss of generality, the 1D nanomaterial are modeled as a stack of parallelipedic cells with rectangular section in which the heat flux flows along the nanowire axis (z-axis) and tranversal dimension in the range 2-50 nm (x-,y- axes).

2. THORETICAL FRAMEWORK

In the case of a semiconductor such as zinc oxide the heat capacity can be written as $C=C_{lattice}+C_{free-e-}+C_{defects}$, where the first contribution accounts for lattice vibrations (phonons), the second for free

(*) Corresponding Author: stefano.distasio1600@gmail.com

electron carrier and the third for lattice defects. Here we neglect the $C_{free\text{-}e\text{-}}$ contribution considering that free electron in ZnO are 6 order of magnitide less numerous with respect to Zn. Details of the Debye dispersion model for phonon heat transfer can be retrieved in several papers [6-8] including our previous work [2]. Here below, we report the equations used for the work here described. First part of work is dedicated to the validation of the model with the standard silicon. We correct several physical constants reported erroneously by previous authors [6-8]. In particular, the sound velocity c_S is here evaluated according to the equation $c_S = \sqrt{E/\rho}$ where E is the Young's modulus (Pa) and ρ is the mass density (kg m^{-3}) of the material. The c_S above is known as the *extensional* velocity of filiform structure such is the case of 1D nanomaterials. Such sound velocity at 300 K is reported in Table I for Silicon and Zinc, together with other physical parameters used in simulations (deponent "D" is for Debye, "phon" for phonons, "melt" for "melting", "cryst" for crystal, c_S is the sound velocity, ρ the mass density and E the Young modulus).

T=300 (K)	E (Pa)	ρ (kg m^{-3})	c_S (m s^{-1})	N_{cryst} (m^{-3})	$\nu_D=k_BT_D/h$ (s^{-1})	T_D (K)	c_V (J kg^{-1} K^{-1})	T_{melt} (K)	ℓ_{phon} (Å)	$\lambda_{T,bulk}$ (W m K)
Si	1.0×10^{11}	2329	8435	6.02×10^{28}	13.44 THz	645	702	1687	400	116
ZnO	0.60×10^{11}	5606	3271	4.15×10^{21}	8.67 THz	416	494	2248	533	23.4

TABLE 1. Physical parameters of Bose-Debye Monte Carlo model for phonon transport in Silicon and Zinc. E, ρ, c_S are the Young modulus, the density and the sound velocity; N_{cryst} and ℓ_{phon} is the crystallographic number density and the phonon mean free path; ν_D, T_D the Debye frequency and temperature; T_{melt} and $\lambda_{T,Bulk}$ the melting temperature and the heat conductivity referred to bulk material.

The phonon mean free path is evaluated for silicon and scaled for zinc oxide through the Grunheisen relationship $\ell_{phon} = 10\,(a/\gamma)\,(T_{melt}/T)$ where $a \approx 0.5$ nm is a scale constant and $\gamma \approx 1$ is the Grunheisen parameter. The thermal conductivity (W m^{-1} K^{-1}) is before the simulations estimated from the kinetic theory as $\lambda_T = (1/3)c_S\,\ell_{phon}\,c_V$ where c_V is the specific heat at constant volume, and, after the simulations, is evaluated through the definition as $\lambda_T = (1/A)(dE/dt)/(dT/dz)$ where **z** is the heat flow direction, that overlaps to the axis of the cell stack modeling the nanopillar.

3. RESULTS AND DISCUSSION

In Figure 1 we report TEM micrographs of samples of original Zn nanopowders synthesized as described elsewhere [1-8]. Thereafter Zn nanostructures undergo oxidation at about 200 °C as described in [8]. Collected powder are typically composed by thick (0.5 μm) nanowires, sponges of much thinner nanotubes with size (40 to 90 nm) controlled by the vapor pressure of the Zn vapor in the flow reactor, crystals with rectangular section (see Figure 1 right) and short pillars (400 nm length) of transverse size about 40 nm, which we called *nanoclubs* [1]. Figure 2 left shows the results of the simulation for a ZnO nanopillar with rectangular transverse section (Δx=10 nm, Δy=10 nm) with length 400 nm, schematized by an horizontal stack of 40 cells. The direction of propagating sound wave **z** is coincident with the stack axis. The transient of temperature is markedly different at different times cconsidered. Time zero is the start of simulation when phonons start to propagate from left hot (500 K) extremity of the stack towards the cold extremity at right (300 K). After about 1 ns, the transient reaches a steady state waveform that is the linear behavior predicted by the Fourier law. Figure 2 right is an example of evaluating heat conductivity (W m^{-1} K^{-1}) from the computation of the energy flow across the 1D nanostructure carried by phonon flux. Thermal conductivity of the silicon nanopillar with a transverse sectio 10x10 nm and a length 400 nm results about a factor 5 smaller with respect to bulk Si, as effect of the inertia to heat flowing exerted by boundary scattering.

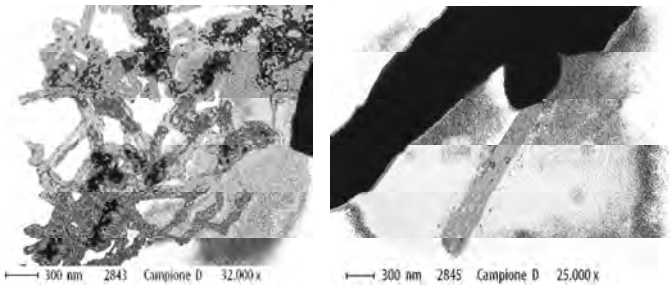

FIGURE 1. Examples of Zinc 1D nanostructures synthesized by CVD process in a gas flow reactor [1].

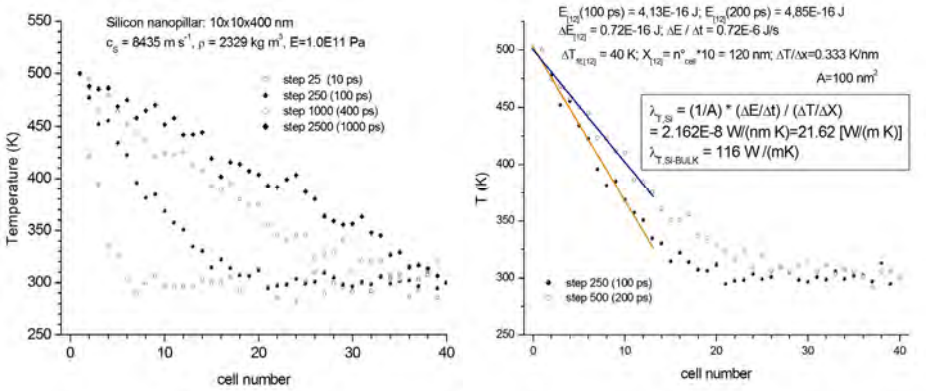

FIGURE 2. Comparison of our results with previous literature [5-7] for a Silicon nanopillar. Left) transients of temperature vs number of cells. The nanopillar is considered positioned along the z-axis with transverse section $\Delta x=\Delta y=10$ nm and total length 400 nm. The abscissa Z is obtained by multiplying the cell number times $\Delta x=10$ nm. Right) Example of heat conductivity calculation for the Si nanopillar at 100 ps time.

After validation of phonon heat transfer model with silicon, we focus attention on zinc oxide, which is the material of nanostructures synthesized in our lab. The nanopillar simulated here (10x10x400 nm) does correspond to the thinnest nanoclubs described in previous experimental work [1].The results obtained are shown in Figure 3. Also in this case a dramatic decreasing of the heat conductivity λ_T as effect of the boundary scattering with respect to bulk zinc oxide is observed. Moreover, λ_T is depending on the transverse size of the ZnO nanopillar so schematized. Further details and computations will be shown in the next mother paper. Figure 3 illustrate the transient temperature as evaluated by phonon heat transfer model in the case of zinc oxide nanopillar. Results as function of section size can not be reported here for limit of format. In the example shown, the transverse section of nanopillar, which is orthogonal to the direction of heat flux (**x**-axis), is a square with size $\Delta y=\Delta z=10$ nm. The nanopillar length is 400 nm and its volume is considered as the stack of 40 cells with longitudinal size $\Delta x=10$ nm. A comment to our result of Figure 3 is that the transient of heat flux to the Fourier ruled steady state (straight line) is significantly longer with respect to previous silicon reference case, in particular the temperature transient is almost over for Si at times about 200 ps and, vice versa, is still far from steady state in the case of ZnO . This yield significant effects on the values of instant heat conductivity in the case of times below 100 ps and/or shorter nanopillar. The complete results of our work will be shown in the mother paper.

6. CONCLUSIONS

The feasibility of a Boltzmann-Debye Monte Carlo phonon heat transfer model to study heat transfer in 1D nanostructures has been here demonstrated both for metal oxide nanomaterials, zinc oxide in the specific case. Main findings are that the thermal conductivity λ_T is depending on the size of transverse section and that at time transients of order 100 ps, λ_T is significantly smaller (a factor about 3) with respect to metal oxide bulk values. This result is interpretated as the effect of impedance with respect to the heat flow represented by boundary scattering events with are more influent for smaller transverse size of ZnO nanopillars. Further, simulations indicate that the temperature regime is reached much faster in zinc oxide 1D nanomaterial with respect to the corresponding reference silicon at parity of geometry or, equivalently, that the transient before steady-state Fourier ruled regime is much longer for ZnO with respect to Si. Further details and results will be published on a mother paper from our group.

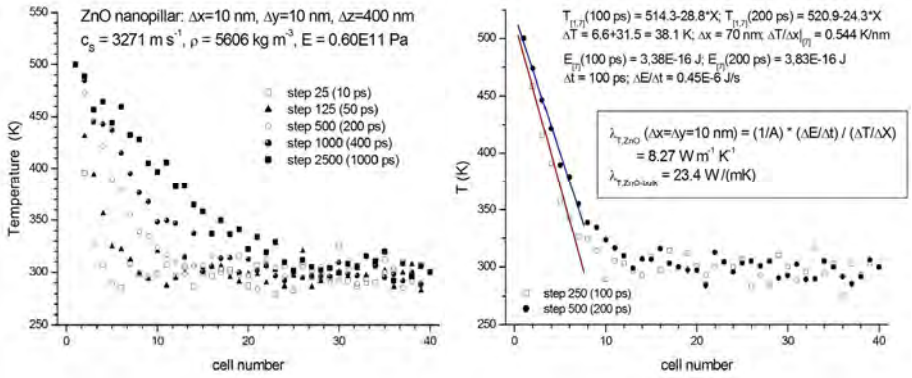

FIGURE 3. Left) Temperature gradients evaluated by phonon heat transfer model here applied to simulate the heat flow in a zinc oxide nanopillar 10x10x400 nm, which corresponds to the actual ZnO nanowires of Fig. 1 previously reported by our group [1]. The abscissa on nanowire axis is cell number times 10 nm.

REFERENCES

[1] S. di Stasio S, Growth of Zinc Hollow Nanofibers and Nanotubes by Thermal Evaporation-Condensation-Deposition Route, *Chemical Physics Letters* 393, 498-503, 2004

[2] S. di Stasio, A. Iazzetta, Transient phonon Heat transport in quasi-1D nanostructures, Proceedings of 1st THERMACOMP Congress, Napoli 8-10 Sept 2009, 362-365, 2009

[3] A. Onischuk, S. V. Vosel, O. V. Borovkova, A. M. Baklanov, V. V. Karasev and S. di Stasio, Experimental study of homogeneous nucleation from the bismuth supersaturated vapor: Evaluation of the surface tension of critical nucleus, *The Journal of Chemical Physics* 136, 224506 1-18, 2012

[4] C. Baratto, G. Sberveglieri, A.A. Onischuk, B. Caruso, S. di Stasio, Low temperature selective NO_2 sensors by nanostructured fibers of ZnO, *Sensors Actuators B* 100, 261-265, 2004

[5] S. di Stasio, V. Dal Santo, DRIFTS Study of Surface Reactivity to NO_2 by Zinc Nanoparticle Aggregates and Zinc Hollow Nanofibers-Powders " *Appl. Surface Sci.* 253, 2899-2910, 2006.

[6] R.B. Peterson, Direct Simulation of Phonon-Mediated Heat Transfer in a Debye Crystal, *Journal of Heat Transfer* 116, 815-822, 1994

[7] D. Lacroix, K. Joulain, D Terris, D Lemonnier, Monte Carlo simulation of phonon confinement in silicon nanostructures: Application to the determination of the thermal conductivity of silicon nanowires, *Applied Physics Letters* 89, 103104-103106, 2006.

[8] A. Majumdar, Microscale Heat C onduction in Dielectric Thin Films, *Journal of Heat Transfer* 115, 7-16, 1993 .

Third International Conference on Computational Methods for Thermal Problems
THERMACOMP2014, June 2-4, 2014, Lake Bled, Slovenia
N. Massarotti, P. Nithiarasu and B. Sarler (Eds.)

THERMO-FLUID-STRESS ANALYSIS IN MICROCHANNELS COOLING OF ELECTRONICS WITH HOT SPOTS

Abas Abdoli, George S. Dulikravich, Genesis Vasquez and Siavash Rastkar
Department of Mechanical and Materials Engineering, MAIDROC Laboratory
Florida International University, Miami, FL 33174,
aabdo004@fiu.edu, dulikrav@fiu.edu, gvasq007@fiu.edu, srast002@fiu.edu

ABSTRACT

Two-layer, single phase fluid, microchannels were studied for cooling of electronic chips with a hot spot. Chip had 2.45 x 2.45 mm footprint with a hot spot of 0.5 x 0.5 mm in its center. Heat fluxes of 1500 W cm^{-2} and 2000 W cm^{-2} were applied at the hot spot, and 1000 W cm^{-2} was applied on the rest of the chip. Each microchannel layer had 20 channels with aspect ratio of 4 to 1. Direction of the second michrochannel layer was shifted by 90 degrees with respect to the first layer. Fully 3-D conjugate heat transfer and stress/deformation analyses were performed to examine the proposed cooling design. For the fluid flow domains, the steady state Navier-Stokes equations were solved.

Key Words: *Electronics Cooling, Single Phase Flow Microchannel, Hot Spot.*

1. INTRODUCTION

Cooling of electronic chips with hot spots having more than 1000 W cm^{-2} heat load is one of challenges of the electronics cooling [1,2]. In one of the recent analysis studies, Alfier *et al.* [3] numerically investigated the hot-spot cooling in 3-D stacked chips with integrated cooling. Gonzales *et al.* [4] performed 2-D microchannel networks optimization. Genetic algorithms have been used by Wei and Joshi [5] to perform single objective optimization in order to minimize overall thermal resistance. Abdoli and Dulikravich [6] performed multi objective optimization for 4-layer branching microchannel configurations with 67 design variables to improve heat removal, decrease temperature non-uniformity, and coolant pumping pressure drop. They also numerically optimized the multi-layer throughflow microchannels [7]. In this paper, a cooling configuration with two layers of microchannels is analysed numerically. The main advantages of using straight through-flow cooling channels rather than branching cooling channels are: a) lower pumping power requirements, b) lower manufacturing cost, c) better uniformity of hot surface temperature; and d) higher reliability in case of obstructions in any of the microchannels.

Two-layer microchannel configuration was designed with 20 channels in each layer. Each channel has the cross section dimension of 240 µm x 60 µm. As figure 1 shows, direction of the second layer microchannels was shifted 90 degrees with respect to the first layer microchannels.

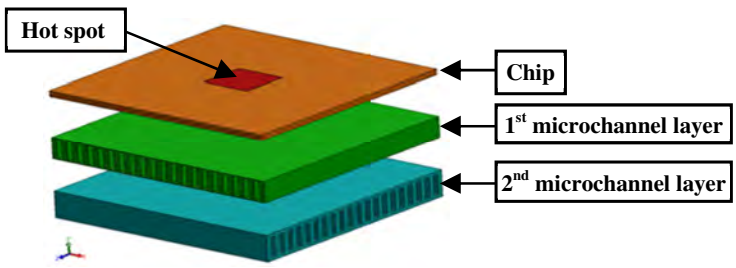

FIGURE 1. Expanded view of two-layer microchannel cooling design.

For conjugate heat transfer analysis, all fluid and solid domains need to be coupled. Forty fluid domains and three solid domains were modelled by using conjugate heat transfer solver in COMSOL Multiphysics software suite. Tetrahedral mesh was generated for each domain with overall 3,500,000 degrees of freedom.

2. ANALYSIS RESULTS

Multi-region, 3-D, steady conjugate heat transfer analysis module of COMSOL Multiphysics software was used for simulations. Water was used as the cooling liquid with the inlet temperature of 300.15 K. The water inlet average velocity was 2 m s^{-1}. The exit static pressure of water was set to 110 kPa. Electronic chip and its substrate material were both assumed to be silicon. A uniform thermal load of 1000 W cm^{-2} was enforced on the top surface of the substrate except the hot spot. Two different uniform heat fluxes were applied at the hot spot. A constant temperature of 300 K was set on the bottom surface of the substrate, while assuming adiabatic side walls.

In the first case, a uniform thermal load of 1500 W cm^{-2} was applied to the hot spot of the chip. Figure 2a illustrates the temperature distribution inside the chip, substrate. Figure 2b shows variations of temperature on the top surface of the silicon chip. As this figure demonstrates, the maximum temperature is 81.4^{o}C, which is located on the hot spot. As figure 2a illustrates, temperature variations in the second microchannel layer are not significant. In other words, this layer does not play a noticeable role in the cooling system. The water flow direction in the first microchannel layer is in the x-direction. In the second michrochannel layer, water flows in the opposite direction of the z-direction. As water moves toward the outlets, its temperature increases. Therefore, higher temperatures can be observed in the upper right section of the figure 2b.

In the second case, a uniform thermal load of 2000 W cm^{-2} was applied on the hot spot of the chip. Figure 2a shows temperature variations on the entire cooling design. As this figure illustrates, effect of the second microchannel layer is not very significant compared to the first layer. Figure 2b shows that the maximum temperature of the top surface is 91.7^{o}C, which is 10.3^{o}C higher than in case 1. The minimum temperature on this surface is same as the minimum temperature in case one, which is 43.2^{o}C. In this case, higher temperature gradients are observed close to the hot spot compared to case 1. This demonstrates that by increasing the heat load on the hot spot, effectiveness of the microchannel cooling decreases.

Linear stress analysis was also performed to determine thermal stresses due to temperature variations within the cooling designs. COMSOL Multiphysics stress deformation analysis module was coupled to its conjugate heat transfer analysis for the multi-physics simulations. All internal and external walls were assumed to be fixed with zero displacement. There are two reasons for this assumption; 1) to obtain maximum possible stresses applied on cooling design, and 2) to enable the cooling design for 3-D stacking.

Figures 3a and 3c demonstrate the von Mises stress distribution in the entire cooling design for the case 1 and case 2. Higher stresses can be observed on the hot spots, on the side and near the inlet of the first layer, where larger temperature variations exist. Figures 3b and 3d illustrate the deformation in five slices of the entire cooling system for case 1 and case2. As these figures show, the maximum deformations in both cases are the same. However, in case 2 more deformation can be observed under the hot spot.

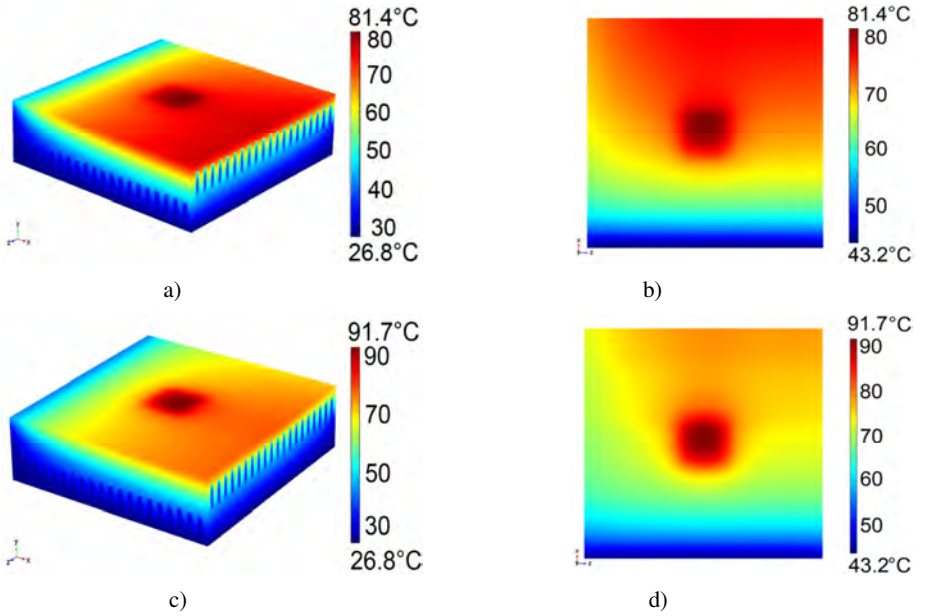

FIGURE 2. Temperature distribution on: a) entire cooling design, and b) top surface of the chip for case 1 (uniform heat flux of the hot spot is 1500 W cm^{-2}), c) entire cooling design, and d) top surface of the chip for case 2 (uniform heat flux of the hot spot is 2000 W cm^{-2}).

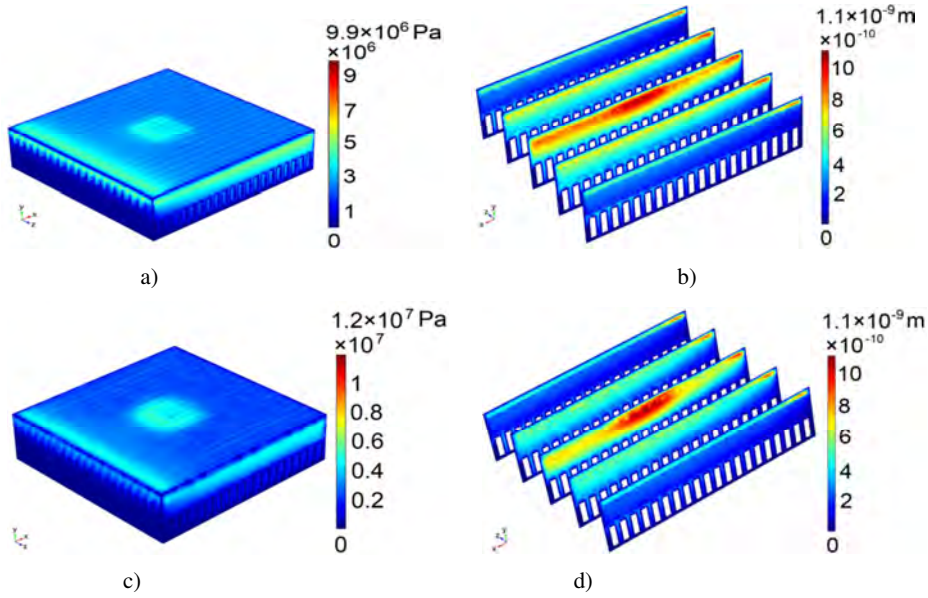

FIGURE 3. Deformation distribution in: a) entire cooling design, and b) five slices of the entire model for case 1 (uniform heat flux of the hot spot is 1500 W cm^{-2}), c) entire cooling design, and d) five slices of the entire model for case 2 (uniform heat flux of the hot spot is 2000 W cm^{-2}).

4. CONCLUSIONS AND RECOMMENDATIONS

In this research, 3-D multi-physics (conjugate heat transfer and thermal stress analyses) were performed to numerically investigate effects of two-layer single phase flow microchannels for cooling electronic chips having a hot spot with up to 2000 W cm^{-2} thermal loads. The thermal load of 1000 W cm^{-2} was applied on the rest of the chip. Results of case 1 in which the thermal load of the hot spot was 1500 W cm^{-2} showed that the maximum temperature on the top surface of the chip was 81.4°C. Results of case 2 in which the hot spot thermal load was 2000 W cm^{-2} showed maximum temperature of the hot spot was increased by 10.3°C to 91.7°C. This shows that the proposed two-layer microchannel configuration can handle 1000 W cm^{-2} background thermal load with a moderate hot spot thermal load. Higher thermal loads will require design optimization of topology of the cooling microchannels, different cooling fluid, introduction of a very thin layer of diamond or of nanoplatelets based high thermal conductivity heat spreader, and altogether different cooling concepts in order to keep the hot spot temperature below 85°C.

ACKNOWLEDGEMENTS

Authors are grateful for partial financial support of this research provided by DARPA via GaTech in the framework of ICECool project under supervision of Dr. Avram Bar-Cohen. The lead author would like to acknowledge the financial support of a Florida International University Dissertation Year Fellowship. The authors also gratefully acknowledge the FIU Instructional and Research Computing Center for providing HPC resources to perform calculations for this project.

REFERENCES

[1] A. Bar-Cohen, Gen-3 thermal management technology: role of microchannels and nanostructures in an embedded cooling paradigm, *Journal of Nanotechnology in Engineering and Medicine,* 4(2), 020907, 2013.

[2] V. Sahu, Y. Joshi and A. Fedorov, Hybrid solid state/fluidic cooling for hot spot removal, *Nanoscale and Microscale Thermophysical Engineering,* 13: 135-150, 2009.

[3] F. Alfieri, S. Gianini, M. K. Tiwari, T. Brunschwiler, B. Michel, and D. Poulikakos, Computational modeling of hot-spot identification and control in 3-D stacked chips with integrated cooling, *Numerical Heat Transfer, Part A*, 65: 201–215, 2014.

[4] M.J. Gonzales, N. Jelisavcic, R.J. Moral, D. Sahoo, G.S. Dulikravich and T.J. Martin, Multi-objective design optimization of topology and performance of branching networks of cooling passages, *International Journal of Thermal Sciences*, 46(11), pp. 1191-1202, 2007.

[5] X. Wei and Y. Joshi, Optimization study of stacked micro-channel heat sinks for micro-electronic cooling, *Proceedings of ITherm*, San Diego, CA, pp. 441–448, 2002.

[6] A. Abdoli and G.S. Dulikravich, Multi-objective design optimization of multi-layer, counterflow micro heat exchangers, *paper HT2013-17738, ASME Heat Transfer Conference*, Minneapolis, MN, July 14-19, 2013.

[7] A. Abdoli and G.S. Dulikravich, Optimized multi-layer throughflow micro heat exchangers, *International Journal of Thermal Sciences,* 78 (2014) 111e123, 2014.

Third International Conference on Computational Methods for Thermal Problems
THERMACOMP2014, June 2-4, 2014, Lake Bled, Slovenia
N. Massarotti, P. Nithiarasu and B. Sarler (Eds.)

NUMERICAL ANALYSIS OF MICRO HEAT EXCHANGERS FOR COOLING OF HIGH CONCENTRATION PHOTOVOLTAIC PANELS

Guerrieri, Daduí Cordeiro[1], Naveira-Cotta, Carolina Palma[2]

[1]Mechanical Eng.Dept., CEFET-RJ UnED Itaguaí, Rio de Janeiro-Brazil, guerrieri@cefet-rj.br
[2] Mechanical Eng.Dept., Federal University of Rio de Janeiro-UFRJ, Rio de Janeiro, Brazil, carolina@mecanica.coppe.ufrj.br

ABSTRACT

This paper presents a numerical analysis of an optimized heat exchanger based on micro-channels for efficient active water cooling of a commercial high concentration photovoltaic (HCPV) system. In the theoretical study, four different cases were analyzed using the finite element method through the computational platform COMSOL Multiphysics 4.2a. Critical comparisons with infrared thermography measurements are performed.

Key Words: *Micro-heat exchanger, Finite elements method, Conjugated problem, Solar energy, High concentration photovoltaics, HCPV, Infrared thermography.*

1. INTRODUCTION

The solar energy market is growing rapidly, becoming increasingly more competitive specially in the world sunnier regions. The high concentration photovoltaic technology (HCPV) is able to concentrate the sunlight to intensities of 1000 suns or more, onto a small area of a solar photovoltaic cell. Since smaller areas of photovoltaic material are required in such HCPV systems, there is a significant reduction in the value of the final product compared to a non-concentrated photovoltaic system for the same total electrical output. HCPV systems operate more efficiently as long as the solar cell is kept cool enough by suitable heat sinks. Most of the commercial HCPV systems are based on passive air-cooled heat sinks, specially due to their simplicity. The main idea of this work is to present the numerical simulation of an alternative heat sink to remove heat more efficiently from a HCPV system, changing the passive air-cooled system to an active water-cooled one, and also allowing the re-use of the rejected heat in a secondary thermohydraulic circuit, such as for water desalination. Tuckerman and Pease [1] in their early work of 1981 studied the heat exchange enhancement in micro-channel heat sinks for electronic devices of high thermal dissipation. At that time, the so-called VLSI circuits (Very-large-scale integrated) could dissipate up to 100 W in small areas, and it was a general belief that the physical limit for heat sinks was on the order of $2x10^5$ W/m^2. Using micro-channels, the authors showed that it would be possible to dissipate heat fluxes as high as 10^7 W/m^2. Parida *et al.*[2] present a fairly complete revision of photovoltaic systems and show some advantages in reducing the amount of silicon, as occurs in HCPV systems, and also present some possible aplications in integrated circuits to re-use the waste heat from the solar panels. Correa *et al.* [3] proposed an optimized micro-heat exchanger for active cooling of a commercial HCPV module that concentrates 1200 suns, using water as working fluid in a closed loop. This optimized micro-heat exchanger based on micro-channels is comprised of 18 micro-channels with 400μm in width and 945μm in depth each. This configuration is here numerically analyzed and compared in four different cases: three of them with a lower power dissipation and the last one for a more realistic situation dealing with a higher power dissipation. All numerical analysis was performed using the commercial platform COMSOL Multiphysics 4.2a. The four cases analyzed correspond to available experimental runs, when the temperatures at the external surface of the micro-heat exchanger were measured through infrared thermography, allowing for validation of the proposed model and solution methodology, as shown below.

Figure 1a shows a typical module of the commercial HCPV system (Sunflower, ATS Pyron) that contains 30 photovoltaic cells. For each cell, using fresnel lens, as schematically shown in Figure 1b, the system is able to concentrate 1200 suns on the photovoltaic material area of 1cm^2.

Figure 1a. Sunflower (ATS Pyron) HCPV system module

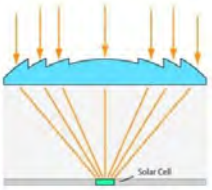

Figure 1b. Schematic drawing of the fresnel lens concentration

2. NUMERICAL ANALYSIS

The computational analysis of the optimized micro-heat exchanger proposed in [3] was performed in the finite element software package COMSOL Multiphysics 4.2a. In the simulation, a 3D transient conjugated problem was considered, involving the solution of the continuity, momentum and thermal energy equations for the fluid domain and heat conduction equation for the solid domain. in a copper micro-heat exchanger with 18 micro-channels with rectangular cross section of 400μm in width and 945μm in depth. Figure 2 shows in detail the main dimensions, in millimeters, of the micro heat exchanger and also shows the type of connection to be considered in the inlet and outlet of the micro-heat sink cover.

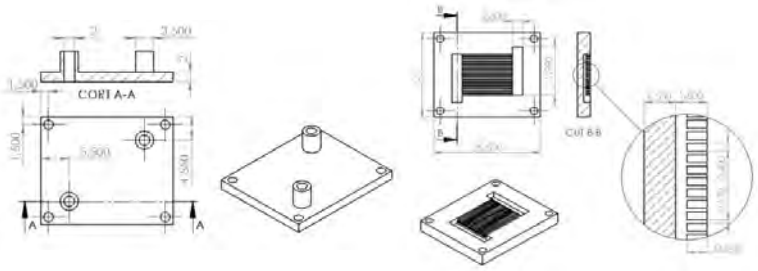

Figure 2. Technical drawing of the micro-heat sink (all dimensions in millimeters)

Figures 3 illustrate the adopted boundary conditions, for all four analyzed cases, which are further detailed in Table 1. In thr present numerical analysis, a known applied heat flux was considered in the central area of 10x10mm at the micro-heat sink bottom wall, indicated by the purple area in Figure 3.a. The rest of the bottom area was considered insulated, as indicated by the purple area in Figure 3.b. We have also considered heat loss by external natural convection and radiation at the entire top cover area and in all lateral walls, as indicated by the purple areas in Figures 3.c and 3.d.

(a) Applied heat flux (bottom)

(b)Insulated area (bottom)

(c) Natural convection and radiation heat losses (top)

(d) Natural convection and radiation heat losses (laterals)

Figure 3 – Adopted boundary conditions in the computational simulation

For all four cases the initial condition was considered as the ambient temperature, the emissivity of all external walls was considered homogeneous and equal to 0.97, due to the graphite ink employed for the infrared thermography. The inlet water temperature and the ambient temperature are in fact different for each

of the four cases, due to the difficulty in controlling these parameters in the experimental analysis. The experimental analysis is not the focus of the present study and was detailed elsewhere [3], but will be here used for validation of the proposed modeling and obtained numerical solutions.

Input data to COMSOL	Case 1	Case 2	Case 3	Case 4
Ambient temperature (°C)	26.7	26.9	26.4	22.0
Volumetric flow rate (mL/min)	10	10	10	20
Applied power (W)	6.6	9.5	12.6	46.6
Water inlet temperature(°C)	27.4	26.4	26.4	41.0

Table 1 – Numerical input data used in the four simulated cases

A careful analysis of the convergence of the solution was carried on for different types and number of elements in the mesh, using the option "physics-controlled mesh" and "user-controlled mesh" on the software platform. For the final results here reported, an adaptive mesh grid with different number and types of elements, with a larger mesh refinement in the fluid region, was used, as illustrated in Figures 4.a and 4.b, and near the edges, as illustrated in Figure 4.c, for the fluid using de "user-controlled mesh", amounting to a total of 2,054,881 elements.

(a) (b) (c)

Figure 4 – Illustration of the adaptive mesh elements employed in the discretization of the whole domain

3. RESULTS

The pressure drop between the entry and outlet of the micro-heat sink was estimated by the numerical analysis for all four cases, providing 35.1 Pa, 34.4 Pa, 40.2 Pa and 97.5 Pa, respectively. Figure 5.a shows the variation of the average temperature on the external top cover surface over time, until reaching steady state, for case 1. Also in this graph are shown four pictures illustrating the spatial distribution of the temperature in this most external surface, for four diffent times, respectively 1s, 10s, 30s and 100s. Figure 5.b. shows the distribution of the velocity profile after reaching steady state for the entire heat exchanger. Figures 6a. and 6b. show the velocity profile in all 18 channels, respectively for cases 1 and 4. In both graphs the inlet is closer to the left, and as can be seen, the average velocity increases as the channels depart from the inlet of the micro-heat exchanger, for all presented cases.

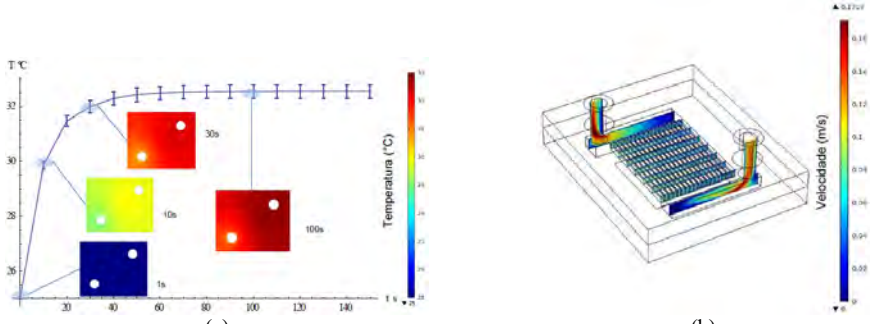

(a) (b)

Figure 5 – a)Mean temperature at the external top surface over time for case 1; b) Velocity field for case 4.

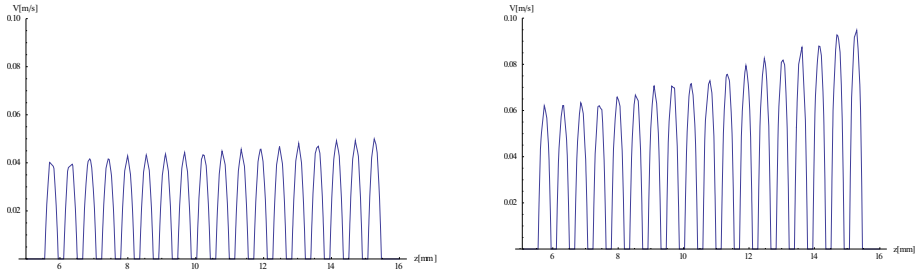

(a) Case 1 (b) Case 4

Figura 6 – Velocity profiles in the 18 micro-channels for a) Case 1; b) Case 4.

Figure 7a shows the comparison between the average temperature at the external surface, provided by the numerical solution (in red) and the experimental analysis (in blue), for the first three cases. In this comparison the largest deviations between the simulation and experiments were 0.66°C, 0.86°C and 1.42°C, respectively, for cases 1, 2 and 3. Figure 7.b shows the two-dimensional temperature distribution at the external surface of the top cover, with a comparison between the experimental (in blue) and theoretical analysis (in red), after the steady state is achieved. In this analysis the maximum deviation between these two analysis was 1.79°C.

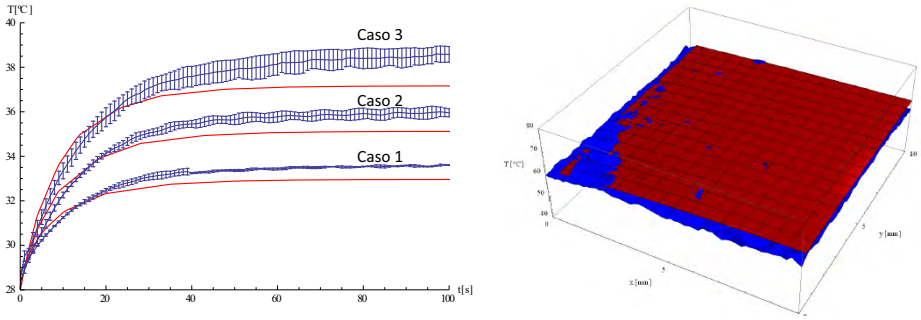

(a) (b)

Figure 7– Comparison between numerical solution (in red) and experimental analysis (in blue) at the external surface of the heat sink top cover, for: a)mean temperature evolution; b) local temperatures at steady state

4. CONCLUSIONS

This work presents a numerical analysis of a micro heat exchanger for efficient active water-cooling of a commercial high concentration photovoltaic (HCPV) system. The theoretical analysis was performed for four different experimental cases in the commercial platform COMSOL Multiphysics 4.2a. The experimental runs employed infrared thermography to measure the external surface of the top cover and a fairly good agreement was achieved between the theoretical and experimental results.

REFERENCES

[1]Tuckerman, B. D. and Pease, R. F. W., “High-Performance Heat Sinking for VLSI”, IEEE Electron Device Letters, vol. 2, nº 5, pp. 126-129, 1981.

[2]Parida, B., Iniyanb, S. and Goicc, R., "A Review of Solar Photovoltaic Technologies", Renewable and Sustainable Energy Reviews, no. 15, pp. 1625-1636, 2011.

[3]Correa, M.; Guerrieri, C. D.; Naveira-Cotta, C. P. and Colman, J., "Design and Manufacture of Microchannel Heat Sinks for High Concentration Photovoltaic Cells", 22nd International Congress of Mechanical Engineering (COBEM 2013), Ribeirão Preto, SP, Brazil, November 2013.

Third International Conference on Computational Methods for Thermal Problems
THERMACOMP2014, June 2-4, 2014, Lake Bled, Slovenia
N. Massarotti, P. Nithiarasu and B. Sarler (Eds.)

THE EFFECT OF GAS-SURFACE MODEL ON THERMAL CREEP FLOW

O. Rovenskaya, G. Croce
DIEG, University of Udine, via delle Scienze 208, 33100 Udine, Italy
olga.rovenskaya@uniud.it, giulio.croce@uniud.it

ABSTRACT

Numerical analysis of the nonlinear rarefied gas flow caused by temperature gradient in a direction tangential to the wall through a planar channel of finite length is carried out based on the S- model kinetic equation under a range of Knudsen number from free-molecular to slip regime. Cercignani-Lampis solid boundary condition is chosen at channel walls. An implicit scheme is applied; the algorithm is optimized via massive parallelization in both physical and velocity spaces. Results showed that the gas-surface scattering model plays distinguished role for highly rarefied conditions.

Key Words: *rarefied gas, Cercignani-Lampis boundary condition, implicit scheme, MPI.*

1. INTRODUCTION

Flows induced solely by the effect of steady temperature field are peculiar to rarefied gases and are an intriguing research subject in rarefied gas dynamics. One of the most famous is the thermal-creep flow, where a temperature gradient tangential to a surface induces a flow in the same direction. It is well known that the choice of gas-surface interacting model has a strong effect on the gas flow [1, 2]. Although the widely used Maxwell diffuse-specular boundary condition provides reliable results in a variety of physical systems, some discrepancies have been found between numerical and experimental data in flows through ducts and tubes [1]. As an alternative, the use of more realistic Cercignani-Lampis (CL) model has become popular in the rarefied gas dynamics community [3]. The CL model successfully overcomes drawbacks of the Maxwell model by adjusting two accommodation coefficients: α_t, accommodation of tangential momentum and α_n, accommodation of kinetic energy of the normal velocity component. The CL boundary condition demonstrates better agreement with the experimental data in comparison with the Maxwell one in [2].

In this work the effect of the CL boundary condition on temperature gradient driven flow is investigated. Mass flow and streamwise heat flux are plotted as a function of the CL accommodation coefficients. Comparison with open literature results is provided. The competing effect of rarefaction and accommodation coefficients on flow is discussed.

2. STATMENT OF THE PROBLEM AND NUMERICAL METHOD

We consider temperature–driven monoatomic gas flow through a planar microchannel of width H and length $l = 10H$, $100H$, connecting two reservoirs. Reservoir sizes are $L_x \times L_y = 30H \times 15H$ for $l = 10H$ and $6H \times 3H$ for $l = 100H$ [5]. The gas in reservoirs far from the channel is in equilibrium at constant temperature T_i and T_e, $T_i < T_e$, and equal pressure $p_i = p_e$. The temperature along walls varies linearly as: $T_w(x) = T_i + (T_e - T_i)x/l$. The flow is a two-dimensional in xOy surface (see Fig. 1). Due to the spatial symmetry of the flow in y direction only half of the domain will be considered.

The S–model of the Boltzmann kinetic equation describing the evolution of distribution function $f = f(t, \mathbf{x}, \boldsymbol{\xi})$ of particle with velocity vector $\boldsymbol{\xi} = (\xi_x, \xi_y, \xi_z)$ at time moment t and in position $\mathbf{x} = (x, y, z)$ in non-dimensional form is written as follows [4]:

$$\frac{\partial f}{\partial t}+\boldsymbol{\xi}\frac{\partial f}{\partial \mathbf{x}}=\frac{8n\sqrt{T}}{5Kn\sqrt{\pi}}\left(S-f\right)=\nu(n,T)\left(S-f\right), \tag{1}$$

$$S(t,\mathbf{x},\boldsymbol{\xi})=M\left(1+\frac{4\mathbf{qc}}{15T^2}\left(\frac{\mathbf{c}^2}{T}-\frac{5}{2}\right)\right), \qquad M(t,\mathbf{x},\boldsymbol{\xi})=\frac{n}{(\pi T)^{3/2}}\exp[-\frac{\mathbf{c}^2}{T}], \tag{2}$$

where $\mathbf{c} = \boldsymbol{\xi} - \mathbf{V}$ is the relative speed of a particle against a background gas, $\mathbf{q}$ is the heat flux vector, $M(t, \mathbf{x}, \boldsymbol{\xi})$ is the local Maxwell distribution function, $\nu(n, T) = \delta n T^{0.5}$ is a collision frequency, $Kn = \lambda_0/H$ is the Knudsen number, λ_0 is a mean free path at reference state. Following [1] we introduce the rarefaction parameter $\delta = p_0 H/\mu_0 v_0 \sim 1/Kn$. Reference state scales are specified by averaged inlet and exit equilibrium values: $T_0 = (T_i+T_e)/2$, $p_0 = (p_i+p_e)/2$ etc. Assuming hard-sphere model the dimensionless viscosity is $\mu = T^{0.5}$.

At inlet and outlet boundaries we impose the Maxwell distribution function $M(t, \mathbf{x}, \boldsymbol{\xi})$ for incoming particles, with pressure p_i and T_i for inlet and p_e and T_e for outlet. Particles coming off the solid wall are emitted with a distribution function assuming the CL scattering kernel, which includes two distinct coefficients (α_n, α_t), and wall temperature T_w [3]. The CL model reduces to diffuse scattering if $(\alpha_n, \alpha_t) = (1, 1)$ and to specular reflection condition if $(\alpha_n, \alpha_t) = (0, 0)$. The extreme case $(\alpha_n, \alpha_t) = (0, 2)$ corresponds to the back scattering: after the collision an impinging molecule with velocity $\boldsymbol{\xi}$ is reemitted with velocity $-\boldsymbol{\xi}$. Specular boundary condition is imposed at symmetry line.

The S-model equation (1) is discretized on a 2D uniform grid in velocity space $\{\boldsymbol{\xi}_\boldsymbol{\Gamma}\} = (\xi_{x\alpha} = -v_{\max}+\alpha\Delta\xi_x,\ \xi_{y\beta} = -v_{\max}+\beta\Delta\xi_y)$, $\alpha, \beta = 1, N_\xi$, $\boldsymbol{\Gamma} = (\alpha, \beta)$ is velocity grid points indices. In the physical space a 2D non uniform grid is defined by nodes (x_i, y_j), for $i = 1, i_{max}$ and $j = 1, j_{max}$ cells. Denoting $f^n_{\boldsymbol{\Gamma},i,j}$ as the approximations of $f(t^n, \boldsymbol{\xi}_\boldsymbol{\Gamma}, x_i, y_j)$ the numerical scheme for the equation (1) is written as:

$$f^{n+1}_{\boldsymbol{\Gamma},i,j} = f^{n}_{\boldsymbol{\Gamma},i,j} - \Delta t/\Delta x\left(F^{n+1}_{\boldsymbol{\Gamma},i+1/2,j} - F^{n+1}_{\boldsymbol{\Gamma},i-1/2,j}\right) - \Delta t/\Delta y\left(F^{n+1}_{\boldsymbol{\Gamma},i,j+1/2} - F^{n+1}_{\boldsymbol{\Gamma},i,j-1/2}\right) + \Delta t\nu^n_{i,j}\left(S^n_{\boldsymbol{\Gamma},i,j} - f^{n+1}_{\boldsymbol{\Gamma},i,j}\right), \tag{3}$$

where the gain term $S_\boldsymbol{\Gamma}$ is positive and treated explicitly. The numerical fluxes $F_{i\pm1/2,j,\boldsymbol{\Gamma}}$ and $F_{i,j\pm1/2,\boldsymbol{\Gamma}}$ are of the second order with minmod limiter function, Δx and Δy are the mesh sizes in the x and y, respectively [4]. Using the storage by index $\boldsymbol{\Gamma}$ the scheme (3) is expressed in matrix form as:

$$\left(I/\Delta t + T_\boldsymbol{\Gamma} + \nu^n\right)\delta f^n_\boldsymbol{\Gamma} = RHS^n_\boldsymbol{\Gamma}, \quad \delta f_\boldsymbol{\Gamma} = f^{n+1}_\boldsymbol{\Gamma} - f^n_\boldsymbol{\Gamma} \qquad \text{for all } \boldsymbol{\Gamma} \tag{4}$$

where I is the identity matrix, $(Tf^n)_{i,j,\boldsymbol{\Gamma}}$ is a matrix with first order fluxes, and right –hand side $RHS^n_\boldsymbol{\Gamma}$ includes the limiters for the second order scheme. The linear system (4) is solved for each velocity point $\boldsymbol{\Gamma}$ by successive LU decomposition [4]. Boundary conditions are treated explicitly and RHS^n contains the boundary terms. The solution of (4) is local in $\boldsymbol{\Gamma}$, therefore parallelizable in velocity space. The computation of the CL boundary condition is local in i, j, thus it is parallelized in physical space. Before solving equation (4) each processor exchanges boundary information with others. The software code was written in C++ with the use of MPI (Message Passing Interface). Computations were run on Intel(R) Xeon(R) E5520 CPU, 2.27 GHz, 8 MB Cache, quad core processors (8 cores); maximum parallel efficiency achieved is 90 %.

3. RESULTS AND DISCUSSIONS

The numerical analysis of temperature gradient flow ($T_e/T_i = 1.1$) through a planar channel of finite length $l = 10$ and 100 and rarefaction levels $0 \le \delta \le 10$ has been carried out using nonlinear S-model equation provided with CL boundary condition at the wall. The global results are expressed in terms of thermal creep mass and streamwise heat flux evaluated at channel mid-section $x = l/2$:

$$M_T(x) = \frac{4l}{\Delta T}\int_0^{1/2} n(x,y)u(x,y)dy, \qquad Q_T(x) = -\frac{4l}{\Delta T}\int_0^{1/2} q_x(x,y)dy, \qquad \Delta T = T_e - T_i \tag{5}$$

A grid with 360 nodes in the streamwise direction, $\Delta x_{min} = 0.1$, and 40 nodes in the transverse direction with $\Delta y_{min} = 0.01$ near the wall is used. Grid independence tests have been done using finer mesh of 480×80 nodes: variations in M_T and Q_T for different grids was less than 0.5%. The velocity space is bounded by $v_{max} \approx 5$. The number of velocity nodes depends on the rarefaction level δ: at $\delta = 10$ we use a 32×32 mesh, increasing up to 128×128 nodes for $\delta << 1$.

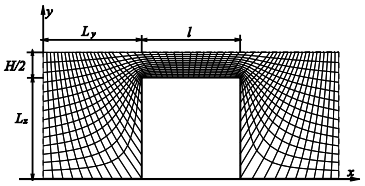

FIGURE 1. Sketch of computational domain

Validation was carried out for channel of $l = 100$ at $\delta = 2$ and accommodation coefficients $0.25 \le (\alpha_n, \alpha_t) \le 1$ comparing with a linearized solution [1]. Figure 2 shows that mass flow M_T and heat flux Q_T are in a good agreement, with differences within 1.5%. Figure 2 demonstrates also a strong dependence of mass flow M_T on both accommodation coefficients, since a mass flow decrease is induced by both kinetic energy losses ($\alpha_n > 0$) and tangential momentum reduction ($\alpha_t > 0$) of particles impinging upon the surface. The dependence on α_t is stronger at smaller α_n: in Figure 2, for the same range of tangential accommodation ($0.25 \le \alpha_t \le 1$) we have a 15% variation in mass flow at $\alpha_n = 0.25$ and an almost negligible 0.2% variation for diffused condition $\alpha_n = 1$. Analogously, for diffused tangential momentum condition $\alpha_t = 1$ mass flow does not depend on α_n, while close to specular tangential momentum ($\alpha_t = 0.25$) we have a 12% M_T variation from $\alpha_n = 0.25$ to $\alpha_n = 1$. Heat flux Q_T behavior is qualitatively similar, but with a weaker dependence on α_n (at most 6.7% for $\alpha_t = 0.25$). On the other hand, since streamwise heat transfer is related mostly to tangential momentum, we have stronger dependence on α_t, up to 22% at $\alpha_n = 0.25$. However, the dependence on α_t vanishes for diffused kinetic energy condition $\alpha_n = 1$.

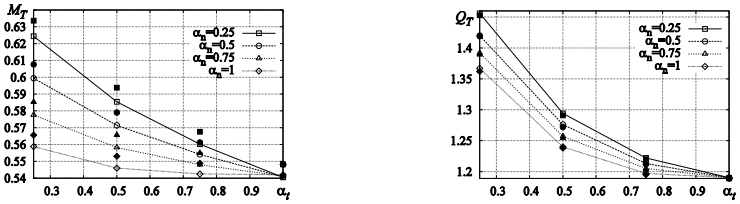

FIGURE 2. M_T and Q_T profiles; $\delta = 2$, $l = 100$. Empty symbols: present; solid ones: ref. [1]

The validated model was applied to an investigation on rarefaction effects on channel performances. We applied the full nonlinear solution to shorter channel, where the use of linearization would be questionable. We chose $l = 10$, including in the domain two large inlet and outlet reservoirs [5]. Figure 3 shows mass flow and heat flux over a wide rarefaction range. Accommodation coefficient α_t varies from 0.25 to 1.75, keeping a fixed $\alpha_n = 0.25$. The higher the rarefaction, the higher the mass flow M_T and heat flux Q_T. At near free-molecular regime ($\delta = 0.02, 0.2$) interactions between particles and the wall become more important than collisions among particles, hence we get higher influence of α_t: M_T and Q_T under near backscattering condition $\alpha_t = 1.75$ is more than 2 times smaller than mass flow and heat flux under near specular reflection $\alpha_t = 0.25$. In the transition regime ($\delta = 2$) M_T near backscattering condition ($\alpha_t = 1.75$) is 80% of the corresponding near specular one, while Q_T is one half of the heat flux computed at $\alpha_t = 0.25$. At the slip regime ($\delta = 10$), the dependence of heat flux on α_t becomes very weak, with maximum difference up to 6%. The mass flow trend is the opposite of that detected in transition or free-molecular regime: M_T increases

with α_t, showing a near backscattering ($\alpha_t = 1.75$) mass flow 28% higher than the near specular reflection $\alpha_t = 0.25$ value. The same behavior of M_T in slip regime has been also observed in [1].

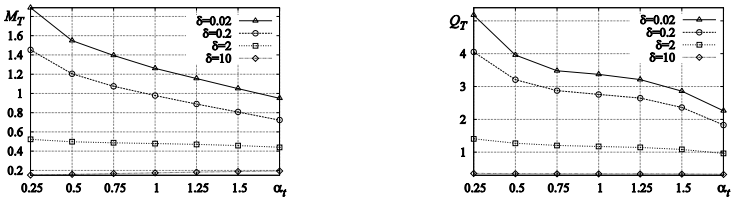

FIGURE 3. M_T and Q_T profiles vs α_t at $\alpha_n = 0.25$; $l = 10$

Figure 4 shows dependence of M_T on energy coefficient α_n at fixed $\alpha_t = 0.25$. For highly rarefied flow ($\delta \leq 2$) M_T decreases monotonically from near specular reflection ($\alpha_n = 0.25$) to perfect accommodation ($\alpha_n = 1$): maximal decrease in M_T reached at $\delta = 0.02$ is 26% and becomes small, 4%, at transition regime $\delta = 2$. Near the slip regime M_T grows with α_n up to a maximal increase, 16%. The heat flux dependence is weaker; the maximum variation between near specular $\alpha_n = 0.25$ and perfectly accommodated condition $\alpha_n = 1$ is 13.8% at $\delta = 0.02$. This variation decreases with δ, and at slip regime Q_T does not depend on normal kinetic energy accommodation α_n.

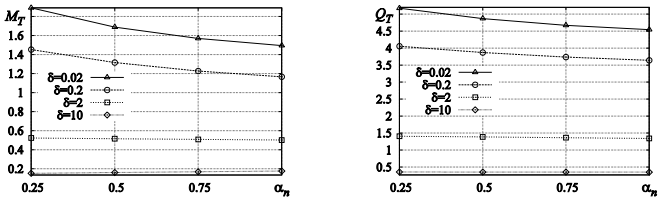

FIGURE 4. M_T and Q_T profiles vs α_n at $\alpha_t = 0.25$; $l = 10$

4. CONCLUSIONS

The effect of the CL gas-surface interaction model on the rarefied gas between parallel plates has been considered on the basis of the S-model kinetic equation. The values of accommodation coefficients in CL model have a huge impact on the flow. This effect is stronger for highly rarefied gas. Thus, in such case the choice of the boundary model is very important.

REFERENCES

[1] F. Sharipov, Application of the Cercignani–Lampis scattering kernel to calculations of rarefied gas flows. I. Plane flow between two parallel plates *European Journal of Mechanics B/Fluids*, 21, 113–123, 2002.

[2] S. Pantazis, S. Varoutis, V. Hauer, C. Day, D. Valougeorgis, Gas-surface scattering effect on vacuum gas flows through rectangular channels, *Vacuum*, 85, 1161-1164, 2011.

[3] C. Cercignani, *Rarefied gas dynamics: From basic concepts to actual calculations*, Cambridge University Press, Cambridge, 2000.

[4] O. I. Rovenskaya, Kinetic analysis of surface roughness in a microchannel, *Computers & Fluids*, 77, 159–165, 2013.

[5] O. I. Rovenskaya, Comparative analysis of the numerical solution of full Boltzmann and BGK model equations for the Poiseuille flow in a planar microchannel, *Computers & Fluids*, 81, 45–56, 2013.

Third International Conference on Computational Methods for Thermal Problems
THERMACOMP2014, June 2-4, 2014, Lake Bled, Slovenia
N. Massarotti, P. Nithiarasu and B. Sarler (Eds.)

NUMERICAL ANALYSIS OF UNSTEADY NATURAL CONVECTION BETWEEN PARALLEL WALLS IN SLIP FLOW REGIME

Pamela Vocale, Marco Spiga
Department of Industrial Engineering, University of Parma, Parco Area delle Scienze 181/A, 43124 Parma, Italy; pamela.vocale@unipr.it, marco.spiga@unipr.it

ABSTRACT

This paper analyses the transient behavior of a Newtonian flow, between parallel surfaces, driven by buoyancy forces, in miniaturized systems. The problem is numerically solved, assuming uniform wall temperature conditions (UWT), and accounting for the rarefaction effect. The numerical solution is validated resorting to analytical solutions available in literature. The first benchmark is carried out thanks to a recent analytical solution obtained for no slip conditions (Kn = 0), in the same geometry, and UWT conditions. A second benchmark is carried out thanks to an analytical solution obtained in slip flow steady state. The benchmarks confirm that the numerical solution provides results quite accurate and reliable.

Key Words: *Free Convection, Gaseous slip flows, Numerical analysis, Microfluidics.*

1. INTRODUCTION

In recent years miniaturized systems have shown a great diffusion in many fields of medicine, biology and engineering. Many papers in literature are devoted to investigate the role played by some effects that in macroscale are negligible. In particular the effects of rarefaction are relevant when the mean free path of particles is not negligible compared to the hydraulic diameter of the duct, as for gas flows in ducts with diameter less than hundreds of micrometers. In this case the hypothesis of continuous medium, is no longer valid [1]; for Knudsen number ranging between 10^{-3} and 10^{-1}, the flow pattern is classified as slip flow, it is analysed using the classical momentum and energy equations, but introducing the hypothesis of velocity slip and temperature jump at the walls of the duct [1].

The slip flow in forced convection in microchannels, has already been analysed in detail. On the contrary, slip flow in natural convection has not received great attention; particularly transient slip flow has been only recently investigated (see for instance [2, 3]). Although these very appreciable contributions, the transient analysis of thermal behavior of gaseous flow gas in laminar free convection in slip flow, under T boundary conditions, has been not yet investigated, at least to the author's best knowledge.

2. MAIN BODY

The considered channel is bounded between two vertical parallel plates, separated by a distance H; it has both ends open at atmospheric pressure. At time $t' \leq 0$, the walls and the stagnant fluid in the duct have uniform temperature T_0. At time t'>0 the temperature of one wall increases to the constant value T_1. Due to buoyancy forces, natural circulation is created inside the channel, and the fluid flows upward if $T_1 > T_0$. The following hypotheses are assumed: 1) the fluid is Newtonian, single-phase, the flow is laminar and fully developed; 2) the Mach number is low and compressibility effects are negligible [4]; 3) fluid properties are constant, except density in the buoyancy term of the motion equation, where it is expressed according to Boussinesq approximation; 4) other effects such as viscous dissipation or radiative heat transfer are absent.

According to the proposed hypotheses, the classical governing equations of momentum and energy are:

$$\rho_0 \frac{\partial u}{\partial t'} = -\frac{\partial p}{\partial \zeta} - \rho_o \, g \left[1 - \beta (T - T_0)\right] + \mu \frac{\partial^2 u}{\partial \xi^2} \tag{1}$$

$$\rho_0 \, c \, u \frac{\partial T}{\partial \zeta} + \rho_0 \, c \frac{\partial T}{\partial t'} = k \, \nabla^2 T \tag{2}$$

The slip flow boundary conditions for the velocity and temperature jump conditions for the temperature are:

$$u_s - u_w = \left| \frac{2 - \sigma_v}{\sigma_v} \lambda \left(\frac{\partial u}{\partial \xi} \right)_w \right| \tag{3}$$

$$\begin{aligned} T_s - T_w &= \frac{2 - \sigma_T}{\sigma_T} \frac{2\gamma}{\gamma + 1} \frac{1}{\mathrm{Pr}} \lambda \left(\frac{\partial T}{\partial \xi} \right) \quad in \ \xi = 0 \\ T_s - T_w &= -\frac{2 - \sigma_T}{\sigma_T} \frac{2\gamma}{\gamma + 1} \frac{1}{\mathrm{Pr}} \lambda \left(\frac{\partial T}{\partial \xi} \right) \quad in \ \xi = H \end{aligned} \tag{4}$$

To obtain general results, the following dimensionless independent variables are introduced:

$$x = \frac{\xi}{H} \qquad z = \frac{\zeta}{H} \qquad t = \frac{\nu t'}{H^2} \tag{5}$$

together with the dimensionless functions:

$$P = (p - p_s) \frac{H^2}{\rho_0 \nu^2 \, Gr} \qquad U = u \frac{H}{Gr \, \nu} \qquad \theta = \frac{T - T_0}{T_1 - T_0} \tag{6}$$

Many authors [5, 6] have proved that being P=0 in the inlet and outlet sections of the channel, the fluid pressure in the duct follows the hydrostatic law $p = p_s$.

3. RESULTS

Equations (1) and (2) with their boundary conditions were solved resorting to the finite element method, by using Comsol Multiphysics® [7]. The numerical procedure was validated by comparing the numerical results with analytical ones available in literature [8]. A good agreement was found. The mesh indipendence analysis was checked by testing different grid sizes. The here presented results were obtained by using a structured mesh with an enhanced refinement close to the wall wich presents better performance in terms of accuracy and requires a reasonable computational effort to run each simulation.

The investigation is carried out assuming air flows at 20°C, with Pr=0.71 and γ=1.4; the accommodation coefficients are assumed, as usual in literature for solid walls, σ_v = σ_T = 0.9. The transient dimensionless velocity distributions are shown in Fig. 1, for four values of Knudsen number, namely Kn=0,01, Kn=0.05 and Kn=0.1. For very low Knudsen numbers (and for continuum flow), the transient solution approaches the steady state distribution when the non-dimensional time becomes comparable with the Prandtl number, as already observed in [6], and [8]. On the contrary, when the slip flow regime becomes more predominant, the transient evolution becomes slower.

Figure 2 describes the transient spatial distribution of the dimensionless temperature distribution; it increases with time and attains its steady state distribution as the non-dimensional time approaches the Prandtl number, as discussed in [8], even for high Knudsen numbers.

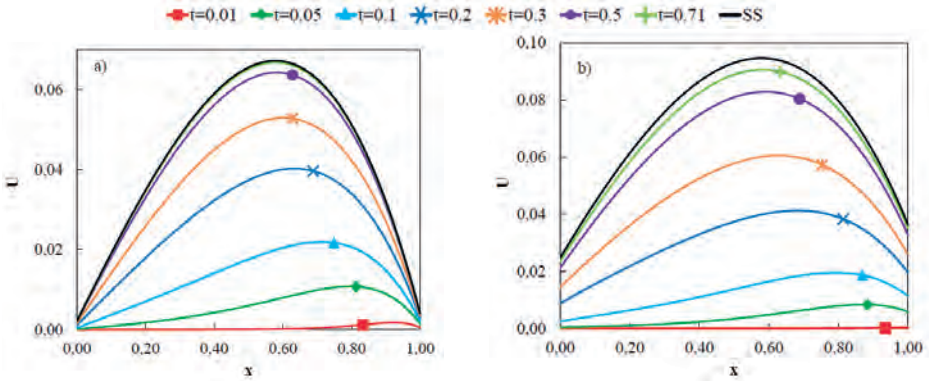

FIGURE 1. Dimensionless velocity distribution: a) *Kn*=0.01; b) *Kn*=0.1.

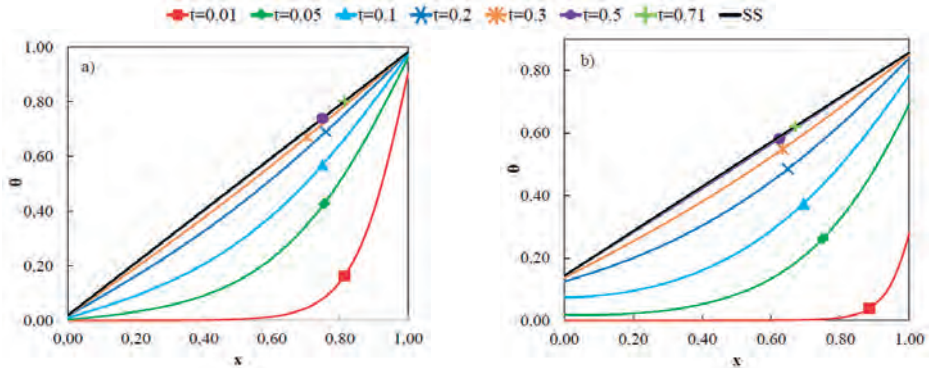

FIGURE 2. Dimensionless temperature distribution: a) *Kn*=0.01; b) *Kn*=0.1.

In Fig. 3, the dimensionless average velocity is shown versus the dimensionless time. In the first stage of the transient (t<0.15) the velocity is almost independent on the Knudsen number; then the increase of the Knudsen number (augmentation of slip at the walls) reduces the skin-friction and increases the mass flow rate.

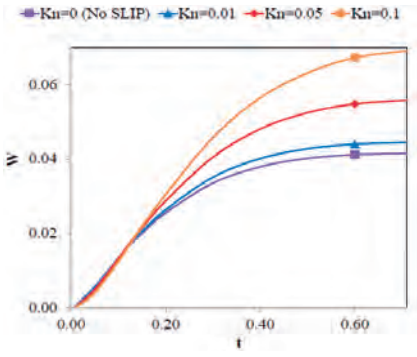

FIGURE 3. Dimensionless average velocity versus time.

While the increase of the Knudsen number increases the flow rate, on the contrary the heat transfer performance is reduced. This is well evident in the evolution of the Nusselt numbers on the cold wall (Figure 4a) and hot wall (Figure 4b) for Knudsen number in the range 0 - 0.1.

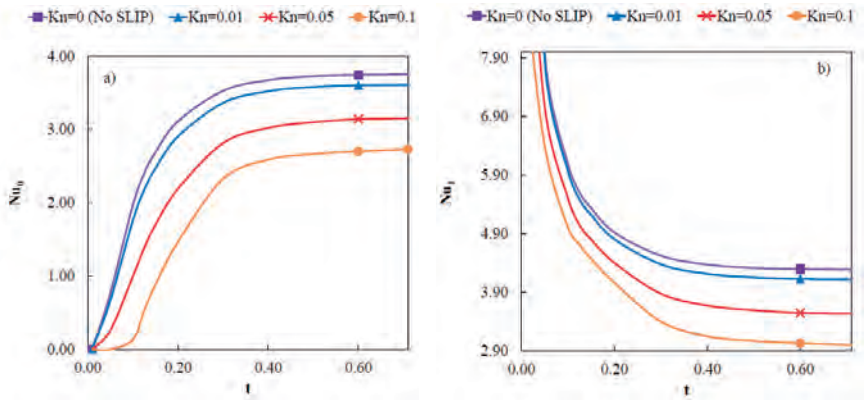

FIGURE 4. Nusselt number at the cold and hot wall: a) *Kn*=0.01; b) *Kn*=0.1.

4. CONCLUSIONS

The transient dynamical and thermal behaviour of the fluid flowing upward in the channel between the parallel walls is so quite determined, emphasizing the role played by the rarefaction effects.

REFERENCES

[1] G. Karniadakis, A. Beskok, and N. Aluru, *Microflows and Nanoflows – Fundamentals and Simulation*, New York, Springer, 2005.

[2] B. Buonomo and O. Manca, Transient natural convection in a vertical microchannel heated at uniform heat flux, *Int. J. Therm. Sci.*, 56, 35-47, 2012.

[3] A.F. Khadrawi and M.A. Al-Nimr, Unsteady natural convection fluid flow in a vertical microchannel under the effect of the dual-phase-lag heat-conduction model, *Int. J. Thermophys*., 28, 1387-1400, 2007.

[4] G.L. Morini, M. Spiga and P. Tartarini, Rarefaction Effects on Friction Factor of Gas Flow in Microchannels, *Superlattices & Microstructures*, 35, 587-599, 2004.

[5] G.L. Morini, D. Cocconi and M. Spiga, Transient Buoyancy Induced Slip Flow in Microchannels, Microfluidics, Toulouse (France), pp. 12-14, December 2006.

[6] A.K. Singh and T. Paul, Transient Natural Convection between Two Vertical Walls Heated/Cooled Asymmetrically, *Int. J. Applied Mechanics and Engineering*, 11, 143-154, 2006.

[7] S. Rainieri, F. Bozzoli, L. Schiavi, and G. Pagliarini, Numerical analysis of convective heat transfer enhancement in swirl tubes, *Int. J. Numerical Methods for Heat and Fluid Flow*, 21, 559-571, 2011.

[8] M. Spiga and P. Vocale, Step Response for Free Convection between Parallel Walls, *submitted to Heat and Mass Transfer*.

ISBN: 978-88-7431-727-1